Accelerator-Based Boron Neutron Capture Therapy

by

William Bruce Howard

B.S., Engineering Physics

United States Military Academy, 1987

Submitted to the Department of Physics
in Partial Fulfillment of the Requirements for the Degree of
Doctor of Philosophy in Physics

at the

Massachusetts Institute of Technology

February 1997

Signature of Author: _____
Department of Physics
January 17, 1997

Certified by:

_____
Professor Jacquelyn Yanch
Thesis Supervisor

_____
Professor Lee Grodzins
Thesis Co-Supervisor

Accepted by:

_____
Professor George Koster
Chairman, Committee on Graduate Students
Department of Physics

Accelerator-Based Boron Neutron Capture Therapy

by

William Bruce Howard

Submitted to the Department of Physics
on January 21, 1997 in Partial Fulfillment of the
Requirements for the Degree of Doctor of Philosophy in
Physics

ABSTRACT

Boron Neutron Capture Therapy (BNCT) is a promising therapy modality for cancer. Clinical trials using BNCT are underway in the US. BNCT works by a selective loading of tumor cells with ^{10}B and subsequent irradiation of the tumor with thermal neutrons. The reaction $^{10}B(n,\alpha)$ is induced and releases approximately 2.3 MeV of energy, most of which is deposited locally. In Accelerator-Based BNCT (AB-BNCT), neutrons for this therapy are produced using ion induced reactions. Three reactions, $^{7}Li(p,n)$ E_p=2.5 MeV, $^{9}Be(p,n)$ E_p=3.0-4.0 MeV, and $^{9}Be(d,n)$ E_d=2.6 MeV are investigated here. Complete data for the $^{9}Be(p,n)$ reaction were not previously available. Therefore, 28 thick target neutron spectra were measured, on an absolute basis, using time-of-flight techniques. Proton energies 3.0, 3.4, 3.7, and 4.0 MeV, and laboratory angles 0-145 degrees were used. The absolute accuracy of the data (better than 25% for most neutron energies) was confirmed by measuring a different reaction with a known spectrum. Using the three reactions, Monte Carlo techniques were used to design therapy beams for AB-BNCT. The reaction $^{7}Li(p,n)$ yielded the highest dose rates. However, given lithium's poor thermal properties, lithium targets will be difficult to develop. Dose rates using $^{9}Be(p,n)$ were also high. Beryllium is known to be an excellent target material. Using $^{7}Li(p,n)$ and $^{9}Be(p,n)$, therapy times of 12-25, and 27-60 minutes, respectively, were predicted (tumor depth 2-6 cm, 15 RBE-Gy total tumor dose, 10 kW accelerator power, 30 ppm boron tumor concentration). Using $^{9}Be(p,n)$ and a 1 mA beam current, nearly equivalent therapy beam parameters were predicted with 4.0 and 3.7 MeV protons. For equivalent accelerator power, 3.7 MeV protons would produce higher dose rates. Using $^{9}Be(d,n)$ resulted in lower dose rates because the reaction's high energy neutrons must be extensively moderated. AB-BNCT therapies would result in an intense neutron and photon radiation field requiring significant facility shielding. Most of the occupational dose comes from (n,γ) reactions in the facility walls. Effective facility shielding has been designed. Effective shielding for the patient can be made from lithium carbonate and polyethylene.

Thesis Supervisor: Jacquelyn C. Yanch
Title: Associate Professor of Nuclear Engineering

Acknowledgments

I would like to thank my thesis advisor, Professor Jacquelyn Yanch for the opportunity to work on this project, and for her patience, support, and guidance. I would also like to thank her for the many times she has been a devoted and caring friend.

I also want to express my appreciation to the members of my thesis committee, especially Dr. Stephen Steadman and Professor Lee Grodzins, for their advice and support.

Much of the funding for this reseach was provided by a fellowship from the Hertz Foundation. I am very thankful for their support. This work was also supported by a US Department of Energy grant (Grant No. DE-FG02-89ER60874).

This work would not have been possible without the assistance of the other members of the Laboratory for Accelerator Beam Applications (LABA). In particular, I would like to thank Haijun Song for his help.

Our collaborators at Newton Scientific have contributed immeasurably to the progress at LABA. I am especially grateful for their patience in answering many technical questions, and for their advice.

The members of The Ohio University Accelerator Laboratory have been very supportive, accommodating, and helpful during the past two years.

I am indebted to the MIT Reactor BNCT group for their contributions. They have been helpful in many ways, particularly in regards to therapy beam design and dosimetry. My thanks especially to Professor Otto Harling, Dr. Ron Rogus, Stead Kiger, and Kent Riley.

Finally, I want to express my deepest appreciation to my wife, Nancy, for all of her help and patience.

Sincerely,

William B. Howard
21 January, 1997

TABLE OF CONTENTS

LIST OF FIGURES

LIST OF TABLES

Simulations Used in Therapy Beam Design

CHAPTER ONE

Introduction

This chapter provides an introduction to BNCT, a promising modality for the treatment of cancer. The first section outlines the basic medical theory of BNCT and its proposed uses. A history of the therapy is provided, along with a presentation of recent progress. One approach to producing neutrons for BNCT is called Accelerator-Based BNCT (AB-BNCT). The unique features of AB-BNCT are described. The BNCT research program and accelerator at the Laboratory for Accelerator Beam Applications (LABA) at MIT are discussed. In the concluding section of this chapter, the new contributions to the field of AB-BNCT which are presented in this thesis will be outlined. These contributions are in the areas of neutron source reaction measurement, therapy beam design and radiation shielding.

I.A BNCT

I.A.1 Medical Theory

Boron Neutron Capture Therapy (BNCT) is a binary radiation therapy for cancer based on the nuclear reaction $^{10}B(n, \alpha)^{7}Li$ [1]. Although this modality is currently being used clinically in Japan and is undergoing clinical trials in the US, several aspects of the therapy are still in the developmental stage. The therapy is binary in the sense that it

relies on two components combining at the tumor site to achieve the desired effect. The first component is a non-toxic, boron-containing pharmaceutical which is delivered to the tumor cells, and to the greatest extent possible, kept out of normal tissue. The second component is a low-energy neutron flux at the location of the tumor. When these two components combine, the fission reaction $^{10}B(n,\alpha)$ is induced. The thermal neutron cross section of this reaction is 3840 barns. The reaction cross section follows a 1/v behavior up to approximately 500 keV. The reaction proceeds to either the ground state or first excited state of ^{7}Li releasing 2.79 MeV or 2.31 MeV, respectively, in the form of kinetic energy of the ^{7}Li and ^{4}He nuclei. The first excited state emits a single 0.48 MeV gamma photon as it decays to the ground state [2]. Since the alpha and ^{7}Li are heavy charged particles, they are densely ionizing and have high linear energy transfer (LET) values (200 - 300 keV/micrometer) and very short ranges in tissue (7 μm for alpha, and 4 μm for ^{7}Li) [3]. Thus, their total combined energy is deposited in a volume approximately the size of a single cell. If high concentrations of ^{10}B can be sufficiently localized in tumor cells, it is theoretically possible to destroy or inhibit these malignant cells without similar negative effects to nearby healthy cells. These concepts are depicted in Figure I-A-1.

BNCT, so illustrated, is deceptively simple. In this section, the medical theory of BNCT will be examined more closely and the various factors influencing its efficacy will be explained. It is important to note that BNCT is, by necessity, an interdisciplinary endeavor. The goal of selectively loading tumor cells with ^{10}B has been addressed primarily by pharmacologists and chemists. The design of neutron therapy beams

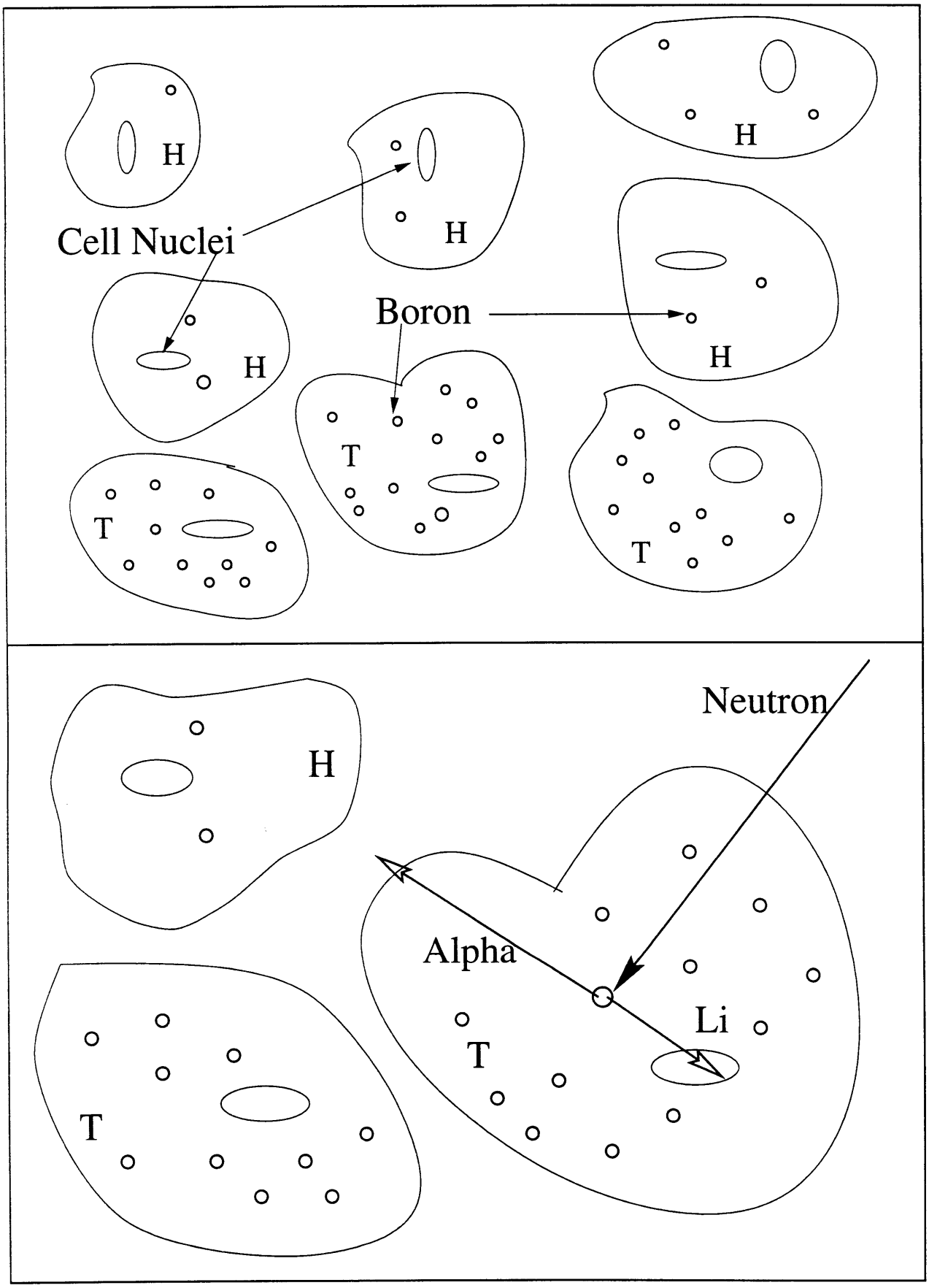

Figure I-A-1: Boron delivered selectively to tumor cells (T), with less absorption by healthy cells (H). Tissue volume is irradiated by low energy neutrons which induce the reaction 10B(n,alpha) The fission products deposit most of their energy in the host cell.

suitable for BNCT has been accomplished mainly by nuclear engineers and physicists. The radiobiologist has added expertise in many areas including microdosimetry and the study of the biological effects of the various radiation dose components. Among other tasks, the physician diagnoses the malignancy, refers the patient to a BNCT facility and designs the treatment plan. Each of these groups must work together to ensure the safe and effective treatment of the patient.

The approach used in radiation oncology for tumor control is to simultaneously maximize radiation absorbed dose to the tumor and minimize the dose to normal tissue. Complete eradication of malignant cells (tumor cure) is desired as even one cell could seed the regrowth of the tumor. However, controlling the growth and spread of the tumor (local control) without complete tumor cell kill could also lead to palliation of pain, elimination of debilitating symptoms, and possibly increased survival times. Controlling or eliminating the tumor requires high radiation doses to tumor cells. In practice, the dose to the tumor is limited by the maximum allowable dose to healthy tissue, or tolerance dose. This holds true for the BNCT modality.

The viability of BNCT, or for any other radiation therapy, depends greatly on the selectivity of the treatment. In BNCT, this selectivity is achieved by preferentially loading the tumor cells with ^{10}B. This differentiation is accomplished by exploiting differences (physiological, chemical or metabolic) between healthy and tumor cells. One approach exploits the blood-brain barrier (BBB), which in normal brain tissue carefully

controls the flow of chemicals in and out of the brain. In regions of rapid tumor growth, this barrier has been shown to be less effective [4]. If a boron-containing chemical can be found which would not penetrate the normal BBB, this same chemical might pass through the "leaky" BBB found in tumor regions and be absorbed into the tumor cells. A second approach uses antibodies which have been tagged with boron [1]. These antibodies seek out antigens on the surface of tumor cells. Other approaches exploit the heightened metabolic rate of tumor cells. These tumor cells might absorb and process more of certain chemicals which can be loaded with boron. A similar approach seeks to tag boron to nucleosides which then would be incorporated into the nuclei of tumor cells. This approach has the advantage of placing the boron where the $^{10}B(n, \alpha)$ reaction can have its greatest effect [1].

Two compounds in current clinical use for the delivery of ^{10}B to tumor cells are sodium borocaptate and p-boronophenylalanine. Sodium borocaptate ($Na_{12}B_{12}H_{11}SH$) is commonly called BSH. BSH has been used clinically for the BNCT treatment of brain tumors in Japan [5]. P-boronophenylalanine is commonly called BPA. BPA is an amino acid analog and is postulated to be taken up by various tumor cells, including melanomas, due to their more active metabolism [6]. BPA has been used in clinical treatment of melanoma patients in Japan and is being used in two clinical trials currently underway in the US.

Unfortunately, it is not likely that boron will ever be delivered solely to tumor cells. There will always be some residual boron in healthy tissue. A more realistic goal is to maximize the concentration of boron in tumor cells relative to healthy cells. This goal is quantified by such values as the uptake ratio, which is the ratio of the concentration of boron in tumor cells (ppm) to the concentration in healthy cells. Some examples of these ratios taken from clinical use and research will be presented later in this chapter.

I.A.2 BNCT dose components

The radiation dose received during a BNCT procedure results from the following reactions:

(1) $^{10}B(n,\alpha)$

(2) neutron capture reactions primarily from the reactions $^{14}N(n,p)$ and $^{1}H(n,\gamma)$

(3) neutron scattering resulting in energetic recoil nuclei

(4) incident photon irradiation which contaminates the therapeutic neutron beam

Of the reactions listed, only (1) delivers radiation dose selectively to the tissue volume containing ^{10}B. The boron concentration in tumor must be sufficiently large to offset the contaminating dose components which accompany the $^{10}B(n,\alpha)$ dose and which are not tumor specific (2,3, and 4). A 0.48 MeV photon, which contributes a non-specific dose component, accompanies 94% of the $^{10}B(n,\alpha)$ reactions. Previous research indicates that this component accounts for less than 0.2% of the total ^{10}B dose when using a

spherical tissue-equivalent model of the head with a uniform distribution of ^{10}B [7]. This 0.48 MeV photon dose component will not be considered further. One advantage of BNCT is that the $^{10}B(n,\alpha)$ reaction produces high LET radiation, and the resultant dose component is weighted by a large relative biological effectiveness (RBE) factor. The RBE weighting factor is used to account for the fact that, for equivalent absorbed doses, different types of radiation (gamma, alpha, heavy charged particles, etc.) result in differing degrees of tissue damage. The RBE is referenced to the damage caused by a standard radiation type (usually 250 kVp x-rays). The RBE is always defined for a specific biological endpoint, such as cell death. The exact value of all weighting factors for BNCT is the topic of continuing research. One set of typical values is: 1.0 for photons, 4.0 for neutrons, and 4.1 for the $^{10}B(n,\alpha)$ reaction [8]. For this reason, physical dose (i.e. no RBE factors) will be used primarily in this thesis. When appropriate, RBE weighted doses will be presented and the RBE values used will be stated.

Neutron capture reactions can occur in many nuclides commonly found in human tissue. These nuclides, and the microscopic cross section for thermal neutron capture are listed in Table I-A-1. For comparison, the reaction $^{10}B(n,\alpha)$ is also listed.

Nuclide	Cross Section (barns)
Boron-10	3840
Oxygen-16	0.0002
Carbon-12	0.0037
Hydrogen-1	0.332
Calcium-40	0.44
Sodium-22	0.536
Nitrogen-14	1.75
Potassium-40	2.07

Table I-A-1. Important thermal neutron radiative capture reactions in human tissue [1].

Although the microscopic cross section for the reaction $^{10}B(n,\alpha)$ is much higher than those listed in Table I-A-1, the value of the $^{10}B(n,\alpha)$ macroscopic cross section is a direct function of the concentration of ^{10}B in the tissue. It is the macroscopic cross section (microscopic cross section multiplied by number density) which determines the relative probabilities of the various reactions in tissue. Since the number densities in tissue of some isotopes, particularly ^{1}H and ^{14}N, are very large, the respective macroscopic cross sections can also be significant. The $^{1}H(n,\gamma)$ reaction produces 2.2 MeV gamma rays which transfer energy to tissue primarily through Compton scattering. The $^{14}N(n,p)$ reaction releases a total kinetic energy of 0.62 MeV which is shared by the proton (0.58 MeV) and ^{14}C nucleus (0.04 MeV). The range of these heavy charged particles is small, and the total kinetic energy is deposited within 1 mm of original ^{14}N nucleus [9].

As neutrons scatter from nuclei in tissue, energy is transferred to these nuclei, which in turn directly ionize atoms in the cell. The amount of energy transfer is dependent on the incident energy of the neutron and on the mass of the target nucleus. In

the case of ^{1}H, the neutron transfers an average of 50% of its energy in an elastic collision. This dose mechanism is tumor non-specific and must be minimized for effective BNCT therapy. The common approach to this problem is to design neutron therapy beams which contain few energetic (fast) neutrons.

Finally, the neutron therapy beam is always contaminated by some photons which are produced concurrently with the neutrons, or later when neutrons interact with material surrounding the therapy port. This photon dose can also be limited during therapy beam design and optimization.

I.A.3 Clinical use of BNCT

BNCT is currently being proposed for treating several forms of malignant tumors, including cervical [10], breast, head and neck [11], and metastatic cancer to the liver [12]. Current clinical research, however, is directed at two forms of cancer: brain (primarily glioblastoma multiforme) and metastatic melanoma (a form of skin cancer). This thesis primarily addresses the use of BNCT to treat tumors located in the brain. These include glioblastoma multiforme and melanoma which has metastasized to the brain. In this section, some clinical information on glioblastoma multiforme and melanoma is provided.

I.A.3.a Glioblastoma Multiforme

The brain contains interstitial cells call glia which perform supportive functions. There are three types of glia cells: (1) astroglia (astrocytes) (2) oligodendroglia and (3) microglia. In the US, gliomas (tumor cells which arise from glia cells) account for approximately 31-49% of all intracranial tumors, and of these, 72-89% are astrocytomas [7]. Astrocytomas are further subdivided into four grades based on malignancy and prognosis, with grade IV the most malignant. The malignancy of brain tumors is judged based on the aggressiveness of the tumor cells and the location of the tumor relative to sensitive structures in the brain. Forty to sixty percent of all gliomas are grade III and IV astrocytomas. Grade IV astrocytomas are known as glioblastoma multiforme (GBM) [13].

GBM is often characterized by a central tumor which is not well vascularized, and the presence of extensions or "fingers" which branch off the main tumor and which are the most active and malignant parts of the tumor. In contrast to the central tumor, the extensions are well vascularized. Metastasis to other locations is rare [7] . The prognosis of all astrocytomas is poor and any cells that escape treatment almost always lead to the regrowth of tumor. After diagnosis, median survival for the most favorable patient populations (based on several prognostic factors) is around 12 months, even with surgery and photon therapy. For elderly patients (age > 60), the median survival drops to 6 months [14]. Despite advances in treatment techniques, the prognosis of these patients is

not improving [15], and as a result, treatment is generally palliative and not curative [13] [1].

I.A.3.b Malignant melanoma

The skin consists of three layers, the epidermis (outermost layer), the dermis (middle layer), and the hypodermis or subcutaneous tissue (deepest layer). Melanin is a pigment which is synthesized from tyrosine in melanocytes. This pigment is found primarily in the epidermis of the skin. Melanin provides the pigmentation of the skin and hair and also serves as a light absorbing material for the skin. Inability to produce melanin leads to an increased susceptibility to sunburn and skin cancer [16] [13] [1].

Malignant melanoma is a cancer of the melanin-producing cell. The incidence of melanoma is rising sharply in the US, with approximately 30,000 new cases each year, resulting in over 6,000 deaths annually. Typically, melanoma is indicated by an enlarging black-brown nodule on the skin, surrounded by erythema. This form of cancer is usually easy to diagnose, but its progression is difficult to predict. Melanoma can take one of several forms. The most dangerous form progresses by growing vertically into the deeper layers of the skin. Tumors which extend into the deeper skin layers are also more likely to metastasize, usually to the regional lymph nodes. Discovery of lymph node metastasis severely degrades the prognosis. The median survival for patients with distant metastases is approximately five months [16] [13] [1]. When the metastasis site is the brain, the

prognosis is very bad, and the tumor is considered untreatable [17]. These tumors are currently being targeted by BNCT.

I.A.4 History of BNCT

I.A.4.a Early results

Most historical accounts of BNCT [18] [1] [19] begin in 1936 with a proposal for such a therapy by Locher [20]. Some initial radiobiological studies, including some with mice. were conducted before World War II [18]. In August 1950 the Brookhaven Graphite Research Reactor (BGRR) was completed, and the use of this reactor for slow neutron therapy was already being considered by the medical department at Brookhaven National Laboratory (BNL). Clinical experiments of boron uptake in brain tumor patients were conducted at the Massachusetts General Hospital (MGH), and in 1951, patients were referred to BNL for BNCT treatments. The first series of patient studies was conducted at BNL and MIT. The following is a summary of the conditions and results [18]:

- The first patient at BNL was irradiated on 15 February 1951, as part of a ten patient study. ^{10}B was delivered intravenously in the form of an aqueous solution of borax. The irradiations lasted 17-40 minutes at 40 MW reactor power. The thermal neutron flux was 0.44-1.93 x 10^{12} neutrons/cm^2-sec. This group had a median survival of 97 days post BNCT.

- A second group of nine patients was treated at BNL using sodium pentaborate with D-glucose. The incident neutron flux was 2.34-3.84 x 10^{12} neutrons/cm^2-sec. This second group suffered from radiation induced dermatitis of the scalp and scalp ulceration. The median survival of this group was 147 days post irradiation.

- A third group of nine patients was irradiated with a neutron flux of 0.39-1.5 x 10^{12} neutrons/cm^2-sec. The boron compound was delivered directly to the internal carotid artery of the affected hemisphere, and no severe dermatitis was experienced. The median survival was 96 days.

- In 1959, the Brookhaven Medical Research Reactor (BMRR) became operational, and between 1959 and 1961, an additional 17 patients were treated using BNCT. The median survival was 87 days, and was considered disappointing.

- Between 1959 and 1961, 18 patients were treated for brain tumors at the MIT reactor. For 16 patients, the ^{10}B carrier used was the p-carboxy derivative of phenylboronic acid. The average survival was six months post BNCT. At MIT the scalp and skull were reflected to prevent the dermatitis seen in the second BNL group [19].

A total of 45 patients were irradiated at BNL, with an additional 18 at MIT. None of these early trials was considered successful. The failure of the early clinical trials has been blamed on two main factors. First, the boron delivery agents were not successful in

sustaining a high concentration of ^{10}B in the tumor cells. This resulted in low values of the tumor-to-healthy-tissue ^{10}B ratios during the therapy. Upon autopsy, it was discovered that radiation damage had occurred in the capillaries of the brain due to the high concentrations of ^{10}B in the patients' blood [7]. Second, the thermal neutrons did not penetrate deep enough to treat deep-seated parts of the tumor [1] . After these disappointing results, clinical trials were halted in the US.

In the 1960s, solutions were sought for both of these deficiencies. Fairchild, at BNL, promoted the use of epithermal neutron beams as a way of treating the deeper portions of the brain [21]. Epithermal neutrons provide greater penetration than thermal neutrons into the organ containing the tumor. The epithermal neutrons are moderated in the tissue volume and arrive at the tumor site with a thermal distribution. There is no exact energy range which defines an ideal epithermal beam for BNCT; however, the lower limit is approximately 0.5-1.0 eV [22] [19] and the upper limit is approximately 20 - 100 keV [22] [19] [23]. The use of epithermal beams for BNCT has been generally accepted in the BNCT community. During the early 1960s, researchers in the US sought a new drug that would enter GBM tumor cells easily, yet not cross the blood brain barrier [4] into healthy tissue. One such compound, BSH, was investigated at MGH and later selected for use in Japan [18] .

I.A.4.b Treatment of GBM in Japan

The most extensive use of BNCT clinically was by Dr. Hiroshi Hatanaka in Japan. Between 1968 and 1992, 119 patients were treated for intracranial tumors. All of these patients were injected with BSH and subsequently irradiated with thermal neutrons from a reactor. To increase neutron penetration, the scalp and skull were resected. Dr. Hatanaka's results are encouraging and have significantly helped spark interest in the BNCT field. For grade III and IV gliomas, with BNCT treatment only, the five and ten year survival rates are reported as 19.3% and 9.6% [5]. The respective numbers for conventional surgery followed by radiotherapy or chemotherapy are 4.6% and 0% [24]. For shallow tumors, the five and ten year survival rates were 58.3% and 29.2%, respectively. The median survival of untreated GBM patients in the US is eight months [16] . The most effective conventional treatment to date, which combines surgery and photon irradiation, results in a 13% survival after three years [7]. Dr. Hatanaka reported tumor-to-blood ratios of boron as high as 8.95, with an average around 1.4, and average boron concentrations in tumor around 15 ppm [5].

I.A.4.c Treatment of melanoma

In the early 1970s Dr. Yutaka Mishima developed a program to treat melanoma by BNCT using a thermal neutron beam [25]. In 1976, he developed a boron containing analog of dopa, BPA. Melanin is formed from dopa, and actively absorbed by tumor cells due to their increased metabolic rate [26]. The first patient treated under this program had been diagnosed with a metastasis to the left occipital region. The location of the

metastasis made surgery impossible. Administration of BPA was via perilesional injection, and the patient was treated with 10^{13} thermal neutrons/cm^2. After 9 months the tumor had regressed with no regrowth [27].

A second patient was treated for a primary melanoma of the foot. This case resulted in regression of the tumor, with no regrowth after 18 months. To date, 16 patients have been treated successfully with thermal BNCT [25]. Specific statistical data on these patients are difficult to obtain.

I.A.5 Recent Progress

By September 1994, two epithermal beams were in operation and ready for clinical trials in the US. The first was at the MIT Research Reactor (MIT-R), and the second was at the Brookhaven Medical Research Reactor (BMRR). On September 6th, 1994 the first BNCT treatment with an epithermal beam was conducted at MIT-R using the boron delivery agent BPA as part of a phase-I clinical study for metastatic melanoma of the extremities [28]. In one year, four subjects, each with subcutaneous metastatic melanoma nodules in the lower extremities, were irradiated. The subjects were first given 400 mg/(kg-body weight) of BPA orally for the purpose of evaluating the pharmacokinetic absorption and excretion of the BPA. After this evaluation, the subjects were given repeat administrations of BPA, prior to each of four neutron irradiation fractions. The maximum total normal tissue dose received by the subjects was between 1000 RBE-cGy and 1250 RBE-cGy. The dose to the tumor was 25-35% higher due to the

preferential absorption of BPA. No negative effects were observed, with the exception of an adverse skin reaction with one of the subjects, which was resolved in two weeks. Two of the four subjects manifested clear tumor regression, which has not reversed. Each of the subjects is still alive [29].

Also in September 1994 (just a few days after the first MIT-R irradiation), a single patient was treated for GBM using BPA as the delivery agent at the BMRR [30]. BNL began a multi-patient trial in February 1995. This trial was designed to evaluate: (1) the performance of BPA as a delivery agent to GBM cells, (2) the safety of BNCT using BPA for GBM treatment, and (3) the efficacy of this treatment for GBM patients[31]. In the period up to February 1996, ten patients were treated with this protocol. As in the MIT-R study, a biodistribution evaluation was conducted. The boron concentrations in tumor were found to be 24.7 ± 12.6 μg ^{10}B/g-tissue (mean $\pm$ standard deviation) for a 250 mg/(kg-body weight) administration of BPA. The tumor-to-blood ratio was approximately 2.0, and the non-necrotic tumor-to-blood ratio was greater than 3.5. The patients were treated to a normal brain endothelium dose of 10.5 Gy-equivalent (peak dose volume of 1 cm^3). No serious complications were experienced [31]. Of these initial ten patients, at least eight experienced recurrence of the tumor. Following BNCT, the median survival time was 13.5 months. Two of the patients are still alive [31]. In the second of two protocols now underway, the tumor dose has been increased over that given in the first protocol.

A recent update indicates that 23 patients have been treated at BNL to date. The life extension was similar to that using conventional radiotherapy, and so the results are encouraging [32]. Conventional radiotherapy is very time consuming for the patient who may not have a long life expectancy. Typical radiotherapy treatment protocols may last six weeks. BNCT procedures may require as little as a few days of the patient's time. Initial analysis of the results indicates that tumor control will require a dose to tumor of approximately 30-50 RBE-Gy [32].

I.A.6 Non-reactor neutron sources

If BNCT proves to be a viable cancer therapy modality, additional sources of neutrons (i.e. other than reactors) would be needed. The death rate from GBM in the US alone is approximately 3200/year [7]. In addition, there are approximately 6,000 deaths from melanoma each year. The total death rate from these two cancers alone is over 25/day. New reactor construction, particularly at a hospital, seems unlikely due primarily to the prohibitive cost of construction and operation. At lease three other reactors in the US have been identified for possible conversion to BNCT facilities [33] although no construction progress has been made to date.

In recent years, alternative sources of neutrons have been investigated. These neutron sources include: ^{252}Cf [23], spallation sources [34], photoneutron sources [35] and accelerator-based (p,n) or (d,n) sources [8][36] [37] [38].

The possibility of a ^{252}Cf source has been investigated, and deemed unlikely primarily because the quantity of radioactive material needed exceeds the total production capacity of the Western world [23]. The other alternative neutron sources listed above are accelerator-based neutron sources. An evaluation of one spallation source, using 72 MeV protons on a tungsten target, found that the predicted dose distributions in a head phantom were comparable to those achievable with existing reactor facilities [34]. The proton currents required are approximately 100 μA. A moderator made of iron and graphite is proposed [39]. A photoneutron source has been proposed which uses 6 MeV electrons striking a material such as tungsten. The resulting Bremsstrahlung photons then create neutrons through interaction with D_2O which also serves as the moderator [40]. Of the accelerator-based neutron sources, spallation and photoneutron sources have received less attention than the charged particle reactions, particularly $^{7}Li(p,n)$ and $^{9}Be(p,n)$.

For the purpose of this thesis, the term Accelerator-Based BNCT (AB-BNCT) will be used to describe the production of neutrons through charged particle induced reactions such as (d,n) or (p,n), as opposed to spallation or photoneutron sources. Section I.B introduces the concepts and terminology used in AB-BNCT. Section I.C will describe the operation of an accelerator built specifically for use in AB-BNCT research. The original research contained in this thesis will be introduced in Section I.D.

I.B Introduction to Accelerator-Based BNCT (AB-BNCT)

The new contributions to BNCT which are contained in this thesis are in the field of AB-BNCT. These contributions are contained in Chapters II, III, and IV. In this section, an introduction to AB-BNCT is provided which will form the foundation for the work presented in the later chapters.

AB-BNCT differs from reactor-based BNCT in the method of generating neutrons and modifying the energy spectrum of these neutrons to create a useful epithermal therapy beam. A typical configuration consists of a neutron producing target, such as beryllium or lithium, which is bombarded by energetic protons or deuterons. This target is surrounded by an object known as a Moderator-Shielding-Reflector-Assembly (MSR). The patient would be placed in front of the MSR and exposed to neutron radiation which is emitted from the therapy port. A diagram representing such a configuration is shown in Figure I-B-1.

Three basic components must work together to create a viable AB-BNCT therapy beam: accelerator, neutron producing target, and MSR. The accelerator produces a charged ion beam containing protons or deuterons at a current, I, and energy E. The ions strike the target inducing a (p,n) or (d,n) reaction. Therefore, the target must be designed to withstand a heat load equal to W=IE. For example, a 1 mA beam of 4 MeV protons delivers 4 kW of power to the target. Neutrons are produced at the target with an energy spectrum written as $Y(\Theta_n,E_n)$, expressed in units such as (neutrons/mC-keV-steradian).

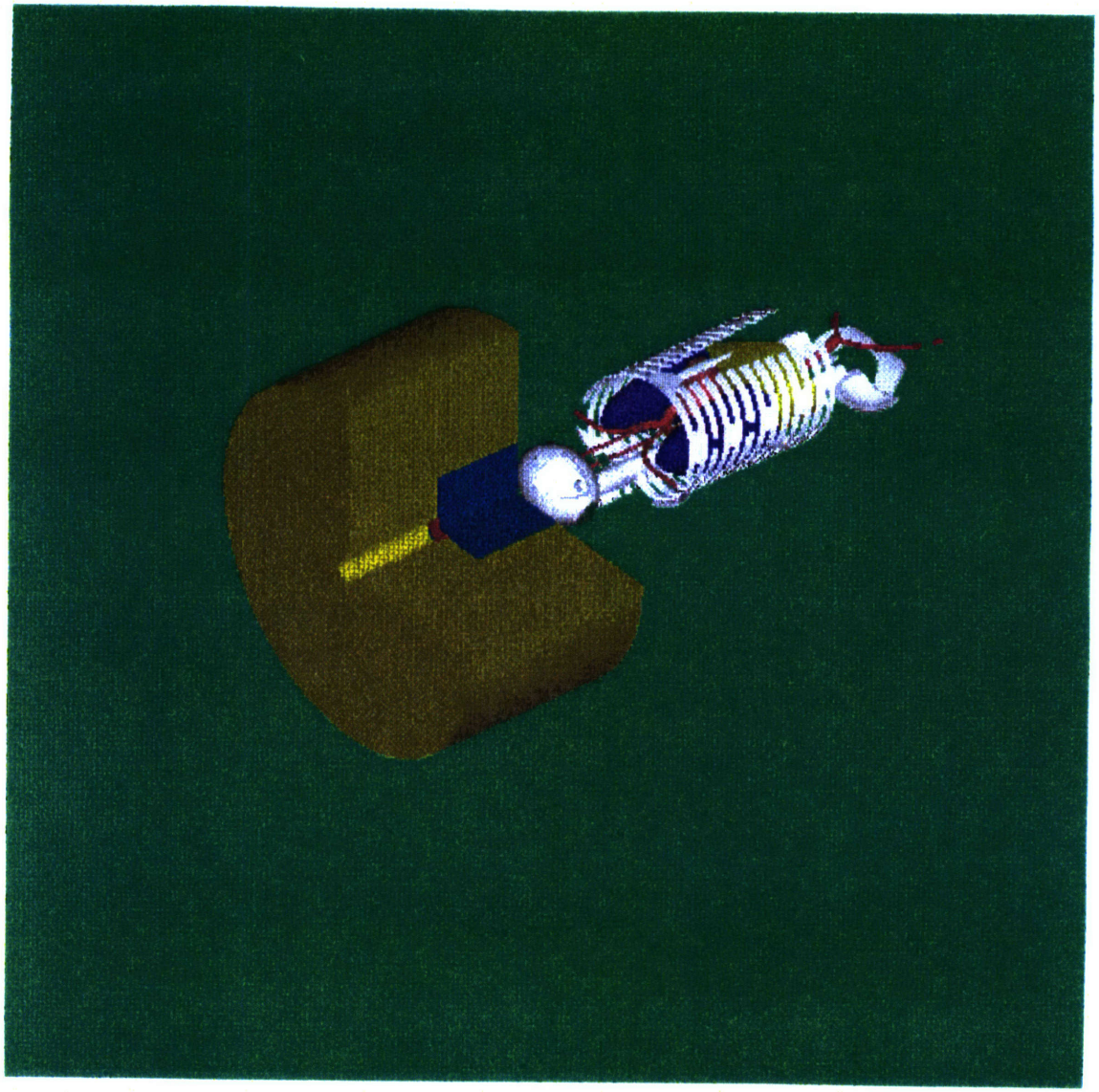

Figure I-B-1: Model of an AB-BNCT system. The reflector is shown in gold. The moderator is shown in blue. The neutron producing target is shown in red.

This spectrum depends on the target material, ion species and ion energy. The total neutron yield of a reaction, $Y_{TOT}(E_{ion})$, is the neutron energy spectrum integrated over all angles, Θ_n, and all neutron energies, E_n. The ideal reaction for AB-BNCT would produce a copious and focused amount of purely epithermal neutrons, with no penetrating contaminant radiation. The neutrons from this reaction could then be used, with very little moderation, as a therapy beam. The kinematics of reactions capable of producing epithermal beams at the target dictate that the ion energy must be kept only slightly above the threshold energy of the reaction, E_{TH}. Unfortunately, this approach generates relatively small neutron yields, since the production cross section is low at E_{TH}. The alternative approach is to use an ion energy significantly above E_{TH}, and generate neutrons with an average energy well above the epithermal range. This neutron beam cannot be used directly on a patient. The primary purpose of the MSR is to decrease the average energy of the neutrons before they reach the patient position. This alternative approach is the one used at LABA, depicted in Figure I-B-1, and described in Chapters II-IV of this thesis.

In the most general sense, the design of an "optimized" AB-BNCT therapy beam is the process of choosing all of the parameters of the combined system (accelerator, target, and MSR) which will provide the most useful therapy beam, in a reasonable amount of time, and with the least amount of other resources (money, space, shielding, etc.). Each design parameter of the basic components depends on the others in a complex way. For example, the optimal MSR components and dimensions depend on the target

reaction and ion energy. Increasing the ion energy increases the neutron production rate at the target, but may result in a less optimal neutron spectrum at the patient position. Also, if the ion energy is increased, the heat load on the target increases if the same beam current is used.

I.B.1 Target system

Charged particle reactions can be divided into two classes: exothermic and endothermic. Exothermic reactions, such as ^{9}Be(d,n) release energy so that the resultant neutrons have a maximum energy in excess of the bombarding charged particle energy. Endothermic reactions, such as ^{7}Li(p,n) absorb energy so that the maximum neutron energy is less than the charged particle energy. Both types are potentially useful for AB-BNCT. The ideal neutron producing reaction for BNCT would have several characteristics. First, the yield of the reaction would be high at low charged particle energies and currents so the accelerator system requirements would be simplified and the BNCT treatment could take place in a reasonable amount of time. Second, the neutron energy spectrum would be as close to epithermal as possible to reduce the need for extensive moderation/filtration. Third, the reaction would not produce penetrating contaminant radiation (gamma-rays). Finally, the target material would be inexpensive, safe to handle, capable of withstanding operating conditions such as high temperature and vacuum, and easily made into a practical target. In all cases, a thick target would be used to produce the maximum neutron yield.

Unfortunately, no target reaction meets these four requirements simultaneously. Previous studies [41] [42] [22] [8] have concluded that three source reactions are currently plausible for AB-BNCT. These reactions are ^{7}Li(p,n), ^{9}Be(p,n) and ^{9}Be(d,n). Chapter II of this thesis examines each of these reactions and describes the neutron energy spectra for each. In Chapter III, the design of MSRs for each reaction is discussed.

I.B.2 Accelerator

An accelerator designed for use in AB-BNCT would be characterized by three main performance parameters: ion current, ion energy and total available power. As a minimum, such an accelerator must be capable of producing ion energies above the threshold for the neutron producing reactions of interest. The highest threshold of the reactions considered here is 2.059 MeV (^{9}Be(p,n)). Beyond this requirement, the method by which the performance parameters are chosen can be illustrated by an example. If the ^{7}Li(p,n) reaction is to be used, the energy spectrum might be calculated or measured at several proton bombarding energies. The resulting spectra could then be used, one at a time, to design MSRs to be used with each proton energy. The combination of target reaction, ion energy, and MSR which resulted in the most optimal beam would then be implemented. These MSR designs would be based, in part, on assumptions concerning issues such as: depth of tumor, total dose to tumor prescribed by a physician, tolerance dose of healthy tissue, and the maximum time allowed for a therapy procedure. At the end of the MSR design process, the therapy beam performance (based, for example on Monte Carlo simulations to predict radiation dose rates in tissue) would be evaluated.

One result of this evaluation would be the determination of the proton current required, for each proton energy, which then sets the performance requirement for the accelerator.

As this example shows, the performance requirements for an accelerator are dependent on the assumptions used in the therapy beam design. Although there is not yet a consensus on these assumptions, the current clinical trials should help resolve some of these issues. It is, however, possible to give an order-of-magnitude approximation to some of the accelerator design specifications. Another example is helpful. As will be shown in Chapter III, it is possible to design an AB-BNCT therapy beam with a tumor dose rate, at a depth in tissue of six cm, of 2.5 cGy/(min-mA of accelerator beam current), using a 4.0 MeV proton beam. Depending on the assumed RBE weighting factors, the RBE-weighted dose rate could range from 6-10 RBE-cGy/min-mA. If one were to assume that a physician prescribed a dose of 15 RBE-Gy, to be delivered in no more than 60 minutes, then a beam current of approximately 2.5 mA would be required, resulting in an accelerator power of 10 kW. These results will, of course, change with changing assumptions. Therapy beams are currently being designed within the AB-BNCT community using ion bombarding energies and ion currents of approximately 2.5-4 MeV and 4-30 mA respectively [43] [44] [45] [46] [47]. The accelerator power requirements, then, are on the order of 10-100 kW.

In addition to adequate energy and current production, a viable accelerator for BNCT would have the following characteristics. First, the production of charged particles must be safe and reliable. Second, the accelerator (including auxiliary systems) must be practical in terms of system cost, ease of use, size and weight. Several types of accelerators have been examined to produce proton beams for AB-BNCT (E_p= 2-4 MeV, I_p = 4-30 mA). These include: radio frequency quadrupole (RFQ), electrostatic quadrupole (ESQ) and electrostatic accelerators. Electrostatic and ESQ accelerators have several properties which make them useful for the AB-BNCT application. First, beam current and energy are continuously tunable over a wide range. Second, continuous current is delivered to the target resulting in lower peak thermal load. Third, higher accelerating gradients are possible resulting in a more compact system. Finally, electrostatic accelerators have high electrical power efficiency which reduces cooling requirements and system operating cost [48]. The accelerator which has been built at LABA for AB-BNCT research is an electrostatic accelerator.

I.C The LABA Accelerator

I.C.1 Description of the accelerator

A detailed description of the LABA accelerator is given in Appendix A. A brief description is given here. When examples are needed to highlight an aspect of the accelerator operation, a proton beam will be assumed. The accelerator at LABA is a tandem electrostatic linear accelerator capable of accelerating protons and deuterons. The accelerator is designed for a maximum terminal voltage of 2.05 MV (a maximum proton

energy of 4.1 MeV) and a maximum power of 10 kW. The accelerator was designed by Newton Scientific Incorporated, Cambridge, MA. A picture of the accelerator is shown in Figure I-C-1. The complete system weighs approximately 1000 kg and measures 3.9 meters from the ion source to the high energy end of the pressure vessel. The largest diameter is 0.94 m. The entire outside surface of the accelerator is at ground potential.

A cut-away drawing of the accelerator, with the major components labeled, is shown in Figure I-C-2. Negative ions, such as H-, are produced in the ion source and injected into the low energy stage of the accelerating structure. The ions experience a constant acceleration provided by the electrodes of the low energy stage, and gain energy as they travel in vacuum towards the positively charged high voltage (HV) terminal. Inside the HV terminal, each ion passes through a stripping foil, where two electrons are stripped, leaving a positive ion, such as H+. These positive ions then experience a repulsive force from the terminal as they enter the high energy stage. The ions exit the accelerating structure, and enter the beam line extension, which is electrically grounded. In its present configuration, the beam line extension passes through a steering magnet, and quadrupole focusing magnet and terminates at the target housing. The steering magnet, quadrupole magnet and target are not shown in Figure I-C-2.

I.C.2 Accelerator performance to date

The accelerator has been operated, for limited duration, at a maximum continuous proton beam current of 0.8 mA at an energy of 2 MeV. The accelerator has been run

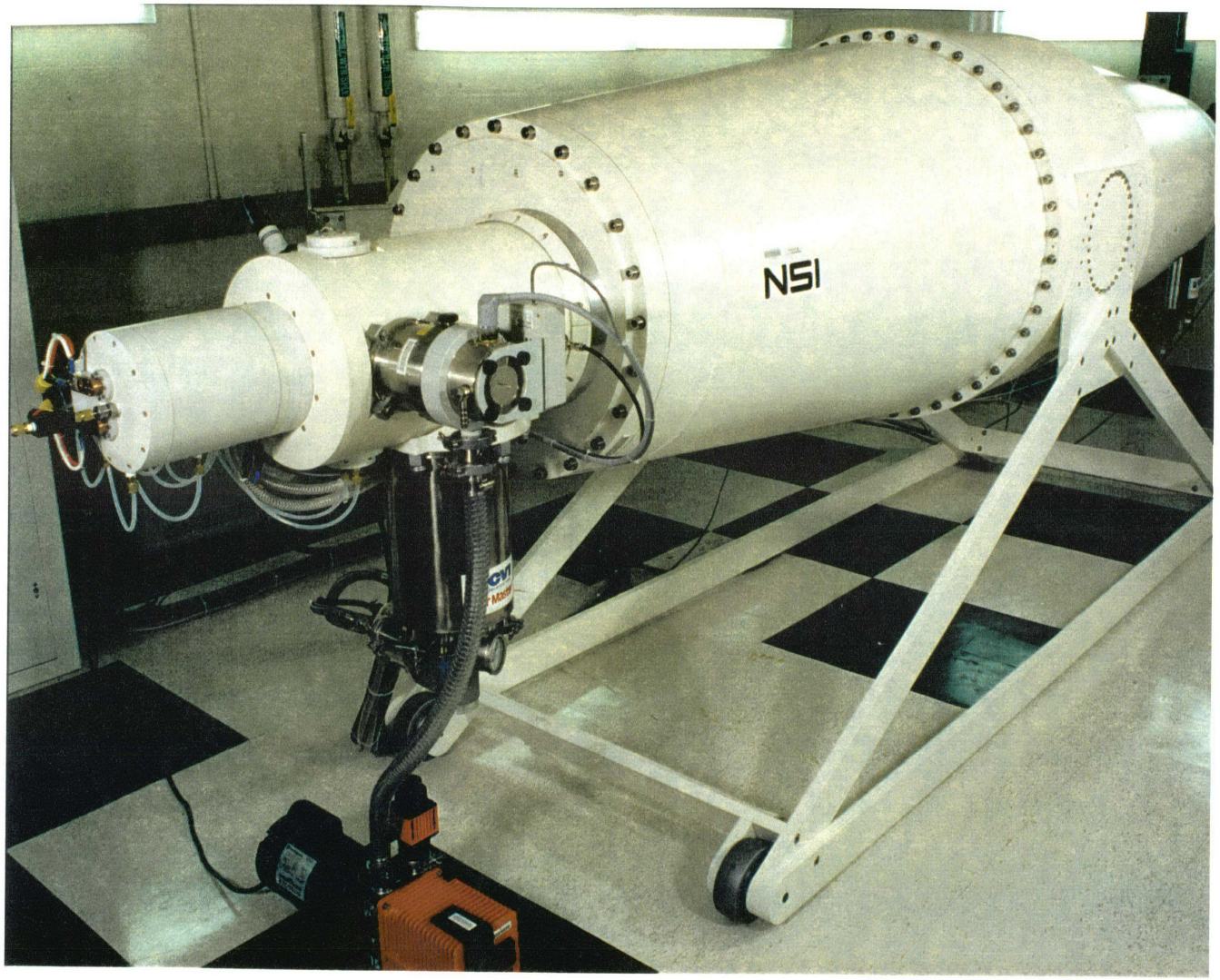

Figure I-C-1: The accelerator at LABA.

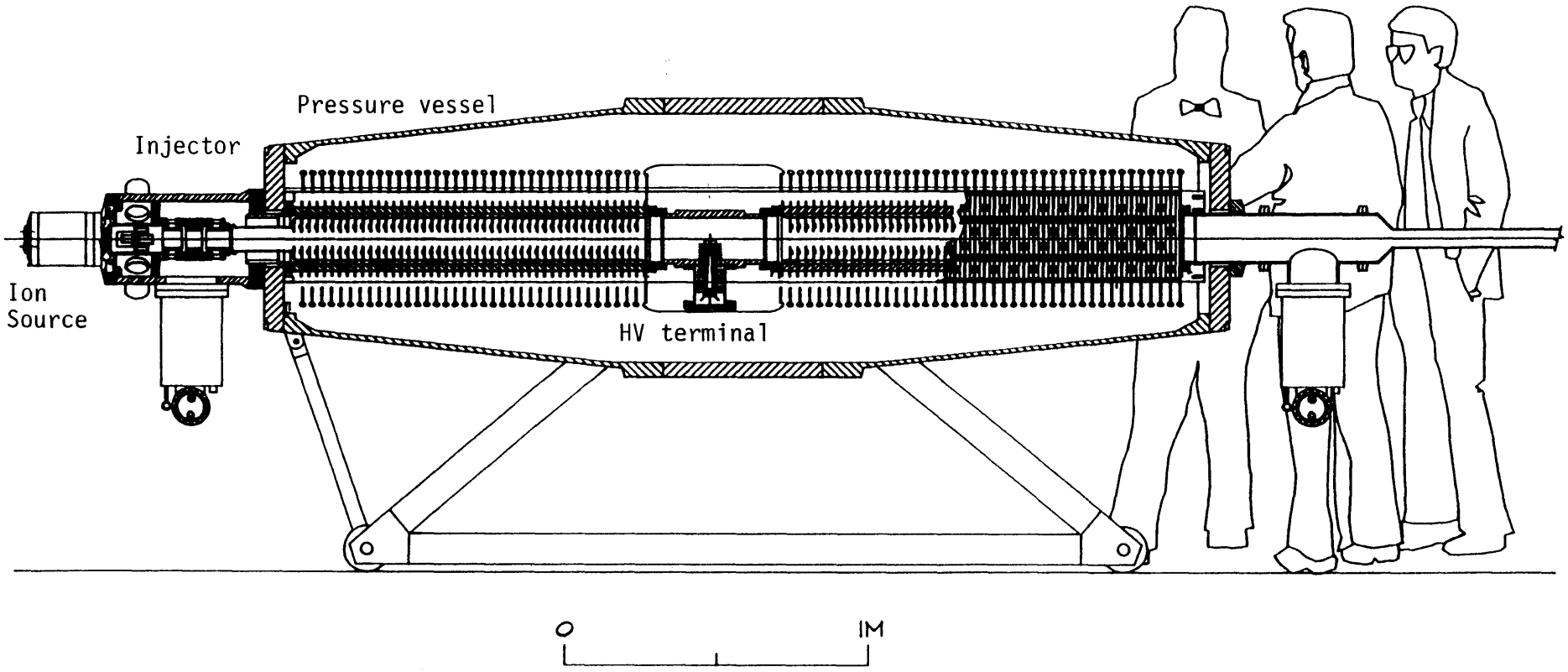

Figure I-C-2: Cut away drawing of the LABA accelerator

routinely with deuteron beam currents up to 50 μA at a beam energy of 2.6 MeV. The ion source current has been as high as 5 mA. The current research program aims to increase both the terminal voltage and the current in a systematic way, and to evaluate the performance of all accelerator systems.

I.D Overview of New Research

For AB-BNCT to become a viable and accepted cancer treatment modality several issues must be resolved. The purpose of this thesis is to address some of these issues, and report on the progress towards a solution for each. During the past few years, significant advances have been made in the field of AB-BNCT, both at LABA, and other facilities. The work presented in the remainder of this thesis will add to these advances. This section introduces the research presented as original contributions to the AB-BNCT field.

The thick target yield and spectra of the reaction ^{9}Be(p,n) have been accurately measured using time-of-flight techniques, using proton bombarding energies which are currently considered useful for AB-BNCT. This research will be presented in Chapter II. An important characteristic of these measurements is that they were accomplished on an absolute basis, without any normalization. The experimental procedures were confirmed indirectly by measuring a second reaction, ^{9}Be(d,n). These measurements are important not only to the BNCT community, but also to the scientific community at large, since this reaction can be used as a neutron source for a variety of applications.

A comparative study of possible therapy beams has been accomplished using three likely neutron source reactions for AB-BNCT (^{9}Be(p,n), ^{9}Be(d,n), ^{7}Li(p,n)), and is presented in Chapter III. Seventy different MSR configurations were studied using Monte Carlo methods. In addition to examining the neutron production at the target, the gamma contamination resulting from (p,γ) reactions was addressed. The designs were compared on the basis of equivalent accelerator current and power. Recommendations are made concerning future beam design. Beam designs based on the reaction ^{9}Be(p,n) were studied for four different proton bombarding energies.

The BNCT dose components were measured experimentally using dual ionization chambers and activation foil analysis. These measurements were accomplished on an absolute basis and were compared with the values predicted by Monte Carlo simulation. Recommendations for further measurements are presented.

The radiation dose rates resulting from operation of the LABA accelerator at a shielded facility were investigated for several neutron producing reactions and MSR configurations. This work is presented in Chapter IV. A system of electron suppression magnets inside the accelerating column of the LABA accelerator appears to have effectively reduced the bremsstrahlung radiation levels which were thought to be problematic. Methods to shield the patient against non-therapeutic radiation dose rates are also examined.

REFERENCES

1. Barth, R.F., A.H. Soloway, and R.G. Fairchild, *Boron neutron capture therapy for cancer.* Scientific American, 1990. **263**(4): p. 100-107.

2. Knoll, G.F., *Radiation detection and measurement.* Second ed. 1989, New York: John Wiley and Sons, Inc. 754.

3. Kiger, W.S.I., *Neutronic design of a fission converter-based epithermal beam for neutron capture therapy*, in *MS Thesis, Nuclear Engineering.* 1996, Massachusetts Institute of Technology: Cambridge, MA. p. 471.

4. Goldstein, G.W. and A.L. Betz, *The blood-brain barrier.* Scientific American, 1986. **250**((5)): p. 74-83.

5. Hatanaka, H. and Y. Nakagawa, *Clinical results of long-surviving brain tumor patients who underwent boron neutron capture therapy.* International Journal of Radiation Oncology Biology Physics, 1994. **28**(5): p. 1061-1066.

6. Mallesch, J.L., *et al.*, *The pharmacokinetics of p-boronophenylalanine fructose in human patients with glioma and metastatic melanoma.* International Journal of Radiation Oncology Biology Physics, 1994. **28**(5): p. 1183-1188.

7. Zamenhof, R.G., *et al.*, *Boron neutron capture therapy for the treatment of cerebral gliomas. I: Theoretical evaluation of the efficacy of various neutron beams.* Medical Physics, 1975. **2**(2): p. 47-60.

8. Yanch, J.C., *et al.*, *Accelerator-based epithermal neutron beam design for neutron capture therapy.* Medical Physics, 1992. **19**(3): p. 709-722.

9. Attix, F.H., *Introduction to radiological physics and radiation dosimetry.* First ed. 1986, New York: John Wiley and Sons.

10. Lorvidhaya, V., *et al. Status report on BNCT for cervical carcinoma in Thailand.* in *Seventh international symposium on neutron capture therapy for cancer.* 1996. Zurich Switzerland: Elsevier Science - To be published.

11. Coderre, J.A. *Application of BNCT to other types of tumors.* in *Seventh international symposium on neutron capture therapy for cancer.* 1996. Zurich, Switzerland: Elsevier Science - to be published.

12. Wallace, S., M. Carolan, and B. Allen. *Treatment planning for boron neutron capture therapy of liver cancer.* in *Seventh international symposium on neutron capture therapy for cancer.* 1996. Zurich, Switzerland: Elsevier Science -to be published.

13. Robbins, S.L., *Pathologic basis of disease.* First ed. 1974, Philadelphia, PA: W. B. Saunders company. 1595.

14. Bauman, G.S., *et al.*, *A prospective study of short-course radiotherapy in poor prognosis glioblastoma multiforme.* International Journal of Radiation Oncology Biology Physics, 1994. **29**(4): p. 835-839.

15. Curran, W.J., *et al.*, *Recursive partitioning analysis of prognostic factors in three radiation therapy oncology group malignant glioma trials.* Journal of the National Cancer Institute, 1993. **85**(9): p. 704-710.

16. Coia, L.R. and D.J.I. Moylan, *Introduction to clinical radiation oncology.* First ed. 1991, Madison WI: Medical Physics publishing. 578.

17. Barth, R.F., *et al.*, *A nude rat model for neutron capture therapy of human intracerebral melanoma.* International Journal of Radiation Oncology Biology Physics, 1994. **28**(5): p. 1079-1088.

18. Slatkin, D.N., *A history of boron neutron capture therapy of brain tumors.* Brain, 1991. **114**: p. 1609-1629.

19. Rogus, R.D., *Design and dosimetry of epithermal neutron beams for clinical trials of boron neutron capture therapy at the MITR-II reactor*, in *Ph.D. Thesis, Nuclear Engineering.* 1994, Massachusetts Institute of Technology: Cambridge, MA.

20. Locher, G.L., *Biological effects and therapeutic possibilities of neutrons.* American Journal of Roentgenology, 1936. **36**: p. 1-13.

21. Fairchild, R.G., *Development and dosimetry of an "epithermal" neutron beam for possible use in neutron capture therapy.* Physics in Medicine and Biology, 1965. **10**: p. 491-504.

22. Wang, C.K. and B.R. Moore, *Thick beryllium target as an epithermal neutron source for neutron capture therapy.* Medical Physics, 1994. **21**(10): p. 1633-1638.

23. Yanch, J.C., J.K. Kim, and M.J. Wilson, *Design of a californium-based epithermal neutron beam for neutron capture therapy.* Physics in Medicine and Biology, 1993. **38**: p. 1145-1155.

24. Rubin, P., *Editor's note.* International Journal of Radiation Oncology Biology Physics, 1994. **28**(5): p. 1055-1056.

25. Mishima, Y. *Selective neutron capture therapy of cancer cells using their specific metabolic activities - melanoma as prototype.* in *Sixth international symposium on neutron captuer therapy for cancer.* 1994. Kobe, Japan: Plenum Press -to be published.

26. Mishima, Y., *et al. Selective melanoma thermal neutron capture therapy for lymph node metastases.* in *Fifth international symposium on neutron capture therapy.* 1992. Columbus, Ohio: Plenum Press.

27. Mishima, Y., *et al., Treatment of malignant melanoma by single thermal neutron capture therapy with melanoma seeking 10B-compound.* The Lancet, 1989. **August 12, 1989**: p. 388-389.

28. Madoc-Jones, H., *et al. A phase-I dose escalation trial of boron neutron capture therapy for subjects with subcutaneous melanoma of the extremities.* in *Sixth international symposium on neutron capture therapy for cancer.* 1994. Kobe, Japan: Plenum Press - to be published.

29. Busse, P., *et al. Long-term clinical follow-up of four subjects with melanoma in the extremities who underwent a phase-I boron neutron capture therapy protocol.* in *Seventh international symposium on neutron capture therapy for cancer.* 1996. Zurich, Switzerland: Elsevier Science - to be published.

30. Coderre, J.A. *BNCT for malignant glioma using BPA: radiation biology and treatment planning.* in *Sixth international symposium on neutron capture therapy for cancer.* 1994. Kobe, Japan: Plenum Press - to be published.

31. Elowitz, E., *et al. A phase I/II trial of boron neutron capture therapy (bnct) for glioblastoma multiforme using intravenous boronphenylalanine-fructose complex and epithermal neutrons - early clinical results.* in *Seventh international symposium on neutron capture therapy for cancer.* 1996. Zurich, Switzerland: Elsevier Science - to be published.

32. Bernard, J., *Personal communication - BNCT progress at MIT and BNL*, . 1996.

33. Brugger, R., *et al. Rapporteurs' report.* in *International workshop on neutron beam design, development and performance for neutron capture therapy.* 1989. Cambridge, MA: Plenum Press.

34. Teichmann, S. and J. Crawford. *Theoretical study of a spallation neutron source for bnct.* in *Seventh international symposium on neutron capture therapy for cancer.* 1996. Zurich, Switzerland: Elsevier Science - to be published.

35. Nigg, D.W., *et al. Experimental investigation of filtered epithermal photoneutron beams for BNCT.* in *Seventh international symposium on neutron capture therapy for cancer.* 1996. Zurich, Switzerland: Elsevier Science - to be published.

36. Howard, W.B., *et al., Measurement of the 9Be(p,n) thick target spectrum for use in accelerator-based Boron Neutron Capture Therapy.* Medical Physics, 1996. **23**(7): p. 1233-1235.

37. Gupta, N., T.E. Blue, and M.C. Dobelbower. *Preliminary testing of a moderator assembly prototype for an accelerator-based neutron source for boron neutron capture therapy.* in *Seventh international symposium on neutron capture therapy for cancer.* 1996. Zurich, Switzerland: Elsevier Science - to be published.

38. Beynon, T.D., *et al. Towards the final design of an accelerator-based facility for clinical boron cancer therapy (BCT).* in *Seventh international symposium on neutron capture therapy for cancer.* 1996. Zurich, Switzerland: Elsevier Science - to be published.

39. Conde, H., *et al., Develpment of spallation neutron sources*, in *Clinical aspects of neutron capture therapy*, R. Fairchild, V. Bond, and A. Woodhead, Editors. 1989, Plenum Press: New York.

40. Nigg, D.W., *et al. An accelerator-based epithermal photoneutron source for bnct.* in *Sixth international symposium on neutron capture therapy for cancer.* 1994. Kobe, Japan: Plenum Press - to be published.

41. Shefer, R.E., R.E. Klinkowstein, and J.C. Yanch, *A versitile, new accelerator design for boron neutron capture therapy: accelerator design and neutron energy considerations*, in *Neutron beam design, development, and performance for neutron capture therapy*, B.a.Z. Harling, Editor. 1990, Plenum Press: New York. p. 259-270.

42. Sears, S., *Production of a neutron beam for use in boron neutron capture therapy*, in *Physics*. 1996, Massachusetts Institute of Technology: Cambridge, MA. p. 77.

43. Tattam, D., *et al. Development and preliminary neutron fluence measurements in the Birmingham bct beam.* in *Seventh international symposium on neutron capture therapy for cancer*. 1996. Zurich, Switzerland: Elsevier Science - to be published.

44. Yanch, J.C., *et al., Research in boron neutron capture therapy at MIT LABA.* Nuclear Instruments and Methods - To Be Published, 1996.

45. Blue, T., *et al. Design of an accelerator-based epithermal neutron source for bnct.* in *Seventh international symposium on neutron capture therapy for cancer*. 1996. Zurich, Switzerland: Elsevier Science - to be published.

46. Chu, W., *et al. Design of a new bnct facility based on esq accelerator.* in *Seventh international symposium on neutron capture therapy for cancer*. 1996. Zurich, Switzerland: Elsevier Science - to be published.

47. Heinzel, V., M. Sokcic-Kostic, and Y. Ronen. *The target and moderator considerations for an accelerator for boron neutron capture therapy.* in *Seventh international symposium on neutron capture therapy for cancer*. 1996. Zurich, Switzerland: Elsevier Science - to be published.

48. Shefer, R.E., *et al. Tandem electrostatic accelerators for BNCT.* in *First international workshop on accelerator-based neutron sources for boron neutron capture therapy, INEL Conference 940976.* 1994. Jackson Hole, WY.

CHAPTER TWO

Neutron Producing Reactions

As mentioned in Chapter I, the ideal neutron producing reaction for AB-BNCT would be prolific, have an average energy in the epithermal range, and produce no penetrating contaminant radiation. No reaction has yet been found which meets all of these criteria simultaneously. Therefore, a common approach is to induce a neutron producing reaction at an energy well above threshold, and moderate the resulting neutrons to epithermal energies. This approach leads to significant heat loading of the target, so an additional requirement is that the target material be practical, especially concerning heat removal. A common feature of these reactions is that the total thick target yield and maximum neutron energy both increase with increasing ion bombarding energy. Thus, a trade-off exists in trying to create a neutron source which is both low energy and prolific. In this chapter, three possible neutron producing reactions are examined: ^{7}Li(p,n), E_p=2.5 MeV; ^{9}Be(p,n) $E_p \leq 4.0$ MeV; and ^{9}Be(d,n), E_d=2.6 MeV. The advantages and problems associated with each reaction in regards to its use for AB-BNCT will be discussed. This will provide the framework for Chapter III, where clinically useful epithermal beam designs based on each of these reactions will be investigated.

II.A ^{7}Li(p,n)

This reaction is a natural choice for AB-BNCT for two reasons. First, the thick target yield is significant even at energies less than 1 MeV above threshold. This means that large amounts of neutrons will be produced at relatively low energies. Second, the threshold of the reaction is low (1.88 MeV) so that accelerator performance requirements and target heating are minimized. Unfortunately, lithium is a poor choice for a high current target material, when its physical and mechanical properties are considered. The thermal conductivity of lithium is 44.0 W/m-°C, and the melting point is 180.7 °C [1]. Further complicating the poor thermal properties of lithium is the fact that pure lithium is a soft metal with the consistency of soft clay. Thus, lithium cannot be formed into a target which will hold vacuum or water pressures without a backing. Since the backing, and not the lithium, would be directly cooled, heat must be conducted first through the lithium target, then across the lithium-backing interface, through the backing, and finally into the coolant. One possible solution to this problem is the use of a lithium compound (such as LiF). However, this results in lower neutron yield per unit current. In this section, the neutron production from a pure lithium target will be presented. Although lithium does not have good physical and mechanical properties, it is quite possible that these limitations can eventually be overcome. AB-BNCT groups are currently working on lithium target designs [2] [3].

II.A.1 Neutron yield and spectra

The thick target neutron yield and angular and energy distributions have been calculated using published cross-section [4] and stopping power [5] data for proton energies from 1.88 to 2.5 MeV [6]. The total thick target neutron yield for E_p=2.5 MeV is 8.96 x 10^{11} neutrons/mC. and the maximum neutron energy is approximately 800 keV. The unit mC (milliCoulomb) refers to the total charge (integrated current) of the proton beam striking the target. The neutron yield is forward peaked as shown in Figure II-A-1. Examples of the angular distributions are shown in Figure II-A-2.

II.A.2 Gamma production

In addition to the production of neutrons, the proton bombardment of lithium also produces gamma rays. At energies below 2.5 MeV, gamma production results from the reaction ^{7}Li(p,p'γ)^{7}Li. This photon has an energy of 478 keV. The thick target absolute gamma yield has been previously reported for proton energies up to 4.2 MeV [7]. Some of the results are presented in Table II-A-1.

Yield of ^{7}Li(p,p'γ)^{7}Li [photons/mC-steradian]		
E_p= 1.7 MeV	E_p= 2.4 MeV	E_p= 3.1 MeV
8.6 x 10^6	2.6 x 10^7	5.6 x 10^7

Table II-A-1: Thick target gamma-ray yield resulting from the proton bombardment of lithium[7].

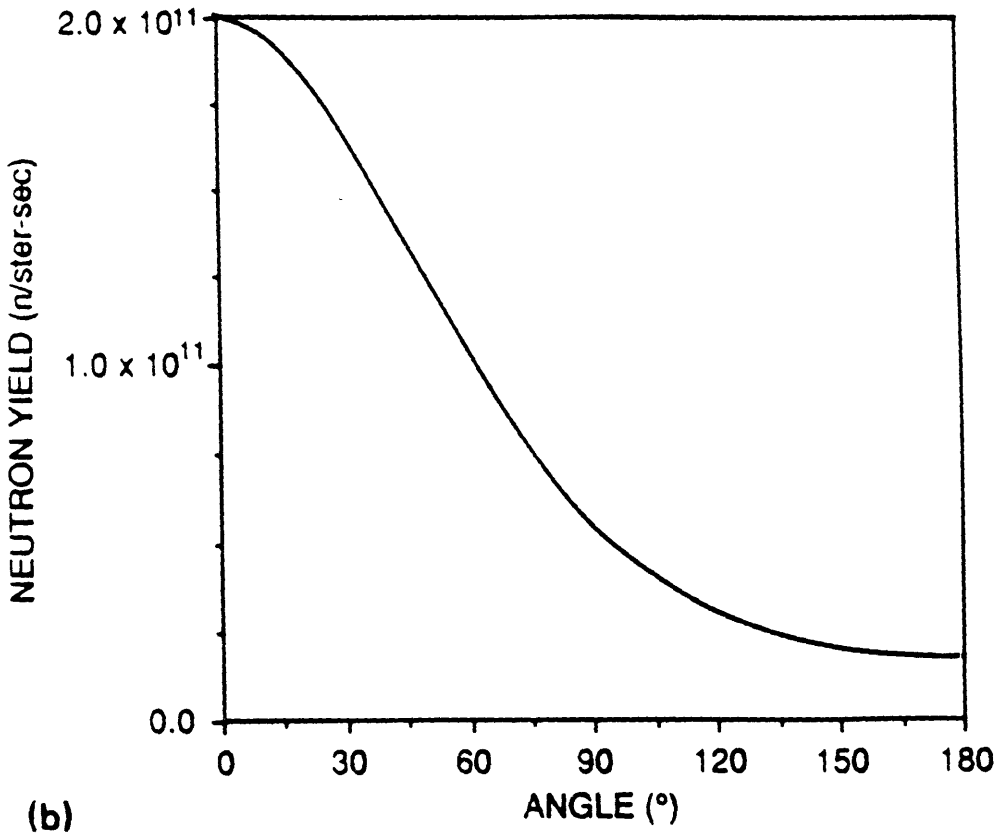

Figure II-A-1: Neutron yield versus angle for $^{7}Li(p,n)$ reaction.

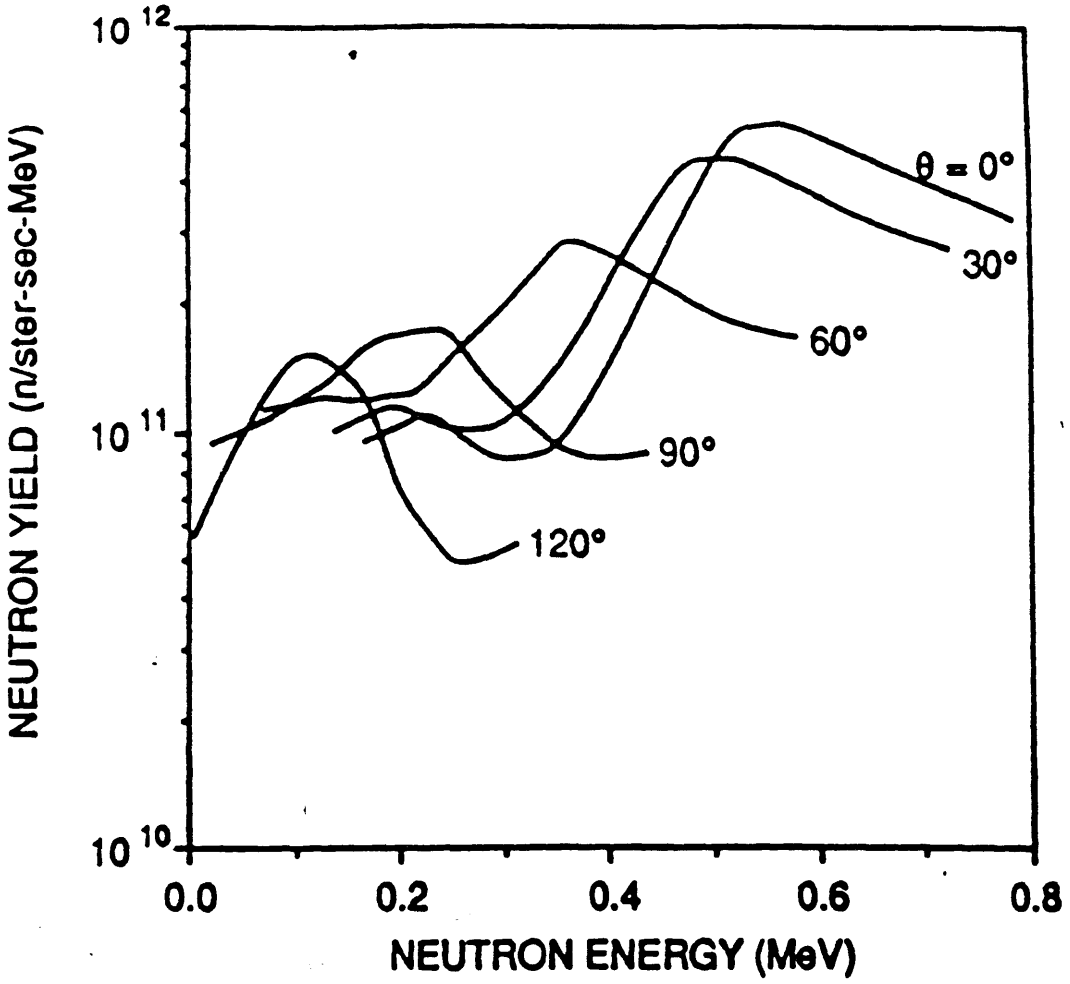

Figure II-A-2: Neutron energy spectrum for $^{7}Li(p,n)$ reaction.

II.B ^{9}Be(d,n)

The second reaction to be considered in this chapter is ^{9}Be(d,n). Unlike lithium, beryllium has excellent thermal properties. Beryllium is better suited as a high current target, when compared with lithium, due to its higher melting point (1290 °C) and superior thermal conductivity (190 W/m °C) [1]. The mechanical and physical properties of beryllium make it an ideal high current target. It can easily be made into a practical target which can withstand both water and vacuum pressures. The ^{9}Be(d,n) reaction is exothermic, in contrast to the two (p,n) reactions discussed in this chapter, and produces energetic neutrons which must be extensively moderated for AB-BNCT. The maximum Q-value of the reaction ^{9}Be(d,n)^{10}B is +4.36 MeV. The reaction may also proceed to many excited states in ^{10}B. There are several endothermic reactions which can also occur, such as (d,2n), (d,pn) and (d,p2n) [8]. The total thick target neutron yield has been measured for deuteron bombarding energies E_d = 2.6-7.0 MeV at 0 degrees[8]. During the measurement of the reaction ^{9}Be(p,n) discussed in Section II-C, some of these measurements were repeated and confirmed. Both sets of measurements were absolute, independent, and were made only at 0 degrees. The angular distribution of the neutron production is not available in the literature. When this reaction is used in Chapter III, it is assumed that the neutron production at 0 degrees is representative of the neutron production at all angles.

The yield of this reaction is a steadily increasing function of deuteron bombarding energy. This relation is shown in Figure II-B-1. Although this reaction is prolific, the

Figure II-B-1: Increase in neutron yield with increasing deuteron energy for the reaction $^{9}Be(d,n)$

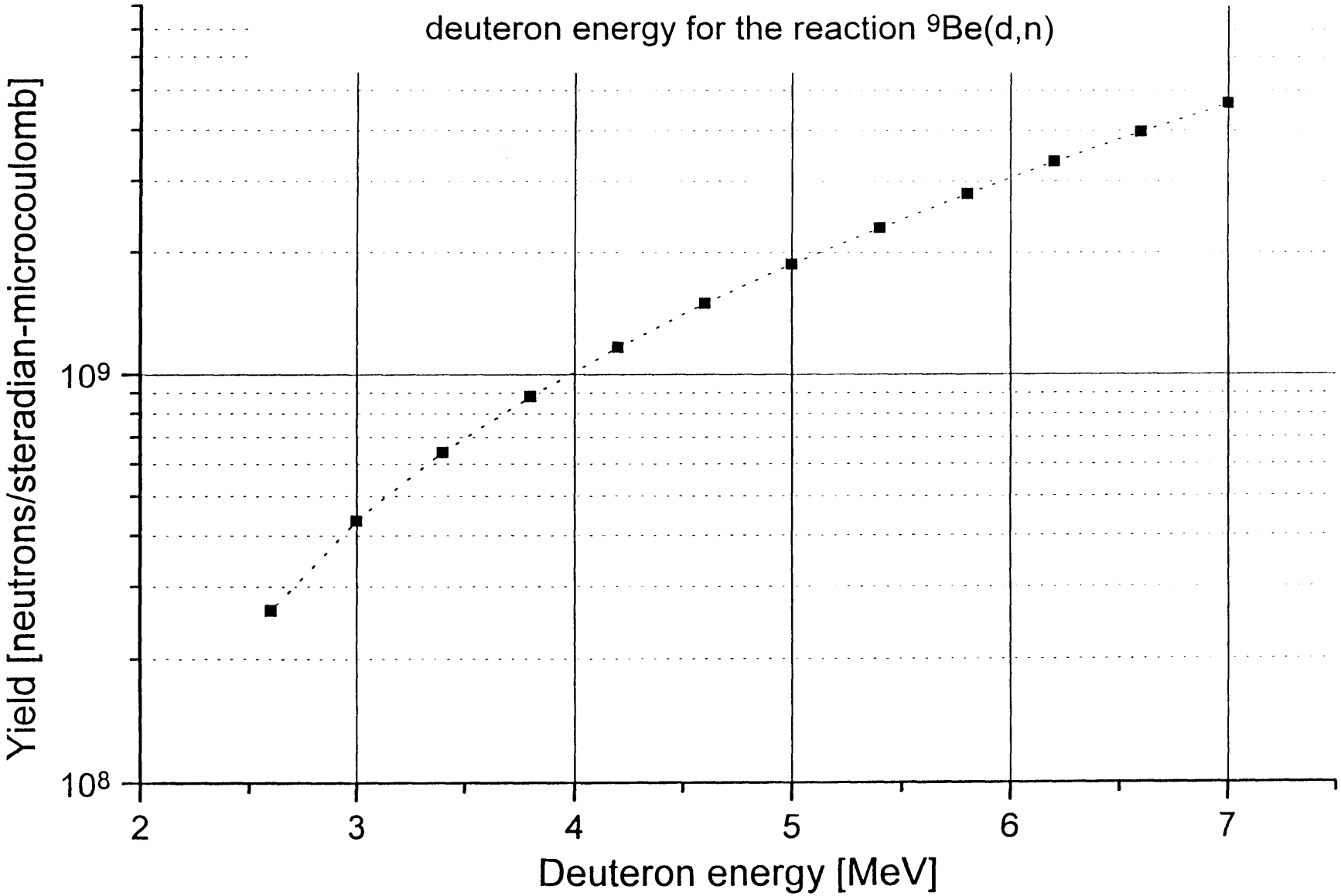

average neutron energy may be problematic for AB-BNCT, because the extensive moderation of the neutrons severely reduces the neutron intensity [9]. Figure II-B-2 depicts the increase in average neutron energy as a function of the incident deuteron energy [8]. Even with the lowest deuteron energy shown (2.6 MeV) the average energy exceeds the maximum neutron energy for the reaction ^{7}Li(p,n), E_p=2.5 MeV (which is approximately 800 keV), and is near the maximum for ^{9}Be(p,n), E_p=4.0 MeV (which is approximately 2.2 MeV). Results which will be presented in Chapter III of this thesis, indicate that the high neutron energy resulting from 2.6 MeV deuteron bombardment is, indeed, a problem for AB-BNCT. These early disappointing results precluded the consideration of higher energy deuteron bombardment. The neutron spectrum of the reaction, using 2.6 MeV deuterons, is shown in Figure II-B-3 [8].

In addition to the production of neutrons, the deuteron bombardment of beryllium also leads to the production of gamma rays. There is only limited data in the literature concerning this reaction. The cross section for photon production reaches a maximum value of 10.1 $\pm$ 3.5 μb at E_d=0.96 MeV [10].

II.C ^{9}Be(p,n)

II.C.1 Introduction

The ^{9}Be(p,n) reaction is the least prolific of the reactions considered in this chapter, at proton or deuteron bombarding energies below 4.0 MeV. However the reaction is still a strong candidate for an AB-BNCT neutron source for two reasons. First,

Figure II-B-2: Increase in average neutron energy with increase in deuteron energy for the reaction $^{9}Be(d,n)$

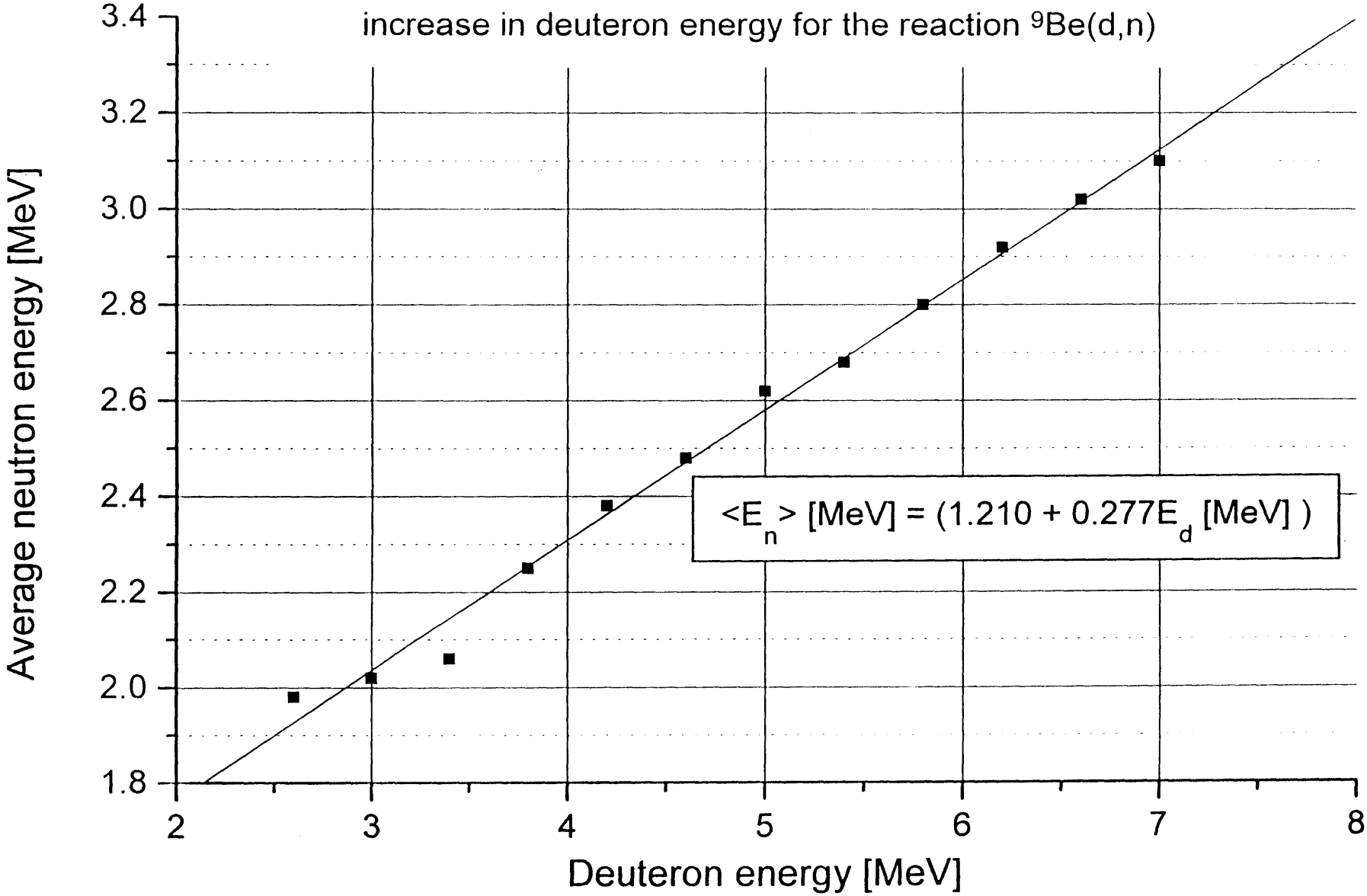

Figure II-B-3: Neutron spectrum of the reaction
$^{9}Be(d,n)$, E_d=2.6 MeV, 0 degrees

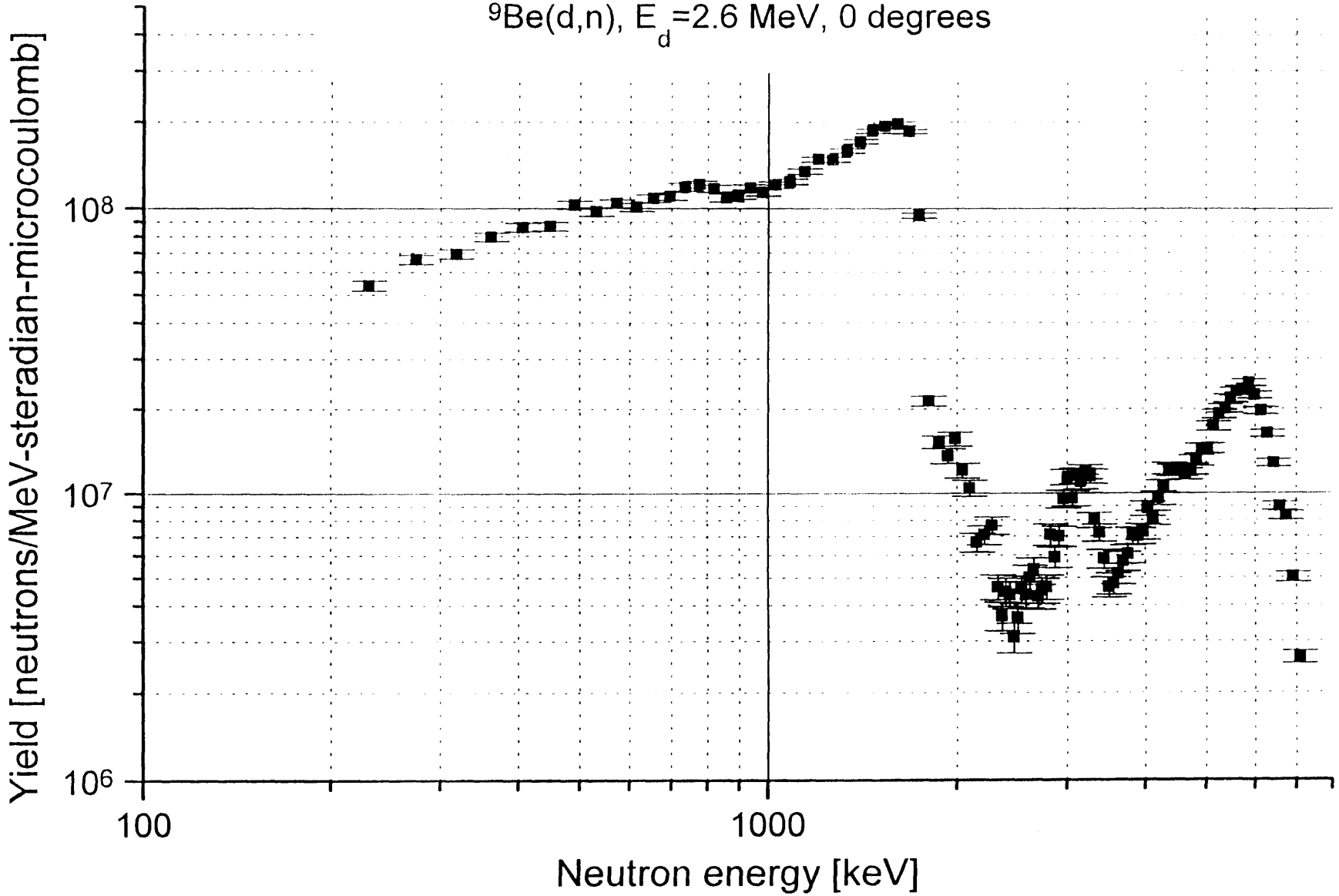

as previously stated, beryllium is an excellent material for a high current target primarily due to the superior thermal and mechanical properties of beryllium compared with lithium discussed in section II.B. Second, since the reaction is endothermic, the average neutron energy is not excessively high even when using E_p=4.0 MeV. At this proton energy, the average neutron energy is below 1 MeV. At lower proton bombarding energies, the average neutron energy is even more favorable. Prior to this work, accurate thick target neutron spectra were not available for proton bombarding energies below 4.0 MeV. This lack of data has prevented the accurate evaluation of the suitability of this reaction for AB-BNCT. The purpose of this section is to provide information about the reaction (at energies $E_p \leq 4.0$ MeV) and to present the measurements which have resulted in such thick target neutron spectra.

One study of this reaction using E_p=4.0 MeV for AB-BNCT was conducted by Wang and Moore in 1994 [11]. This study was based on calculated neutron yields and spectra, and no experimental measurements were made. The calculations were based on the limited data which were available in 1994, and which are discussed in Section II.C.1.b. The study concluded that this reaction would be slightly better for AB-BNCT than the reaction ^{7}Li(p,n). The research by Wang and Moore provided much of the motivation for the measurements presented here.

II.C.1.a Neutron production channels

The reaction ^{9}Be(p,n), as it is generally discussed, is actually several distinct reactions. Throughout this thesis, the notation ^{9}Be(p,n) will symbolize, collectively, all reactions in which neutrons are produced from the proton bombardment of beryllium. A list of all known reactions which take place below E_p=4.0 MeV, is presented in Table II-C-1. The first of these reactions is more accurately symbolized as ^{9}Be(p,n)^{9}B. This reaction proceeds through the formation of a compound nucleus, ^{10}B. When the reaction proceeds directly to the ground state of ^{9}B, the neutrons generated are referred to as the "ground state group", and given the notation n_0. The threshold of this reaction is 2.059 MeV. The threshold for the reaction to proceed to the first excited state of ^{9}B, generating the n_1 neutron group, is approximately 4.64 MeV [12], and therefore this reaction channel is not considered in this section.

Reaction	Q Value
^{9}Be(p,n)^{9}B	-1.9
^{9}Be(p,p'n)^{8}Be	-1.7
^{9}Be(p,p')^{9}Be* $\rightarrow$ n + α + α	-1.6
^{9}Be(p,p')^{9}Be* $\rightarrow$ α + ^{5}He $\rightarrow$ n + α	-2.5

Table II-C-1: Neutron producing reactions for ^{9}Be(p,n), $E_p \leq 4.0$ MeV [13].

One unique aspect of the isotope ^{9}Be is that it has the lowest neutron binding energy (1.67 MeV) of any stable isotope. As a result, the three-body breakup of ^{9}Be can occur for incident proton energies as low as 1.85 MeV [12]. This process is labeled as ^{9}Be(p,p'n)^{8}Be. The last two reactions are often collectively referred to as (p,p')(n) reactions, which proceed through the excited state ^{9}Be* [12].

II.C.1.b Previous measurements

Some of the first quantitative measurements of the $^{9}Be(p,n)$ reaction were made in the early 1950s using photographic film [14]. These studies used a thin beryllium target, and proton energies near 3.8 MeV. The results clearly showed the existence of a large n_0 group. and a significant lower energy neutron continuum. Since that time, many other measurements have been made at proton energies from threshold to 4.0 MeV. Table II-C-2 contains a list of these studies, as compiled by Byrd [15]. It is important to note that many of these measurements were undertaken to investigate the properties of a particular nuclear energy level. These experiments often consisted of relative measurements of neutron production at various laboratory angles, and in each case, thin targets were used. In most experiments, the neutron group of interest was the n_0 group, and the researchers would deliberately detect only neutrons in this group.

In the late 1950s two important experiments were conducted to generate the neutron excitation function [16] [17]. The excitation function is the total thin-target neutron production cross section, integrated over all angles and neutron energies, as a function of the proton bombarding energy. The excitation function is shown in Figure II-C-1. The cross section rises rapidly from threshold to a value of 160 mb, at a resonance of E_p=2.56 MeV. A second resonance was identified at 4.6 MeV [12]. Between these two resonances, the neutron production is attributed to a third broad resonance centered at 3.5 MeV [17] [12]. This broad resonance is believed to be responsible for the neutron production below the 2.56 MeV peak as well [17].

Reference (note a)	Year	E_n (note b)	Proton energies used [MeV]	Angles measured [laboratory] (note c)	Absolute Error [%] (note d)
Marion (16)	1956	none	2.1-5.1	(5) 0-150	(7-10)
		none	2.1-2.8	4π	
Marion & Levin (12)	1959	n_o	2.3-5.6	0,90	(10)
		none	2.3-5.8	90	
Gibbons & Macklin (17)	1959	none	2.1-5.4	4π	see note d
Albert (28)	1961	none	2.0-4.3	(10) 0-120	(25)
Kelsey (29)	1963	n_o	2.5-4.1	(9) 0-150	(10)
Walker (30)	1963	n_o	3.5-10.9	(9) 0-150	(20)
Bair (31)	1964	none	4-14.3	4π	(6)

Table II-C-2: Measurements of ^{9}Be(p,n) for $E_p \leq 4.0$ MeV[15].

Notes: (a) The number in parenthesis corresponds to the reference number at the end of this chapter.
(b) "none" indicates that the neutron energies were not evaluated. "n_o" indicates that only the n_o group was measured.
(c) The number in parenthesis is the number of angles measured.
(d) Numbers in parenthesis have been assigned by the author of the review article. In the case of the research by Gibbons and Macklin, Byrd claims that this number is stated in the original work, as 3%. This does not seem to be supported by a careful reading of the original work. No clear statement of absolute error is reported in the original paper.

Because the threshold of the reaction ^{9}Be(p, p'n)^{8}Be is less than that of the ^{9}Be(p,n_o)^{9}B reaction, it is possible to evaluate the cross section of the former reaction below E_p=2.059 MeV. This value has been determined to be less than 1 μb [17]. At proton bombarding energies up to approximately 2.5 MeV, neutron production is dominated by the n_o group. Above approximately 3.0 MeV, the neutrons generated from (p, p'n) and (p,p')(n) reactions are more significant, and form a continuum of neutrons which is noticeable in the energy spectrum [12]. An exact evaluation of the percentage of neutrons in this continuum is difficult since the continuum extends through the n_o (and at higher energies, n_1) group [12]. One report states that the continuum neutron cross

Figure II-C-1: Excitation function of the reaction $^{9}Be(p,n)$ for $E_p \leq 4.0$ MeV

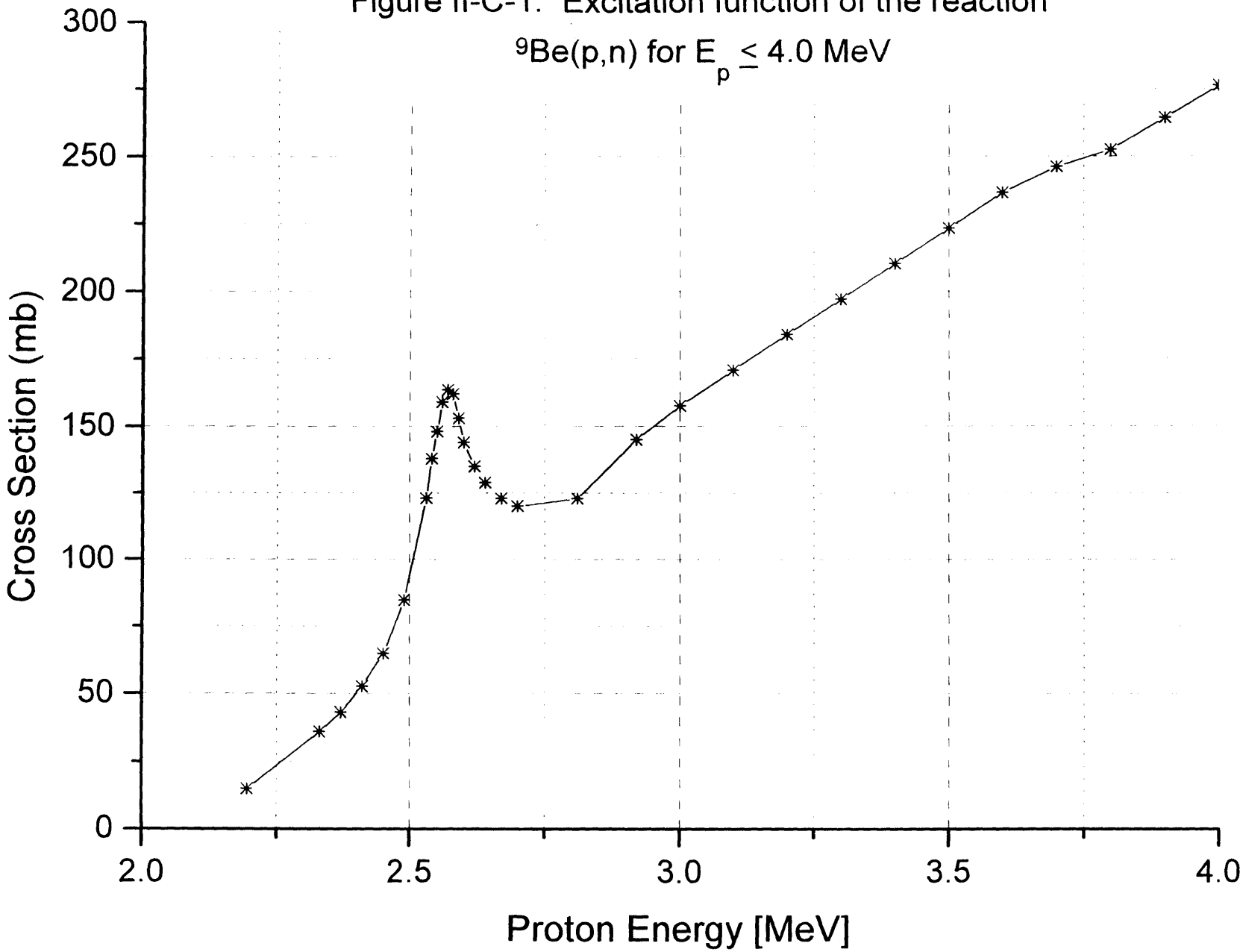

section at 90°, E_p=4.6 MeV, is 25 mb/steradian, compared with 11 mb/steradian for the n_o group. The corresponding figures at E_p=2.7 MeV are reported as 6 mb/steradian and 5 mb/steradian, respectively [12]. Another estimation is that the n_o contribution drops from 65% at E_p=2.5 MeV, to 30% at 5 MeV, and 5% at 18 MeV [15]. At much higher energies (above 15 MeV), the low energy continuum dominates the spectrum [18] [19].

As shown in Table II-C-2, there have been few studies which examine the neutron energy spectra in the energy range E_p< 4.0 MeV. One such experiment, using a thin target and E_p=4.5 MeV, found clear evidence for a low energy continuum, and anisotropy in the neutron production [12].

II.C.1.c Gamma production

In addition to the production of neutrons, the proton bombardment of beryllium results in a significant production of gamma rays. At energies below 5 MeV, gamma production comes from only two sources: proton capture (which is relatively insignificant), and the $^9Be(p,\alpha)^6Li^*(\gamma)^6Li$ reaction [16]. The latter reaction produces a 3.562 MeV gamma photon. The thick target absolute gamma yield has been previously reported at energies up to 4.2 MeV [7]. A sample of these results is presented in Table II-C-3.

Yield of $^9Be(p,\alpha_1\gamma)^6Li$ [photons/mC-steradian]				
E_p= 1.7 MeV	E_p= 2.4 MeV	E_p= 3.1 MeV	E_p= 3.8 MeV	E_p= 4.2 MeV
0.1×10^6	2.5×10^7	2.5×10^9	5.1×10^9	6.2×10^9

Table II-C-3: Thick target gamma-ray yield resulting from the proton bombardment of beryllium[7].

II.C.1.d Introduction to recent measurements

Because the thick target neutron production spectra data did not exist in the literature for the reaction ^{9}Be(p,n), using proton energies below 4.0 MeV, it was necessary to use neutron time-of-flight (TOF) to attain these data experimentally. It would theoretically be possible to calculate the thick target spectra knowing the double differential cross section, $d^2\sigma/d\Omega_n dE_n$ as a continuous function of E_p, E_n, and Ω_n. However, this type of information is incomplete in the literature, and as previously mentioned, many of the experiments were performed to specifically limit, or discriminate against, the low energy neutron continuum. For these reasons the direct approach of measuring the thick target spectra was chosen.

These measurements were carried out primarily for use in AB-BNCT research. However, because the neutron production threshold of this reaction is low and the thermal properties of beryllium are favorable for heat removal, the reaction is an important high intensity source of neutrons for many applications. One possible use of detailed spectral information is the use of this reaction as a calibration standard for neutron detectors. Other possible uses are neutron radiography, neutron interrogation of materials, and the calibration of dosimeters [18].

The goal of this project was to accurately measure the neutron spectra, and to provide a data set which would be useful to the scientific community. An important aspect of this goal is that absolute measurement of the reaction was desired. In many cases, relative measurements are adequate for the needs of the scientific community. For AB-BNCT applications, absolute measurements are needed since the radiation dose rates are proportional to the absolute yield of the reaction. As will be shown below, the total neutron yields at various proton bombarding energies estimated by these measurements differed from the predicted values. Therefore, a relative measurement scaled to the absolute predicted yield would have been in error. As will be discussed below, the measured and predicted values of total yield differ by approximately 20% for E_p=3.7 MeV and by approximately 25% for E_p=4.0 MeV. The data presented in this section are absolute - no normalization has been used.

The TOF measurements were made at the Ohio University Accelerator Laboratory (OUAL) during two series of experiments in November 1995 and August 1996, using 4.0, 3.7, 3.4, and 3.0 MeV protons. In this section, the November 1995 measurements will be collectively referred to as Group A, and those taken in August 1996 as Group B. The complete data set is located in Appendix B. Appendix B includes a graph of each neutron spectrum measured. This appendix also contains the data in tabular form. These tables provide the neutron yield and total statistical uncertainty for each energy bin, and each spectrum. The remainder of Section II.C will describe these measurements in detail

including the method of calibrating the neutron detectors, and a presentation of some of the results. The section will conclude with some suggestions for further measurements.

II.C.2 Experimental methods and equipment

II.C.2.a Introduction to time-of-flight

Standard TOF techniques were used in the determination of the neutron energy spectra from the reaction ^{9}Be(p,n). Neutron TOF is a method of determining the kinetic energy of a neutron by measuring its velocity, since $E_{KIN}=mv^2/2$. (The neutron energies measured in this experiment were less than 2.5 MeV; therefore, a non-relativistic treatment is appropriate.) The velocity is determined by the simple equation velocity=length/time, or more completely: $V=(X_2-X_1)/(T_2-T_1)$. The quantity (X_2-X_1) is the "path length" or "L". The quantity (T_2-T_1) is the time-of-flight (TOF), or T. Typically, L is held constant by fixing the location of the neutron source (in this case, a beryllium target) and the neutron detectors. To measure TOF, one must accurately determine both T_2 and T_1. In the case of charged particle induced reactions, such as ^{9}Be(p,n), a pulsed proton beam is used and a circuit called a "beam pick-off" (BPO) generates an electronic signal just before the proton pulse strikes the target. The BPO starts the timing sequence at T_1. If a neutron is produced at the target, in the direction of a neutron-sensitive detector located at $X=X_2$, then a neutron event will cause a second electronic signal to be generated at T_2. Normally, a time-to-amplitude converter (TAC) charges a capacitor for a period of time equal to T_2-T_1 creating a voltage proportional to

the TOF. This voltage amplitude is then digitized using the TOF analog-to-digital converter (TOF-ADC).

Rearranging $E=mv^2/2$ yields, $v=(2E/m)^{1/2}$. Dividing both sides of this equation by c yields: $(v/c) = (2E/mc^2)^{1/2}$. Since mc^2 for a neutron is 939.55 MeV, $(v/c)=(2E/939.55)^{1/2}$, where E is measured in units of MeV. As an example, the velocity of a 1 MeV neutron is: $v=(3x10^8 \text{ m/s})(2\bullet 1/939.55)^{1/2} = 1.38x10^7$ m/sec. Using a path length of 10 m results in a TOF of 723 nanoseconds. Repeating this same calculation for a 950 keV neutron, yields TOF=741 nanoseconds. So, to resolve the difference between a 950 keV neutron, and a 1 MeV neutron, the detector and associated electronics must respond faster than 18 nanoseconds. Because energy is a function of the square of the velocity, the fast timing requirements are more stringent for higher energies. For a 10 m flight path, the TOF difference between a 2 MeV and a 1.95 MeV neutron is 6.5 nsec. These examples illustrate the need for fast timing circuits for neutron TOF measurements.

Since the energy information is encompassed in the values of L and T, the uncertainty of the energy has two components: $\Delta L/L$ and $\Delta T/T$. The ΔL uncertainty is primarily due to the thickness of the detector (the neutron producing target is thin, and the distance from the target to the midpoint of the detectors can be accurately measured). When a neutron event is detected, one only knows that the event was generated somewhere in the active volume of the detector. For example, a 1 cm thick neutron detector used at L=10 m, would have $\Delta L/L = 0.001$. The uncertainty in the timing

resolution is more complex, and depends on the choice of detector and circuit components. Typical timing circuits and detector arrangements have ΔT on the order of 1 nsec. For the measurements presented here, this is also approximately the width of one TOF-ADC channel.

Low-energy neutron TOF measurements are hindered by an effect called "wrap-around". If two successive proton pulses, N and N+1, arrive at the target and produce neutrons with various energies, it is possible that the fastest neutrons created in the second pulse will arrive at the detector before the slowest neutrons of the first pulse. Since the neutron detector cannot distinguish which pulse the neutrons came from, these signals must be discarded. This is called "wrap-around". The wrap-around problem effectively sets a limit on the lowest energy neutrons which can be resolved. The problem is more severe for faster pulse rate frequencies, and longer flight paths. Unfortunately, long flight paths are preferred in TOF measurements, as they allow for small values of the relative uncertainties of L and T, i.e., $\Delta L/L$ and $\Delta T/T$ are lower since L and T are larger. Lowering the pulse rate frequency lengthens the time required for the measurements. Therefore, there is a trade-off between experimental quality and speed of measurements on the one hand, and the lower energy limit of neutron measurement on the other.

II.C.2.b The Ohio University TOF facility

OUAL utilizes a tandem Van de Graaff accelerator, with a maximum terminal voltage of 4.5 MV, to produce proton pulses for neutron TOF measurements. A picture of the accelerator is shown in Figure II-C-2. H^- ions are produced in a ion source when positive cesium ions are made to strike the cathode target made of titanium hydride. Hydrogen atoms are sputtered from the cathode and gain electrons though charge exchange with cesium, which has deposited on the cathode surface. These sputtered atoms, now negatively charged, are repelled from the cathode and accelerated to ground potential. Electron suppression is accomplished through the use of permanent magnets mounted to the source housing. A negative voltage applied to the ion source causes the H^- ions to be injected into the low-energy extension of the accelerator. In this extension, the DC beam is chopped by allowing the beam to pass through the aperture of the klystron buncher at a frequency, $f=5/2^n$ MHz (n=0-6). Experiments at OUAL are usually conducted at f=5/8 MHz or f=5/16 MHz. For these measurements, f=5/16 MHz was used, allowing neutron energies down to 70 keV to be measured. The width of the chopped beam (FWHM) is approximately 50 nsec. The klystron buncher produces a pulsed beam with a width of approximately 750 psec [20].

The bunched beam is then accelerated in the low energy stage of the tandem Van de Graaff towards the high voltage terminal. Inside the terminal, a thin carbon foil stripper (2-3 $\mu g/cm^2$) removes 2 electrons and the resultant proton is accelerated away from the terminal to the end of the accelerating column. The axis of the accelerator is

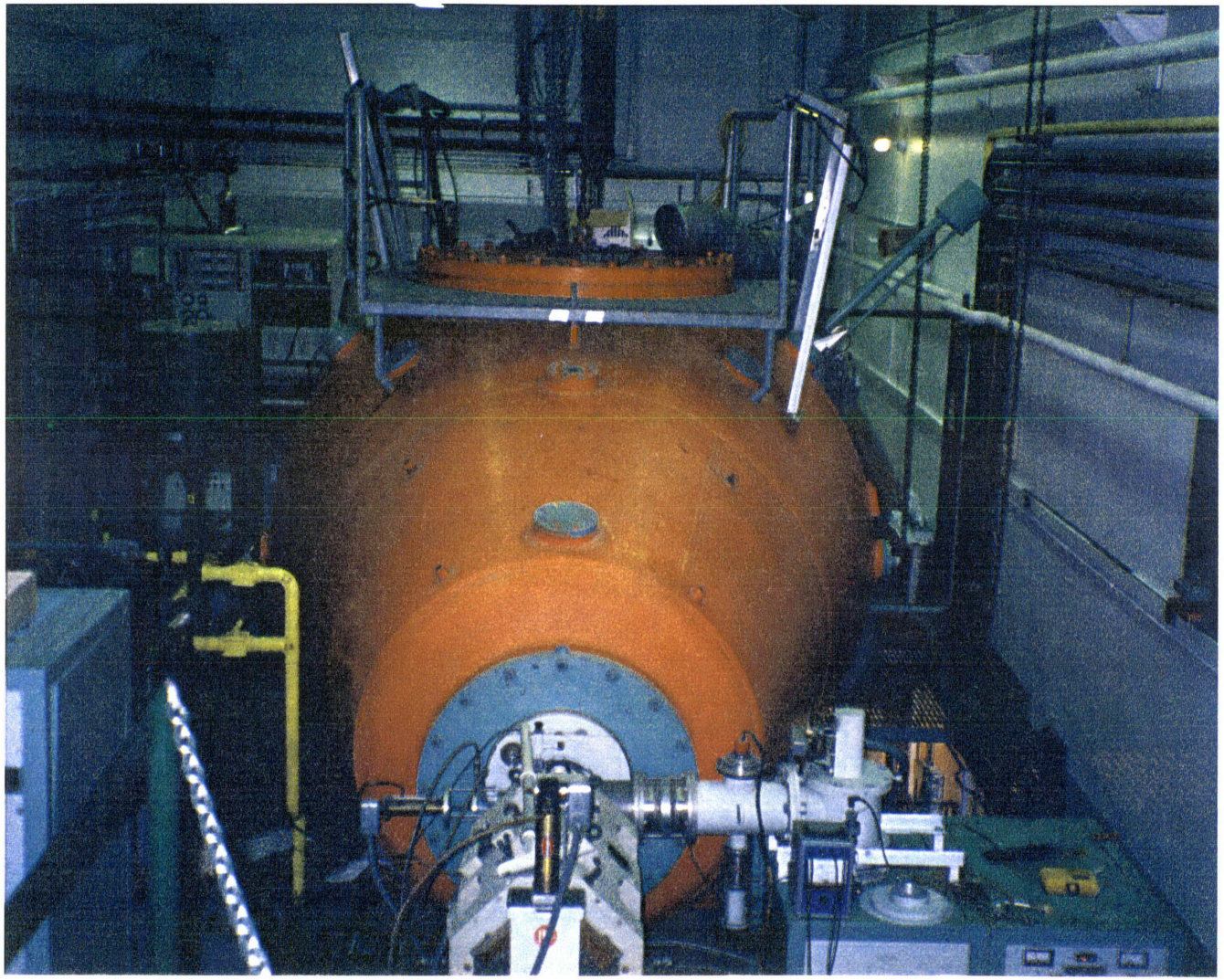

Figure II-C-2: The accelerator at OUAL

perpendicular to the axis of the flight tunnel, so the beam must be redirected by using the beam swinger [21]. The main components of the beam swinger are two magnets which alter the direction of the beam -45° and +135° respectively so that the proton beam direction changes by a net +90°. The entire swinger gantry is counterbalanced to allow rotation about the axis of the accelerator. Thus, the detectors can be set to record data for laboratory angles from -4° to +160° simply by rotating the swinger. Before striking the target, the beam passes through a capacitor circuit beam pick off used to generate the TOF record for a detected event. The target chamber is mounted at the end of the beam swinger gantry. The chamber contains a target wheel capable of holding eight targets which can be selected remotely. A picture of the target housing is shown in Figure II-C-3. The evacuated beam tube terminates at an extension called the "snout", which protrudes into the target chamber. An electron suppression screen is connected to this snout by an insulated bushing. Below the target wheel is a Faraday cup. During measurements, a 300 Volt battery is connected to an electron suppression screen to repel any secondary electrons back onto the target or chamber walls. The current on the snout, chamber walls, target wheel and Faraday cup, are combined to form the integrated current reading [21].

After the first series of measurements (Group A) a calculation of the total measured yield was made. The result was lower than expected (based on calculations using the excitation function [17] and stopping powers of protons in beryllium [22]), and several possible reasons for this disagreement were considered. The first is that a

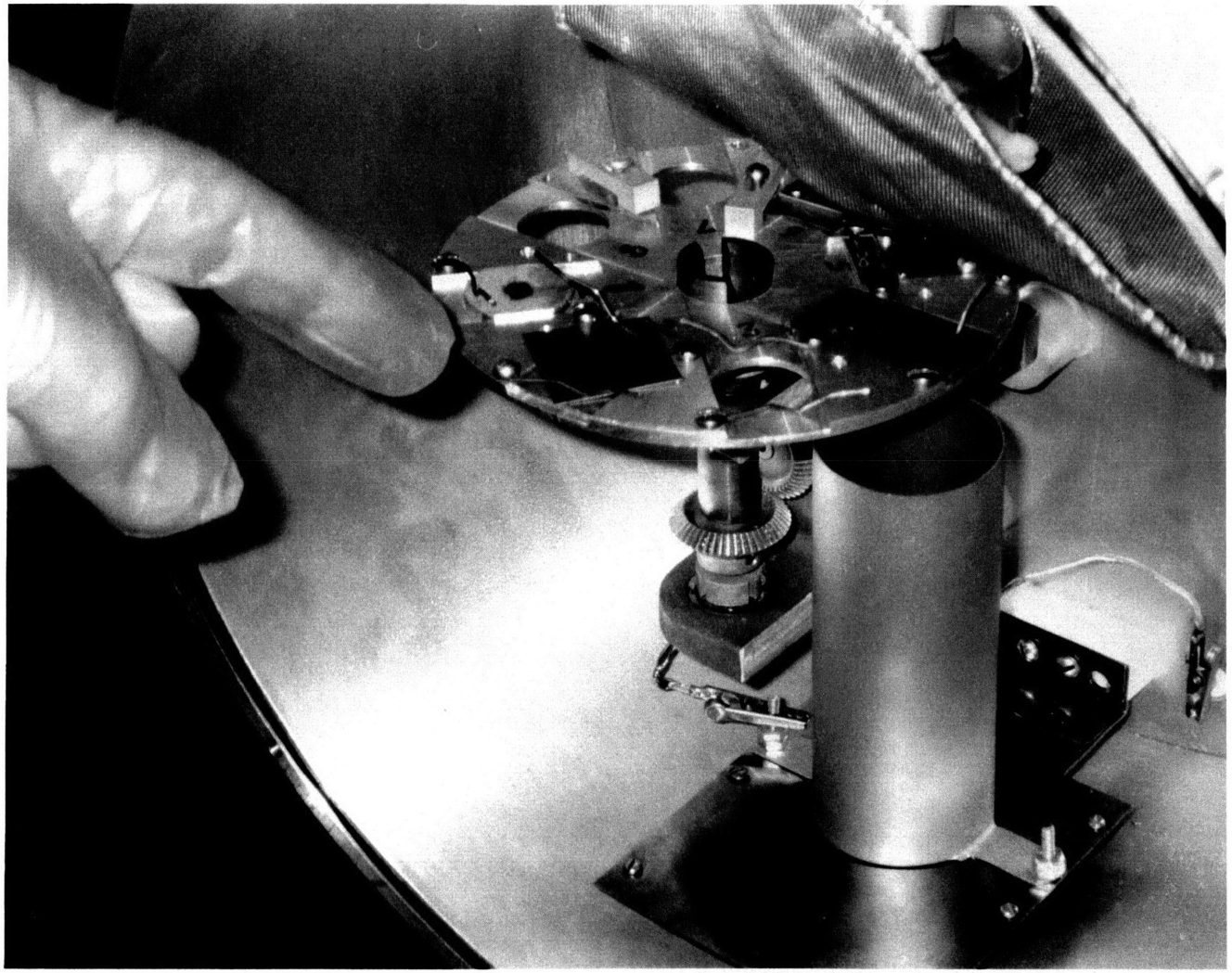

Figure II-C-3: Target chamber at OUAL.

significant portion of the yield was contained at angles greater than 110 degrees (not measured in Group A). One other possibility was that the charge collection circuit was not functioning correctly, and was introducing a systematic error. For this reason, the charge integrating circuit was tested extensively before the Group B measurements. A testing circuit was devised to ensure that the charge on each possible surface was being added to the current reading. The variation of current on the target wheel with changing electron suppression screen voltage was measured. It was determined that above 50 volts, the variation diminished rapidly and then remained steady over the remainder of the measurements, indicating that this voltage is enough to suppress the most energetic secondary electrons. With the beam running, the target wheel was rotated between various targets and blanks (open slots which allow the current to be collected on the Faraday cup). No variation on integrated current with target wheel position was seen. Additionally, a free floating current source (dry cell battery) and a resistor circuit, were used to check the absolute accuracy of the charge collection. This series of tests confirmed that the accuracy of the charge collection is better than 2 %. The charge collection circuit was identical for the Group A and Group B measurements, but was not tested before the Group A measurements.

The targets used for these measurements were 2.5 cm square, and 0.25 or 0.5 mm thick, and 99% pure in their beryllium content. These targets were thick enough to stop 4 MeV protons. Neutrons produced at the target must pass through a 30 cm collimator in a 1.2 m thick concrete wall before reaching the flight tunnel. The flight tunnel is

constructed with eight sections of concrete water conduit, which is buried beneath approximately 3 m of earth. The inner diameter of the conduit is 2.13 m and each section is 3.35 m long. A detector array capable of holding seven detectors is located at any distance from 4 to 30 m. For these measurements, a 10 m flight path was used. A picture of the flight tunnel, looking towards the target chamber, and showing the back of the detector array, is provided in Figure II-C-4. A diagram of the OUAL TOF facility is shown in Figure II-C-5.

II.C.2.c Neutron detectors

The evaluation of neutron spectra at energies below approximately 500 keV, and up to 2.5 MeV, requires the use of detectors which can generate discernible signals from the interaction of low and high energy neutrons. To yield accurate energy information, the detectors must also have the ability of generating fast timing information. Four lithium-loaded glass scintillators were used based on their fast response time and sensitivity to low, as well as high, energy neutrons [23]. The lithium glass detectors contained 6.6% weight fraction of lithium, which was enriched to 95% ^{6}Li. The detectors were 1.27 cm thick and 12.7 cm in diameter.

Lithium glass detectors work by creating a luminescence at a cerium activator site (Ce^{3+}) in a glass matrix. The energy to activate this site comes from the reaction $^{6}Li(n,\alpha)^{3}H$. For thermal neutrons, the triton carries away 2.72 MeV of energy, and the alpha particle 2.04 MeV. These charged particles then induce ionization along their paths

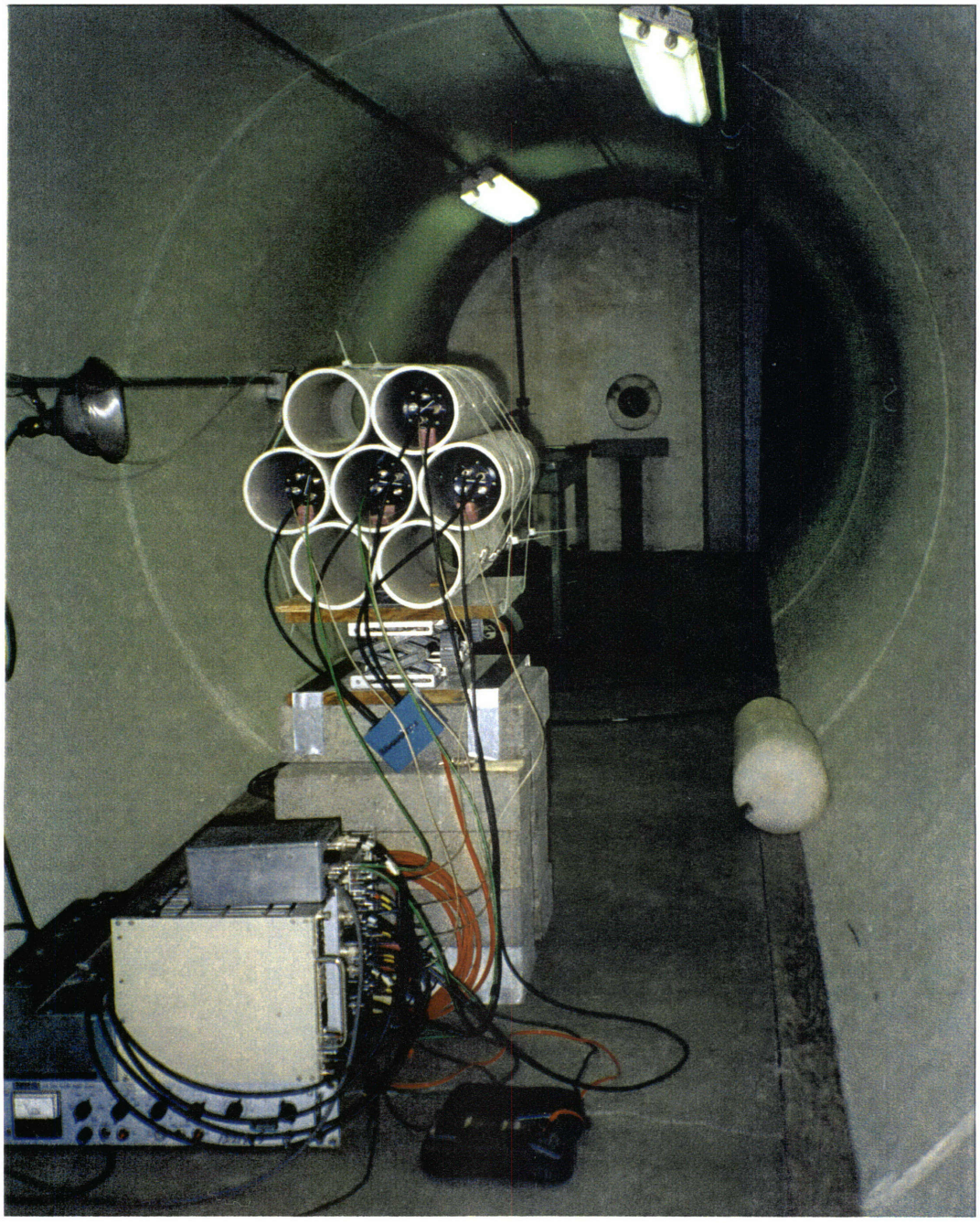

Figure II-C-4: TOF tunnel and detectors at OUAL.

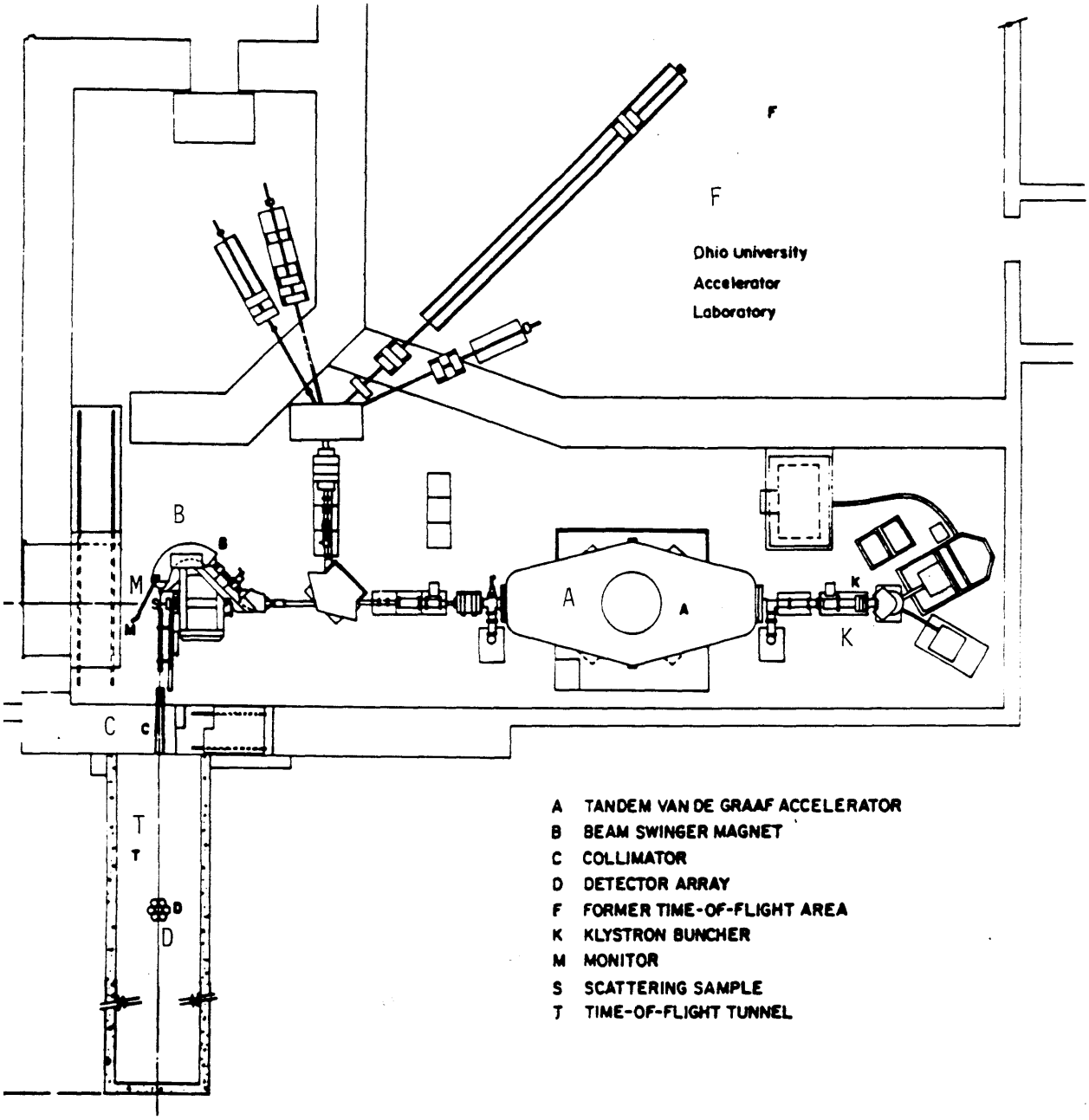

Figure II-C-5: OUAL Facility

through the glass. The secondary electrons created in turn activate the cerium centers, which give off light. This light is then collected by a photomultiplier tube [24].

The efficiency of the lithium-glass detectors were determined in a two step process. First, the neutron spectrum at 120° from the reaction Al(d,n), using 7.44 MeV deuterons, was measured using fission detectors. A stopping aluminum target was used, and the neutrons were detected using TOF techniques, with a fission chamber furnished by Argonne National Laboratory. The fission chamber used ultra-pure methane as a counting gas, and was composed of four ^{235}U foils: U-235-J, U-235P, U-235S, and U-235T, which have been previously described [25]. The Al(d,n) spectrum used for the calibration is shown in Figure II-C-6. The lithium-loaded glass scintillators were then used to measure the Al(d,n) spectra. Comparisons between the known and measured spectra of Al(d,n) yielded the intrinsic efficiency data for the detectors.

This calibration process works well at higher energies, but is problematic at low energies because the yield of the calibration reaction, Al(d,n), drops off rapidly below 300 keV. This occurs precisely near the rapid change in lithium glass efficiency caused by the 250 keV peak in the $^{6}Li(n,\alpha)$ cross section. For these measurements, the shape of the lithium glass efficiency curve below 250 keV was taken from the literature [23]. The absolute magnitude of the curve below 250 keV was then scaled to match the experimentally determined efficiency at 250 keV. The efficiency of the detectors was analyzed separately for data Groups A and B. For Group A, the scaling factor used to

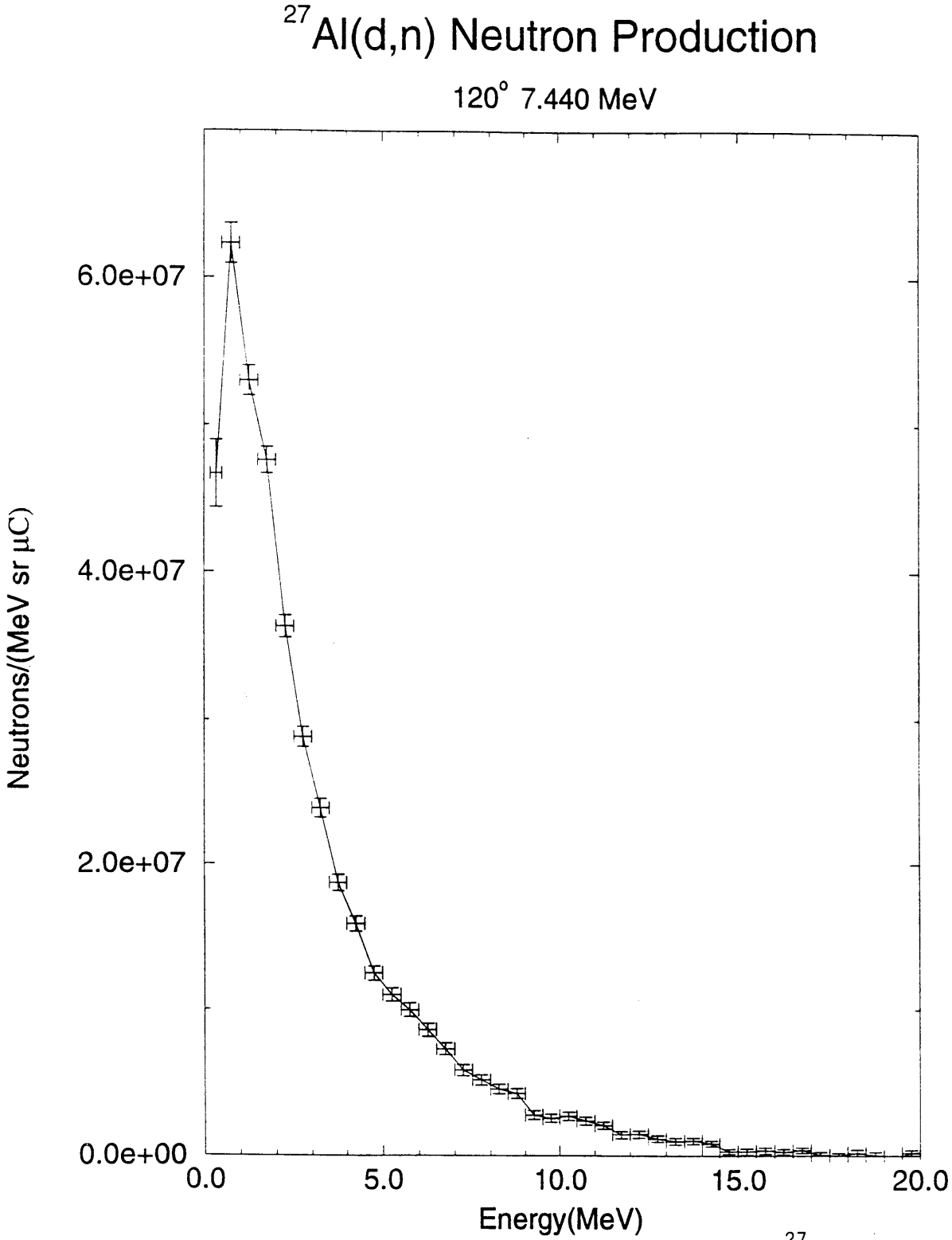

Figure II-C-6: Neutron spectrum for the reaction ^{27}Al(d,n)

match the data in the literature was near 1.0. For Group B, the detector efficiencies measured at OUAL were lower than the data in the literature. Below 250 keV, the data in the literature were multiplied by 0.756. The difference in the scaling factors (1.0 and 0.756) results from differences in the photomultiplier bias voltages. These efficiency curves were then fitted by polynomial equations to yield efficiency functions that are continuous in energy. This process resulted in a lithium glass efficiency curve shape very similar to those of Neill et al., over the region of interest for these measurements ($E_n < 3$ MeV) [23]. The average lithium glass efficiency used in the analysis of the Group A measurements is shown in Figure II-C-7.

II.C.2.d Data processing

The TOF, energy, pulse shape discrimination (PSD), and routing information (detector number) for each detector event are generated by the electronic components and circuits depicted in Figure II-C-8. The result of this process is the generation and storage of a series of data files containing the channel signals for several analog-to-digital converters (ADC). Each of these ADC data files corresponds to a different physical quantity such as the integrated light yield of the detected event, or the time-of-flight.

During the experiments, these ADC data files were stored temporarily on the data acquisition computer, and then transferred to a UNIX workstation to be analyzed. The analysis of the ADC data to produce the neutron spectrum is accomplished with a single FORTRAN program which executes a number of processing steps. The first step is the

Figure II-C-7: The average lithium glass efficiency used for Group A

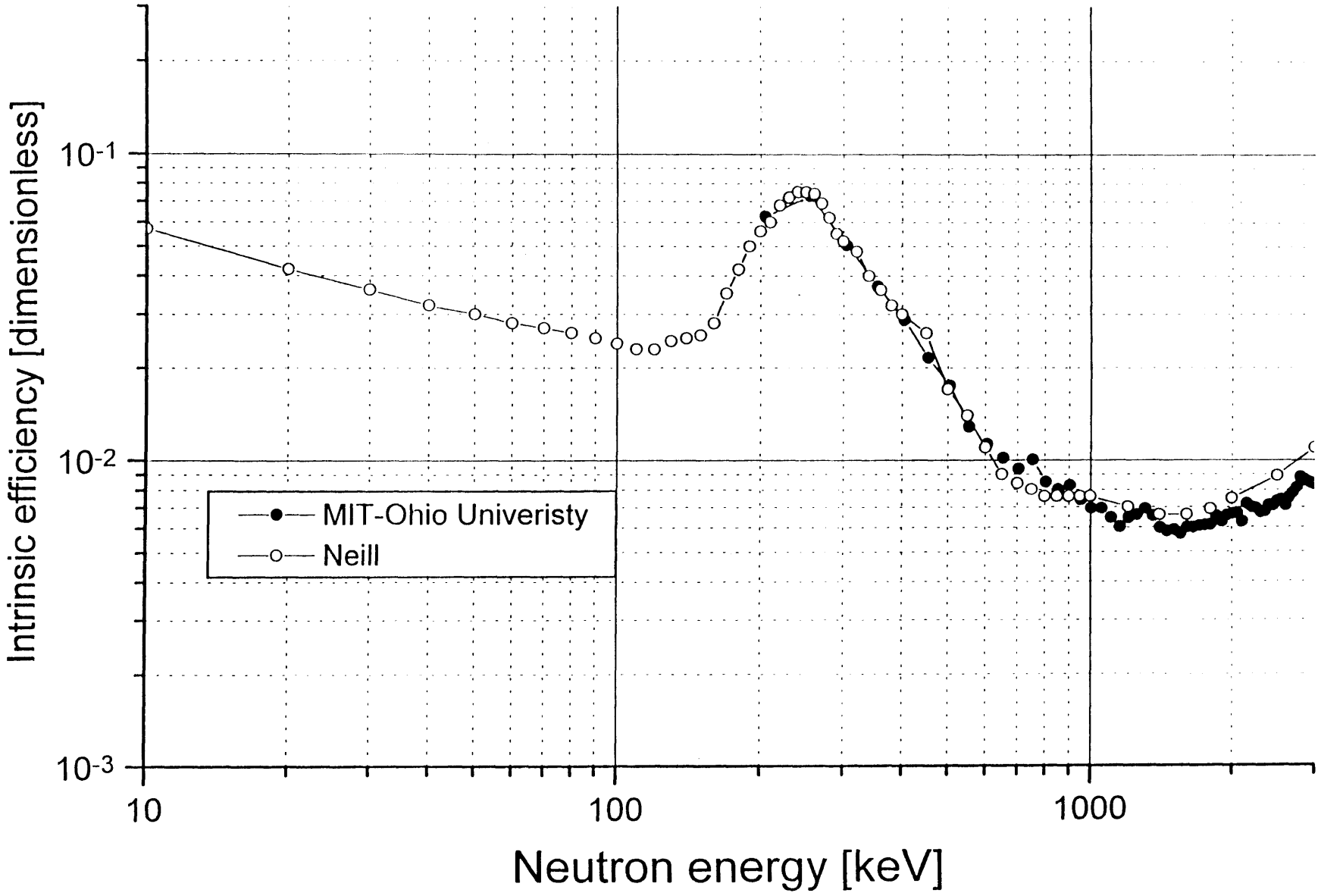

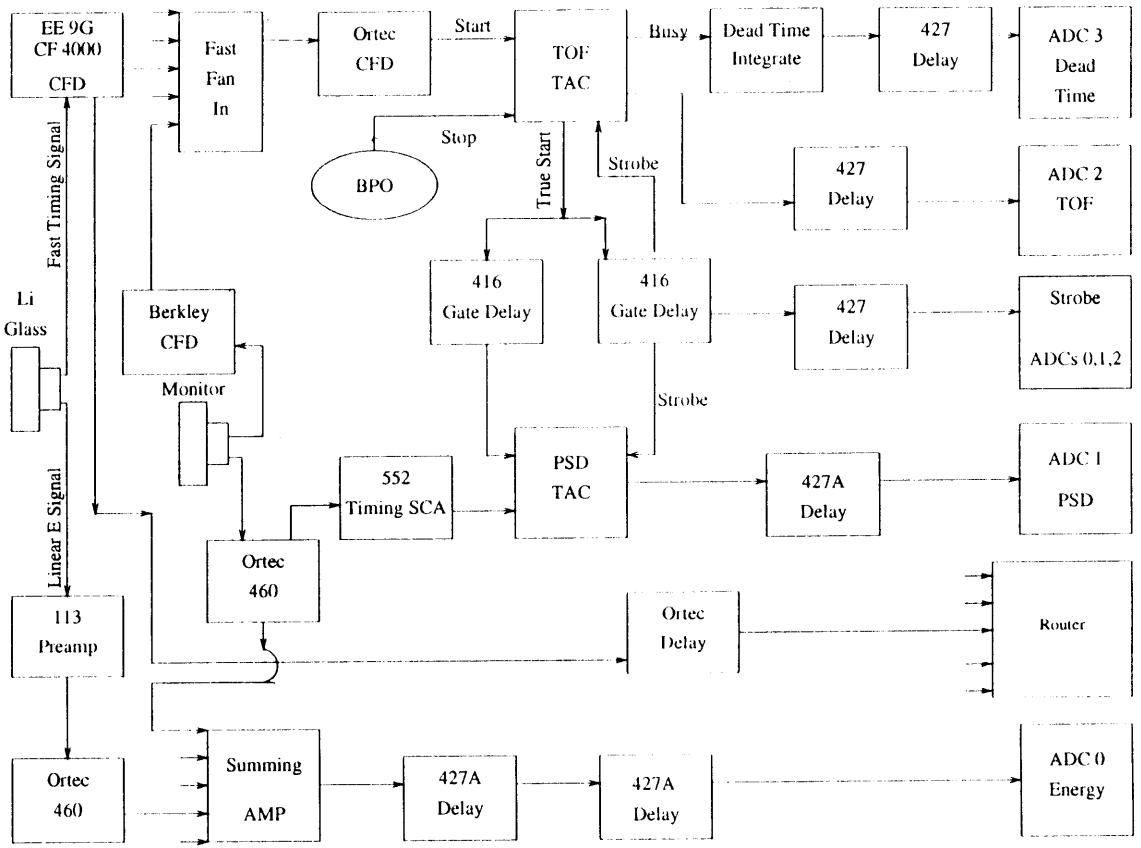

Figure II-C-8: TOF electronics circuit.

assignment of flight times, and corresponding neutron energies, for the various TOF-ADC channels. The methodology used for this assignment has been previously described [26]. The linearity of the time-to-amplitude converter is determined and used to subtract the background signal on a channel-by-channel basis. Next, each of these net signals is converted to neutron yield by dividing by the intrinsic detector efficiency, which is expressed as a continuous function of energy. The methodology used to generate this function will be discussed later. The individual detector yields are then grouped in energy bins, and finally, the various detectors are added together to form the total neutron yield for each energy bin. The propagation of the total statistical error is accomplished with the same FORTRAN program.

II.C.2.e Statistical and systematic error

The total statistical counting error is calculated during the execution of the FORTRAN processing program. The statistical error decreases with increasing total charge impinging on the target. As in the case of pulse rate frequency, there is a trade off between experimental quality, and length of the measurements. Calculations were made prior to the experiments to determine the number of counts in each channel of the TOF-ADC which would result in a statistical counting uncertainty of approximately 5%, using 25 keV energy bin widths, near E_n=1 MeV. During the measurements, the data were monitored and evaluated against this calculation. To achieve this degree of statistical quality, each configuration of angle and energy required an average of 3 hours for

acquisition. The total acquisition time of the data set was approximately 100 hours for the Groups A and B combined.

In addition to the statistical error, there are several factors which add to the systematic error of the results. The solid angle subtended by the detectors is measured by determining the diameter of the detector surface and the neutron path length. These are determined to within 2 mm. The detectors are aligned with the target by using an alignment telescope, and the flight path is measured by a metal ruler embedded in the flight tunnel. A calculation using the maximum expected deviations results in a solid angle uncertainty of 2%. The total integrated charge has been discussed above, and an absolute error of 2% is assigned to this value. The solid angle factor and integrated charge are multiplying factors for the data, and would affect the absolute value of the data, but not the shape of the individual spectra.

The uncertainty in the shape of the spectra is affected primarily by two quantities in addition to the counts in the TOF ADC channels. These are: the energy uncertainty and the detector efficiency uncertainty. Since the energy measurement is essentially a velocity measurement, it depends on accurate assignment of path length and TOF. The accuracy of the path length has two contributions: distance from target to detector face, and thickness of the detector. For a 10 m flight path (measured to within 2 mm), and a 1.27 cm thick detector, the $\Delta L/L$ uncertainty is approximately 0.1%. The timing uncertainty is dependent on a few factors. The width of the proton pulse, as discussed

above, is approximately 750 psec. The accuracy of the timing is optimized by taking the neutron event timing from one of the first dynodes in the photomultiplier tube amplifying chain. The neutron channels are assigned energies based on the position of the gamma peak, which results from gamma rays produced at the target. The width of this gamma peak is approximately 1-1.5 TOF-ADC channels, or approximately 1.5 nsec. The remainder of the timing uncertainty comes from the electronics, and accounts for an additional 1-1.5 nsec [21]. The total uncertainty in the timing is approximately 4 nsec. Since energy is proportional to TOF^2, the uncertainty affects the higher energy portion of the neutron spectra more than the lower portion. As mentioned in section II.C.2.a, the TOF difference between 2 MeV and 1.95 MeV neutrons is 6.5 nsec. Since the neutron spectra are binned in 20-50 keV bins, neutrons in the lower energy portions of the spectra are more accurately assigned to a bin, since the width of an energy bin (expressed in TOF) is large compared with the timing uncertainty. If a neutron with an energy near 2 MeV is assigned to the incorrect TOF ADC channel, it could more easily result in that neutron being counted in the wrong energy bin as well, since fewer TOF ADC channels make up that energy.

Finally, the accuracy of the shape and magnitude of the spectra are both affected by the accuracy of the detector efficiency calibration. The interaction cross section of the fission foils is known to better than 3%; however, the weight, and hence, thickness of the foils has an uncertainty of $\pm$ 5% [25]. The efficiency calibration is also dependent on the statistical quality of the Al(d,n) measurements, which is approximately 5% , combined

with a systematic error of approximately 5% [27]. At energies below 250 keV, the efficiency determination is dependent on the accuracy of the initial calibration data in the literature [23]. The error introduced by transcribing this data from the literature is difficult to judge. Considering all of these effects, the detector calibration efficiency is assigned an error of 15% above 250 keV, and 20% below 250 keV.

The total error in the absolute magnitude of the neutron spectra data, then, is estimated to be less than 20 % above 250 keV, and 25% below 250 keV. At the higher energy portion of the various spectra, there is some additional inaccuracy in the shape of the curves due to the previously mentioned effects of timing uncertainty. This shape uncertainty is most easily seen by examining the highest energy portion of each spectrum. Here, the yield should drop rapidly to zero at an energy dictated by kinematics. How slowly the yield drops gives an indication of the timing, and hence energy, uncertainty. This drop would be even sharper for even faster detectors such as plastic scintillators.

II.C.2.f Confirmation of spectra using ^{9}Be(d,n) reaction

To confirm the accuracy of the detector calibration procedure, and all other aspects of the measurement process (time calibration, charge collection accuracy, programming, etc.), the measurement of the Group B ^{9}Be(p,n) spectra was immediately preceded by thick target measurements of the reaction ^{9}Be(d,n). This reaction was measured (on an absolute basis) at 0°, for E_d=2.6-7.0 MeV, at 400 keV intervals. These results were then compared to data in the literature [8]. One such comparison, using 4.6

MeV deuterons, is shown in Figure II-C-9. The error bars reflect only the total statistical error. The ^{9}Be(d,n) data are discussed in section II-B.

The agreement between the two data sets is very good above 500 keV. Between 600 keV and 3 MeV, the maximum dissagreement is about 10%. In the region above 1 MeV, Meadows presents a third set of data which agrees with his earlier data to within 10% [8]. The neutron energy spectrum above 1 MeV shown in Figure II-C-9 is consistent with both sets of measurements. Between 250 keV and 500 keV, the neutron spectra measured at OUAL consistently fall below those of Meadows by approximately 25%. The maximum disagreement is near 290 keV. At this energy, the stated statistical uncertainty of the Meadows data is 4.1%, in addition to a total systematic error of 4%.

The discrepancy between 250 keV and 500 keV is difficult to explain because the cross section of the ^{6}Li(n,α) reaction and the efficiency of the lithium glass detectors are well known in this energy region. As shown in Figure II-C-7, the lithium glass efficiency determined during these measurements agrees well with the results of Neill. One possibility is that Meadows used different cross sections to determine the fission foil detector efficiencies. Also, because Meadows used fission foil detectors for his measurements, he avoided the difficulty of calibrating lithium glass detectors, and his calibration procedures had one less step than those used by MIT/OUAL in August 1996. By reducing the number of calibration steps, Meadows' data would potentially have fewer sources of error.

Figure II-C-9: Comparison of OUAL/MIT and Meadows measurement of $^{9}Be(d,n)$, E_d=4.6 MeV neutron spectrum

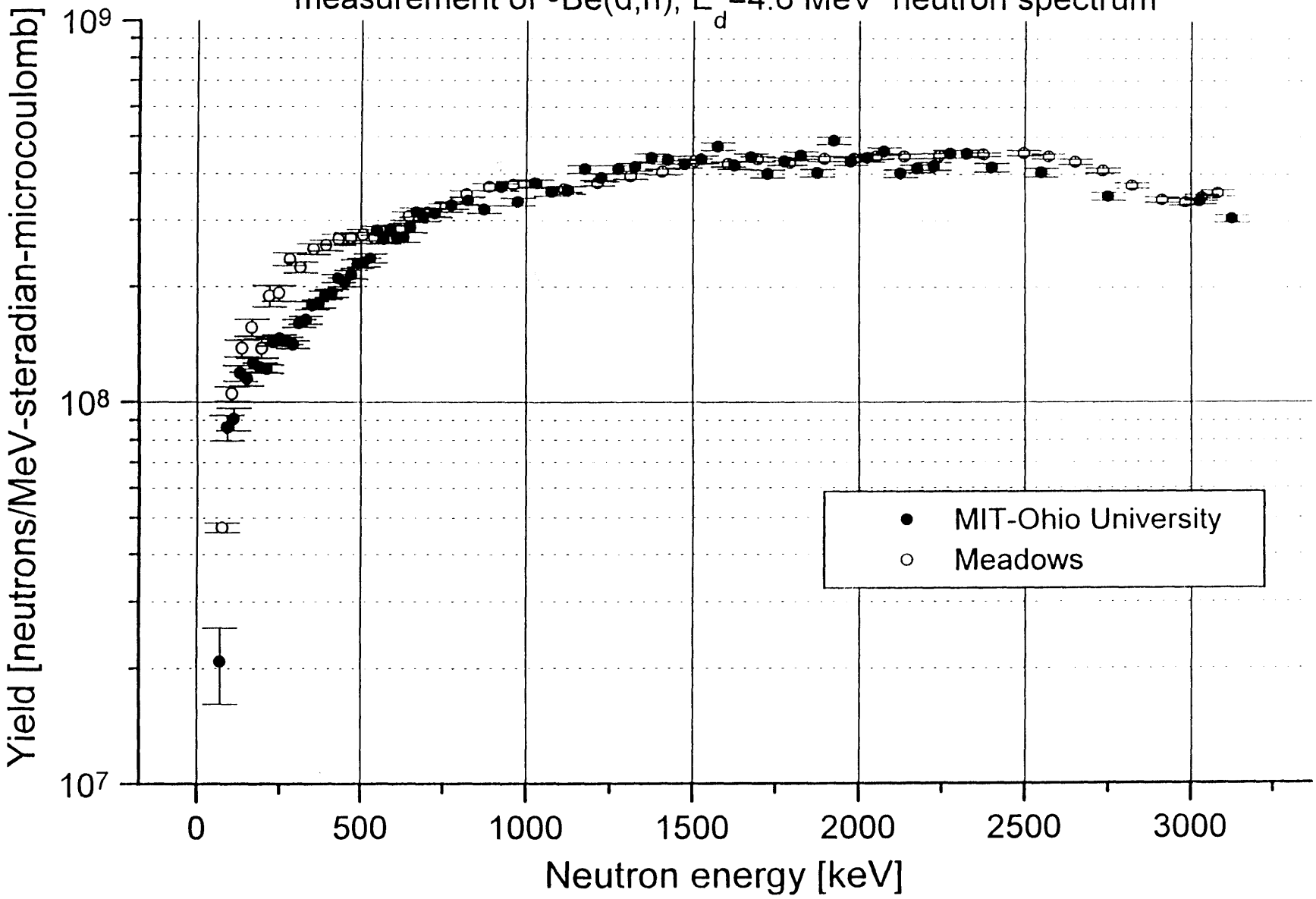

II.C.3 Results and discussion

The neutron spectra were measured at the various combinations of energy and angle shown in Table II-C-4. Graphs of the complete data set are included in Appendix B. This appendix also includes the numerical values for each of the following quantities: midpoint of energy bin, absolute yield and total statistical uncertainty. Since the statistical error is included in a complete form in the appendix, some of the graphs in this section will not include error bars. This allows the clear presentation of several data sets on one graph, for reasons of comparison. Samples of the neutron energy spectra for the various combinations of angle and energy are shown in Figure II-C-10 and Figure II-C-11. Figure II-C-10 shows neutron energy spectra at 3 angles using 4.0 MeV protons. For clarity, the total statistical error is shown only at 0.25, 0.5, 1.0, and 1.5 MeV. Figure II-C-11 depicts the 0 degree spectrum at the various proton bombarding energies, with representative errors shown.

Proton bombarding energy (MeV)	Laboratory Angle
4.0	0,20,40,60,80,110,115,120,125,130,135,145
3.7	0,20,40,60,80,110,115,120,125,130,135,145
3.4	0,40
3.0	0,40

Table II-C-4: Combinations of energies and angles for which the neutron spectra of ^{9}Be(p,n) were measured.

Since the complete data set was acquired at two different times (Groups A and B), it was important to ensure that the results were repeatable. Group A contains laboratory angles from 0 to 110 degrees. The Group B measurements were made primarily to examine the angles greater than 110 degrees. However, to ensure consistency, the laboratory angles 0, 20, 60 and 110 were repeated in August 1996 (Group B) for E_p=4.0

Figure II-C-10: $^{9}Be(p,n)$ neutron spectra at 3 angles for E_p = 4.0 MeV. Group B data are presented.

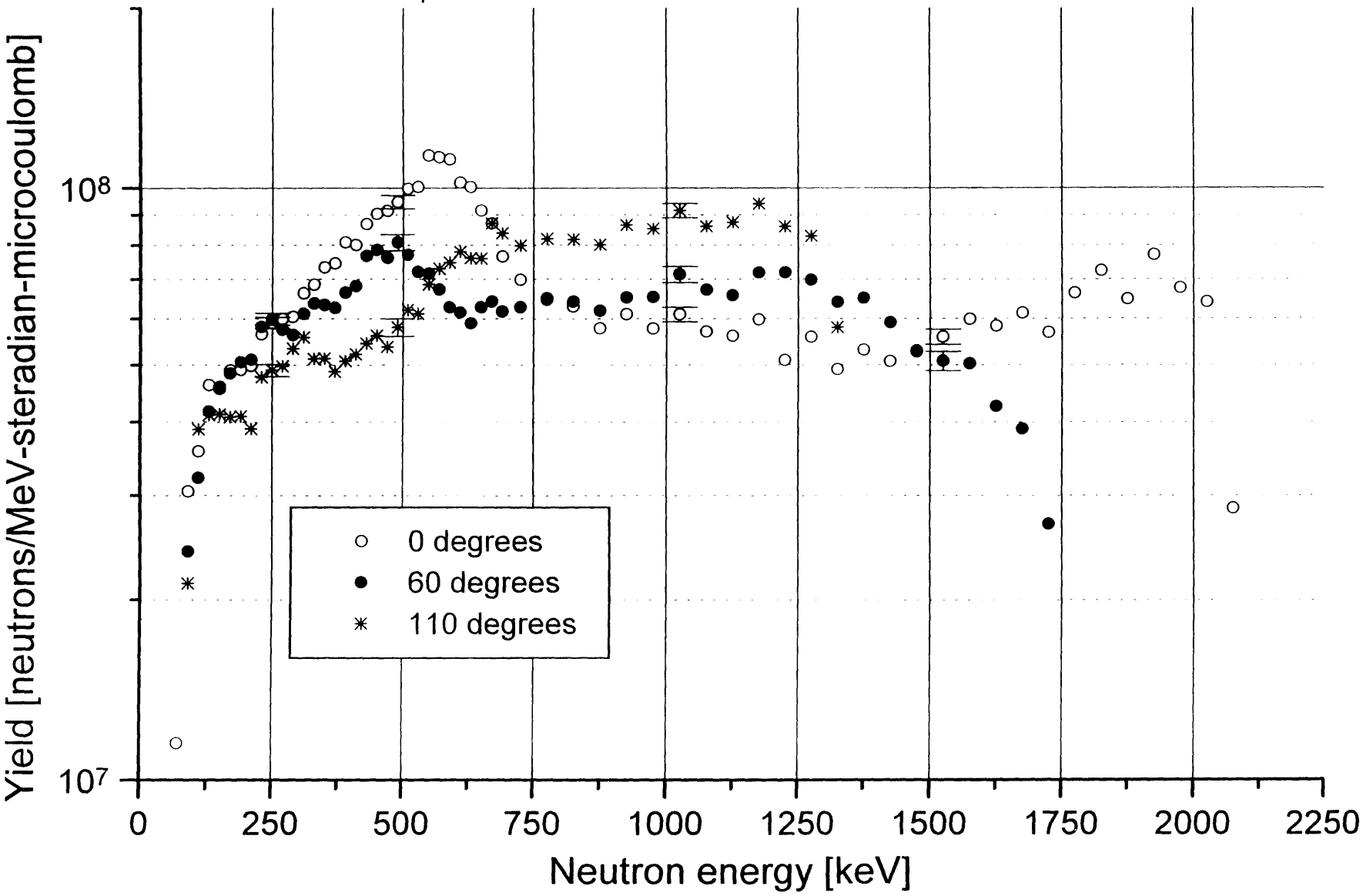

Figure II-C-11: $^{9}Be(p,n)$ neutron spectrum at 0 degrees for 4 energies. Group B data are presented.

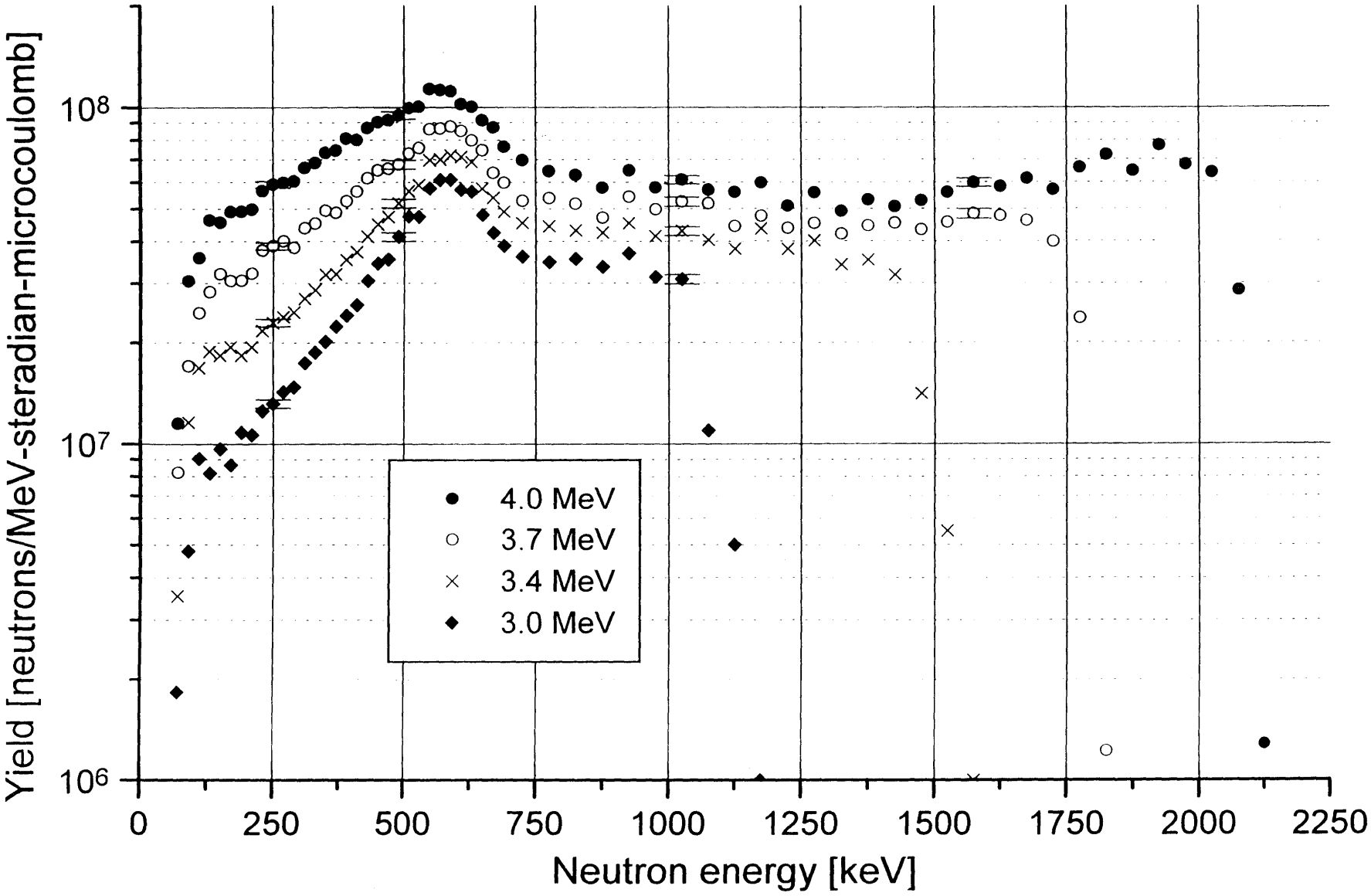

and 3.7 MeV. For E_p=3.4, 3.0 MeV, the 0 degree measurements were also repeated. One such comparison of these data is shown in Figure II-C-12. The error bars reflect only the total statistical error.

The agreement between Groups A and B varies as a function of neutron energy. Over the neutron energy range 250 keV - 1.875 MeV, the maximum disagreement is approximately 20%. The agreement between 250 keV and 2 MeV is within the total statistical and systematic error. Over this interval, neither spectrum is consistently higher than the other. One important distinction between the two is that the Group B appears to have better timing accuracy. The drop in the neutron spectrum near 2.1 MeV should be rapid for timing configurations with small values of $\Delta T/T$. This is the case with the Group B results, but the Group A drop much less rapidly to zero. One possible explanation for the discrepancies concerns the charge collection circuit. The target charge collection circuit was tested extensively before the Group B measurements, but not before the Group A measurements. It is possible that some part of the circuit was different, or not functioning the same during the Group A measurements.

Below 250 keV, the results from Group A are consistently higher than Group B. The disagreement between the two groups is as high as a factor of 2.0. There are two possible explanations for this discrepancy. First, the lower energy portion has many more TOF-TAC channels than the upper energy portion, for an equivalent sized energy bin. The lower portion is, therefore, much more susceptible to errors in background

Figure II-C-12: Comparison of Group A and Group B results

E_p = 4.0 MeV, 0degrees

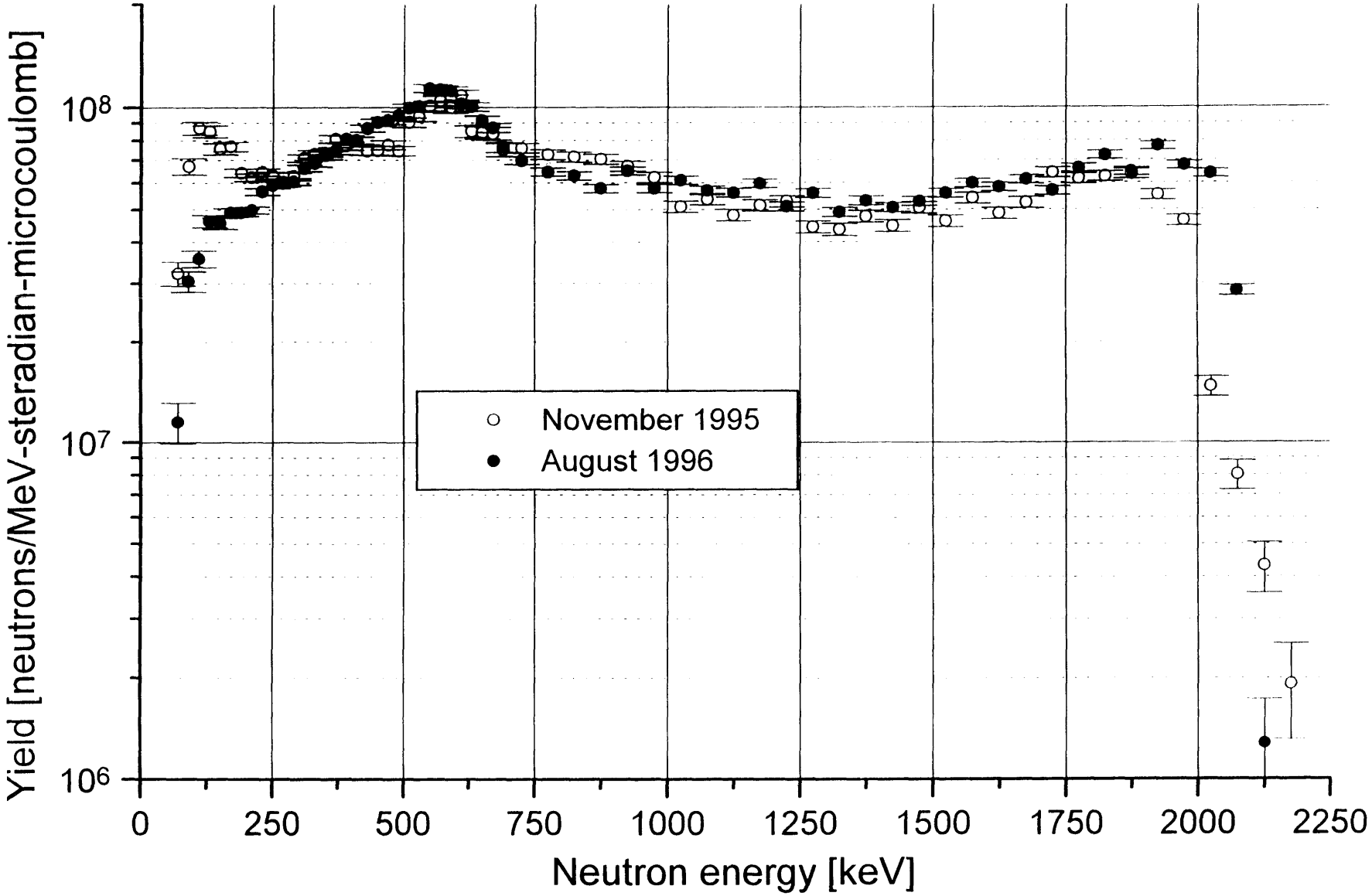

subtraction and the linearity of the TAC channels. A small error in the background subtraction, which is done channel-by-channel, would multiply to a larger error for the lower energy bins. Second, during the calibration of the lithium glass detectors, the ^{27}Al(d,n) spectrum is fit to a smooth curve. As the yield of this reaction begins to drop at lower neutron energies (below 500 keV) it is difficult to determine what features of the neutron spectrum are real, and which ones are statistical anomalies. A great improvement to these measurement techniques would be a calibration standard which was more prolific, and better defined, at energies below 500 keV.

The possibility that one of the detectors was not functioning properly was examined to determine if this could have caused the discrepancy between Groups A and B. The detectors were found to give equivalent neutron spectra when their signals were treated individually or as a group (with a single detector, the statistical error is noticeably higher).

If the ^{9}Be(d,n) data by Meadows, presented above, are taken to be accurate, then below 250 keV, the shape of the ^{9}Be(d,n) spectra should be monotonically decreasing. There is agreement in this aspect between the Meadows measurement and that of OUAL/MIT. This would indicate that the efficiencies of the detectors used in the Group B calculations had the correct shape, if not the correct magnitude.

If one compares the magnitude of the spectra (Group A to Group B, and Meadows to OUAL/MIT), the spectra measured in August 1995 seem to be low near 250 keV. The discrepancy in the total angular yield (E_p=4.0 MeV, 0 degrees) between the Group A and Group B measurements is approximately 3%.

The explanation of the shape of the various neutron spectra is the topic of ongoing research at OUAL. Several contributing reactions have been previously reported as discussed earlier in this chapter. The neutrons produced with energies above 1 MeV are believed to be due primarily to the reaction $^{9}Be(p,n_0)^{9}B$ which proceeds through the compound nucleus ^{10}B. It is important to note that the best information on the reaction would come from thin target measurements, and not thick target measurements. However, a simple calculation might help to explain the neutron energy spectrum for 0°, and E_p=4.0 MeV. The spectra at other energies could have similar explanations. The calculation would differ, of course, because the differential cross sections vary with angle. The calculation is based on an excitation curve for neutrons in the n_0 group, 0° laboratory angle, measured by Marion [12]. Data for this calculation were extracted from Figure 5 of Marion's paper, to which he assigns an absolute uncertainty of 30%. The excitation function at 0° is generally flat in the region 2.8 MeV< E_p<3.6 MeV. This differs from the excitation function for all angles (also presented in the same paper), which has a large broad resonance centered at 3.5 MeV. As mentioned previously, the contribution to the neutron production from the continuum neutrons is expected to

increase from approximately 35% at E_p=2.5 MeV to 70% at 5 MeV. A linear fit to these two data points was used in the following calculation.

For this calculation, one must consider the thick beryllium target as being made of several thin targets stacked together. The calculations below used a 10 keV thickness. First, since the yield is of the order $1x10^{12}$ neutrons/mC, only 16 in 100,000 protons actually produce a neutron. It is safe, then, to consider a beam of uniform intensity passing through the target, slowing down, and eventually stopping. As the proton beam passes through the first thin layer of beryllium, with energy 4 MeV, it produces neutrons in the n_o group corresponding to an energy E_{No} (near 2.2 MeV). The protons lose some energy traversing this thin layer, and in the following layer, produce fewer neutrons due to the lower cross section, and these neutrons have a slightly lower energy. This process continues until the protons reach the resonance at 2.56 MeV. Here, although the n_o group has less energy, the production actually increases. When the total neutron production is combined, it would be composed of several groups of n_o neutrons, decreasing in intensity and energy, from the maximum energy down to threshold. The one exception from this pattern would be the n_o neutrons produced from the 2.56 MeV resonance. As a final step the expected yield based on the data by Marion was multiplied by a correction factor for the continuum neutrons, using the two data points at E_p=2.5 and 5 MeV, discussed above, and the spectrum was normalized. This result can be compared with the actual normalized measured result from the Group B data. This comparison is shown in Figure II-C-13. It should be emphasized that this comparison is qualitative, and not quantitative

Figure II-C-13: Results of a calculation used to illustrate the possible source of neutrons in the 0 degree, E_p = 4.0 MeV spectrum

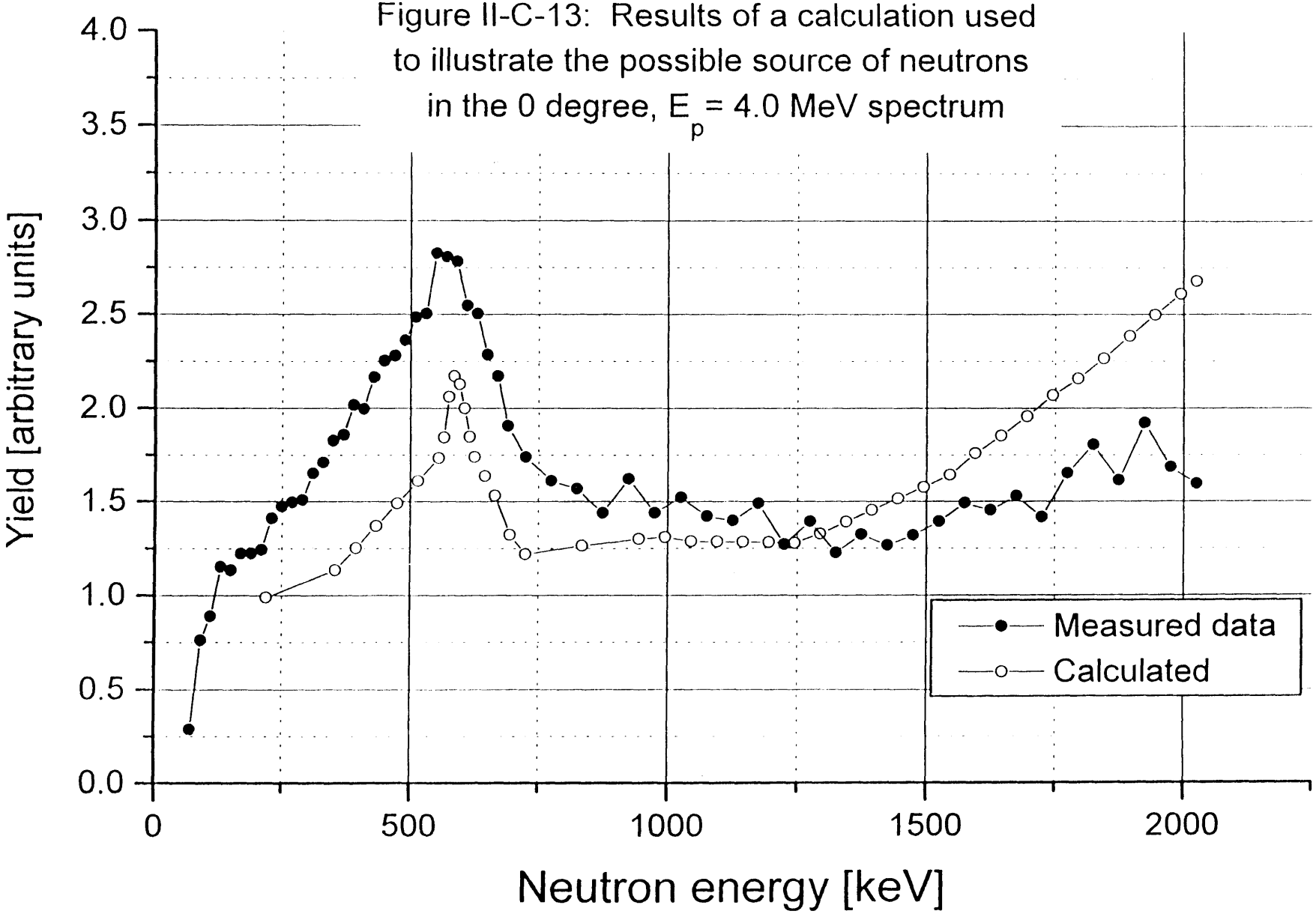

in nature due to the large uncertainty of Marion's data, and the assumption concerning the continuum contribution. However, the general agreement in the shape of the two spectra, especially the peak near 600 keV suggests that the production of the n_o neutrons can account for the basic shape of the 0° spectrum.

The neutron production near 500 keV may also have some contribution from the decay of the second (2.443 MeV) excited state of ^{9}Be. The ^{9}Be nucleus is excited via the reaction ^{9}Be(p,p'n). A peak near this energy has been seen before in experiments using a stilbene crystal for neutron detection [13]. Finally, a group of neutrons with energies centered around 500 keV was previously reported using a proton bombarding energy of 4.5 MeV. This peak existed only at the forward angles [12].

The neutron production at 0 degrees can be further examined by comparing the results using various proton bombarding energies. Figure II-C-14 shows three "subtracted" spectra. To generate the first subtraction spectrum, the spectrum using 3.7 MeV protons was subtracted from that using 4.0 MeV protons. This was repeated using 3.4 and 3.7 MeV, and finally for 3.0 and 3.4 MeV. The large peaks on the right hand side of the graph are probably accounted for by those neutrons in the n_o group which are produced from protons with energies between the respective values (such as 4.0 and 3.7 MeV). The neutrons in the subtracted spectra near 500 keV could be from the ^{9}Be(p,p'n) reaction mentioned above. The remaining neutrons could be explained by the various

Figure II-C-14: "Subtracted" spectra for $^{9}Be(p,n)$

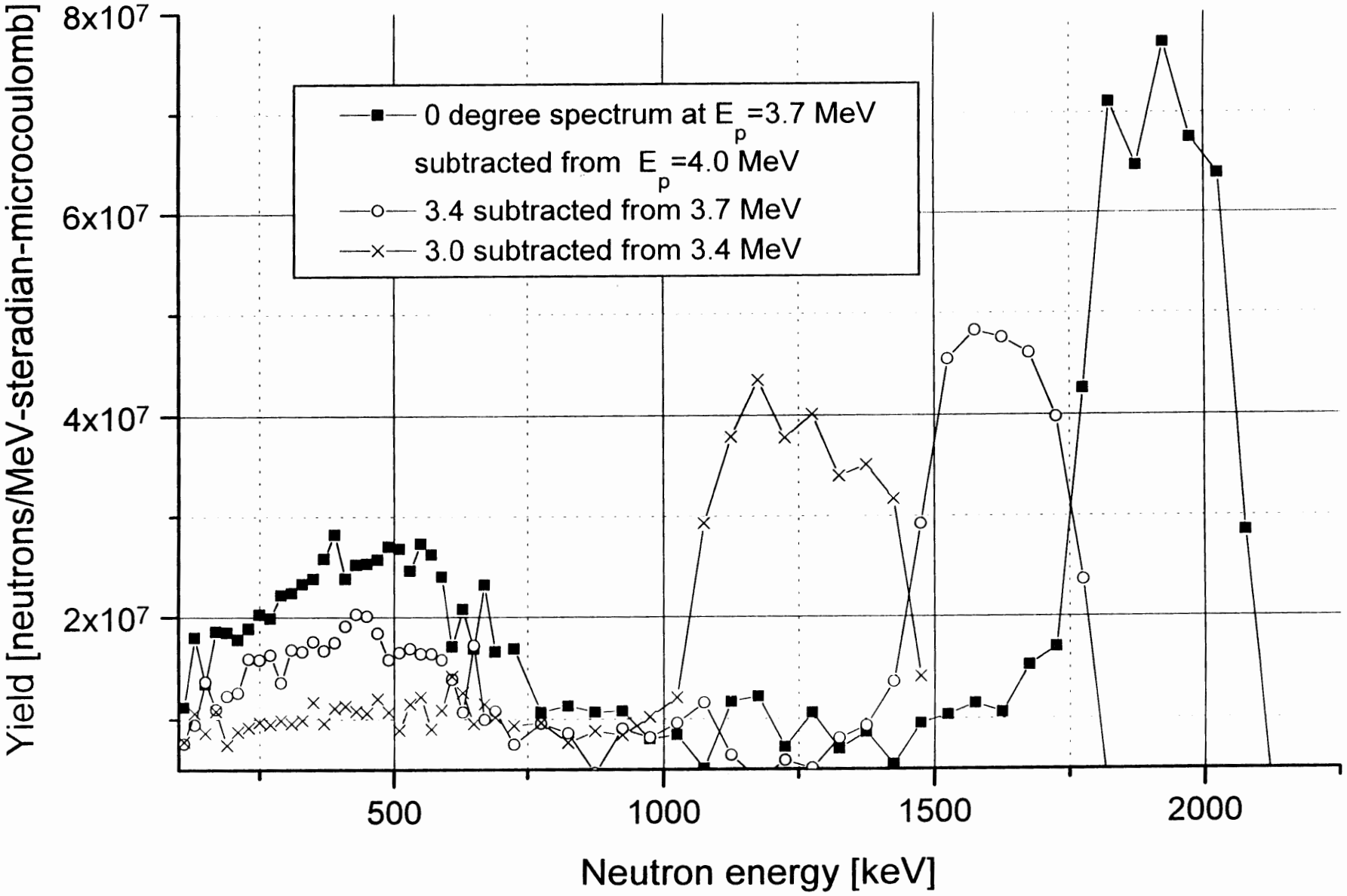

other continuum reactions. Again, the qualitative nature of this comparison should be emphasized. A more precise explanation could be gained by measuring thin target spectra.

II.C.4 Total yield calculations

The total neutron yield of the reaction can be estimated by integrating the various neutron spectra over the measured energy range and solid angle. During the November 1995 experiments, only the forward angles (1-110 degrees) were measured, and the estimated total yield for E_p=4.0 MeV was significantly less than the value predicted (1.36 x 10^{12} neutrons/mC) on the basis of published cross sections obtained using a 4π detector [17], and stopping powers of beryllium [22]. The experiments in August 1996 were, therefore, carried out to measure the backward angles. Using a proton bombarding energy of 4.0 MeV, the absolute total yield is now estimated to be 1.05 x 10^{12} neutrons/mC, based on the more complete data set (0 - 145 degrees). The neutron yield estimated from the complete set of neutron spectra now agrees within 23% with the predicted data. Unfortunately, the magnitude of the experimental error in the published cross sections is not clearly stated in the literature [17]. However, it is reasonable to assume an error of at least 10 - 15% based on other experiments of this type. Considering the 15-20% total error presented here, the agreement between the two values is good. The same comparison can be made for a proton bombarding energy of 3.7 MeV.

The agreement here is better between the measured and predicted total thick target yield (7.77×10^{11} and 9.63×10^{11} neutrons/mC, respectively), with the measured value 80.7% of the predicted value.

II.C.5 Conclusions and suggestions for future measurements

A complete data set now exists for the absolute thick target yield of ^{9}Be(p,n) for E_p=4.0, 3.7 MeV. There is general agreement between the shapes and magnitudes of the Groups A and B results with the exception of the unresolved differences near 250 keV. Additionally, the data have been confirmed indirectly through the measurement of the ^{9}Be(d,n) spectra at several energies. The greatest addition to this data set would be the acquisition of neutron energy spectra at increasingly lower neutron energies. Another useful addition to the data set would be to continue the measurements at proton bombarding energies below 3.7 MeV to near threshold. The shape of the total reaction spectrum seems to be based on the shape of the expected ^{9}Be(p,n_o) spectrum, to which the low energy continuum is added. To further refine an understanding of the shape of the spectra, thin target measurements would probably be required.

The ^{9}Be(p,n) reaction is a potentially valuable calibration source for neutron detectors. The spectrum at 0 degrees is generally flat for E_p=4.0 MeV, and the neutron yield is appreciable at least down to 200 keV. These qualities make the reaction an ideal choice for calibrating neutron detectors (provided the low energy neutrons can be

accurately measured). The possibility of more accurately determining a single energy spectrum of this reaction for calibration purposes is being investigated at OUAL.

One valuable future research project would be a more careful measurement of the lower energy portion of the neutron spectrum. The best configuration for this experiment would be a shorter flight path, and lower proton pulse rate frequency. The acquisition time increases for the lower frequency, but can be offset by the shorter flight path (which increases the solid angle of the detector). Both changes would further reduce the wrap-around problem allowing for lower energy neutron measurement. The negative consequence is that the $\Delta L/L$ uncertainty increases with the shorter path length. Another possibility is to measure the reaction $^{9}Be(p,n)$ directly with the fission foil detectors. The disadvantage is that the efficiency of these detectors is quite low (on the order or 10^{-5}) due to the requirement for very thin foils. However, since the foils are thin, the $\Delta L/L$ uncertainty is quite low, and the detectors can be used at short flight paths. The result would be a second useful calibration source (in addition to the $^{27}Al(d,n)$ reaction) for neutron detectors.

REFERENCES

1. Baker, H. and D. Benjamin, eds. *Metals Handbook.* 9 ed. . Vol. 2. 1979, American Society for Metals: Metals Park, OH.

2. Beynon, T.D., *et al. Towards the final design of an accelerator-based facility for clinical boron cancer therapy (BCT).* in *Seventh international symposium on neutron capture therapy for cancer.* 1996. Zurich, Switzerland: Elsevier Science - to be published.

3. Zhu, N., *et al. A target assembly cooling design for a BNCT application.* in *Seventh international symposium on neutron capture therapy for cancer.* 1996. Zurich, Switzerland: Elsevier Science - to be published.

4. Liskien, H. and A. Paulson, *Neutron production cross sections and energies for the reactions 7Li(p,n)7Be and 7Li(p,n)7Be*.* Atomic Data Nuclear Tables, 1975. **15**: p. 57.

5. *Nuclear data tables, part 3*, . 1960, National Academy of Science: Washington, DC.

6. Yanch, J.C., *et al.*, *Accelerator-based epithermal neutron beam design for neutron capture therapy.* Medical Physics, 1992. **19**(3): p. 709-722.

7. Kiss, A.Z., *et al.*, *Measurement of relative thick target yields for PIGE analysis on light elements in the proton energy interval 2.4-4.2 MeV.* Journal of Radioanalytical and Nuclear Chemistry, 1985. **89**(1): p. 123-141.

8. Meadows, J.W., *The thick target 9Be(d,n) neutron spectra for deuteron energies between 2.6 and 7.0 MeV*, . 1991, Argonne National Laboratory: Argonne, IL.

9. Yanch, J. and R. Shefer. *Deuteron-based reactions for epithermal neutron beam design.* in *Seventh international symposium on neutron capture therapy for cancer.* 1996. Zurich, Switzerland: Elsevier Science - to be published.

10. Ajzenberg-Selove, F., *Energy levels of light nuclei A=11-12.* Nuclear Physics, 1990. **506**(1): p. 1-158.

11. Wang, C.K. and B.R. Moore, *Thick beryllium target as an epithermal neutron source for neutron capture therapy.* Medical Physics, 1994. **21**(10): p. 1633-1638.

12. Marion, J.B. and J.S. Levin, *Investigaion of the 9Be(p,n)9B and 9Be(p,alpha-gamma)6Li reactions.* Physical Review, 1959. **115**(1): p. 144-149.

13. Lone, M.A. and B.C. Robertson, *Characteristics of neutrons from beryllium targets bombarded with protons, deuterons, and alpha particles.* Nuclear Instruments and Methods, 1981. **189**: p. 515-523.

14. Johnson, V.R., F. Ajzenberg, and M.J. Wilson-Laubenstein, *Neutron spectrum for protons on 9Be.* Physical Review, 1950. **79**: p. 187-188.

15. Byrd, R.C., *et al.*, *Cross-section measurement and Lane model analysis for the 9Be(p,n)9B reaction.* Nuclear Physics, 1983. **A399**: p. 94-118.

16. Marion, J.B., *Excited states in 10B.* Physical Review, 1956. **103**: p. 713-717.

17. Gibbons, J.H. and R.L. Macklin, *Total neutron yields from light elements under proton and alpha bombardment.* Physical Review, 1959. **114**(2): p. 571-580.

18. Brede, H.J., *et al.*, *Neutron yields from thick Be targets bombarded with deuterons or protons.* Nuclear Instruments and Methods in Physics, 1989. **A274**: p. 332-344.

19. Lone, M.A., *et al.*, *Thick target neutron yields and spectral distributions from the 7Li(p,n) 7Li(d,n) and 9Be(p,n) 9Be(d,n) reactions.* Nuclear Instruments and Methods, 1977. **143**: p. 331-344.

20. Bainum, D.E., *Neutron inelastic scattering from closed-shell nuclei*, in *Ph.D. Thesis, Physics*. 1977, Ohio University: Athens, Ohio.

21. Finlay, R.W., *et al.*, *The Ohio University beam swinger facility.* Nuclear Instruments and Methods, 1982. **198**: p. 197-206.

22. Ziegler, J.F., *TRIM-95*, . 1995, IBM: Yorktown, NY.

23. Neill, J.M., *et al.*, *Calibration and use of a 5-inch lithium glass detector.* Nuclear Instruments and Methods, 1970. **82**: p. 162-172.

24. Spowart, A.R., *Neutron scintillating glasses: part 1.* Nuclear Instruments and Methods, 1976. **135**: p. 441-453.

25. Meadows, J.W., *Characteristics of the samples in the FNG fission deposit collection*, . 1990, Argonne National Laboratory: Argonne, IL.

26. Baker, C.A., C.J. Batty, and L.E. Williams, *Calibration of time-to-amplitude converters.* Nuclear Instruments and Methods, 1968. **59**: p. 125-130.

27. Massey, T.N., *et al.*, *Neutrons produced by proton and deuteron bombardment of beryllium.* Nuclear Instruments and Methods - To Be Published, 1996.

28. Albert, R.D., S.D. Bloom, and N.K. Glendenning, *(p,n) angular distributions from mirror nucleus targets: 13C, 11B, and 9Be.* Physical Review, 1961. **122**(3): p. 862-869.

29. Kelsey, C.A., *The polarization of neutrons from the 9Be(p,n)9B reaction.* Nuclear Physics, 1963. **45**: p. 235-242.

30. Walker, B., *et al.*, *Angular distribution and polarization of neutrons from the 9Be(p,n)9B and 11B(p,n)11C reactions.* Physical Review, 1965. **137**(6B): p. 1504-1508.

31. Bair, J., C. Jones, and H. Willard, *Neutrons from the proton bombardment of 6Li, 7Li, 9Be, 11B, and 18O.* Nuclear Physics, 1964. **53**: p. 209-218.

CHAPTER THREE

Therapy Beam Design and Verification

This chapter describes the methodology of designing a useful therapy beam with a neutron producing reaction as the starting point. The reactions considered are: ^{7}Li(p,n), E_p=2.5 MeV, ^{9}Be(p,n), E_p=4.0 , 3.7 , 3.4 and 3.0 MeV, and ^{9}Be(d,n), E_d=2.6 MeV. This is the first detailed evaluation of the reaction ^{9}Be(p,n) based on the measured data presented in Section II.C. It is convenient to clarify two terms at the outset of this process. The "target spectrum" is defined as the neutron production at the surface of the target as a function of energy and angle. The "therapy beam" is the neutron beam to which a patient would be directly exposed. This therapy beam also contains non-therapeutic or "contaminant" radiation in the form of photons and fast and thermal neutrons. The photons are created at the target (as discussed in Chapter II) and in (n,γ) reactions in the MSR. In each of the reactions listed above, the neutron target spectrum is dominated by energies much greater than what are optimal for an AB-BNCT therapy beam. To produce a useful therapy beam, a structure is placed between the neutron producing target and the patient. This structure, which is called a Moderating-Shielding-Reflector assembly, or MSR, serves three functions: tailor the energy spectrum to a more optimal distribution, conserve neutron fluence, and reduce non-therapeutic dose to the

patient. The tailoring of the energy spectrum sometimes involves the use of materials known as "filters" or "resonant scatterers". Fast neutron filters are made of specific isotopes which have neutron scattering or absorption cross sections which are larger at high energies than at epithermal energies. These filters work by preferentially scattering or absorbing the fast neutrons, thereby lowering the average neutron energy. Some common fast neutron filter materials for BNCT are aluminum, titanium, fluorine, and sulfur [1]. Thermal neutron filters contain materials such as ^{6}Li or ^{10}B which have a high thermal neutron cross section. Thermal neutron filters are used to absorb thermal neutrons before they can interact with materials in the MSR which could create (n,γ) radiation. Thermal neutron filters are also used at the therapy port to reduce the thermal neutron components ($^{14}N(n,p)$ and $^{10}B(n,\alpha)$) to the first few centimeters of the brain.

This chapter begins with a discussion of the specific objectives of this research. The model used in the evaluation of the various beam designs is then discussed and the MSR materials used in this study are presented. The therapy beam design process is outlined followed by a presentation of the results. The last sections in the chapter describe an experimental procedure which can be used to confirm the results of these simulations. Results from measurements using the MSR currently installed at LABA are presented.

III.A Objectives and design criteria

III.A.1 Objectives

The objectives of the research presented here are to evaluate three reactions as potential AB-BNCT neutron sources, design MSRs for use with these reactions, and to predict the various dose rate components that would result from using these reactions and MSRs. As will be discussed below, this evaluation procedure is somewhat hindered by the fact that specific design goals are ill-defined. However, by using a consistent set of criteria, the beam designs can be evaluated and compared.

Despite much effort devoted to the design of therapy beams for BNCT, there is not yet a general agreement concerning the optimal therapy beam parameters, or therapy dose rates, for BNCT. The current clinical trials (Section I.A.5) should result in more definitive guidance on these issues. Moreover, there is not a uniform method used to design therapy beams. Some research groups use therapy beam figures-of-merit as an intermediate step in finding a suitable MSR configuration [1] [2]. Eventually, a therapy beam is evaluated based on the prediction of the various dose components that would result in a patient. Ideally, these predictions should be confirmed experimentally.

The method of predicting these dose components is more widely uniform. Typically, a transport simulation program, such as the Monte Carlo N-Particle Transport Code System (MCNP) [3], is used to estimate the neutron and photon fluences that would occur within the patient, and these fluences are converted to absorbed dose rates using

fluence-to-kerma conversion factors for the various dose components. To equate kerma to absorbed dose, the condition of charged particle equilibrium must exist [4]. This condition is met by choosing tallying volumes for the MCNP model which are large relative to the ranges of charged particles created in the simulation. The ranges of the reaction products of $^{10}B(n,\alpha)$ in tissue are each less than 10μm. The maximum energy of recoil protons resulting from fast neutron elastic scattering is equal to the maximum neutron energy in the organ volume. For example, the most energetic neutrons in the target spectra of the $^{9}Be(p,n)$ reaction for $E_p \leq 4.0$ MeV, have energies around 2.2 MeV. At the therapy port, the therapy spectrum is dominated by neutrons well below 1 MeV. The maximum recoil proton energy in the organ volume is thus approximately a few MeV or less. The range of 3 MeV protons in tissue is less than 0.1 mm and is about 1 mm for 10 MeV protons [4]. The maximum energy of secondary electrons would be on the order of 1 MeV. The range of a 1 MeV electron in water is approximately 0.44 cm [4]. For these simulations, the cell volumes in the MCNP model were approximately 1 cm^3. Since 1 cm is large compared to the ranges of all reaction products, the kerma approximation to dose is valid. Once the physical dose rates have been predicted, RBE weighting factors can be used to determine more accurately the therapeutic efficacy of the design.

Because there are limited data and consensus on the acceptable dose rates (both therapeutic and contaminant) for BNCT, specific therapy beam design goals are ill-defined. For the simulations presented here, which are based on the treatment of brain

tumors, a consistent trade-off exists. The fast neutron dose rate is usually the most problematic of the non-therapeutic or "contaminant" dose rate components. This dose rate is inversely proportional to the amount of moderating material between the target and the therapy port. For very small moderator volumes, the AD is zero, since the fast neutron dose rate exceeds the therapeutic dose rate component, which is primarily the ^{10}B dose. Increasing the moderator volume decreases the fast neutron dose rate, because the average neutron energy is lowered. However, this also decreases the therapeutic dose rate for two reasons. First the therapy port now subtends a smaller solid angle seen by the target. Second, since the moderator surface area has increased, the neutron leakage rate increases. The process of finding the MSR configuration which maximizes the therapeutic dose to tumor, while limiting the fast neutron dose at shallow depths in the tissue, is often governed by this trade off.

III.A.2 Design parameters

The specific design parameter used here is that the fast neutron dose rate should be no more than 15% of the total tumor dose rate at a depth of 0.5 cm (with no RBE weighting factors used). With this limitation, the possible therapy beams are examined on the basis of the dose rate to tumor at 2 cm (which is generally near the location of maximum tumor dose rate) and at 6 cm. The design is accomplished without the use of RBE values. Based on these criteria, the most favorable combinations of target material, ion energy, and MSR are then presented with different sets of RBE weighting factors. In all the simulations, a ^{10}B concentration in tumor of 30 ppm was assumed.

III.B The MCNP model

The Monte Carlo Code MCNP [3] was used to optimize the design of an MSR for each of the target reactions and incident charged particle energies. MCNP was used to model the geometry of the accelerator beam tube leading to the target, moderator, reflector, shielding, neutron filters, and a cylindrical head phantom [5]. The target housing was modeled as being similar to the prototype beryllium target discussed in Appendix A. The model included a volume of light water coolant behind the target. A three dimensional model of this configuration is shown in Figure III-B-1. The moderator volume is shown in blue and the reflector is gray. The water which cools the target is shown in yellow. The thermal neutron filters are very thin, and would not normally be easily seen at this scale, so they have been increased in thickness and shown in red. The cylindrical head phantom is shown in green and magenta.

The various dimensions of the MSR components are indicated in Figure III-B-2. Throughout this chapter, this figure will be used as a reference when discussing these dimensions. This drawing is not to scale.

The head phantom was modeled as a cylindrical volume 16 cm long and 16 cm in diameter based on a 50%/50% by weight average of gray and white matter [5]. This volume was divided into a series of 13 disks and 8 shells, for a total of 104 MCNP defined cells, as shown in Figure III-B-3. The cylindrical shells are shown in alternate colors of green and magenta. The axial centerline, which is referred to often in this

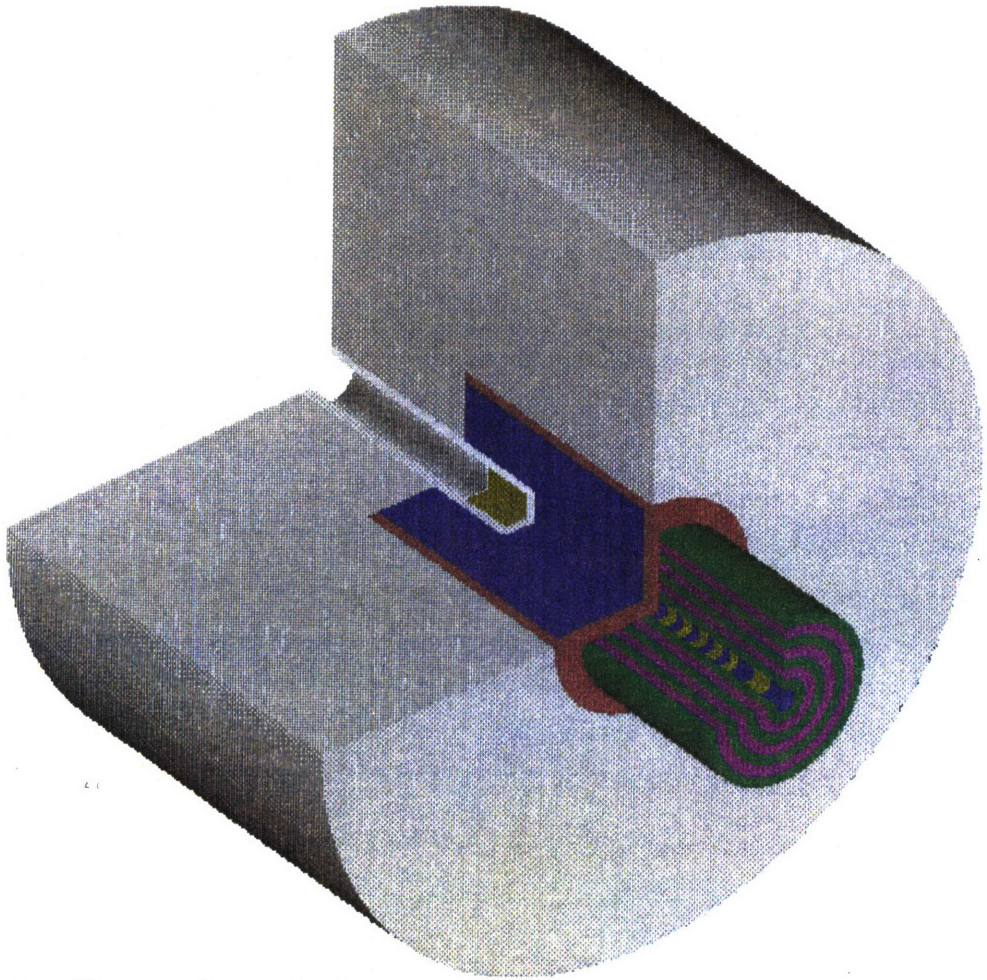

Figure III-B-1: Therapy beam design Model. Components shown as: reflector (grey) moderator (blue) thermal neutron filters (red) target coolant (yellow).

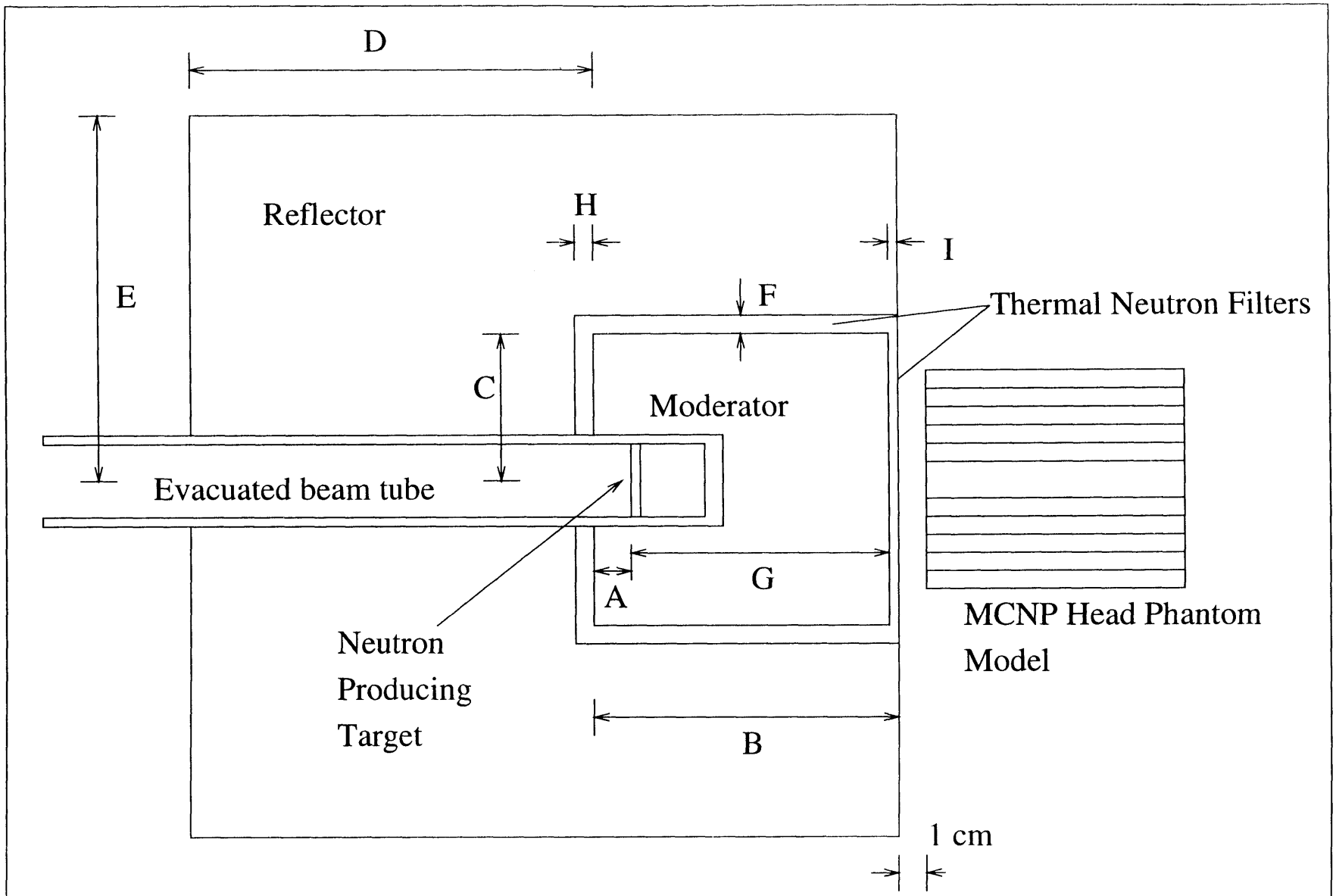

Figure III-B-2: Two dimensional drawing of the MCNP model showing the location of various components and critical dimensions

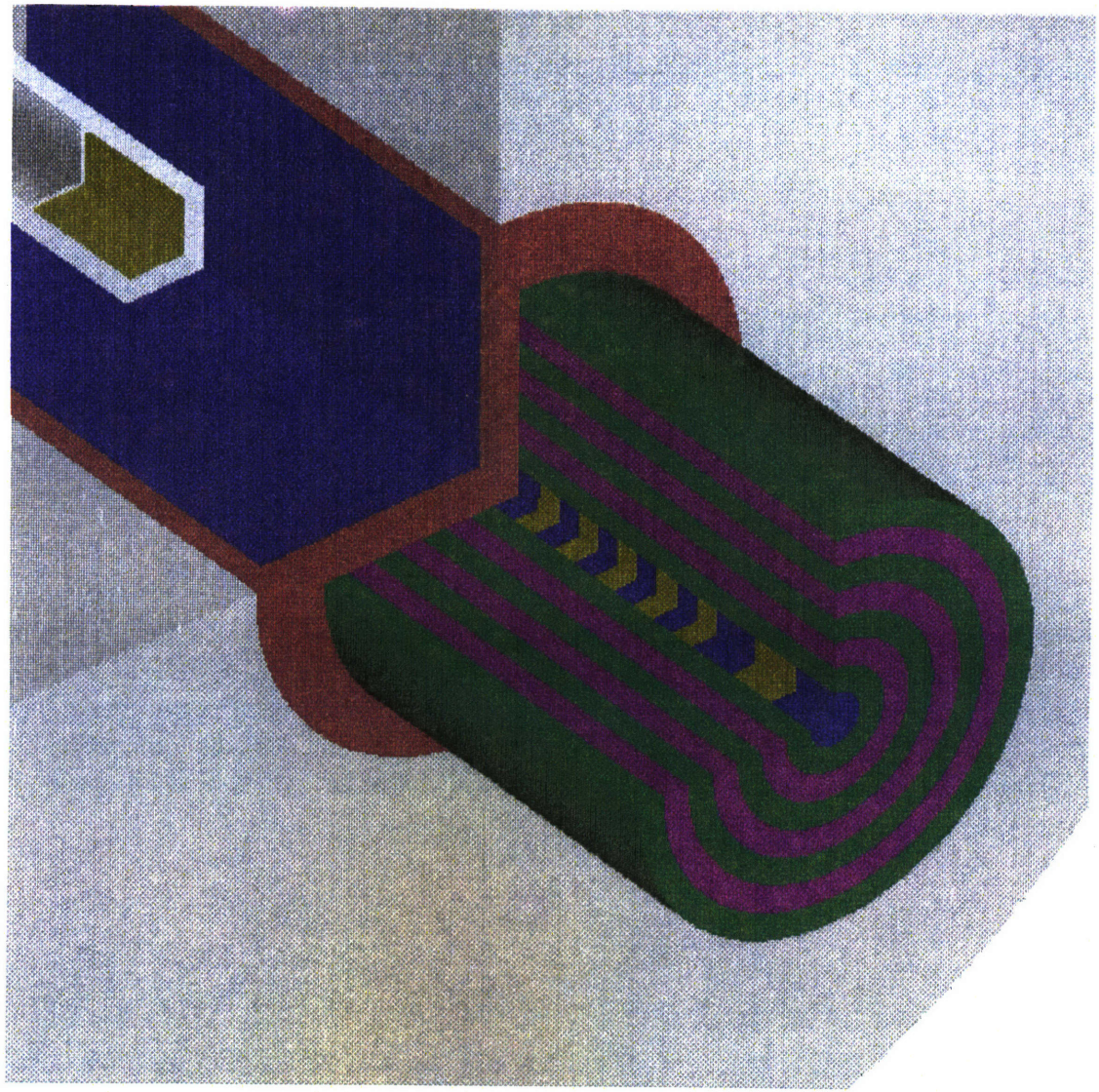

Figure III-B-3: Model of head for therapy beam design.

chapter is at the center of the phantom. The axial centerline is segmented into disks as shown in alternating colors of blue and yellow. The outer cylinders are also segmented in this way. To calculate the various dose components, tallies were used to determine the neutron and photon fluences in each of the 104 head phantom cells. These fluences were then converted to kerma using published fluence to kerma conversion factors for neutrons [6] photons [7] and the ^{10}B reaction [7]. As mentioned previously, kerma was assumed to be equal to absorbed dose for the purposes of these optimizations. Dose rates were calculated by multiplying the tally results by neutron yield (neutrons/min-mA). Dose rates are expressed in the units "cGy/min-mA of accelerator current". The result of each simulation was a list of the various BNCT dose rate components, in units of cGy/min-mA, for all of the 104 cells of the head phantom. All the simulations presented in this thesis were performed with a tissue model. No "in-air" studies were undertaken.

The target spectra were input into the model using the MCNP source definition specifications. These target spectra, and the methods used to measure or calculate them were discussed in Chapter II. For the reaction $^{9}Be(p,n)$ using E_p=3.4 and 3.0 MeV protons, a complete set of angular distributions still does not exist. The neutron spectrum of these reactions was estimated by using the neutron spectrum of E_p=3.7 MeV and truncating an appropriate amount of the high energy portion of the angular distributions. The total neutron production rate was then normalized using 75% of the rate predicted from published cross sections [8] and stopping powers [9] as discusses in Section II-C.

For the data presented in that section, the total measured neutron production rates for E_p=4.0 and 3.7 MeV were approximately 75% of the predicted values.

In the case of the reactions ^{7}Li(p,n) and ^{9}Be(p,n), separate MCNP simulations were conducted to evaluate the effect of the (p,γ) reactions at the target. These simulations will be discussed with the results in Section III.E.

III.C MSR materials

The materials chosen for a MSR must not only perform their primary function well, but must also be practical from a combined engineering, safety, and economic perspective. Ideally, all MSR materials should not be expensive, exotic, heavy, corrosive, explosive, toxic, unstable, or flammable. For the materials examined in this study, the majority of these constraints were easily met. The work presented here draws on the therapy design experience of many groups, including work previously done at LABA. The selection of materials for the MSR was based on the experience gained from working with similar neutron spectra, particularly from the ^{7}Li(p,n) reaction [10]. The experience at LABA has also shown that the choice of many of the materials will impact the results in a predictable way. For example, when choosing between lead and graphite as a reflector material, a slightly larger moderator volume must be used with a lead reflector than with a graphite reflector to achieve the same relative dose rates between the BNCT therapy components. Graphite, being a lower Z material, provides more moderation than

lead. By using a graphite reflector, the moderator volume is reduced, and the total therapy dose rate, for equivalent fast neutron contamination, tends to increase.

III.C.1 Moderator materials

A good moderator would reduce the average energy of the target spectrum neutrons using the smallest volume of material. Since the reflector is not ideal, the neutron leakage from the therapy beam is proportional to the surface area of the moderator. For this reason, a small moderator is desirable. There are two processes by which a neutron can lose energy as it traverses the moderator. If the incident neutron has enough energy to excite the target nucleus, an inelastic collision can occur. Below these energies only elastic scattering can occur, which is effective for lowering the neutron energies down to the 0.1 eV range. Below this energy, the thermal motion of the target nuclei is important, and the neutrons reach a state of thermal equilibrium with the moderator medium. In elastic scattering, a neutron of initial energy E_o is scattered at a center-of-mass angle Θ with a new energy E. The difference in neutron energy, E_o - E, is transferred to the kinetic energy of the recoiling nucleus of mass number A. An elementary application of kinematics yields the following equation, and inequality:

Equation III-C-1[11]: $$E = \frac{E_o}{(A+1)^2}(A^2 + 1 + 2A\cos\theta)$$

Equation III-C-2[11]: $$E_0\left(\frac{A-1}{A+1}\right)^2 \leq E \leq E_0$$

The inequality clearly shows that low weight nuclei are favored for neutron moderation. In addition to its ability to moderate neutrons, a good moderator should produce little contaminant penetrating radiation through reactions such as radiative capture. Some materials, commonly called filters, allow the selective scattering and moderation of higher energy neutrons. The ideal filter would have a high fast neutron scattering cross section, a low epithermal scattering cross section, and a low (n,γ) cross section. An example of such a filter material is ^{27}Al. The relevant cross section data for ^{27}Al is shown in Figure III-C-1. A list of materials which could be used as filters was compiled by Kiger, and is reproduced in Table III-C-1 [1].

Material	Average number of elastic collisions from 2 MeV to 10 keV	Absorption cross section E_n=0.025 eV [barns]	Scattering cross section E_n=0.025 eV [barns]	Total cross section E_n=0.025 eV [barns]	Epithermal total cross section [barns]	Fast total cross section [barns]
Al	73.3	0.241	1.4	1.64	1.55	3.04
O	44.2	0.0004	4.2	4.2	3.74	2.52
F	52.1	0.001	3.9	3.9	3.63	3.25
AlF3		0.244	13.1	13.3	12.4	12.8
Al_2O_3		0.483	15.4	15.9	14.3	13.6
Ti	128.6	5.8	4	9.8	13.3	3.55
D_2Ti		5.8	18	23.8	20.0	8.43
TiF_4		5.8	19.6	25.4	27.8	16.6
S	86.5	0.52	1.1	1.62	1.09	2.8
Al_2S_3		2.04	6.1	8.14	6.38	14.5

Table III-C-1: Possible therapy beam filter materials for BNCT.

For this work, two possible moderator/filter materials were examined: D_2O and a mixture of 30%Al-70%AlF_3. These materials have been examined during previous studies by researchers at LABA [10] and other groups [1] and found to function well as moderator materials. The second will be referred to simply as Al-AlF_3 in this chapter.

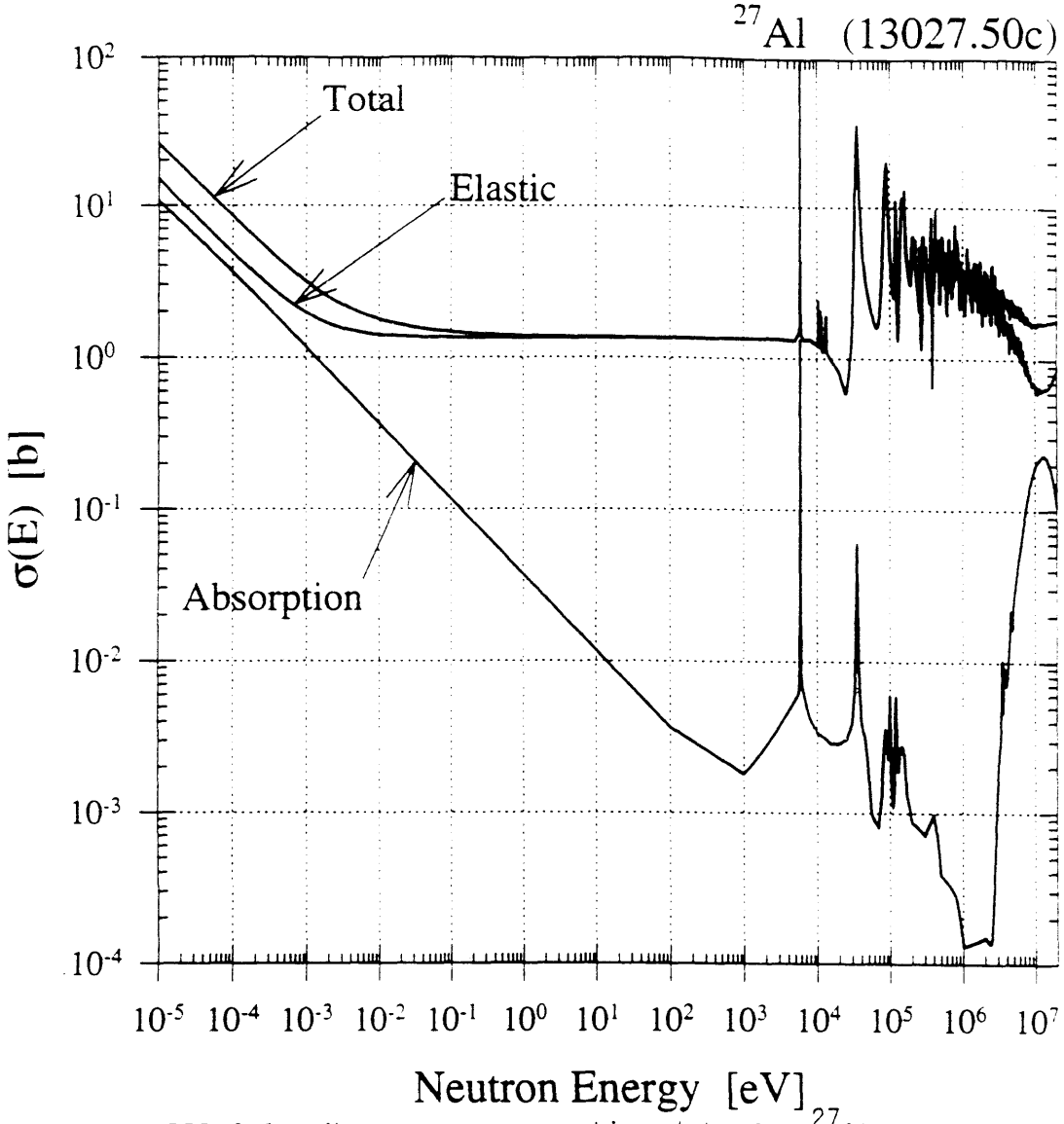

Figure III-C-1: Neutron cross section data for ^{27}Al
(figure used with the permission of W.S. Kiger)

III.C.2 Reflector materials

The purpose of the reflector is to redirect the neutrons escaping the moderator volume back into the moderator. A good reflector material would have a high macroscopic cross section for scattering so that neutrons penetrate only a short distance into the reflector before scattering. The scattering should be isotropic in the laboratory frame so that neutrons have an equally likely chance of being directed back into the moderator as opposed to being scattered deeper into the reflector [1]. The reflector should also not produce large amounts of high energy photons.

Two reflector materials, lead and graphite, were chosen based on prior experience at LABA and results from other research groups [1] [10] [12]. Additionally, two other reflector materials, bismuth and nickel, were initially tested with the reaction ^{9}Be(p,n), E_p=4.0 MeV. Neither material proved to be better than lead or graphite, and were not examined further. The use of nickel as a reflector material has been shown to produce an unacceptably high photon dose rate [1] which was confirmed by work at LABA, including these initial simulations.

III.C.3 Thermal neutron filter

The thermal neutron filter performs two functions. When placed between the moderator and the reflector, it decreases the number of (n,γ) reactions in the reflector. When placed between the moderator and the patient, it decreases the thermal neutron (^{14}N(n,p)^{14}C) and boron (^{10}B(n,α)) doses to the first few centimeters of the patient tissue,

and suppresses the (n,γ) reactions induced in this tissue. An ideal thermal neutron filter would capture thermal neutrons selectively, without emitting a photon. Previous experience has shown that a ^{6}Li containing compound such as $^{6}LiCO_3$ works well as a filter material [10]. One advantage of ^{6}Li-based filter materials is that the reaction $^{6}Li(n,\alpha)$ produces no gamma radiation. For these simulations, a thin layer of ^{6}Li was used in the model.

III.D The optimization methodology

To optimize the therapy beam, the critical dimensions of the MSR, and the materials which comprise its component parts, were varied in a systematic way. The initial configurations were chosen based on previous experience and results using the $^{7}Li(p,n)$, E_p=2.5 MeV, reaction [10]. A compilation of the configurations used in this thesis is provided in a series of Tables at the beginning of Appendix C. These tables list the neutron source reaction and ion energy, and the MSR components and dimensions.

Since this optimization procedure is multi-variable in nature, it is not trivial to find the set of parameters and materials which will produce the best therapy beam. Computer time eventually limits the number of configurations which can be simulated, and it is not practical to vary every parameter independently of the others. Therefore, the chronological order of this systematic variation is important. The most critical elements of the optimization (for a given reaction and ion energy) are the moderator material and dimensions.

As the moderator was being designed, the reflector was initially made much larger than the expected optimal size. The reason for this approach is that a reflector of exaggerated size should result in the best performance, all other factors being equal. As neutrons escape the sides and back of the moderator, they enter the reflector. If the reflector is thin, some neutrons may pass through the reflector and escape into air, at which point they are very unlikely to contribute to the patient dose. As the reflector thickness is increased, some of the neutrons which otherwise would have escaped, are reflected back into the moderator. At some unknown thickness, adding more reflector has no effect on the dose to the patient, since all neutrons entering the reflector have either been captured or reflected back into the moderator. An exaggerated thickness will be used initially, and near the end of the optimization procedure, a determination will be made as to how much this reflector volume can be reduced without affecting the results. Other than system weight and cost, there should not be any adverse effect of an oversized reflector. The validity of this approach, based on the simulation results, will be discussed in Section III.E.

To begin the process of designing an optimized therapy beam, a reaction (^{9}Be(p,n), E_p=4.0 MeV), moderator material (D_2O), and reflector material (graphite) were chosen. The moderator length and diameter were varied using an oversized reflector and the simulation results were evaluated. The moderator dimensions resulting in the highest dose rates at 2 cm and 6 cm, subject to the limit of 15% fast neutron contamination at a depth of 0.5 cm discussed above, were recorded. Next, the various reflector materials

were used with this same reaction and the moderator dimensions were varied slightly to find the highest dose rate at 2 cm and 6 cm while keeping the fast neutron contamination below 15%. As mentioned above, two of the reflector materials (nickel and bismuth) showed no significant improved performance over lead and graphite, and were no longer considered. In particular, use of a nickel reflector resulted in a high photon contamination. In the third step, the moderator material was changed, and the design process was repeated with the same reaction using graphite and lead reflectors.

The result of this initial set of simulations was a configuration which was close to being optimized (i.e. close to the final design chosen) for the reaction ^{9}Be(p,n), E_p=4.0 MeV. For the other reactions, the moderator size was adjusted either to a larger volume for more energetic reactions (^{9}Be(p,n), E_d=2.6 MeV), or to a smaller one for less energetic reactions (^{9}Be(p,n), E_p=3.7, 3.4, 3.0 MeV and the ^{7}Li(p,n) reaction). The moderator volume must also be adjusted for the reflector material (increase volume for lead reflector compared with graphite), and the moderator material (increase volume for Al-AlF_3 compared with D_2O).

Three effects were examined using the best MSR resulting from the initial set of simulations using ^{9}Be(p,n), E_p=4.0 MeV. First, the effect of moving the target position relative to the rest of the MSR was examined. The target surface location was changed relative to the back of the moderator (critical dimension A in Figure III-B-2). Second, dimensions A and G were varied together so that the total length of moderator between the target and therapy port remained constant. Third, the reflector thickness was varied to

determine the smallest thickness which could be used without noticeably changing the therapy dose components.

Each of these simulations was executed using three million neutron histories. Neutron importance weighting in the brain phantom cells was used as a variance reduction technique. Variance reduction is used within MCNP to increase the precision of the results by reducing the statistical uncertainty of the MCNP output [3]. The value of these weighting factors is shown in Figure III-D-1. The MSR in this diagram is located to the left. As shown, the neutron importance factor of the first disk is 1.0 increasing to 1.2 in the second disk. The neutron importance factor does not vary radially from the axial centerline. No photon weighting factors were used.

Using three million histories, the typical statistical uncertainties (1σ) at a depth of 2 cm for the various dose components were approximately: 10% for fast neutrons, 7% for photons, and 3% for thermal neutrons. Once the MSR materials and critical dimensions were selected in this manner, a second simulation was executed, for some of the more promising configurations, using 9-10 million histories to generate results with smaller statistical uncertainty. The typical errors using 10 million histories were approximately: 6% for fast neutrons, 3-4% for photons, and 1-2% for thermal neutrons. For each of the configurations in the optimization, the dose components along the axial centerline of the brain phantom were graphed and evaluated. An example of such a

1	1.2	1.4	1.5	1.7	2	2.3	2.7	3.3	3.5	3.7	4.6	5.7
1	1.2	1.4	1.5	1.7	2	2.3	2.7	3.3	3.5	3.7	4.6	5.7
1	1.2	1.4	1.5	1.7	2	2.3	2.7	3.3	3.5	3.7	4.6	5.7
1	1.2	1.4	1.5	1.7	2	2.3	2.7	3.3	3.5	3.7	4.6	5.7
1	1.2	1.4	1.5	1.7	2	2.3	2.7	3.3	3.5	3.7	4.6	5.7
1	1.2	1.4	1.5	1.7	2	2.3	2.7	3.3	3.5	3.7	4.6	5.7
1	1.2	1.4	1.5	1.7	2	2.3	2.7	3.3	3.5	3.7	4.6	5.7
1	1.2	1.4	1.5	1.7	2	2.3	2.7	3.3	3.5	3.7	4.6	5.7
1	1.2	1.4	1.5	1.7	2	2.3	2.7	3.3	3.5	3.7	4.6	5.7
1	1.2	1.4	1.5	1.7	2	2.3	2.7	3.3	3.5	3.7	4.6	5.7
1	1.2	1.4	1.5	1.7	2	2.3	2.7	3.3	3.5	3.7	4.6	5.7
1	1.2	1.4	1.5	1.7	2	2.3	2.7	3.3	3.5	3.7	4.6	5.7
1	1.2	1.4	1.5	1.7	2	2.3	2.7	3.3	3.5	3.7	4.6	5.7

Figure III-D-1: Neutron importance weighting for therapy beam design.

graph, using the results of a simulation with 3 million histories, is shown in Figure III-D-2. The error bars on the various dose components indicate the statistical error (1σ) generated by MCNP. Each dose component is calculated by MCNP when the program convolves the neutron and photon fluences in each of the 104 phantom cells with the appropriate fluence-to-kerma conversion factors. The entire set of these graphs (which do not show the statistical errors) is included in Appendix C.

III.E Therapy beam design results and discussion

A total of 70 simulations were completed and evaluated for the reactions outlined above. As was noted previously, the initial results using the reaction ^{9}Be(d,n) were sufficiently disappointing that further consideration of this reaction for beam optimization was suspended in favor of devoting more resources to the other simulations. The results using the reaction ^{9}Be(d,n) will be presented last, and the remainder of the discussion will focus on the results using the reactions ^{9}Be(p,n) and ^{7}Li(p,n).

It is important to note that these simulations were compared, initially, on the basis of expected dose rates in phantom for equivalent accelerator beam currents. This comparison can be deceptive. For example, from the standpoint of target heat removal or required accelerator power, a 1 mA beam of protons for E_p=2.5 MeV is not equivalent to a 1 mA beam for E_p=4.0 MeV. One method of addressing this issue is to compare the results based on equal power to the target, that is, the product of beam energy and current. In the case of the reaction ^{9}Be(p,n), where multiple proton energies were used, the results

Figure III-D-2: An example of the dose components using a typical MSR configuration

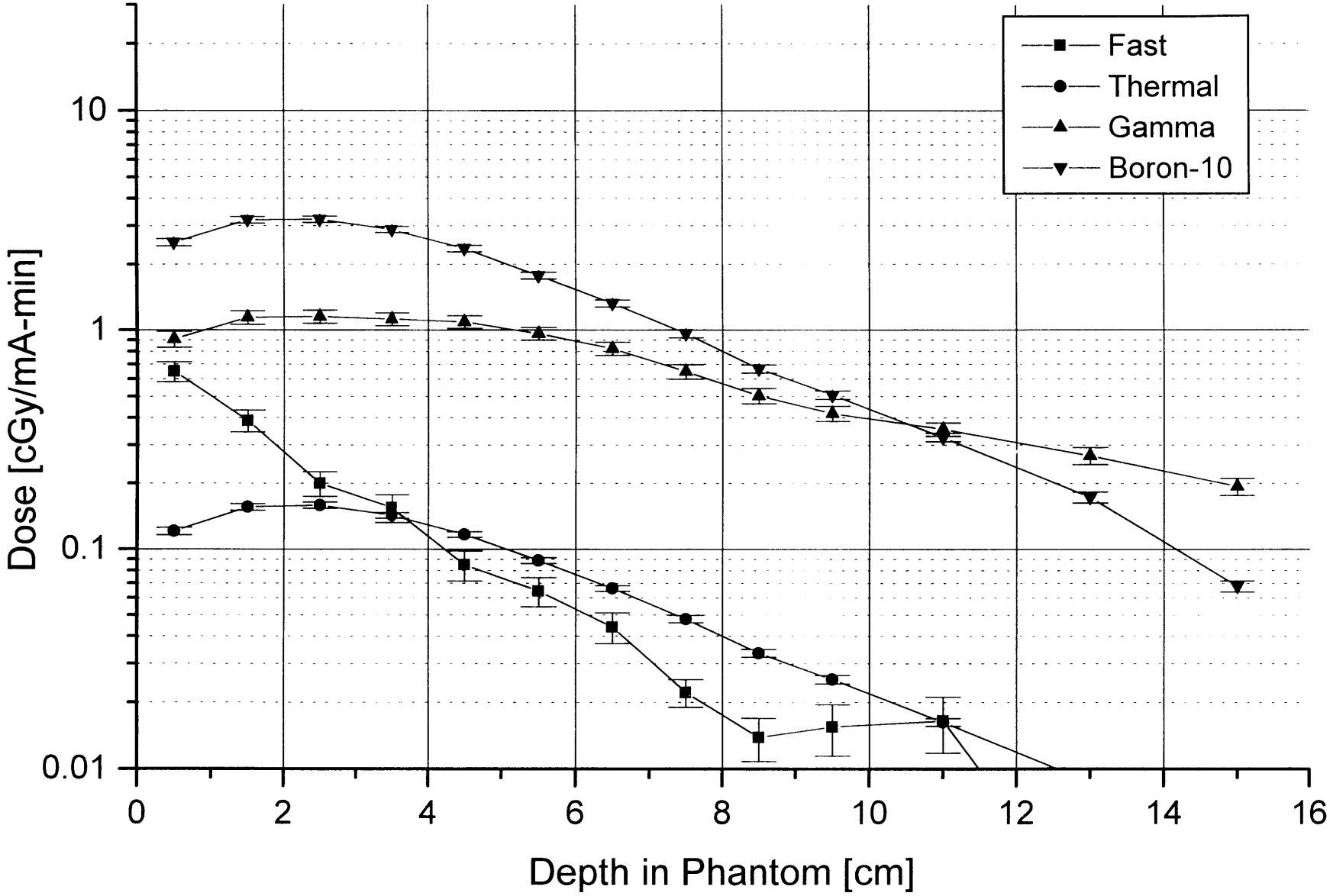

of the various energies were compared on the basis of equivalent proton current and on the basis of equivalent accelerator power. A comparison of the $^{7}Li(p,n)$ and $^{9}Be(p,n)$ reactions was made on the basis of equivalent total accelerator power.

A comment concerning the notation used in the figures of this section is needed. The MSR configuration is annotated with a series of numbers and letters which designate the size and composition of the moderator, and the composition of the reflector. When the reaction and ion energy is obvious, it is not included in the nomenclature. For example the designation, 27x10g-d, signifies a moderator 27 cm long, with a 10 cm radius. This moderator is surrounded by a graphite reflector (g), and the moderator is filled with D_2O (d). When the reaction $^{7}Li(p,n)$ is used, the designation is prefaced by a "li" as in li27x10g-d. When the $^{9}Be(p,n)$ reaction is used, the designation is prefaced by a 2 digit number representing the proton energy in units of MeV. Thus, 3.4-27x10g-d indicates that a proton bombarding energy of 3.4 MeV was used. The various designations are shown in Table III-E-1.

Moderator Material	Designation
D_2O	d
Al-AlF_3	a
Reflector Material	Designation
Graphite	g
Lead	pb
Bismuth	bi
Nickel	ni
Neutron source reactions	Designation prefaced by
$^{7}Li(p,n)$, E_p=2.5 MeV	li
$^{9}Be(p,n)$, E_p=4.0 MeV	4.0
$^{9}Be(p,n)$, E_p=3.7 MeV	3.7
$^{9}Be(p,n)$, E_p=3.4 MeV	3.4
$^{9}Be(p,n)$, E_p=3.0 MeV	3.0

Table III-E-1: MSR designations for Section III.E.

Although the total tumor dose rates at 2 cm and 6 cm were both examined, these two rates are related. Figure III-E-1 shows the total tumor dose rate at 6 cm as a function of the total tumor dose rate at 2 cm for 24 representative simulations, which include both (p,n) reactions and all proton energies. Since the two values are linearly related, the simulations will only be compared based on the total tumor dose rate at 2 cm and the Fast Neutron Fraction. The Fast Neutron Fraction (FNF) is defined here as the ratio: (fast neutron dose rate at 0.5 cm) / (total dose rate to tumor at a depth of 0.5 cm). One of the stated design goals is that the FNF should be less that 0.15. Because the statistical uncertainty of the results is on the order of a few percent, configurations with FNFs close to, but higher than, 0.15 should not be disregarded.

III.E.1 Results using the ^{9}Be(p,n) reaction

III.E.1.a Initial results using 4.0 MeV protons

The ^{9}Be(p,n) reaction was first evaluated using a proton bombarding energy of 4.0 MeV. Figure III-E-2 indicates the total tumor dose rate (without RBE weighting factors) at a depth of 2 cm, and the FNF. On a graph of this type, the best possible design would be located at the upper left hand corner, indicating both low fast neutron contamination, and high total tumor dose rate. There are several features of this plot which are important.

Figure III-E-1: Total tumor dose rate at 6 cm as a funtion of the total tumor dose rate at 2 cm for representative simulations using both (p,n) reactions and all proton energies.

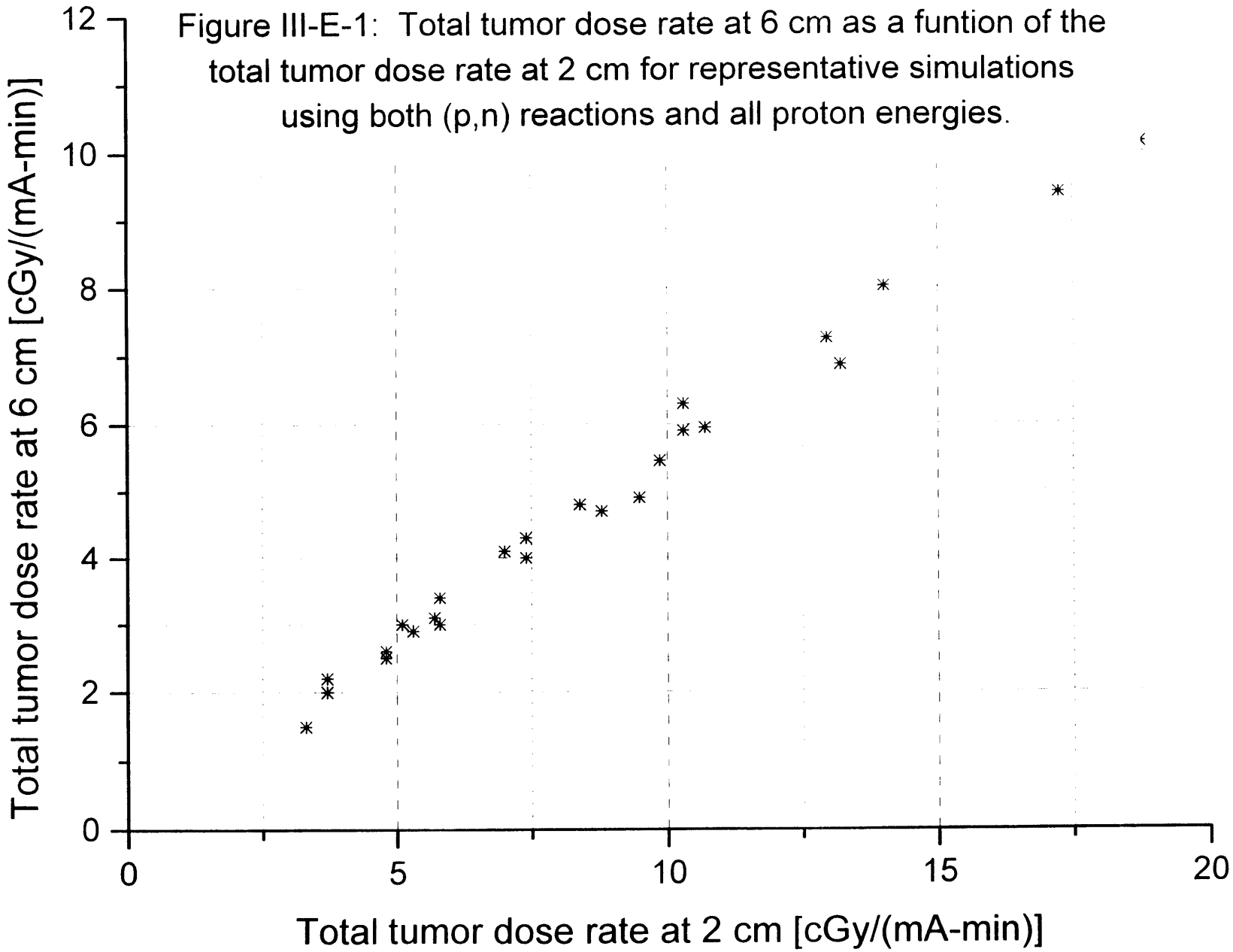

Figure III-E-2: Comparison of therapy beam simulation results for $^{9}Be(p,n)$, E_p = 4.0 MeV

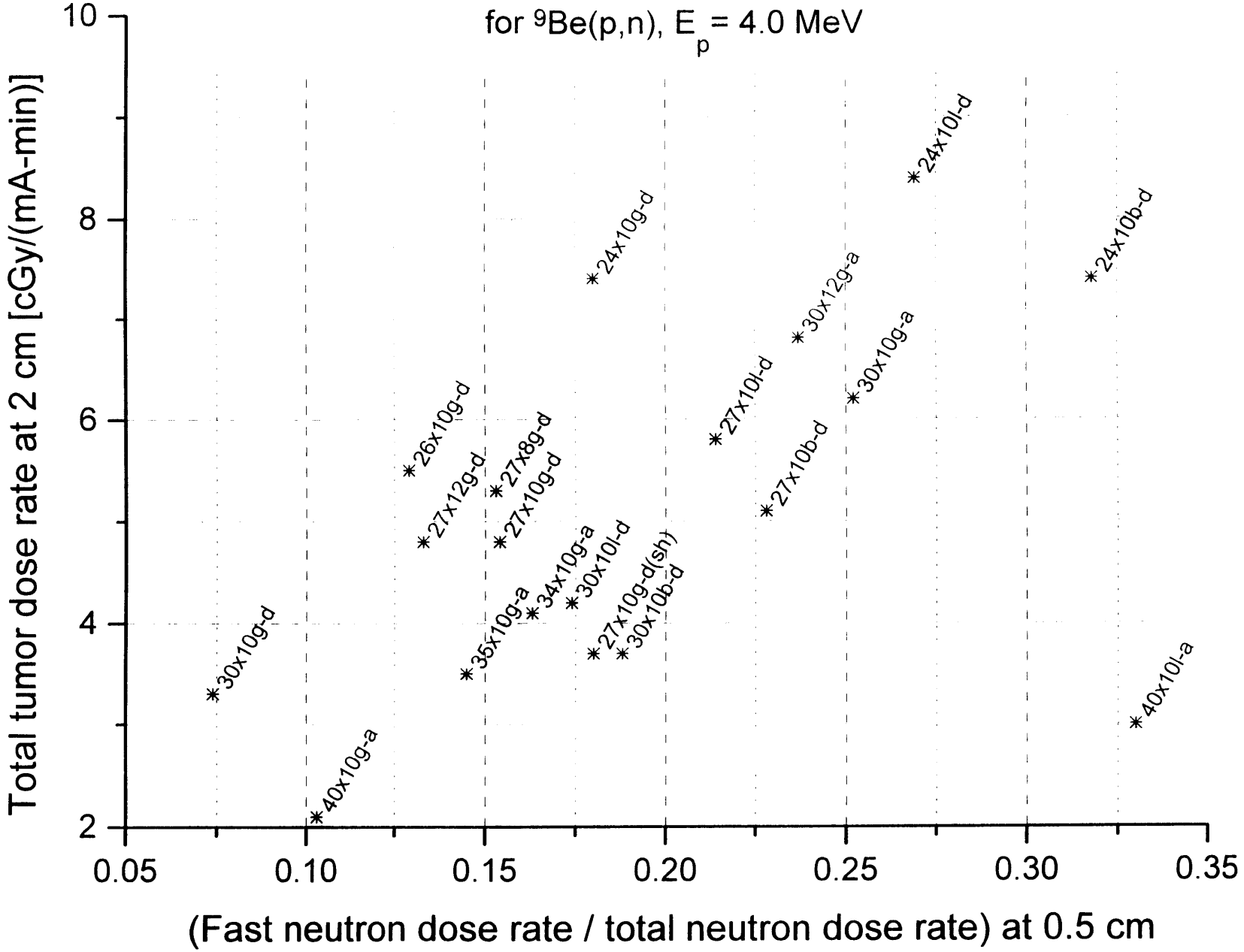

First, on the basis of this comparison, the worst combination of moderator and reflector is Lead-Al/AlF_3. This combination leads to both a low total tumor dose rate, and a high FNF. This is due to the reduced moderating capabilities of both materials when compared with D_2O and graphite. Smaller moderator volumes, such as 4.0-35x10l-a and 4.0-30x10l-a resulted in higher FNF, and are not shown on this graph.

Second, the best combination is Graphite-D_2O. With a FNF less than 0.15, total tumor dose rates in excess of 5 cGy/(min-mA) were predicted. This combination would have the best moderating capability, which is reflected in these results. A graph showing the dose components for the configuration 4.0-27x10g-d is shown in Figure III-E-3. This configuration results in predicted total tumor dose rates at 2 cm and 6 cm of 4.2 and 2.1 cGy/(mA-min), respectively.

Another trend, which is to be expected, is indicated on this graph. With any given combination of reflector/moderator, the data points move from the upper right to the lower left as the length of the moderator is increased. This is due to the trade-off between dose rate and FNF which was mentioned previously.

Finally, if only the Graphite-D_2O combinations are considered, a moderator size close to 27x10 best meets the design criteria specified. This is the configuration that was selected after the first series of simulations, and was used in the evaluation of the effects of target location and reflector size discussed later in this chapter. It should be noted that

Figure III-E-3: Results of a therapy beam simulation using 27x10cm D_2O Moderator,Graphite Reflector, $^{9}Be(p,n)$ 4 MeV

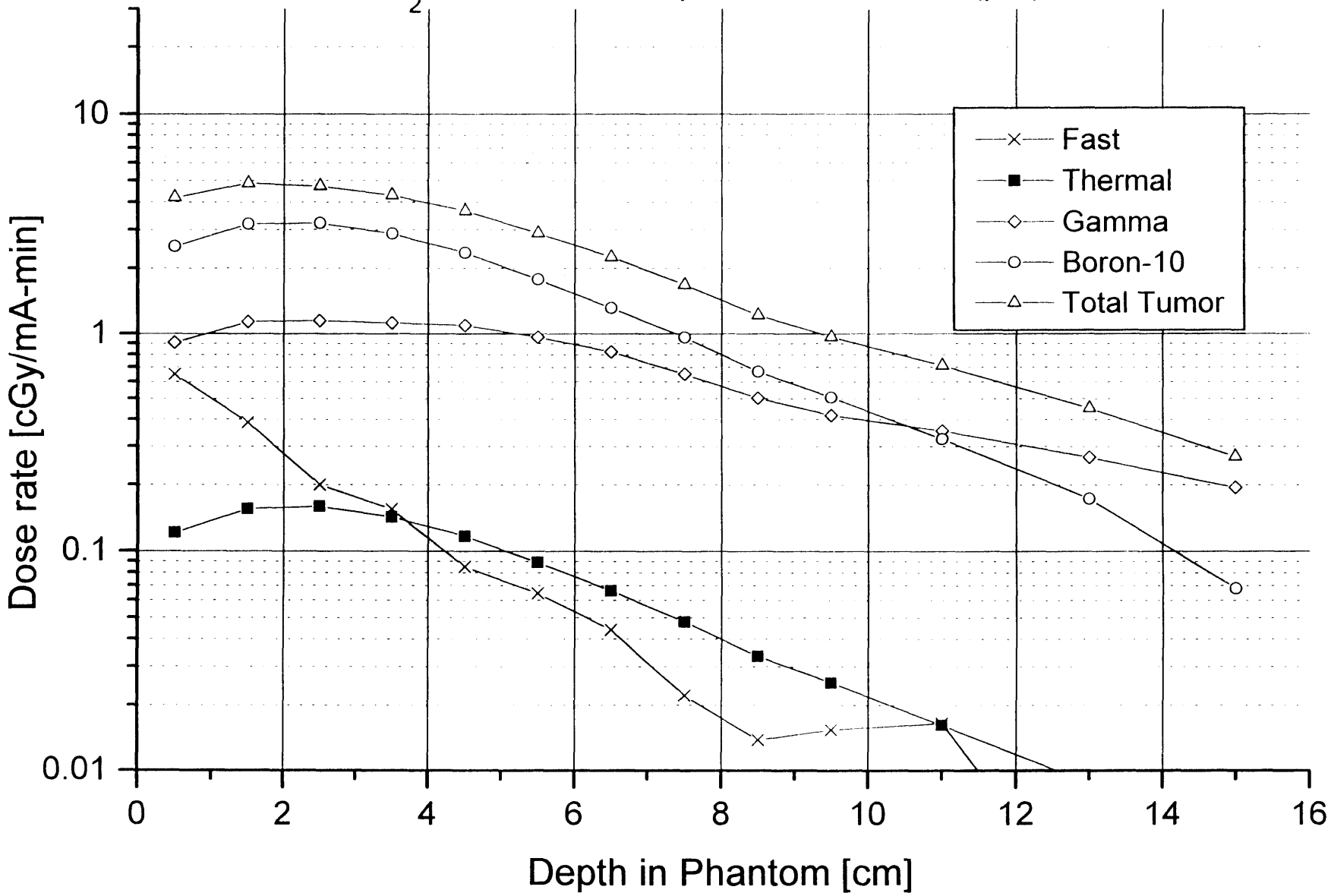

4 configurations: 4.0-26x10g-d, 4.0-27x12g-d, 4.0-27x8g-d, and 4.0-27x10g-d, have FNF = 0.14 $\pm$ 0.02, and total tumor dose rates of 5.2 $\pm$ 0.4 cGy/(mA-min). As stated above, for 3 million histories, the statistical uncertainties are 3-10 % for each of the components. Therefore, these various configurations can be said to be equivalent.

III.E.1.b Results using 3.7 MeV protons

The results of the simulations using the reaction $^{9}Be(p,n)$, E_p=3.7 MeV are shown in Figure III-E-4. Based on the experiences gained using 4.0 MeV protons for this reaction, three combinations of reflector/moderator were selected: Graphite-D_2O, Graphite-Al/AlF_3, and Lead-D_2O. Solid lines on the graph segregate these combinations. Due to the fewer number of simulations, the trends mentioned in Section III.E.1.a are more clearly visible. The best configuration found was 3.7-25x10g-d. The results using this configuration are shown in Figure III-E-5. The predicted total tumor dose rates at 2 and 6 cm are 5.2 and 2.7 cGy/(mA-min), respectively, and the FNF is 0.15.

III.E.1.c Results using 3.4 and 3.0 MeV protons

The results of simulations using 3.4 and 3.0 MeV protons are shown in Figure III-E-6 and Figure III-E-7. The best configurations are 3.4-23x10g-d and 3.0-21x10g-d respectively. The 3.4-23x10g-d design resulted in total tumor dose rates at 2 and 6 cm of 4.2 and 2.2 cGy/(mA-min) respectively, and the FNF is 0.16. The 3.0-21x10g-d configuration resulted in dose rates at 2 and 6 cm of 2.8 and 1.5 cGy/(mA-min) respectively, and the FNF is 0.15.

Figure III-E-4: Comparison of therapy beam simulation results for $^{9}Be(p,n)$, E_p = 3.7 MeV

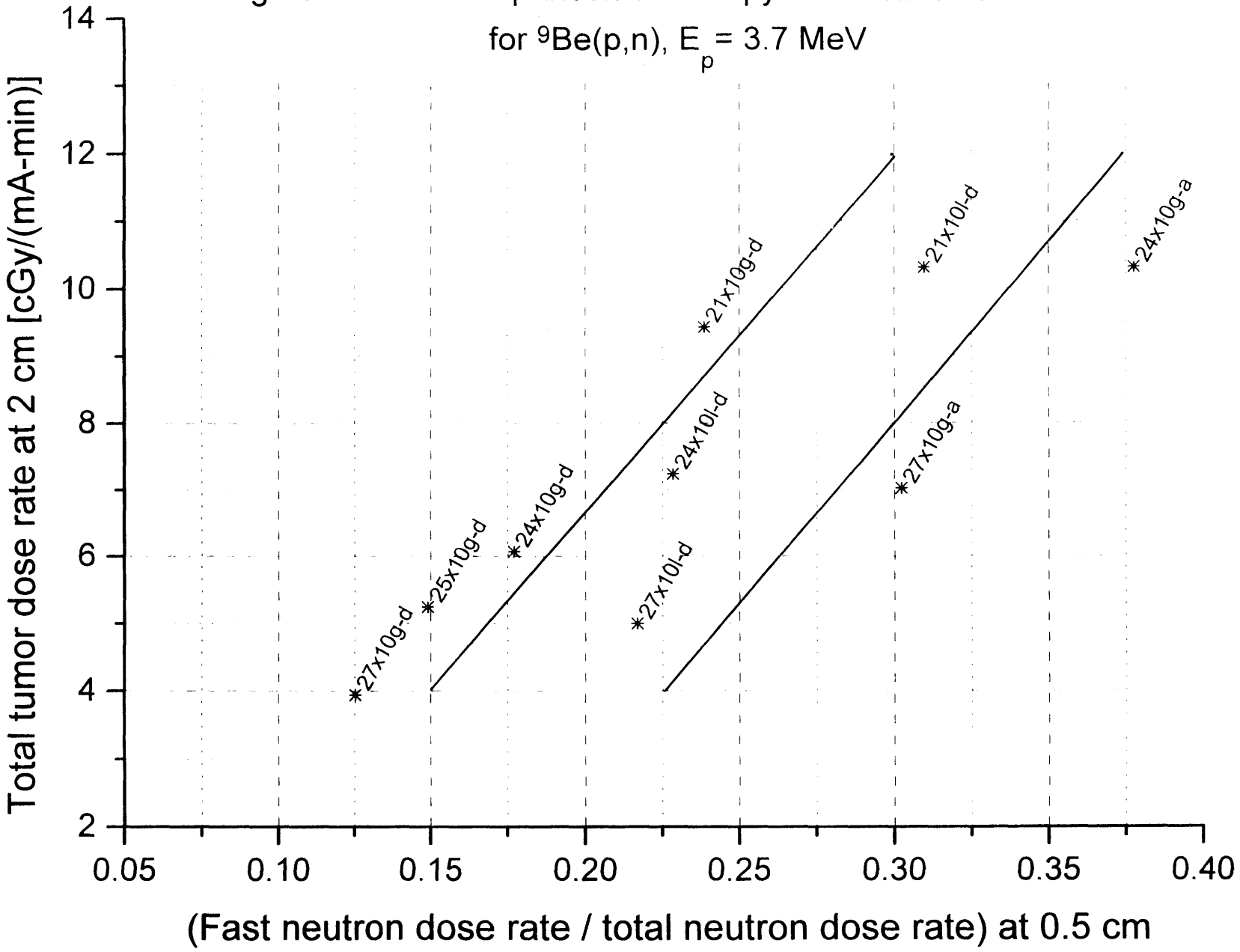

Figure III-E-5: Results of a therapy beam simulation using 25x10cm D_2O Moderator,Graphite Reflector, $^{9}Be(p,n)$ 3.7 MeV

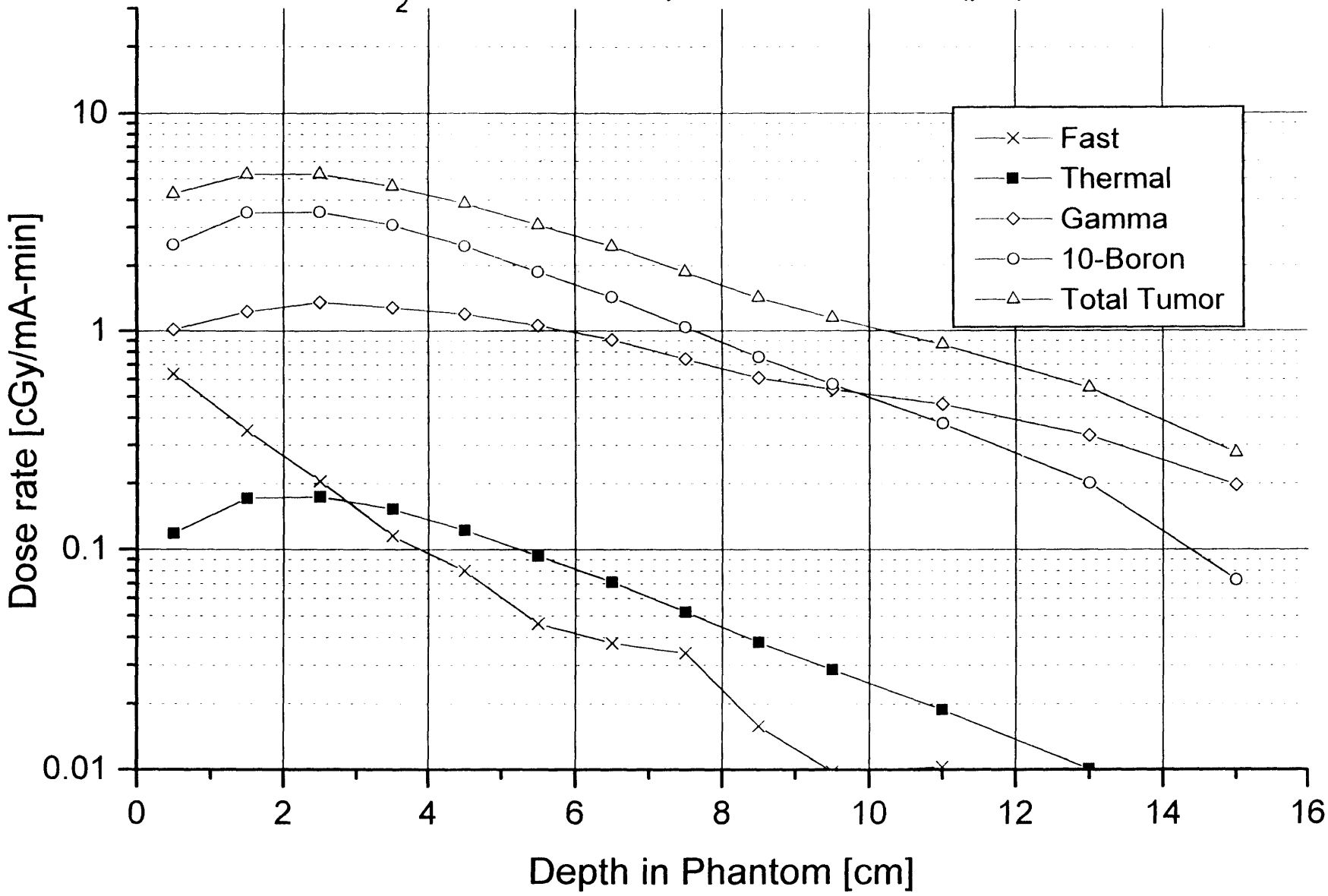

Figure III-E-6: Comparison of therapy beam simulation results for $^{9}Be(p,n)$, E_p=3.4 MeV

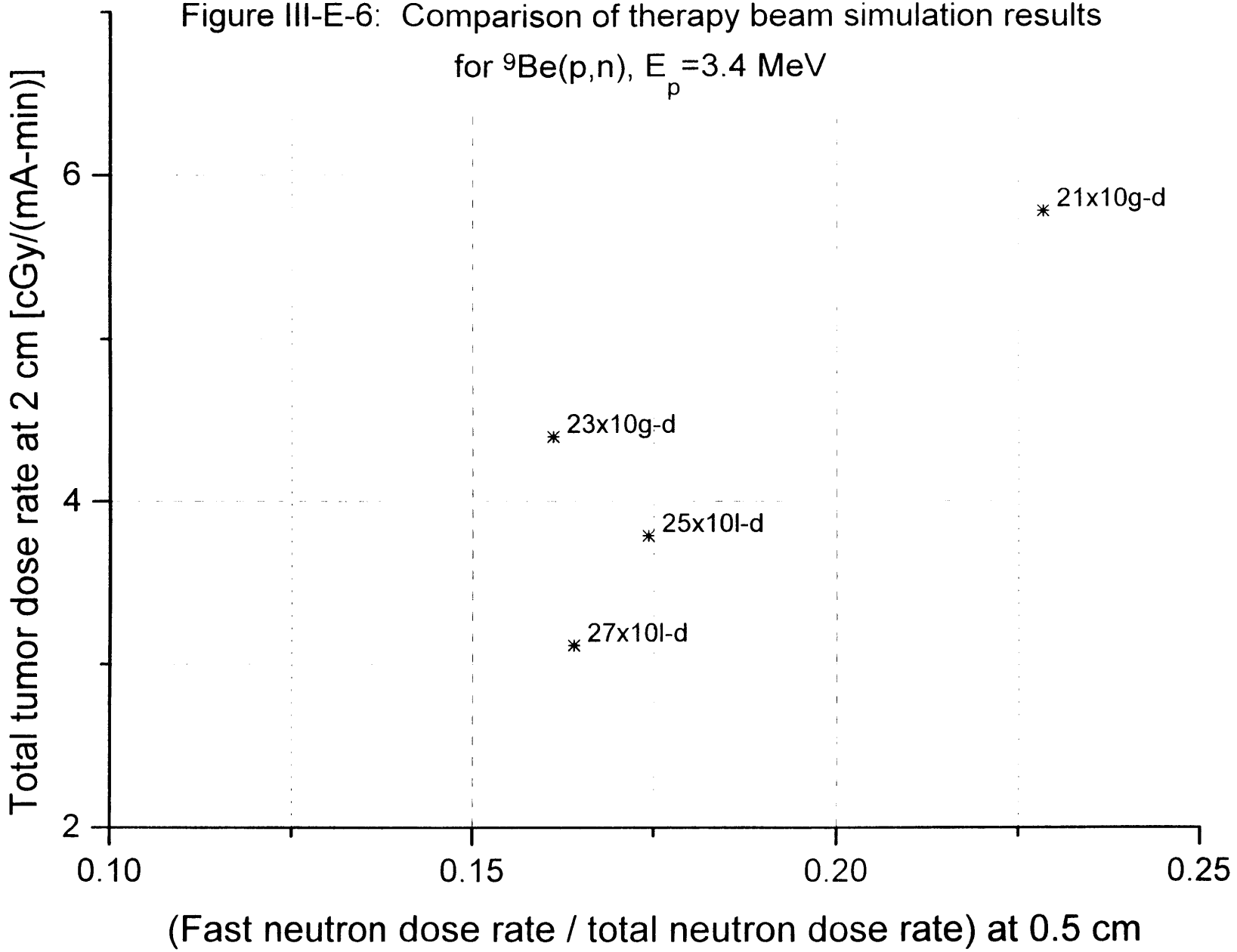

Figure III-E-7: Comparison of therapy beam simulation results for $^{9}Be(p,n)$, E_p = 3.0 MeV

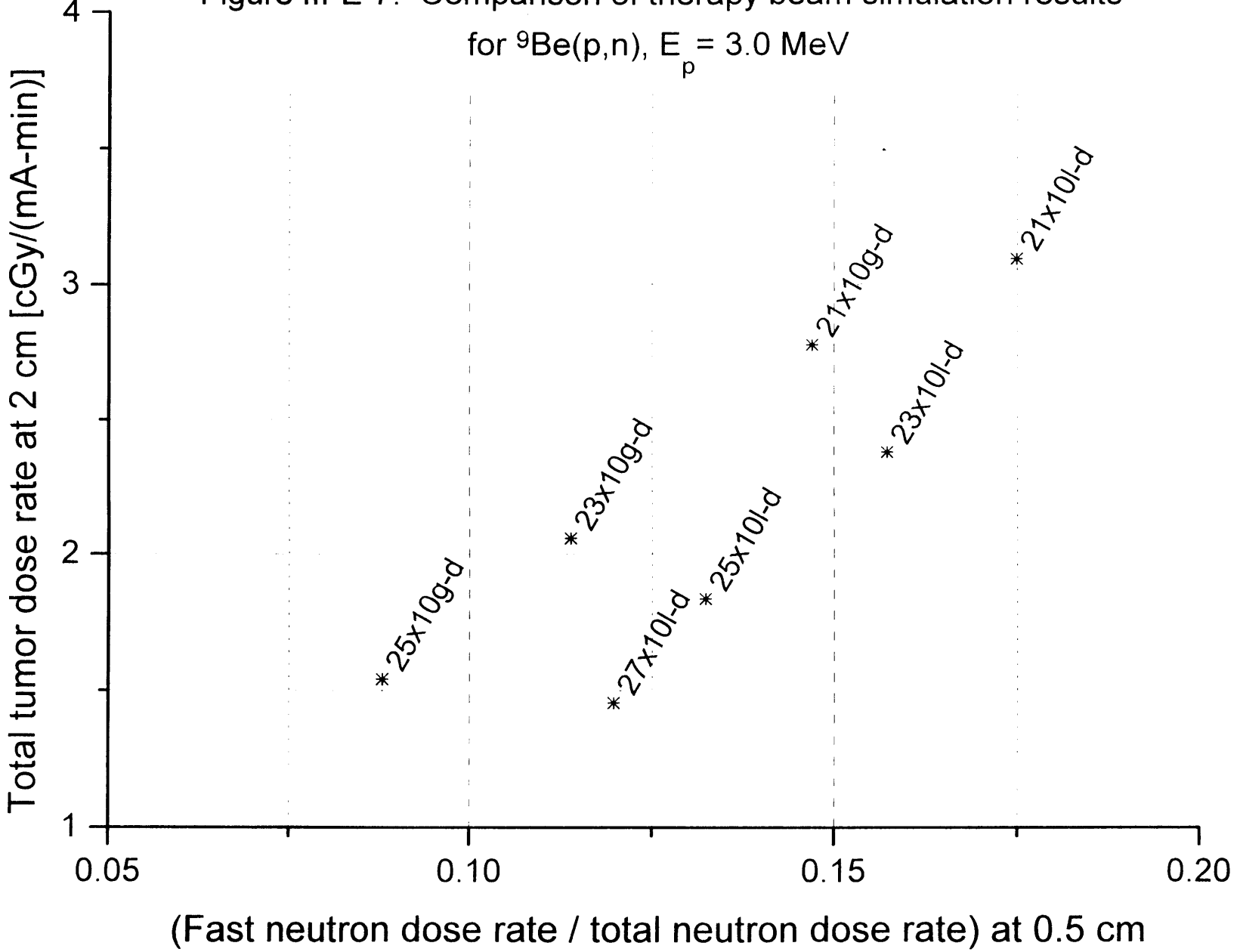

III.E.1.d Combined results for proton energies 4.0, 3.7, 3.4, and 3.0 MeV

As mentioned in the introduction to this chapter, the comparison of results from the same reaction, using variable ion energies, can be made based on equivalent current, or equivalent accelerator power. The first of these comparisons is shown in Figure III-E-8, and the second comparison is shown in Figure III-E-9. When comparing different proton energies on the basis of equal accelerator current, one interesting result is that the combinations 3.7gr-d-25x10, 4gr-d-27x8, and 4gr-d-27x10 are nearly equivalent. This indicates that the reduction in yield between the 4.0 and 3.7 MeV proton beams would be sufficiently compensated by the smaller moderator volume needed when using the 3.7 MeV beam.

When compared on the basis of accelerator power, the performance of the 3.7 MeV beam relative to the 4.0 MeV beam is superior. Additionally, the combinations 3.4-23x10g-d and 4.0-27x8g-d have nearly equivalent results. This is an important result for AB-BNCT. This indicates that for a given dose rate and FNF, there is a choice of how those endpoints can be achieved. For some accelerator designs, it may be much easier to deliver 10 kW to the target using 3.4 MeV protons than using 4.0 MeV protons. Using a lower proton energy would require a lower terminal voltage for the accelerator. This may reduce system cost, size and complexity. The LABA accelerator has not yet been run at multi-milliAmpere beam currents. Therefore, it is difficult to predict which combination of beam energy and current can be most easily produced.

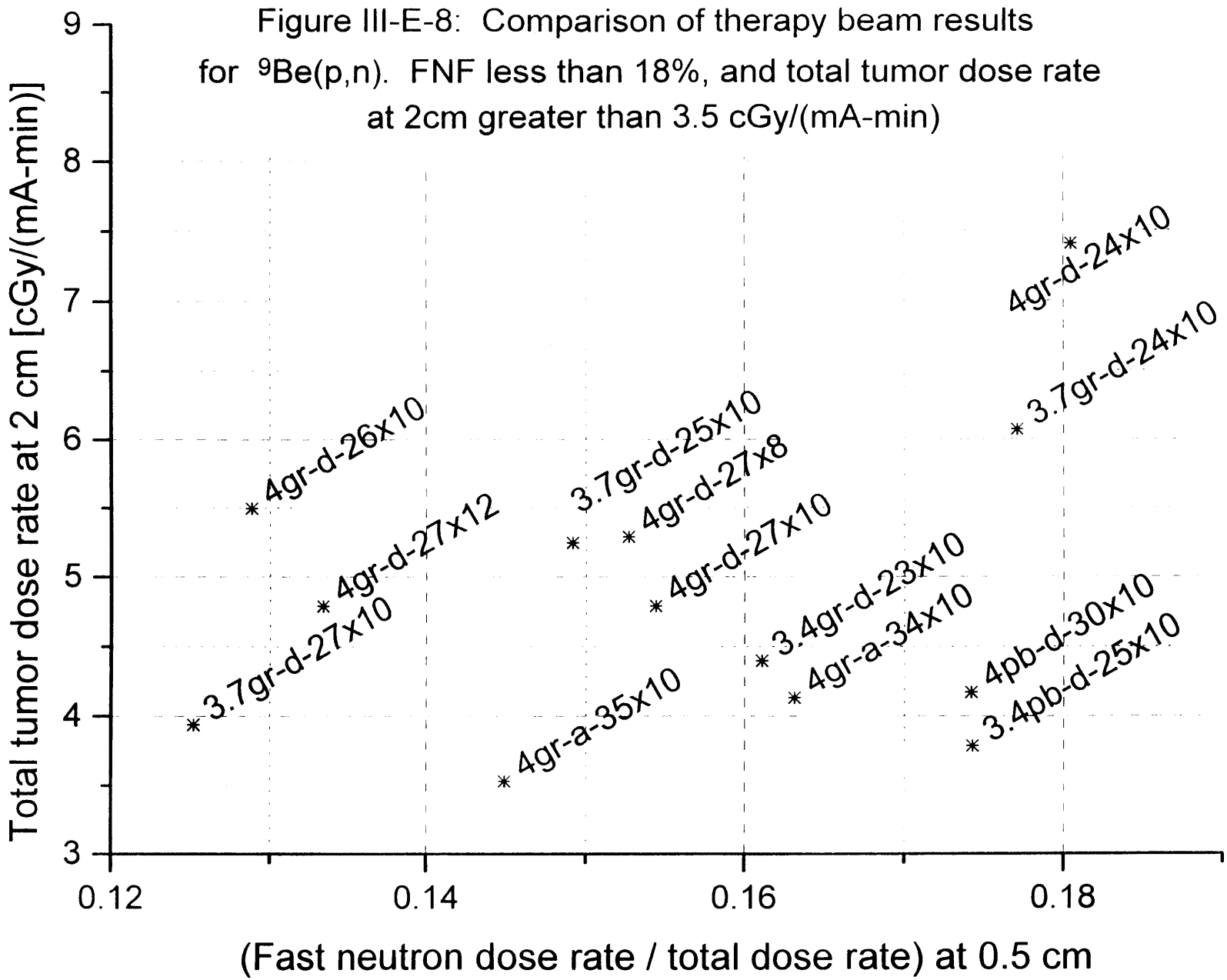
Figure III-E-8: Comparison of therapy beam results
for 9Be(p,n). FNF less than 18%, and total tumor dose rate
at 2cm greater than 3.5 cGy/(mA-min)
Total tumor dose rate at 2 cm [cGy/(mA-min)]
(Fast neutron dose rate / total dose rate) at 0.5 cm
9
8
7
6
5
4
3
0.12
0.14
0.16
0.18
4gr-d-26x10
4gr-d-27x12
3.7gr-d-27x10
3.7gr-d-25x10
4gr-d-27x8
4gr-d-27x10
4gr-a-35x10
3.4gr-d-23x10
4gr-a-34x10
4gr-d-24x10
3.7gr-d-24x10
4pb-d-30x10
3.4pb-d-25x10

Figure III-E-9: Comparison of therapy beam simulation results for $^{9}Be(p,n)$ using equivalent accelerator power

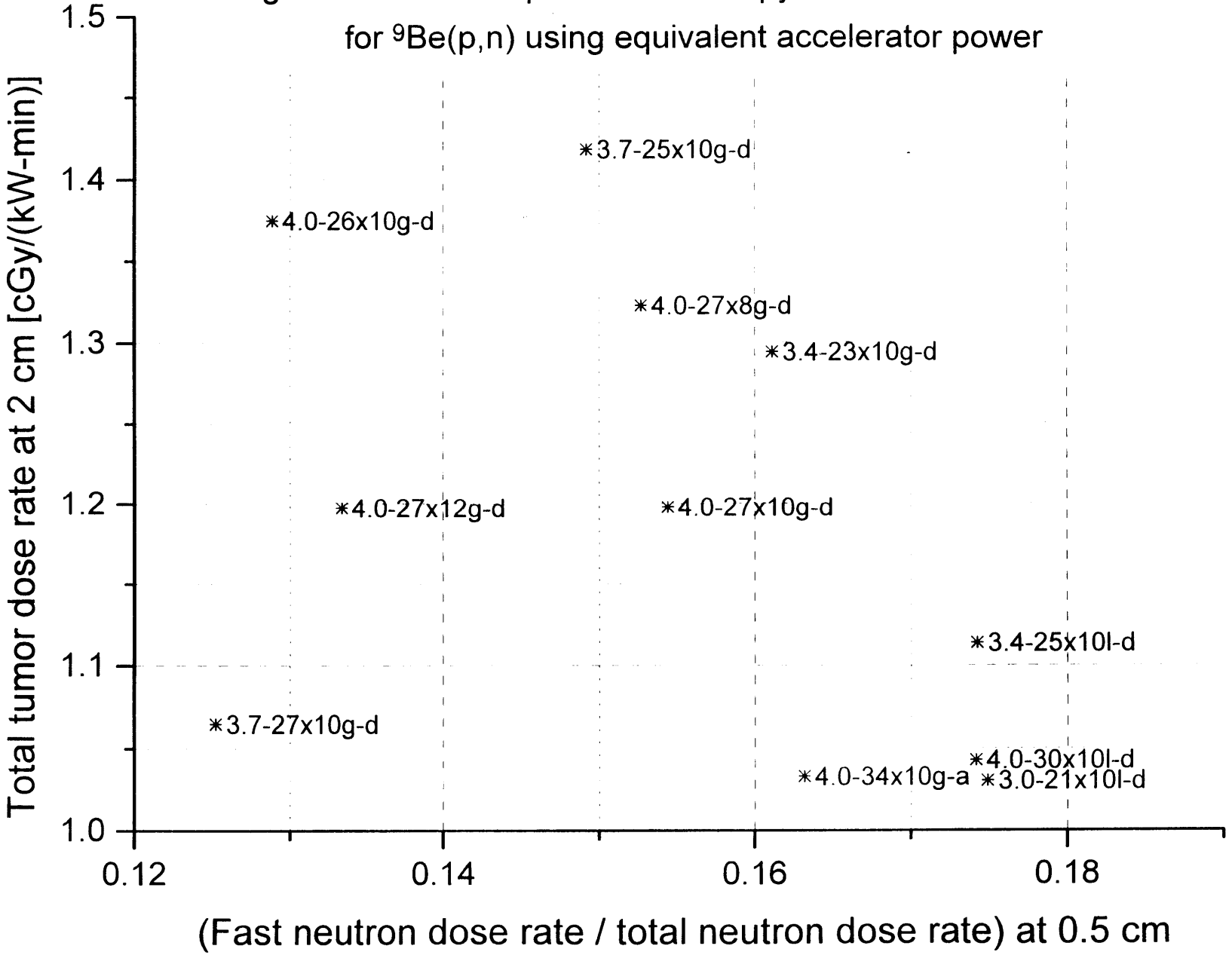

Finally, this raises the question of how far this trend can be followed. That is, if 3.7 MeV and 3.4 MeV proton energies can produce therapy beams similar to those produced using E_p=4.0 MeV, can a MSR designed using 3.0 MeV protons also produce a therapy beam with equivalent performance based on total accelerator power? What is the lower limit? The best result for each proton energy is summarized in Table III-E-2 below. In this table, dose rates are compared based on equivalent power.

Proton beam energy [MeV]	Size of moderator (length x radius) [cm]	Moderator material	Reflector material	FNF	Total tumor dose rate at 2 cm [cGy/(kW-min)]	Total tumor dose rate at 6 cm [cGy/(kW-min)]
4.0	26 x 10	D_2O	Graphite	.13	1.37	0.71
3.7	25 x 10	D_2O	Graphite	.15	1.42	0.74
3.4	23 x 10	D_2O	Graphite	.16	1.29	0.66
3.0	21 x 10	D_2O	Graphite	.15	.925	0.48

Table III-E-2: Summary of ^{9}Be(p,n) beam design results compared on the basis of equivalent accelerator power.

The results presented in Table III-E-2 should be interpreted carefully. On the basis of this comparison, there does not seem to be a clear advantage to using the 4.0 MeV proton beam. It is unlikely that an accelerator would be able to produce more power using 4.0 MeV protons than using 3.7, 3.4 or 3.0 MeV protons. The opposite is not true. Although the total tumor dose rates using E_p=3.0 MeV are significantly lower than those using E_p=3.7 MeV, it is possible that the power capacity of an accelerator would be greater at the lower proton energy. A final judgment on the best MSR configuration and proton energy can occur only when the relation between maximum power and beam energy is considered.

III.E.2 Results using the ^{7}Li(p,n) reaction

A comparison of the results using the ^{7}Li(p,n) reaction is shown in Figure III-E-10. Based on the trends discussed above, the data points for li20x10g-d and li22x10g-d indicate that a configuration such as li21x10g-d might be optimal for this reaction. It appears that there would be three configurations which might provide similar beam performance: li21x10g-d, li22x10pb-d and li22x10bi-d. The results using the configuration li22x10g-d are presented in Figure III-E-11. Since this configuration results in a FNF more than 2 percentage points less than the other two, with only slightly lower dose rates, it can be considered the best design.

III.E.3 Comparing the ^{7}Li(p,n) and ^{9}Be(p.n) reactions

A comparison between the ^{7}Li(p,n) and ^{9}Be(p,n) reactions, on the basis of equivalent accelerator power is shown in Figure III-E-12. When the two (p,n) reactions are compared on this basis, the advantages of the ^{7}Li(p,n) reaction are clearly visible. Since this reaction has both a low average neutron energy and high total yield, the total tumor dose rates at 2 cm are more than a factor of 2 greater than designs based on the ^{9}Be(p,n) reaction, for equivalent FNFs. For equivalent performance, the ^{7}Li target would need to withstand only half the heat load of the beryllium target. If target designs based on lithium are found to be capable of handling the required heat loads, the ^{7}Li(p,n) reaction would be the better reaction.

Figure III-E-10: Comparison of therapy beam simulation results for $^{7}Li(p,n)$, E_p = 2.5 MeV

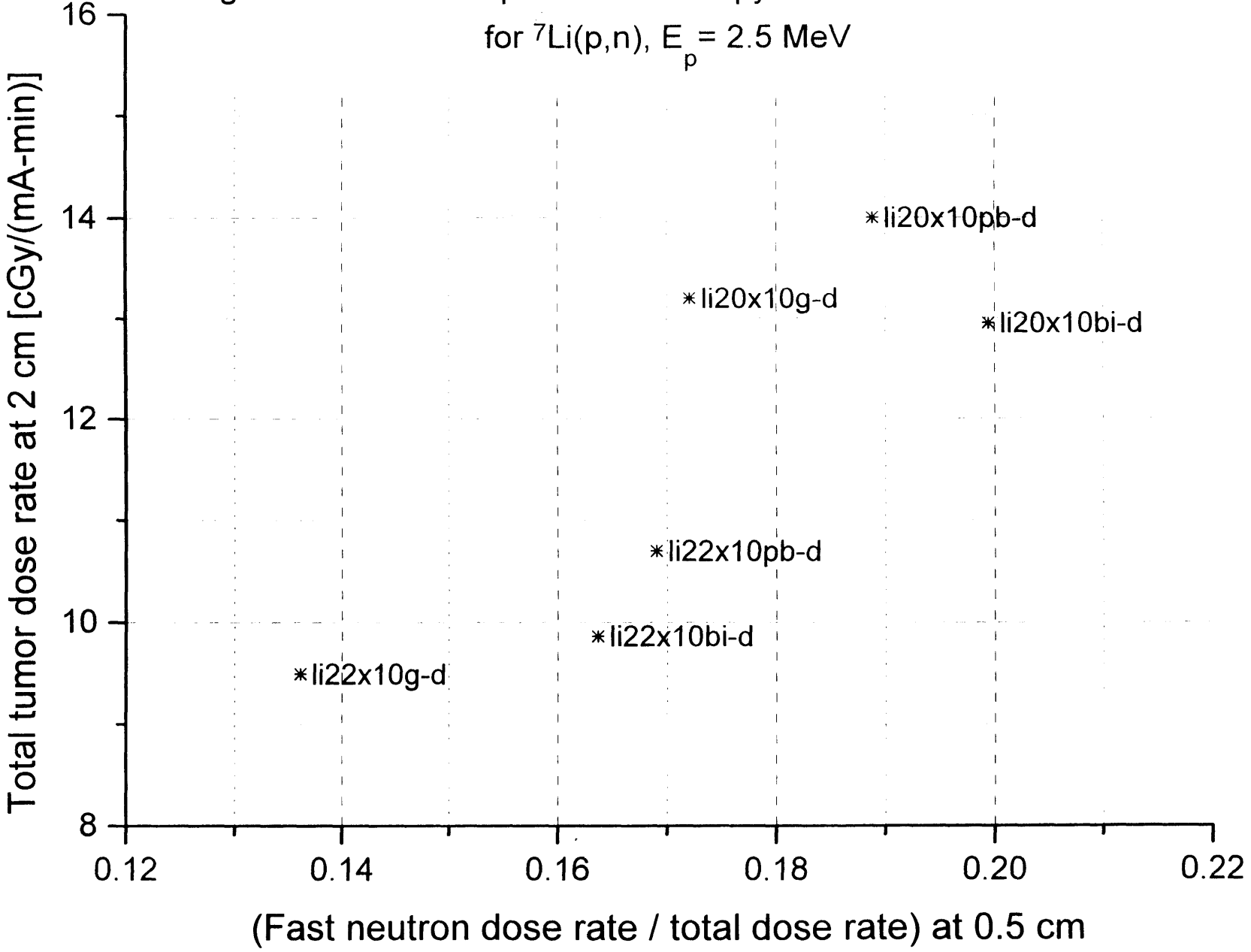

Figure III-E-11: Results of a therapy beam simulation using 22x10D_2O Moderator, Graphite Reflector, $^7Li(p,n)$ 2.5 MeV

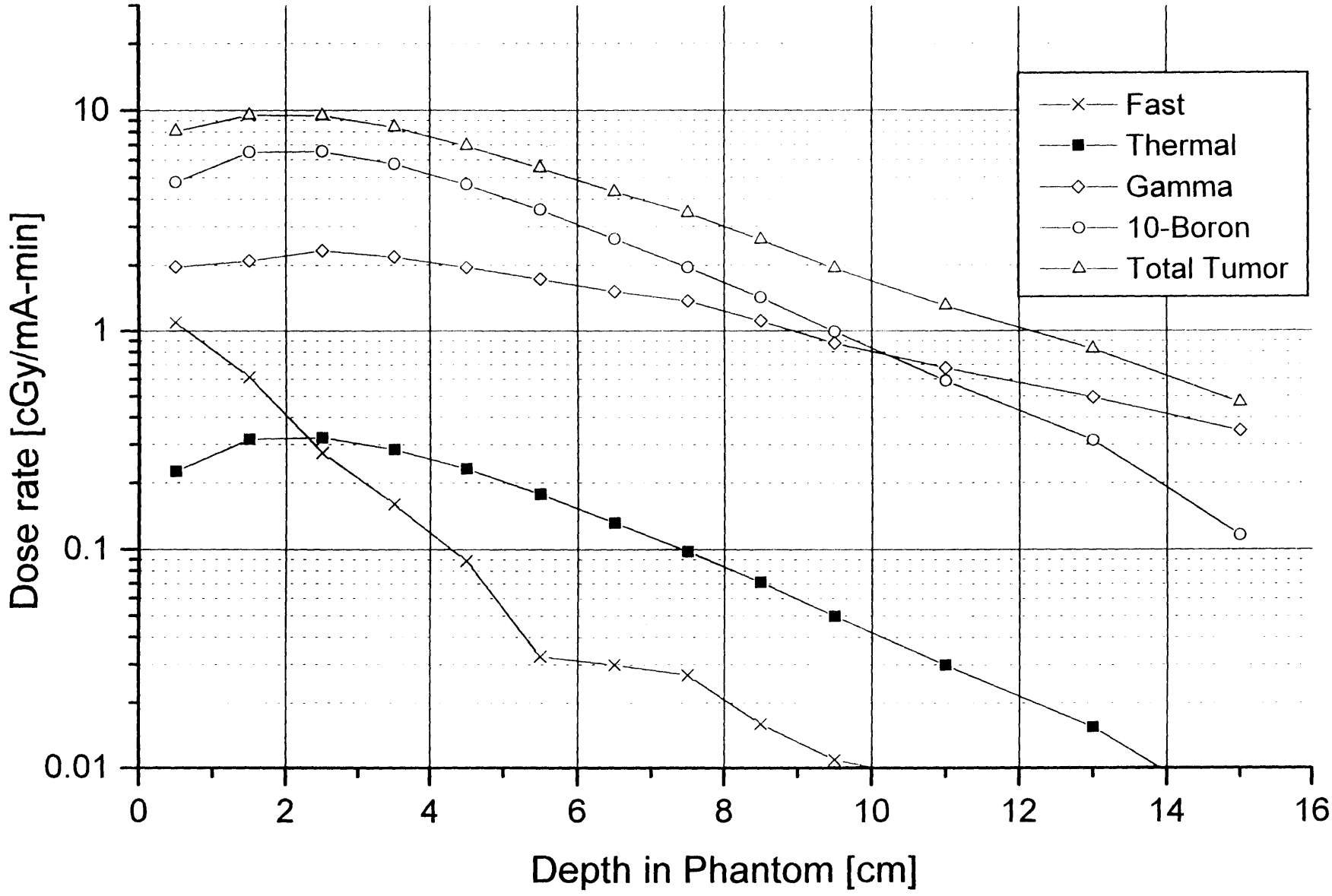

Figure III-E-12: Comparison of therapy simulation results for $^{7}Li(p,n)$ and $^{9}Be(p.n)$ using equivalent accelerator power

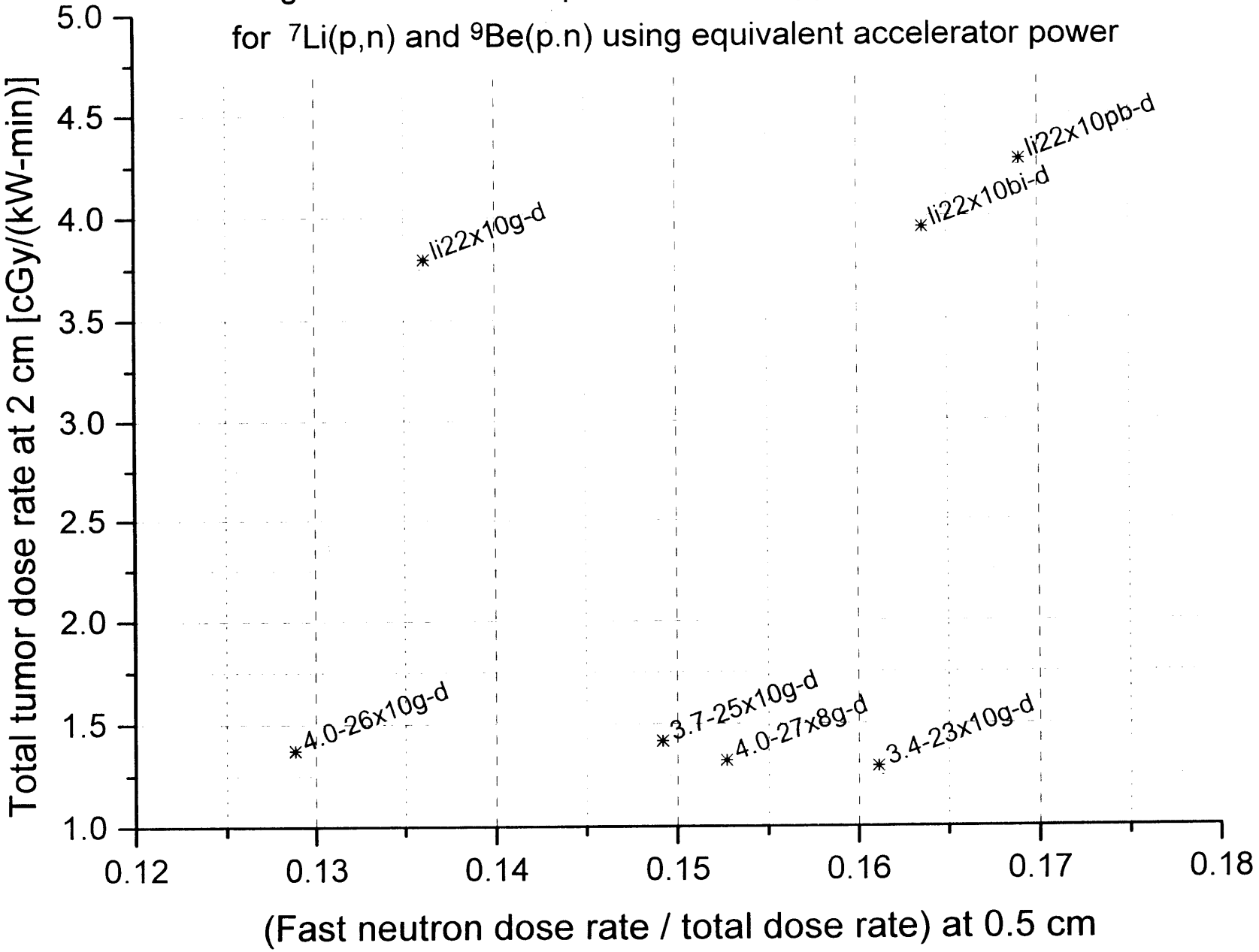

An important point which has been made above should be repeated. The $^{7}Li(p,n)$ reaction was examined using E_p=2.5 MeV, which is the lowest energy of the (p,n) reactions considered here. An accelerator may be able to produce significantly more power at this lower proton energy than it would at E_p=4.0 MeV. The final comparisons can be made only when two things are known: (1) the relationship between maximum available accelerator power and proton energy, and (2) the capability of lithium targets to withstand heat loads.

III.E.4 Gamma production at the target

As mentioned in Chapter II, the two (p,n) reactions are known to produce some contaminant photon radiation at the target. The evaluation of the dose rates in phantom resulting from this photon radiation required a separate MCNP simulation since MCNP will allow only one radiation source definition (neutron or photon).

In the case of the $^{9}Be(p,n)$ reaction, the photon production was evaluated using two MSR configurations: 4.0-27x10g-d and 4.0-34x10g-a. These two combinations result in similar performance measures without the target photon production considered. The AlF_3/Al moderator was expected to provide more shielding against the gamma production at the target than the D_2O moderator based on the higher average Z value of AlF_3/Al. The photon dose rates as a function of depth in the phantom were added to the previous results for these configurations, and the results are presented in Figure III-E-13 and Figure III-E-14.

Figure III-E-13: Results of a therapy beam simulation using 27x10cm D_2O Moderator,Graphite Reflector, $^9Be(p,n)$ 4 MeV Including the gamma production at the target

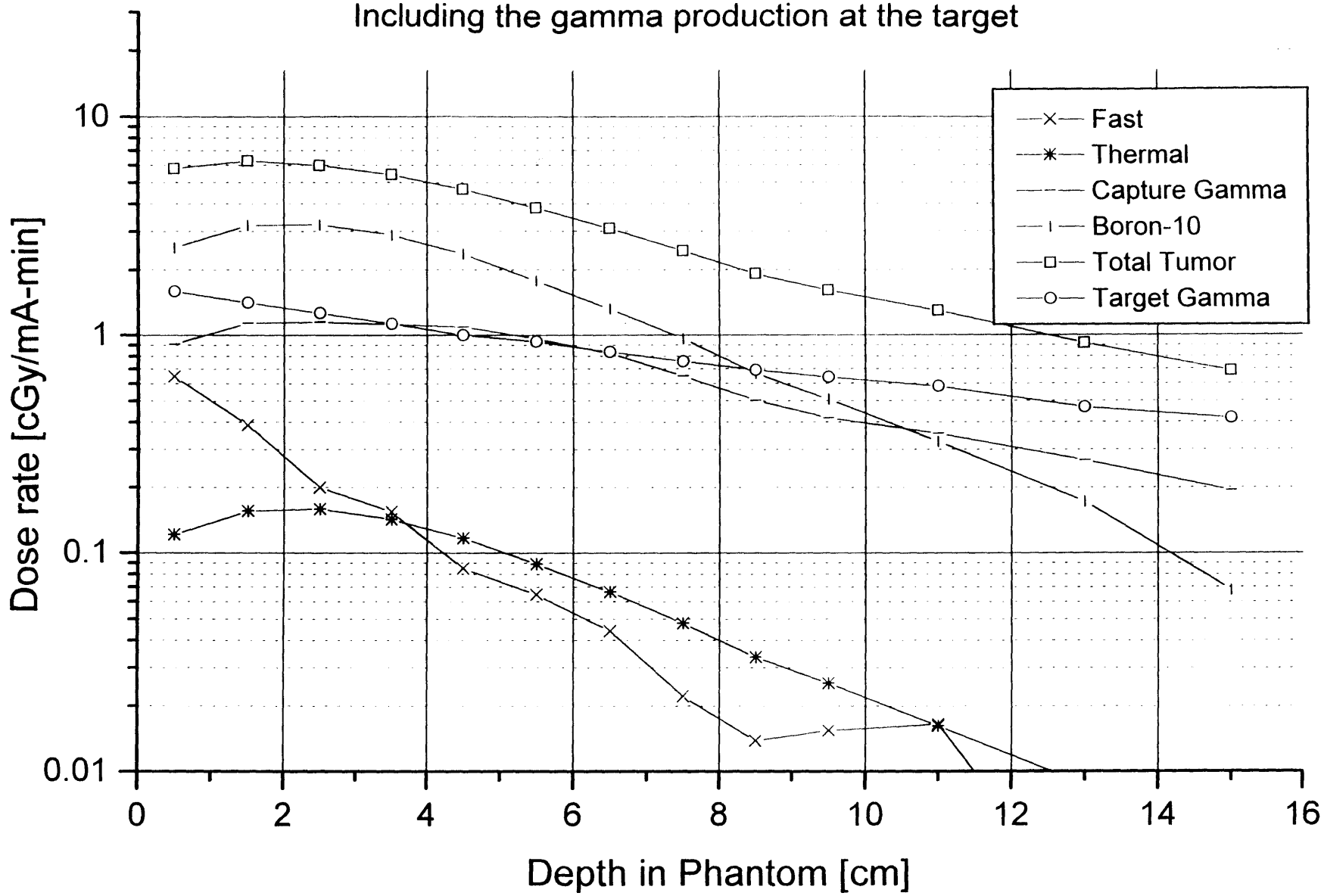

Figure III-E-14: Results of a therapy beam simulation using
34x10cm- 70% AlF_3 - 30% Al - Moderator, Graphite Reflector, $^{9}Be(p,n)$ 4 MeV
Including the gamma production at the target

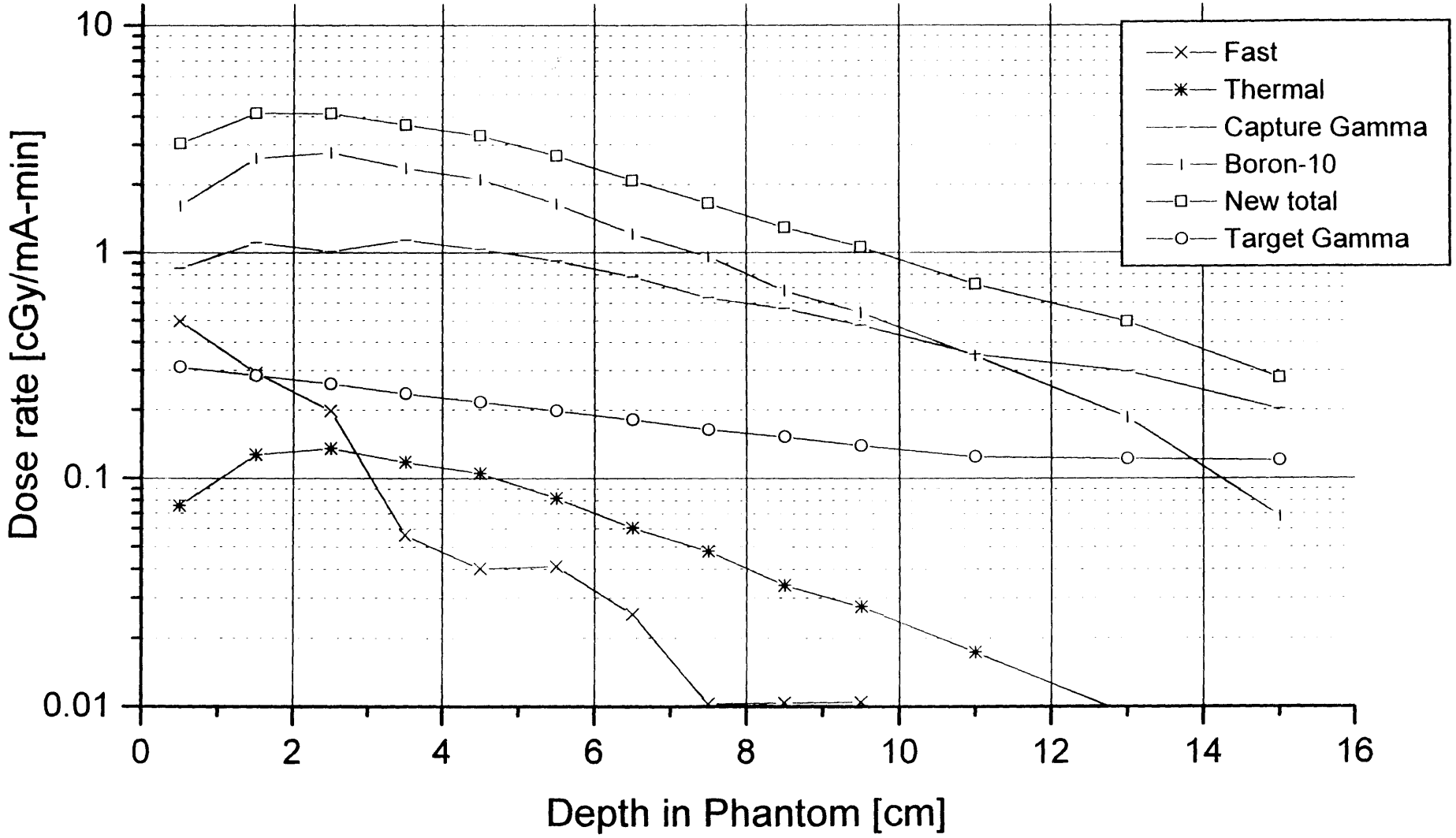

The additional dose rate at 0.5 cm using the 4.0-27x10g-d combination was 1.7 cGy/(mA-min) and was approximately equivalent in magnitude to the (n,γ) dose rate. When using the MSR configuration 4.0-34x10g-a, the photon dose rate resulting from gamma production at the target was approximately 30% of the (n,γ) dose rate. Due to the low value of RBE for photons, the resultant additional dose to the patient may eventually be considered insignificant.

In the case of the ^{7}Li(p,n) reaction, the photon dose rate resulting from gamma production at the target was evaluated using the configuration li22x10g-d. This dose component was then added to the others. The results are shown in Figure III-E-15. The target gamma photon dose rate is approximately 3 orders of magnitude lower than the (n,γ) dose rate. The target gamma energy was low enough (478 keV) that the moderator and reflector provided adequate shielding.

III.E.5 Effect of changing target location

The effect of varying the location of the neutron source relative to the moderator and therapy port was investigated using two series of simulations. In both series, the configuration 4.0-27x10g-d, with the target initially located 2 cm into the moderator, was used. In the first series, the distance from the back of the moderator to the target (dimension A on Figure III-B-2) was varied from the initial value (A=3) while keeping the distance between the target and the therapy port (dimension G on Figure III-B-2) constant. The results of this series are shown in Figure III-E-16. The target location was

Figure III-E-15: Results of a therapy beam simulation using 22x10cm D_2O Moderator,Graphite Reflector, $^7Li(p,n)$ 2.5 MeV Including the gamma production at the target

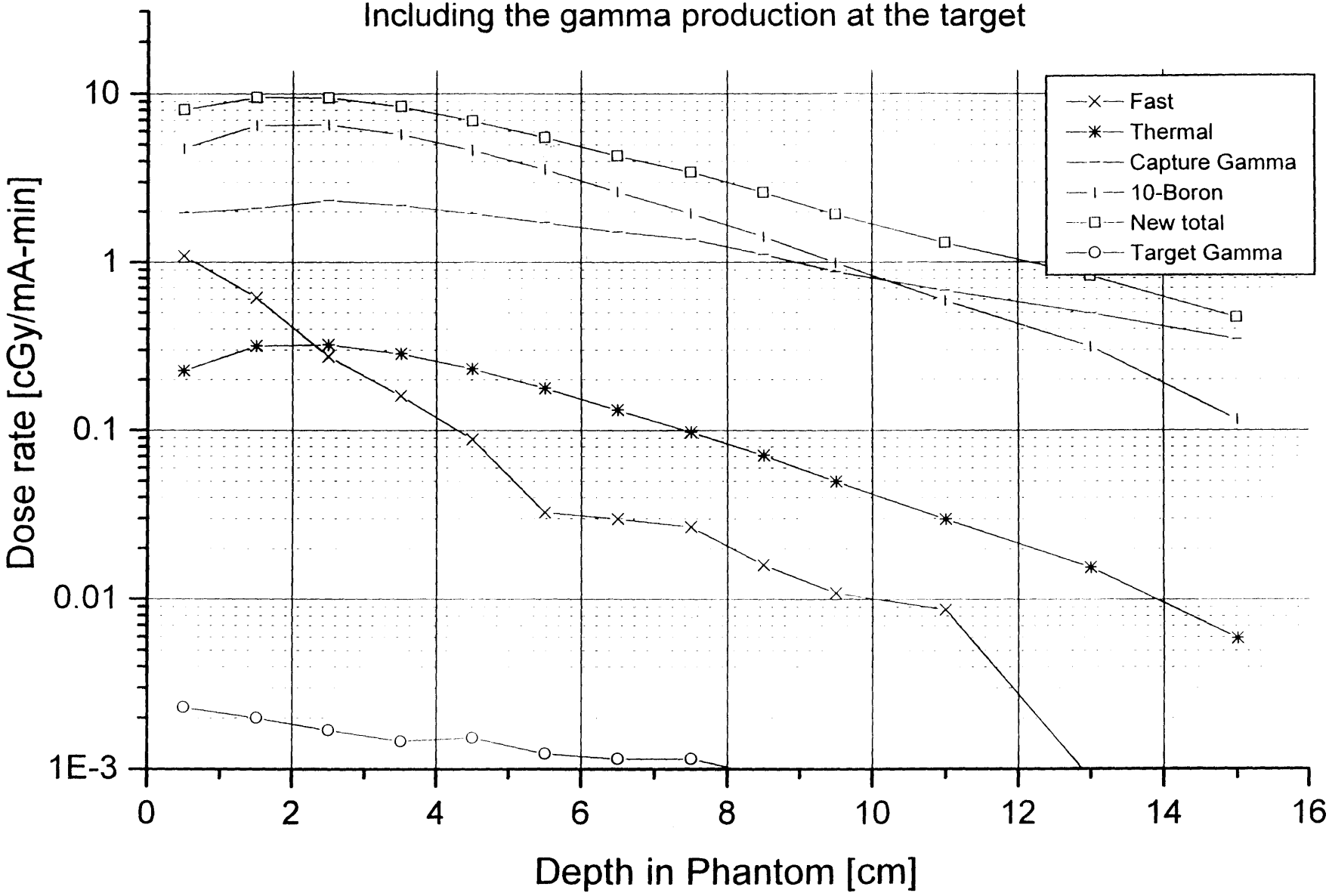

6 – Figure III-E-16: Comparison of results varying target location (A) while keeping target to therapy port distance (G) constant

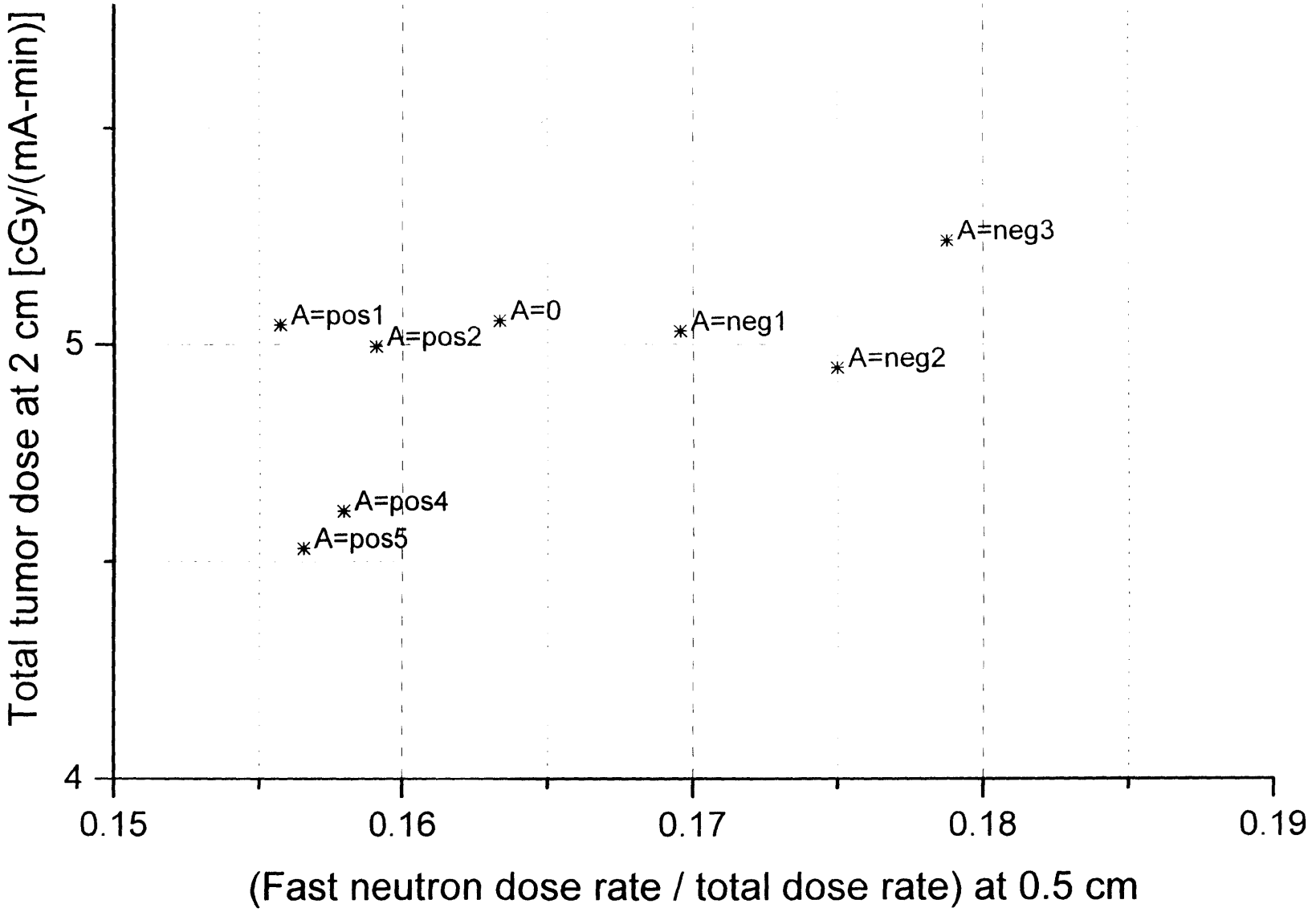

varied over a total distance of 8 cm. Negative values of "A" indicate that the target was located behind the interface of the back of the moderator and the reflector. The notation "A=pos2" indicates that A = 2 cm. The results indicate that the total tumor dose rate is not significantly affected by the amount of moderating material between the back of the moderator and the target. However, the FNF decreases as A is increased from negative to positive values. The total tumor dose rate at 2 cm varied less than 5 % during this series.

For the second series, the moderator dimensions (G and C) were not changed, but the target location (A) was varied from -3 to +5. Results of this series are shown in Figure III-E-17. The configuration with A = +5 resulted in the best performance. One interpretation of the results shown in Figure III-E-17 might be that the additional dose rate at 2 cm is simply the result of the additional fast neutron dose rate because the FNF using this configuration is higher than the others on the graph. An examination of the results, shown in Figure III-E-18, shows that this is not the case.

III.E.6 Results using ^{9}Be(d,n) reaction

As stated in the beginning of the chapter, the results using the reaction ^{9}Be(d,n), E_d = 2.6 MeV were disappointing. The results using this reaction with a 40x10 cm D_2O moderator and graphite reflector are shown in Figure III-E-19. The fast neutron component at 0.5 cm is higher than the therapeutic ^{10}B dose. Based on the experience gained during these simulations, the moderator length would need to be increased by at least 5-10 cm to lower the FNF to a value near 0.15. Since the ^{10}B dose rate is already

Figure III-E-17: Comparison of results varying target location (A) while keeping moderator length (B) constant

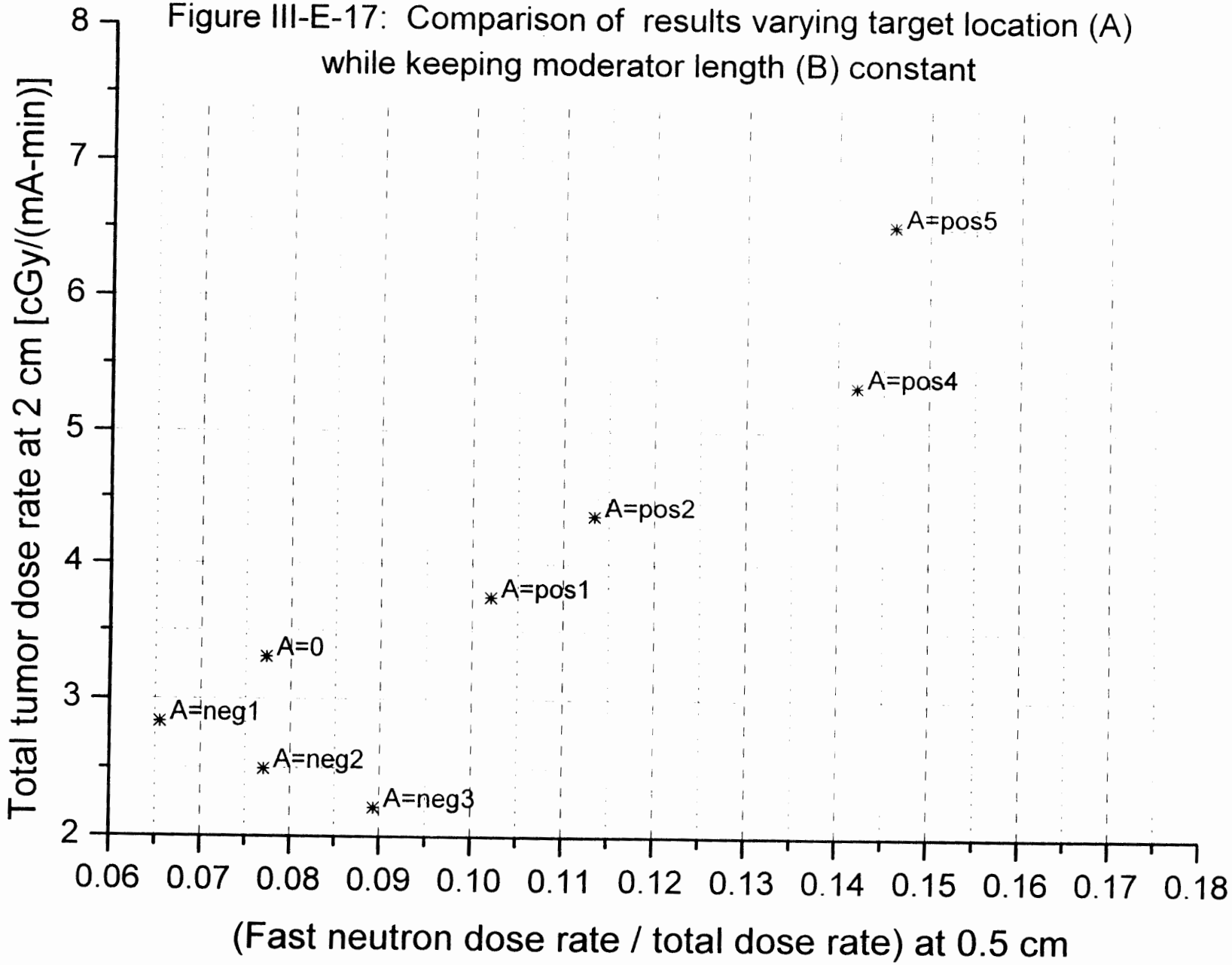

Figure III-E-18: Results of a therapy beam simulation using 27x10cm D_2O Moderator,Graphite Reflector, $^9Be(p,n)$ 4 MeV Target is located 5 cm into the reflector (A = +5)

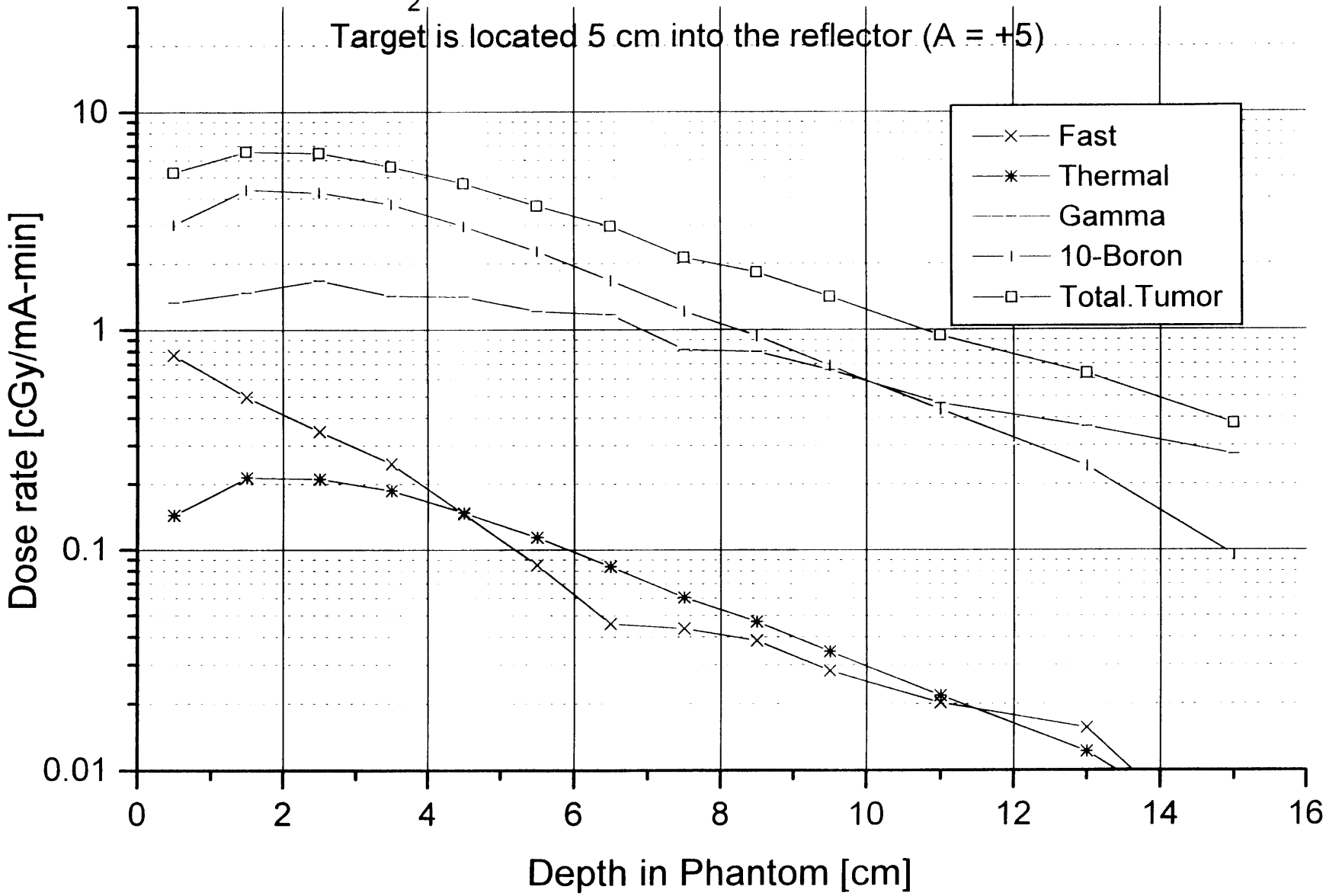

Figure III-E-19: Results of a therapy beam simulation using 40x10cm D_2O Moderator,Graphite Reflector, $^{9}Be(d,n)$ E_d = 2.6 MeV

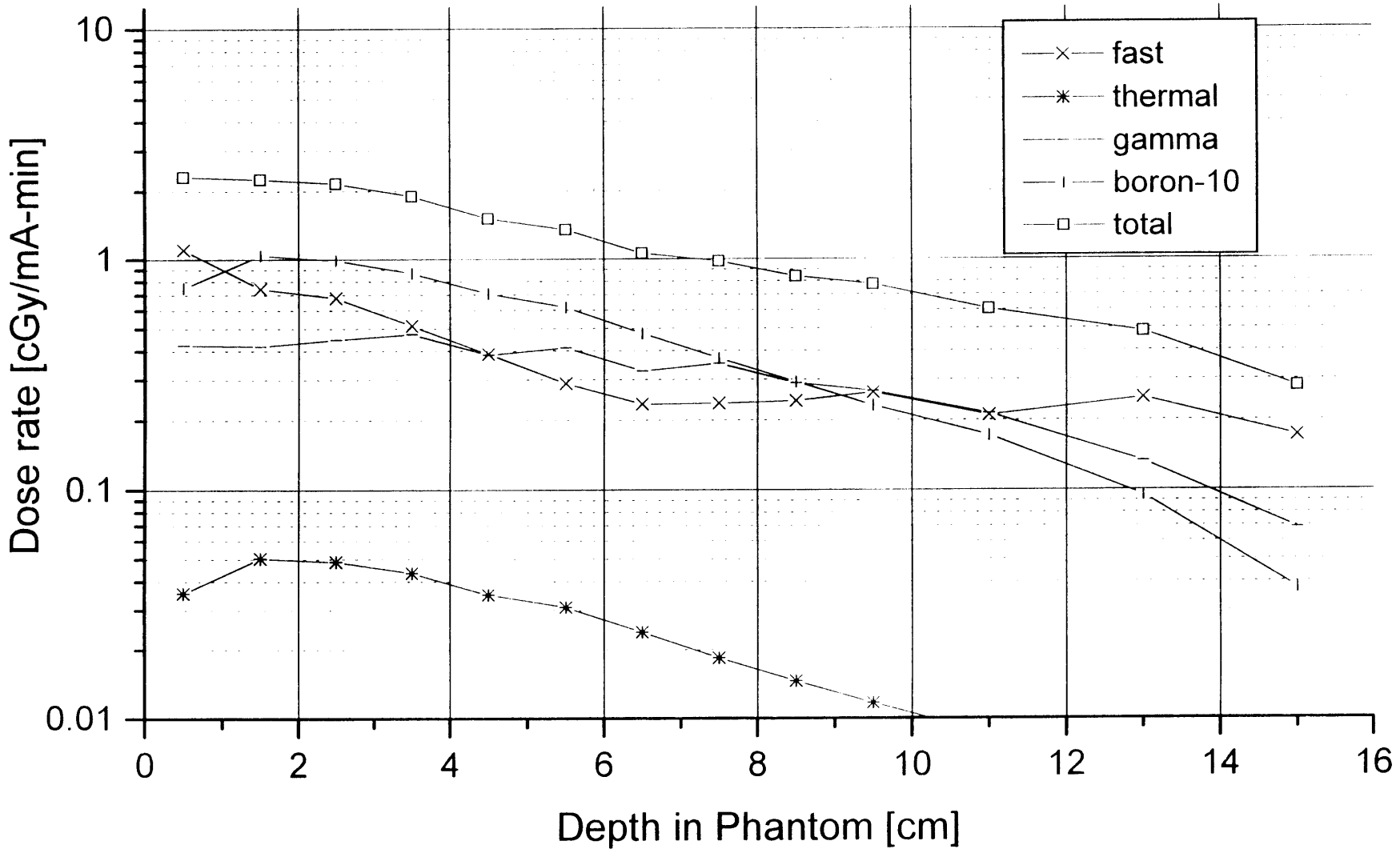

low in comparison with other results, and will be reduced by the larger moderator volume, the investigation of this reaction as an AB-BNCT source was suspended.

III.E.7 Effect of reflector diameter

All the simulations conducted in this chapter used a 34 cm radius reflector (dimension E in Figure III-B-2). At the conclusion of the simulations, the configuration (4.0-27x10g-d) was used with reflector radii between 45 and 15 cm. All reflector radii greater than 25 cm showed nearly identical behavior for all dose components and at all depths up to 6 cm. Although the dose components are very similar at depths greater than 6 cm, the statistical uncertainty becomes significant at greater depths and the comparison is less accurate. Four reflector radii (22, 20, 17 and 15 cm) were evaluated below 25 cm. The reflector with a radius of 22 cm shows an induced photon dose component which is approximately 5% lower than the reflector with a 25 cm radius at depths in phantom less than 6 cm. The thermal neutron dose also drops approximately 5-10% when the reflector radius is decreased from 25 to 22 cm. As the reflector radius is reduced to 17 and 15 cm, these differences are more apparent. For the 15 cm radius reflector, the ^{10}B dose rate has dropped to 2.3 cGy/(min-mA) at a depth of 2 cm compared with a dose rate of 3.2 cGy/(min-mA) for the 34 cm radium reflector. These simulations are included in Appendix C.

These results indicate that, for this particular configuration (4.0-27x10g-d), the optimal reflector size is near 25 cm. If the reflector is made larger than 25 cm, the

neutrons which enter the additional volume of the reflector will not contribute significantly to the therapy dose of the patient. Any neutrons which escape the reflector sides or back should be immediately shielded against since they will interact with the therapy room walls or the body of the patient. These results indicated that the reflector radius should be approximately 25 cm, and that the reflector should be surrounded by a moderating material and thermal neutron absorber.

III.E.8 Conclusions regarding therapy beam design

In every variation presented in this chapter, the combination of a graphite reflector and D_2O performed better than other combinations. Two promising results of this study were the MSR configurations 3.7-25x10g-d and li22x10g-d. A third promising result was the configuration 4.0-27x10g-d with the target at A = +5. This configuration will be referred to as 4.0-27x10g-d(A=+5). These three designs are presented with two sets of RBE values. These RBE values are the same as those used for a previous AB-BNCT beam design study [10], and are given in Table III-E-3.

Dose component	RBE value set A	RBE value set B
^{10}B (30 ppm)	2.3	4.1
Fast neutrons	2.2	4.0
Thermal neutrons	2.2	4.0
Photons	1.0	1.0

Table III-E-3: RBE values for sets A and B.

Results of these three configurations, with both sets of RBE values are shown in Figures III-E-20 through III-E-25. The configuration and RBE values are given in the figure caption. A summary of some of the results is given in Table III-E-4.

Figure III-E-20: Results of a therapy beam simulation using
22x10cm D_2O Moderator,Graphite Reflector, $^{7}Li(p,n)$ E_p = 2.5 MeV
With RBE set A: ^{10}B, all neutrons = 2.3 ; Photons = 1.0

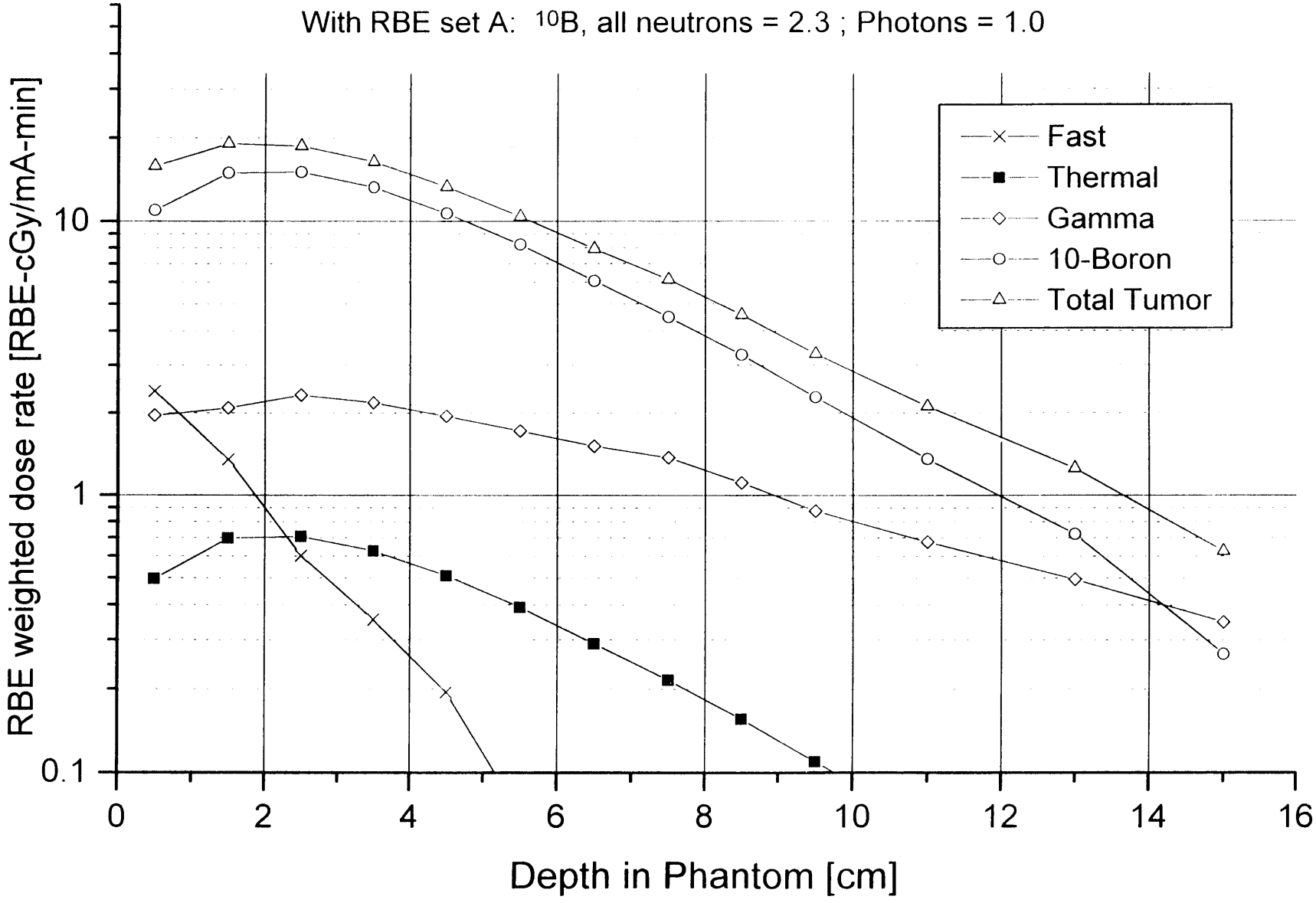

Figure III-E-21: Results of a therapy beam simulation using
25x10cm D_2O Moderator,Graphite Reflector, $^{9}Be(p,n)$ E_p = 3.7 MeV
With RBE set A: ^{10}B, all neutrons = 2.3 ; Photons = 1.0

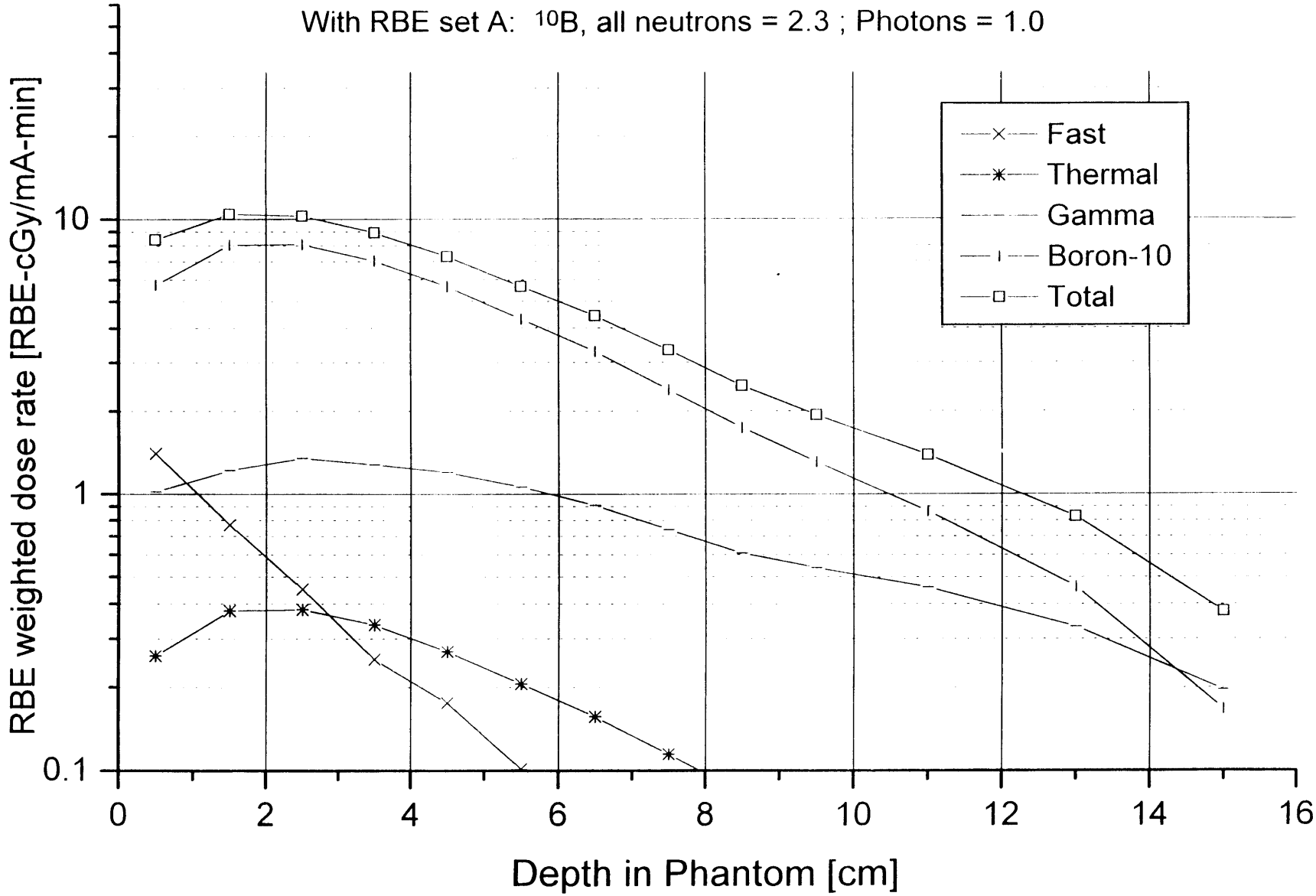

Figure III-E-22: Results of a therapy beam simulation using
27x10cm D_2O Moderator,Graphite Reflector, $^{9}Be(p,n)$ E_p = 4.0 MeV
Target located 5 cm into moderator
With RBE set A: ^{10}B, all neutrons = 2.3 ; Photons = 1.0

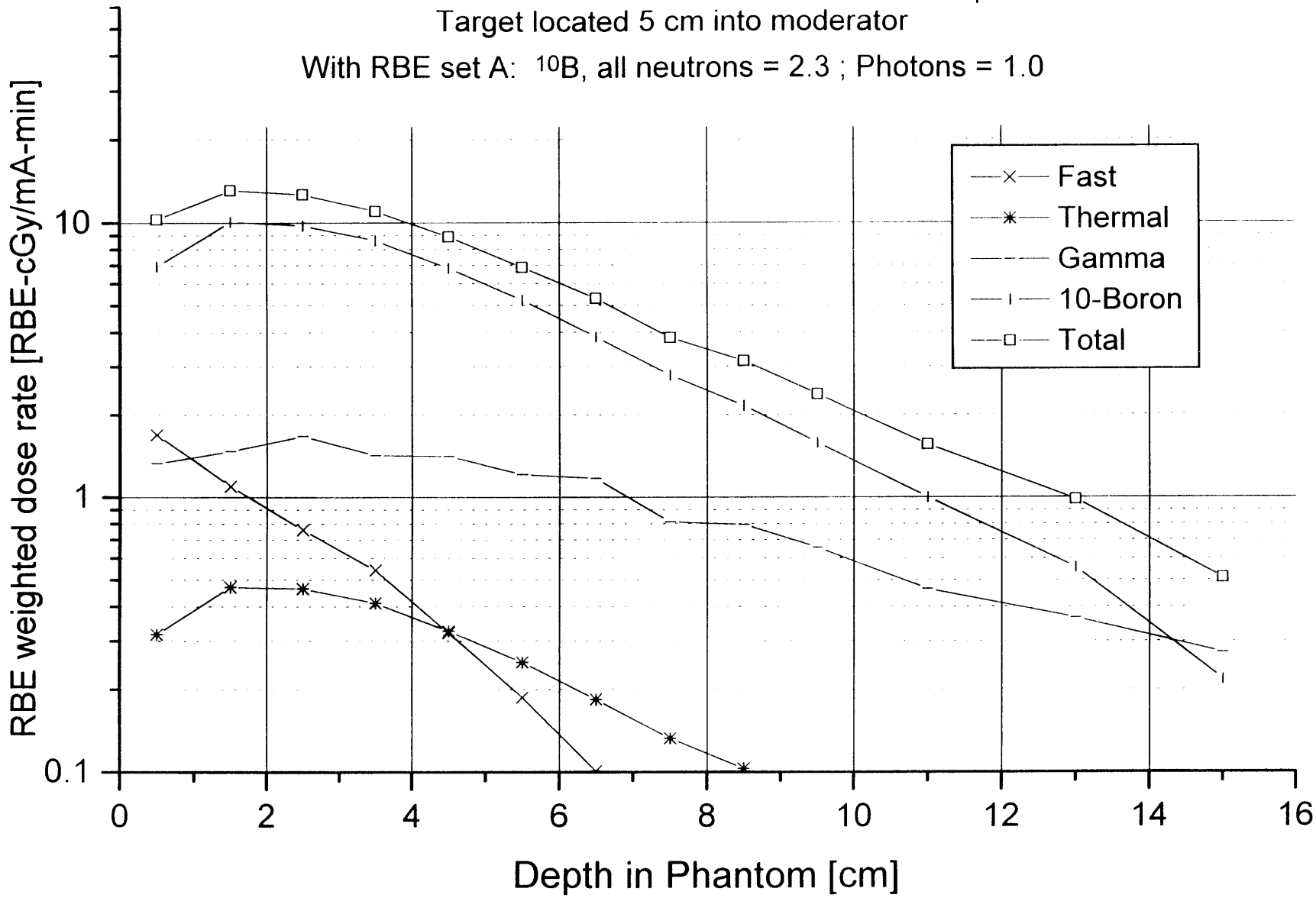

Figure III-E-23: Results of a therapy beam simulation using
22x10cm D_2O Moderator,Graphite Reflector, $^7Li(p,n)$ E_p = 2.5 MeV
With RBE set B: ^{10}B= 4.1, all neutrons = 4.0 ; Photons = 1.0

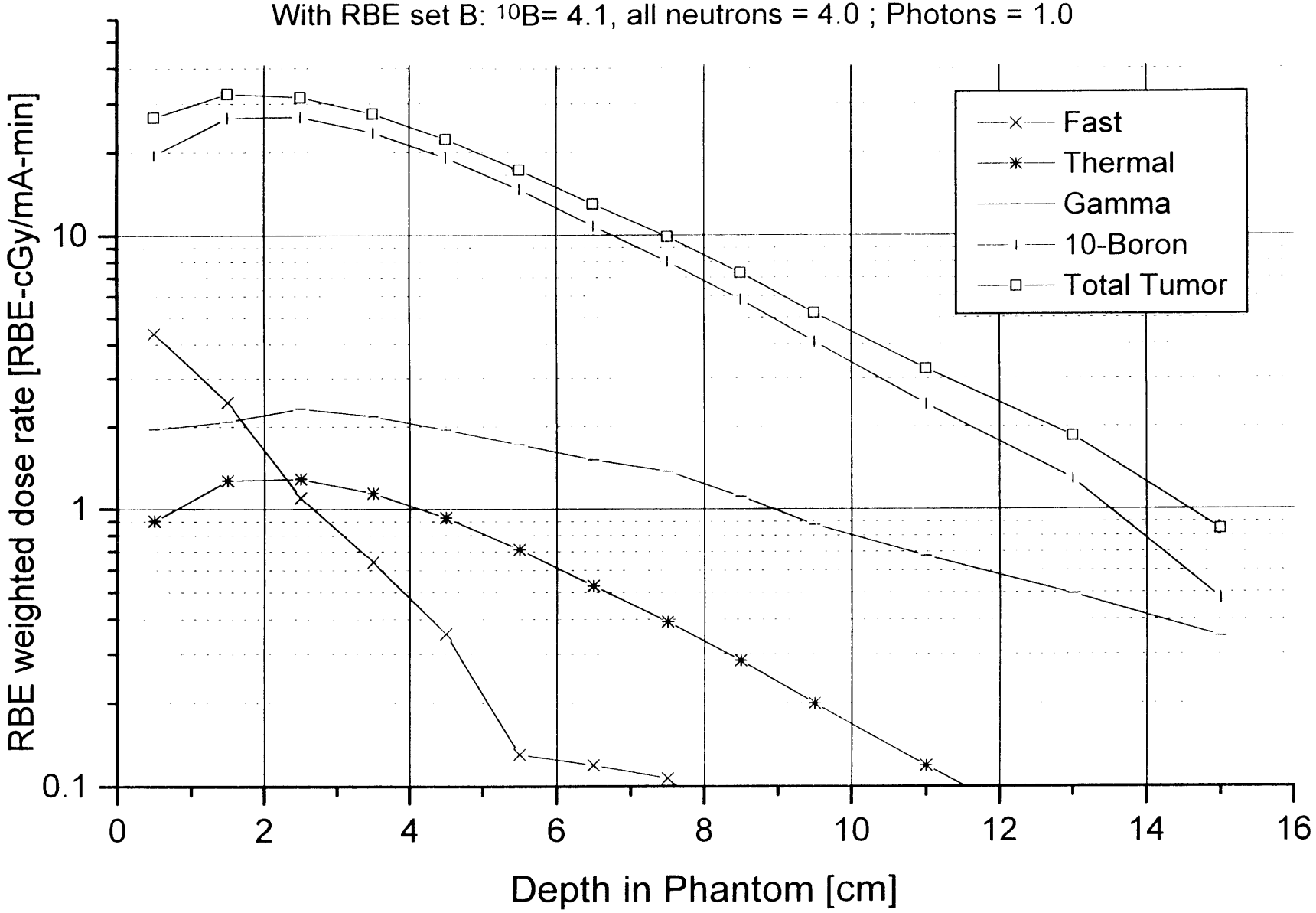

Figure III-E-24: Results of a therapy beam simulation using
25x10cm D_2O Moderator,Graphite Reflector, $^{9}Be(p,n)$ E_p = 3.7 MeV
With RBE set B: ^{10}B= 4.1, all neutrons = 4.0 ; Photons = 1.0

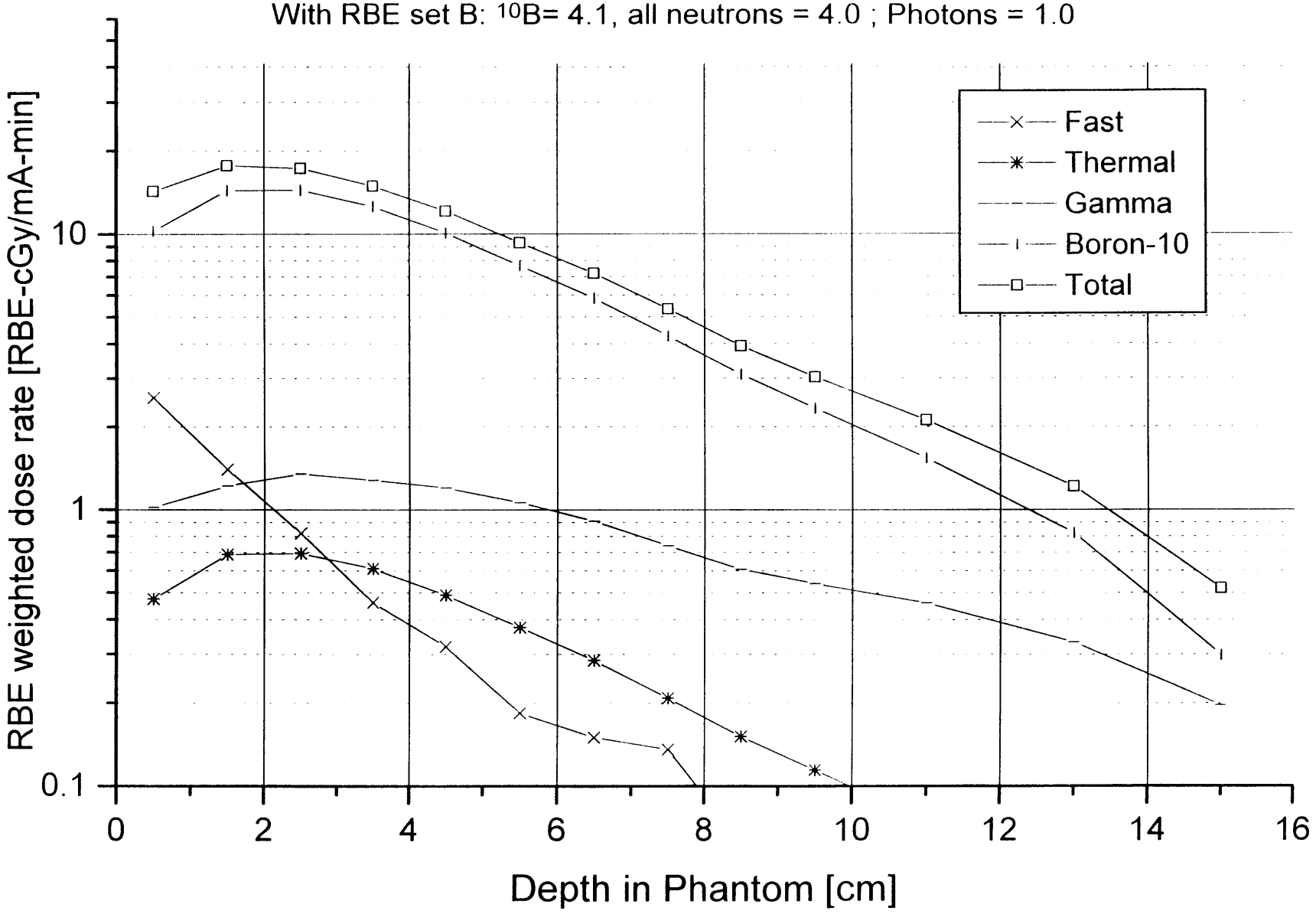

Figure III-E-25: Results of a therapy beam simulation using
27x10cm D_2O Moderator,Graphite Reflector, $^{9}Be(p,n)$ E_p = 4.0 MeV
Target located 5 cm into moderator
With RBE set B: ^{10}B= 4.1, all neutrons = 4.0 ; Photons = 1.0

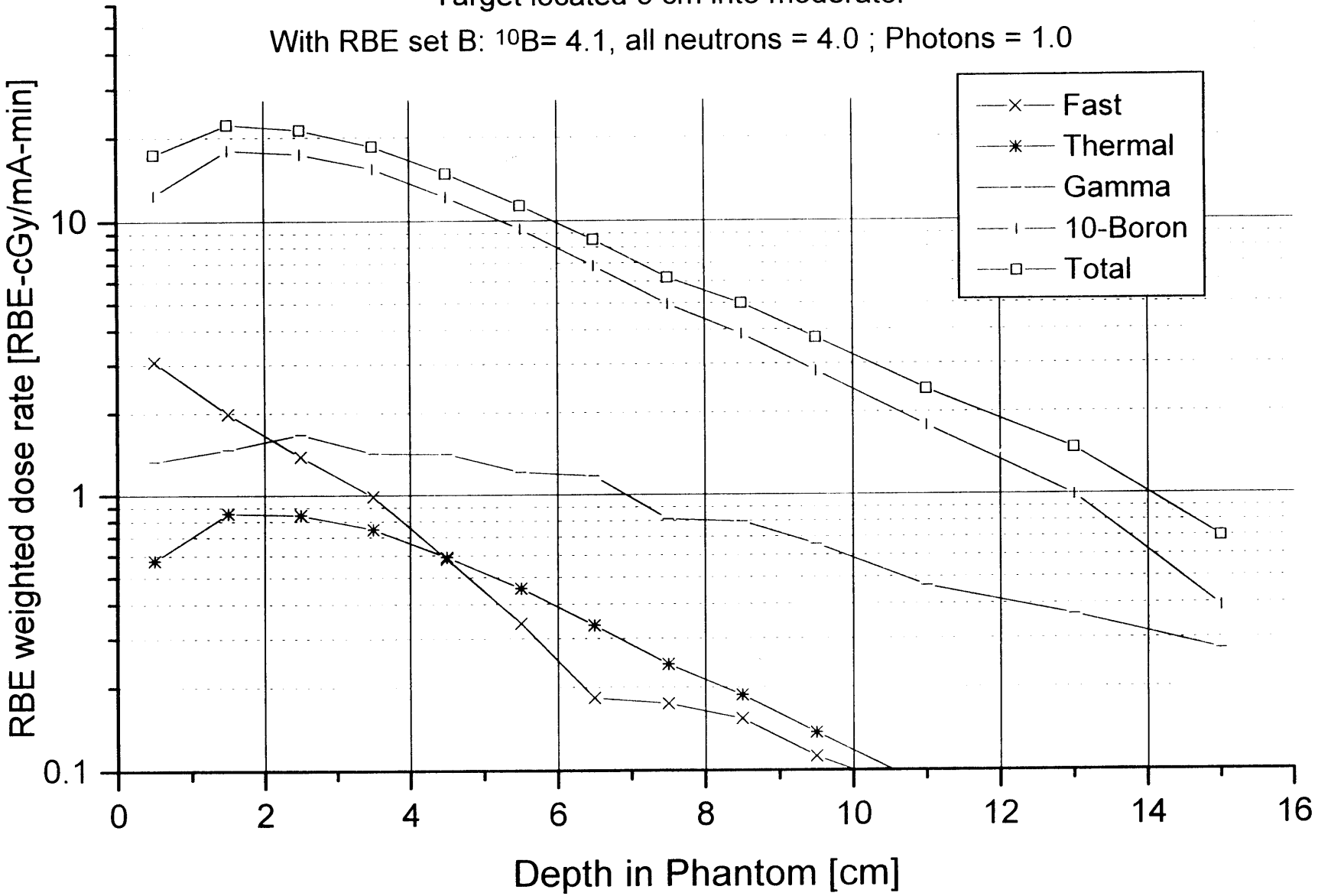

	RBE Set A		RBE Set B	
Configuration	RBE weighted dose rate at 2 cm RBE-cGy/ (mA-min)	RBE weighted dose rate at 4 cm RBE-cGy/ (mA-min)	RBE weighted dose rate at 2 cm RBE-cGy/ (mA-min)	RBE weighted dose rate at 4 cm RBE-cGy/ (mA-min)
li22x10g-d	18	15	32	25
3.7-25x10g-d	10.1	8	17	13
4.0-27x10g-d (A=+5)	13	10	22	15

Table III-E-4: Summary of promising results using two sets of RBE weighting factors

When compared only on the basis of therapy beam performance, the reaction ^{7}Li(p,n) is a superior neutron source for AB-BNCT. Using the examples in Table III-E-4, the RBE-weighted dose rate at 4 cm is more than 60% higher than the next best configuration using the ^{9}Be(p,n) reaction. However, as previously stated, the poor thermal and mechanical properties of lithium present a significant obstacle to creating an AB-BNCT therapy beam based on the ^{7}Li(p,n) reaction.

One surprising result is the variation of dose rates with target position when the moderator length is fixed. This variation was only examined for the reaction ^{9}Be(p,n) E_p=4.0 MeV, and should be researched more carefully in the future. When using the configuration 4.0-27x10g-d, the dose rate at 2 cm increased from 4.3 cGy/(min-mA) with the target 2 cm into the moderator to a rate of 6.5 cGy/(min-mA) with the target 5 cm into the moderator. The FNF increased when the target was placed 5 cm into the moderator; however, the FNF in both cases was below 0.15.

The time required for a BNCT therapy procedure depends on many variables including tumor location and prescribed dose. During MIT-R's recent Phase I trial, patients with melanoma of the extremities were administered radiation doses of approximately 15-20 RBE-Gy. Two of the five patients showed partial tumor response. One of the five patients has demonstrated complete tumor response (no evidence of tumor) after 19 months [13]. For the purpose of the calculations presented below, a tumor dose of 15 RBE-Gy, assuming tumor depths of 2, 4 and 6 cm, will be considered. These results can be easily scaled to higher total tumor doses.

The results presented in Table III-E-4 show that RBE-weighted dose rates at 4 cm depth in excess of 8 and 13 RBE-cGy/(mA-min) are predicted for RBE sets A and B, respectively, using any of the configurations listed. Using the RBE Set B values and an accelerator power of 10 kW, the time required to deliver a total tumor dose of 15 RBE-Gy to depths of 2, 4 and 6 cm are listed in Table III-E-5. The times listed in Table III-E-5 are certainly possible, and reasonable.

Configuration	Time required to deliver a tumor dose of 15 RBE-Gy to a depth of 2 cm [min]	Time required to deliver a tumor dose of 15 RBE-Gy to a depth of 4 cm [min]	Time required to deliver a tumor dose of 15 RBE-Gy to a depth of 6 cm [min]
li22x10g-d	12	15	25
3.7-25x10g-d	31	39	70
4.0-27x10g-d (A=+5)	27	35	60

Table III-E-5: Times required to deliver 15 RBE-Gy to tumor depths of 2, 4, and 6 cm

Based on the cumulative results presented in this chapter, two approaches to AB-BNCT therapy design appear to be promising. First is the development of AB-BNCT therapy beams based on the reaction ^{7}Li(p,n). To be able to use this reaction, a viable target assembly must be designed and tested to withstand accelerator powers of at least 10 kW. If this is possible, then it might be possible to deliver a total tumor dose of 15 RBE-Gy, at a depth of 6 cm, in less than 30 minutes.

The second promising approach is to investigate the use of the reaction ^{9}Be(p,n) using proton bombarding energies below 3.7 MeV. When compared with other configurations using the ^{9}Be(p,n) reaction on the basis of equivalent accelerator power, the configuration 3.7-25x10g-d showed the best performance. The total tumor dose rate at 2 cm from the configuration 3.4-23x10g-d was only 10% below that of 3.7-25x10g-d. The target position was only varied when using the reaction ^{9}Be(p,n) E_p=4.0 MeV, and it is possible that the total tumor dose rates could be increased by 10-20% by optimizing the target location for the other reactions and energies. The decrease in proton energy may reduce the accelerator performance requirements and allow for greater current production.

Finally, these simulations clearly show that there is a trade-off between FNF and total tumor dose rate. For example, in Figure III-E-4 the FNF and dose rate at 2 cm both increase steadily as the moderator length decreases using a graphite reflector and D_2O moderator. The dose rate increases by almost a factor of 2 when the moderator length decreases from 27 cm to 21 cm. For these moderator lengths, the FNF increases from

0.15 to 0.24. It may be possible to tolerate a FNF higher than 0.15. If a FNF as high as 0.25 can be tolerated, then the therapy times listed in Table III-E-5 could be decreased by as much as a factor of two. Since the fast neutron dose decreases rapidly with depth in tissue, it should be possible to decrease the effect of the fast neutron dose by irradiating the patient from various directions. This would spread the fast neutron dose over a larger area, and potentially allow for a higher FNF. If a higher FNF could be tolerated, this could also decrease the accelerator power required to deliver a specific dose to the tumor. For example, Figure III-E-10 indicates that it might be possible to achieve an increase in dose rate of approximately 50% by decreasing the length of the D_2O moderator from 22 cm to 19 cm when using the $^{7}Li(p,n)$ reaction. This should result in a FNF of approximately 0.20. This increase in dose rate could be used to reduce the therapy times listed in Table III-E-5. This increased dose rate could instead be used to reduce the amount of current needed for the therapy. By reducing the amount of current, the heat load on the lithium target would decrease. For example, if a configuration of li19x10g-d were used with a FNF of 0.19 which resulted in a 50% increase in dose rate at depth, the total tumor dose rate at 4 cm would be 37.5 RBE-cGy/(min-mA) (RBE set B values). This increased dose rate could be used to decrease the power requirements of the accelerator and the heat load on the target by 50% while maintaining the therapy times listed in Table III-E-5.

III.F Experimental verification

To confirm the predictions of the Monte Carlo simulations, experiments were conducted to measure the BNCT radiation dose components with the reaction $^{9}Be(d,n)$ E_d=2.6 MeV as the neutron source. This reaction was used because a beryllium target was available at LABA, and the accelerator could be operated reliably at a deuteron energy of 2.6 MeV. Two dosimetry techniques were used to measure these components. To resolve the fast neutron and gamma dose rates, the dual ionization chamber (IC) technique was used. The thermal fluence was determined from activation foil analysis, and the thermal neutron and ^{10}B dose rates were then calculated using fluence-to-kerma conversion. These measurements relied heavily on techniques developed by the MIT Reactor BNCT group (referred to here as MIT-R) [14] [15]. When appropriate, this chapter will use the same notation as that used by the MIT-R group, which will allow easy comparison between the results of the MIT-R and LABA groups. The following sections outline the theory of the two dosimetry techniques, the methodology of implementing them, and the experimental results. The dual ionization chamber technique is explained first (Section III.F.1), followed by the activation foil methods (Section III.F.2). The experimental results are presented and discussed in the remainder of the chapter.

III.F.1 The dual ionization chamber technique

The dual ionization chamber technique is a method of separating two dose components of a mixed radiation field (fast neutrons and photons) which simultaneously

deliver dose to a target volume of material. When a radiation detector is placed in such a mixed field, part of the detector signal is attributed to one dose component (fast neutrons) and part to the other (photons). Since the detector generally yields only one signal, the detector system is analogous to a single mathematical equation with two unknowns. To resolve the two unknowns, a second detector (equation) is needed. The two known values are the detector signals (charge collected from the ICs) and the two unknowns are the dose components.

The technique relies on the differential responses of the ICs to fast neutron and photon radiation. If the response of the detectors is expressed as the amount of charge collected on the anode per unit absorbed dose that would occur in brain tissue at the location of the IC, then the charges collected at the anodes of the two detectors are:

Equation III-F-1: $A_1D_\gamma + B_1D_n = Q_1$

Equation III-F-2: $A_2D_\gamma + B_2D_n = Q_2$

Where:

A_1, A_2 = Response of detectors 1 and 2 to photon radiation in brain tissue {C/cGy}

B_1, B_2 = Response of detectors 1 and 2 to fast neutron radiation in brain tissue {C/cGy}

Q_1, Q_2 = Charge collected on the anode.

The solutions to these equations are:

Equation III-F-3: $$D_\gamma = \frac{B_2Q_1 - Q_2B_1}{A_1B_2 - A_2B_1}$$

Equation III-F-4: $D_n = \frac{A_1 Q_2 - Q_1 A_2}{A_1 B_2 - A_2 B_1}$

The dual IC technique was applied to the measurement of photon and fast neutron doses by using two small chambers, inserted one at a time, in a water-filled phantom. This phantom was located in front of the MSR currently used at LABA. To relate the charge collected by an electrode of an IC to the dose deposited in the walls of the IC, cavity theory must be used. To relate the dose deposited in the walls of the IC to the dose that would be deposited in brain tissue, other relationships must be used. These conversion factors are included in the A and B values in the equations above, which is why these constants are expressed as dose in brain per unit charge collected in an ionization chamber. The determination of the A and B values is a complex process which has many steps. In the following paragraphs, the dual ionization chamber method will be developed more completely. First, the equipment used in these measurements will be described. Then, the method of determining the constants (A_1, A_2, B_1, B_2) experimentally or theoretically will be presented.

III.F.1.a Equipment used

III.F.1.a.(i) Ionization chambers, flushing gas, and high voltage supply

The two detectors were manufactured by the Far West Company and are referred to as the tissue equivalent chamber (TE) and the carbon-graphite chamber (CG). The TE chamber has an outer diameter of 9.59 mm and a wall thickness of 2.51 mm. The

corresponding values for the CG chamber are 7.87 mm and 1.65 mm, respectively [15]. The TE wall results in transient charged particle equilibrium for photons up to 0.7 MeV and charged particle equilibrium for neutrons up to 15 MeV. The corresponding values for the CG chamber are 0.8 MeV and 17 MeV [15]. A picture of the detectors is shown in Figure III-F-1.

The chambers are flushed with gas using the connections near the chamber base. The TE chamber is flushed with TE gas (64.4 % CH_4, 32.4 % CO_2, and 3.2 % N_2 by partial pressure). The CG chamber is flushed with CO_2 (99% purity). The gas flow through the chambers is monitored by using a remote video camera which focuses on a sensitive flow meter. The high voltage (HV) terminal of the chambers is connected to a HV supply which is set to +250 V. A standard coaxial cable with HV termination is used. The HV is applied to the outside of the IC, so that positive ions created in the ionization process are repelled to the center electrode for collection. The electron current path is through the HV supply to ground. This circuit can be run as easily in reverse with -250 V applied to the HV terminal. In this case, electrons are collected at the electrometer.

III.F.1.a.(ii) Water-filled brain phantom, and automated dosimetry system

A realistic head phantom designed and constructed by the MIT-R group was used in these measurements [16]. The head phantom is made mostly of acrylic, and filled with water. Tube guides on the bottom of the phantom allow the insertion of watertight

Figure III-F-1: Picture of Far West ionization chamber

butyrate tubes. These tubes house the ICs and gold activation foils used during the dosimetry measurements. A small hole has been drilled in the top of the phantom to allow excess water to escape as the ICs are pushed deeper into the phantom.

When the phantom was previously used by the MIT-R group or the LABA group, the IC had to be manually repositioned after each data point (depth in phantom). For the MIT-R group, the time required to insert all shielding materials, including a water shutter, and then remove them was approximately 20 minutes. The interval for the LABA group was approximately 10 minutes. To improve the efficiency of this process, a new phantom stand and stepper motor system was built to allow the remote repositioning of the IC. A picture of the head phantom and new phantom stand is shown in Fig. III-F-2. The IC base is locked into position in an aluminum holder called the "carriage". The carriage is moved up and down by a stepper motor controlled by a personal computer. Slots or "keys" in the carriage body ride along L-shaped "rails" to keep the carriage from twisting or tilting. The system is monitored remotely by a video camera to ensure that the IC is moving the correct distance. Marks on the butyrate tubes can be seen on the video display. The stepper motor and rails are mounted on a plate that moves freely so that the IC can be inserted into any of the tube guides. Once the stepper motor has been positioned, the plate is fixed to the phantom stand to make a rigid system. During a recent measurement by the MIT-R group, this automated system reduced the time for the experiment from 15 to 5 hours [17].

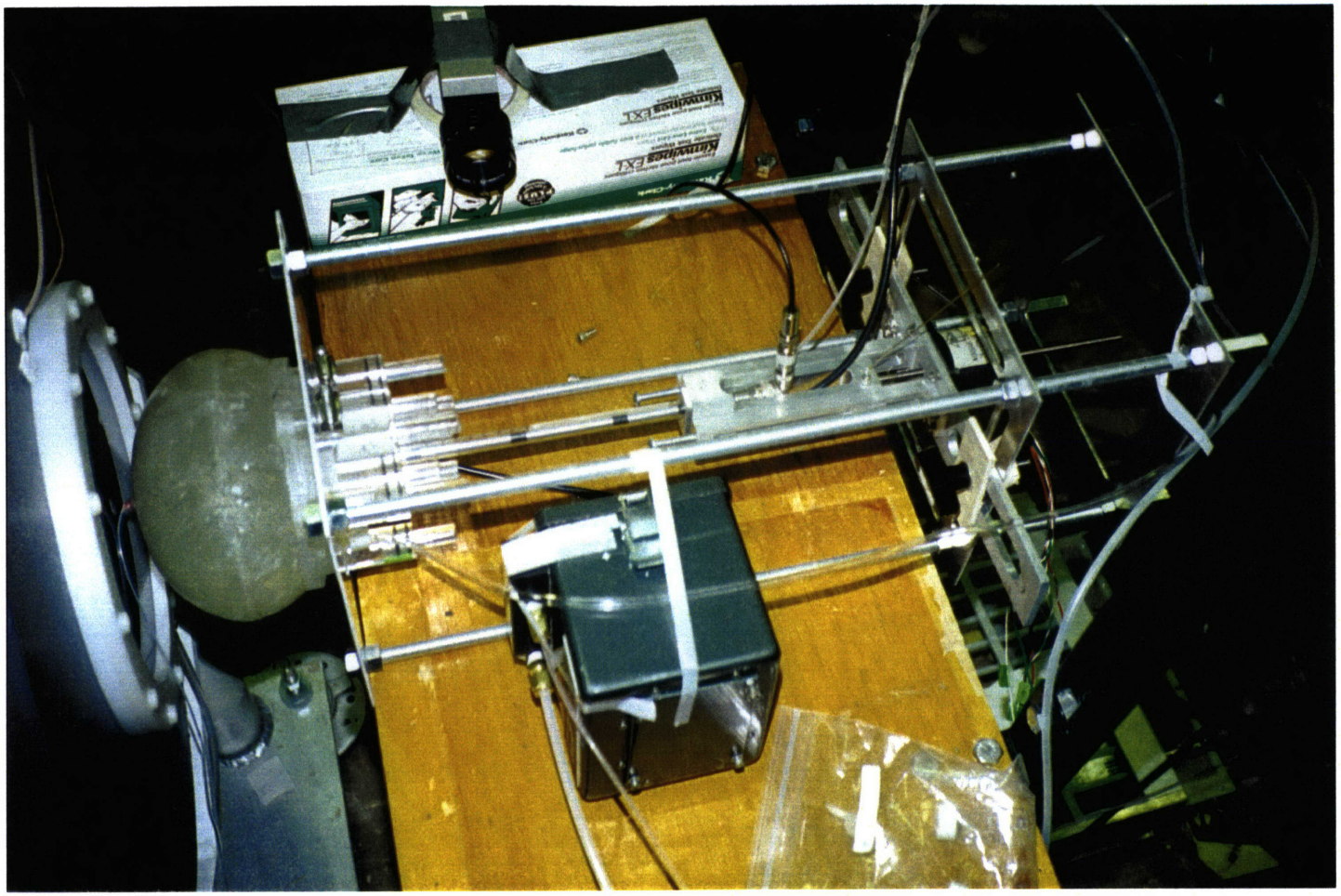

Figure III-F-2: Picture of dosimetry phantom and stand.

III.F.1.a.(iii) Charge collection and electrometer

The center electrode of the IC collects the positive ions created in an ionization event. This charge collected in the ionization chambers passes to a low noise triaxial cable which terminates at a sensitive electrometer (Keithly model 617) located at the accelerator control station. The current collection cable is very sensitive, so all instruments are turned on at least one hour before the measurements and movement of the cable is strictly avoided during the experiments.

III.F.1.b Calibration of the ionization chambers

The purpose of the IC calibration is to determine the four constants A_{TE}, A_{CG}, B_{TE}, and B_{CG}, which indicate the response of the chambers to photon and neutron irradiation, respectively. The values of A_{TE} and A_{CG} are found directly by exposing the chambers to a known photon exposure from a ^{60}Co source. The values for B_{TE}, and B_{CG}, are found by first determining the ratio B/A for each detector, and then multiplying by the respective A value. $(B/A)_{TE}$ is calculated using the Bragg-Gray relation, and $(B/A)_{CG}$ is taken from previously published results [14]. The remainder of Section III.F.1.b will discuss each step of this process in detail.

The calibration of the ICs requires many calculations. Some of these calculations require knowledge of the neutron and photon energy spectra at the location of the dose measurement. To attain this information for the LABA group, MCNP was used to estimate the neutron and photon spectra along the axial centerline of the MIT-R brain

phantom when exposed to the measurement conditions (^{9}Be(d,n) reaction, E_d=2.6 MeV, current LABA MSR). The brain phantom in the MCNP model was filled with water. The photon and neutron fluences were estimated at 1 cm and 7 cm. In a second simulation, most of the phantom was filled with water but a center channel in the phantom was filled with air to model the butyrate tube inserted into the phantom. The purpose of the second simulation was to estimate the effect of the air on the dosimetry measurements. Some of the results of these simulations are shown in Figure III-F-3.

The photon fluence was nearly constant as a function of depth in the phantom, and did not vary in a statistically significant way when the center channel was modeled with air. The neutron spectra, as shown in Figure III-F-3, do vary significantly with depth in the phantom. For most of the neutron energies, the intensity drops by an order of magnitude when the point of interest is moved from 1 cm to 7 cm. Because the neutron and photon spectra do not change significantly when air is added to the model, these results indicate that the air in the butyrate tubes should not significantly affect the results of these measurements.

III.F.1.b.(i) Determining the A values

The A values of the detectors are determined in two steps. First, the detectors are exposed to a ^{60}Co source at an accredited laboratory (AAPM Calibration Laboratory, University of Wisconsin). Because the IC walls do not provide charged particle equilibrium for the ^{60}Co source, buildup caps were machined by the MIT-R BNCT group

Figure III-F-3: Neutron spectra in head phantom resulting from the reaction $^{9}Be(d,n)$, E_d = 2.6 MeV

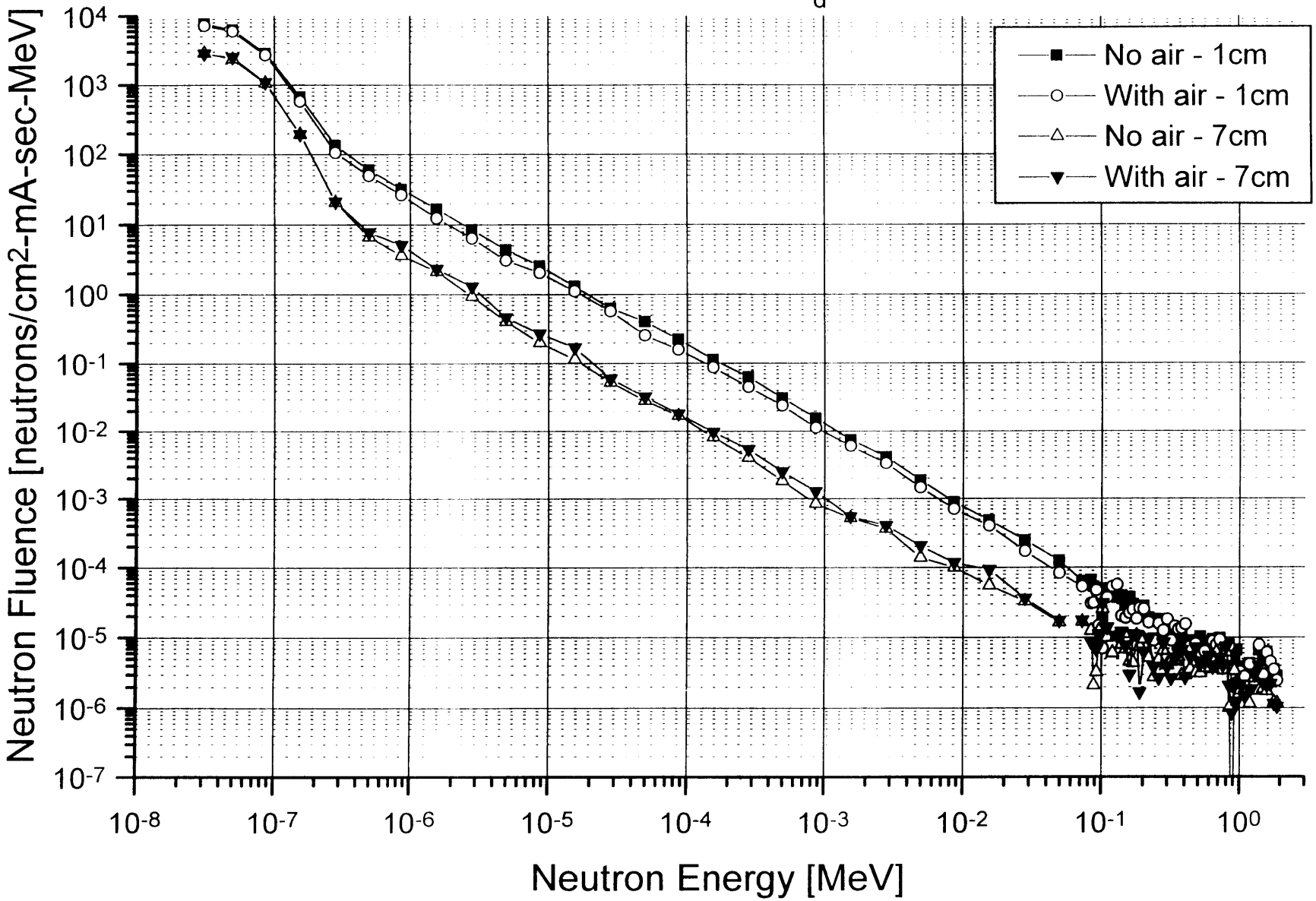

and used in the calibration [15]. This initial step provides the exposure calibration constant in units of R/C. During the exposure calibration, the ICs are open to air. During the measurements, the detectors are purged continuously with gas, so air-to-gas correction factors must be determined. The MIT-R group has determined these factors experimentally by exposing the chambers to a ^{137}Cs beam under the exposure calibration conditions and while purging them with gas. The air-to-gas correction factor is 1.57 for the TE chamber, and 1.19 for the CG chamber [15]. The chambers are periodically checked against the ^{137}Cs source as a consistency check [15].

The first step has provided a calibration factor in units of R/C, and the second step must provide a calibration factor in units of cGy/C. This procedure is discussed in detail in the literature [4]. To accomplish this, an equation relating absorbed dose in tissue to exposure is needed. This equation is [4] :

Equation III-F-6: $D_{tissue} = 0.876\ \beta_{tissue}\ A_c\ X\ (\mu_{en}/\rho)_{air}^{tissue}$

The factor 0.876 is a conversion factor arising from the radiation units. Beta is the charged particle equilibrium constant, and expresses the fact that the kerma is lower than the absorbed dose. When indirectly ionizing radiation enters a slab of material, the kerma is a monotonically decreasing function of depth in the slab. The absorbed dose, however, first rises to a maximum as more charged particles are created and then decreases steadily. At a depth where transient charged particle equilibrium (TCPE)

exists, the absorbed dose and kerma as a function of depth will be linearly related, but the absorbed dose will be higher [4]. The value of β varies slightly with photon energy and has a value around 1.003-1.005 [4]. The MIT-R group uses a value of 1.004 [15]. The displacement correction factor, A_c, occurs because the dosimeter displaces some tissue material. During calibration, the chamber is mostly void. If tissue were to replace the chamber the dose at the center of the volume of tissue would go down. A_c accounts for the decrease in the dose due to the attenuation of the photons in the tissue now replacing the chamber. The value is less than 1.0 because the tissue provides some self-shielding [4]. The effect should be small and the value should be close to, but less than, 1.0. The value of A_c is dependent on the outer diameter of the IC and has a value for the ICs used here of approximately 0.988-0.99 [4] [15]. The quantity $(\mu_{en}/\rho)_{air}^{tissue}$ is the relative mass energy absorption coefficient of tissue to air, $(\mu_{en}/\rho)_{air}^{tissue} = (\mu_{en}/\rho)^{tissue} /(\mu_{en}/\rho)_{air}$. Values of these coefficients as a function of photon energy are given in the literature [4]. These coefficients were weighted based on the information provided by the MCNP simulation discussed above. The value $(\mu_{en}/\rho)_{air}^{tissue}$ was 1.047 at a depth of 1 cm and 1.054 at a depth of 7 cm. These values differ by less than 0.7%, which is much less than the statistical uncertainty in the fluence simulations on which they are based. An average value of 1.0505 is used in these calculations at all depths. This yields: $A_{TE}= 4.9 \times 10^{-11}$ C/(cGy dose in brain), and $A_{CG}= 8.8 \times 10^{-11}$ C/(cGy dose in brain). The MIT-R group uses a value of 1.1 for $(\mu_{en}/\rho)_{air}^{tissue}$ which results in the values: $A_{TE}= 4.67 \times 10^{-11}$ C/(cGy dose in brain) and $A_{CG}= 7.62 \times 10^{-11}$ C/(cGy dose in brain)[15].

III.F.1.b.(ii) Determining the $(B/A)_{TE}$ value

Attix has derived a relationship, based on the Bragg-Gray relation, for the neutron-to-gamma sensitivity ratio [4]. This relationship is:

Equation III.F.7: $$\left(\frac{B}{A}\right)_{TE,i} = \frac{\left(F_n\right)_i^{TE}\left(\overline{W_\gamma/e}\right)_g\left(\overline{S\gamma/\rho}\right)_g^{TE}}{\left(\frac{\mu_{en}}{\rho}\right)_i^{TE}\left(\overline{W_n/e}\right)_g\left(\overline{S_n/\rho}\right)_g^{TE}}, i = brain, muscle$$

Where:

$\left(F_n\right)_i^{TE}$ = neutron kerma factor ratio of TE plastic to tissue

$\left(\frac{\mu_{en}}{\rho}\right)_i^{TE}$ = mass energy absorption coefficient ratio of A-150 TE plastic to tissue

$\left(\overline{W_n/e}\right)_g$, $\left(\overline{W_\gamma/e}\right)_g$ = the average energy needed to produce an ion pair for neutrons (photons) in TE gas

$\left(\overline{S_n/\rho}\right)_g^{TE}$, $\left(\overline{S\gamma/\rho}\right)_g^{TE}$ = mass collision stopping power ratio of TE plastic to TE gas for neutron (electron) secondaries.

Since the elemental composition of TE plastic, and the TE flushing gas are very similar, the two mass collision stopping power ratios are close to unity [4]. The ratio $(\mu_{en}/\rho)_i^{TE}$ is near unity and varies only by several percent over the photon energy range 0.2-8 MeV [15]. Thus, Equation III-F-7 is reduced to:

Equation III-F-8: $$\left(\frac{B}{A}\right)_{TE,i} = \frac{(F_n)_i^{TE}\left(\overline{W_\gamma/e}\right)_g}{\left(\overline{W_n/e}\right)_g}, i = brain, muscle$$

The factor $(F_n)_{brain}^{TE}$ accounts for the fact that there is a mismatch between the kerma factors for A-150 plastic and brain. A-150 plastic has about twice the amount of nitrogen as brain, so the TE chamber over responds at low neutron energies. The agreement is actually very good for A-150 plastic and ICRU muscle, and is also very good for brain tissue above about 20 keV. Below 20 keV, the discrepancies are approximately 50% [15]. Without correcting for this effect, the response of the TE chamber would be approximately 50% too high. Using tabulated values of neutron kerma factors, and convolving these with the expected neutron energy distribution, the value of $(F_n)_{brain}^{TE}$ can be calculated [15]. This calculation has been repeated for the neutron energy distribution in phantom predicted by MCNP for the reaction ^{9}Be(d,n), E_d=2.6 MeV, using the current MSR existing at LABA. The calculated values of $(F_n)_{brain}^{TE}$ are 1.44 and 1.53 at depths of 1 and 7 cm respectively.

The ratio W_n/W_e has been calculated by Goodman as a function of neutron energy in the range 0.1-20 MeV [18]. This function is complex, but the magnitude of the changes are small. Over this energy range, the value of W_n/W_e changes from a maximum value of approximately 1.12 to a minimum value around 1.055. For neutron energies expected at the brain phantom location of the MCNP model used here, the most appropriate value is around 1.10.

The value of $(B/A)_{TE}$ can now be calculated as 1.31 for 1 cm and 1.39 for 7 cm. The MIT-R group uses a value of 0.92 for brain and 0.95 for muscle and does not account for the change of these values with depth [15]. The MIT-R group first calculates the $(B/A)_{TE}$ values as a function of energy, and then averages these values over the energy range 0.1 - 10 MeV. In this energy range, the value of $(F_n)_{brain}^{TE}$ is close to 1.0. The value used here (1.31 or 1.39) is significantly different from the value used by the MIT-R group because the $(B/A)_{TE}$ value has been determined by convolving the $(F_n)_{brain}^{TE}$ values with the expected neutron energy distribution in the phantom. This neutron energy distribution is greatest at energies where the value of $(F_n)_{brain}^{TE}$ is approximately 1.5 - 2.0. During the analysis of this data, the value of $(B/A)_{TE}$ was varied between the values 0.9 and 1.4. The effect of this variation is discussed in Section III.F.3.

III.F.1.b.(iii) Determining the $(B/A)_{CG}$ value

Like $(B/A)_{TE}$, $(B/A)_{CG}$ depends on the neutron energy spectrum to which the detector is exposed. The ratio $(B/A)_{CG}$ has been calculated and measured by several

researchers. Their results, as compiled by the ICRU, are shown in Table III-F-1 [19]. The relative neutron sensitivity for graphite ICs filled with a variety of gases (including CO_2) at atmospheric pressure has also been studied using a 2 cm^3 spherical cavity [19]. The latter study shows that the neutron sensitivity ratio is monotonically decreasing below 2.5 MeV, and that the calculated value at 2.5 MeV is near 0.07 for a CO_2 filled chamber. This value (0.07) from the second study would be an approximation for the upper limit on the ratio $(B/A)_{CG}$ for these measurements. Using the results in Table III-F-1, the value of $(B/A)_{CG}$ is 0.07 (computed) and 0.08 (measured) for a 2 MeV neutron beam. Both studies show that $(B/A)_{CG}$ is decreasing with decreasing neutron energy in the range $E_n < 2$ MeV. Table III-F-I also indicates that 0.07 would be an approximation for the upper limit of $(B/A)_{CG}$. The lower limit is not available from these data.

Neutron Energy (MeV)	Calculated value of relative neutron sensitivity	Observed value of relative neutron sensitivity
0.7	0.05	0.07±0.006
2	0.07	0.08±0.01
5	0.07	0.11±0.01

Table III-F-1: Summary of previous $(B/A)_{CG}$ values as compiled by the ICRU [19].

Ashtari performed similar calculations using the MITR-I therapy beam, and arrived at a value of 0.0437 [14]. The MITR-I therapy beam was designed as a thermal neutron beam. Ashtari did not include the thermal neutron component of the spectrum in her calculations in an attempt to approximate a value of $(B/A)_{CG}$ for an epithermal beam. This value is now used by the MIT-R group [15].

A calculation of the type made by Ashtari was not made for the LABA neutron beam. The best information available at this time indicates that the value of $(B/A)_{CG}$ should be less than 0.07. The value 0.04 was chosen as an initial value for the calculations, and the variation of the results using values in the range 0.01-0.07 was analyzed. Changing the value from 0.01-0.07 changed the fast neutron and photon doses by less than 5%. Because this variation was small, the value 0.04 was used for the rest of the calculations. The effect of this variation is discussed in Section III.F.3. The value 0.04 indicates that the CG chamber response is due almost entirely to the photon dose, and that the neutron dose contributes only approximately 4% to the detector signal.

At this point, it is possible to state the values to be used for the A and B factors.

$A_{TE} = 4.9 \times 10^{-11}$ C/(cGy-in brain)

$A_{CG} = 8.8 \times 10^{-11}$ C/(cGy-in brain)

$B_{TE} = 6.42 \times 10^{-11}$ C/(cGy-in brain) at a depth of 1 cm

$B_{TE} = 6.81 \times 10^{-11}$ C/(cGy-in brain) at a depth of 7 cm

$B_{CG} = 0.35 \times 10^{-11}$ C/(cGy-in brain)

III.F.1.c Corrections to the ionization chamber signals

Some correction factors must be applied to the ionization currents because the measurements did not take place under the same conditions as the calibration. The chambers were calibrated with a gas flow rate of 5 cc/min. It is difficult to regulate the

gas flow at this low rate, so a rate near 20 cc/min was used instead and a correction factor was applied. This correction factor was taken from a graph produced by the MIT-R group [15].

The gas temperature was measured with a thermometer to make a correction to the calibration constant. This correction factor is a result of applying the ideal gas law. Because the pressure of the gas in the chamber (assumed to be ideal) varies with the temperature of the gas, it is the gas temperature and not the room temperature which should be measured. The thermometer was held to the end of the gas flow tube before it was connected to the IC. The temperature correction factor is f_T=(measured temperature in °K)/(293 °K). The correction for barometric pressure differences was not made. Previous results have shown that the magnitude of this correction is about 1% [15]. For the combined effects of flow rate and temperature, the correction factors are 0.996 for the CG chamber and 0.983 for the TE chamber.

III.F.1.d Thermal neutron response of the ionization chambers

To ensure that the IC signals are attributed only to photon and fast neutron doses, the response of the chambers to thermal neutrons must be subtracted from the signals. As stated previously, there is a large nitrogen kerma mismatch between A-150 plastic and brain, because the former has about twice the amount of nitrogen as the latter. The thermal response of both detectors has been studied by the MIT-R group [14] [15]. The study used a subtraction method in which the detectors were irradiated with and without a

layer of $^{6}Li_2CO_3$ surrounding the sensitive volume. The result was a determination of the correction factors: $f_\phi = 4.77 \times 10^{-20}$ C/(min-n/cm^2) for the TE chamber and $f_\phi = 1.50 \times 10^{-20}$ C/(min-n/cm^2) for the CG chamber [15].

The ionization current attributed to the thermal neutron flux is:

Equation III-F-9: $I_\phi = f_\phi \phi_{2200}$

The method used to determine ϕ_{2200} is described in section III.F.2

III.F.1.e Dual ionization chamber measurement techniques

The ionization current is calculated by dividing the charge collected at the electrometer by the time on a stopwatch. The first step is to measure the "dark current" which is the current flowing through the IC circuit with voltage applied to the IC, but with no radiation field. The value of this dark current at 1 cm was 0.126×10^{-10} C/min-mA for the TE chamber and 0.074×10^{-10} C/min-mA for the CG chamber. Next, the accelerator beam is directed onto the neutron producing target, and charge begins to collect at the electrometer. After the accelerator beam reaches a steady-state condition, the stopwatch is started, and readings from the electrometer and target current meter are recorded every minute for 15 minutes. The values of the IC currents were (without black current subtraction): 3.38×10^{-10} C/min-mA for the TE chamber and 3.2×10^{-10} C/min-mA for the CG chamber. The IC is then pushed farther into the phantom (more shallow

depth), for the next measurement. The IC is then manually removed and the entire process is repeated with the second IC.

III.F.2 The activation foil - cadmium difference method

Activation foil analysis using the cadmium difference method is used to determine the thermal neutron flux. This flux is used to calculated the thermal neutron and ^{10}B dose components. and to make the thermal neutron IC current correction described above. Bare gold foils exposed to a neutron flux with epithermal and thermal components will be activated by both components. The reaction in the gold foil is $^{197}Au(n,\gamma)^{198}Au$ which has a thermal cross section of 98.8 barns [20]. The energy of the gamma photon is 411 keV and it is emitted in 95% of the reactions [21] . A gold foil covered by cadmium will respond only to the epithermal flux because the thermal neutrons are captured in the cadmium before reaching the foil. The cadmium cutoff energy is approximately 0.5 eV [15].

The thermal neutron flux is proportional to the saturated activity of the bare gold foil. The saturated activity of the cadmium covered foil serves as a correction factor which accounts for the amount of activity induced in a bare foil by epithermal neutrons. For a pure thermal neutron field, the thermal flux can be measured directly as [22]:

Equation III-F-10: $$\varphi = \frac{MW}{A_v \cdot \sigma}\left(\frac{A_{sat}}{m}\right)_{bare}$$

Where:

MW = molecular weight of gold

A_v = Avogadro's number

A_{sat} = saturation activity. The saturation activity is the activity that will be reached as the irradiation time approaches infinity, and can easily be calculated [22].

σ = microscopic neutron absorption cross section

m = mass of gold foil

The thermal neutron flux in a mixed field must be calculated by applying a correction factor as [15]:

Equation III-F-11: $$\varphi = \frac{MW}{A_v \cdot \sigma}\left(\left(\frac{A_{sat}}{m}\right)_{bare} - F_{cadmium}\left(\frac{A_{sat}}{m}\right)_{cadmium}\right)$$

Where:

F_{cd} = A correction factor to account for the absorption of neutrons above the cadmium cut off, by the cadmium covers. For 0.020" thick Cd covers, a value of 1.02 is used [15].

As noted by Rogus, the flux calculated in this way is more appropriately called the 2200 m/sec flux, or ϕ_{2200} because the cadmium foils capture many of the neutrons in the higher energy regions of a thermal Maxwellian distribution [15].

III.F.2.a Calculation of the ^{10}B and ^{14}N dose rates

Once the ϕ_{2200} is known, the ^{10}B and ^{14}N dose rates are calculated using the fluence-to-kerma conversion factor method. For the ^{14}N dose, the MIT-R group has calculated the value in brain tissue of 1.401×10^{-11} cGy cm^2/n. The kerma factor for a 1 ppm concentration of ^{10}B is 8.66×10^{-12} cGy cm^2/n [15]. For 30 ppm, the kerma factor is multiplied by 30.

III.F.2.b Experimental techniques - activation foils

The use of activation foils in conjunction with the dual IC method requires at least two more experiments. The two ICs must first be used one at a time as described above. Then, the activation foils (bare and Cd covered) are used one at a time at the same radial and depth locations in the phantom.

Gold foils cut approximately square to weigh near 7 mg were used in the measurements. The bare foils are taped to a thin acrylic rod which is then inserted into one of the butyrate tubes. The MIT-R group tapes the gold foils at 1 cm intervals. The MIT-R group uses Cd-covered foils only at 2 cm intervals because placing them at closer intervals could lead to flux suppression. In the measurements presented here, the bare and cadmium-covered foils were located at 1 and 7 cm only. The tube is filled with water, and tapped repeatedly to remove all the air bubbles which cling to the tape. The tube is then capped and inserted into the phantom. At the start of irradiation, a complete recording of all relevant times is kept to be used in the calculation of the saturation

activity. For these measurements, a beam current of approximately 10 μA was used for 45 minutes.

During the measurements presented here, the accelerator power supply failed while irradiating the Cd-covered gold foils, and it was not possible to use the Cd-covered foils in the analysis. In the calculations, it was assumed that the ratio of $(A_{sat}/m)_{bare}/(A_{sat}/m)_{Cd}$ was the same as that determined by the MIT-R group, 2.45 [15]. The bare foils were then counted on a germanium detector at MIT, which was calibrated on the same day of the readings. The calibration is made with a National Institute of Standards mixed radionuclide source. This mixed source contains many isotopes which emit gamma photons with a variety of energies. One of these isotopes, ^{125}Sb emits a photon with an energy 427.9 keV which is near that of the gold photon. The efficiency of the detector is calculated at this point and used in the calculations[23]. From this measurement, the saturation activity was determined. Using this method, the values of ϕ_{2200} were 2.4 x 10^8 neutrons/(cm^2-sec-mA) and 7.7 x 10^7 neutrons/(cm^2-sec-mA) at depths of 1 and 7 cm respectively.

III.F.3 Results and discussion

Measurements of the BNCT dose components were made, using the techniques described above, at two locations in the phantom (1 and 7 cm) along the axial centerline. No normalization was used. Table III-F-2 contains a list of the various dose components calculated by these methods. The table also includes the predicted values from MCNP.

Dose component	Predicted at 1 cm [cGy/(mA-min)]	Measured at 1 cm [cGy/(mA-min)]	Predicted at 7 cm [cGy/(mA-min)]	Measured at 7 cm [cGy/(mA-min)]
Fast neutron	1.8	2.17	0.54	0.81
Thermal neutron	0.3	0.25	0.12	0.065
Photon	2.3	3.40	1.5	1.54
30 ppm ^{10}B	5.8	4.55	2.4	1.2

Table III-F-2: Measured and simulated dose components in an elliptical phantom using the reaction ^{9}Be(d,n) E_d=2.6 MeV.

To compare the predicted and measured values, the following formula was used:

discrepancy = |measured-predicted| /predicted

When compared in this way, the discrepancies at 1 cm are 20%, 16%, 48%, 21% for the fast neutron, thermal neutron, photon and ^{10}B dose rates, respectively. The discrepancies at 7 cm are more severe except in the case of the photon dose, where the discrepancy is 2%. There are several possible sources of error in the experimental and predicted results presented here which may explain these discrepancies.

The MIT-R group, which has used this method extensively, estimates that the total experimental error in the photon and fast neutron dose components are 17% and 9% respectively. The error in the thermal neutron and ^{10}B dose components is estimated to be 7.4% [15]. The MIT-R group has found that their experimental results, using the phantom, agree with MCNP predictions of the dose components to within 15% [24].

The measured values at 1 and 7 cm are higher than the predicted values for the fast neutron and photon components (measured with the dual ionization chambers) and lower than the predicted values for the thermal neutron and ^{10}B components (measured by activation foil analysis). Since these components are measured in two different ways,

these discrepancies are not necessarily inconsistent. In both cases, one of the largest sources of error is the uncertainty of the total integrated ion beam current striking the target. The current striking the neutron producing target was recorded at 1 min intervals. The total charge on the target was then computed by integrating these currents over the 1 minute intervals assuming that the current was constant during the intervals. Typical measured ion beam currents were 10-12 μA. The ion beam current meter showed fluctuations of ± 5% during the one minute intervals and the current over the entire measurement period fluctuated by 20%. The accuracy of the ion beam current reading depends on the accuracy of the meter and the design of the charge collection circuit. To create the circuit, a conductive wire was attached to the beryllium target holder. A second wire was connected to the beam tube to collect secondary electrons and any beam current which did not reach the target. These two wires were joined and connected to the ion beam current meter. Before steering the ion beam onto the target, the beam was intentionally steered onto the beam tube and the beam current was measured. The beam was then steered onto the target, and no other adjustments were made to the accelerator operating parameters. The ion beam was directed onto the neutron producing target by adjusting the steering and focusing magnets so that the neutron production at the target was maximized. This neutron production rate was measured by a large volume neutron detector placed approximately 60 cm from the MSR therapy port. The currents measured when the beam was directed on target, and when the beam was intentionally off the target, agreed to within 10 - 15%. More precise charge collection systems, like the one described at OUAL in Chapter II, are accurate to within a few percent. Based on the

fluctuations observed during the data collection process and the inaccuracy of the charge collection circuit, the total integrated charge on the target is a potentially large source of systematic error. The experimental error assigned to the total integrated charge is at least 5% and possibly as high as 20%.

The signal to noise ratios of the ion chambers (net currents/dark currents) at 1 cm were 25:1 for the TE chamber and 42:1 for the CG chamber and approximately 10:1 for both chambers at 7 cm. The values of the dark currents were very small, and would not affect the accuracy of the results more than a few percent.

The gas flow meters could be read to an accuracy of approximately 5% (20 $\pm$ 1 cc/min) due to the size of the floating ball in the flow meters. The fluctuations of these readings were approximately 10% (20 $\pm$ 2 cc/min). These fluctuations should affect the IC signals by approximately 1% based on the data provided by the MIT-R group [15]. The accuracy of the IC electrometer is known to be approximately 0.5% based on calibration results [15].

Another source of systematic error is the calculation of the photon and neutron sensitivities of the detectors. The A values are determined by direct calibration with an associated error of $\pm$ 2% [15]. The B values are derived from the calculated or assumed (B/A) values. Since the B values are the products of the respective (B/A) and A values, the uncertainties in the A values affect the accuracy in the B values. The values of

$(B/A)_{TE}$ and $(B/A)_{CG}$ used in these calculations were 1.31 and 0.04, respectively. To assess the effect that these values have on the final measured dose rates, these values were varied independently between 0.9 - 1.4 and 0.01 - 0.07, respectively. When the value of $(B/A)_{TE}$ was varied between 0.9 and 1.4, the photon dose rate varied between 3.36 and 3.41 cGy/(min-mA) or approximately 2%. The fast neutron dose rate, however, varied between 3.20 and 2.03 cGy/(min-mA). This indicates that the fast neutron dose is very sensitive to the value of $(B/A)_{TE}$, while the photon dose is not. When the value of $(B/A)_{CG}$ was varied between 0.01 and 0.07, the photon dose rate varied between 3.46 and 3.33 cGy/(min-mA) or approximately 3%. The fast neutron dose rate varied between 2.11 and 2.22 cGy/(min-mA) or about 5%. Therefore, neither dose component is very sensitive to value of $(B/A)_{CG}$. Since the choice of B/A values does not appear to greatly affect the photon dose calculation, another explanation must exist.

A more significant source of the discrepancies is the source definition used in the simulations. The source definition was a pure neutron spectrum without any photon production. There is little information in the literature concerning the gamma production at the target from the deuteron bombardment of beryllium. The gamma production is relatively weak, with a maximum cross section of 10.1 ± 3.5 μb [25]. This gamma production was not modeled, and might account for some of the discrepancy. Another source of photon dose is the various (n,γ) reactions in the MSR. This photon component depends on the original neutron spectrum which was taken from the literature and available only at 0 degrees. Since the neutron production was not known at other angles,

the production was assumed to be isotropic. This might account for a significant error which is difficult to assess without knowing the correct spectrum.

One other possible source of photons which was not accounted for in the simulation was the (n,γ) reactions in the walls of the vault. This source of radiation will be examined in Chapter IV. The results of Chapter IV indicate that, using the neutron producing reaction ^{7}Li(p,n), the (n,γ) reactions in the walls could account for approximately 0.02 cGy/(min-mA) at a location near the brain phantom for a well-shielded MSR. Results in Chapter IV also clearly indicate that use of an unshielded MSR results in much more contaminant radiation (neutron and photon) because thermal neutrons are not captured near the MSR. From these results of Chapter IV, we can estimate the photon dose rate that would have existed during these measurements at a location near the phantom, resulting from (n,γ) reactions in the walls of the vault. Since the MSR used in these measurements is unshielded, this photon dose rate component might have been on the order of 0.02 - 0.2 cGy/(min-mA). This additional photon dose component might account for a significant part of the discrepancy between the measured and simulated results. This photon dose component, however, should be approximately uniform over the volume of the phantom.

Because the disagreement between measured and predicted photon dose rate is so large at 1 cm and so small at 7 cm, one might expect some type of geometric explanation for the differences. Since the detector is very close to the phantom surface and the

therapy port during the 1 cm measurement, one possible explanation of the discrepancies, based on geometry, is that a low energy photon field exists outside the phantom. The low energy photon field might penetrate 1 cm into the phantom easily, but not significantly penetrate to depths of 7 cm. This would cause the photon dose rate at 1 cm to be higher than expected, but not affect the 7 cm photon dose measurement.

The accuracy of the gold foil activation method is dependent on several factors. The gold foils are weighed to an accuracy of $\pm$ 1%. The statistical uncertainty resulting from the counting process was approximately 1.5% for the gold foil at 1 cm and 2.5 % for the foil at 7 cm. The total systematic error resulting from uncertainties in the position of the gold foils, the cross sections of Cd and Au, timing, and self absorption of the 411 keV photon in the gold foil have been analyzed extensively by the MIT-R group. These various factors result in uncertainties of less than 4%[15]. As discussed above, the uncertainty in the total integrated charge is potentially much greater than these other factors, and could be as high as 20%.

Considering all possible sources of error, the most likely reasons for the disagreement between simulated and measured results are: (1) the inaccuracy of the neutron source definition, (2) the fact that two photon dose components ((n,γ) reactions in the vault walls, and photon production at the target) were not included in the model, (3) the large uncertainty in the total charge on the target. Numbers (1) and (3) would affect

both the neutron and photon dose components while (2) would only affect the photon dose components.

III.G Conclusions regarding dosimetry techniques

In Section III-F, the dual ionization chamber method, as it has been implemented at LABA, has been described. At a depth in phantom of 1 cm, the discrepancies between measured and simulated neutron dose components were between 16% and 21%. This disagreement can be attributed both to experimental error and inaccuracies in the MCNP model as discussed above. The disagreement between the measured and simulated photon dose rates was much larger (48%). This disagreement can also be attributed to errors in both measurements and simulations. Possible sources of this disagreement have been discussed above.

These are the first results using this dosimetry method at LABA. The measurements were made on an absolute basis (no normalization used) and in all cases the simulated and measured dose components agreed to within a factor of 2. The level of accuracy is encouraging for initial results, but will not be sufficient to definitively confirm the results of Monte Carlo beam design. The confirmation of Monte Carlo-based designs will be very important in the development of AB-BNCT. Four changes to the experimental methods might help to resolve these discrepancies, and improve these initial results.

First, a neutron source should be used for which the neutron and photon production at the target is more accurately known. If possible, two neutron sources, such as ^{7}Li(p,n) E_p=2.5 MeV and ^{9}Be(p,n) E_p=3.7 MeV, should be used. In the case of the ^{7}Li(p,n) reaction, the photon production at the source is known to be very small and well shielded by the moderator. By using this neutron source, one could eliminate photon production at the target as a possible source of error.

Second, the MSR should be shielded and the (n,γ) reactions in the vault walls more accurately modeled. One possible experiment could be conducted in which the MSR is alternately shielded and left unshielded. Comparing the results would give a direct indication of the effect of contaminant photon radiation inside the vault, and specifically around the therapy port. This type of experiment could also be used to confirm some of the results which will be presented in Chapter IV.

Third, a second method of experimentally determining dose within the phantom should be developed. This method should be independent in as many respects as possible from the dual ionization chamber and activation foil methods. One possibility is the use of thermoluminescent detectors (TLDs). TLDs are used at the Brookhaven National Laboratory (BNL) BNCT group for therapy beam dosimetry [26]. By using LiF TLDs which have been sufficiently depleted of their ^{6}Li content, BNL can directly measure the photon dose component. Usually, these TLDs are problematic in mixed neutron and photon fields because any ^{6}Li(n,α) reactions in the TLDs will result in the deposition of a

large amount of energy which can hide the photon dose component. That is, unless the LiF TLDs have a very small amount of ^{6}Li, the neutron sensitivity can be much larger than the photon sensitivity and will not allow the accurate measurement of the photon dose component [27]. Recently, researchers at BNL have reported that they have improved these methods by using LiF TLDs which are surrounded by ^{6}Li shields. The shields are designed to absorb thermal neutrons so that the TLD measures only the photon dose component [26].

Fourth, the experimental procedures must be improved to reduce the systematic errors. The most important of these changes would be an improved charge collection and ion beam profiling system for the accelerator. This system should be designed to measure the current or charge impinging the target with an accuracy of 5 % or less.

REFERENCES

1. Kiger, W.S.I., *Neutronic design of a fission converter-based epithermal beam for neutron capture therapy*, in *MS Thesis, Nuclear Engineering*. 1996, Massachusetts Institute of Technology: Cambridge, MA. p. 471.
2. Wang, C.K. and B.R. Moore, *Thick beryllium target as an epithermal neutron source for neutron capture therapy.* Medical Physics, 1994. **21**(10): p. 1633-1638.
3. Briesmeister, J.F., *MCNP - A general Monte Carlo N-particle transport code, Version 4A*, . 1993, Los Alamos National Laboratory: Los Alamos, NM.
4. Attix, F.H., *Introduction to radiological physics and radiation dosimetry*. First ed. 1986, New York: John Wiley and Sons.

5. Brooks, R., G. DiChiro, and M.R. Keller, *Explaination of cerebral white-gray contrast in computed tomography.* Journal of Computer Assisted Tomography, 1980. **4**: p. 489-491.

6. Caswell, R.S., J.J. Coyne, and M.L. Randolph, *Kerma factors of elements and compounds for neutron energies below 30 MeV.* Int. J. Appl. Radiat. Isot., 1982. **33**: p. 1227-1262.

7. Zamenhof, R.G., *et al.*, *Boron neutron capture therapy for the treatment of cerebral gliomas. I: Theoretical evaluation of the efficacy of various neutron beams.* Medical Physics, 1975. **2**(2): p. 47-60.

8. Gibbons, J.H. and R.L. Macklin, *Total neutron yields from light elements under proton and alpha bombardment.* Physical Review, 1959. **114**(2): p. 571-580.

9. Ziegler, J.F., *TRIM-95.* . 1995, IBM: Yorktown, NY.

10. Yanch, J.C., *et al.*, *Accelerator-based epithermal neutron beam design for neutron capture therapy.* Medical Physics, 1992. **19**(3): p. 709-722.

11. Segre, E., *Nuclei and Particles*. Second ed. 1977: W. A. Benjamin, Inc.

12. Howard, W.B., *et al.*, *Measurement of the 9Be(p,n) thick target spectrum for use in accelerator-based Boron Neutron Capture Therapy.* Medical Physics, 1996. **23**(7): p. 1233-1235.

13. Busse, P., *et al. Long-term clinical follow-up of four subjects with melanoma in the extremities who underwent a phase-I boron neutron capture therapy protocol.* in *Seventh international symposium on neutron capture therapy for cancer*. 1996. Zurich, Switzerland: Elsevier Science - to be published.

14. Ashtari, M., *Biological and physical studies of boron neutron capture therapy*, in *Ph.D. Thesis, Nuclear Engineering*. 1982, Massachusetts Institute of Technology: Cambridge, MA. p. 313.

15. Rogus, R.D., *Design and dosimetry of epithermal neutron beams for clinical trials of boron neutron capture therapy at the MITR-II reactor*, in *Ph.D. Thesis, Nuclear Engineering*. 1994, Massachusetts Institute of Technology: Cambridge, MA.

16. Harling, O.K., *et al.*, *Head phantoms for neutron capture therapy.* Medical Physics, 1995. **22**: p. 579-583.

17. Riley, K., *Personal communication - automated IC system*, . 1996.

18. Goodman, L.J. and J.J. Coyne, *Wn and neutron kerma for methane-based tissue-equivalent gas.* Radiation Research, 1980. **82**: p. 13-26.

19. ICRU, *ICRU Report 26, Neutron dosimetry for biology and medicine*. 1977, Washington D.C.: ICRU.

20. Walker, F. and F. Parrington, *Nuclides and Isotopes*. 14th ed. 1989, San Jose, CA: General Electric Company.

21. Lederer, C. and V. Shirley, *Table of Isotopes*. 7th ed. 1978, New York: John Wiley and Sons.

22. Knoll, G.F., *Radiation detection and measurement*. Second ed. 1989, New York: John Wiley and Sons, Inc. 754.

23. Gone, J.-K., *Laboratory Report - High resolution gamma ray spectroscopy*, . 1994, Massachusetts Institute of Technology: Cambridge, MA.

24. Kiger, W., *Personal communication - MIT-R dosimetry results*, . 1997.

25. Ajzenberg-Selove, F., *Energy levels of light nuclei A=11-12.* Nuclear Physics, 1990. **506**(1): p. 1-158.

26. Liu, H.B. and J. Capala. *Measuring gamma dose with 7LiF-TLDs in a mixed field.* in *Seventh international symposium on neutron capture therapy for cancer*. 1996. Zurich, Switzerland: Elsevier Science - to be published.

27. Liu, H.B., *Personal communication - TLD detectors for BNCT*, . 1996.

CHAPTER FOUR

Facility and Patient Shielding Evaluations

This chapter describes the Monte Carlo methods used to estimate the neutron and photon dose rates in a variety of locations in the vicinity of the LABA accelerator. Using an iterative approach of design and Monte Carlo evaluation, the existing radiation shielding was evaluated and improvements were designed and built. The purpose of this shielding is to protect those working in and around the LABA facility. Improvements to the facility shielding will be presented. The initial design process was carried out under the assumption that the reaction ^{7}Li(p,n), with E_p=2.5 MeV, would be used to produce neutrons for the research at LABA [1]. The Monte Carlo simulations used to predict dose rates near the facility have been repeated for the ^{7}Li(p,n) reaction and for the reactions ^{9}Be(p,n), E_p=4.0 and 3.7 MeV. These reactions were examined because therapy beam designs based on them were shown to be promising.

Although the reaction ^{9}Be(d,n) E_d=2.6 MeV was shown in Chapter III to be less useful for producing therapy beams, it is a convenient source of neutrons for the LABA facility because the reaction is prolific and a beryllium target is already available for use. Because the LABA group will be using this reaction as a neutron source, it was necessary

to evaluate the dose rates near the vault that would result from its use. This reaction will be used with deuteron currents in the microampere range. Therefore, when this reaction is being considered, the evaluation of dose rates is based on an assumption of a 50 μA deuteron current.

Simulations were also conducted to evaluate a preliminary shielding design which would reduce the non-therapeutic dose to the patient during an AB-BNCT procedure to treat brain cancer. This evaluation was conducted using the ^{7}Li(p,n) reaction as a source of neutrons. The results of this study will be presented in Section IV.B.

IV.A Facility shielding evaluation and dose assessment

IV.A.1 Purpose

The purpose of these simulations was two-fold: (1) to design additional shielding at the LABA facility to ensure that the AB-BNCT research could be conducted safely and (2) to predict the radiation dose rates at locations in and near the facility. If AB-BNCT proves to be a clinically useful therapy, the most likely location of a new facility would be a hospital. A critical aspect of AB-BNCT is the demonstration that the therapy can be conducted in an environment which is safe for the hospital staff. This work and other similar studies [2] will help answer those concerns and eventually lead to realistic hospital-based facility designs. This section begins with a description of the MCNP model of the LABA facility.

IV.A.2 Description of the building before renovation

The LABA facility is located in MIT building NW13. A large scale drawing of the area is shown in Figure IV-A-1. Building NW13 faces almost due north, with the main entrance on Albany Street. The vault and LABA facility are located in the back of the building in the basement. There is a railroad line which runs parallel to Albany Street behind building NW13. Prior to the construction of the laboratory, most of the basement was used to store equipment and was unsuitable for immediate use. Within the proposed laboratory space was an existing vault which had been used for research using radiation sources. Although the laboratory is located entirely in the basement, this vault has a high ceiling which extends into the ground floor of NW13. A drawing of the facility's basement level, based on original blueprints of the building, is shown in Figure IV-A-2. A drawing of the first floor, which shows the vault's extension into that level, is shown in Figure IV-A-3. This ground floor has not been renovated. Cinder block construction is used for many of the walls in the basement. The ceiling between the basement and first floors is approximately 10-12 inches thick. This thickness was measured through several vents and passageways which exist in the ceiling. The walls of the vault are approximately 3 feet thick. The ceiling and vault walls are made of solid concrete.

Above the vault is a small crawl space which contains plumbing and heating equipment for the building. Access to this area is possible, but very difficult. After climbing a small ladder, one must crawl through a maze of pipes to arrive at any location where one could sit or stand. Because access to this area is so difficult, it is considered to

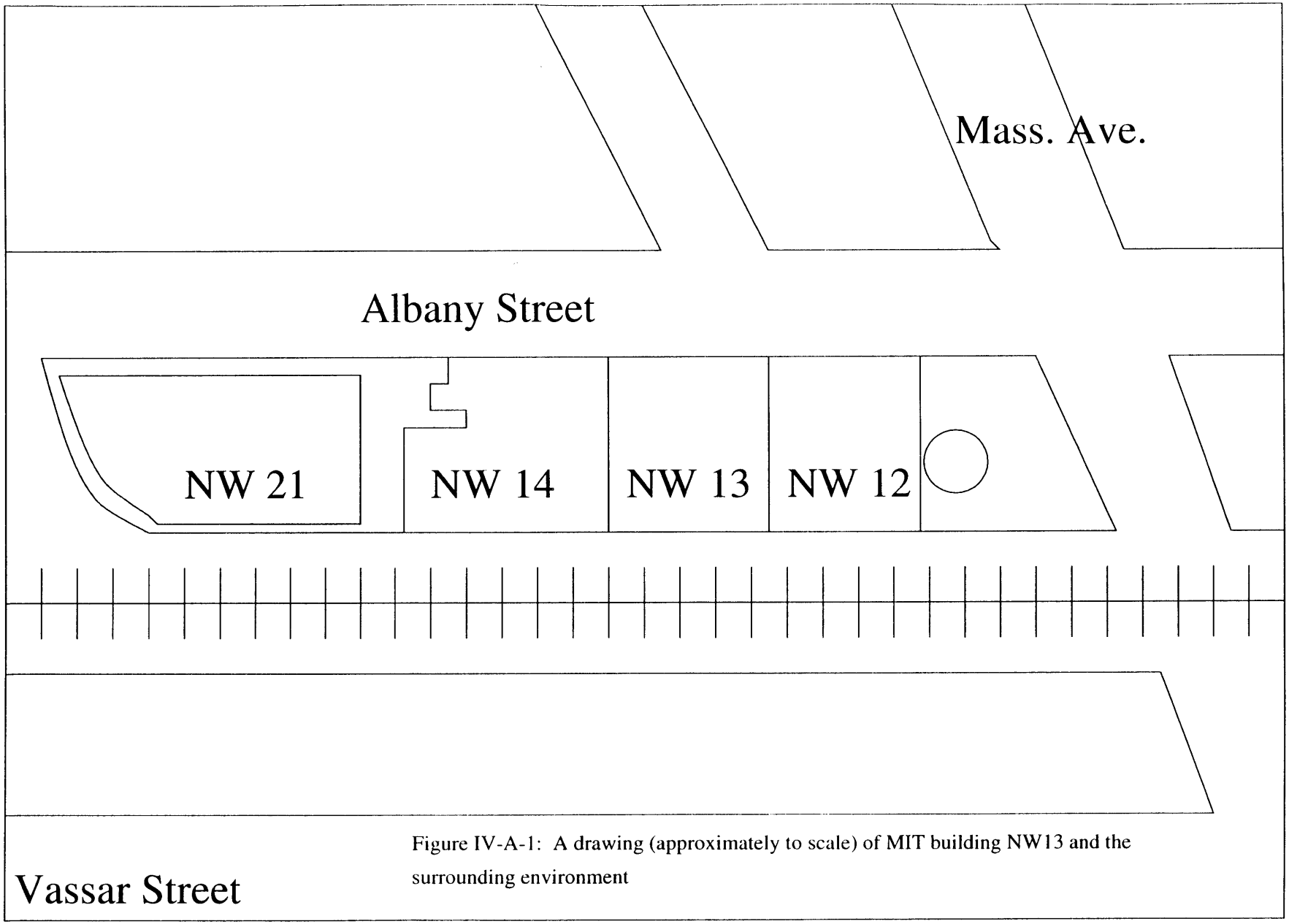

Figure IV-A-1: A drawing (approximately to scale) of MIT building NW13 and the surrounding environment

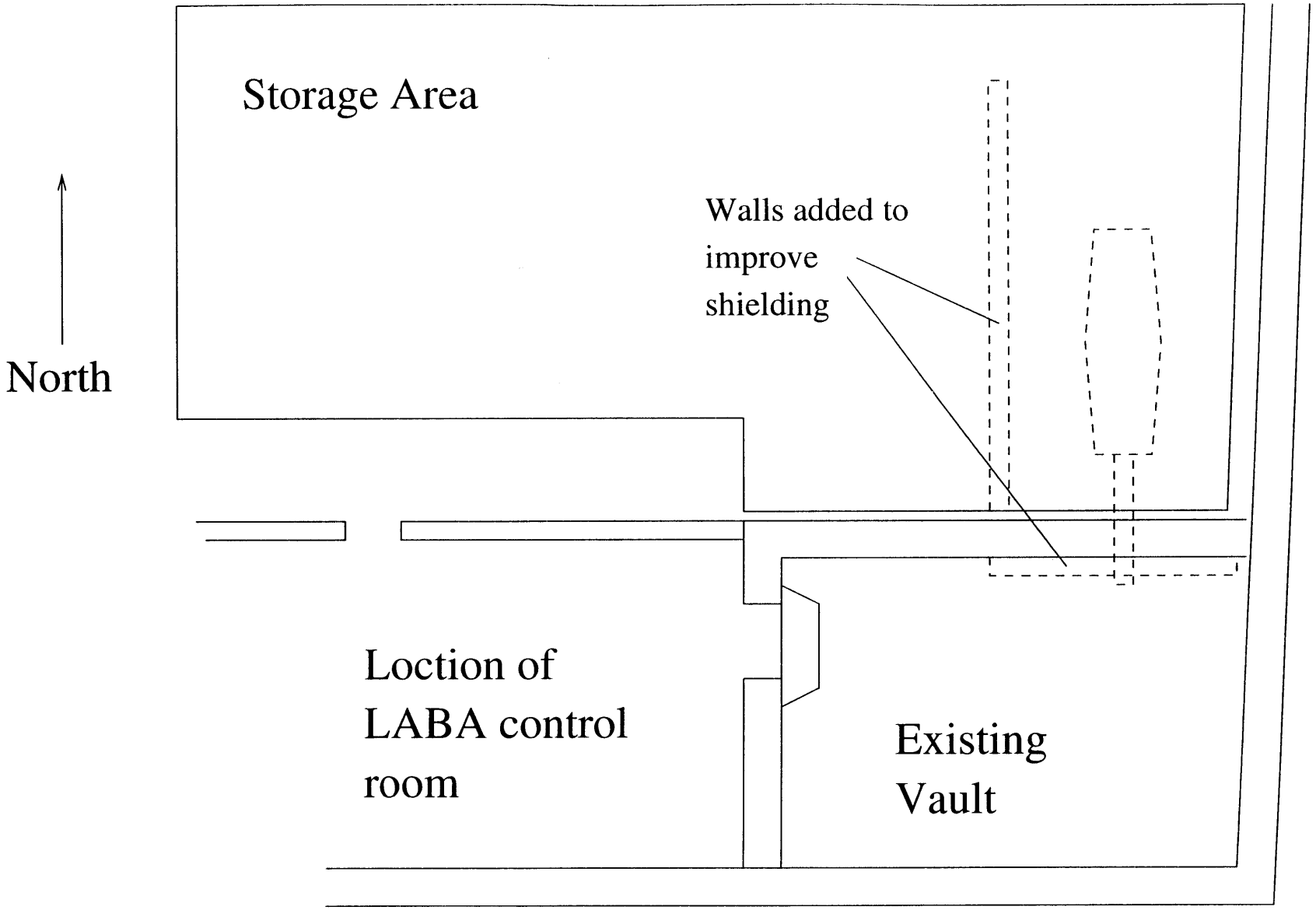

Figure IV-A-2: The basement of MIT building NW-13 in the vicinity of the LABA facility prior to renovations. Approximately to scale

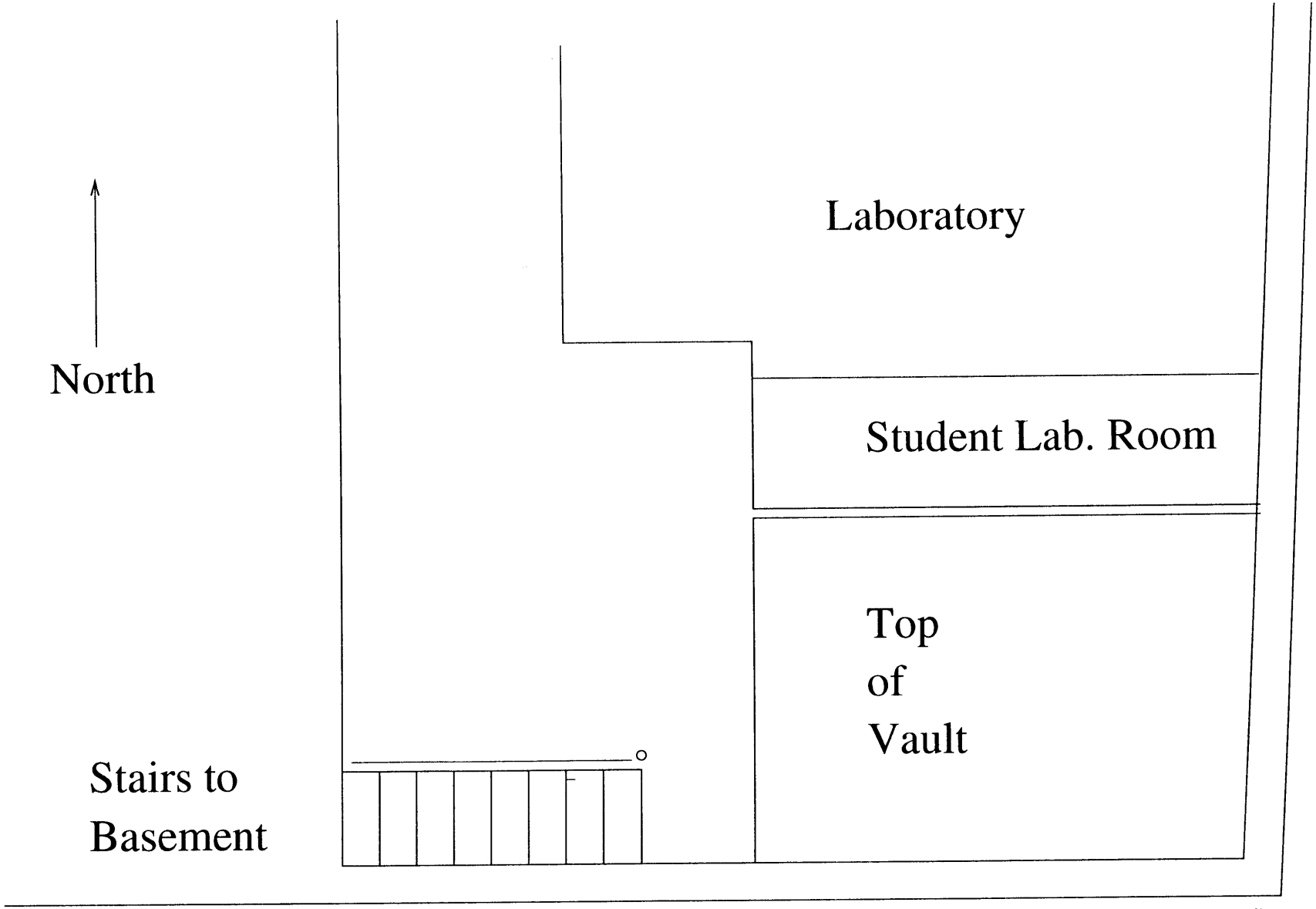

Figure IV-A-3: The ground floor of MIT building NW13, in the vicinity of the LABA facility. The vault is shown extending into this floor.

be only rarely occupied for the purposes of radiation safety evaluations. A primary concern in designing the radiation shielding is the student laboratory located north of the vault on this ground floor. The area on the south side of the vault is not excavated below street level. The east side of the vault below street level borders a boiler room in NW12. The area in the basement to the west of the vault is the control room, which was not significantly changed during the renovations. The area north of the vault in the basement was a storage room prior to the renovations and is now used to house the LABA accelerator and a radio-frequency quadrupole accelerator of another laboratory.

IV.A.3 Geometrical model for MCNP

The Monte Carlo N-Particle Transport Code System (MCNP) [3] was used to model the accelerator, existing radiation vault and two floors of MIT buildings NW12 and NW13. Wall, floor and door thicknesses and material composition were input as accurately as possible in the model. Schematic illustrations of the basement and first floor levels of the model are shown in Figure IV-A-4 and Figure IV-A-5. These have been produced by MCNP's internal two dimensional plotting routine and represent bird's-eye views of both levels. The circles indicating the locations of dose estimation, and the shaded walls added as part of the shielding design are discussed below. The accelerator was modeled as a hollow, 1.25 cm thick, aluminum cylindrical shell of radius 83 cm. A small hollow cylindrical proton beam tube was located at one end and extended through the wall and into the radiation vault. The MSR was modeled in the vault.

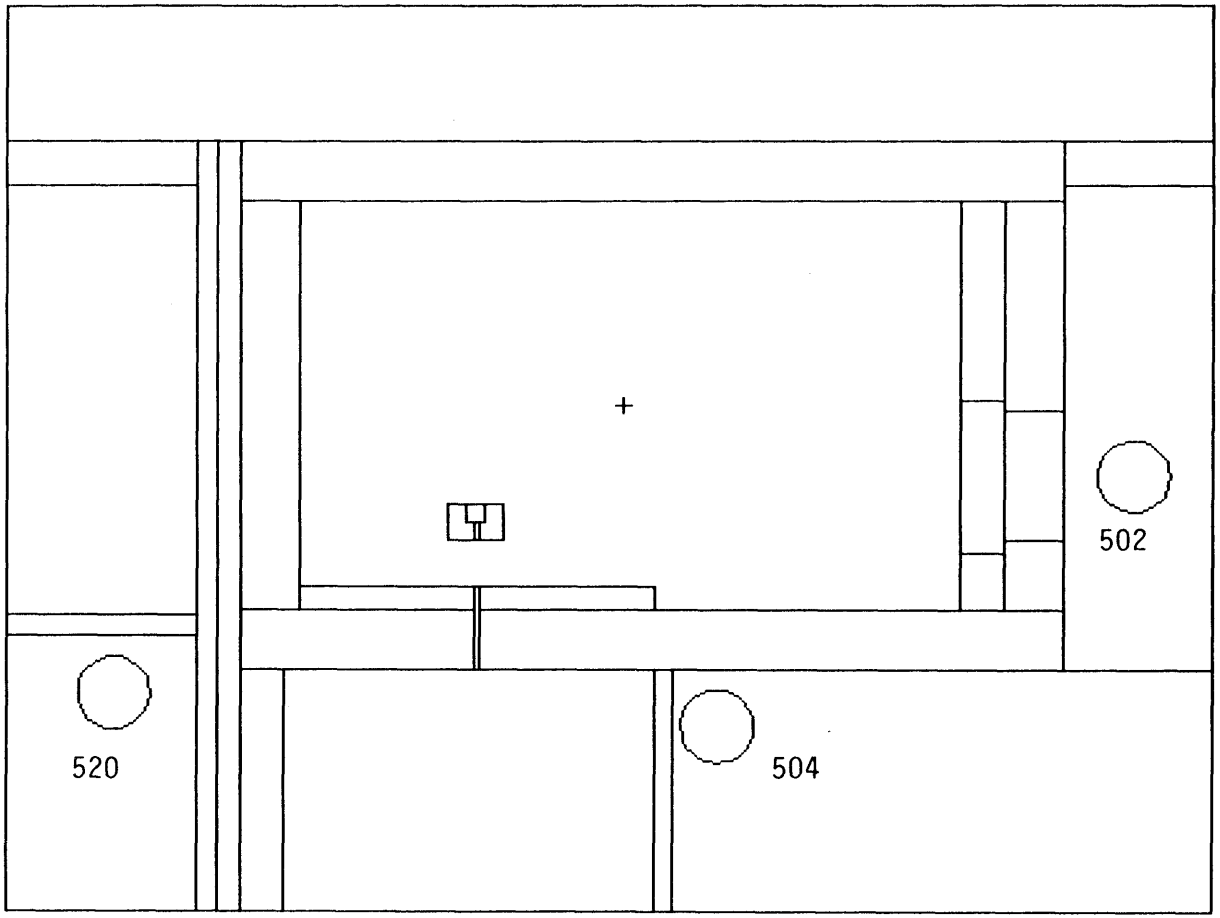

Figure IV-A-4: MCNP model, basement of MIT building NW13.

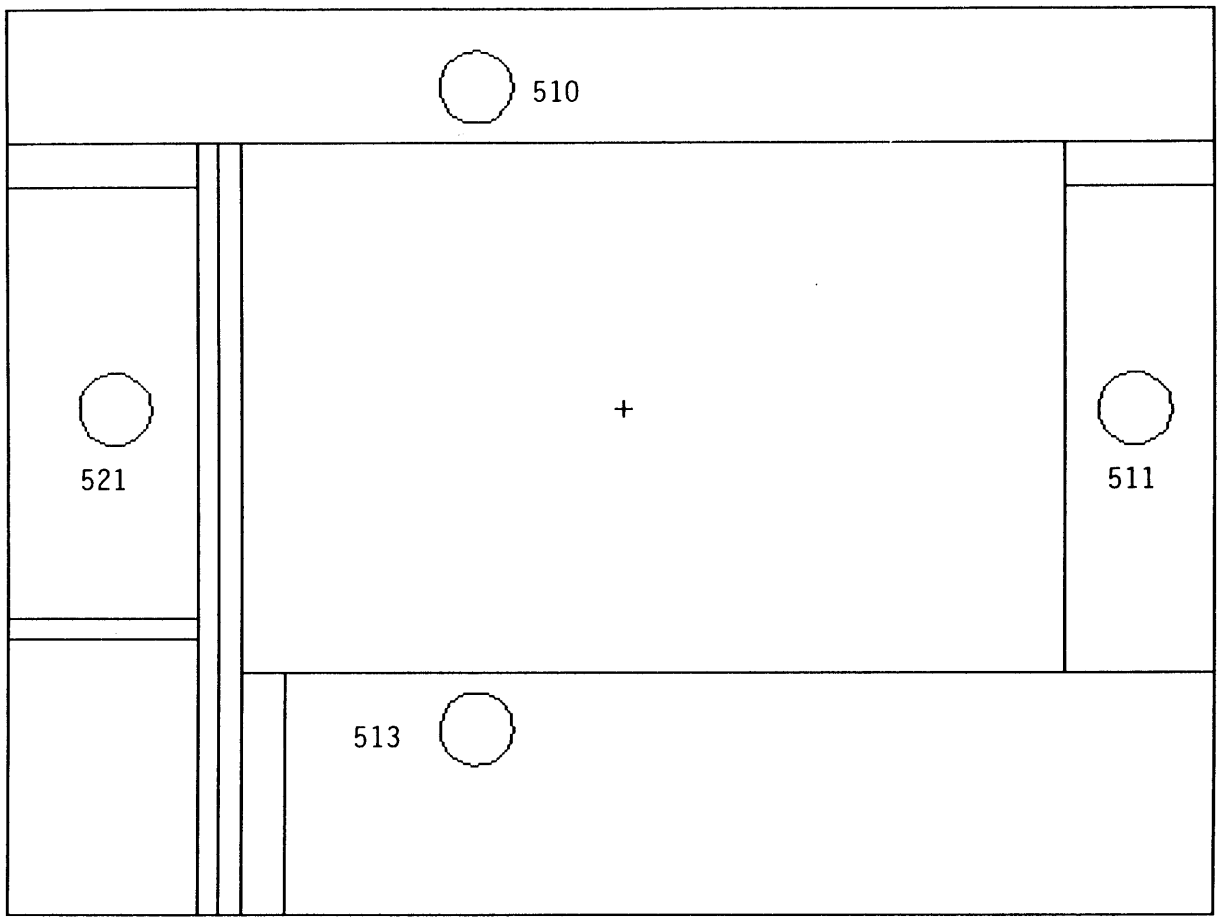

Figure IV-A-5: MCNP model, first floor of MIT building NW13.

Three sets of simulations were evaluated. The purpose of the first set of simulations was to determine the dose rates surrounding the facility when the MSR is made only of a moderator and reflector. For the $^{9}Be(p,n)$ E_p=4.0 MeV reaction a 27 cm long, 10 cm radius D_2O moderator surrounded by a graphite reflector was chosen. For the same reaction using 3.7 MeV protons, the length of the moderator was reduced to 24 cm. For the $^{7}Li(p,n)$ reaction, a 24 cm diameter, 19 cm length D_2O moderator was chosen. The moderator and reflector dimensions used for the $^{7}Li(p,n)$ and $^{9}Be(p,n)$ reactions were based on realistic therapy beam designs which were presented in Chapter III.

A second set of simulations were also conducted for the $^{9}Be(p,n)$ E_p=4.0 MeV and $^{7}Li(p,n)$ reactions using a MSR which was designed for the latter reaction [4]. A drawing showing the cross section of this MSR is shown in Figure IV-A-6. This MSR is more complex than the MSR used in the first set of simulations. It contains a 19 cm long, 24 cm diameter D_2O moderator surrounded by a lead reflector. The lead reflector is surrounded on all sides by a large volume of D_2O (with a passage left for a therapy port). At the boundaries of all materials, a thermal neutron filter made of ^{6}Li was used. The purpose of the second set of simulations was to determine the dose rates surrounding the facility when the more complex MSR is used. The simulation using the $^{7}Li(p,n)$ reaction was repeated to generate better statistical results than were published earlier [1].

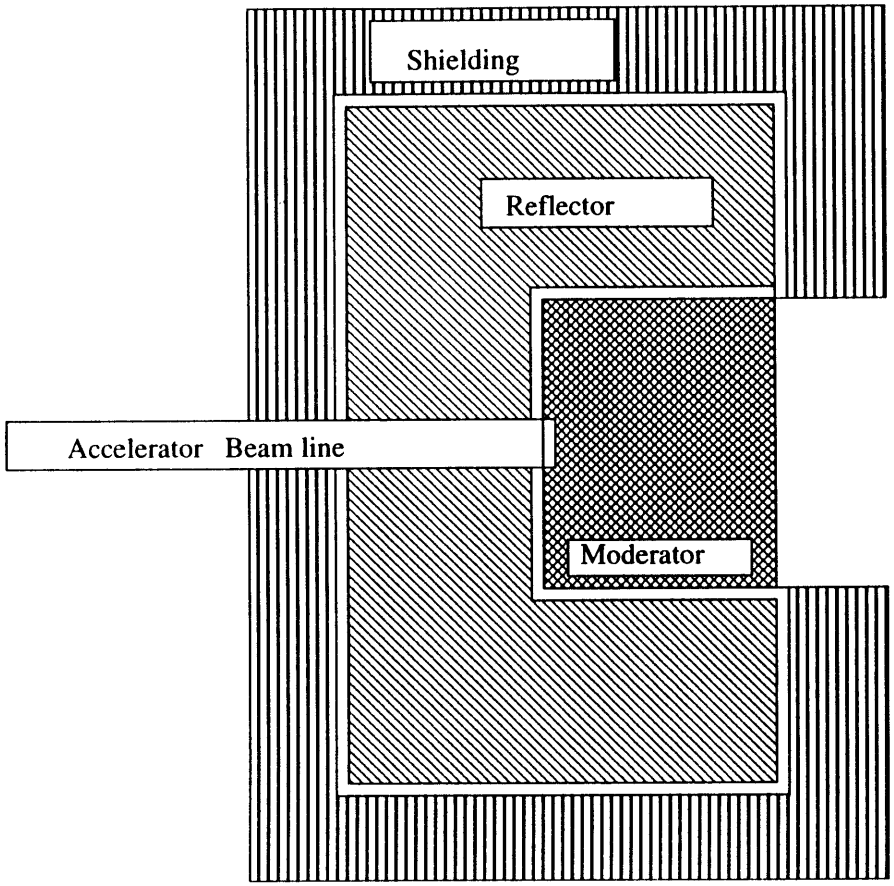

Figure IV-A-6: MSR designed for the reaction 7Li(p,n)

Finally, a simulation was evaluated to determine the dose rates which would be expected, at locations surrounding the LABA facility, from use of the $^{9}Be(d,n)$, E_d=2.6 MeV reaction and the MSR currently in use at LABA. The MSR which is currently in use was modeled since it will be used during the initial experiments at LABA. This MSR contains a 27 cm long, 24 cm diameter D_2O moderator surrounded by a lead reflector. This MSR has no additional shielding and uses no thermal neutron filters.

IV.A.4 Radiation sources

There are three distinct sources of radiation from the LABA accelerator that must be considered. The first source is a pure gamma field which is created by proton or deuteron bombardment of the target via the reactions (p,γ) or (d,γ). The strength of these sources and the energy of the photons released in these reactions was presented in Chapter II. The photon production from the $^{7}Li(p,\gamma)$ reaction was shown in Chapter III to be adequately shielded by the MSR. The gamma production from $^{9}Be(d,n)$ is relatively weak (maximum cross section of approximately 10.1 $\pm$ 3.5 μbarn [5]) and was not considered. The dose rates at locations surrounding the facility resulting from the $^{9}Be(p,\gamma)$ reaction were not thought to be significant. This assessment was based on the dose rates at the therapy port from this reaction as determined in Chapter III. This assessment was confirmed by a single simulation which will be presented.

The second source of radiation is a pure photon field which is created in the acceleration process. Stray electrons can be produced in the evacuated accelerating tube

as protons or deuterons strike the aluminum electrodes. These electrons experience an accelerating force directed towards the positively charged HV terminal. Bremsstrahlung radiation is created when these electrons strike the aluminum electrodes of the accelerating structure or some other part of the evacuated beam tube. The LABA accelerator has been designed with strong samarium-cobalt (SmCo) magnets which deflect these electrons. The strength of this magnetic field is approximately 100 Gauss on the axis of the accelerating tube [6]. Since these secondary electrons could be produced anywhere along the accelerator, the most appropriate model for the Bremsstrahlung radiation would be a line source extending the length of the accelerator. The accelerator beam tube and aluminum pressure vessel provide a considerable amount of shielding for these x-rays. The beam tube is made primarily of aluminum electrodes and glass insulators. The pressure vessel is made of aluminum which has a thickness of approximately 1.25 cm.

Prior to construction of the LABA facility, the expected intensity of the Bremstrahlung radiation during operating conditions was not known. An estimation of the intensity was based on simulations from a coupled electron - photon Monte Carlo code called TIGER [7] and measurements from an existing accelerator similar to the LABA accelerator located at Washington University in St. Louis, MO (referred to in this section as the St. Louis accelerator). The St. Louis accelerator does not use SmCo magnets for electron suppression. Separate TIGER simulations were conducted using 300, 440 and 500 keV electrons striking a 0.254 cm thick aluminum target [8]. These

TIGER simulations produced three Bremsstrahlung spectra, each of which was used as the source definition in a MCNP model of the accelerator at St. Louis. These MCNP simulations produced three different estimates of the dose rates inside and outside of the shielding structure at the St. Louis accelerator. Results of the simulations of the St. Louis accelerator were compared with actual measurements taken at that location using an ionization chamber [9]. The spectrum resulting from the 440 keV electrons best fit the available measured data. This spectrum was then used as an approximation to the Bremstrahlung production for the LABA accelerator during the evaluation of the shielding requirements and dose assessments previously reported [1]. Recent measurements during operation of the accelerator indicate that the Bremsstrahlung radiation field intensity is much lower than estimated above [6] and might not contribute in a measurable way to the dose rates at the LABA facility.

The third and most important source of radiation is the neutron beam that is created when the accelerated ion beam strikes the lithium or beryllium target. This source of radiation was presented in Chapter II. Of the three sources, the neutron source is unique in its ability to create a second penetrating radiation field at distances far from the original source of radiation. As the neutrons interact with materials in the vault, especially the hydrogen contained in concrete, gamma rays are created through (n,γ) reactions. Neutrons which have traveled a distance of many meters from the MSR could be captured in the walls of the vault releasing high energy photons close to the location of those working in the laboratory. Photons which are created at the target and MSR also

can create a secondary photon field far from the MSR. These secondary photons are reduced in energy from the primary photons created near the MSR and are not as penetrating.

The same geometrical model of the accelerator and building structure can be used in the determination of dose rates resulting from the three sources of radiation. Three separate MCNP simulations were required because the MCNP program allows only one radiation source definition for a simulation.

IV.A.5 Dose rate prediction

Radiation dose rates were estimated by tallying particle fluence (either neutron or photon) in cylindrical volumes of tissue equivalent material [10] built into the model. Particle fluence was converted to dose using fluence to kerma conversion factors for neutrons [11] and photons [12]. The cylindrical volumes were modeled at 11 locations as depicted as circles in Figure IV-A-4 and Figure IV-A-5. The number beside each circle is the reference number for the tables and discussion in this chapter. One of the cylinders (510) was modeled outside the building near existing railroad tracks, which is the closest location accessible to the public.

IV.A.6 Shielding evaluation and improvement

The shielding surrounding the neutron producing target must be adequate to keep radiation dose rates at locations surrounding the facility acceptably low. For these

simulations, the acceptable dose rates were taken from the Code of Massachusetts Regulations [Massachusetts, 1988 #114]. There should be no accessible location where any individual could be exposed to a dose equivalent rate of greater than 2 mrem/hr. The dose rates at locations accessible to the general public should be less than 0.2 mrem/hr.

The first step in the design process was to evaluate the existing radiation shielding which was provided by the radiation vault. Early results from these simulations indicated that additional shielding on the north side of the vault was needed. A concrete wall was proposed which would be a permanent structure on the inside north wall of the vault. To design the proper thickness and location of this concrete wall, and the thicknesses of the concrete walls which would form the accelerator room, dose rates were estimated and wall thicknesses changed in an iterative manner. Seven such iterations were needed to arrive at the final design.

Based on practical building constraints and an iterative examination of shielding design and dose assessment, an effective shielding improvement for the laboratory was developed. This design is shown in Figure IV-A-7. The location and orientation of the accelerator has been chosen to take advantage of the existing shielding available. Cinder block walls have been added to form the laboratory rooms and also to provide shielding. Additionally, a wall made of 30.5 cm thick concrete blocks was added to the inside north wall of the vault; this wall was needed to reduce the predicted dose rate to the students in the laboratory directly above the accelerator.

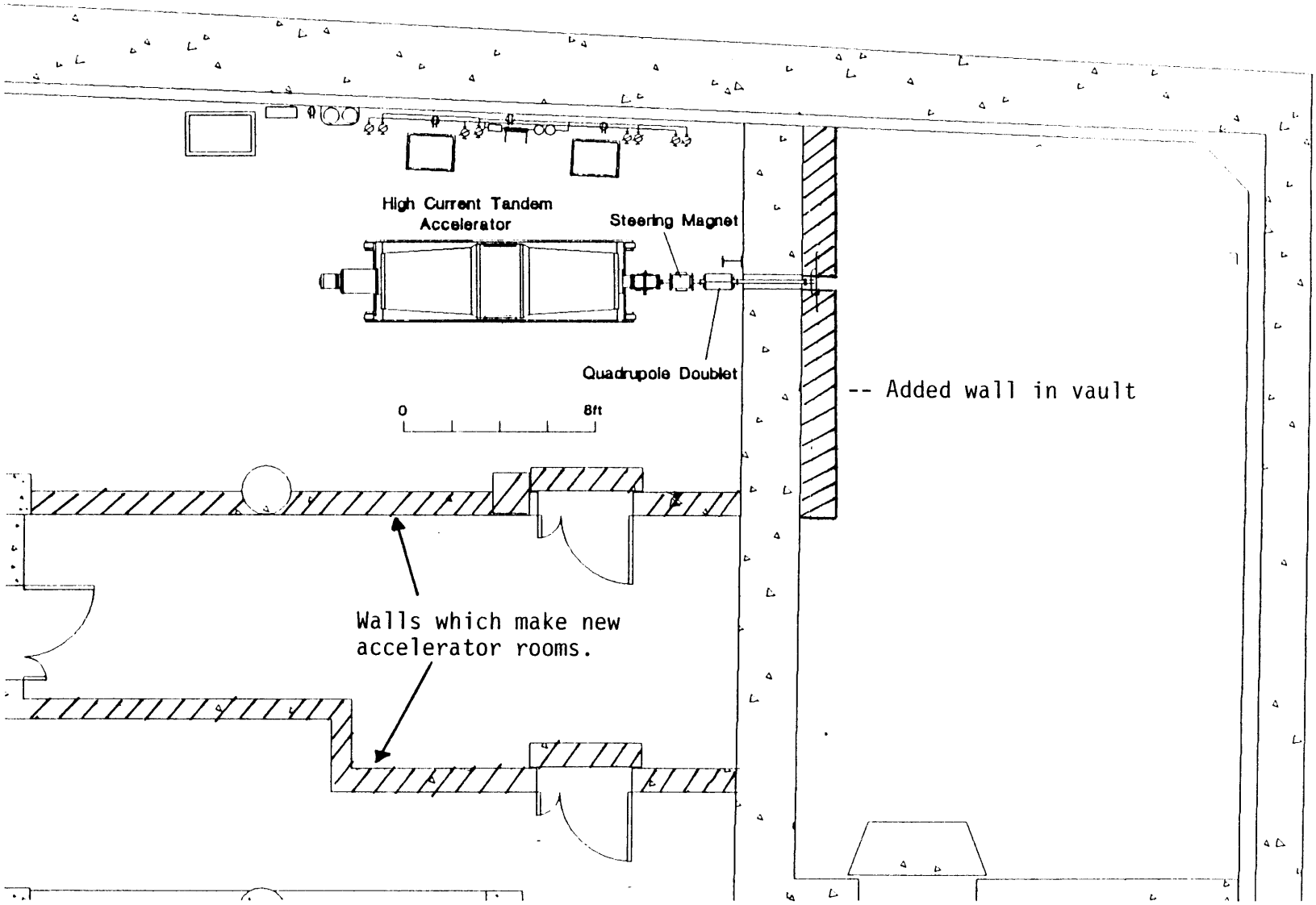

Figure IV-A-7: Shielding improvements to MIT building NW13.

IV.A.7 Dose estimations

Estimates of dose rates produced by the accelerator and target reactions in areas adjacent to the proposed laboratory were calculated using MCNP as described above. The additional shielding presented in Figure IV-A-7 was included in all simulations discussed in the remainder of the chapter. Table IV-A-1 shows the predicted dose rates at three locations which results from the Bremsstrahlung radiation produced in the accelerator [1]. These are the locations closest to the accelerator.

Reference Number	Gamma dose equivalent rate [mrem/hr-mA]	Relative Error (1 standard deviation)
504	0.02	0.01
513	0.03	0.01
543	0.001	0.05

Table IV-A-1: Predicted photon dose rates from Bremsstrahlung radiation. A 1 mA beam of 2.5 MeV protons was assumed.

Tables IV-A-2 and IV-A-3 show the predicted dose rates which result from the (p,n) reactions. The first table shows the results when the MSR shown in Figure IV-A-6 is used. The second table shows the results when the MSRs made of only a moderator and reflector are used.

Results using the MSR shown in Figure IV-A-6				
Cell reference number	Neutron Dose rate using the ^{7}Li(p,n) E_p=2.5 MeV reaction [mrem/(hr-mA)]	Statistical error (1 standard deviation)	Neutron Dose rate using the ^{9}Be(p,n) E_p = 4.0 MeV reaction [mrem/(hr-mA)]	Statistical error (1 standard deviation)
502	0.09	0.11	0.3	0.09
504	0.003	0.3	0.01	0.3
510	0.005	0.25	0.02	0.3
511	0.004	0.25	0.009	0.2
513	0.007	0.24	0.02	0.17
530	0.07	0.09	0.9	0.06
531	0.07	0.08	0.2	0.06
Cell reference number	Photon Dose rate using the ^{7}Li(p,n) E_p=2.5 MeV reaction [mrem/(hr-mA)]	Statistical error (1 standard deviation)	Photon Dose rate using the ^{9}Be(p,n) E_p = 4.0 MeV reaction [mrem/(hr-mA)]	Statistical error (1 standard deviation)
502	1.7	0.09	4.8	0.07
504	0.3	0.23	0.4	0.3
510	0.5	0.22	0.7	0.3
511	0.2	0.24	0.6	0.2
513	0.2	0.27	0.3	0.3
530	2.2	0.08	6.0	0.06
531	2.6	0.07	7.3	0.05

Table IV-A-2: Dose rates resulting from the use of the MSR in Figure IV-A-6.

Results using the MSRs containing only a moderator and a reflector						
Cell #	Neutron Dose rate using the ^{7}Li(p,n) E_p=2.5 MeV reaction mrem/(hr-mA)	Statistical error 1 standard deviation	Neutron Dose rate using the ^{9}Be(p,n) E_p = 4.0 MeV reaction mrem/(hr-mA)	Statistical error 1 standard deviation	Neutron Dose rate using the ^{9}Be(p,n) E_p = 3.7 MeV reaction mrem/(hr-mA)	Statistical error 1 standard deviation
502	0.9	0.02	1.5	0.06	1.0	0.05
504	0.03	0.08	0.04	0.07	0.03	0.08
510	0.04	0.07	0.05	0.07	0.04	0.06
511	0.06	0.06	0.05	0.06	0.04	0.06
513	0.05	0.06	0.05	0.07	0.04	0.07
520	0.0003	0.67	0.00008	0.6	0.0001	0.66
521	0.002	0.36	0.002	0.2	0.002	0.24
530	0.6	0.02	0.69	0.02	0.5	0.02
531	0.8	0.02	0.9	0.02	0.7	0.02
Cell #	Photon Dose rate using the ^{7}Li(p,n) E_p=2.5 MeV reaction mrem/(hr-mA)	Statistical error 1 standard deviation	Photon Dose rate using the ^{9}Be(p,n) E_p = 4.0 MeV reaction mrem/(hr-mA)	Statistical error 1 standard deviation	Photon Dose rate using the ^{9}Be(p,n) E_p = 3.7 MeV reaction mrem/(hr-mA)	Statistical error 1 standard deviation
502	11.5	0.02	16.5	0.02	14	0.02
504	1.55	0.05	2.34	0.06	1.8	0.06
510	2.75	0.04	4.2	0.04	3.5	0.04
511	1.75	0.05	2.5	0.06	2.1	0.06
513	0.75	0.08	1.3	0.07	1.0	0.08
520	0.047	0.34	0.04	0.44	0.44	0.31
521	0.36	0.12	0.5	0.13	0.44	0.12
530	14.5	0.02	22.8	0.02	17.6	0.02
531	20	0.02	30	0.02	24.4	0.02

Table IV-A-3: Results using a simple moderator and reflector.

A single simulation was executed to evaluate the effect of gamma production at the target for the reaction ^{9}Be(p,n) E_p= 4.0 MeV using only a moderator and reflector. The highest dose rate was at cell 531, with a value of 2.4 x 10^{-3} mrem/hr-mA and a statistical error of 0.2. This result confirms the earlier assessment that photon production at the target does not produce a high dose rate outside the shielded vault.

The results of the simulation using the reaction ^{9}Be(d,n) and the MSR currently in existence at LABA are shown in Table IV-A-4. Since this reaction will be used at currents of approximately 10 -50 μA, for limited periods of time, the results are presented assuming a beam current of 50 μA. The highest photon dose-equivalent rate at 50 μA is 2.5 mrem/(hr-mA). At location 510 the photon dose-equivalent rate at 50 μA is 0.3 mrem/(hr-mA). To reduce these dose rates further, additional shielding should be added around the MSR.

Results using MSR existing at LABA		
Cell reference number	Neutron dose rate using ^{9}Be(d,n) E_d=2.6 MeV reaction, 50 μA. [mrem/hr]	Statistical error (1 standard deviation)
502	.1	0.06
504	.004	0.02
510	0.01	0.2
511	.01	0.3
513	.01	0.3
530	0.15	0.07
531	0.1	0.06
Cell reference number	Photon dose rate using ^{9}Be(d,n) E_d=2.6 MeV reaction, 50 μA. [mrem/hr]	Statistical error (1 standard deviation)
502	1.5	0.01
504	0.2	0.03
510	0.3	0.05
511	0.2	0.03
513	0.1	0.04
530	1.5	0.01
531	2.5	0.01

Table IV-A-4: Dose rates resulting from the use of the MSR currently being used at LABA and the reaction ^{9}Be(d,n), assuming a beam current of 50 μA.

IV.A.8 Discussion

One clear conclusion which can be made from examining Tables IV-A-2 and IV-A-3 is that the shielding surrounding the moderator and reflector is very important to the reduction of dose rates outside the vault. The more complex MSR was designed for the $^{7}Li(p,n)$ reaction, and the comparisons presented here will be based on that reaction unless stated otherwise. For all the simulations, the highest photon dose rate occurred directly above the vault at location 531. The highest neutron dose rates occurred at locations 502, 530, and 531. At location 531, the photon dose rate was reduced from 20 mrem/(hr-mA) to 2.6 mrem/(hr-mA) when the additional shielding surrounding the moderator and reflector was added. At the same location, the neutron dose rate was reduced from 0.8 mrem/(hr-mA) to 0.07 mrem/(hr-mA).

The neutron dose rate accounts for a small fraction of the total absorbed dose rate at any of the tally locations. For example, using the more complex MSR, the neutron and photon dose rates at location 531 are 0.07 mrem/(hr-mA) and 2.6 mrem/(hr-mA), respectively. The total dose equivalent rate is thus not very sensitive to the number which is used for the quality factor to convert absorbed dose rate to dose equivalent rate. For these results a quality factor of 10 was used.

Some of the dose rates predicted using the more complex MSR are still higher than the allowed values discussed above. In particular, at location 510 (accessible to the general public) the photon dose rate is 0.5 mrem/(hr-mA). At location 531, the photon

dose rate is 2.6 mrem/(hr-mA). A final simulation was evaluated which used the more complex MSR and the reaction ^{7}Li(p,n) as a source of neutrons. For this final simulation, an additional shielding layer of water and boric acid was added around the sides of the MSR, but not the back or front. This volume was modeled as a cylindrical shell 10 cm thick which contained water which was saturated in its boric acid content. The boric acid was enriched to 90% ^{10}B. This additional shielding reduced the photon dose rate at location 531 from 2.6 mrem/(hr-mA) to 0.9 mrem/(hr-mA). A similar reduction was seen at the other locations. This additional boric acid shielding would be very inexpensive. To reduce the photon dose rates even further, similar boric acid shields could be added along the inside of the vault walls.

IV.A.9 Initial measurements of the Bremsstrahlung radiation

Some initial measurements have been made of the Bremsstrahlung radiation field produced by the accelerator. The accelerator beam was made to terminate on a beam stop in the vault which was not neutron producing. This ensured that the photon dose rates had no (n,γ) components. Two radiation survey meters (Ludlum model 19 and Victoreen model 450P) were placed one at a time 24 inches from the axial centerline of the accelerator, and monitored remotely by a video camera. The readings were taken using a 1.8 MeV proton beam at currents of 10-140 μA. The background readings for the two detectors were approximately 10 μrem/hr and 30 μrem/hr respectively. The dose rate was measurable when a beam current of 10 μA was used, and the dose rate did not vary significantly with increasing beam current. At a beam current of 140 μA, the dose rates

measured by the two detectors were approximately 30 μrem/hr and 55 μrem/hr. respectively. After subtracting background readings, the dose rates were 20 μrem/hr and 25 μrem/hr, respectively.

IV.A.10 Concluding remarks regarding facility shielding

For the first year of research, while the accelerator is being tested and a high current target is being developed, the accelerator will most often be run at currents in the range 10-500 μA. During this time, the dose rates should be measured experimentally to confirm the results of these simulations.

The dose rates resulting from the Bremsstrahlung radiation of the accelerator may be much lower than predicted. A systematic study of these dose rates should be conducted at various beam energies and currents. If the dose rates are very low, the shielding requirements could be significantly reduced.

The simulation results also indicate that shielding near the MSR is very important. Neutrons which are not part of the useful therapy beam should be moderated to thermal energies and captured as close to the MSR as possible. These simulations indicate that an inexpensive and effective solution would be the addition of shielding layers containing boric acid and water. Without this additional shielding, the dose rates at multi-milliampere currents would probably exceed 2 mrem/hr at several locations.

IV.B Patient shielding evaluation

During an AB-BNCT therapy procedure, the patient would be exposed to a mixed neutron and photon radiation field. As a result, in addition to the therapeutic and contaminant doses to the target organ which were discussed in Chapter II, the patient would receive a non-therapeutic radiation dose to the rest of the body. For an AB-BNCT treatment of a brain tumor, the upper torso would receive the largest part of this dose. This section describes the Monte Carlo methods used to estimate the radiation dose rates to which the patient will be exposed and to investigate a way in which this dose might be reduced. One shielding configuration is presented and various materials which might be used for this shielding are evaluated.

A diagram of a possible AB-BNCT scenario was shown in Chapter I (Figure I-B-1). In this configuration, the patient's head is placed as near as possible to the therapy port of the MSR. There is very little space available to shield the patient's torso. Other possible configurations for AB-BNCT exist, such as irradiation of the brain from one side of the head, or the irradiation of an extremity. The positioning of the patient shown in Figure I-B-1, however, presents a difficult configuration in regards to shielding the rest of the patient's body. This scenario will be used as a model to examine ways in which the dose to the patient's torso can be reduced. All other configurations should be as easy or easier to shield.

IV.B.1 Methodology

The Monte Carlo simulation code, MCNP, was used for all analysis and shielding design. The neutron spectrum from the reaction ^{7}Li(p,n), E_p=2.5 MeV was used as the initial radiation source. The results of this shielding study should not depend strongly on the neutron source reaction as long as a MSR which has been designed for the reaction is used. As shown in Chapter III, the therapy beam spectra resulting from either (p,n) reaction can be made to have very similar characteristics. The ^{7}Li(p,n) reaction has been shown to provide a therapy beam with a greater intensity, but the shapes of the various dose components are similar when compared with the ^{9}Be(p,n) reaction (E_p = 4.0, 3.7, 3.4, 3.0 MeV) if optimized beams are considered. The ^{9}Be(p,n) source reaction would also have a (p,γ) component which was not examined here.

The laboratory, MSR and patient phantom were included in the MCNP model. Neutron and photon fluences were estimated at several locations within the patient model and these fluences were then converted to neutron and photon dose rates using fluence to kerma conversion factors for neutrons [11] and photons [12]. For all calculations, a quality factor of 10 was used for neutrons, and 1 for photons. In addition, the contributions to patient dose rate from neutron radiative capture reactions in the patient and the walls of the therapy room were assessed separately. In all calculations, a proton current of 4 mA was assumed.

Because the therapy is assumed to be targeted at the brain, the location of the highest dose to the patient from extra-cranial radiation would be in the upper torso and neck. Figure IV-B-1 shows a three dimensional representation of the phantom used in the MCNP model. The MSR consists of a D_2O moderator (blue) surrounded by a lead reflector (gray) and a D_2O shielding volume (green). Layers of ^6Li (magenta) absorb thermal neutrons. The patient is modeled as three connected cylinders for the head (red), neck (gray) and torso (blue). Tissue equivalent material fills the phantom [10]. A larger scale drawing of Figure IV-B-1 is shown in Figure IV-B-2. The MCNP defined cells shown in green are the cells in which neutron and photon fluences were estimated and converted to absorbed dose.

To protect the body of the patient, a volume of shielding material, similar to a neck brace, was modeled around the neck of the patient phantom. This shielding is shown in yellow in Figure IV-B-1 and Figure IV-B-2. This volume was initially filled with air and data from this simulation were used as a baseline for comparison. The volume was then filled with other materials and the simulation results were compared for efficacy in reducing patient dose rates. The shielding design is difficult because there is limited space for shielding materials. It is important to place the patient as close as possible to the beam therapy port to maximize the therapeutic dose rate. The design is also difficult because neutron capture reactions in various materials create a mixed field of photons and neutrons.

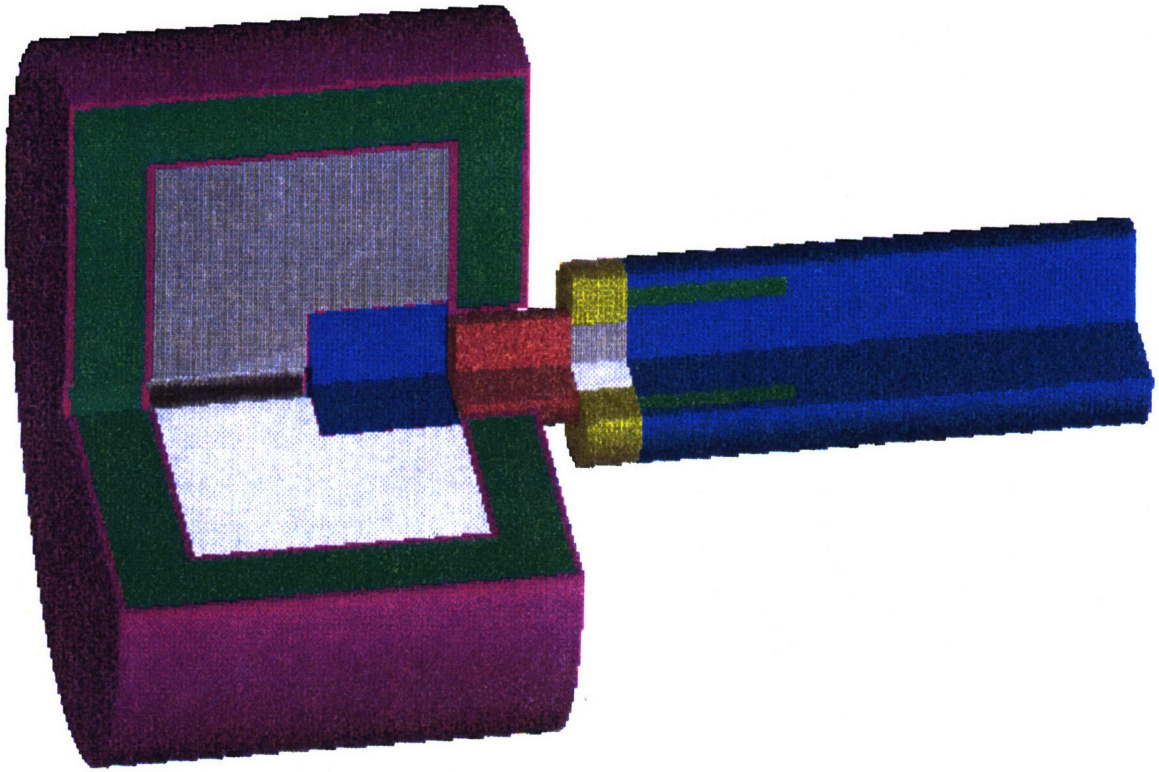

Figure IV-B-1: MCNP model for patient shielding evaluation.

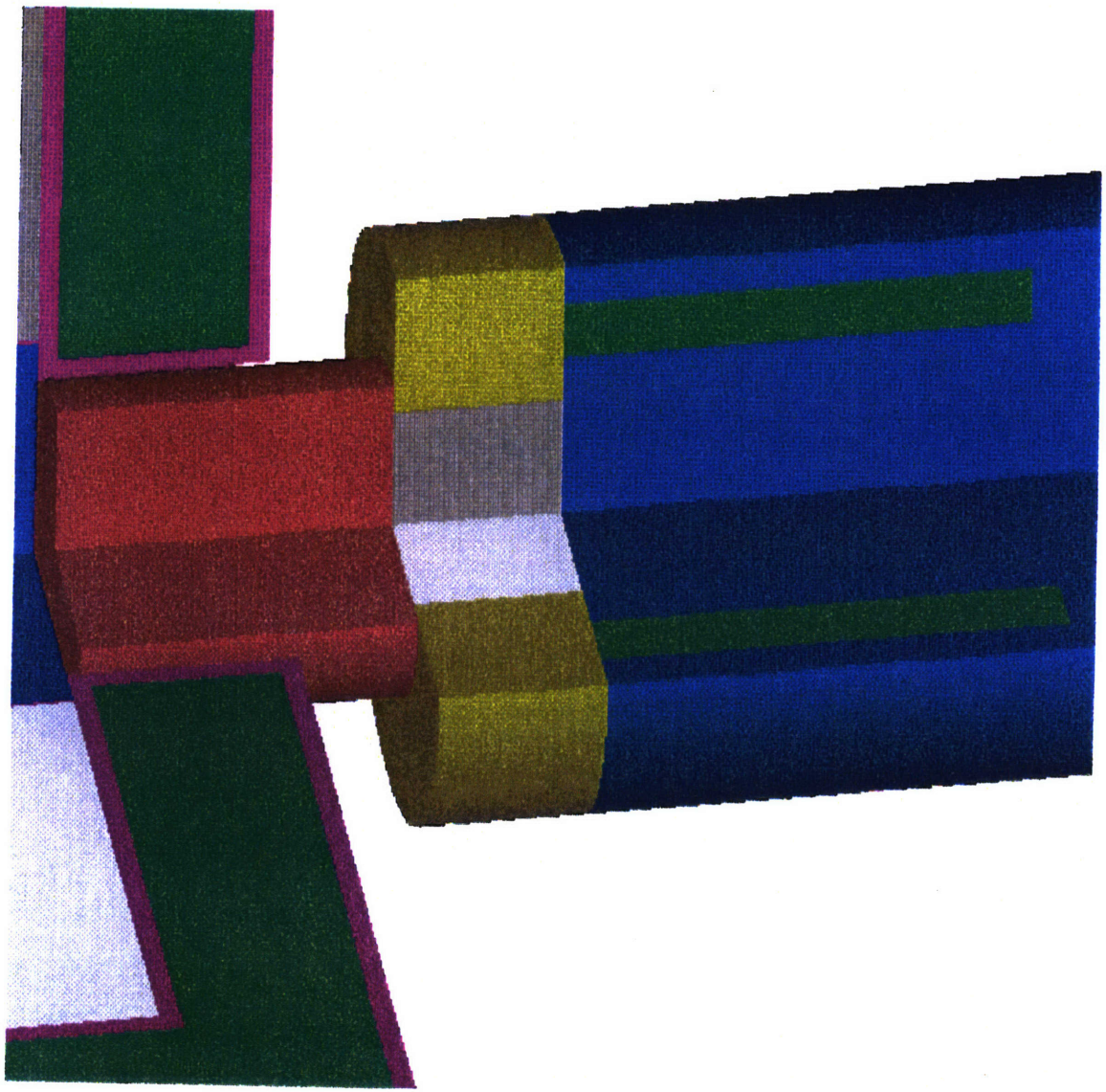

Figure IV-B-2: Patient model in MCNP shielding simulations.

The ideal material for mixed neutron and gamma shielding has the following properties: high fraction of low-Z materials for efficient neutron thermalization, large cross section for a neutron capture reaction with limited gamma production, inexpensive and safe to handle, and the ability to attenuate photons created in gamma capture reactions. Three materials were chosen for comparison: D_2O, lithium carbonate (Li_2CO_3), and a 50-50 mixture by molecular fraction of polyethylene and lithium carbonate. Lithium based compounds were chosen because the $^{6}Li(n,\alpha)$ reaction has a high thermal cross section (940 barns) and no associated gamma photons. Although the reaction $^{10}B(n,\alpha)$ has a higher cross section (3840 barns), 94% of the residual ^{7}Li is left in an excited state which emits a 0.48 MeV gamma photon. For the initial comparison of shielding materials, natural lithium, which is 7.5% ^{6}Li and 92.5% ^{7}Li was used.

IV.B.2 Results

The absorbed dose rates or dose equivalent rates as a function of depth in the phantom torso, measured from the neck down, were evaluated and graphed. To evaluate the relative efficacies of the different shielding materials, the dose rates at a depth of 3 cm in the cylinder and at a radial distance halfway between the extent of the neck cylinder and the extent of the cylinder modeling the torso were compared. A comparison of the various shielding materials, based on their ability to shield against photon radiation, is shown in Figure IV-B-3.

Figure IV-B-3: Photon dose rate in phantom torso during simulated AB-BNCT procedure using the reaction $^{7}Li(p,n)$ E_p = 2.5 MeV, 4mA, and three different shields

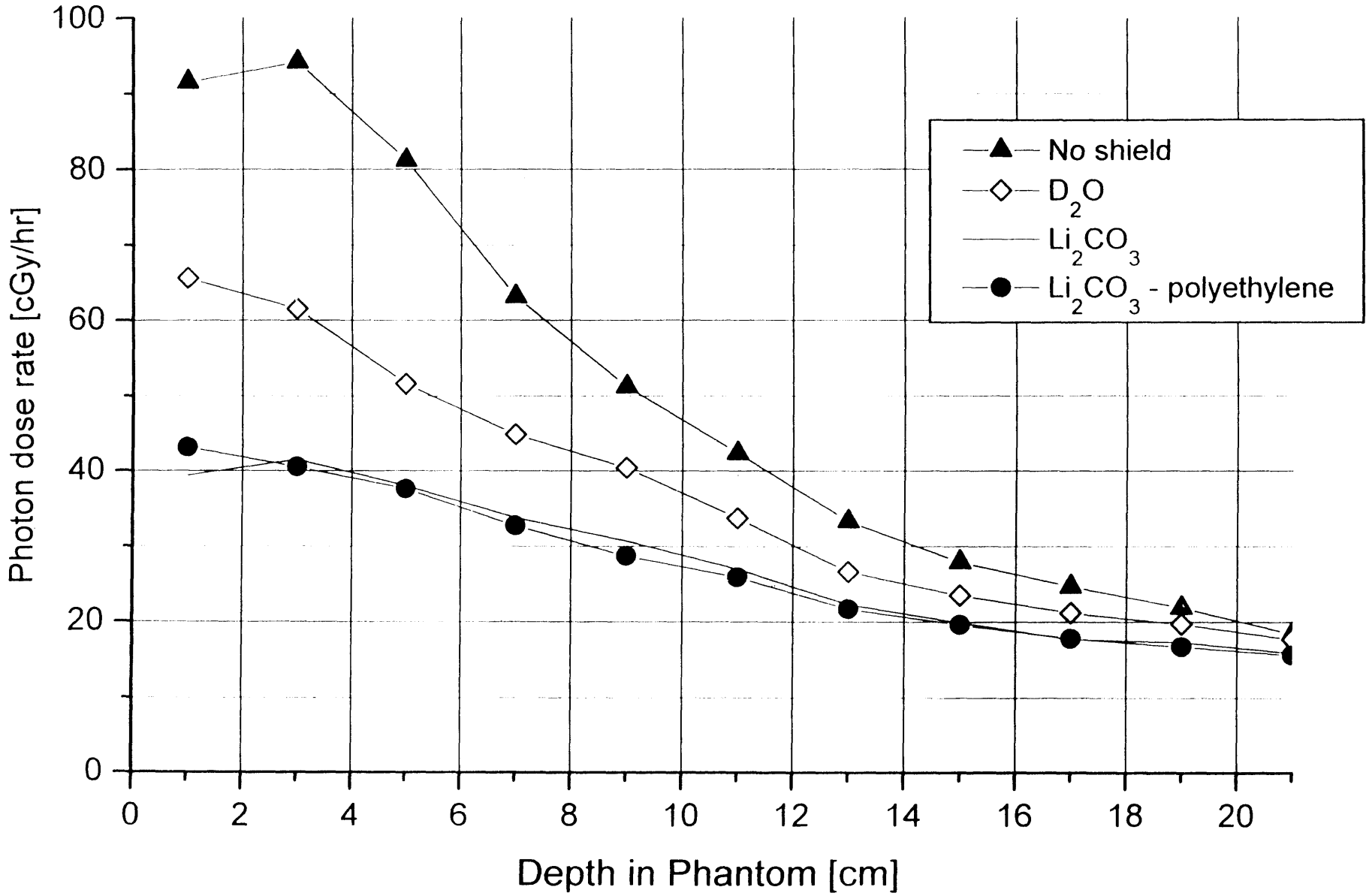

The ability of the shielding materials to shield against neutron radiation is shown in Figure IV-B-4. Based on the simulations, the best patient shielding material considered in this study is the 50-50 mixture of polyethylene and lithium carbonate. When natural lithium is used in the mixture, the total dose equivalent rate at a depth of 3 cm has been reduced to approximately 30% of the total unshielded rate. This unshielded rate includes photon production in the therapy room walls and the head phantom in the model.

IV.B.2.a Effect of increasing ^{6}Li enrichment

Natural lithium is 7.5% ^{6}Li and 92.5% ^{7}Li. To study the effects of enriching the lithium in its ^{6}Li content, the ratio of ^{6}Li to ^{7}Li was increased in increments, up to a 90% enrichment of ^{6}Li. This enriched lithium was used in place of the natural lithium in the 50-50 mixture of lithium carbonate and polyethylene. A comparison was carried out for the following enrichments: natural, 30%, 50%, 70%, and 90%. The numerical results are summarized in Table IV-B-1.

Shielding material used	Percentage reduction in neutron dose rate from unshielded phantom	Percentage reduction in photon dose rate from unshielded phantom
Heavy Water	63%	35%
Lithium Carbonate	75%	55%
50-50 mixture of lithium carbonate and polyethylene	81%	57%
50-50 mixture with 50% enrichment of ^{6}Li	85%	60%
50-50 mixture with 90% enrichment of ^{6}Li	87%	63%

Table IV-B-1: Summary of numerical results for using enriched lithium in shielding volume.

This table indicates that ^{6}Li enrichment can provide an additional 5-6 % reduction in the neutron and photon dose rates to the patient's torso.

Figure IV-B-4: Neutron dose rate in phantom torso during simulated AB-BNCT procedure using the reaction $^{7}Li(p,n)$ E_p = 2.5 MeV, 4mA, and three different shields

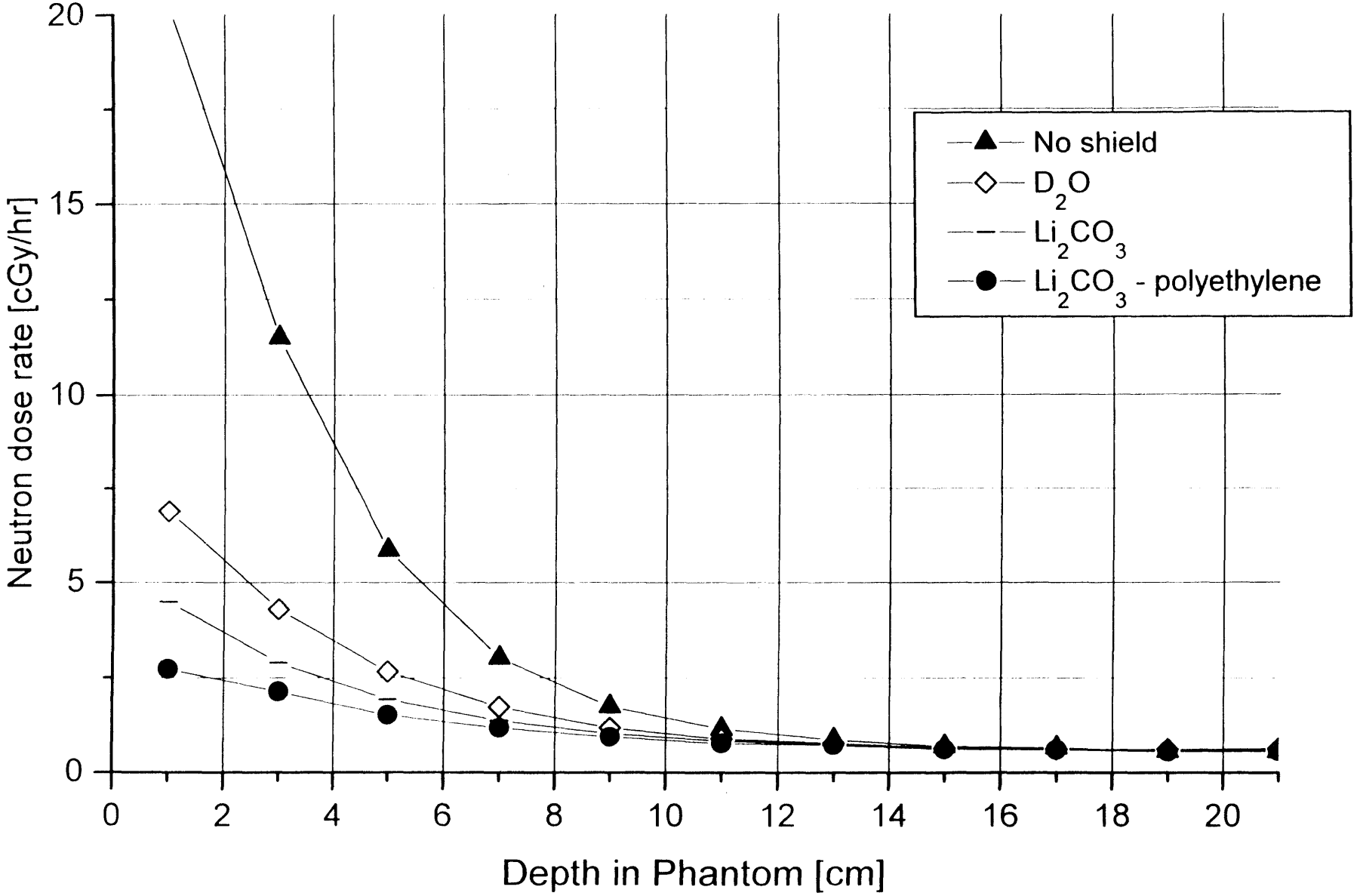

IV.B.2.b Gamma Capture Reactions

In addition to the gamma capture reactions that occur in the structures surrounding the target and those that occur in the torso, there are two other sources of gamma radiation to consider. MCNP allows the user to assess the contribution from each of the sources separately. The contribution to patient dose from gamma capture reactions in the therapy walls (which were modeled as solid concrete) accounts for less than 4% of the total unshielded dose equivalent rate. There are methods to reduce this contribution to the patient dose, such as covering the walls with ^{10}B or ^{6}Li loaded paint [13]. Since this contribution was small, these methods were not investigated further at this time. A more important source of dose to the torso is the gamma capture reactions in the brain, which accounts for approximately 13% of the total unshielded dose equivalent rate. This contribution establishes a lower limit on dose reduction to the patient. The various contributions to the photon dose rate are depicted in Figure IV-B-5.

IV.B.3 Concluding remarks regarding patient shielding

Dose rates to the patient's torso can be significant, reaching levels as high as 50 cSv/(hr-mA) (unshielded). These dose rates have been shown to be easily reduced by a simple shielding design consisting of a 50-50 mixture of lithium carbonate and polyethylene contained in a volume around the patient's neck. The reduction of the total dose equivalent rate at 3 cm by this shielding material was approximately 70% using naturally occurring lithium. The use of lithium enriched in its ^{6}Li content can further reduce these dose rates. Thirty percent of the photon dose rate to the torso at 3 cm

Figure IV-B-5: Photon dose rate in phantom torso during simulated AB-BNCTprocedure showing the various contributions to the unshielded dose rates using the reaction $^{7}Li(p,n)$ E_p = 2.5 MeV, 4mA. No shield was used.

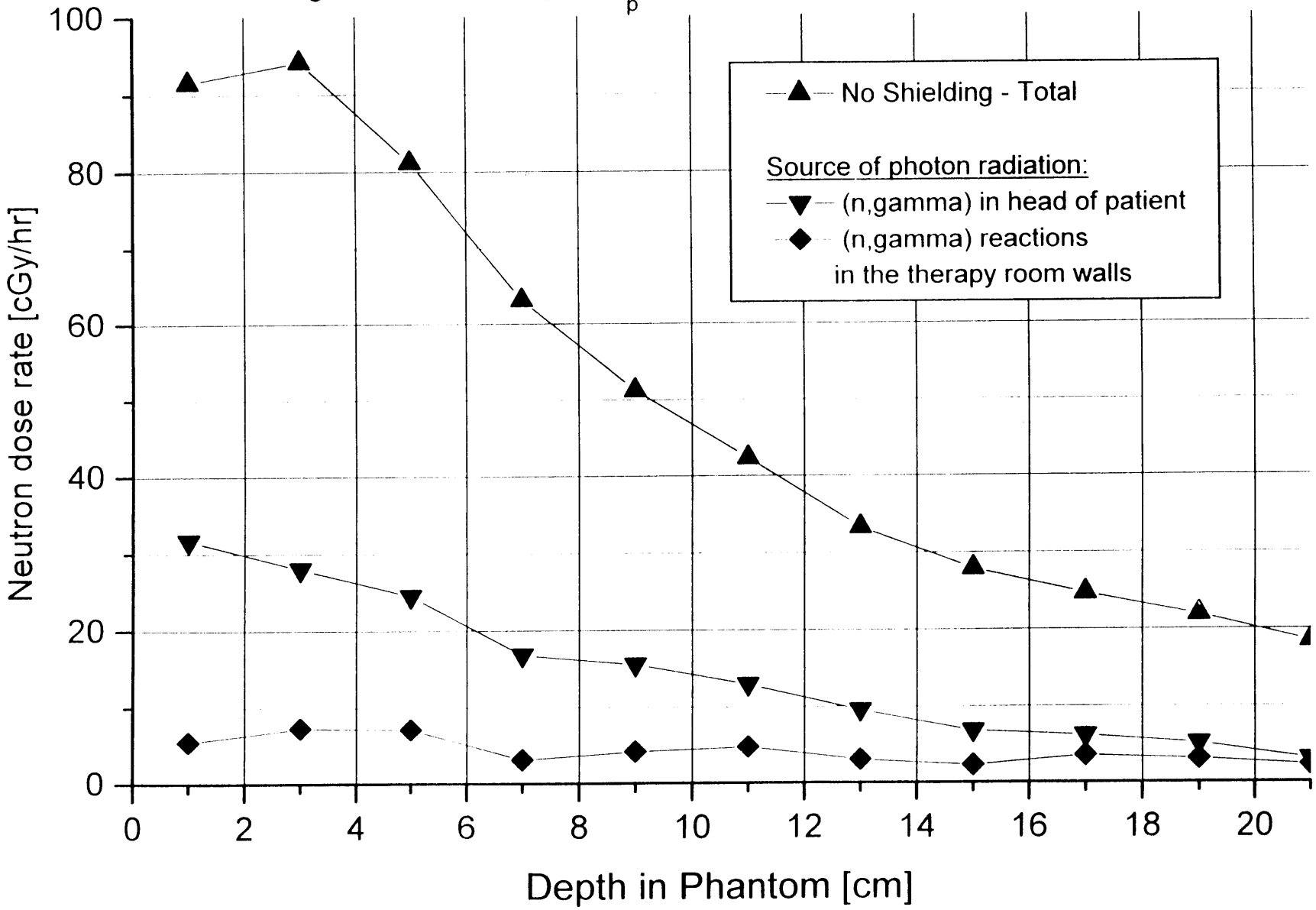

originates in (n,γ) reactions in the brain, and presents a level below which the photon dose component might not be reduced. More advanced shielding designs should be developed if AB-BNCT is be used clinically.

REFERENCES

1. Howard, W.B. and J.C. Yanch, *Shielding design and dose assessment for accelerator-based neutron capture therapy.* Health Physics, 1995. **68**(5): p. 723-730.
2. Evans, J.F. and T.E. Blue, *Shielding design of a treatment room for an accelerator-based epithermal neutron irradiation facility for BNCT.* Health Physics, 1996. **71**(5): p. 692-699.
3. Briesmeister, J.F., *MCNP - A general Monte Carlo N-particle transport code, Version 4A*. . 1993, Los Alamos National Laboratory: Los Alamos, NM.
4. Yanch, J.C., *et al.*, *Accelerator-based epithermal neutron beam design for neutron capture therapy.* Medical Physics, 1992. **19**(3): p. 709-722.
5. Ajzenberg-Selove, F., *Energy levels of light nuclei A=11-12.* Nuclear Physics, 1990. **506**(1): p. 1-158.
6. Shefer, R. and R. Klinkowstein. *A high current electrostatic accelerator for boron neutron capture therapy.* in *Fifth international conference on applications of nuclear techniques*. 1996. Crete, Greece: SPIE - to be published.
7. Halbleib, J.A., *et al.*, *ITS Version 3.0: The integrated TIGER series of coupled electron photon monte carlo transport codes.*, . 1992, Sandia National Laboratory.
8. Hughey, B., *Personal communication - TIGER simulation studies*, . 1993.
9. Shefer, R.E., *Personal communicaton - Radiation measurements at St. Louis accelerator*, . 1993.
10. Brooks, R., G. DiChiro, and M.R. Keller, *Explaination of cerebral white-gray contrast in computed tomography.* Journal of Computer Assisted Tomography, 1980. **4**: p. 489-491.

11. Caswell, R.S., J.J. Coyne, and M.L. Randolph, *Kerma factors of elements and compounds for neutron energies below 30 MeV.* Int. J. Appl. Radiat. Isot., 1982. **33**: p. 1227-1262.

12. Zamenhof, R.G., *et al.*, *Boron neutron capture therapy for the treatment of cerebral gliomas. I: Theoretical evaluation of the efficacy of various neutron beams.* Medical Physics, 1975. **2**(2): p. 47-60.

13. Rogus, R.D., *Design and dosimetry of epithermal neutron beams for clinical trials of boron neutron capture therapy at the MITR-II reactor*, in *Ph.D. Thesis, Nuclear Engineering*. 1994, Massachusetts Institute of Technology: Cambridge, MA.

CHAPTER FIVE

Summary and Conclusions

During the past five years, there has been considerable progress towards making BNCT a viable therapy modality for cancer. The progress has been made in many different disciplines which affect the success of BNCT and AB-BNCT. This chapter contains a summary of the important results contained in this thesis and concluding remarks based on these results. The research presented in this thesis will be useful to the BNCT community, especially to those working in the field of AB-BNCT. This research will be even more meaningful and useful after the results of the current clinical trials have been clearly understood and analyzed.

V.A Summary of Research

Prior to the research presented here, data needed to assess the thick target spectra of the reaction ^{9}Be(p,n) $E_p \leq 4.0$ MeV were not available in the literature. Therefore, these spectra were measured using time-of-flight techniques. A total of 28 neutron spectra were measured using four proton energies: 4.0, 3.7, 3.4 and 3.0 MeV. These data are useful, not only for the BNCT community, but also for the larger scientific community. The accuracy of the data has been confirmed, indirectly, through the measurement of a second neutron producing reaction.

Eight of these spectra were measured twice (November 1995 and August 1996). These repeated measurements show agreement of 20% or better over most of the neutron energy range. There is a significant disagreement between the repeated measurements at neutron energies below 250 keV. The disagreement accounts for less than 3% of the total neutron yield. Possible sources of this discrepancy were discussed, but not resolved. Previous results indicate that low energy neutrons (less than 100 keV) produced at the target do not significantly affect the efficacy of AB-BNCT since they are absorbed in the MSR before reaching the therapy port [1]. Therefore, these discrepancies would not significantly affect the results of this thesis.

The estimated total thick target yields of the reaction ^{9}Be(p,n), using proton bombarding energies of 4.0 and 3.7 MeV, were found to be approximately 20-25% lower than the yields based on the thin target excitation function [2] and stopping powers of protons in beryllium [3].

In Chapter III, Monte Carlo techniques were used to design therapy beams for each of the three reactions examined in Chapter II: ^{7}Li(p,n) E_p=2.5 MeV, ^{9}Be(d,n) E_d=2.6 MeV and ^{9}Be(p,n) E_p=4.0, 3.7, 3.4, and 3.0 MeV. Of these reactions, ^{7}Li(p,n) E_p=2.5 MeV is clearly the best neutron source when the reactions are compared on the basis of the neutron energy spectrum at the target. Although a lithium target capable of withstanding heat loads of 10 kW has not yet been designed, this obstacle may some day be removed. Designs based on the ^{9}Be(p,n) reaction produced less intense therapy beams

compared with ^{7}Li(p,n)-based designs. However, high current targets made of beryllium will be much easier to design and fabricate. A comparison of the dose rates from three therapy beam designs is given in Table V-1 below. Results using the reaction ^{9}Be(d,n) were disappointing. The average neutron energy of this reaction is sufficiently high to require extensive moderation. The added volume of moderator reduces the epithermal neutron flux available at the therapy port, and results in a low total tumor dose rate.

Contaminant photon radiation would be produced at the neutron producing target for each of these reactions. There are few data in the literature concerning the photon production which results from the deuteron bombardment of beryllium. The cross section for photon production reaches a maximum value of 10.1 ± 3.5 μb at E_d=0.96 MeV [4]. For the reaction ^{7}Li(p,n), the photon production is prolific but the photon energy is low (478 keV), and can be easily shielded. For the reaction ^{9}Be(p,n) the photon production is prolific, and the photon is energetic (3.562 MeV). The photons from proton bombardment of beryllium must be carefully considered during therapy beam design. When using a D_2O moderator, the photon dose which results from photons produced at the beryllium target can be approximately equal to the photon dose which results from all neutron capture reactions.

An important result for AB-BNCT was the demonstration in Chapter III that the reaction ^{9}Be(p,n) could be used as a neutron source with proton energies at or below 4.0 MeV. When compared on the basis of equal accelerator current, the total tumor dose

rates were approximately equal for the best results using 3.7 or 4.0 MeV protons. When compared on the basis of equal accelerator current, the design based on 3.7 MeV protons was superior. This research indicates that even lower proton bombarding energies might yield sufficiently high dose rates. If lower proton energies are used, this might significantly reduce the performance requirements of the accelerator and target systems.

The location of the target relative to the moderator and therapy port also is a significant factor for therapy beam design. The variation of total tumor dose with target position was studied using one MSR configuration. For this configuration, the total tumor dose at a depth of 2 cm varied by a factor of three when the target position was moved incrementally over an 8 cm distance.

The time required to produce total tumor doses of 15 RBE-Gy at depths of 2, 4, and 6 cm was presented in Chapter III. These results are repeated in Table V-1 below. The therapy times are based on a ^{10}B concentration in tumor of 30 ppm and an accelerator power of 10 kW. The RBE values used were: 4.1 ($^{10}B(n,\alpha)$ reaction), 4.0 (fast and thermal neutrons) and 1.0 photons. The current clinical trials should provide a better understanding of the doses needed for therapeutic efficacy. These results can easily be scaled to higher or lower tumor doses.

Therapy beam configuration	Time required to deliver a tumor dose of 15 RBE-Gy to a depth of 2 cm [min]	Time required to deliver a tumor dose of 15 RBE-Gy to a depth of 4 cm [min]	Time required to deliver a tumor dose of 15 RBE-Gy to a depth of 6 cm [min]
li-22x10g-d	12	15	25
3.7-25x10g-d	31	39	70
4.0-27x10g-d (A=+5)	27	35	60

Table V-1: Time required to deliver 15 RBE-Gy to tumor depths of 2, 4, and 6 cm.

Verification of the Monte Carlo simulation results was conducted using dual ionization chamber and activation foil techniques. The agreement between simulation and experimental results varied from 2% to 48% depending on the dose component and measurement location. In all cases, the measured values (which were not normalized) agreed within a factor of two with the simulation results. This agreement is encouraging since this is the first use of these dosimetry techniques by the LABA group, but will not be sufficient for future work. Some suggestions to improve these dosimetry techniques were presented.

In Chapter IV, the shielding of the patient and research staff was investigated using Monte Carlo techniques. The LABA facility was used as a model. The use of an unshielded MSR (moderator and reflector only) resulted in dose rates at locations surrounding the laboratory which exceeded the occupational limits. Most of this dose rate is attributed to (n,γ) reactions in the facility walls. When a shielded MSR was used, the highest photon dose rate at a location outside the LABA vault dropped significantly (from 20 mrem/hr-mA using the unshielded MSR to 2.6 mrem/hr-mA using the shielded

MSR). When the shielded MSR was surrounded by an additional shielding layer made of water and boric acid, this dose rate dropped further to 0.9 mrem/hr-mA.

A simple patient shielding design was investigated. Using a shield similar to a neck brace, dose rates in the upper torso were examined. A shield made of a 50/50 mixture of lithium carbonate and polyethylene yielded the best results. This shielding material reduced the photon dose rate by 63% and the neutron dose rate by as much as 87%.

V.B Conclusions

There are three conditions under which AB-BNCT will be a viable cancer therapy.

- First, the efficacy of BNCT as a cancer therapy modality must be clearly demonstrated in clinical trials. Initial results of the current US clinical trials are encouraging in this respect. These trials should result in a better understanding of the doses required for tumor control or eradication.
- Second, a high current target must be developed and tested to ensure that it can reliably withstand heat loads of approximately 10 kW. The design of high current lithium targets will be especially challenging. Since target failure might cause extensive damage to the accelerator system, a comfortable margin of error should be considered when investigating the heat removal capacity of the target assembly. The

design of high current targets for BNCT was addressed in Chapter I, and research in this area is underway at LABA.

- Third, the production of reliable and sustainable high-current ion beams must be demonstrated at ion energies which are useful for AB-BNCT. The reliable production of high current ion beams is, perhaps, the greatest challenge facing AB-BNCT. One research objective at LABA is to steadily increase the ion beam energy and current produced by the accelerator located at the laboratory.

If these conditions are met, this research indicates that a total tumor dose of 15 RBE-Gy can be delivered to depths up to 6 cm in less than an hour using therapy beam designs based on the ^{7}Li(p,n) or ^{9}Be(p,n) reactions, and an accelerator power of 10 kW. This research also demonstrates that radiation shielding designs for the patient and facility, which are effective, inexpensive and practical, can be achieved.

REFERENCES

1. Howard, W.B., *et al.*, *Measurement of the 9Be(p,n) thick target spectrum for use in accelerator-based Boron Neutron Capture Therapy.* Medical Physics, 1996. **23**(7): p. 1233-1235.
2. Gibbons, J.H. and R.L. Macklin, *Total neutron yields from light elements under proton and alpha bombardment.* Physical Review, 1959. **114**(2): p. 571-580.
3. Ziegler, J.F., *TRIM-95*, . 1995, IBM: Yorktown, NY.
4. Ajzenberg-Selove, F., *Energy levels of light nuclei A=11-12.* Nuclear Physics, 1990. **506**(1): p. 1-158.

APPENDIX A

Operation of the LABA Accelerator

The accelerator at LABA is a tandem electrostatic linear accelerator capable of accelerating protons and deuterons. The accelerator is designed for a maximum terminal voltage of 2.05 MV and a maximum power of 10 kW. The accelerator was designed by Newton Scientific Incorporated, Cambridge, MA. A picture of the accelerator is shown in Figure A-1. The complete system weighs approximately 1000 kg and measures 3.9 meters from the ion source to the high energy end of the pressure vessel. The largest diameter is 0.94 m. The entire outside surface of the accelerator is at ground potential. A cut-away drawing of the accelerator, with the major components labeled, is shown in Figure A-2.

A thorough description of the accelerator can be accomplished by dividing the system into components, and treating each separately. The systems to be described are: ion source and extraction system, injector, high voltage generation, accelerating column, and stripping foils. Also included is a description of a prototype high current beryllium target which is currently being tested at LABA, and an update on the accelerator performance to date. For the following discussion, a proton beam is assumed.

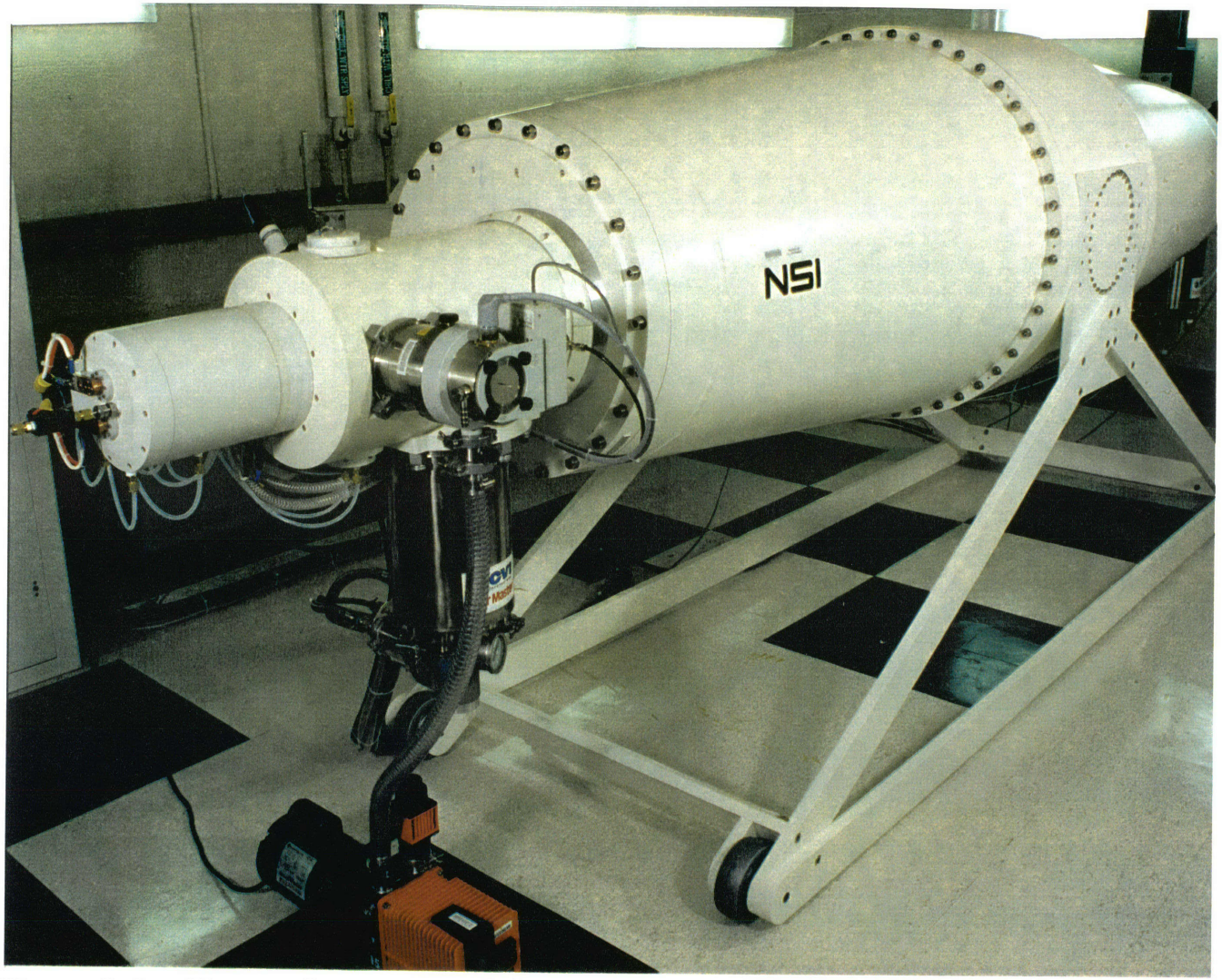

Figure A-1: The accelerator at LABA.

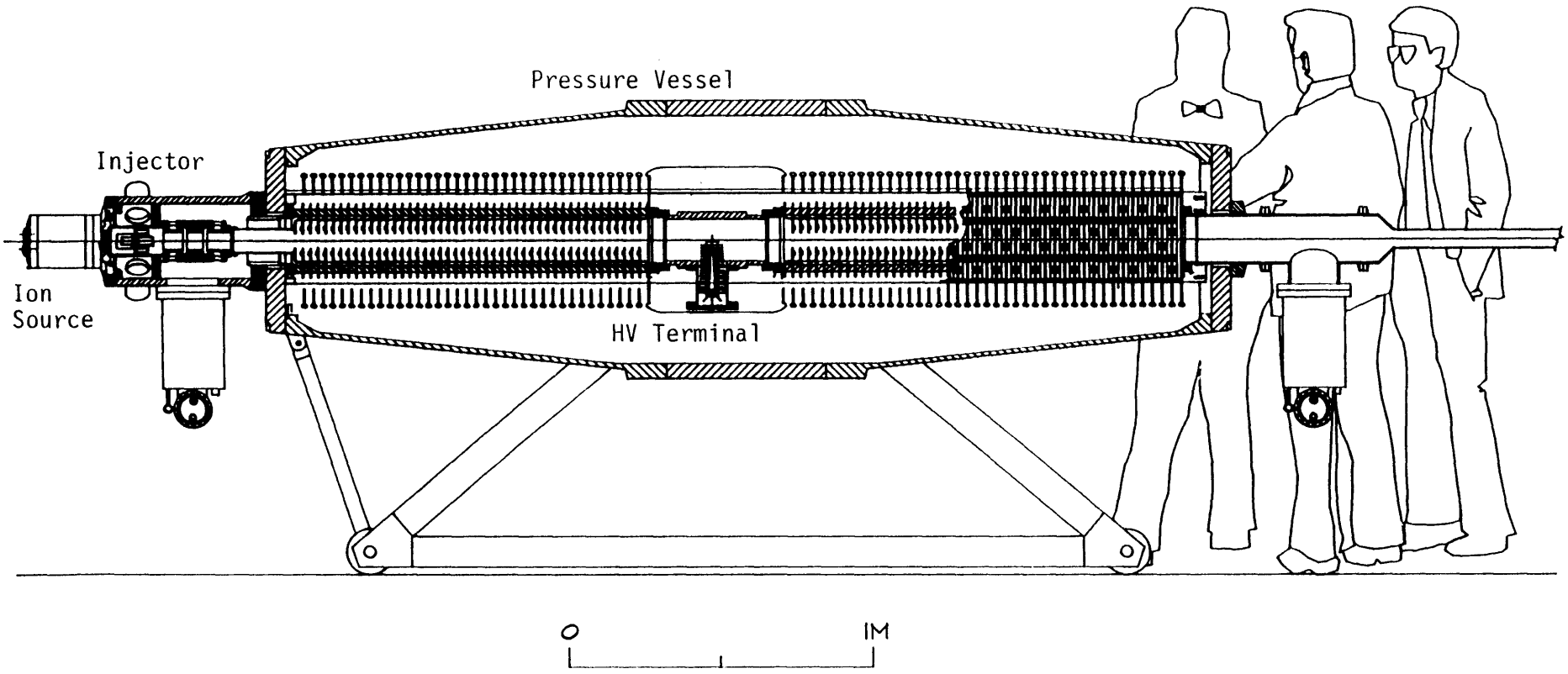

Figure A-2: Cut away drawing of the LABA accelerator.

A.1 Ion source

The purpose of the ion source is to produce a high current beam of H- ions, with low electron contamination. Two main types of H- ion sources exist: surface-production sources and volume-production sources. The ion source used on the LABA accelerator is a volume production multicusp type in which H- ions are produced through the process of dissociative attachment. A simplified drawing of the ion source is shown in Figure A-3. Volume-production sources have lower emittance and do not require cesium, but have the disadvantages of higher source gas pressure and electron contamination [1]. During the 1980s, multi-cusp ion sources based on volume-production techniques were developed [2-4]. Control of electron currents is accomplished through the use of electron suppression magnets and traps [3].

Electrons are introduced to the ion source volume when they are boiled off the cathode. The anode (inner surface of the ion source) is held at a potential of 100 volts relative to the cathode. Hydrogen enters the ion source in the form of H_2 gas. Excited rotational and vibrational states are formed when fast electrons collide with the H_2 molecules, or when these molecules strike the walls of the ion source. The H- ions are created in a process known as dissociative attachment (DA). This process can be written as[5]:$e + H_2(v'', J) > H_2^- > H^- + H$.

The notation $H_2(v'', J)$ means that the hydrogen gas molecule is in the vibrational state v'', and the rotational state J. It is assumed that the molecule is in the electronic

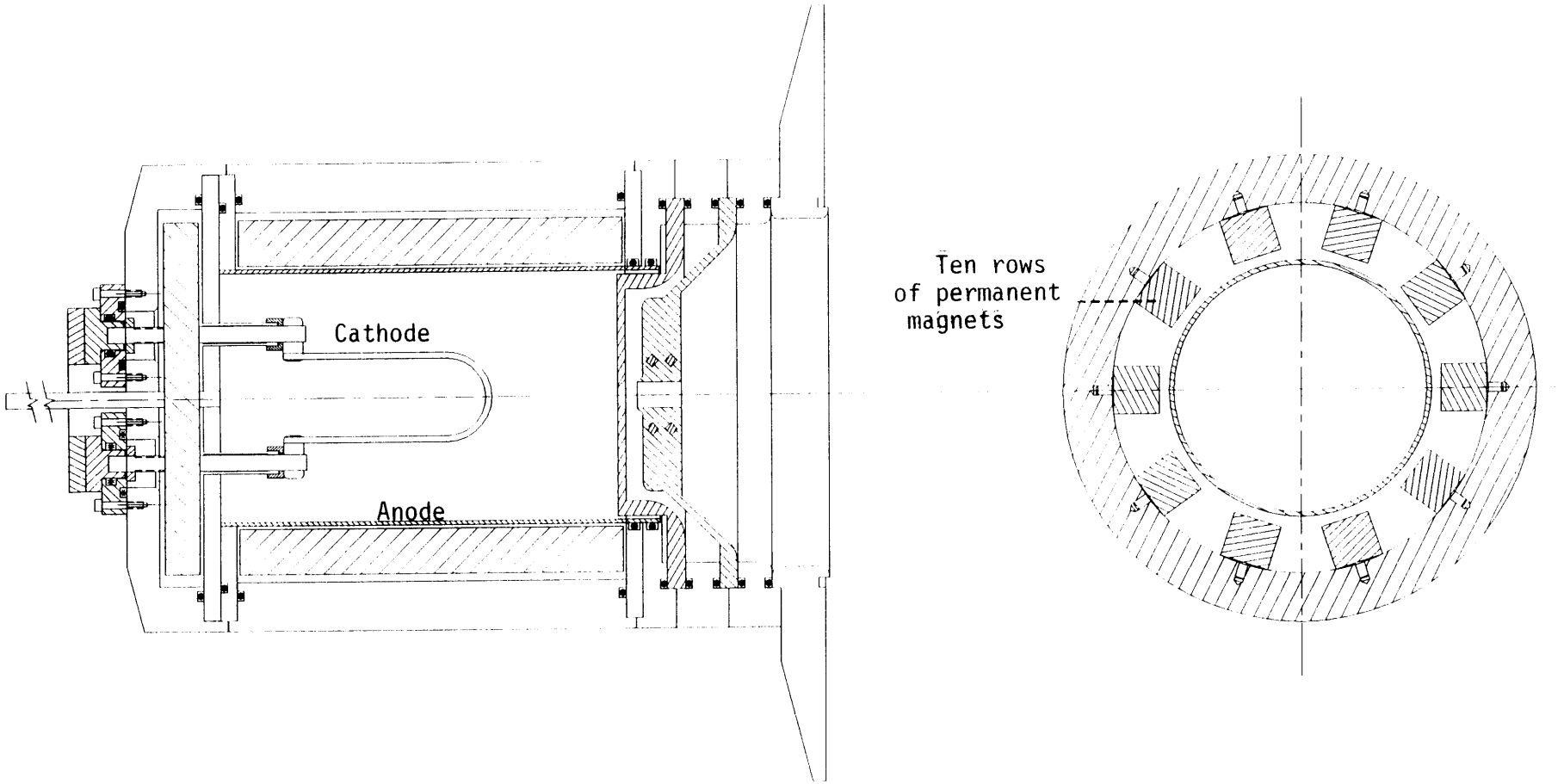

Figure A-3: The LABA accelerator ion source.

ground state. Calculations have shown that the cross section for DA as a function of electron energy has the following characteristics: (a) for a given value of (v'', J), the cross section peaks at threshold, and then decreases monotonically as electron energy increases (b) for a given electron energy, the cross section is enhanced if the molecule is initially in an excited state (i.e. v'', J, not both 0) (c) for a given internal energy determined by (v'', J), the vibrational excitation, v'', is more important in enhancing the cross section than rotational excitation [5].

The ion chamber is divided by a magnetic filter into two volumes, the "source chamber", and the "extraction chamber" [2]. This separation of the two volumes is needed to allow two processes (the induction of excited vibrational states of hydrogen gas, and the dissociative attachment of electrons) to occur in the same system [3]. In this way, collisions between H- ions and fast electrons are suppressed. Such collisions would easily strip the extra electron which is bound by ≈ 0.75 eV. H- ions are extracted by an extraction electrode. The extraction of electron currents is reduced through the use of electron suppression magnets (100 G).

Ten rows of permanent magnets surround the inner surface of the ion source. Adjacent rows of magnets have opposite orientations. This creates a multi-cusp magnetic field. The cusps form "magnetic mirrors" which reflect many of the electrons and the plasma back into the ion source volume and prevent them from striking the anode. In this way the ion and electron densities remain generally uniform over the cross section of the

ion source. The confining magnetic field decreases the thermal load on the cathode and ion source, allowing for greater density and higher current production.

A.2 Injector

The purpose of the injector is two-fold: (1) to prepare the ion beam so that the beam envelope will slowly converge once it has entered the accelerating tube, (2) to minimize the distance between the ion source and the accelerating column so that expansion of the beam envelope due to space charge effects is minimized [6]. H- ions are extracted from the ion source at approximately 1-3 keV. Electrons are swept from the extracted beam by electron suppression magnets. Other ion species are filtered from the beam by two orthogonal (x-y) Wein filters, which are also used for steering. The Wein filters produce perpendicular electric and magnetic fields which can be adjusted to exactly cancel for the desired ion species. Before entering the accelerator, the beam energy is increased to 20 keV. The injector Einzel lens is designed to create an apparent source of ions at a distance d from the entrance to the accelerating tube. As ions enter the electric fields of the accelerator tube, they experience a strong focusing effect due to equipotential surfaces which extend from the first accelerating electrodes. This strong focusing occurs with a focal length of f. To create a slow convergence of the beam envelope in the first stage of the accelerator, the source length, d, is made slightly larger than f [7].

A.3 High voltage generation

The purpose of the HV generation circuit is to deliver high current to the HV terminal at the center of the accelerator. A schematic diagram of the components is shown in Figure A-4. The HV generator is a cascade multiplier type, which is based on the original work of Cockcroft and Walton [8]. The design is unique in that it is the first accelerator to use a switching power supply which incorporates an integral series-fed cascade multiplier. The circuit consists of two basic components: (1) the switching converter, and (2) the cascade multiplying circuit (CMC). This design has a 'wall plug' power efficiency of greater than 90% [7].

The purpose of the converter is to produce, at high efficiency, a variable pulse-width power supply of 300 volts (peak) at a frequency of approximately 30 kHz, which will drive the cascade multiplier. The converter, which is rated at 12 kW, must function at high efficiency for reasons of economy and heat dissipation. At 95% efficiency, the driver would still need to dissipate 240 W of heat. To control the temperature of the unit, active water cooling is used. The converter is based on the use of emitter-follower transistor circuits [6].

As shown in Figure A-4, the converter is coupled to the CMC by a 1:100 transformer, which increases the voltage from the driver by a factor of 200. The CMC is mounted directly on the accelerating column, thereby reducing system size. The purpose of the CMC is to rectify the AC voltage from the converter to a DC voltage at the

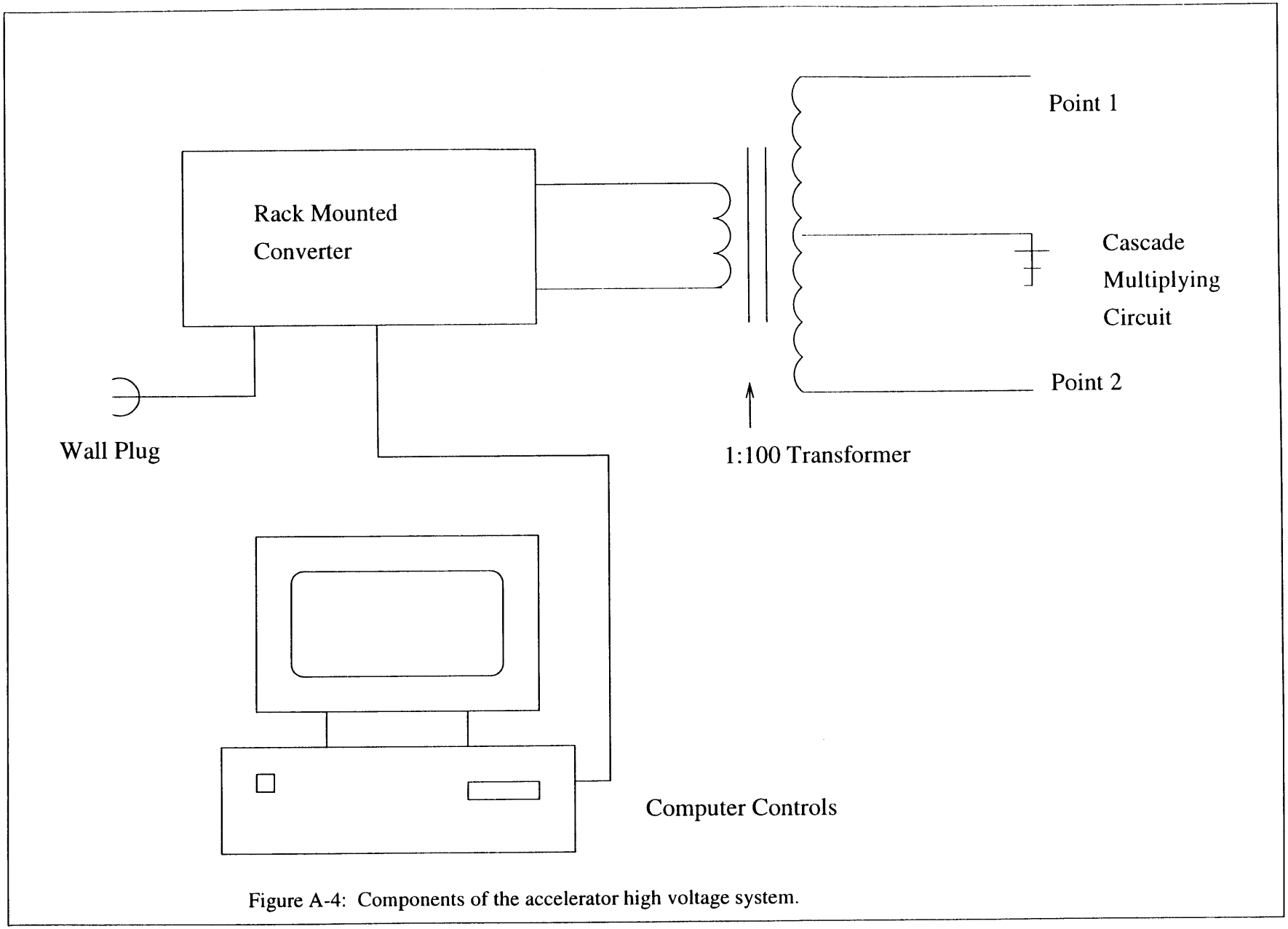

Figure A-4: Components of the accelerator high voltage system.

terminal. The operation of the CMC can best be explained by examining the charging circuit in detail. Figure A-5 shows a schematic drawing of the first few stages of the CMC.

The top 1/2 of the first stage is drawn in Figure A-6. Initially C_{11} and C_{01} are uncharged. As the converter voltage at Point 1 turns positive, Point 1 is biased positive with respect to ground. Thus, D_{11} acts as an open switch, and D_{01} as a closed switch. The equivalent circuit under these conditions is also shown in Figure A-6. These conditions cause C_{11} and C_{01} to charge.

As the driver voltage at Point 1 turns negative, D_{11} is now a closed switch, and D_{01} is an open switch. This condition, and the equivalent circuit is shown in Figure A-7. At this point, the current flow is from ground, through D_{11}, past Point A, to C_{11}. Since C_{01} is electrically isolated, it cannot discharge, so Point B maintains its voltage.

The result is an oscillating voltage at Point A, but an approximate DC voltage at Point B. As current is drawn by the load (in this case the HV terminal), capacitor C_{01} will discharge, and the voltage at Point B will drop until it is charged again during the positive voltage swing at Point 1. Adding the mirror bottom half of the CMC simply doubles the charging rate of the system (the capacitors labeled C_{0X} in Figure A-5 are charged twice as often). The result is that after a single stage, $V_B=2V_o$ DC, with a small ripple caused by the load. After 2 stages, $V_E=4V_o$ DC. In this way, after a sufficient number of stages, the

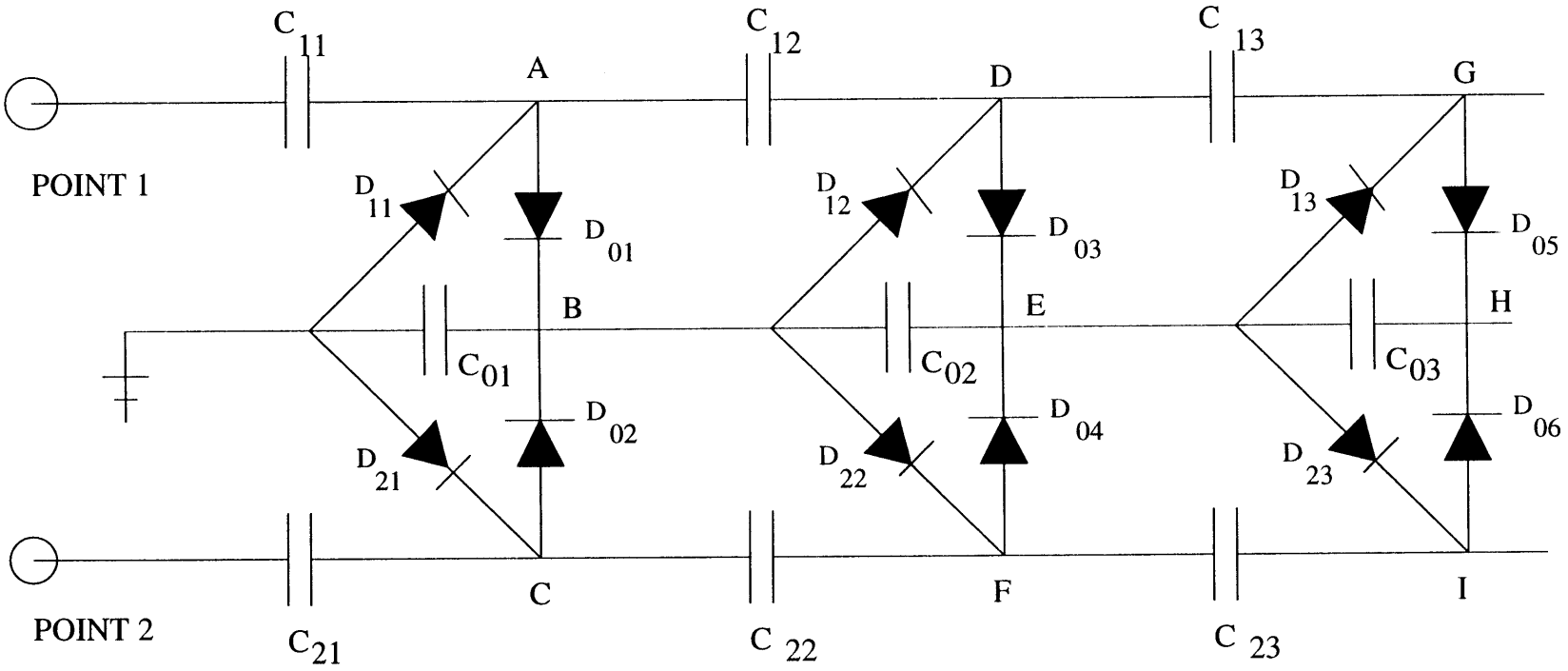

Figure A-5: Schematic drawing showing the first few stages of the CMC.

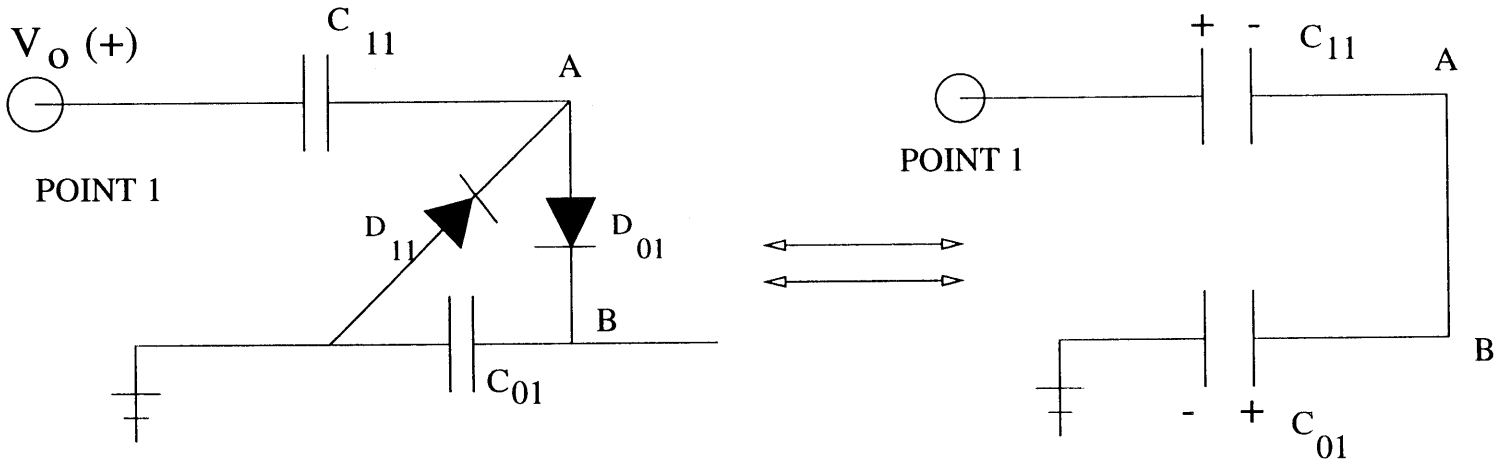

Figure A-6: First half cycle of the CMC operation

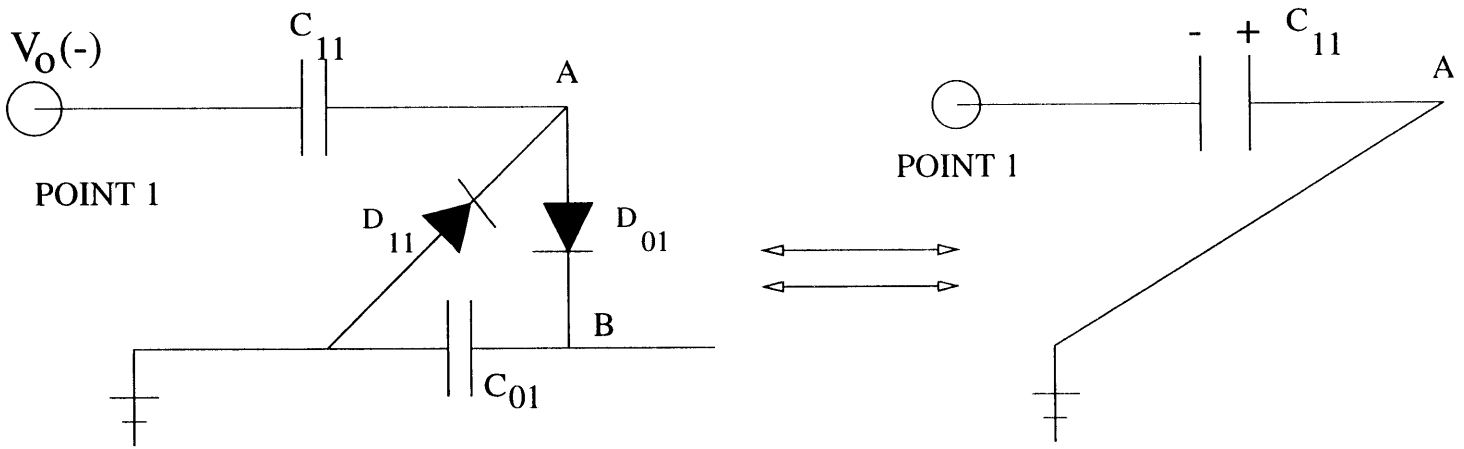

Figure A-7: Second half cycle of the CMC operation

HV is connected to the center of the CMC, and is charged. The high capacitance of the CMC and the high capacitance of the HV terminal guarantee that the voltage ripple on the terminal is very small (less than 0.5%) [6].

A.4 Accelerating column

The accelerating column consists of two stages, the low energy stage (from the injector to the HV terminal) and the high energy stage (from the HV terminal to the end of the accelerator). Both stages are made of a series of aluminum dished electrodes which are insulated from each other by glass rings. The accelerating tubes were manufactured by Vivirad High Voltage Corporation, Billerica, MA. The electrodes are dished to prevent secondary electrons from striking the glass insulators.

In many electrostatic accelerators, the electrodes are alternately tilted forward and backward to suppress the transport of secondary electrons. The suppression of secondary electrons is needed to prevent the creation of intense bremsstrahlung radiation. This radiation creates a radiation safety hazard, and can damage components of the accelerator. By tilting the electrodes, electrons are deflected out of the beam. The heavier ions, such as protons, are not sufficiency deflected, and as they pass through the next electrode (tilted opposite to the previous one) the net effect on their trajectory is negligible. In the LABA accelerator, the electrodes are not tilted. Electron suppression is accomplished instead by a series of samarium-cobalt magnets mounted in channels on each of the

electrodes. The electrons, due to a high q/m, are swept from the field, and the heavy ion species experience a negligible deflection.

The voltage existing on the HV terminal is distributed linearly along the accelerating column using 200 MΩ resistors. The low energy stage has 47 electrodes, and the high energy stage has 52. The low energy stage is on the left of Figure A-8, with the electrodes shown as a series of silver-colored plates along the axial center of the beam tube. The HV terminal is shown as a polished silver cylindrical shell in the middle of the photograph. The resultant electric field gradient is uniform in each stage. For a terminal voltage of 2.05 MV, the gradient in the low energy stage is 17.17 kV/cm and the gradient in the high energy stage is 15.52 kV/cm [9]. These field gradients are greater than can be supported by the dielectric strength of atmospheric pressure air, so the accelerating column is surrounded by approximately 100 psi of sulfer-hexaflouride (SF_6). This gas pressure is safely maintained by surrounding the accelerating column by an aluminum pressure vessel.

A.5 Stripping foils

Carbon stripping foils are mounted in a small bracket and attached to a carousel in the HV terminal. In this way, 80 stripping foils can be available for use. The 1.6 cm diameter stripping foils are very thin (5-10 $\mu g/cm^2$) and nearly 100% efficient at stripping the two electrons from the ion species. The stripping foils have limited lifetimes which

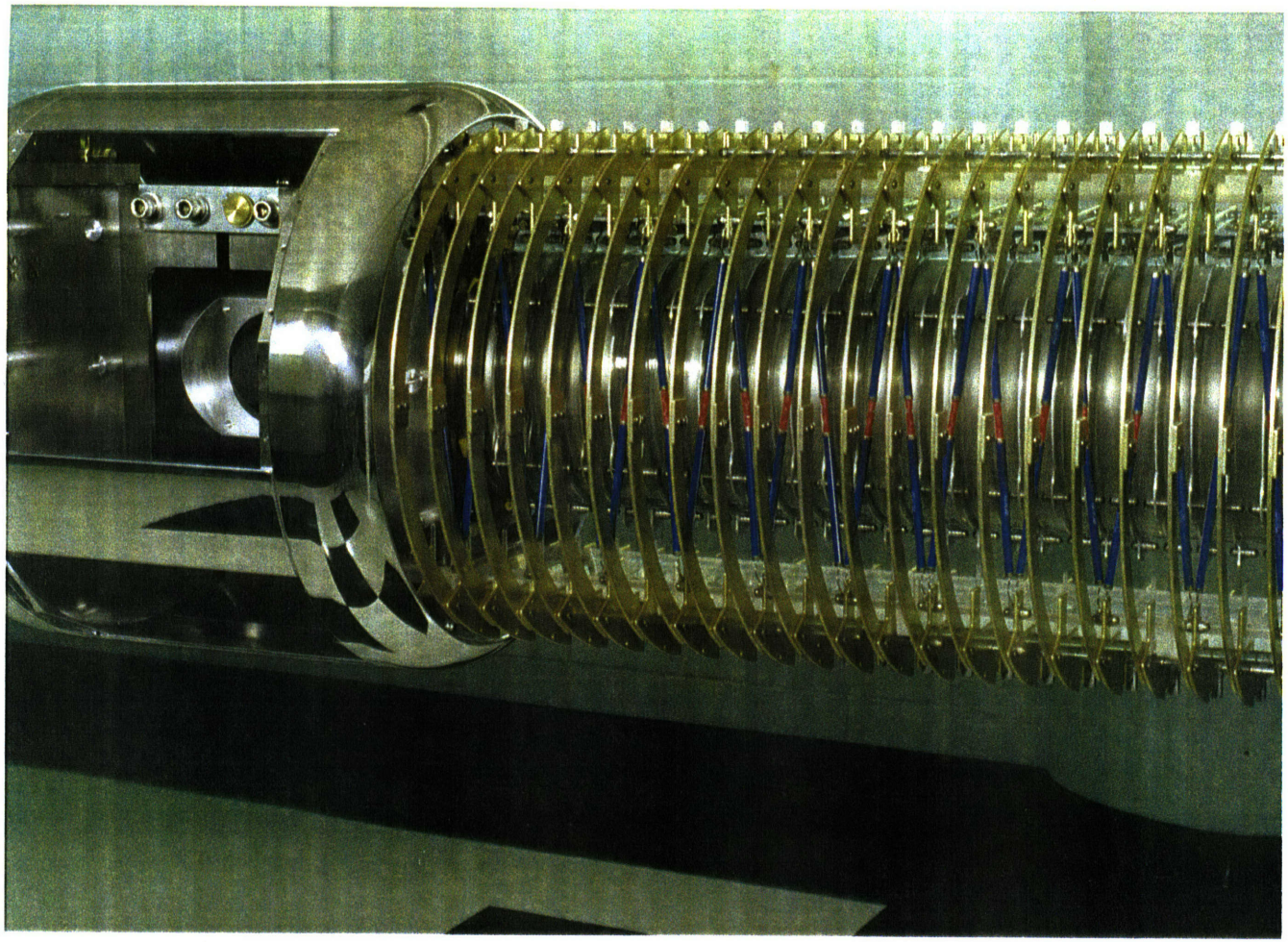

Figure A-8: Accelerating column removed from the pressure vessel.

are estimated to be approximately 100 mA-hours. As a new foil is needed, the carousel rotates a new foil into the active position [9].

A.6 Prototype high current beryllium target

As mentioned in Section I.B, targets used in the production of neutrons for AB-BNCT will need to withstand heat loads produced by the ion beam. Since the maximum power rating of the LABA accelerator is 10 kW, a prototype beryllium target was designed to test the possibility of removing heat loads of this magnitude. A picture of the prototype design is shown in Figure A-9. The target consists of a cube-shaped stainless steel housing which is 6.25 cm long on each side. The center of this cube has been removed, and a flange has been welded onto one side for connection to the evacuated beam line. A 0.254 cm thick, 4.445 cm diameter, 99% pure beryllium target is brazed into the housing. Two thermocouples have been attached to the back side of the target so that target temperature can be monitored at the center and edge of the target. The back of the target housing is removable, and made to accommodate a large diameter water supply.

Development and testing of the cooling system is currently underway at LABA. The target will be cooled by a submerged jet supplying chilled water at a rate of 10 l/min. Theoretical calculations and initial tests indicate that power greater than 10 kW can be removed by the system. The initial tests were conducted with a second prototype which is similar to the first in all aspects except that an aluminum target was used in place of the beryllium[10]. The thermal properties of aluminum are similar to beryllium.

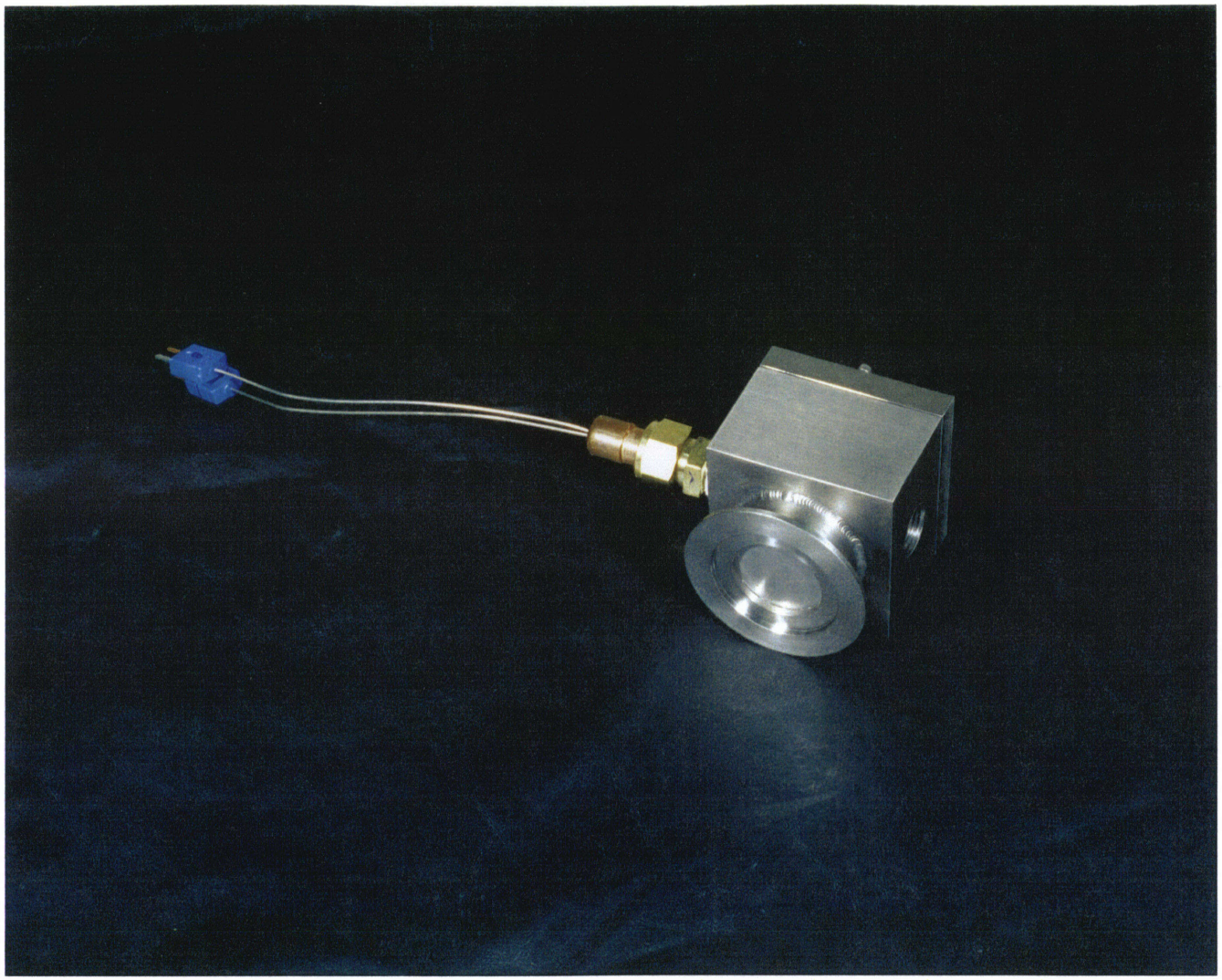

Figure A-9: Prototype high current beryllium target.

A.7 Accelerator performance to date

The accelerator has been operated, for limited duration, at a maximum continuous proton beam current of 0.8 mA at an energy of 2 MeV. The accelerator has been run routinely with deuteron beam currents up to 50 μA at a beam energy of 2.6 MeV. The ion source current has been as high as 5 mA. The current research program aims to increase both the terminal voltage and the current in a systematic way, and to evaluate the performance of all accelerator systems.

REFERENCES

1. Leung, K.N., *et al.*, *Optimization of H- production from a small multicusp ion souce.* Review of Scientific Instruments, 1989. **60**(4): p. 531-538.
2. Leung, K.N., K.W. Ehners, and M. Bacal, *Extraction of volume-produced H- ions from a multicust source.* Review of Scientific Instruments, 1983. **54**(1): p. 56-61.
3. Holmes, A.J.T., G. Dammertz, and T.S. Green, *H- and electron production in a magnetic multiple source.* Review of Scientific Instruments, 1985. **56**(9): p. 1697-1702.
4. Kendall, K.R., *et al.*, *Measurement on a dc volume H- multicust ion source for TRIUMF.* Review of Scientific Instruments, 1986. **57**(7): p. 1277-1281.
5. Wadehra, J.M., *Dissociative attachment to rovibrationally excited H_2.* Physical Review A, 1984. **29**(1): p. 106-110.
6. Klinkowstein, R., *Personal communication - accelerator design*, . 1995.
7. Shefer, R.E., *et al. Tandem electrostatic accelerators for BNCT.* in *First international workshop on accelerator-based neutron sources for boron neutron capture therapy, INEL Conference 940976.* 1994. Jackson Hole, WY.
8. Cockcroft, J.D. and T.S. Walton, Proc. Royal Society, 1932. **A136**: p. 619.

9. Shefer, R. and R. Klinkowstein. *A high current electrostatic accelerator for boron neutron capture therapy.* in *Fifth international conference on applications of nuclear techniques*. 1996. Crete, Greece: SPIE - to be published.

10. Blackburn, B.W., *et al.*, *Development of a high-power, water-cooled beryllium target for the production of neutrons in a high-current tandem accelerator.* Nuclear Instruments and Methods - To Be Published, 1996.

APPENDIX B

Neutron Spectra from the ^{9}Be(p,n) Reaction

This appendix contains the measured neutron spectra of the reaction ^{9}Be(p,n). These measurements were described in Section II.C of this thesis. Tables B-1 through B-8 contain the numerical data in tabular form. There are two sets of data (referred to as Group A and Group B in Section II.C). The first set was acquired in November 1995 and the second set was acquired in August 1996. There is a separate table for each acquisition date and proton bombarding energy. For example, Table B-1 contains the data from the November 1995 measurements using 4.0 MeV protons. The acquisition dates and proton energies are listed in the heading of the tables. The data for each neutron spectrum is given as a series of yields with associated total statistical errors. The data points represent the yield of a particular energy bin. The energy at the center of this bin is provided. The bin widths are 20 keV up to a neutron energy of 700 keV and are 50 keV for neutron energies above 700 keV. For example, the energy bin centered at 690 keV represents all neutrons with energies from 680 - 700 keV. The energy bin centered at 725 keV represents all neutrons with energies from 700 - 750 keV. The units of the neutron

spectra are neutrons/(MeV-steradian-microCoulomb). Graphs of each of the spectra follow the tables. Each of the graphs is labeled with the acquisition date, proton bombarding energy, and laboratory angle.

Table B-1: Neutron energy spectra from the reaction 9Be(p,n) E(p)=4.0 MeV
Measured November 1995

Units of spectra are: neutrons/(MeV-steradian-microcoulomb)

Energy at Center of Bin [keV]	0 degree spectrum	0 degree % statistical error	20 degree spectrum	20 degree % statistical error	40 degree spectrum	40 degree % statistical error
70	3.22E+07	8.31%	2.54E+07	11.40%	2.90E+07	7.72%
90	6.72E+07	5.47%	5.63E+07	6.94%	6.28E+07	4.96%
110	8.69E+07	4.30%	7.62E+07	5.11%	8.16E+07	3.92%
130	8.50E+07	3.98%	7.65E+07	4.59%	8.43E+07	3.52%
150	7.56E+07	3.79%	7.84E+07	3.93%	8.01E+07	3.25%
170	7.67E+07	3.13%	7.70E+07	3.27%	7.93E+07	2.80%
190	6.42E+07	2.86%	6.44E+07	2.96%	6.69E+07	2.60%
210	6.23E+07	2.60%	6.33E+07	2.64%	6.52E+07	2.41%
230	6.45E+07	2.45%	6.74E+07	2.46%	6.76E+07	2.31%
250	6.30E+07	2.44%	6.48E+07	2.45%	6.57E+07	2.30%
270	6.03E+07	2.49%	6.23E+07	2.51%	6.17E+07	2.35%
290	6.26E+07	2.55%	6.51E+07	2.56%	6.45E+07	2.39%
310	7.09E+07	2.57%	7.04E+07	2.61%	6.76E+07	2.44%
330	7.30E+07	2.62%	7.33E+07	2.67%	7.04E+07	
350	7.22E+07	2.68%	7.11E+07	2.75%	6.91E+07	[illegible]
370	8.07E+07	2.68%	7.79E+07	2.76%	7.39E+07	2.55%
390	7.71E+07	2.77%	7.54E+07	2.85%	7.35E+07	2.60%
410	7.97E+07	2.78%	7.59E+07	2.88%	7.27E+07	2.64%
430	7.46E+07	2.90%	7.52E+07	2.95%	6.92E+07	2.72%
450	7.47E+07	2.99%	7.03E+07	3.13%	6.69E+07	2.83%
470	7.75E+07	3.06%	7.48E+07	3.19%	6.97E+07	2.89%
490	7.45E+07	3.24%	7.13E+07	3.39%	7.11E+07	2.97%
510	9.03E+07	3.13%	8.08E+07	3.37%	7.92E+07	2.98%
530	9.40E+07	3.23%	9.12E+07	3.36%	8.34E+07	3.04%
550	1.01E+08	3.27%	9.71E+07	3.42%	8.94E+07	3.09%
570	1.04E+08	3.35%	9.73E+07	3.56%	8.17E+07	3.33%
590	9.98E+07	3.54%	1.02E+08	3.61%	7.91E+07	3.50%
610	1.08E+08	3.54%	9.59E+07	3.88%	8.06E+07	3.60%
630	8.52E+07	4.03%	8.31E+07	4.24%	7.13E+07	3.87%
650	8.43E+07	4.15%	8.60E+07	4.26%	8.28E+07	3.67%
670	8.38E+07	4.25%	8.49E+07	4.39%	7.79E+07	3.86%
690	7.51E+07	4.53%	7.31E+07	4.80%	7.80E+07	3.87%
725	7.59E+07	3.26%	7.52E+07	3.39%	7.43E+07	2.96%
775	7.27E+07	3.35%	7.17E+07	3.48%	7.02E+07	3.05%
825	7.16E+07	3.40%	7.37E+07	3.47%	6.83E+07	3.11%
875	7.04E+07	3.42%	6.96E+07	3.55%	6.92E+07	3.08%
925	6.72E+07	3.43%	6.40E+07	3.63%	6.94E+07	3.03%
975	6.22E+07	3.52%	6.09E+07	3.68%	5.97E+07	3.20%
1025	5.09E+07	3.85%	5.30E+07	3.90%	5.58E+07	3.26%
1075	5.36E+07	3.77%	5.34E+07	3.92%	5.67E+07	3.26%

CONTINUED ON NEXT PAGE

Table B-1: Neutron energy spectra from the reaction 9Be(p,n) E(p)=4.0 MeV
Measured November 1995

Units of spectra are: neutrons/(MeV-steradian-microcoulomb)

Energy at Center of Bin [keV]	0 degree spectrum	0 degree % statistical error	20 degree spectrum	20 degree % statistical error	40 degree spectrum	40 degree % statistical error
1125	4.81E+07	3.94%	5.20E+07	3.91%	5.18E+07	3.36%
1175	5.14E+07	3.84%	4.82E+07	4.12%	5.25E+07	3.36%
1225	5.28E+07	3.79%	4.90E+07	4.07%	5.51E+07	3.29%
1275	4.43E+07	4.12%	4.59E+07	4.19%	4.78E+07	3.49%
1325	4.36E+07	4.13%	4.16E+07	4.39%	4.49E+07	3.57%
1375	4.77E+07	3.97%	4.53E+07	4.22%	4.60E+07	3.56%
1425	4.47E+07	4.06%	4.42E+07	4.23%	4.52E+07	3.55%
1475	5.06E+07	3.84%	4.62E+07	4.15%	4.41E+07	3.61%
1525	4.62E+07	3.97%	4.61E+07	4.09%	4.10E+07	3.69%
1575	5.39E+07	3.69%	4.86E+07	3.98%	4.03E+07	3.72%
1625	4.86E+07	3.81%	4.80E+07	3.94%	3.50E+07	3.92%
1675	5.24E+07	3.67%	5.13E+07	3.80%	3.61E+07	3.85%
1725	6.42E+07	3.36%	5.68E+07	3.61%	3.73E+07	3.77%
1775	6.17E+07	3.37%	5.10E+07	3.72%	3.03E+07	4.09%
1825	6.26E+07	3.33%	4.90E+07	3.76%	1.91E+07	5.26%
1875	6.36E+07	3.29%	4.85E+07	3.76%	5.32E+06	13.60%
1925	5.52E+07	3.42%	3.63E+07	4.22%	2.45E+06	25.10%
1975	4.64E+07	3.69%	1.45E+07	7.58%	1.95E+06	32.40%
2025	1.47E+07	6.77%	3.82E+06	21.30%		
2075	8.04E+06	9.83%	4.46E+06	17.00%		
2125	4.32E+06	16.90%	1.58E+06	46.50%		
2175	1.92E+06	31.60%	1.23E+06	53.20%		
2225	6.61E+05	92.60%				

Table B-1: Neutron energy spectra from the reaction 9Be(p,n) E(p)=4.0 MeV
Measured November 1995

Units of spectra are: neutrons/(MeV-steradian-microcoulomb)

Energy at Center of Bin [keV]	60 degree spectrum	60 degree % statistical error	80 degree spectrum	80 degree % statistical error	110 degree spectrum	110 degree % statistical error
70	3.09E+07	6.86%	1.52E+07	12.40%	2.73E+07	7.56%
90	6.89E+07	4.38%	4.04E+07	6.38%	6.13E+07	4.72%
110	8.21E+07	3.73%	5.75E+07	4.57%	7.49E+07	3.92%
130	8.42E+07	3.39%	5.74E+07	4.15%	7.09E+07	3.72%
150	8.18E+07	3.11%	5.46E+07	3.77%	6.93E+07	3.36%
170	7.91E+07	2.74%	5.63E+07	3.08%	6.21E+07	3.00%
190	6.95E+07	2.53%	4.72E+07	2.82%	5.31E+07	2.73%
210	6.52E+07	2.38%	4.48E+07	2.57%	5.11E+07	2.50%
230	6.64E+07	2.29%	4.75E+07	2.42%	5.37E+07	2.37%
250	6.38E+07	2.29%	4.75E+07	2.39%	5.15E+07	2.37%
270	5.63E+07	2.36%	3.82E+07	2.55%	5.01E+07	2.41%
290	6.02E+07	2.39%	4.06E+07	2.59%	5.34E+07	2.44%
310	6.36E+07	2.44%	4.48E+07	2.63%	5.29E+07	2.53%
330	6.36E+07	2.50%	4.85E+07	2.65%	5.03E+07	2.65%
350	6.07E+07	2.57%	4.65E+07	2.74%	4.92E+07	2.72%
370	6.85E+07	2.57%	5.14E+07	2.75%	5.22E+07	2.76%
390	7.04E+07	2.59%	5.01E+07	2.83%	5.25E+07	2.81%
410	6.81E+07	2.65%	4.53E+07	2.98%	5.22E+07	2.86%
430	6.67E+07	2.71%	4.11E+07	3.16%	4.96E+07	2.97%
450	6.46E+07	2.81%	3.86E+07	3.38%	4.88E+07	3.09%
470	6.22E+07	2.95%	3.74E+07	3.60%	5.08E+07	3.17%
490	6.02E+07	3.10%	3.74E+07	3.78%	5.04E+07	3.31%
510	6.18E+07	3.21%	4.11E+07	3.81%	5.56E+07	3.33%
530	6.17E+07	3.38%	4.15E+07	4.01%	6.01E+07	3.38%
550	6.44E+07	3.47%	4.61E+07	4.00%	6.33E+07	3.46%
570	6.45E+07	3.62%	4.86E+07	4.08%	6.94E+07	3.46%
590	6.51E+07	3.74%	5.14E+07	4.12%	7.66E+07	3.42%
610	6.77E+07	3.83%	5.93E+07	3.99%	8.07E+07	3.46%
630	6.21E+07	4.05%	5.71E+07	4.11%	7.27E+07	3.68%
650	7.17E+07	3.84%	5.90E+07	4.14%	8.11E+07	3.57%
670	7.29E+07	3.88%	6.38E+07	4.05%	8.57E+07	3.54%
690	7.30E+07	3.89%	5.99E+07	4.20%	8.55E+07	3.55%
725	7.51E+07	2.89%	6.07E+07	3.08%	8.68E+07	2.73%
775	7.62E+07	2.89%	6.31E+07	3.05%	8.58E+07	2.76%
825	7.55E+07	2.93%	6.60E+07	3.02%	9.01E+07	2.73%
875	7.77E+07	2.89%	6.89E+07	2.96%	9.04E+07	2.73%
925	7.39E+07	2.91%	6.65E+07	2.96%	9.10E+07	2.69%
975	6.62E+07	3.00%	6.06E+07	3.05%	8.36E+07	2.75%
1025	6.15E+07	3.07%	5.64E+07	3.11%	7.74E+07	2.81%
1075	6.27E+07	3.07%	5.61E+07	3.14%	7.88E+07	2.80%

CONTINUED ON NEXT PAGE

Table B-1: Neutron energy spectra from the reaction 9Be(p,n) E(p)=4.0 MeV
Measured November 1995

Units of spectra are: neutrons/(MeV-steradian-microcoulomb)

Energy at Center of Bin [keV]	60 degree spectrum	60 degree % statistical error	80 degree spectrum	80 degree % statistical error	110 degree spectrum	110 degree % statistical error
1125	6.03E+07	3.09%	5.41E+07	3.16%	7.37E+07	2.85%
1175	6.31E+07	3.06%	5.54E+07	3.15%	7.72E+07	2.82%
1225	6.19E+07	3.08%	5.32E+07	3.20%	7.16E+07	2.89%
1275	5.50E+07	3.22%	4.94E+07	3.29%	5.13E+07	3.27%
1325	5.05E+07	3.32%	4.43E+07	3.43%	1.14E+07	8.11%
1375	5.19E+07	3.30%	4.19E+07	3.54%	3.99E+06	20.20%
1425	4.55E+07	3.46%	3.88E+07	3.64%	2.35E+06	32.00%
1475	4.47E+07	3.50%	3.43E+07	3.87%	1.44E+06	51.60%
1525	3.94E+07	3.67%	1.41E+07	6.51%		
1575	3.86E+07	3.70%	2.74E+06	25.60%		
1625	3.09E+07	4.06%				
1675	1.88E+07	5.38%				
1725	4.28E+06	16.80%				
1775	2.03E+06	31.20%				
1825	1.63E+06	37.90%				
1875	1.54E+06	39.30%				

Table B-2: Neutron energy spectra from the reaction 9Be(p,n) E(p)=3.7 MeV
Measured November 1995

Units of spectra are: neutrons/(MeV-steradian-microcoulomb)

Energy at		0 degree		20 degree		40 degree
Center of Bin	0 degree	% statistical	20 degree	% statistical	40 degree	% statistical
[keV]	spectrum	error	spectrum	error	spectrum	error
70	1.37E+07	15.10%	2.20E+07	9.47%	1.57E+07	12.70%
90	4.22E+07	6.74%	5.13E+07	5.58%	4.35E+07	6.34%
110	4.57E+07	5.94%	6.55E+07	4.39%	5.21E+07	5.18%
130	5.01E+07	4.91%	5.75E+07	4.36%	5.10E+07	4.72%
150	4.13E+07	4.88%	5.29E+07	4.02%	5.39E+07	3.95%
170	4.21E+07	3.79%	5.03E+07	3.37%	5.19E+07	3.30%
190	3.46E+07	3.37%	4.17E+07	3.04%	4.37E+07	2.97%
210	3.41E+07	2.90%	4.00E+07	2.71%	4.10E+07	2.68%
230	3.51E+07	2.66%	4.32E+07	2.50%	4.48E+07	2.47%
250	3.52E+07	2.61%	4.15E+07	2.49%	4.12E+07	2.49%
270	3.39E+07	2.68%	3.90E+07	2.56%	3.78E+07	2.58%
290	3.58E+07	2.74%	4.15E+07	2.61%	4.12E+07	2.61%
310	3.92E+07	2.79%	4.46E+07	2.67%	4.38E+07	2.68%
330	4.18E+07	2.83%	4.84E+07	2.69%	4.57E+07	2.74%
350	4.01E+07	2.94%	4.87E+07	2.74%	4.56E+07	2.79%
370	4.53E+07	2.93%	5.14E+07	2.79%	4.98E+07	2.81%
390	4.84E+07	2.92%	5.24E+07	2.83%	4.89E+07	2.89%
410	5.01E+07	2.92%	5.40E+07	2.84%	5.03E+07	2.90%
430	4.86E+07	3.02%	5.23E+07	2.93%	5.11E+07	2.95%
450	4.91E+07	3.11%	5.21E+07	3.03%	4.96E+07	3.08%
470	5.14E+07	3.18%	5.42E+07	3.10%	5.26E+07	3.13%
490	4.62E+07	3.50%	5.72E+07	3.16%	5.71E+07	3.15%
510	5.61E+07	3.35%	6.31E+07	3.17%	6.47E+07	3.13%
530	6.01E+07	3.42%	6.71E+07	3.24%	7.11E+07	3.15%
550	6.54E+07	3.45%	7.38E+07	3.25%	6.80E+07	3.36%
570	7.23E+07	3.43%	8.02E+07	3.26%	6.97E+07	3.47%
590	7.23E+07	3.55%	7.96E+07	3.38%	6.33E+07	3.77%
610	6.86E+07	3.80%	7.83E+07	3.54%	6.38E+07	3.92%
630	5.75E+07	4.23%	6.51E+07	3.93%	5.65E+07	4.24%
650	5.82E+07	4.32%	6.64E+07	3.98%	6.22E+07	4.11%
670	6.14E+07	4.28%	6.81E+07	4.01%	6.69E+07	4.04%
690	5.63E+07	4.51%	6.05E+07	4.29%	6.41E+07	4.14%
725	5.38E+07	3.33%	6.35E+07	3.08%	6.25E+07	3.09%
775	4.63E+07	3.61%	5.57E+07	3.28%	6.20E+07	3.12%
825	4.92E+07	3.53%	5.89E+07	3.22%	6.39E+07	3.11%
875	4.68E+07	3.60%	5.74E+07	3.25%	6.13E+07	3.15%
925	4.67E+07	3.53%	5.67E+07	3.21%	5.96E+07	3.13%
975	4.13E+07	3.71%	4.97E+07	3.37%	5.42E+07	3.23%
1025	3.99E+07	3.73%	4.64E+07	3.44%	4.85E+07	3.37%
1075	3.88E+07	3.81%	4.62E+07	3.47%	5.09E+07	3.31%

CONTINUED ON NEXT PAGE

Table B-2: Neutron energy spectra from the reaction 9Be(p,n) E(p)=3.7 MeV
Measured November 1995

Units of spectra are: neutrons/(MeV-steradian-microcoulomb)

Energy at Center of Bin [keV]	0 degree spectrum	0 degree % statistical error	20 degree spectrum	20 degree % statistical error	40 degree spectrum	40 degree % statistical error
1125	3.65E+07	3.87%	4.22E+07	3.58%	4.69E+07	3.40%
1175	3.68E+07	3.89%	4.09E+07	3.67%	4.88E+07	3.37%
1225	3.86E+07	3.78%	4.00E+07	3.70%	4.87E+07	3.36%
1275	3.12E+07	4.23%	3.78E+07	3.79%	4.03E+07	3.66%
1325	3.14E+07	4.17%	3.68E+07	3.82%	3.99E+07	3.66%
1375	3.29E+07	4.09%	3.84E+07	3.75%	3.90E+07	3.72%
1425	2.98E+07	4.26%	3.70E+07	3.79%	3.71E+07	3.77%
1475	3.43E+07	3.97%	3.93E+07	3.69%	3.65E+07	3.82%
1525	3.17E+07	4.07%	3.68E+07	3.76%	2.61E+07	4.51%
1575	3.19E+07	4.07%	3.60E+07	3.81%	1.16E+07	7.82%
1625	3.16E+07	4.00%	2.87E+07	4.20%	8.47E+05	78.90%
1675	2.91E+07	4.17%	1.72E+07	5.69%	8.88E+05	74.90%
1725	1.23E+07	7.22%	8.48E+06	9.51%		
1775	6.86E+06	10.90%	5.40E+06	13.10%		
1825	6.01E+06	12.00%	5.02E+06	13.80%		
1875	4.44E+06	15.40%	3.68E+06	17.90%		
1925	2.73E+06	22.00%	2.30E+06	25.20%		
1975	2.96E+06	21.40%	1.83E+06	32.70%		
2025	1.13E+06	48.40%				

Table B-2: Neutron energy spectra from the reaction 9Be(p,n) E(p)=3.7 MeV
Measured November 1995

Units of spectra are: neutrons/(MeV-steradian-microcoulomb)

Energy at Center of Bin [keV]	60 degree spectrum	60 degree % statistical error	80 degree spectrum	80 degree % statistical error	110 degree spectrum	110 degree % statistical error
70	1.70E+07	10.60%	7.34E+06	24.50%	2.13E+07	9.09%
90	4.36E+07	5.74%	3.34E+07	7.43%	4.27E+07	6.12%
110	5.89E+07	4.34%	4.24E+07	5.73%	5.65E+07	4.65%
130	5.36E+07	4.21%	3.70E+07	5.70%	5.39E+07	4.35%
150	5.34E+07	3.72%	3.87E+07	4.71%	4.89E+07	4.06%
170	5.06E+07	3.18%	3.83E+07	3.77%	4.45E+07	3.49%
190	4.34E+07	2.87%	3.18E+07	3.34%	3.95E+07	3.04%
210	4.21E+07	2.60%	3.09E+07	2.91%	3.75E+07	2.73%
230	4.37E+07	2.45%	3.57E+07	2.58%	3.97E+07	2.53%
250	4.03E+07	2.46%	3.32E+07	2.59%	4.02E+07	2.48%
270	3.72E+07	2.55%	2.86E+07	2.76%	4.03E+07	2.52%
290	4.00E+07	2.59%	3.05E+07	2.82%	4.48E+07	2.53%
310	4.22E+07	2.65%	3.58E+07	2.80%	4.34E+07	2.66%
330	4.35E+07	2.72%	3.99E+07	2.80%	4.32E+07	2.75%
350	4.24E+07	2.80%	4.01E+07	2.86%	4.21E+07	2.84%
370	5.00E+07	2.75%	4.74E+07	2.80%	4.56E+07	2.86%
390	5.11E+07	2.79%	4.31E+07	2.96%	4.42E+07	2.97%
410	5.47E+07	2.76%	4.06E+07	3.08%	4.56E+07	2.97%
430	5.30E+07	2.84%	3.66E+07	3.29%	4.43E+07	3.07%
450	5.49E+07	2.89%	3.46E+07	3.52%	4.40E+07	3.19%
470	5.65E+07	2.97%	3.61E+07	3.63%	4.51E+07	3.30%
490	4.85E+07	3.28%	3.29E+07	4.01%	4.47E+07	3.46%
510	5.26E+07	3.33%	3.67E+07	4.00%	5.21E+07	3.39%
530	5.28E+07	3.49%	4.08E+07	4.00%	5.56E+07	3.46%
550	5.29E+07	3.67%	4.38E+07	4.07%	5.97E+07	3.51%
570	5.39E+07	3.80%	4.81E+07	4.06%	6.74E+07	3.46%
590	5.33E+07	3.97%	4.91E+07	4.18%	6.75E+07	3.58%
610	6.36E+07	3.78%	5.36E+07	4.16%	7.64E+07	3.51%
630	5.22E+07	4.24%	5.82E+07	4.02%	7.18E+07	3.66%
650	6.25E+07	3.95%	5.84E+07	4.11%	7.80E+07	3.59%
670	6.48E+07	3.95%	6.22E+07	4.06%	8.12E+07	3.59%
690	6.85E+07	3.85%	6.17E+07	4.08%	8.00E+07	3.62%
725	6.70E+07	2.93%	6.08E+07	3.05%	8.15E+07	2.77%
775	6.90E+07	2.91%	6.25E+07	3.03%	7.83E+07	2.82%
825	7.12E+07	2.91%	6.90E+07	2.94%	8.11E+07	2.81%
875	6.91E+07	2.93%	6.96E+07	2.93%	8.40E+07	2.77%
925	6.94E+07	2.89%	6.77E+07	2.92%	7.89E+07	2.80%
975	6.20E+07	2.99%	6.12E+07	3.01%	6.95E+07	2.90%
1025	5.77E+07	3.05%	5.49E+07	3.11%	5.87E+07	3.07%
1075	6.09E+07	3.01%	5.50E+07	3.13%	3.98E+07	3.66%
1125	5.49E+07	3.11%	4.82E+07	3.28%	8.16E+06	10.70%
1175	5.81E+07	3.07%	5.25E+07	3.19%	3.99E+06	20.60%
1225	5.12E+07	3.21%	4.49E+07	3.40%	2.50E+06	31.40%
1275	4.73E+07	3.31%	2.05E+07	5.19%	6.72E+05	110.00%
1325	3.89E+07	3.60%	1.16E+06	60.90%		
1375	3.22E+07	3.96%				
1425	1.74E+07	5.60%				

Table B-3: Neutron energy spectra from the reaction 9Be(p,n) E(p)=3.4 MeV
Measured November 1995

Units of spectra are: neutrons/(MeV-steradian-microcoulomb)

Energy at Center of Bin [keV]	0 degree spectrum	0 degree % statistical error	40 degree spectrum	40 degree % statistical error
70	8.72E+06	19.20%	1.16E+07	10.52%
90	2.14E+07	10.30%	2.53E+07	6.48%
110	2.45E+07	8.53%	3.22E+07	5.00%
130	3.05E+07	6.20%	3.12E+07	4.58%
150	2.56E+07	6.05%	2.93E+07	4.13%
170	2.69E+07	4.46%	2.72E+07	3.49%
190	2.30E+07	3.79%	2.42E+07	3.01%
210	2.19E+07	3.23%	2.19E+07	2.74%
230	2.15E+07	2.97%	2.32E+07	2.52%
250	2.17E+07	2.87%	2.31E+07	2.48%
270	2.16E+07	2.94%	2.18E+07	2.55%
290	2.27E+07	3.02%	2.26E+07	2.62%
310	2.53E+07	3.06%	2.56E+07	2.63%
330	2.87E+07	3.03%	2.73E+07	2.66%
350	2.76E+07	3.16%	2.72E+07	2.72%
370	3.18E+07	3.11%	3.05E+07	2.71%
390	3.22E+07	3.17%	3.17E+07	2.73%
410	3.19E+07	3.23%	3.24E+07	2.74%
430	3.41E+07	3.23%	3.46E+07	2.73%
450	3.53E+07	3.29%	3.48E+07	2.80%
470	3.80E+07	3.32%	4.07E+07	2.75%
490	3.98E+07	3.39%	4.23E+07	2.81%
510	4.34E+07	3.43%	4.80E+07	2.79%
530	5.13E+07	3.33%	5.59E+07	2.75%
550	5.43E+07	3.41%	5.73E+07	2.83%
570	5.78E+07	3.46%	5.59E+07	2.95%
590	5.83E+07	3.57%	5.40E+07	3.07%
610	5.85E+07	3.71%	5.45E+07	3.17%
630	5.00E+07	4.08%	4.94E+07	3.34%
650	4.91E+07	4.22%	5.13E+07	3.35%
670	4.72E+07	4.43%	5.20E+07	3.38%
690	4.53E+07	4.53%	4.97E+07	3.46%
725	4.28E+07	3.36%	5.22E+07	2.66%
775	3.89E+07	3.55%	4.88E+07	2.73%
825	4.18E+07	3.44%	4.95E+07	2.73%
875	4.05E+07	3.48%	5.01E+07	2.71%
925	4.21E+07	3.35%	4.95E+07	2.69%
975	3.66E+07	3.55%	4.47E+07	2.75%
1025	3.24E+07	3.73%	3.85E+07	2.88%
1075	3.18E+07	3.81%	4.35E+07	2.78%
1125	2.74E+07	4.05%	3.64E+07	2.94%
1175	3.17E+07	3.79%	3.76E+07	2.93%
1225	2.81E+07	4.02%	3.60E+07	2.97%
1275	2.57E+07	4.20%	2.61E+07	3.38%
1325	2.51E+07	4.22%	1.08E+07	5.62%
1375	2.29E+07	4.45%	6.51E+06	8.36%
1425	1.23E+07	6.65%	2.48E+06	18.87%
1475	3.87E+06	17.60%	1.10E+06	41.27%

Table B-4: Neutron energy spectra from the reaction 9Be(p,n) E(p)=3.0 MeV
Measured November 1995

Units of spectra are: neutrons/(MeV-steradian-microcoulomb)

Energy at Center of Bin [keV]	0 degree spectrum	0 degree % statistical error
70	3.50E+06	24.25%
90	1.08E+07	10.32%
110	1.69E+07	6.42%
130	1.68E+07	5.68%
150	1.60E+07	4.99%
170	1.58E+07	3.90%
190	1.33E+07	3.38%
210	1.28E+07	2.91%
230	1.37E+07	2.62%
250	1.40E+07	2.55%
270	1.37E+07	2.60%
290	1.48E+07	2.63%
310	1.73E+07	2.62%
330	1.92E+07	2.62%
350	1.92E+07	2.66%
370	2.19E+07	2.64%
390	2.34E+07	2.63%
410	2.42E+07	2.64%
430	2.62E+07	2.61%
450	2.68E+07	2.66%
470	2.90E+07	2.68%
490	3.12E+07	2.70%
510	3.74E+07	2.64%
530	4.20E+07	2.63%
550	4.58E+07	2.65%
570	4.96E+07	2.66%
590	5.07E+07	2.70%
610	5.04E+07	2.78%
630	4.21E+07	2.99%
650	4.05E+07	3.10%
670	3.77E+07	3.25%
690	3.36E+07	3.43%
725	3.37E+07	2.68%
775	3.23E+07	2.72%
825	3.40E+07	2.69%
875	3.31E+07	2.71%
925	3.07E+07	2.74%
975	2.64E+07	2.87%
1025	1.66E+07	3.49%
1075	5.28E+06	7.83%
1125	1.11E+06	31.47%

Table B-5: Neutron energy spectra from the reaction 9Be(p,n) E(p)=4.0 MeV
Measured August 1996

Units of spectra are: neutrons/(MeV-steradian-microcoulomb)

Energy at Center of Bin [keV]	0 degree spectrum	0 degree % statistical error	20 degree spectrum	20 degree % statistical error	60 degree spectrum	60 degree % statistical error
70	1.15E+07	13.90%	1.11E+07	16.40%	8.54E+06	24.10%
90	3.05E+07	7.16%	2.85E+07	8.60%	2.41E+07	11.40%
110	3.56E+07	5.75%	3.96E+07	5.93%	3.21E+07	8.05%
130	4.62E+07	4.25%	4.51E+07	4.83%	4.17E+07	5.79%
150	4.55E+07	3.81%	4.83E+07	4.05%	4.59E+07	4.70%
170	4.90E+07	2.99%	5.07E+07	3.18%	4.84E+07	3.59%
190	4.91E+07	2.57%	4.76E+07	2.75%	5.06E+07	2.91%
210	4.98E+07	2.37%	4.94E+07	2.49%	5.11E+07	2.62%
230	5.65E+07	2.25%	5.79E+07	2.31%	5.81E+07	2.42%
250	5.90E+07	2.21%	5.86E+07	2.28%	5.99E+07	2.37%
270	5.99E+07	2.22%	5.99E+07	2.28%	5.75E+07	2.41%
290	6.04E+07	2.25%	6.22E+07	2.31%	5.63E+07	2.48%
310	6.62E+07	2.27%	6.68E+07	2.35%	6.12E+07	2.53%
330	6.85E+07	2.31%	6.70E+07	2.42%	6.37E+07	2.60%
350	7.33E+07	2.34%	7.43E+07	2.43%	6.33E+07	2.69%
370	7.45E+07	2.36%	7.09E+07	2.49%	6.26E+07	2.76%
390	8.08E+07	2.36%	7.51E+07	2.50%	6.64E+07	2.77%
410	8.00E+07	2.39%	7.69E+07	2.52%	6.81E+07	2.80%
430	8.68E+07	2.42%	8.23E+07	2.57%	7.66E+07	2.83%
450	9.04E+07	2.47%	8.63E+07	2.63%	7.85E+07	2.93%
470	9.14E+07	2.53%	8.39E+07	2.74%	7.61E+07	3.09%
490	9.47E+07	2.58%	9.02E+07	2.78%	8.08E+07	3.16%
510	9.97E+07	2.61%	9.67E+07	2.80%	7.69E+07	3.35%
530	1.00E+08	2.66%	9.41E+07	2.90%	7.20E+07	3.57%
550	1.13E+08	2.63%	1.05E+08	2.88%	7.15E+07	3.73%
570	1.13E+08	2.69%	1.06E+08	2.94%	6.72E+07	3.98%
590	1.12E+08	2.73%	1.06E+08	2.98%	6.27E+07	4.23%
610	1.02E+08	2.85%	9.90E+07	3.11%	6.15E+07	4.36%
630	1.00E+08	2.89%	8.69E+07	3.31%	5.88E+07	4.52%
650	9.15E+07	3.02%	8.44E+07	3.40%	6.27E+07	4.44%
670	8.71E+07	3.11%	8.44E+07	3.44%	6.41E+07	4.46%
690	7.64E+07	3.29%	7.70E+07	3.59%	6.16E+07	4.56%
725	6.97E+07	2.66%	6.68E+07	2.88%	6.27E+07	3.24%
775	6.46E+07	2.73%	6.29E+07	2.95%	6.49E+07	3.20%
825	6.29E+07	2.75%	6.47E+07	2.92%	6.41E+07	3.22%
875	5.77E+07	2.82%	5.78E+07	3.03%	6.18E+07	3.25%
925	6.50E+07	2.74%	6.38E+07	2.96%	7.11E+07	3.12%
975	5.77E+07	2.86%	5.83E+07	3.07%	6.52E+07	3.23%
1025	6.10E+07	2.86%	5.80E+07	3.14%	7.13E+07	3.19%
1075	5.69E+07	2.93%	5.78E+07	3.15%	6.70E+07	3.28%

CONTINUTED ON NEXT PAGE

Table B-5: Neutron energy spectra from the reaction 9Be(p,n) E(p)=4.0 MeV
Measured August 1996

Units of spectra are: neutrons/(MeV-steradian-microcoulomb)

Energy at Center of Bin [keV]	0 degree spectrum	0 degree % statistical error	20 degree spectrum	20 degree % statistical error	60 degree spectrum	60 degree % statistical error
1125	5.60E+07	2.95%	5.56E+07	3.21%	6.57E+07	3.32%
1175	5.97E+07	2.92%	5.68E+07	3.22%	7.17E+07	3.24%
1225	5.09E+07	3.08%	5.17E+07	3.33%	7.18E+07	3.23%
1275	5.58E+07	3.00%	5.20E+07	3.35%	6.97E+07	3.30%
1325	4.91E+07	3.14%	5.09E+07	3.37%	6.40E+07	3.41%
1375	5.31E+07	3.06%	5.36E+07	3.32%	6.50E+07	3.41%
1425	5.07E+07	3.10%	5.08E+07	3.37%	5.91E+07	3.53%
1475	5.28E+07	3.03%	4.75E+07	3.44%	5.26E+07	3.68%
1525	5.58E+07	2.97%	5.06E+07	3.35%	5.08E+07	3.74%
1575	5.98E+07	2.90%	5.65E+07	3.20%	5.02E+07	3.75%
1625	5.82E+07	2.89%	5.26E+07	3.25%	4.25E+07	3.99%
1675	6.13E+07	2.84%	5.68E+07	3.14%	3.89E+07	4.15%
1725	5.68E+07	2.87%	5.02E+07	3.25%	2.69E+07	4.94%
1775	6.62E+07	2.74%	5.55E+07	3.11%	7.26E+06	12.20%
1825	7.23E+07	2.66%	6.19E+07	2.98%		
1875	6.47E+07	2.72%	5.19E+07	3.13%		
1925	7.70E+07	2.60%	5.88E+07	3.01%		
1975	6.75E+07	2.67%	4.61E+07	3.23%		
2025	6.39E+07	2.69%	3.14E+07	3.78%		
2075	2.85E+07	3.56%	1.84E+06	30.90%		
2125	1.28E+06	34.80%				

Table B-5: Neutron energy spectra from the reaction 9Be(p,n) E(p)=4.0 MeV
Measured August 1996

Units of spectra are: neutrons/(MeV-steradian-microcoulomb)

Energy at Center of Bin [keV]	110 degree spectrum	110 degree % statistical error	115 degree spectrum	115 degree % statistical error	120 degree spectrum	120 degree % statistical error
70	5.56E+06	33.30%	7.49E+06	24.40%	8.25E+06	22.70%
90	2.13E+07	11.70%	2.46E+07	10.10%	2.09E+07	12.00%
110	3.88E+07	6.25%	3.13E+07	7.47%	3.16E+07	7.51%
130	4.11E+07	5.38%	3.45E+07	6.18%	3.46E+07	6.23%
150	4.12E+07	4.69%	4.13E+07	4.70%	3.77E+07	5.06%
170	4.08E+07	3.71%	3.89E+07	3.85%	3.91E+07	3.84%
190	4.09E+07	3.01%	4.04E+07	3.07%	4.13E+07	3.04%
210	3.89E+07	2.73%	4.01E+07	2.75%	3.85E+07	2.78%
230	4.77E+07	2.45%	4.69E+07	2.50%	4.59E+07	2.50%
250	4.90E+07	2.40%	5.01E+07	2.42%	4.99E+07	2.41%
270	4.98E+07	2.40%	5.22E+07	2.42%	5.18E+07	2.41%
290	5.33E+07	2.43%	5.38E+07	2.46%	4.86E+07	2.50%
310	5.58E+07	2.49%	5.15E+07	2.59%	4.83E+07	2.62%
330	5.12E+07	2.64%	4.92E+07	2.73%	4.54E+07	2.78%
350	5.13E+07	2.74%	5.07E+07	2.81%	4.82E+07	2.84%
370	4.87E+07	2.86%	4.99E+07	2.90%	5.02E+07	2.88%
390	5.08E+07	2.89%	5.14E+07	2.94%	5.16E+07	2.92%
410	5.22E+07	2.91%	5.14E+07	3.00%	5.33E+07	2.94%
430	5.44E+07	3.02%	5.56E+07	3.07%	5.46E+07	3.08%
450	5.62E+07	3.14%	5.81E+07	3.18%	5.81E+07	3.16%
470	5.37E+07	3.37%	5.68E+07	3.37%	5.87E+07	3.30%
490	5.80E+07	3.42%	6.10E+07	3.43%	6.03E+07	3.43%
510	6.21E+07	3.46%	6.24E+07	3.55%	6.12E+07	3.56%
530	6.12E+07	3.60%	6.17E+07	3.69%	6.47E+07	3.58%
550	6.85E+07	3.56%	7.38E+07	3.54%	7.35E+07	3.52%
570	7.29E+07	3.56%	7.52E+07	3.61%	7.26E+07	3.65%
590	7.46E+07	3.60%	7.44E+07	3.71%	7.40E+07	3.69%
610	7.79E+07	3.59%	7.34E+07	3.80%	8.01E+07	3.62%
630	7.60E+07	3.67%	7.41E+07	3.83%	7.23E+07	3.84%
650	7.59E+07	3.73%	7.71E+07	3.82%	7.93E+07	3.73%
670	8.71E+07	3.54%	7.83E+07	3.84%	7.61E+07	3.86%
690	8.38E+07	3.61%	7.78E+07	3.86%	7.73E+07	3.84%
725	7.97E+07	2.80%	8.17E+07	2.84%	7.86E+07	2.86%
775	8.19E+07	2.78%	8.12E+07	2.86%	7.90E+07	2.87%
825	8.18E+07	2.79%	8.21E+07	2.85%	8.26E+07	2.83%
875	8.00E+07	2.80%	8.28E+07	2.84%	7.75E+07	2.88%
925	9.15E+07	2.72%	9.19E+07	2.78%	9.02E+07	2.78%
975	8.53E+07	2.79%	8.47E+07	2.87%	8.43E+07	2.85%
1025	9.15E+07	2.77%	9.44E+07	2.82%	9.38E+07	2.80%
1075	8.59E+07	2.84%	9.04E+07	2.87%	9.04E+07	2.84%
1125	8.74E+07	2.83%	8.95E+07	2.89%	8.70E+07	2.89%
1175	9.39E+07	2.80%	9.55E+07	2.86%	9.34E+07	2.85%
1225	8.59E+07	2.87%	8.76E+07	2.94%	8.01E+07	3.00%
1275	8.27E+07	2.93%	7.45E+07	3.13%	4.76E+07	3.72%
1325	5.79E+07	3.33%	1.71E+07	6.80%	2.68E+06	32.70%
1375	5.08E+06	18.20%	2.51E+06	34.80%	1.10E+06	77.70%
1425	2.37E+06	35.70%	2.41E+06	34.90%		

Table B-5: Neutron energy spectra from the reaction 9Be(p,n) E(p)=4.0 MeV
Measured August 1996

Units of spectra are: neutrons/(MeV-steradian-microcoulomb)

Energy at Center of Bin [keV]	125 degree spectrum	125 degree % statistical error	130 degree spectrum	130 degree % statistical error	135 degree spectrum	135 degree % statistical error
70	9.56E+06	19.40%	9.35E+06	20.20%	6.28E+06	27.90%
90	2.16E+07	11.50%	1.97E+07	12.70%	2.05E+07	11.50%
110	3.26E+07	7.23%	3.04E+07	7.82%	2.74E+07	8.10%
130	3.92E+07	5.58%	3.45E+07	6.30%	3.43E+07	6.00%
150	4.11E+07	4.71%	3.94E+07	4.94%	3.57E+07	5.05%
170	3.90E+07	3.83%	3.76E+07	3.98%	3.93E+07	3.71%
190	3.85E+07	3.12%	3.79E+07	3.18%	3.65E+07	3.13%
210	4.02E+07	2.73%	3.74E+07	2.83%	3.92E+07	2.71%
230	4.76E+07	2.47%	4.70E+07	2.50%	4.81E+07	2.44%
250	5.20E+07	2.39%	5.22E+07	2.40%	5.24E+07	2.37%
270	5.35E+07	2.39%	4.78E+07	2.47%	4.52E+07	2.45%
290	4.39E+07	2.56%	4.34E+07	2.59%	4.26E+07	2.55%
310	4.79E+07	2.62%	4.68E+07	2.66%	4.47E+07	2.63%
330	4.85E+07	2.72%	4.58E+07	2.80%	4.44E+07	2.76%
350	4.98E+07	2.80%	4.90E+07	2.85%	4.68E+07	2.82%
370	5.19E+07	2.83%	4.75E+07	2.96%	4.58E+07	2.91%
390	5.17E+07	2.91%	5.05E+07	2.97%	5.12E+07	2.87%
410	5.36E+07	2.93%	4.98E+07	3.05%	5.07E+07	2.94%
430	5.75E+07	3.01%	5.57E+07	3.09%	5.43E+07	3.02%
450	5.59E+07	3.20%	5.50E+07	3.27%	5.61E+07	3.14%
470	5.91E+07	3.28%	5.46E+07	3.45%	5.43E+07	3.34%
490	5.87E+07	3.45%	6.16E+07	3.43%	5.82E+07	3.40%
510	6.44E+07	3.46%	6.48E+07	3.51%	6.21E+07	3.45%
530	6.58E+07	3.54%	6.24E+07	3.69%	6.14E+07	3.59%
550	7.50E+07	3.47%	6.36E+07	3.82%	6.77E+07	3.57%
570	7.35E+07	3.61%	7.25E+07	3.70%	6.81E+07	3.67%
590	7.35E+07	3.68%	6.95E+07	3.85%	6.62E+07	3.80%
610	7.16E+07	3.80%	7.09E+07	3.89%	7.15E+07	3.73%
630	7.07E+07	3.87%	6.84E+07	4.00%	6.88E+07	3.84%
650	7.34E+07	3.86%	7.47E+07	3.90%	7.02E+07	3.86%
670	8.08E+07	3.73%	7.53E+07	3.94%	7.41E+07	3.81%
690	7.78E+07	3.81%	8.13E+07	3.80%	7.62E+07	3.77%
725	7.55E+07	2.89%	7.55E+07	2.93%	7.24E+07	2.89%
775	7.78E+07	2.87%	7.58E+07	2.93%	7.71E+07	2.84%
825	7.94E+07	2.85%	7.91E+07	2.89%	7.89E+07	2.82%
875	8.03E+07	2.84%	7.88E+07	2.89%	7.67E+07	2.84%
925	9.29E+07	2.75%	9.24E+07	2.78%	8.97E+07	2.74%
975	8.53E+07	2.83%	8.73E+07	2.85%	9.07E+07	2.74%
1025	9.36E+07	2.80%	9.41E+07	2.83%	9.71E+07	2.73%
1075	9.07E+07	2.83%	8.72E+07	2.91%	9.23E+07	2.78%
1125	8.72E+07	2.88%	8.59E+07	2.94%	8.46E+07	2.87%
1175	9.31E+07	2.85%	8.98E+07	2.92%	7.75E+07	2.98%
1225	6.60E+07	3.20%	3.25E+07	4.55%	7.09E+06	13.00%
1275	1.03E+07	10.00%	3.34E+06	27.60%	2.85E+06	30.00%
1325	1.92E+06	44.30%	3.79E+05	221.00%	1.46E+06	55.30%
1375	1.23E+06	69.10%				

Table B-5: Neutron energy spectra from the reaction 9Be(p,n) E(p)=4.0 MeV
Measured August 1996

Units of spectra are: neutrons/(MeV-steradian-microcoulomb)

Energy at Center of Bin [keV]	145 degree spectrum	145 degree % statistical error
70	7.21E+06	24.30%
90	2.05E+07	11.40%
110	2.97E+07	7.47%
130	3.23E+07	6.22%
150	3.50E+07	5.07%
170	3.70E+07	3.80%
190	3.54E+07	3.14%
210	4.01E+07	2.66%
230	4.88E+07	2.41%
250	4.44E+07	2.42%
270	4.21E+07	2.47%
290	4.13E+07	2.55%
310	4.24E+07	2.64%
330	4.16E+07	2.78%
350	4.42E+07	2.83%
370	4.42E+07	2.91%
390	4.68E+07	2.92%
410	4.59E+07	3.01%
430	5.05E+07	3.06%
450	5.22E+07	3.18%
470	5.08E+07	3.38%
490	5.18E+07	3.53%
510	5.91E+07	3.47%
530	5.26E+07	3.80%
550	6.26E+07	3.64%
570	6.23E+07	3.76%
590	6.31E+07	3.82%
610	6.41E+07	3.86%
630	6.10E+07	4.00%
650	6.53E+07	3.93%
670	7.63E+07	3.69%
690	7.43E+07	3.74%
725	7.21E+07	2.86%
775	7.50E+07	2.83%
825	7.87E+07	2.78%
875	7.92E+07	2.78%
925	9.54E+07	2.66%
975	9.14E+07	2.70%
1025	1.00E+08	2.67%
1075	9.36E+07	2.73%
1125	7.68E+07	2.91%
1175	1.43E+07	7.44%
1225	2.01E+06	40.70%

Table B-6: Neutron energy spectra from the reaction 9Be(p,n) E(p)=3.7 MeV
Measured August 1996

Units of spectra are: neutrons/(MeV-steradian-microcoulomb)

Energy at		0 degree		20 degree		60 degree
Center of Bin	0 degree	% statistical	20 degree	% statistical	60 degree	% statistical
[keV]	spectrum	error	spectrum	error	spectrum	error
70	8.21E+06	17.10%	6.69E+06	31.70%	6.13E+06	22.90%
90	1.70E+07	11.00%	1.53E+07	18.30%	1.99E+07	9.60%
110	2.45E+07	7.30%	2.81E+07	9.38%	2.26E+07	7.87%
130	2.82E+07	5.83%	3.00E+07	7.88%	2.98E+07	5.61%
150	3.20E+07	4.65%	2.90E+07	6.94%	2.93E+07	4.97%
170	3.05E+07	3.79%	2.84E+07	5.23%	3.04E+07	3.80%
190	3.05E+07	3.08%	2.93E+07	3.87%	3.11E+07	3.06%
210	3.21E+07	2.71%	3.08E+07	3.19%	3.06E+07	2.75%
230	3.76E+07	2.47%	3.55E+07	2.78%	3.57E+07	2.50%
250	3.87E+07	2.42%	3.66E+07	2.68%	3.65E+07	2.45%
270	4.01E+07	2.42%	3.76E+07	2.68%	3.58E+07	2.47%
290	3.83E+07	2.50%	3.77E+07	2.77%	3.59E+07	2.54%
310	4.38E+07	2.52%	4.15E+07	2.83%	3.89E+07	2.60%
330	4.52E+07	2.60%	4.23E+07	2.96%	4.04E+07	2.68%
350	4.94E+07	2.62%	4.59E+07	3.00%	4.24E+07	2.73%
370	4.86E+07	2.69%	4.44E+07	3.14%	4.20E+07	2.81%
390	5.27E+07	2.69%	5.01E+07	3.07%	4.64E+07	2.79%
410	5.62E+07	2.68%	5.12E+07	3.11%	4.77E+07	2.81%
430	6.16E+07	2.73%	5.23E+07	3.27%	5.58E+07	2.80%
450	6.51E+07	2.79%	5.95E+07	3.27%	6.09E+07	2.85%
470	6.57E+07	2.89%	6.17E+07	3.39%	6.36E+07	2.92%
490	6.77E+07	2.97%	6.27E+07	3.54%	6.84E+07	2.96%
510	7.29E+07	3.00%	6.83E+07	3.55%	6.48E+07	3.13%
530	7.58E+07	3.04%	7.13E+07	3.60%	5.67E+07	3.40%
550	8.61E+07	3.00%	8.47E+07	3.46%	6.09E+07	3.42%
570	8.64E+07	3.07%	8.06E+07	3.65%	5.80E+07	3.61%
590	8.77E+07	3.11%	8.57E+07	3.62%	5.93E+07	3.64%
610	8.50E+07	3.19%	8.70E+07	3.66%	5.54E+07	3.83%
630	7.95E+07	3.31%	7.28E+07	4.04%	4.97E+07	4.09%
650	7.46E+07	3.44%	6.71E+07	4.30%	5.73E+07	3.88%
670	6.38E+07	3.74%	6.50E+07	4.45%	6.04E+07	3.83%
690	5.98E+07	3.86%	5.64E+07	4.83%	5.99E+07	3.85%
725	5.28E+07	3.02%	5.57E+07	3.43%	5.64E+07	2.95%
775	5.38E+07	3.01%	5.28E+07	3.53%	5.67E+07	2.95%
825	5.16E+07	3.06%	5.17E+07	3.56%	6.05E+07	2.89%
875	4.70E+07	3.16%	4.65E+07	3.72%	6.00E+07	2.89%
925	5.42E+07	3.04%	5.27E+07	3.56%	6.74E+07	2.82%
975	4.96E+07	3.15%	4.85E+07	3.70%	6.09E+07	2.93%
1025	5.25E+07	3.15%	5.00E+07	3.75%	6.60E+07	2.90%
1075	5.18E+07	3.18%	4.71E+07	3.86%	6.31E+07	2.96%
1125	4.43E+07	3.40%	4.64E+07	3.91%	5.80E+07	3.06%
1175	4.75E+07	3.34%	4.91E+07	3.85%	6.52E+07	2.97%
1225	4.37E+07	3.45%	4.11E+07	4.19%	6.21E+07	3.02%

Table B-6: Neutron energy spectra from the reaction 9Be(p,n) E(p)=3.7 MeV
Measured August 1996

Units of spectra are: neutrons/(MeV-steradian-microcoulomb)

Energy at Center of Bin [keV]	0 degree spectrum	0 degree % statistical error	20 degree spectrum	20 degree % statistical error	60 degree spectrum	60 degree % statistical error
1275	4.52E+07	3.43%	4.54E+07	4.01%	6.39E+07	3.01%
1325	4.20E+07	3.53%	4.33E+07	4.10%	5.51E+07	3.17%
1375	4.44E+07	3.47%	4.43E+07	4.08%	5.30E+07	3.23%
1425	4.52E+07	3.43%	3.85E+07	4.35%	4.84E+07	3.33%
1475	4.33E+07	3.47%	4.26E+07	4.07%	3.34E+07	3.88%
1525	4.55E+07	3.40%	4.22E+07	4.09%	5.70E+06	12.40%
1575	4.83E+07	3.32%	4.43E+07	3.98%	8.65E+05	68.60%
1625	4.76E+07	3.30%	4.05E+07	4.10%		
1675	4.61E+07	3.33%	3.85E+07	4.18%		
1725	3.98E+07	3.49%	2.69E+07	4.95%		
1775	2.36E+07	4.39%	2.47E+06	32.40%		
1825	1.22E+06	41.60%				

Table B-6: Neutron energy spectra from the reaction 9Be(p,n) E(p)=3.7 MeV
Measured August 1996

Units of spectra are: neutrons/(MeV-steradian-microcoulomb)

Energy at Center of Bin [keV]	110 degree spectrum	110 degree % statistical error	115 degree spectrum	115 degree % statistical error	120 degree spectrum	120 degree % statistical error
70	3.97E+06	33.30%	7.29E+06	18.10%	2.86E+06	46.00%
90	1.54E+07	11.60%	1.44E+07	12.20%	9.83E+06	17.80%
110	2.06E+07	8.15%	2.43E+07	6.97%	1.69E+07	9.76%
130	2.59E+07	6.03%	2.54E+07	6.05%	2.43E+07	6.34%
150	2.63E+07	5.18%	2.73E+07	4.98%	2.38E+07	5.59%
170	2.81E+07	3.86%	2.86E+07	3.79%	2.66E+07	3.99%
190	2.69E+07	3.20%	2.74E+07	3.15%	2.57E+07	3.26%
210	2.84E+07	2.77%	2.83E+07	2.76%	2.80E+07	2.78%
230	3.36E+07	2.50%	3.44E+07	2.48%	3.41E+07	2.49%
250	3.54E+07	2.43%	3.82E+07	2.39%	3.98E+07	2.38%
270	3.90E+07	2.41%	4.09E+07	2.38%	4.29E+07	2.36%
290	4.30E+07	2.41%	4.32E+07	2.41%	4.10E+07	2.43%
310	4.57E+07	2.47%	4.36E+07	2.49%	4.02E+07	2.54%
330	4.28E+07	2.60%	4.18E+07	2.60%	4.12E+07	2.62%
350	4.55E+07	2.64%	4.40E+07	2.66%	4.28E+07	2.68%
370	4.47E+07	2.71%	4.48E+07	2.70%	4.44E+07	2.71%
390	4.65E+07	2.74%	4.48E+07	2.76%	4.54E+07	2.76%
410	4.56E+07	2.81%	4.79E+07	2.76%	4.68E+07	2.78%
430	4.85E+07	2.88%	4.98E+07	2.85%	5.05E+07	2.84%
450	5.29E+07	2.93%	5.23E+07	2.93%	5.32E+07	2.92%
470	5.26E+07	3.06%	5.36E+07	3.03%	5.16E+07	3.08%
490	5.23E+07	3.20%	5.70E+07	3.09%	5.41E+07	3.16%
510	6.10E+07	3.13%	5.97E+07	3.15%	5.88E+07	3.18%
530	6.12E+07	3.23%	5.94E+07	3.25%	5.86E+07	3.28%
550	6.73E+07	3.22%	6.68E+07	3.21%	6.57E+07	3.24%
570	6.41E+07	3.37%	6.67E+07	3.30%	6.62E+07	3.32%
590	7.36E+07	3.25%	7.25E+07	3.25%	6.84E+07	3.34%
610	7.12E+07	3.35%	6.86E+07	3.38%	6.87E+07	3.39%
630	7.31E+07	3.34%	7.00E+07	3.39%	6.75E+07	3.45%
650	7.30E+07	3.39%	7.22E+07	3.39%	6.89E+07	3.47%
670	7.94E+07	3.32%	7.75E+07	3.34%	7.89E+07	3.32%
690	7.80E+07	3.35%	7.85E+07	3.33%	7.73E+07	3.35%
725	7.64E+07	2.64%	7.48E+07	2.65%	7.02E+07	2.70%
775	7.64E+07	2.65%	7.84E+07	2.62%	7.43E+07	2.66%
825	7.88E+07	2.63%	7.91E+07	2.62%	7.85E+07	2.63%
875	7.44E+07	2.68%	7.39E+07	2.67%	7.35E+07	2.68%
925	8.40E+07	2.62%	8.46E+07	2.60%	8.01E+07	2.64%
975	7.44E+07	2.71%	7.47E+07	2.70%	7.18E+07	2.73%
1025	7.66E+07	2.73%	7.59E+07	2.73%	6.92E+07	2.81%
1075	6.64E+07	2.86%	6.01E+07	2.94%	2.70E+07	4.14%
1125	3.45E+07	3.70%	7.59E+06	9.77%	3.12E+06	21.40%
1175	2.55E+06	26.30%	2.73E+06	24.30%	2.19E+06	30.30%
1225	1.98E+06	32.20%	8.49E+05	71.10%		

Table B-6: Neutron energy spectra from the reaction 9Be(p,n) E(p)=3.7 MeV
Measured August 1996

Units of spectra are: neutrons/(MeV-steradian-microcoulomb)

Energy at		125 degree		130 degree		135 degree
Center of Bin	125 degree	% statistical	130 degree	% statistical	135 degree	% statistical
[keV]	spectrum	error	spectrum	error	spectrum	error
70	4.34E+06	30.40%	6.50E+06	21.50%	2.92E+06	46.10%
90	1.59E+07	11.30%	1.43E+07	13.00%	1.10E+07	16.30%
110	2.24E+07	7.58%	2.01E+07	8.69%	2.12E+07	8.13%
130	2.61E+07	5.99%	2.65E+07	6.13%	2.10E+07	7.32%
150	2.88E+07	4.84%	2.49E+07	5.58%	2.44E+07	5.57%
170	2.71E+07	3.95%	2.69E+07	4.07%	2.62E+07	4.08%
190	2.76E+07	3.15%	2.69E+07	3.26%	2.72E+07	3.20%
210	2.87E+07	2.76%	3.01E+07	2.75%	2.91E+07	2.76%
230	3.65E+07	2.46%	3.75E+07	2.46%	3.89E+07	2.43%
250	4.14E+07	2.36%	4.38E+07	2.35%	4.38E+07	2.34%
270	4.33E+07	2.36%	4.09E+07	2.39%	3.80E+07	2.42%
290	3.94E+07	2.45%	3.81E+07	2.49%	3.63E+07	2.50%
310	4.08E+07	2.53%	3.93E+07	2.57%	3.83E+07	2.57%
330	4.11E+07	2.62%	4.12E+07	2.64%	3.83E+07	2.68%
350	4.24E+07	2.69%	4.19E+07	2.73%	4.08E+07	2.73%
370	4.21E+07	2.76%	4.16E+07	2.80%	4.07E+07	2.80%
390	4.50E+07	2.77%	4.42E+07	2.81%	4.51E+07	2.77%
410	4.77E+07	2.76%	4.58E+07	2.83%	4.50E+07	2.82%
430	4.92E+07	2.87%	4.87E+07	2.91%	4.72E+07	2.92%
450	5.26E+07	2.93%	4.97E+07	3.02%	5.03E+07	2.99%
470	5.27E+07	3.06%	5.32E+07	3.08%	4.98E+07	3.13%
490	5.56E+07	3.12%	5.28E+07	3.23%	5.13E+07	3.24%
510	5.54E+07	3.25%	5.64E+07	3.27%	5.60E+07	3.25%
530	5.83E+07	3.28%	5.58E+07	3.39%	5.18E+07	3.47%
550	6.64E+07	3.23%	6.56E+07	3.29%	6.51E+07	3.27%
570	7.05E+07	3.24%	6.21E+07	3.46%	6.33E+07	3.40%
590	6.98E+07	3.31%	6.73E+07	3.41%	6.47E+07	3.43%
610	6.95E+07	3.37%	6.77E+07	3.46%	6.47E+07	3.49%
630	7.04E+07	3.39%	6.28E+07	3.62%	6.06E+07	3.64%
650	6.61E+07	3.53%	7.15E+07	3.46%	6.32E+07	3.62%
670	7.60E+07	3.37%	7.49E+07	3.44%	7.36E+07	3.43%
690	7.46E+07	3.40%	7.23E+07	3.50%	6.69E+07	3.58%
725	7.23E+07	2.68%	7.30E+07	2.70%	6.92E+07	2.72%
775	7.37E+07	2.67%	7.46E+07	2.69%	7.12E+07	2.70%
825	7.58E+07	2.66%	7.55E+07	2.68%	7.33E+07	2.69%
875	7.05E+07	2.71%	7.23E+07	2.71%	7.20E+07	2.70%
925	8.10E+07	2.64%	8.00E+07	2.67%	7.87E+07	2.66%
975	7.24E+07	2.73%	6.53E+07	2.84%	5.72E+07	2.94%
1025	5.99E+07	2.94%	2.95E+07	4.03%	6.47E+06	11.60%
1075	4.78E+06	14.60%	3.99E+06	17.80%	2.65E+06	25.40%
1125	3.14E+06	21.20%	3.97E+06	17.80%	9.79E+05	65.40%
1175	2.86E+06	23.70%	2.47E+06	28.30%		

Table B-6: Neutron energy spectra from the reaction 9Be(p,n) E(p)=3.7 MeV
Measured August 1996

Units of spectra are: neutrons/(MeV-steradian-microcoulomb)

Energy at Center of Bin [keV]	145 degree spectrum	145 degree % statistical error
70	4.92E+06	28.90%
90	1.46E+07	13.10%
110	2.35E+07	7.71%
130	2.49E+07	6.56%
150	2.57E+07	5.54%
170	2.56E+07	4.26%
190	2.82E+07	3.20%
210	3.14E+07	2.72%
230	4.04E+07	2.42%
250	3.76E+07	2.42%
270	3.71E+07	2.45%
290	3.49E+07	2.55%
310	3.57E+07	2.65%
330	3.69E+07	2.74%
350	3.85E+07	2.81%
370	3.97E+07	2.85%
390	4.20E+07	2.86%
410	4.32E+07	2.89%
430	4.44E+07	3.01%
450	4.70E+07	3.10%
470	4.66E+07	3.26%
490	4.87E+07	3.35%
510	5.20E+07	3.40%
530	4.87E+07	3.62%
550	5.85E+07	3.47%
570	5.52E+07	3.67%
590	6.17E+07	3.56%
610	5.98E+07	3.68%
630	6.04E+07	3.70%
650	6.41E+07	3.65%
670	6.94E+07	3.57%
690	6.54E+07	3.67%
725	6.46E+07	2.80%
775	6.96E+07	2.75%
825	7.17E+07	2.73%
875	6.83E+07	2.76%
925	7.05E+07	2.76%
975	1.48E+07	6.01%
1025	2.39E+06	29.90%
1075	1.40E+06	48.50%

Table B-7: Neutron energy spectra from the reaction 9Be(p,n) E(p)=3.4 MeV
Measured August 1996

Units of spectra are: neutrons/(MeV-steradian-microcoulomb)

Energy at Center of Bin [keV]	0 degree spectrum	0 degree % statistical error
70	3.52E+06	31.25%
90	1.16E+07	12.67%
110	1.68E+07	8.27%
130	1.88E+07	6.70%
150	1.83E+07	5.90%
170	1.94E+07	4.30%
190	1.83E+07	3.49%
210	1.94E+07	2.94%
230	2.17E+07	2.65%
250	2.29E+07	2.55%
270	2.38E+07	2.54%
290	2.46E+07	2.60%
310	2.70E+07	2.65%
330	2.86E+07	2.72%
350	3.18E+07	2.73%
370	3.19E+07	2.80%
390	3.52E+07	2.77%
410	3.71E+07	2.78%
430	4.13E+07	2.81%
450	4.49E+07	2.85%
470	4.73E+07	2.92%
490	5.19E+07	2.93%
510	5.64E+07	2.96%
530	5.88E+07	2.99%
550	6.97E+07	2.91%
570	7.00E+07	2.97%
590	7.19E+07	2.99%
610	7.12E+07	3.05%
630	6.88E+07	3.11%
650	5.74E+07	3.40%
670	5.39E+07	3.53%
690	4.90E+07	3.69%
725	4.53E+07	2.87%
775	4.43E+07	2.91%
825	4.30E+07	2.93%
875	4.23E+07	2.96%
925	4.52E+07	2.92%
975	4.14E+07	3.02%
1025	4.29E+07	3.03%
1075	4.03E+07	3.13%
1125	3.79E+07	3.22%
1175	4.35E+07	3.08%
1225	3.78E+07	3.23%

Table B-8: Neutron energy spectra from the reaction 9Be(p,n) E(p)=3.0 MeV
Measured August 1996

Units of spectra are: neutrons/(MeV-steradian-microcoulomb)

Energy at Center of Bin [keV]	0 degree spectrum	0 degree % statistical error
70	1.83E+06	50.45%
90	4.78E+06	25.35%
110	9.05E+06	12.43%
130	8.18E+06	12.05%
150	9.67E+06	8.72%
170	8.65E+06	6.94%
190	1.08E+07	4.28%
210	1.06E+07	3.57%
230	1.25E+07	3.00%
250	1.32E+07	2.84%
270	1.43E+07	2.78%
290	1.47E+07	2.85%
310	1.74E+07	2.85%
330	1.87E+07	2.92%
350	2.01E+07	2.97%
370	2.23E+07	2.93%
390	2.41E+07	2.93%
410	2.58E+07	2.91%
430	3.05E+07	2.89%
450	3.43E+07	2.90%
470	3.53E+07	2.99%
490	4.13E+07	2.94%
510	4.75E+07	2.90%
530	4.73E+07	2.98%
550	5.75E+07	2.87%
570	6.10E+07	2.88%
590	6.10E+07	2.93%
610	5.69E+07	3.04%
630	5.62E+07	3.08%
650	4.78E+07	3.33%
670	4.24E+07	3.56%
690	3.88E+07	3.72%
725	3.60E+07	2.89%
775	3.46E+07	2.93%
825	3.54E+07	2.91%
875	3.35E+07	2.96%
925	3.67E+07	2.90%
975	3.13E+07	3.08%
1025	3.08E+07	3.17%
1075	1.09E+07	5.55%
1125		
1175		
1225		

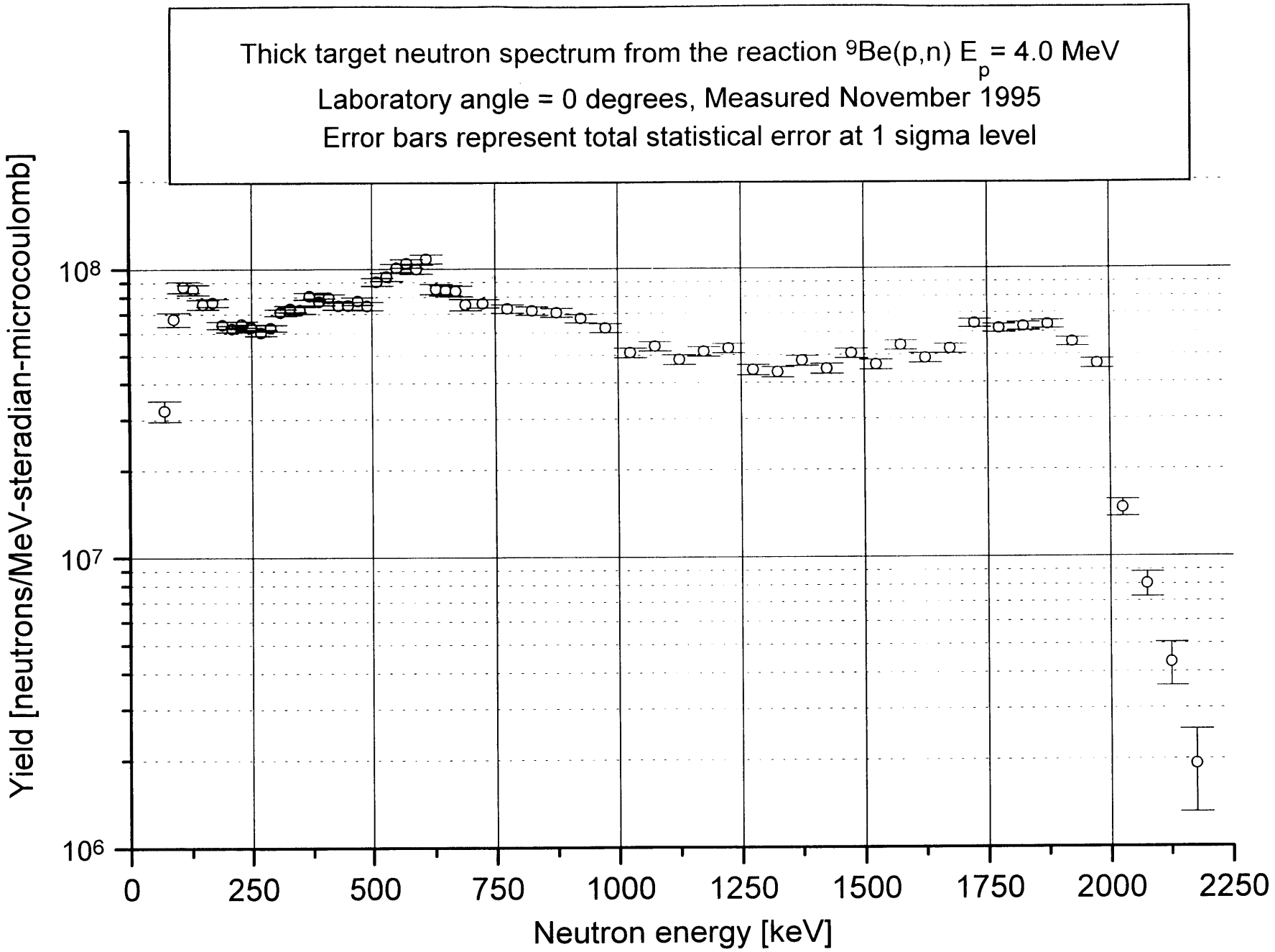
Thick target neutron spectrum from the reaction $^{9}Be(p,n)$ E_p = 4.0 MeV
Laboratory angle = 0 degrees, Measured November 1995
Error bars represent total statistical error at 1 sigma level
Yield [neutrons/MeV-steradian-microcoulomb]
10^8
10^7
10^6
0
250
500
750
1000
1250
1500
1750
2000
2250
Neutron energy [keV]

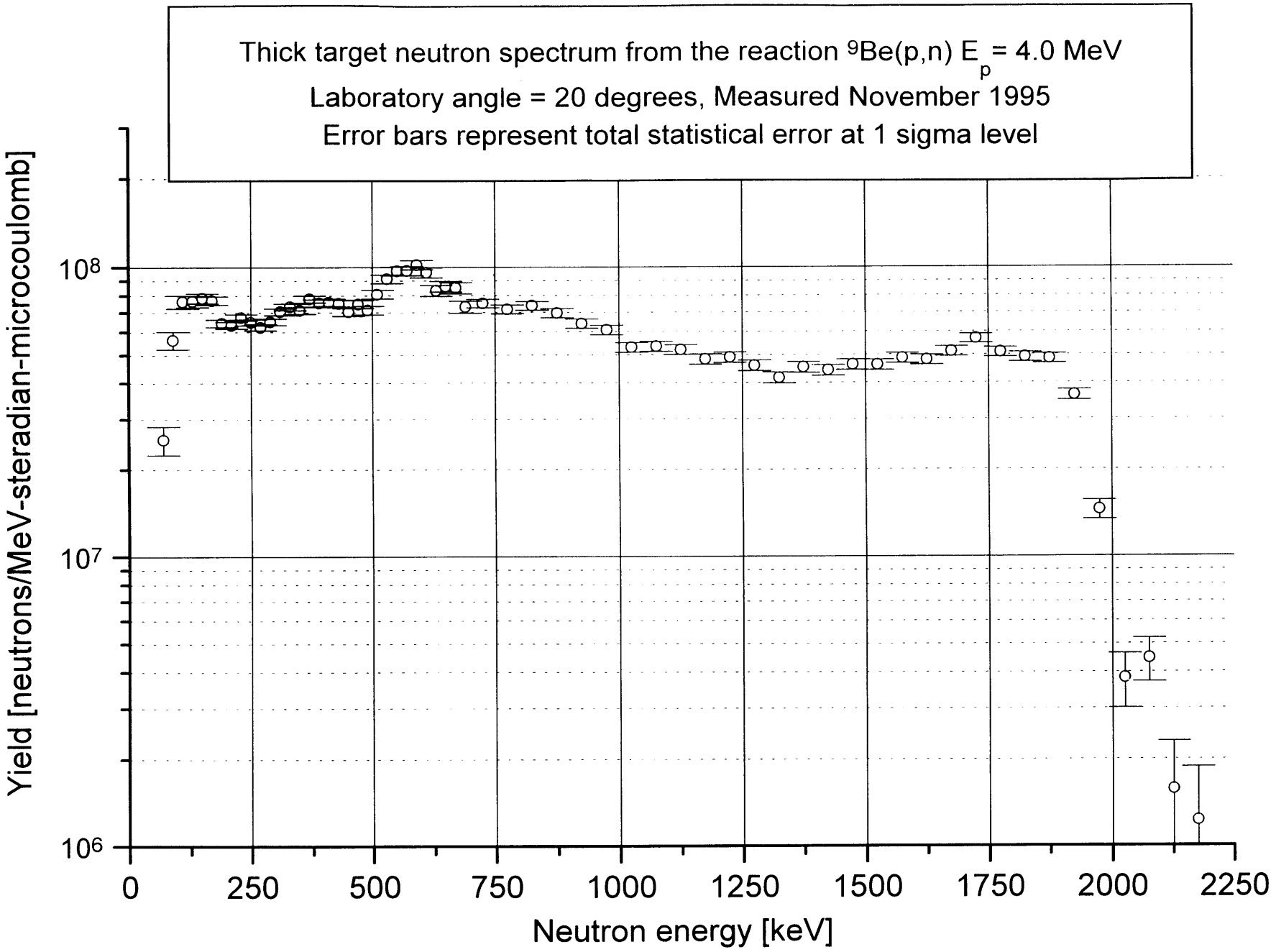
Thick target neutron spectrum from the reaction $^{9}Be(p,n)$ E_p = 4.0 MeV
Laboratory angle = 20 degrees, Measured November 1995
Error bars represent total statistical error at 1 sigma level
Yield [neutrons/MeV-steradian-microcoulomb]
10^8
10^7
10^6
0
250
500
750
1000
1250
1500
1750
2000
2250
Neutron energy [keV]

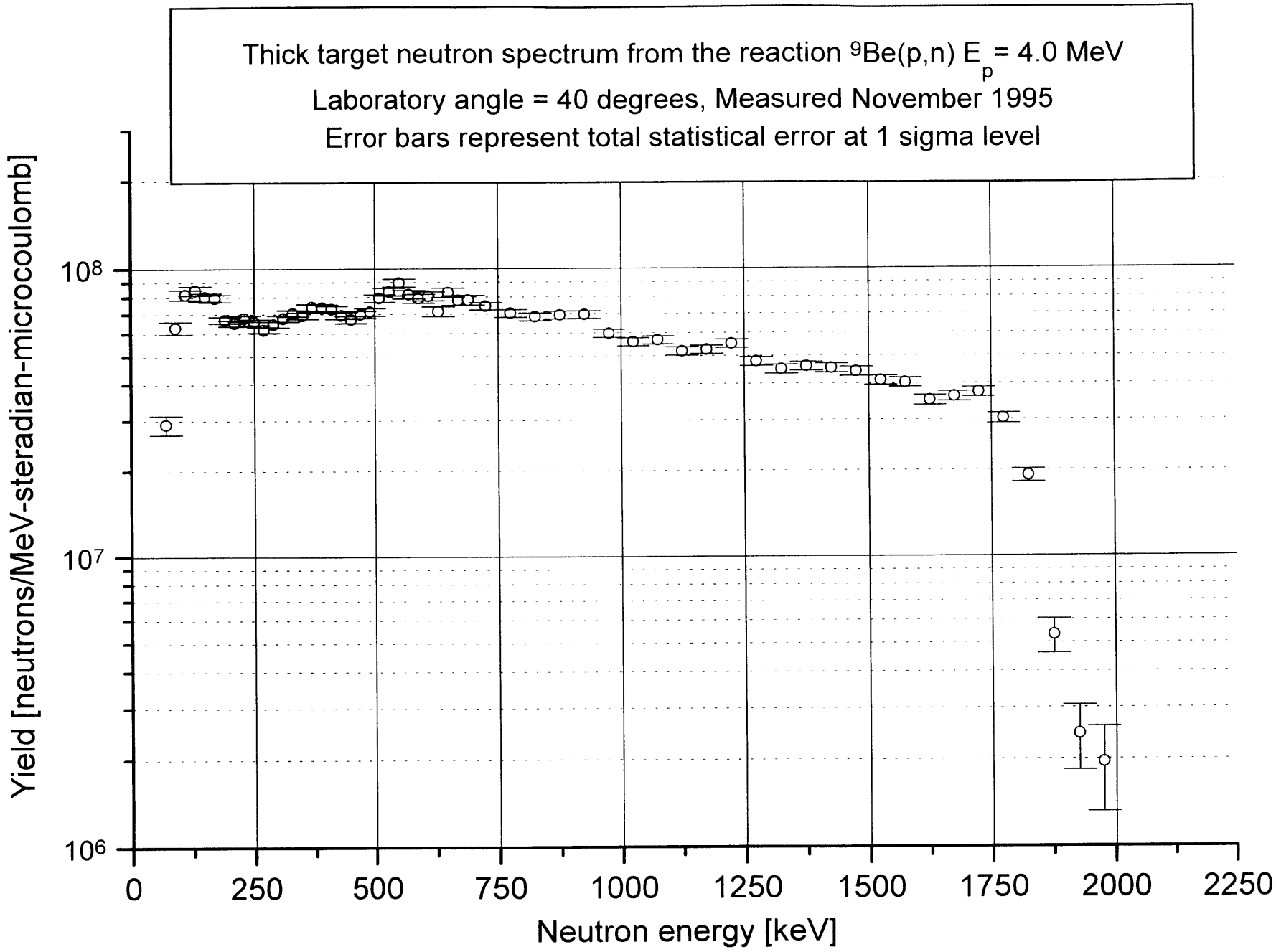
Thick target neutron spectrum from the reaction $^{9}Be(p,n)$ E_p = 4.0 MeV
Laboratory angle = 40 degrees, Measured November 1995
Error bars represent total statistical error at 1 sigma level
Yield [neutrons/MeV-steradian-microcoulomb]
10^8
10^7
10^6
0
250
500
750
1000
1250
1500
1750
2000
2250
Neutron energy [keV]

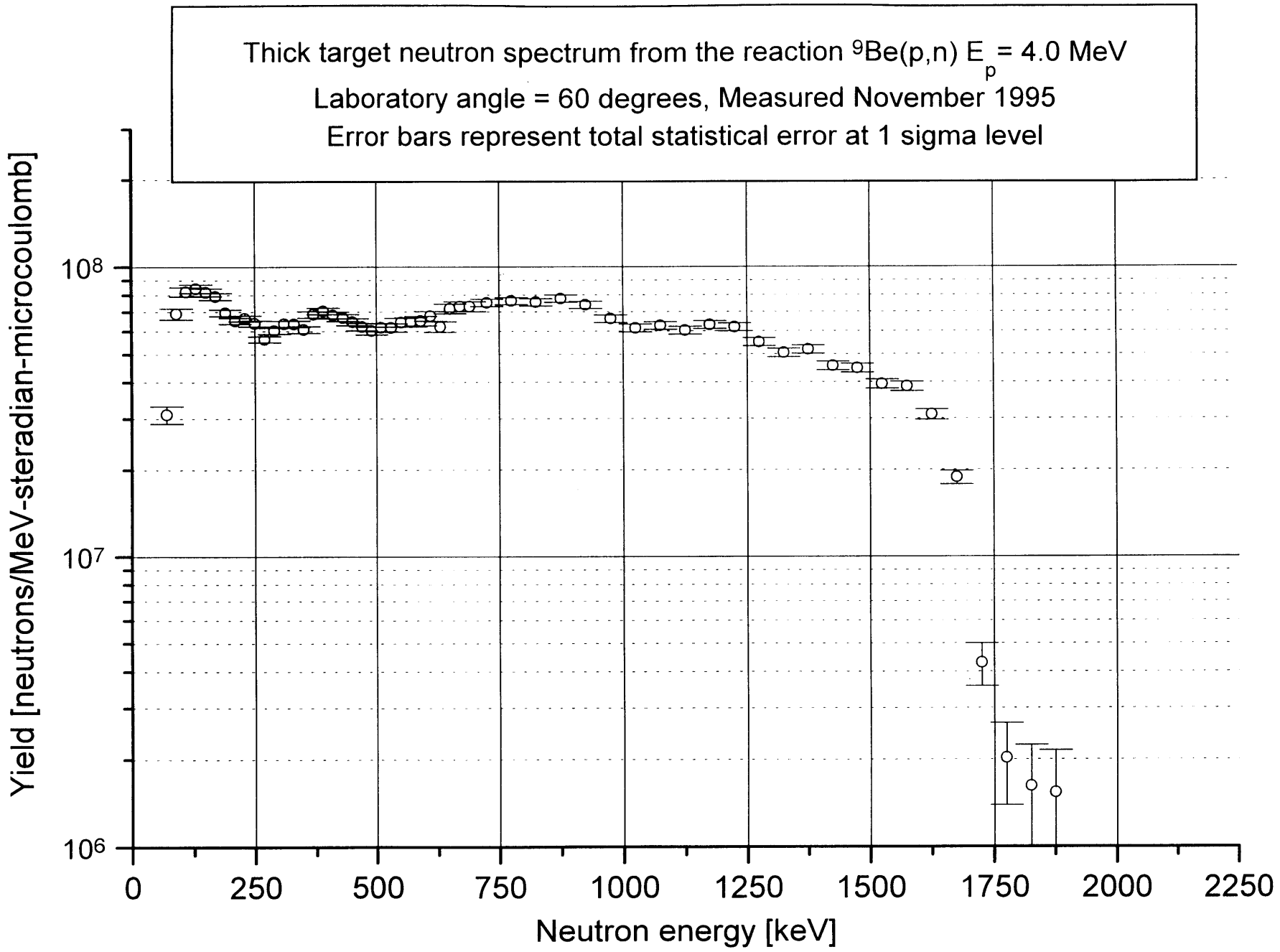
Thick target neutron spectrum from the reaction $^{9}Be(p,n)$ E_p = 4.0 MeV
Laboratory angle = 60 degrees, Measured November 1995
Error bars represent total statistical error at 1 sigma level
Yield [neutrons/MeV-steradian-microcoulomb]
10^8
10^7
10^6
0
250
500
750
1000
1250
1500
1750
2000
2250
Neutron energy [keV]

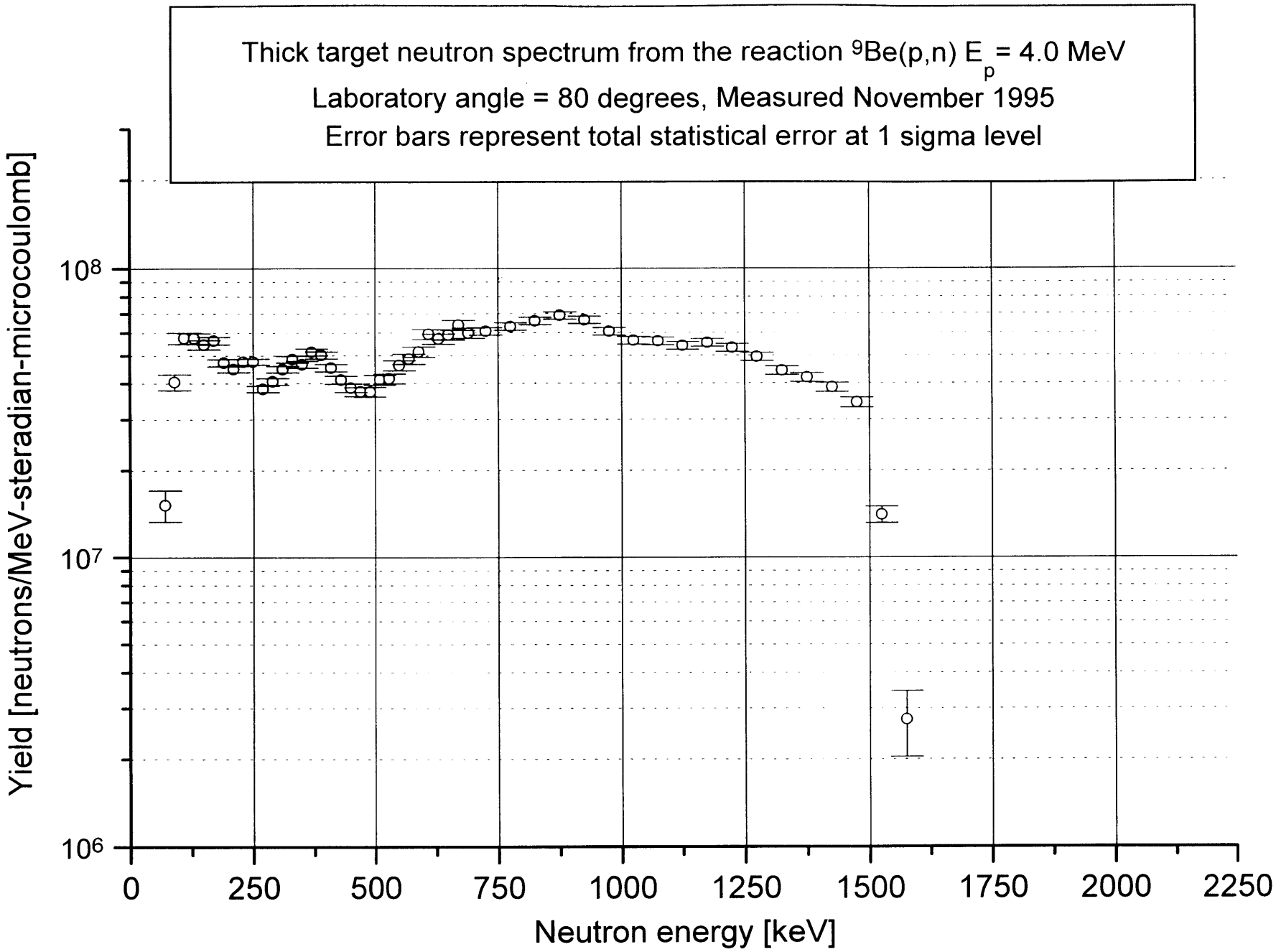
Thick target neutron spectrum from the reaction $^{9}Be(p,n)$ E_p = 4.0 MeV
Laboratory angle = 80 degrees, Measured November 1995
Error bars represent total statistical error at 1 sigma level
Yield [neutrons/MeV-steradian-microcoulomb]
10^8
10^7
10^6
0
250
500
750
1000
1250
1500
1750
2000
2250
Neutron energy [keV]

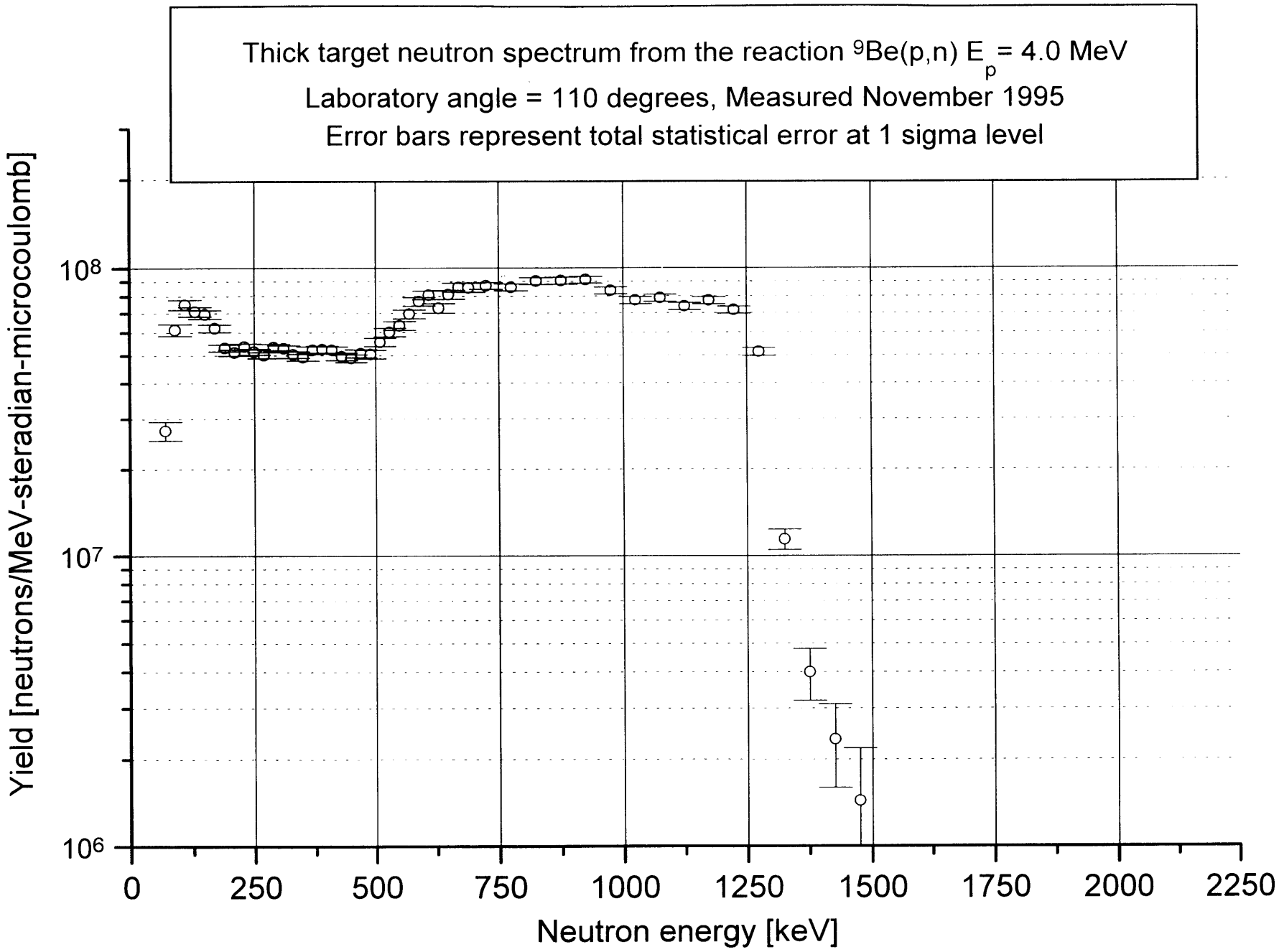
Thick target neutron spectrum from the reaction $^{9}Be(p,n)$ E_p = 4.0 MeV
Laboratory angle = 110 degrees, Measured November 1995
Error bars represent total statistical error at 1 sigma level
Yield [neutrons/MeV-steradian-microcoulomb]
10^8
10^7
10^6
0
250
500
750
1000
1250
1500
1750
2000
2250
Neutron energy [keV]

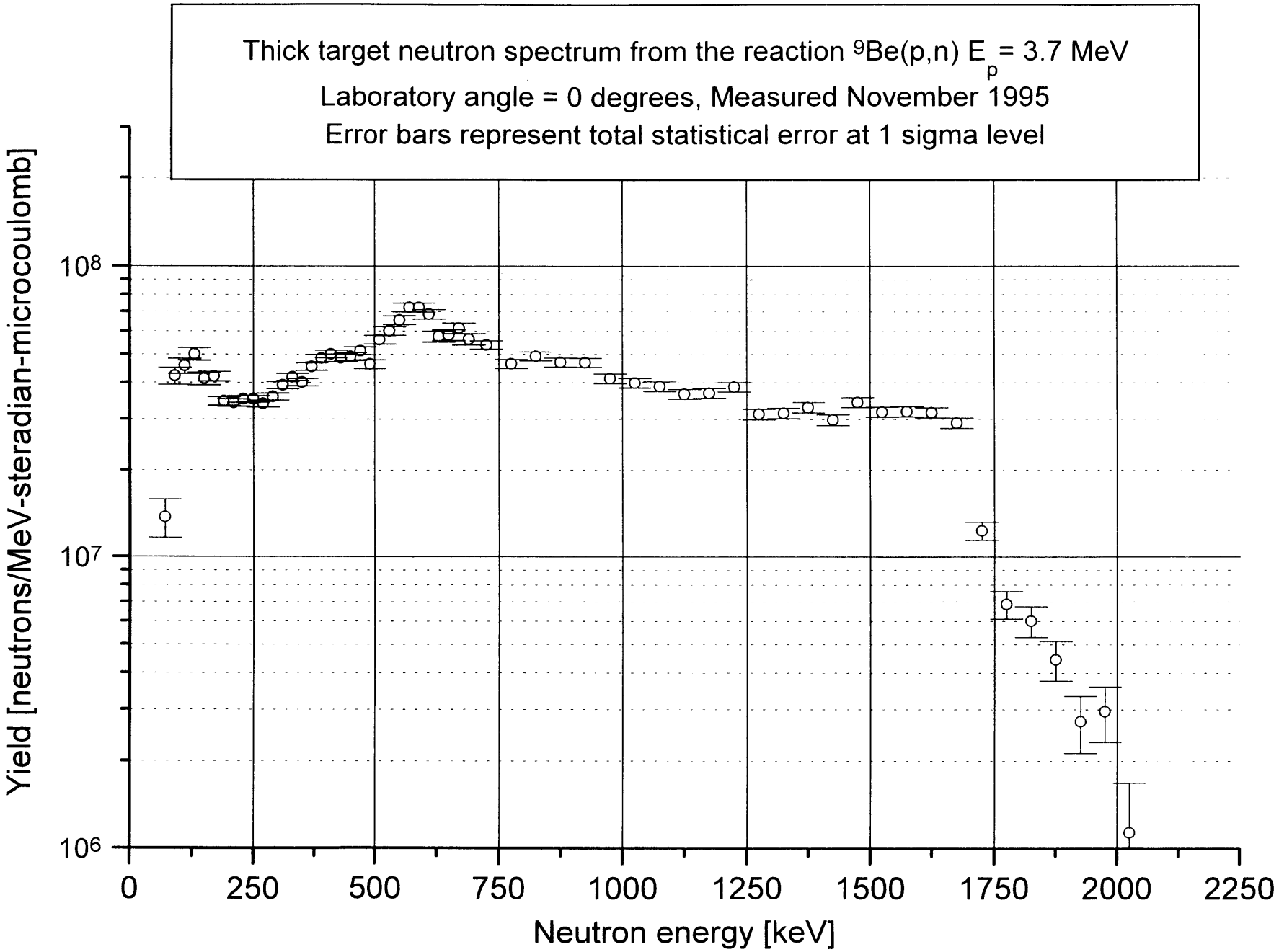
Thick target neutron spectrum from the reaction $^{9}Be(p,n)$ E_p = 3.7 MeV
Laboratory angle = 0 degrees, Measured November 1995
Error bars represent total statistical error at 1 sigma level
Yield [neutrons/MeV-steradian-microcoulomb]
10^8
10^7
10^6
0
250
500
750
1000
1250
1500
1750
2000
2250
Neutron energy [keV]

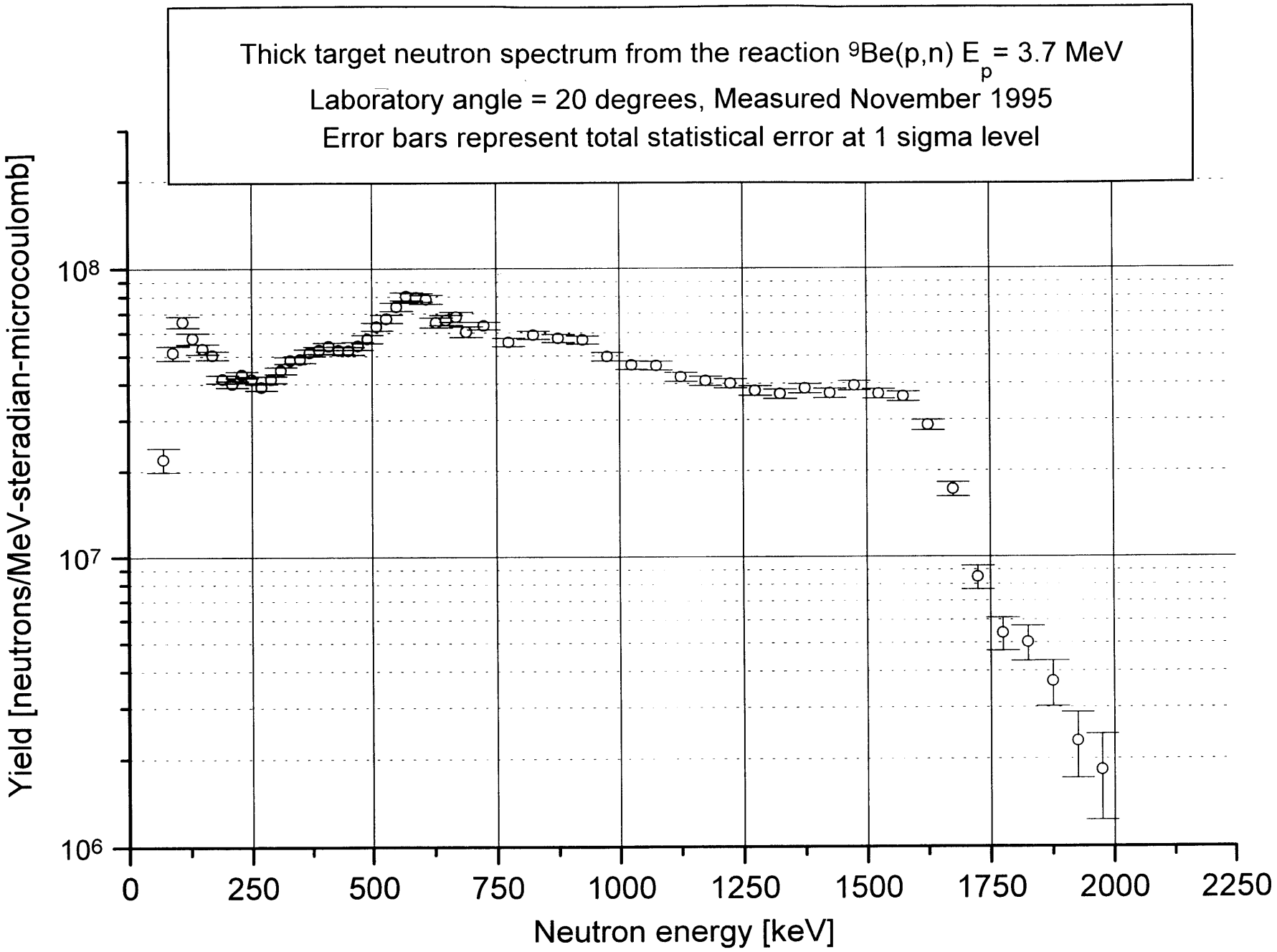
Thick target neutron spectrum from the reaction $^{9}Be(p,n)$ E_p = 3.7 MeV
Laboratory angle = 20 degrees, Measured November 1995
Error bars represent total statistical error at 1 sigma level
Yield [neutrons/MeV-steradian-microcoulomb]
10^8
10^7
10^6
0
250
500
750
1000
1250
1500
1750
2000
2250
Neutron energy [keV]

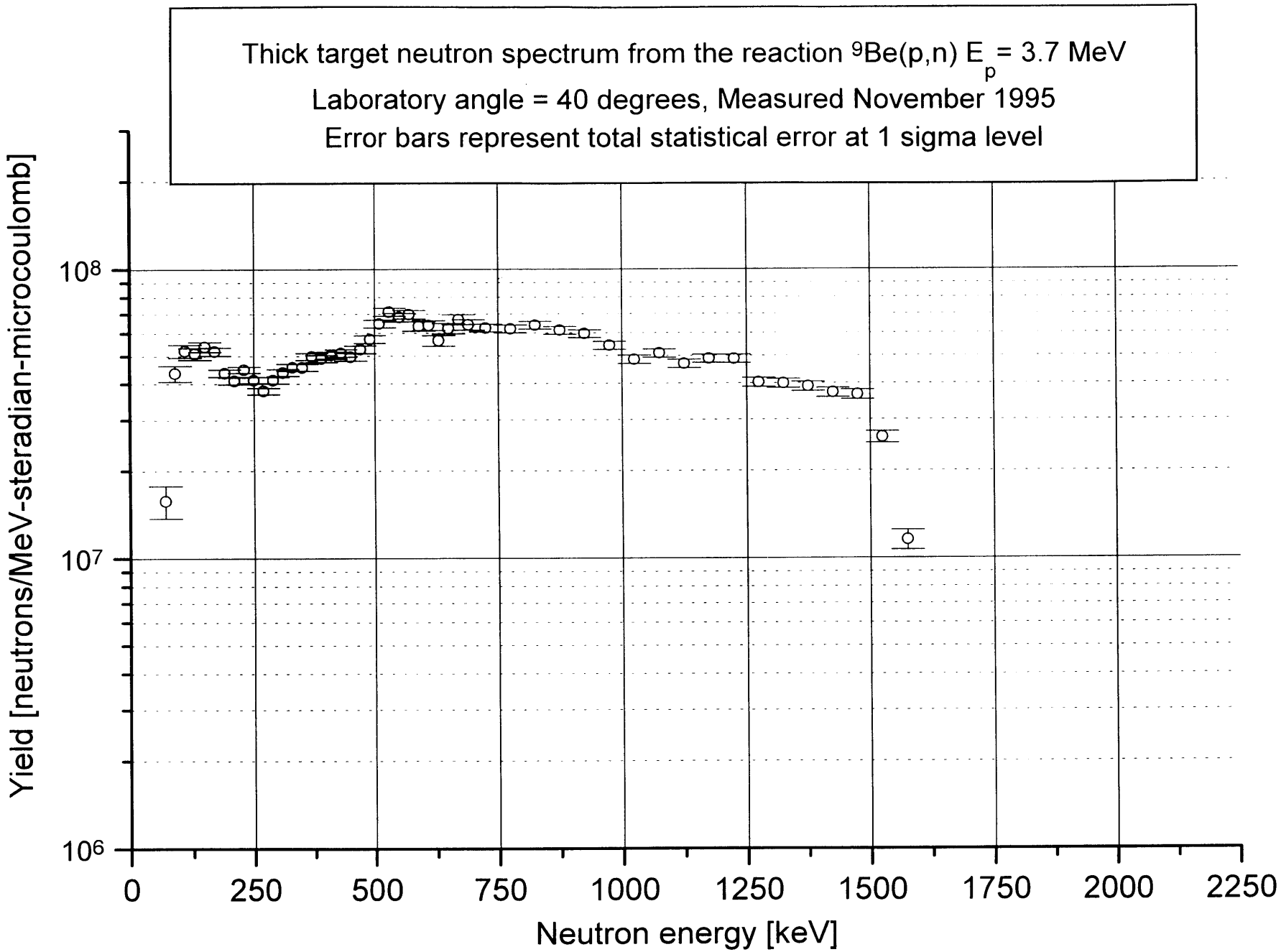
Thick target neutron spectrum from the reaction $^{9}Be(p,n)$ E_p = 3.7 MeV
Laboratory angle = 40 degrees, Measured November 1995
Error bars represent total statistical error at 1 sigma level
Yield [neutrons/MeV-steradian-microcoulomb]
10^8
10^7
10^6
0
250
500
750
1000
1250
1500
1750
2000
2250
Neutron energy [keV]

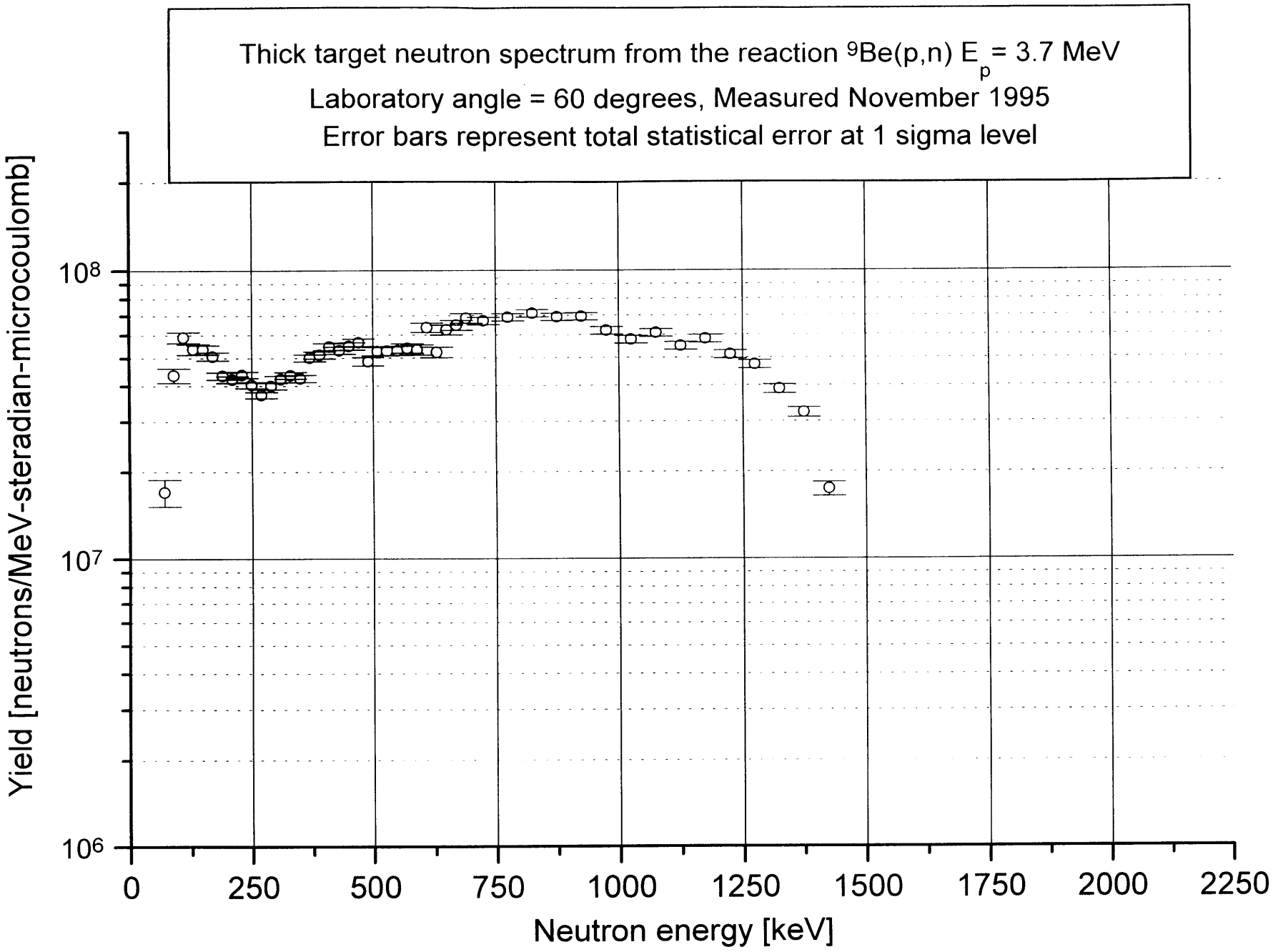
Thick target neutron spectrum from the reaction $^{9}Be(p,n)$ E_p = 3.7 MeV
Laboratory angle = 60 degrees, Measured November 1995
Error bars represent total statistical error at 1 sigma level
Yield [neutrons/MeV-steradian-microcoulomb]
10^8
10^7
10^6
0
250
500
750
1000
1250
1500
1750
2000
2250
Neutron energy [keV]

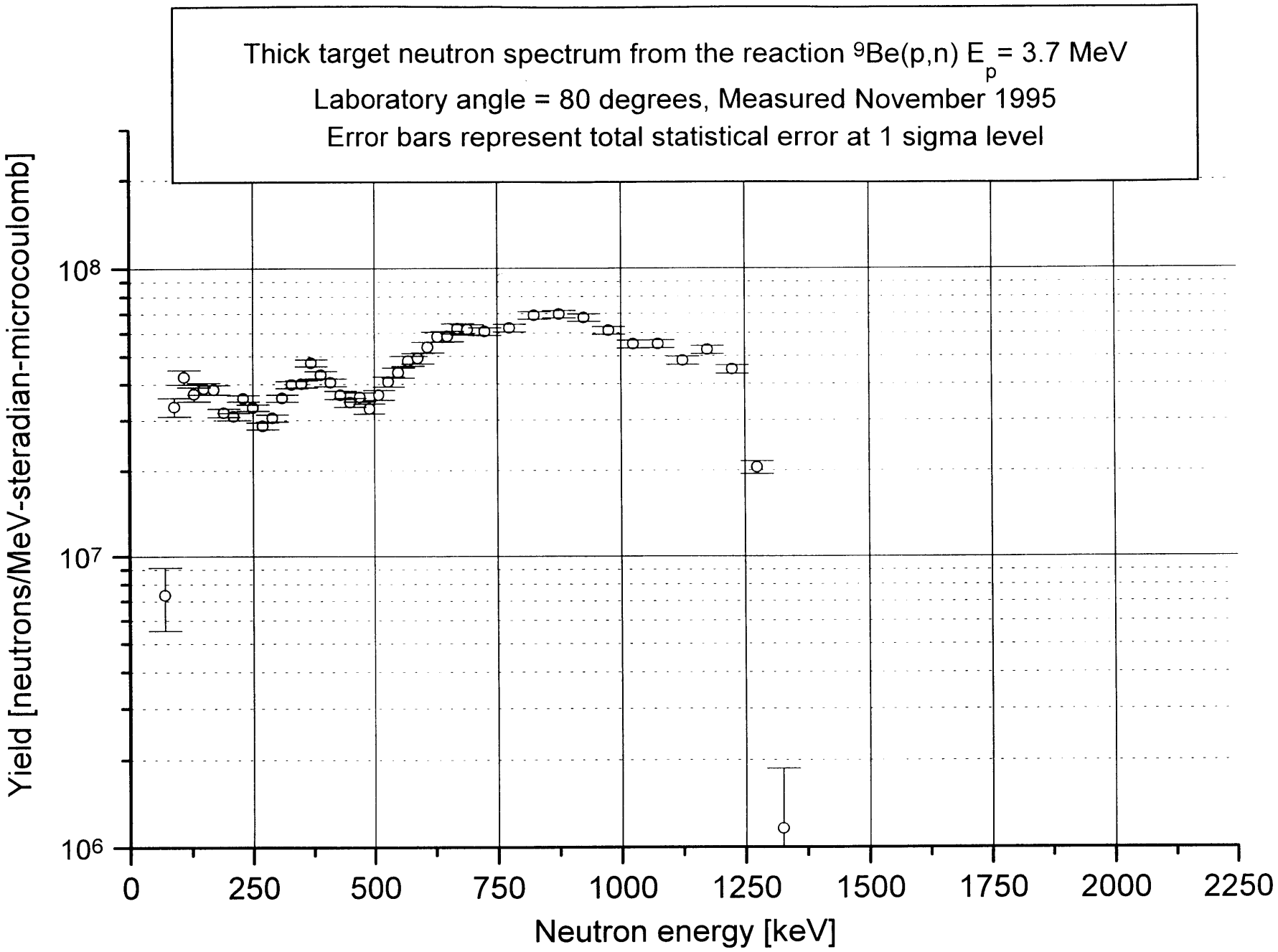
Thick target neutron spectrum from the reaction $^{9}Be(p,n)$ E_p = 3.7 MeV
Laboratory angle = 80 degrees, Measured November 1995
Error bars represent total statistical error at 1 sigma level
Yield [neutrons/MeV-steradian-microcoulomb]
10^8
10^7
10^6
0
250
500
750
1000
1250
1500
1750
2000
2250
Neutron energy [keV]

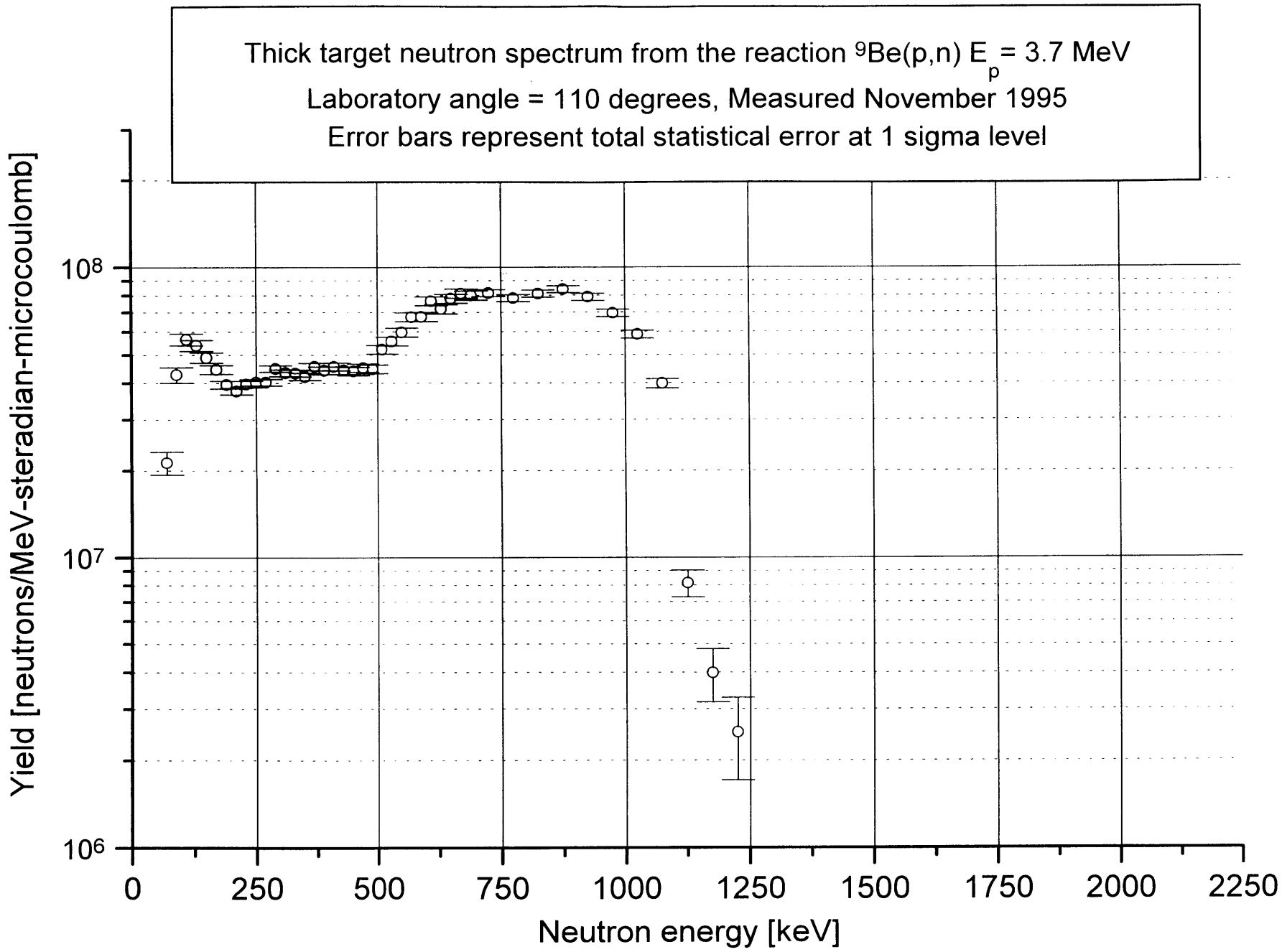
Thick target neutron spectrum from the reaction $^{9}Be(p,n)$ E_p = 3.7 MeV
Laboratory angle = 110 degrees, Measured November 1995
Error bars represent total statistical error at 1 sigma level
Yield [neutrons/MeV-steradian-microcoulomb]
10^8
10^7
10^6
0
250
500
750
1000
1250
1500
1750
2000
2250
Neutron energy [keV]

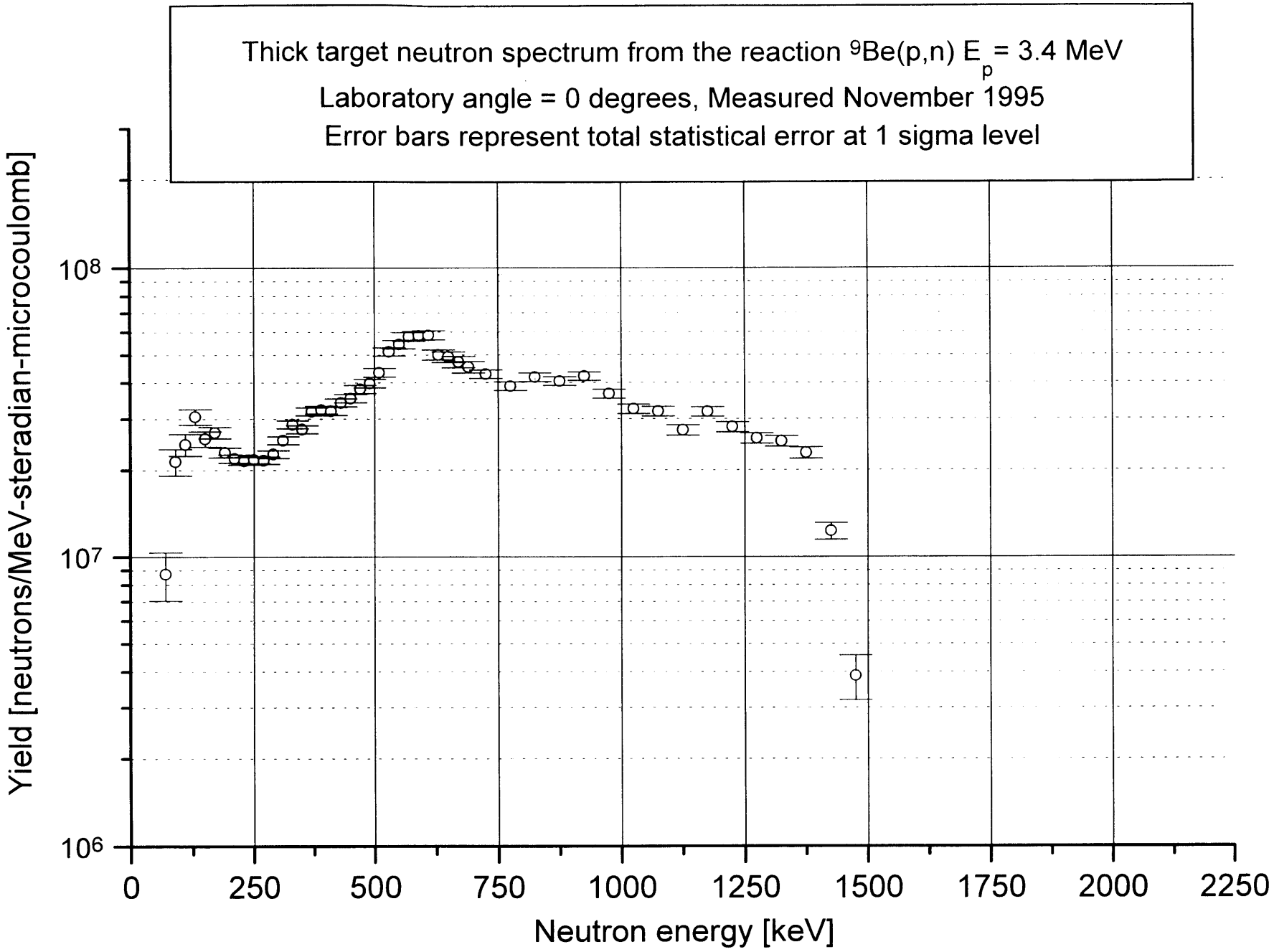
Thick target neutron spectrum from the reaction $^{9}Be(p,n)$ E_p = 3.4 MeV
Laboratory angle = 0 degrees, Measured November 1995
Error bars represent total statistical error at 1 sigma level
Yield [neutrons/MeV-steradian-microcoulomb]
10^8
10^7
10^6
0
250
500
750
1000
1250
1500
1750
2000
2250
Neutron energy [keV]

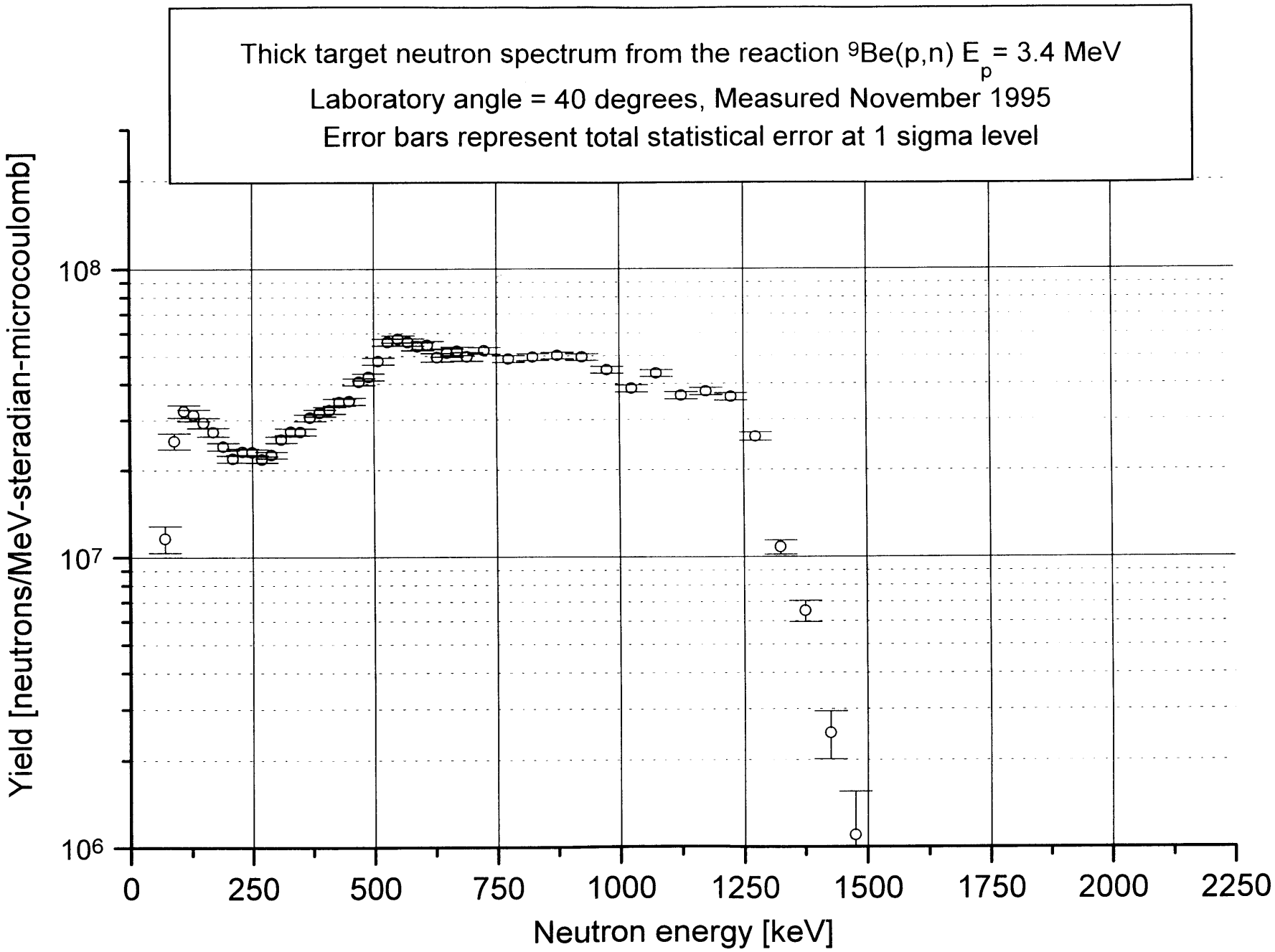
Thick target neutron spectrum from the reaction $^{9}Be(p,n)$ E_p = 3.4 MeV
Laboratory angle = 40 degrees, Measured November 1995
Error bars represent total statistical error at 1 sigma level
Yield [neutrons/MeV-steradian-microcoulomb]
10^8
10^7
10^6
0
250
500
750
1000
1250
1500
1750
2000
2250
Neutron energy [keV]

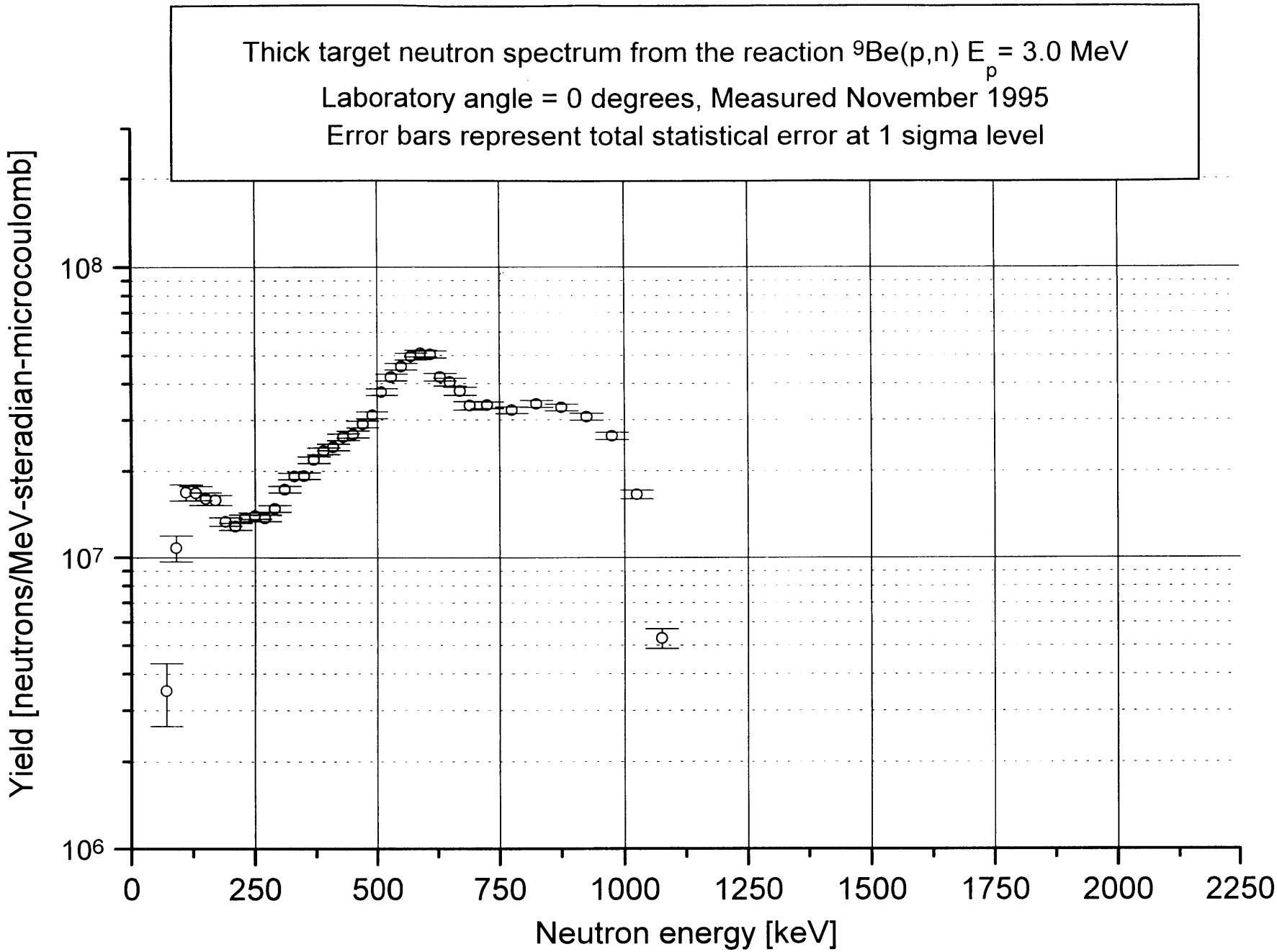
Thick target neutron spectrum from the reaction $^{9}Be(p,n)$ E_p = 3.0 MeV
Laboratory angle = 0 degrees, Measured November 1995
Error bars represent total statistical error at 1 sigma level
Yield [neutrons/MeV-steradian-microcoulomb]
10^8
10^7
10^6
0
250
500
750
1000
1250
1500
1750
2000
2250
Neutron energy [keV]

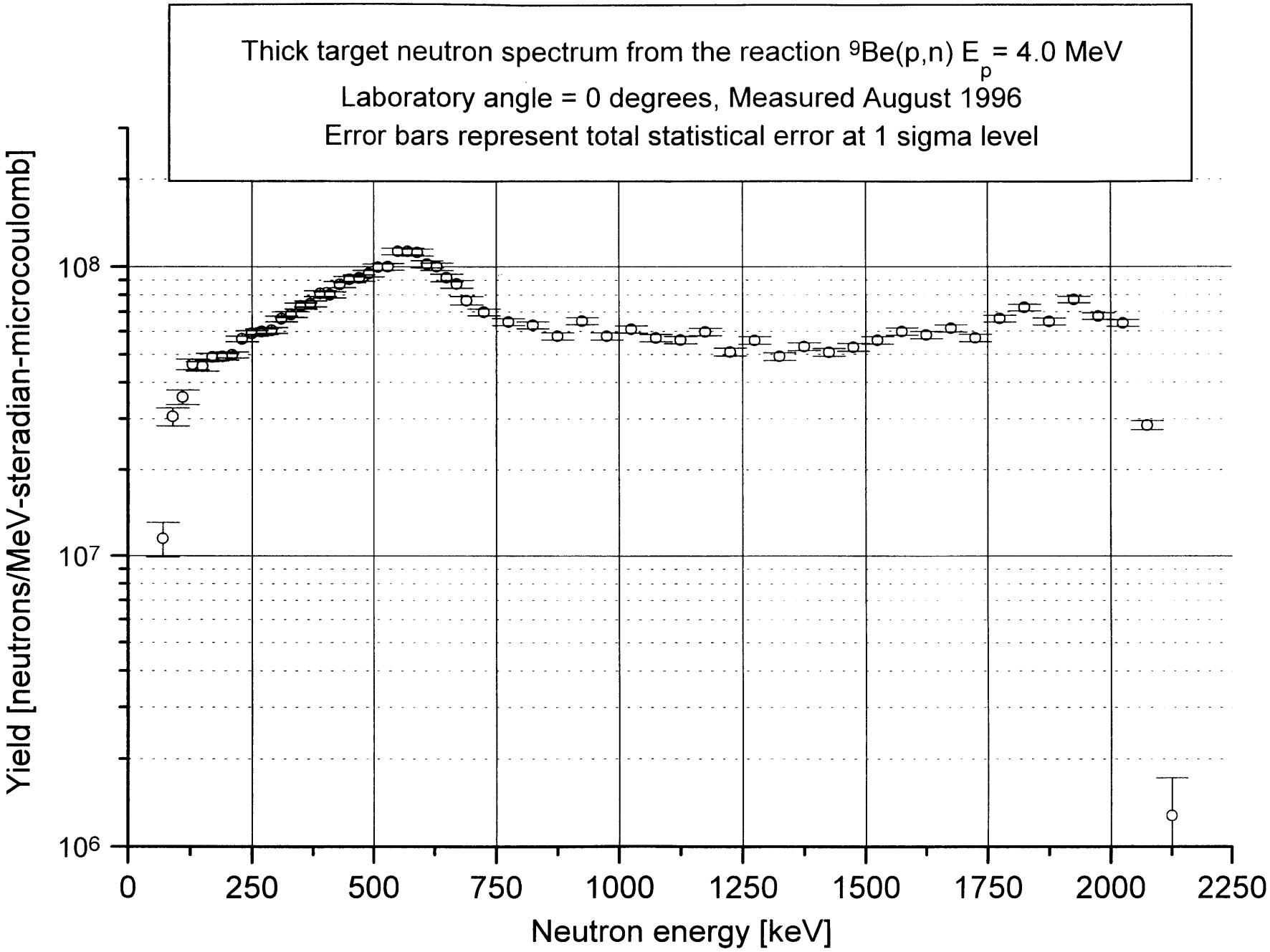
Thick target neutron spectrum from the reaction $^{9}Be(p,n)$ E_p = 4.0 MeV
Laboratory angle = 0 degrees, Measured August 1996
Error bars represent total statistical error at 1 sigma level
Yield [neutrons/MeV-steradian-microcoulomb]
10^8
10^7
10^6
0
250
500
750
1000
1250
1500
1750
2000
2250
Neutron energy [keV]

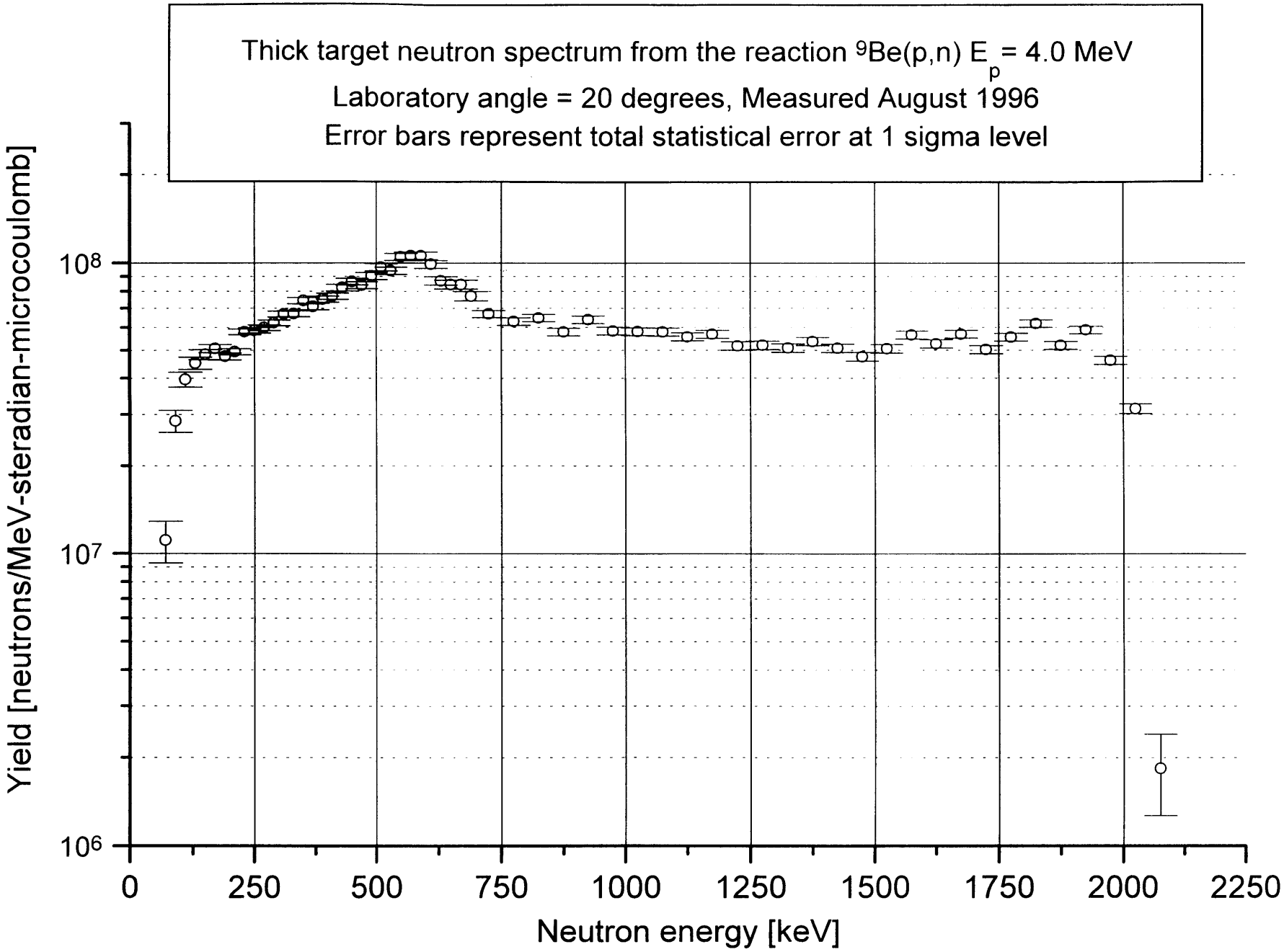
Thick target neutron spectrum from the reaction $^{9}Be(p,n)$ E_p = 4.0 MeV
Laboratory angle = 20 degrees, Measured August 1996
Error bars represent total statistical error at 1 sigma level
Yield [neutrons/MeV-steradian-microcoulomb]
10^8
10^7
10^6
0
250
500
750
1000
1250
1500
1750
2000
2250
Neutron energy [keV]

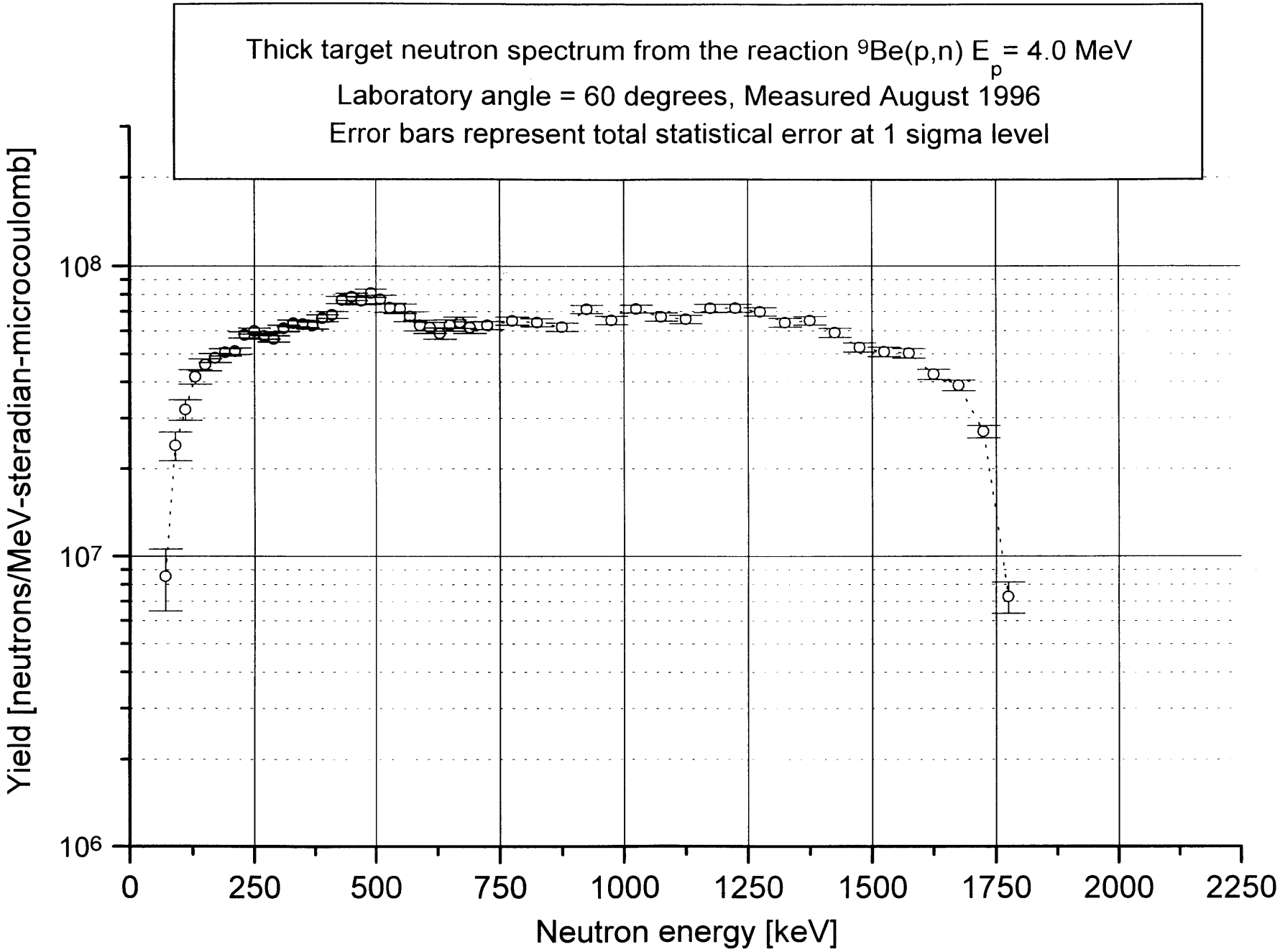
Thick target neutron spectrum from the reaction $^{9}Be(p,n)$ E_p = 4.0 MeV
Laboratory angle = 60 degrees, Measured August 1996
Error bars represent total statistical error at 1 sigma level
Yield [neutrons/MeV-steradian-microcoulomb]
10^8
10^7
10^6
0
250
500
750
1000
1250
1500
1750
2000
2250
Neutron energy [keV]

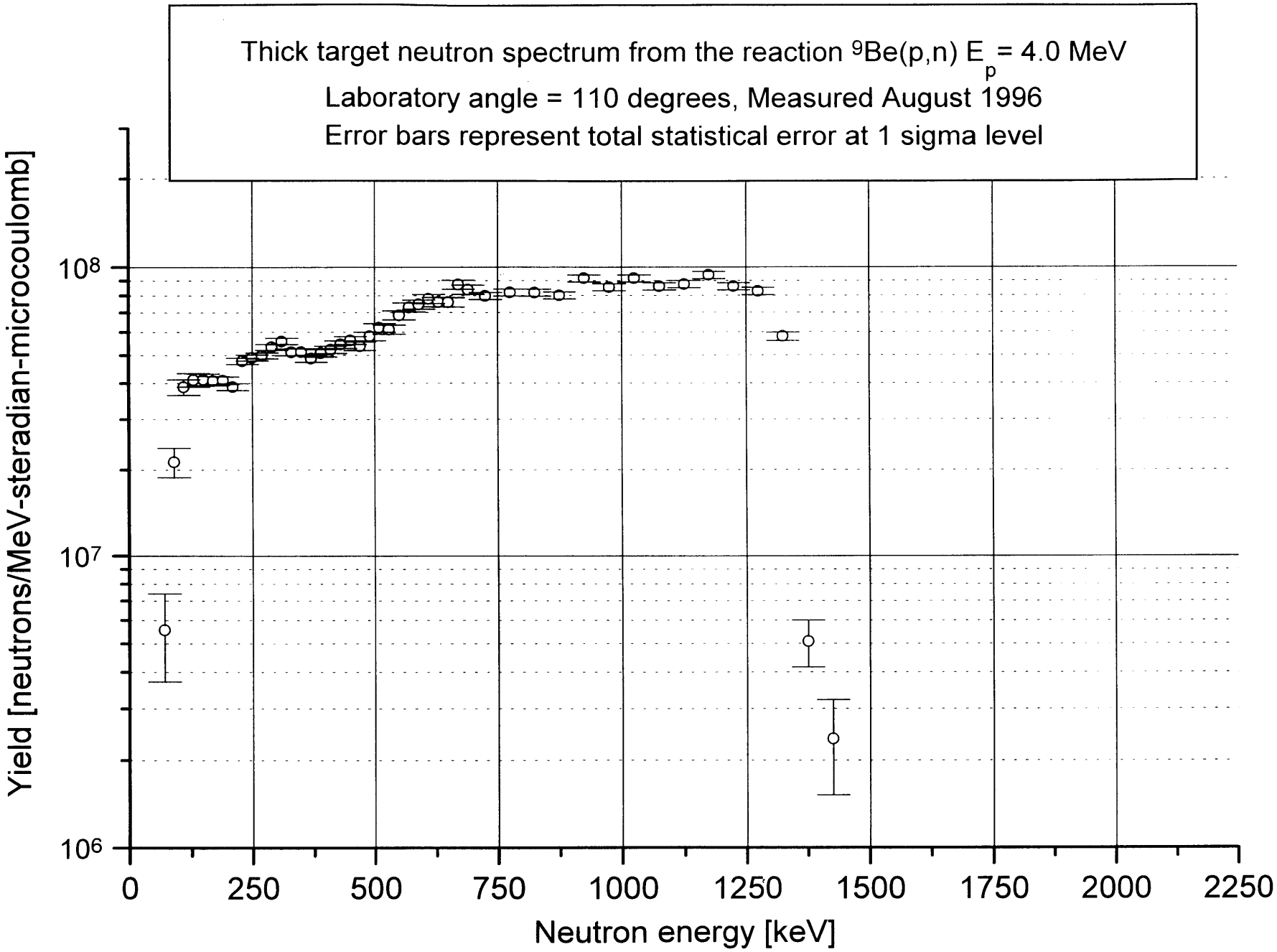
Thick target neutron spectrum from the reaction $^{9}Be(p,n)$ E_p = 4.0 MeV
Laboratory angle = 110 degrees, Measured August 1996
Error bars represent total statistical error at 1 sigma level
Yield [neutrons/MeV-steradian-microcoulomb]
10^8
10^7
10^6
0
250
500
750
1000
1250
1500
1750
2000
2250
Neutron energy [keV]

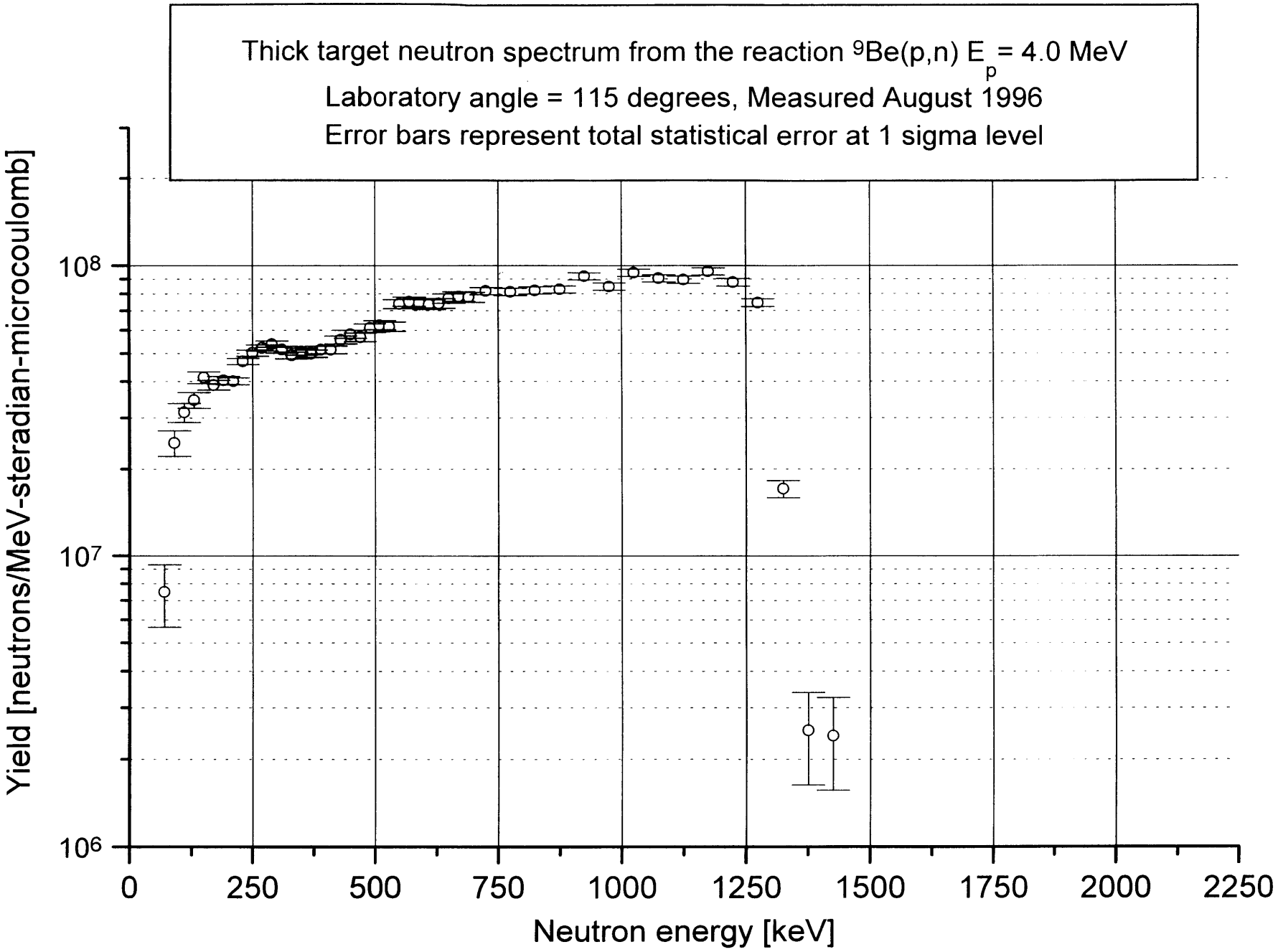
Thick target neutron spectrum from the reaction $^{9}Be(p,n)$ E_p = 4.0 MeV
Laboratory angle = 115 degrees, Measured August 1996
Error bars represent total statistical error at 1 sigma level
Yield [neutrons/MeV-steradian-microcoulomb]
10^8
10^7
10^6
0
250
500
750
1000
1250
1500
1750
2000
2250
Neutron energy [keV]

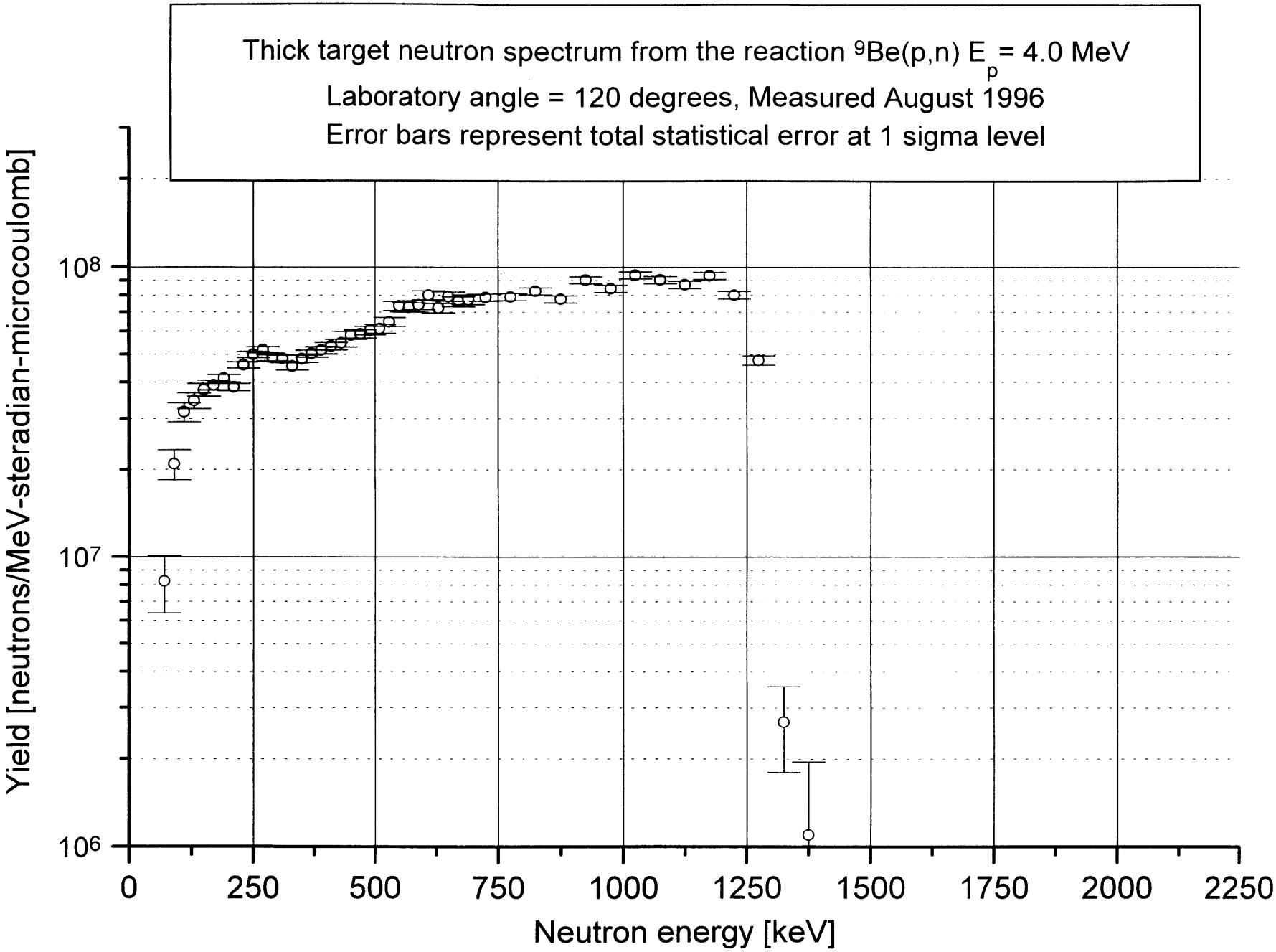
Thick target neutron spectrum from the reaction $^{9}Be(p,n)$ E_p = 4.0 MeV
Laboratory angle = 120 degrees, Measured August 1996
Error bars represent total statistical error at 1 sigma level
Yield [neutrons/MeV-steradian-microcoulomb]
10^8
10^7
10^6
0
250
500
750
1000
1250
1500
1750
2000
2250
Neutron energy [keV]

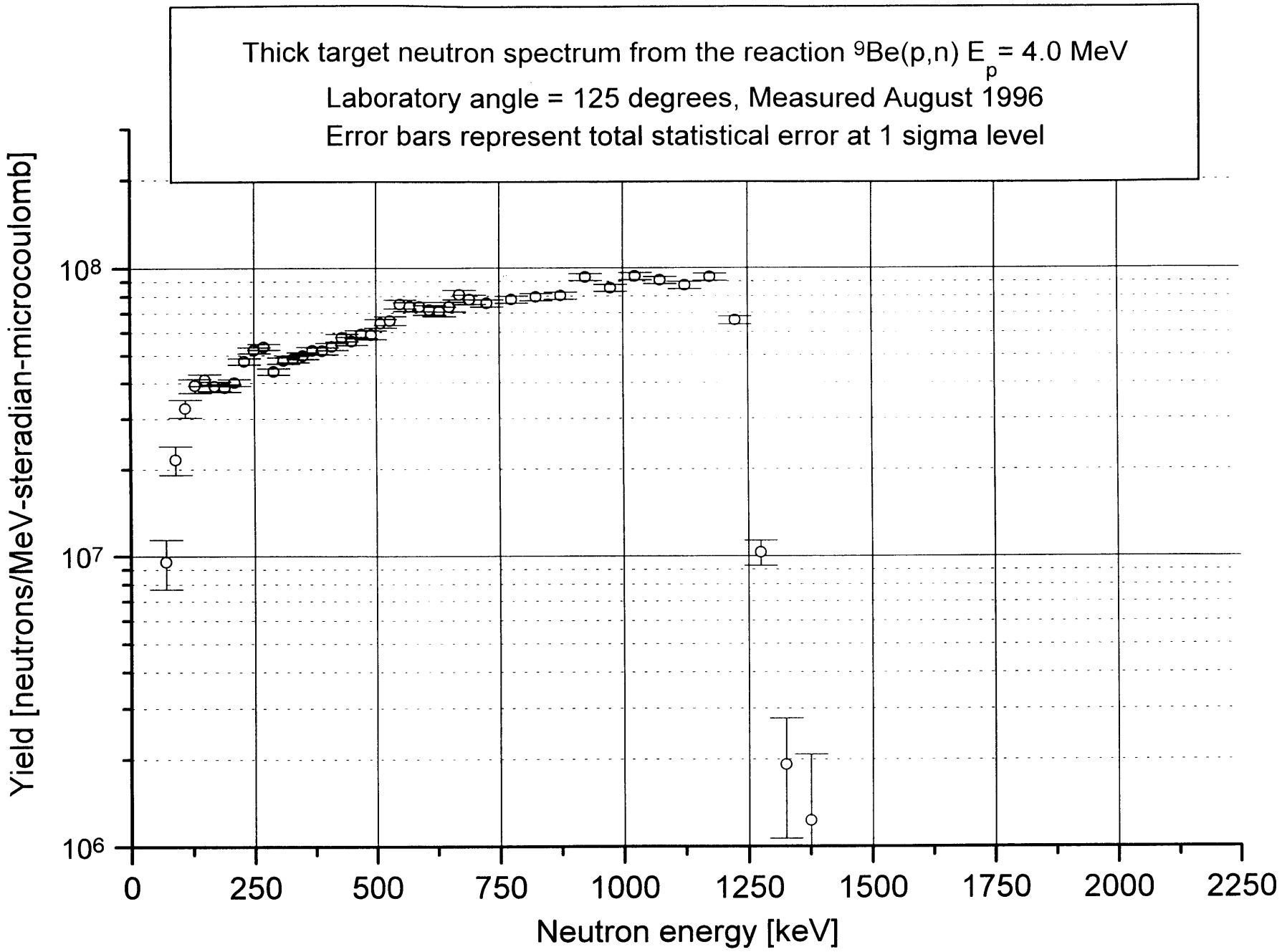
Thick target neutron spectrum from the reaction $^{9}Be(p,n)$ E_p = 4.0 MeV
Laboratory angle = 125 degrees, Measured August 1996
Error bars represent total statistical error at 1 sigma level
Yield [neutrons/MeV-steradian-microcoulomb]
10^8
10^7
10^6
0
250
500
750
1000
1250
1500
1750
2000
2250
Neutron energy [keV]

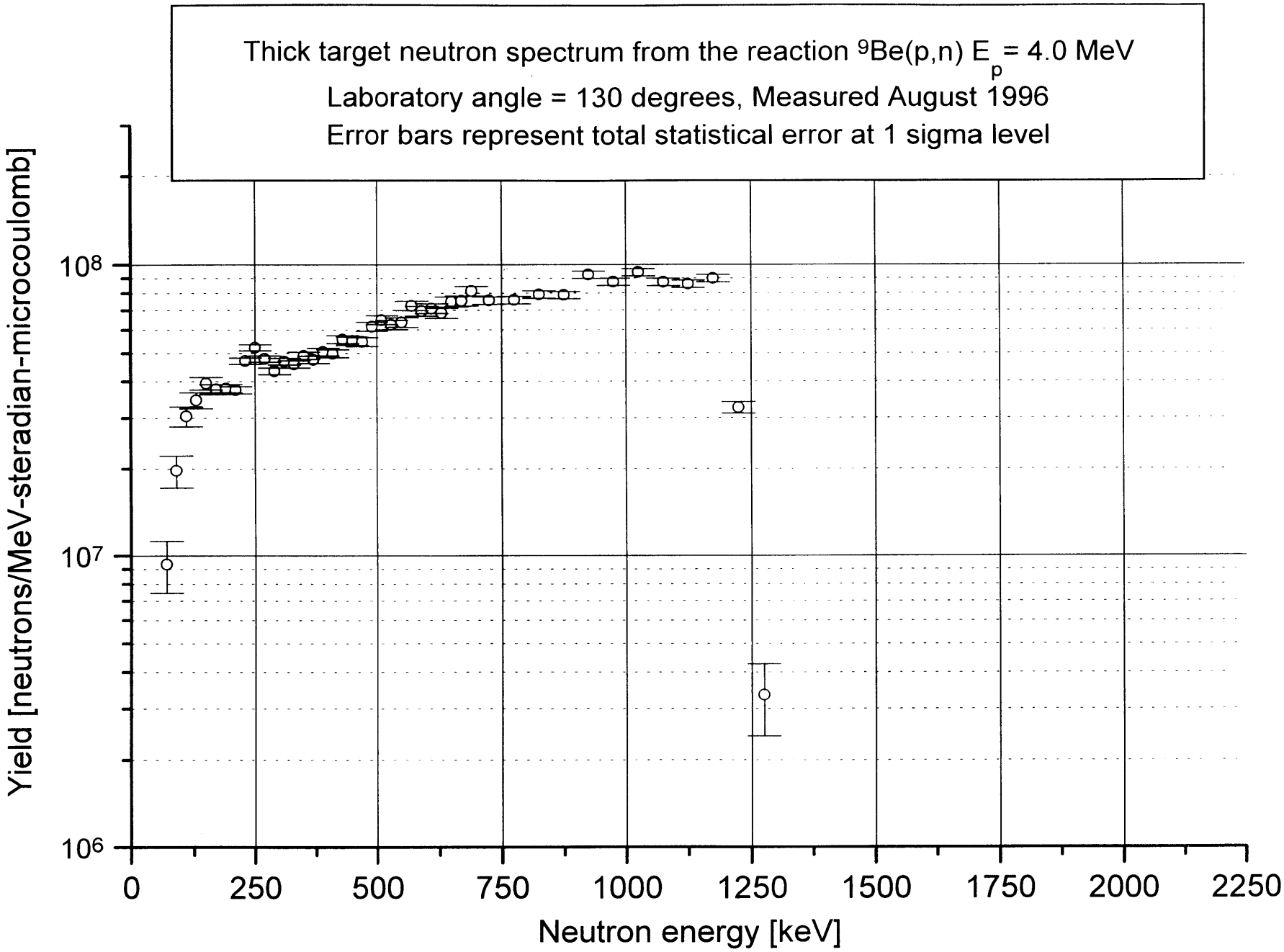
Thick target neutron spectrum from the reaction $^{9}Be(p,n)$ E_p = 4.0 MeV
Laboratory angle = 130 degrees, Measured August 1996
Error bars represent total statistical error at 1 sigma level
Yield [neutrons/MeV-steradian-microcoulomb]
10^8
10^7
10^6
0
250
500
750
1000
1250
1500
1750
2000
2250
Neutron energy [keV]

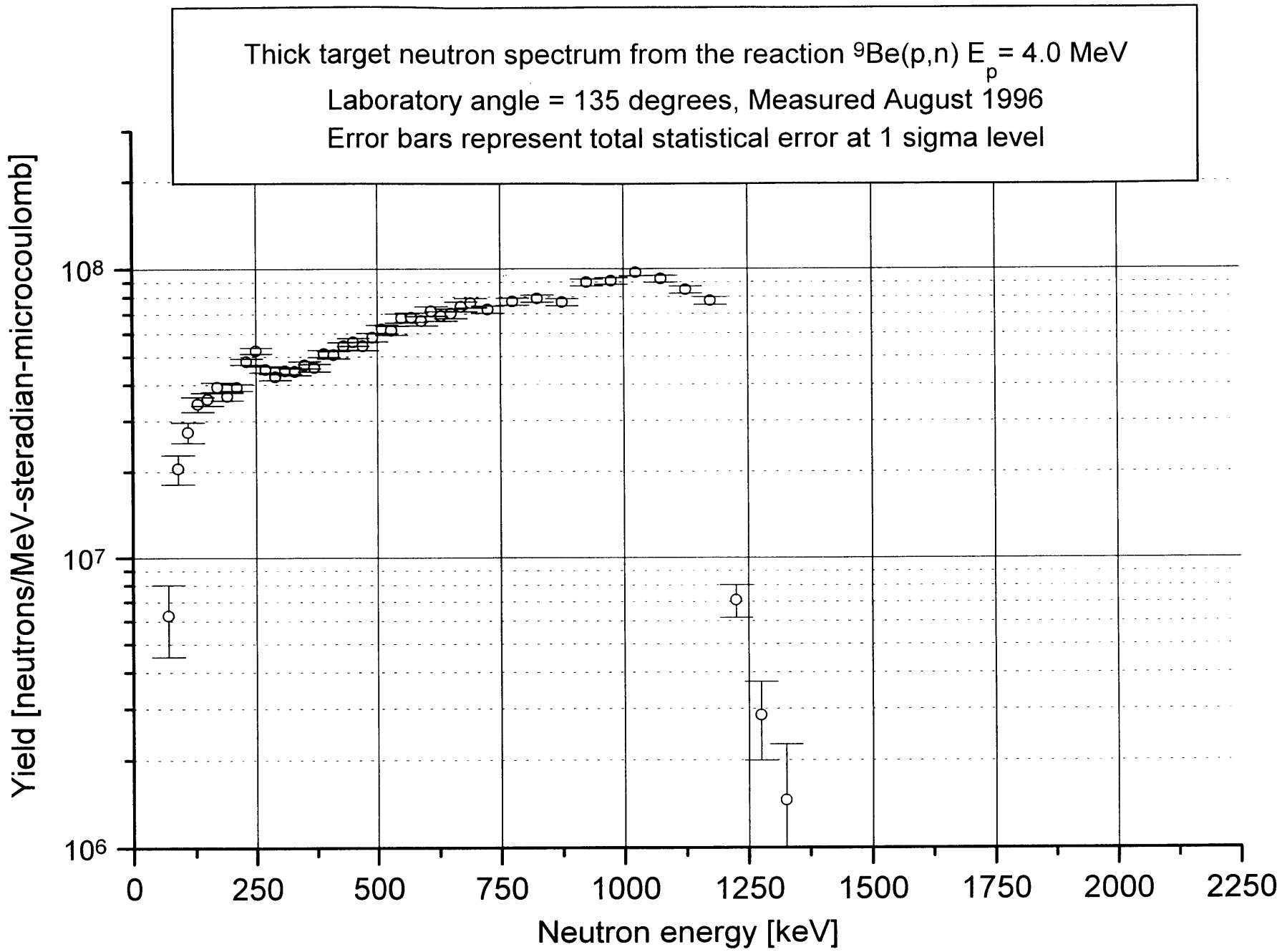
Thick target neutron spectrum from the reaction $^{9}Be(p,n)$ E_p = 4.0 MeV
Laboratory angle = 135 degrees, Measured August 1996
Error bars represent total statistical error at 1 sigma level
Yield [neutrons/MeV-steradian-microcoulomb]
10^8
10^7
10^6
0
250
500
750
1000
1250
1500
1750
2000
2250
Neutron energy [keV]

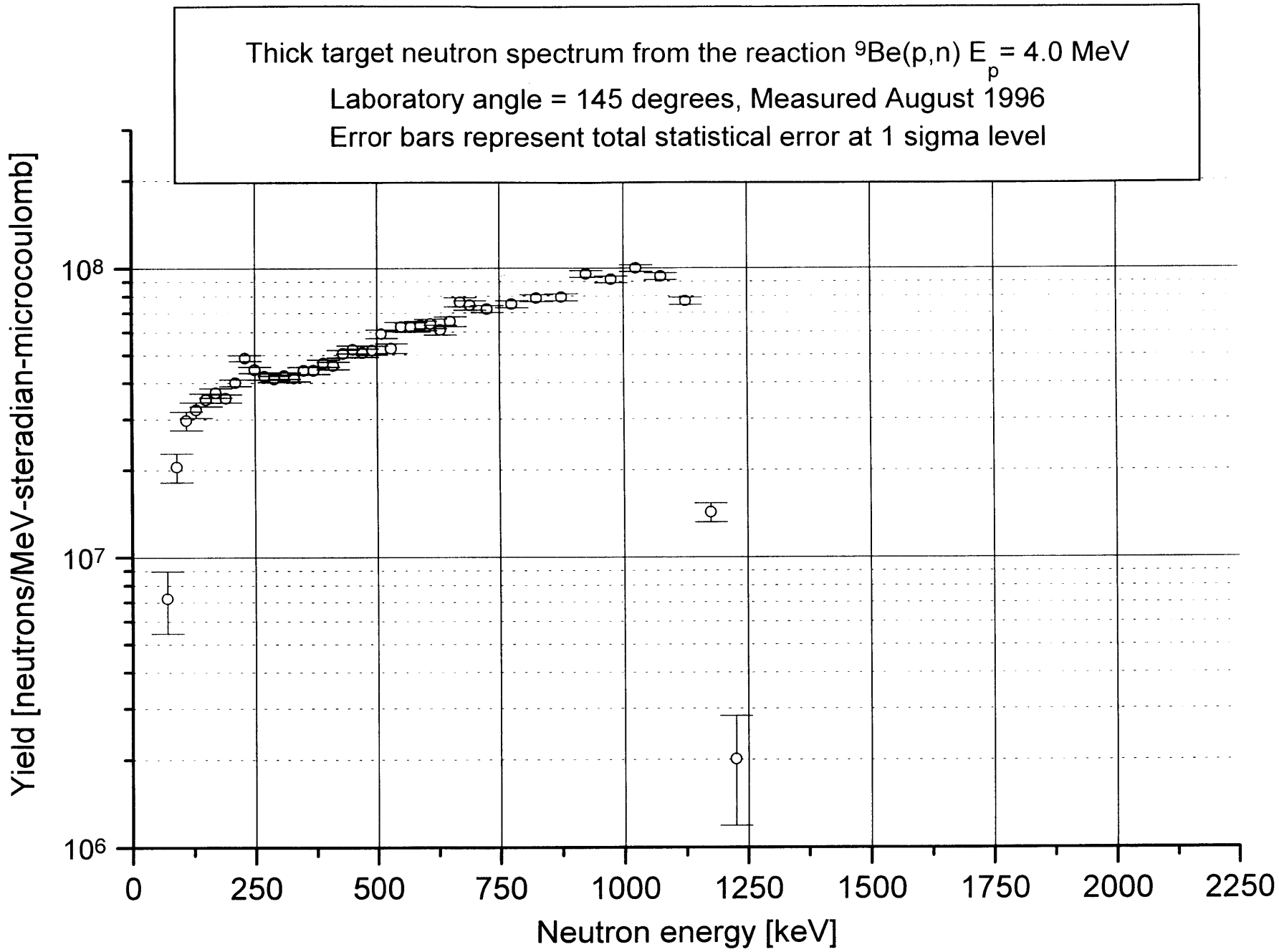
Thick target neutron spectrum from the reaction $^{9}Be(p,n)$ E_p = 4.0 MeV
Laboratory angle = 145 degrees, Measured August 1996
Error bars represent total statistical error at 1 sigma level
Yield [neutrons/MeV-steradian-microcoulomb]
10^8
10^7
10^6
0
250
500
750
1000
1250
1500
1750
2000
2250
Neutron energy [keV]

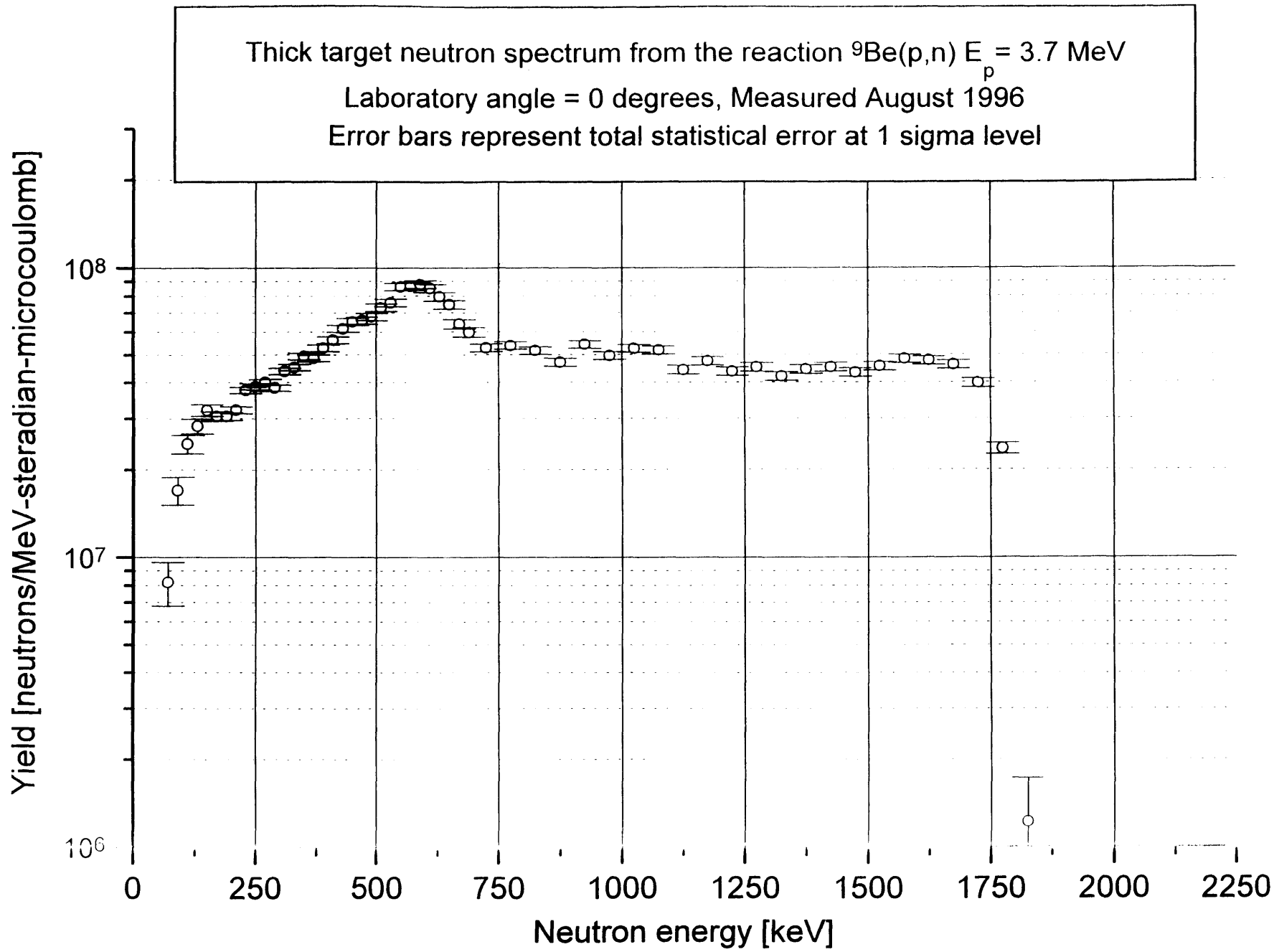
Thick target neutron spectrum from the reaction $^{9}Be(p,n)$ E_p = 3.7 MeV
Laboratory angle = 0 degrees, Measured August 1996
Error bars represent total statistical error at 1 sigma level
Yield [neutrons/MeV-steradian-microcoulomb]
10^8
10^7
10^6
0
250
500
750
1000
1250
1500
1750
2000
2250
Neutron energy [keV]

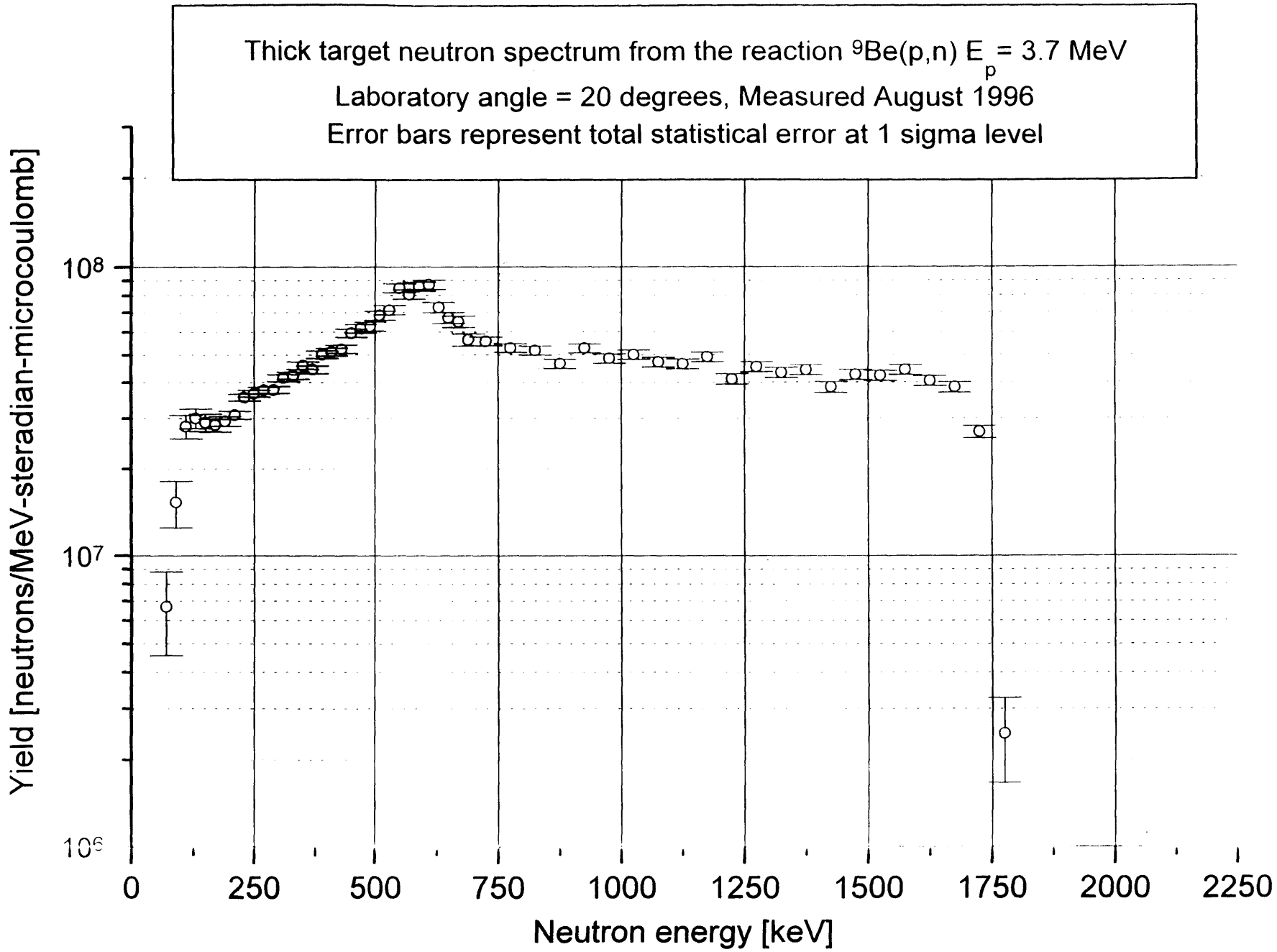
Thick target neutron spectrum from the reaction $^{9}Be(p,n)$ E_p = 3.7 MeV
Laboratory angle = 20 degrees, Measured August 1996
Error bars represent total statistical error at 1 sigma level
Yield [neutrons/MeV-steradian-microcoulomb]
10^8
10^7
10^6
0
250
500
750
1000
1250
1500
1750
2000
2250
Neutron energy [keV]

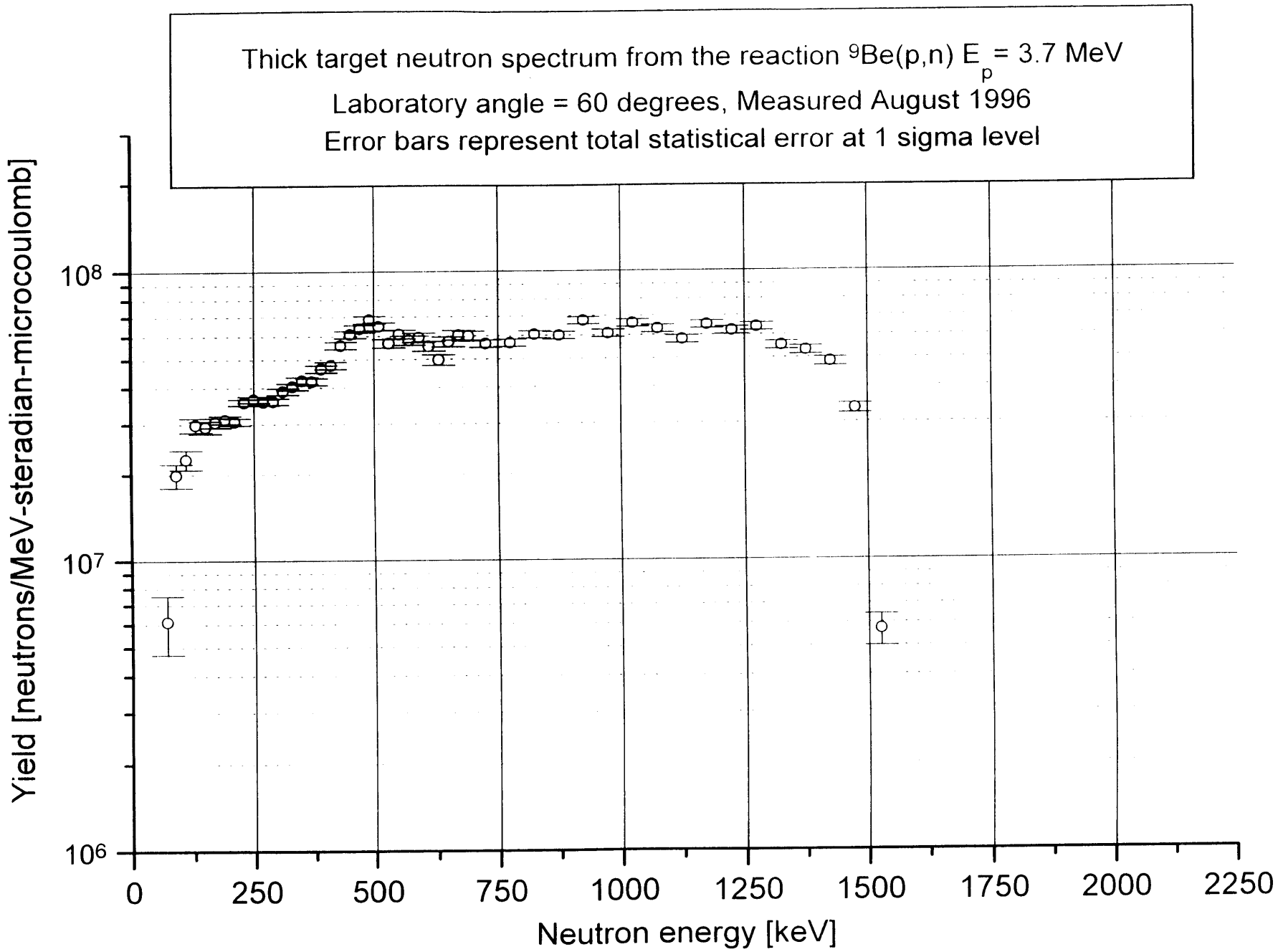
Thick target neutron spectrum from the reaction $^{9}Be(p,n)$ E_p = 3.7 MeV
Laboratory angle = 60 degrees, Measured August 1996
Error bars represent total statistical error at 1 sigma level
Yield [neutrons/MeV-steradian-microcoulomb]
10^8
10^7
10^6
0
250
500
750
1000
1250
1500
1750
2000
2250
Neutron energy [keV]

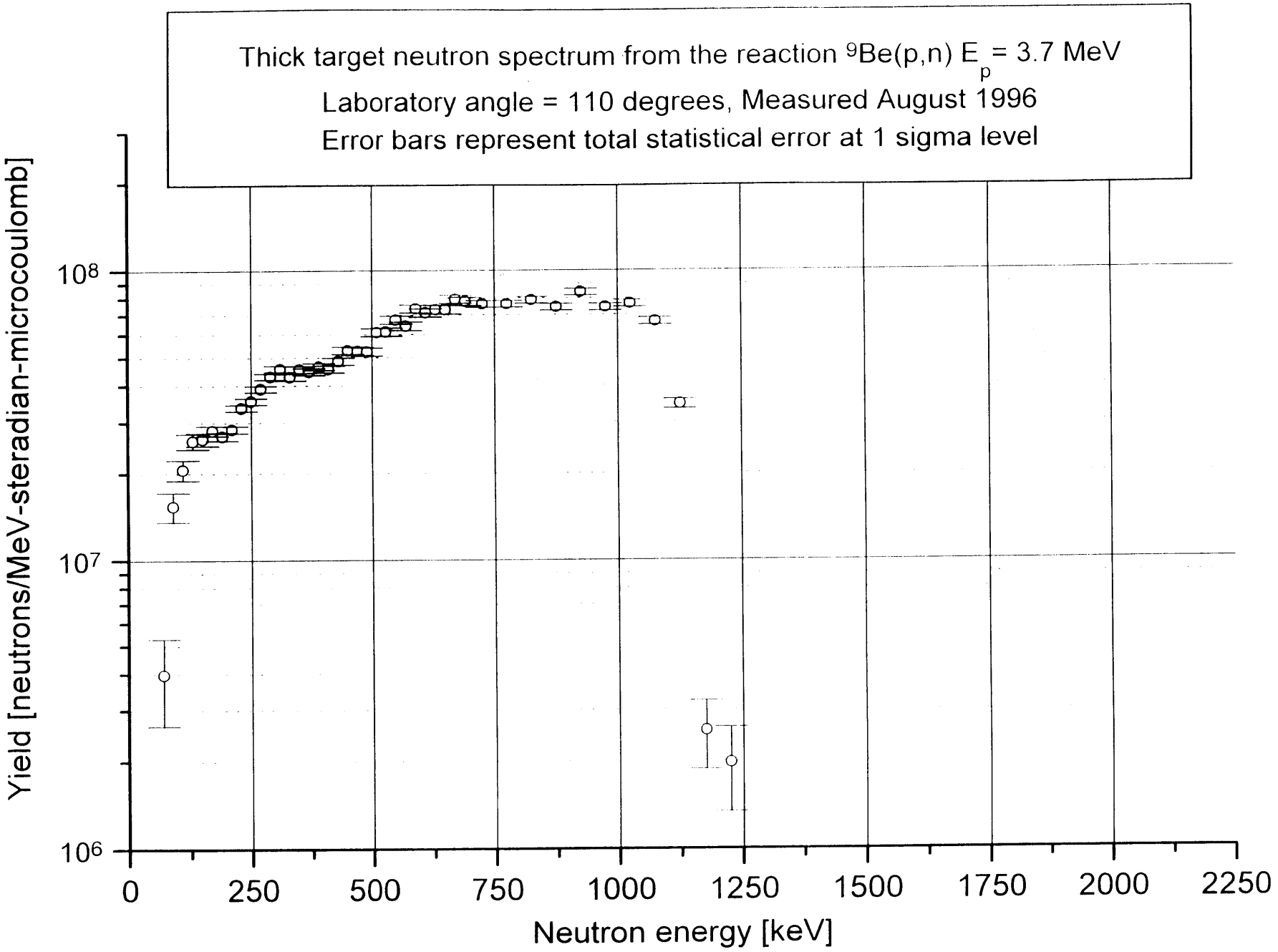
Thick target neutron spectrum from the reaction $^{9}Be(p,n)$ E_p = 3.7 MeV
Laboratory angle = 110 degrees, Measured August 1996
Error bars represent total statistical error at 1 sigma level
Yield [neutrons/MeV-steradian-microcoulomb]
10^8
10^7
10^6
0
250
500
750
1000
1250
1500
1750
2000
2250
Neutron energy [keV]

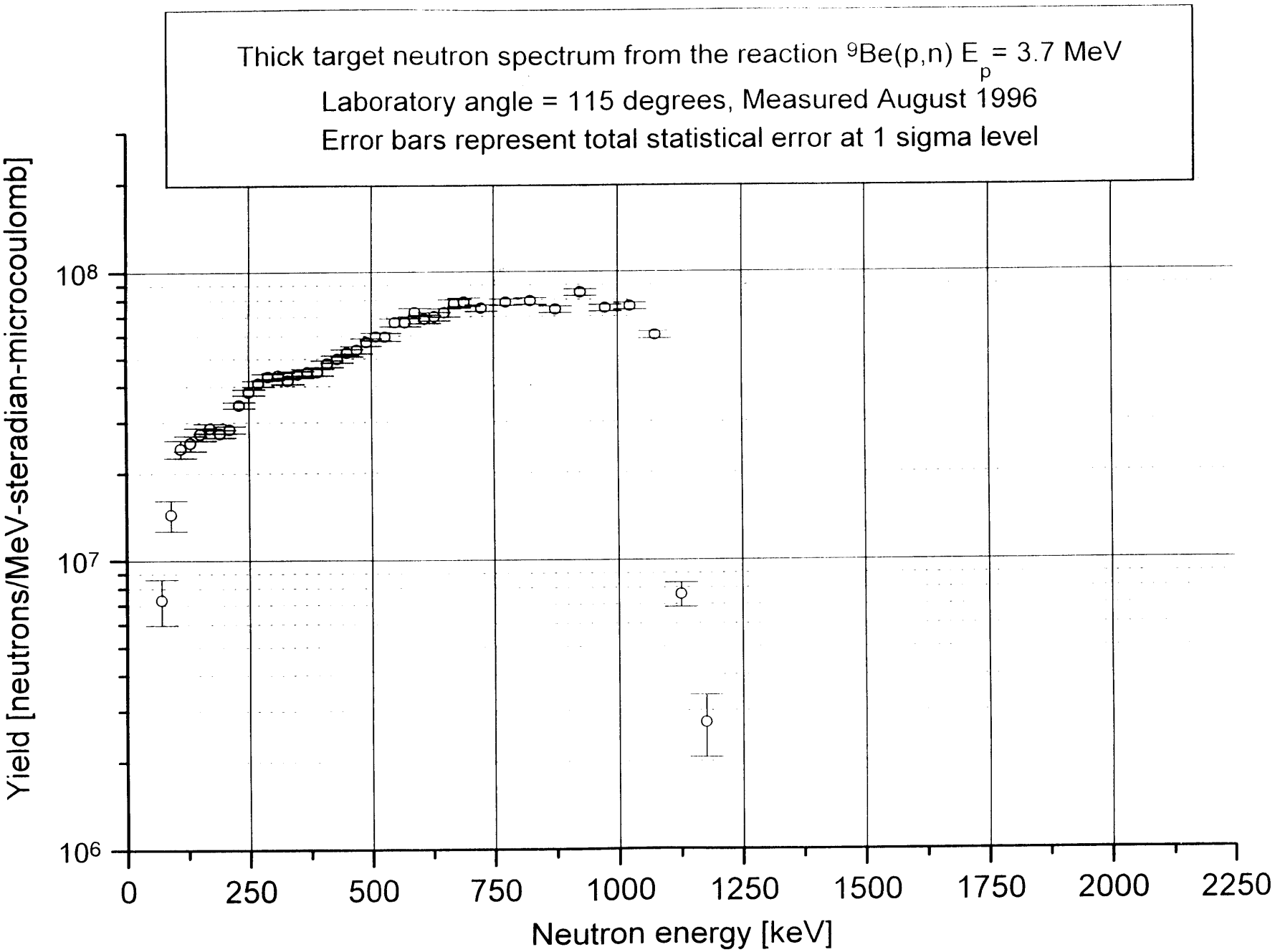
Thick target neutron spectrum from the reaction $^{9}Be(p,n)$ E_p = 3.7 MeV
Laboratory angle = 115 degrees, Measured August 1996
Error bars represent total statistical error at 1 sigma level
Yield [neutrons/MeV-steradian-microcoulomb]
10^8
10^7
10^6
0
250
500
750
1000
1250
1500
1750
2000
2250
Neutron energy [keV]

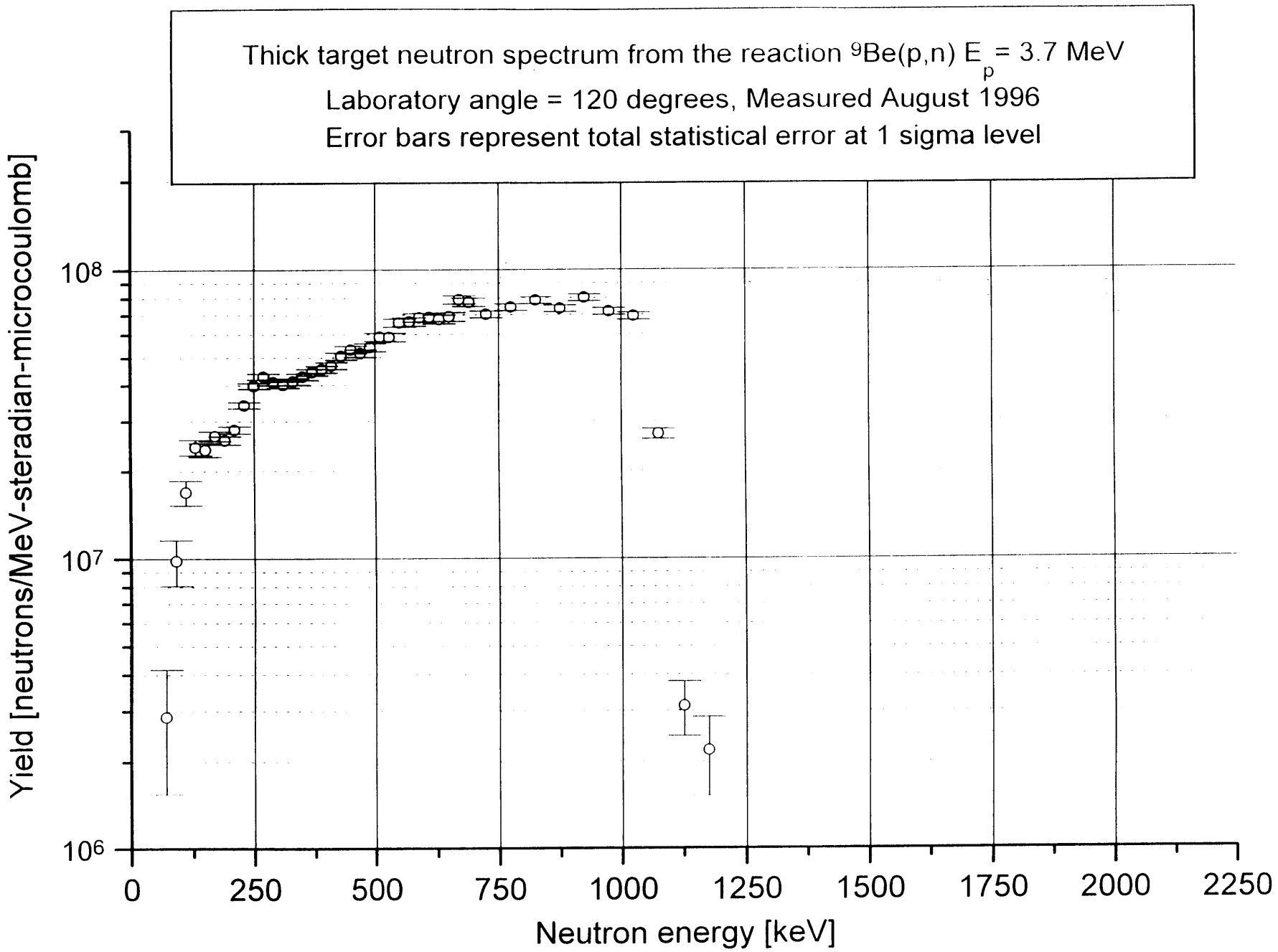
Thick target neutron spectrum from the reaction $^{9}Be(p,n)$ E_p = 3.7 MeV
Laboratory angle = 120 degrees, Measured August 1996
Error bars represent total statistical error at 1 sigma level
Yield [neutrons/MeV-steradian-microcoulomb]
10^8
10^7
10^6
0
250
500
750
1000
1250
1500
1750
2000
2250
Neutron energy [keV]

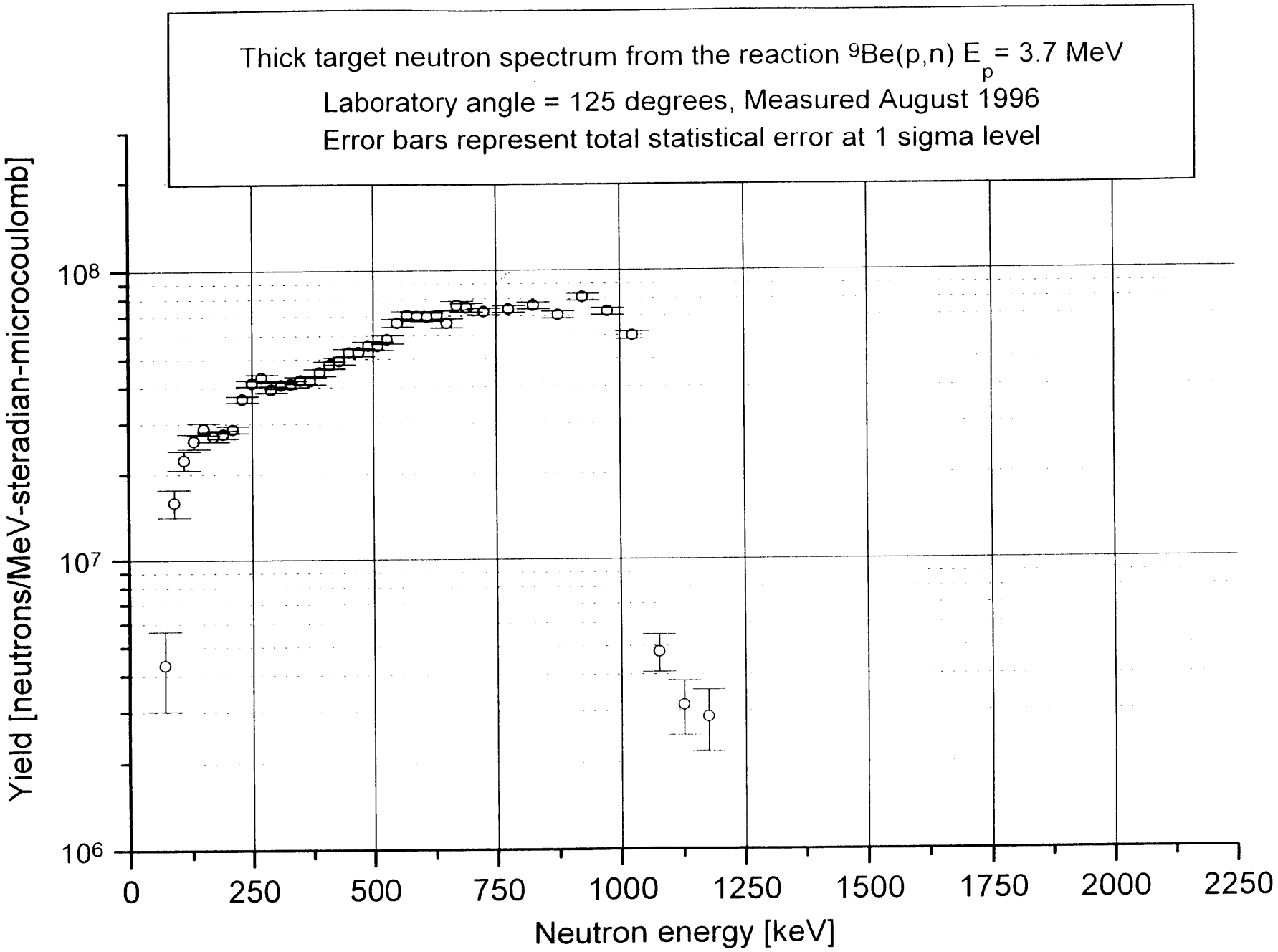
Thick target neutron spectrum from the reaction $^{9}Be(p,n)$ E_p = 3.7 MeV
Laboratory angle = 125 degrees, Measured August 1996
Error bars represent total statistical error at 1 sigma level
Yield [neutrons/MeV-steradian-microcoulomb]
10^8
10^7
10^6
0
250
500
750
1000
1250
1500
1750
2000
2250
Neutron energy [keV]

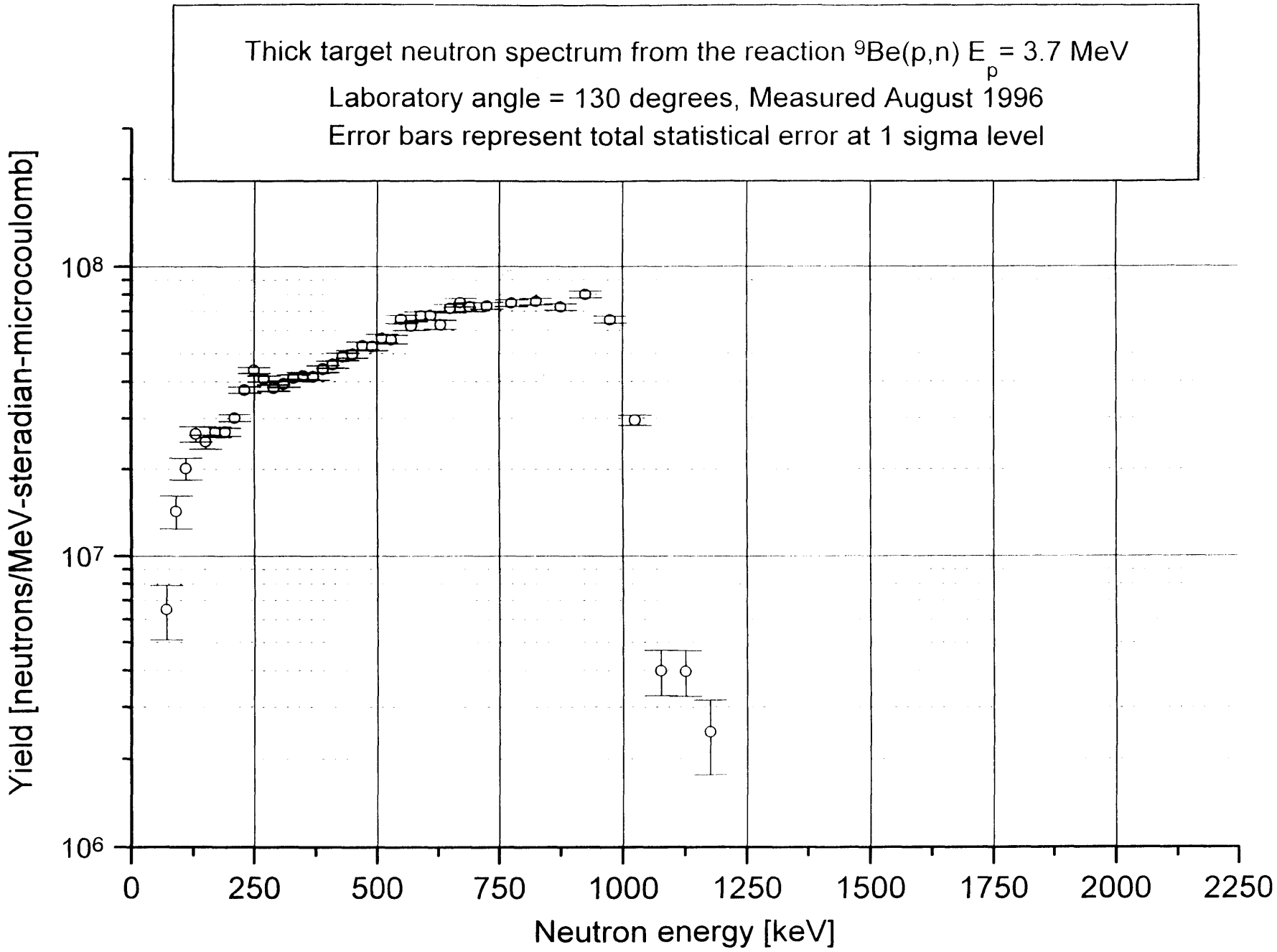
Thick target neutron spectrum from the reaction $^{9}Be(p,n)$ E_p = 3.7 MeV
Laboratory angle = 130 degrees, Measured August 1996
Error bars represent total statistical error at 1 sigma level
Yield [neutrons/MeV-steradian-microcoulomb]
10^8
10^7
10^6
0
250
500
750
1000
1250
1500
1750
2000
2250
Neutron energy [keV]

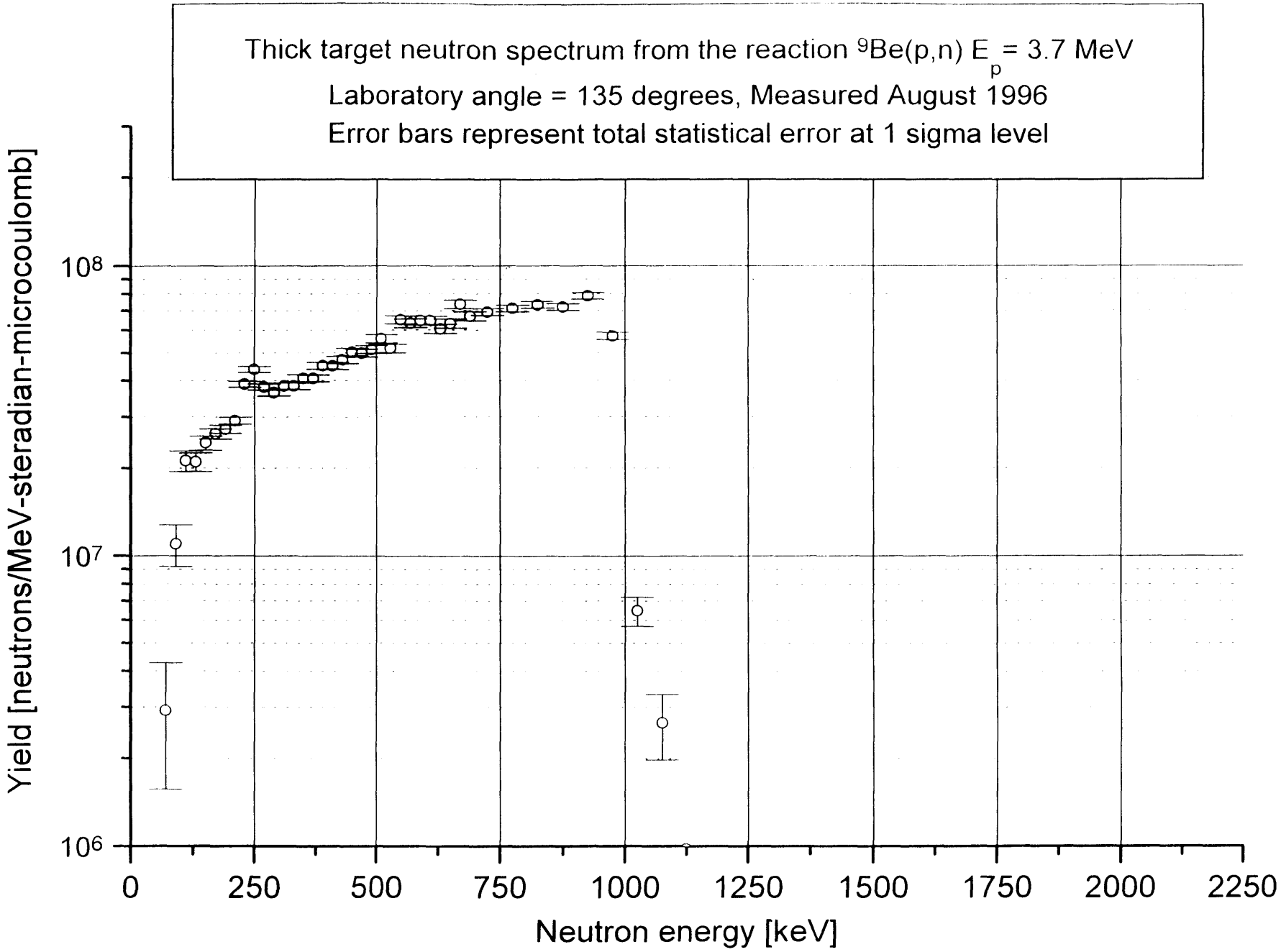
Thick target neutron spectrum from the reaction $^{9}Be(p,n)$ E_p = 3.7 MeV
Laboratory angle = 135 degrees, Measured August 1996
Error bars represent total statistical error at 1 sigma level
Yield [neutrons/MeV-steradian-microcoulomb]
10^8
10^7
10^6
0
250
500
750
1000
1250
1500
1750
2000
2250
Neutron energy [keV]

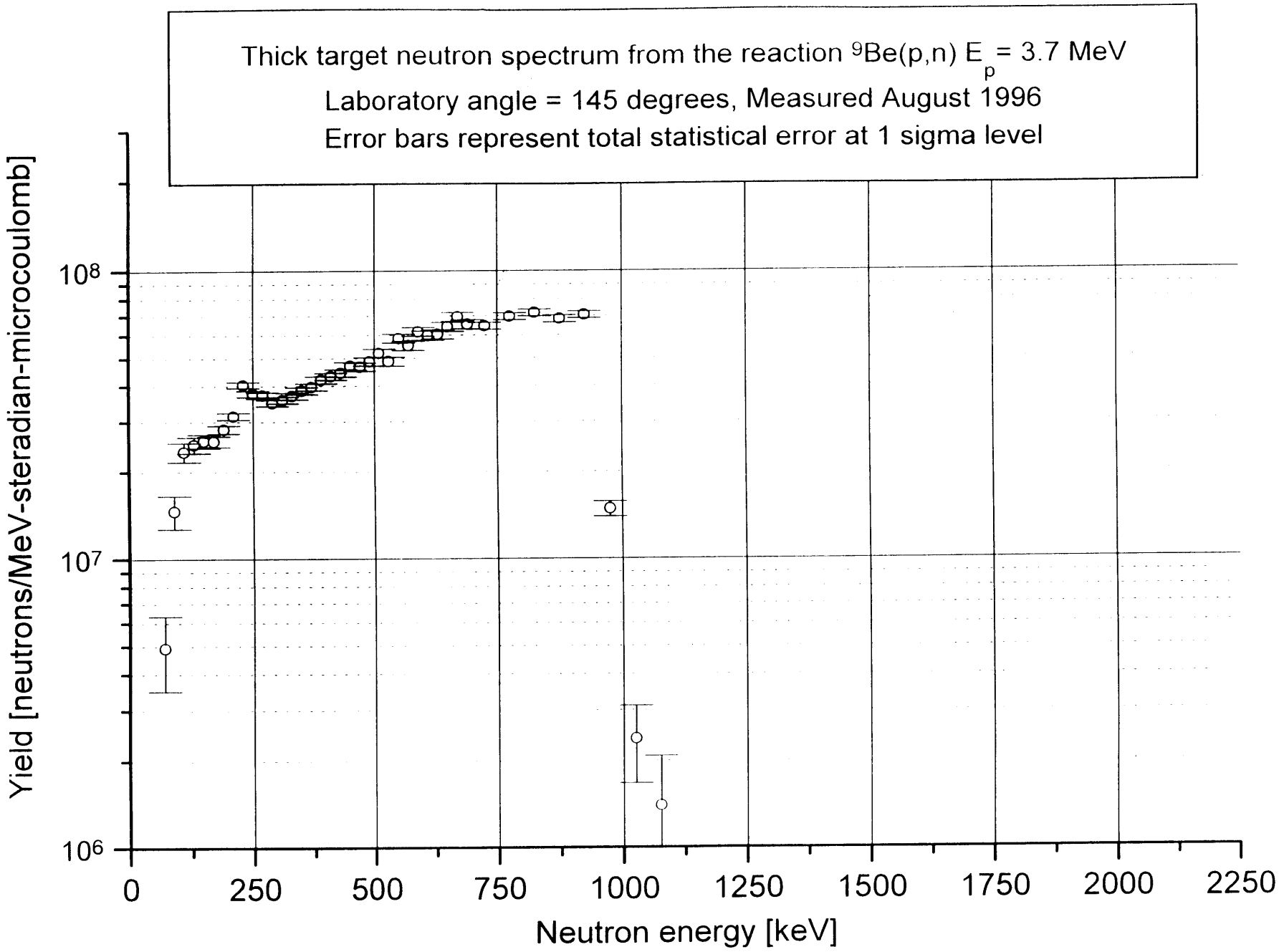
Thick target neutron spectrum from the reaction $^{9}Be(p,n)$ E_p = 3.7 MeV
Laboratory angle = 145 degrees, Measured August 1996
Error bars represent total statistical error at 1 sigma level
Yield [neutrons/MeV-steradian-microcoulomb]
10^8
10^7
10^6
0
250
500
750
1000
1250
1500
1750
2000
2250
Neutron energy [keV]

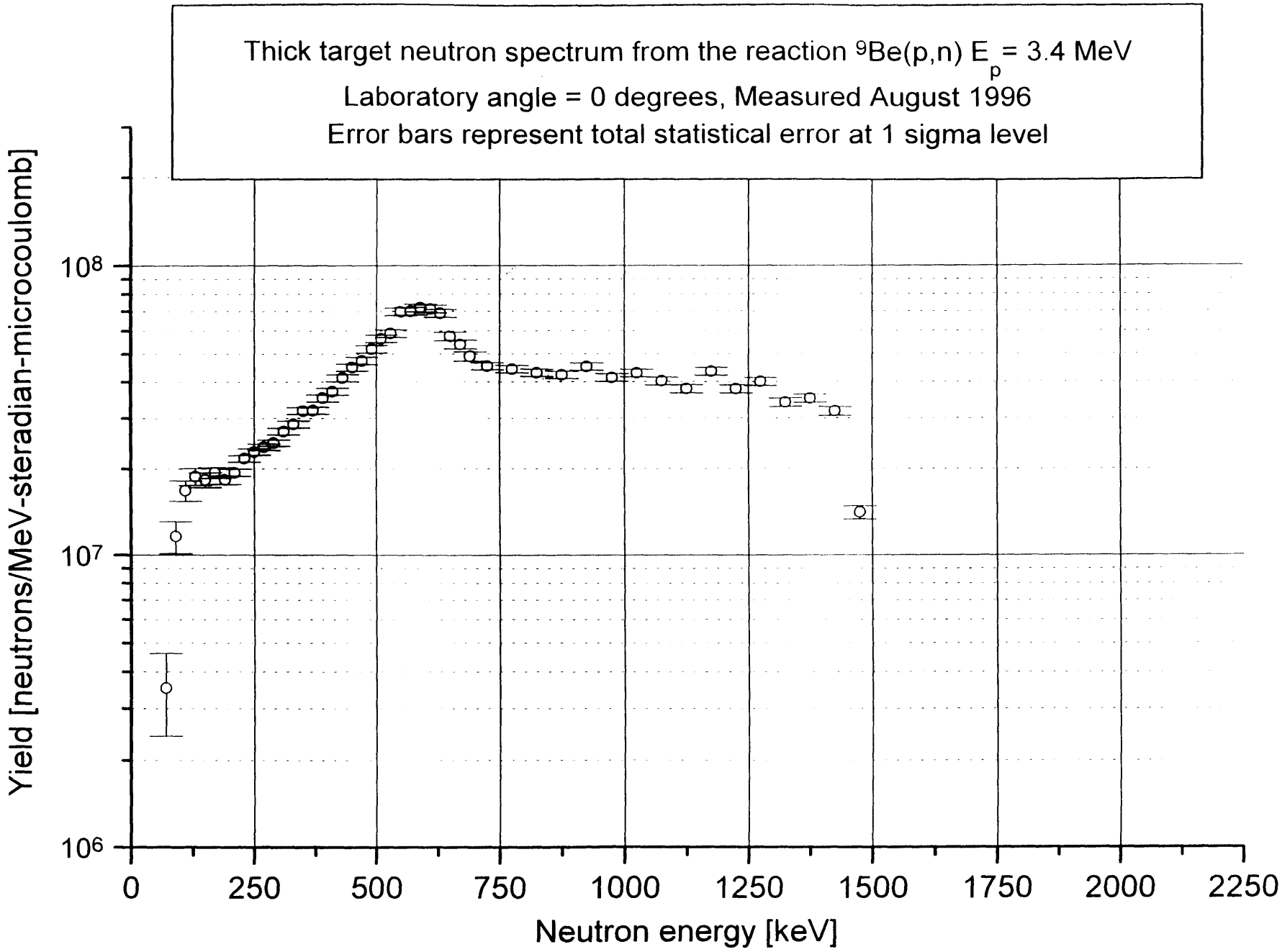
Thick target neutron spectrum from the reaction $^{9}Be(p,n)$ E_p = 3.4 MeV
Laboratory angle = 0 degrees, Measured August 1996
Error bars represent total statistical error at 1 sigma level
Yield [neutrons/MeV-steradian-microcoulomb]
10^8
10^7
10^6
0
250
500
750
1000
1250
1500
1750
2000
2250
Neutron energy [keV]

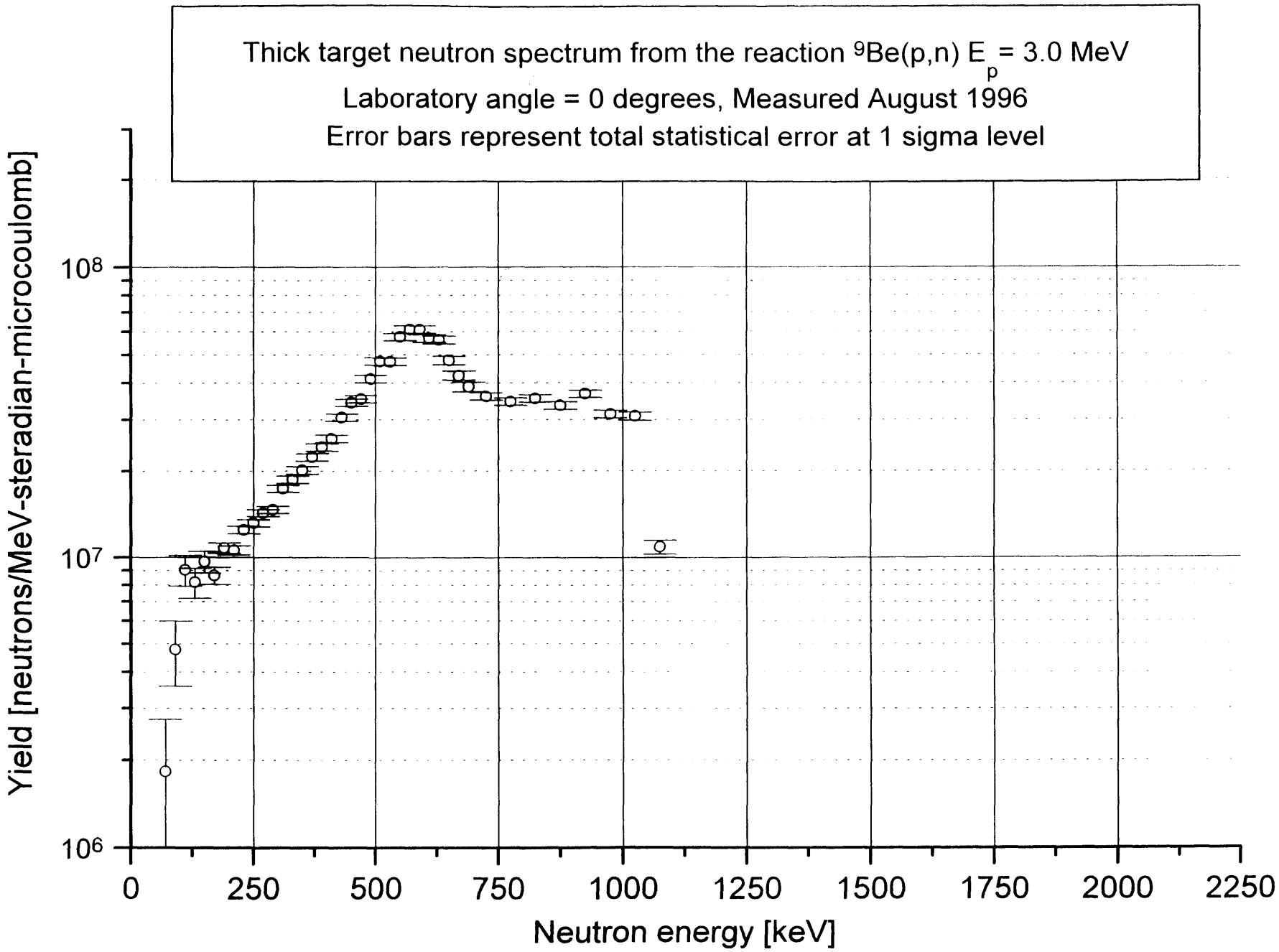
Thick target neutron spectrum from the reaction $^{9}Be(p,n)$ E_p = 3.0 MeV
Laboratory angle = 0 degrees, Measured August 1996
Error bars represent total statistical error at 1 sigma level
Yield [neutrons/MeV-steradian-microcoulomb]
10^8
10^7
10^6
0
250
500
750
1000
1250
1500
1750
2000
2250
Neutron energy [keV]

APPENDIX C

Simulations Used in Therapy Beam Design

This appendix contains graphs depicting the results of the therapy beam design simulations discussed in Chapter III. The graphs are divided into seven groups. Each group is preceded by a table which lists the configurations in the group, and the values of the MSR dimensions which were varied in that group. The dimensions are referenced to Figure III-B-2, found in Chapter III.

The first group consists of the results using the reaction ^{7}Li(p,n). The remaining groups consist of the results from the reaction ^{9}Be(p,n). The reaction, proton energy, moderator and reflector materials, and moderator dimensions are annotated on each graph and are listed in the tables.

Table C-1: Therapy beam design configurations
for the reaction
7Li(p,n) E(p)=2.5 MeV

The following dimesions were not varied:
A=3 cm, C=10 cm, D=34 cm, E=34 cm, F=0.03 cm, H=0.03 cm, I=0.03 cm

Simulation Designation	Moderator material	Reflector material	Target Location [cm] (dimension A)	Moderator Length [cm] (dimension B)	Target to port Distance [cm] (dimension G)
li-gr-d20x10	D2O	Graphite	3	20	17
li-gr-d22x10	D2O	Graphite	3	22	19
li-pb-d18x10	D2O	Lead	3	18	15
li-pb-d20x10	D2O	Lead	3	20	17
li-pb-d22x10	D2O	Lead	3	22	19
li-bi-d18x10	D2O	Bismuth	3	18	15
li-bi-d20x10	D2O	Bismuth	3	20	17
li-bi-d22x10	D2O	Bismuth	3	22	19

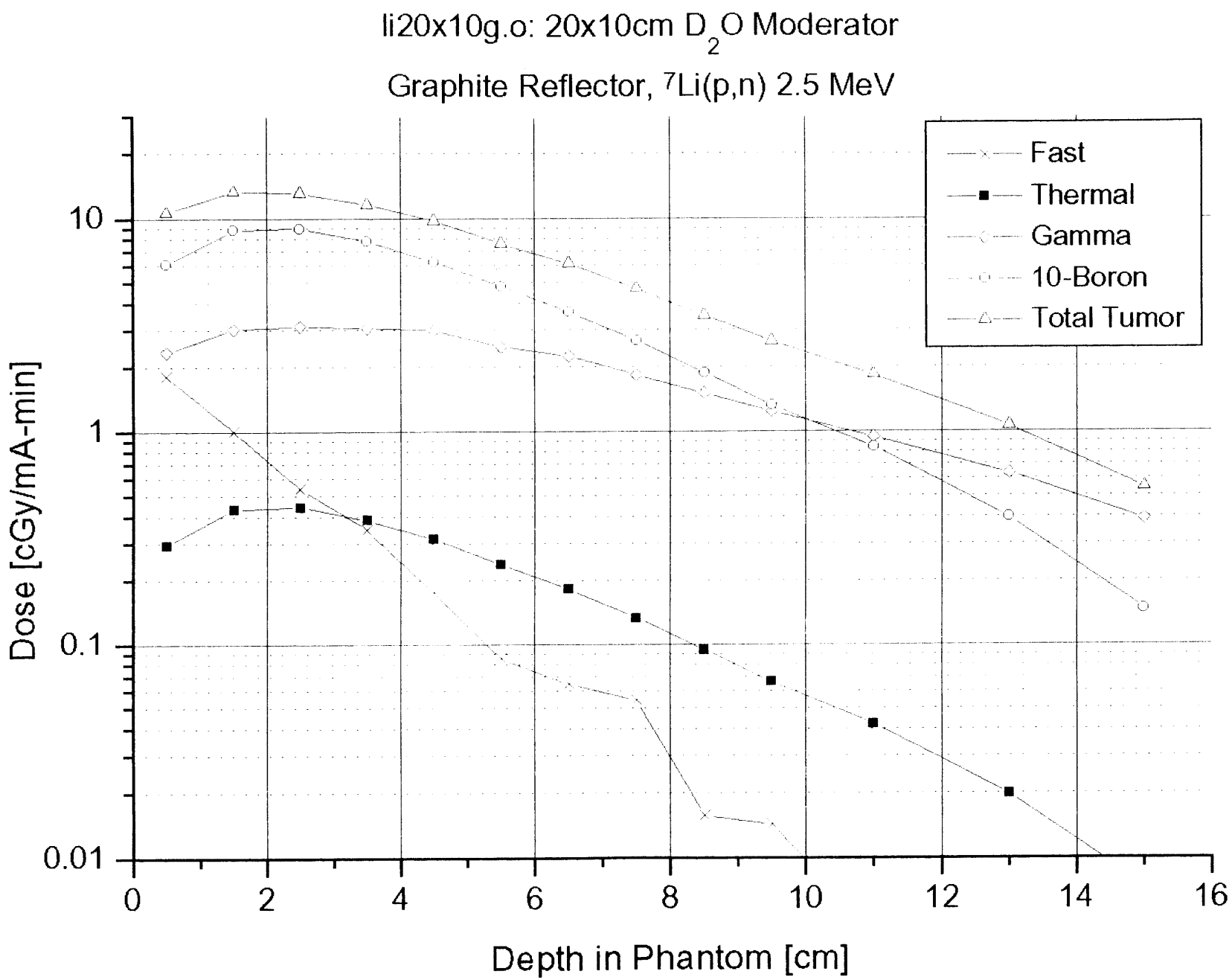
li20x10g.o: 20x10cm D2O Moderator
Graphite Reflector, 7Li(p,n) 2.5 MeV
Fast
Thermal
Gamma
10-Boron
Total Tumor
Dose [cGy/mA-min]
10
1
0.1
0.01
0
2
4
6
8
10
12
14
16
Depth in Phantom [cm]

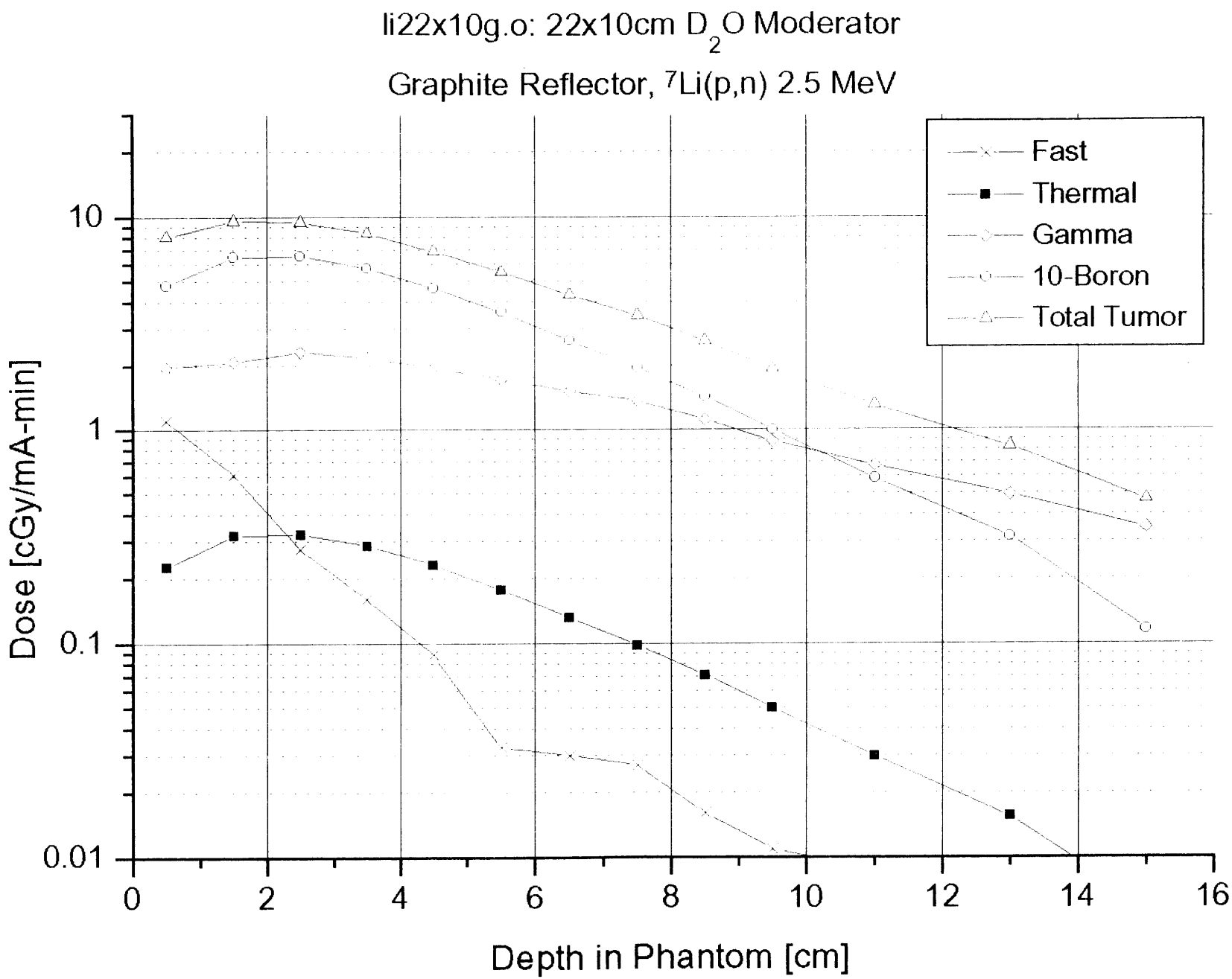
li22x10g.o: 22x10cm D2O Moderator
Graphite Reflector, 7Li(p,n) 2.5 MeV
Fast
Thermal
Gamma
10-Boron
Total Tumor
Dose [cGy/mA-min]
10
1
0.1
0.01
0
2
4
6
8
10
12
14
16
Depth in Phantom [cm]

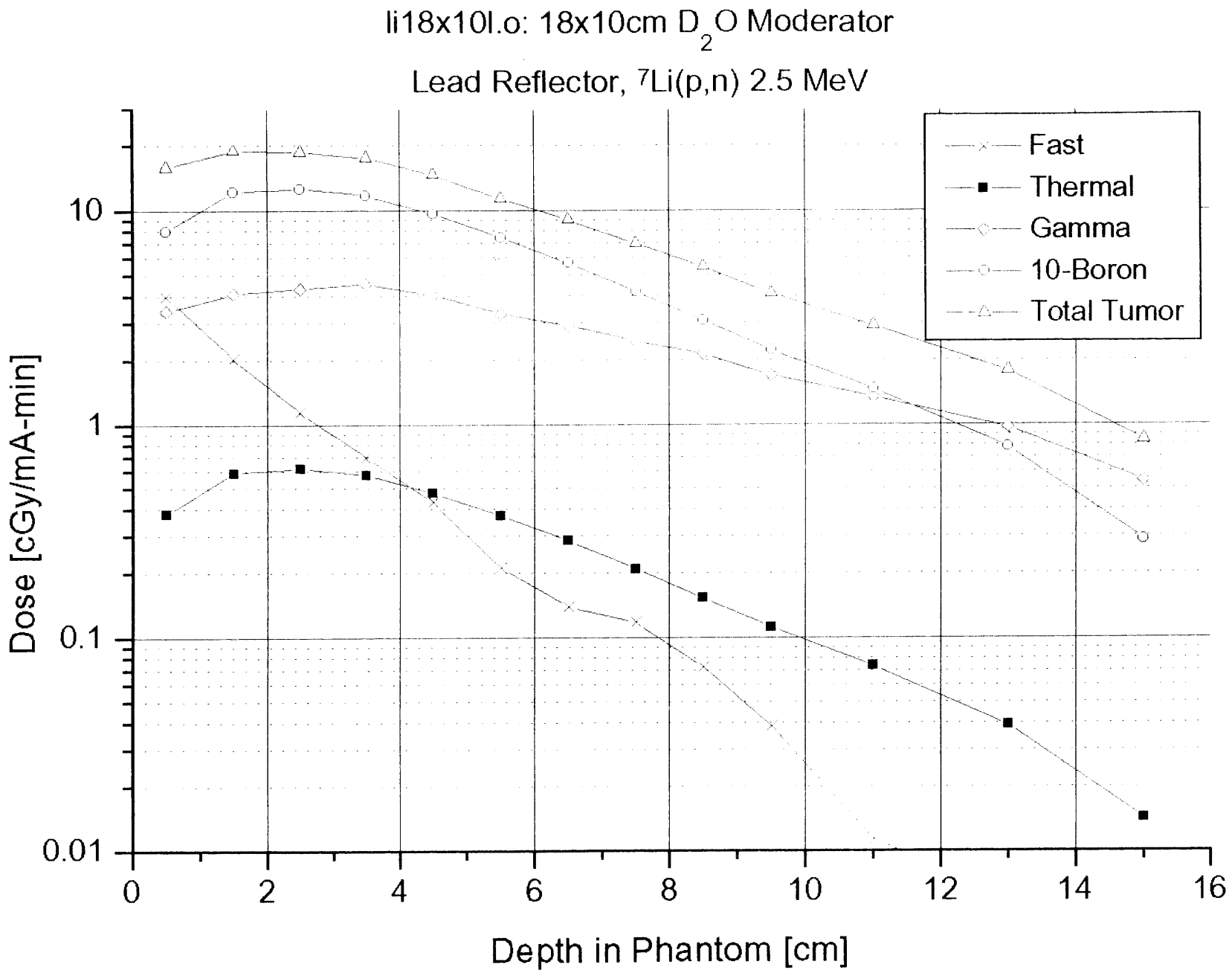
li18x10l.o: 18x10cm D2O Moderator
Lead Reflector, 7Li(p,n) 2.5 MeV
Fast
Thermal
Gamma
10-Boron
Total Tumor
Dose [cGy/mA-min]
10
1
0.1
0.01
0
2
4
6
8
10
12
14
16
Depth in Phantom [cm]

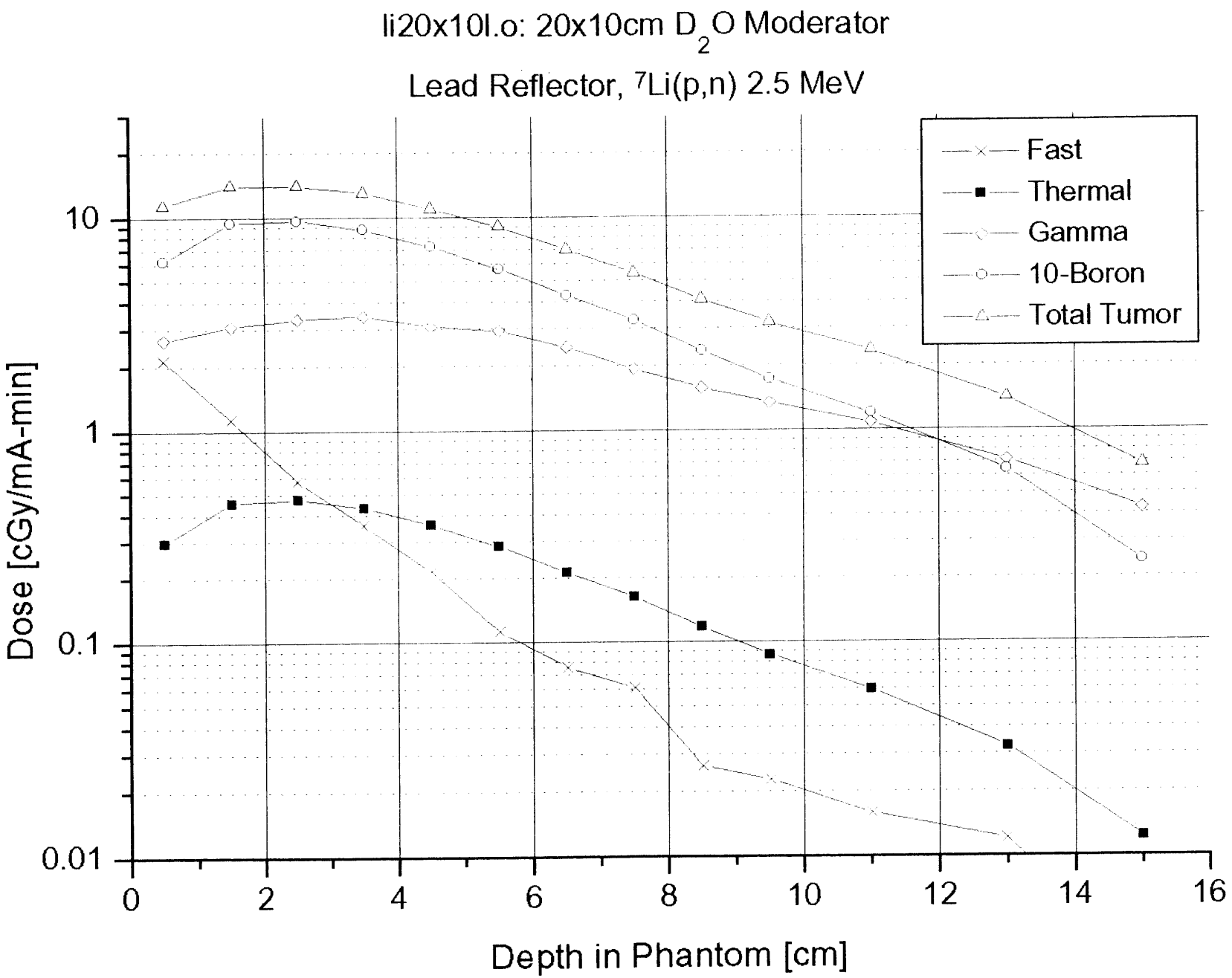
li20x10l.o: 20x10cm D2O Moderator
Lead Reflector, 7Li(p,n) 2.5 MeV
Fast
Thermal
Gamma
10-Boron
Total Tumor
Dose [cGy/mA-min]
10
1
0.1
0.01
0
2
4
6
8
10
12
14
16
Depth in Phantom [cm]

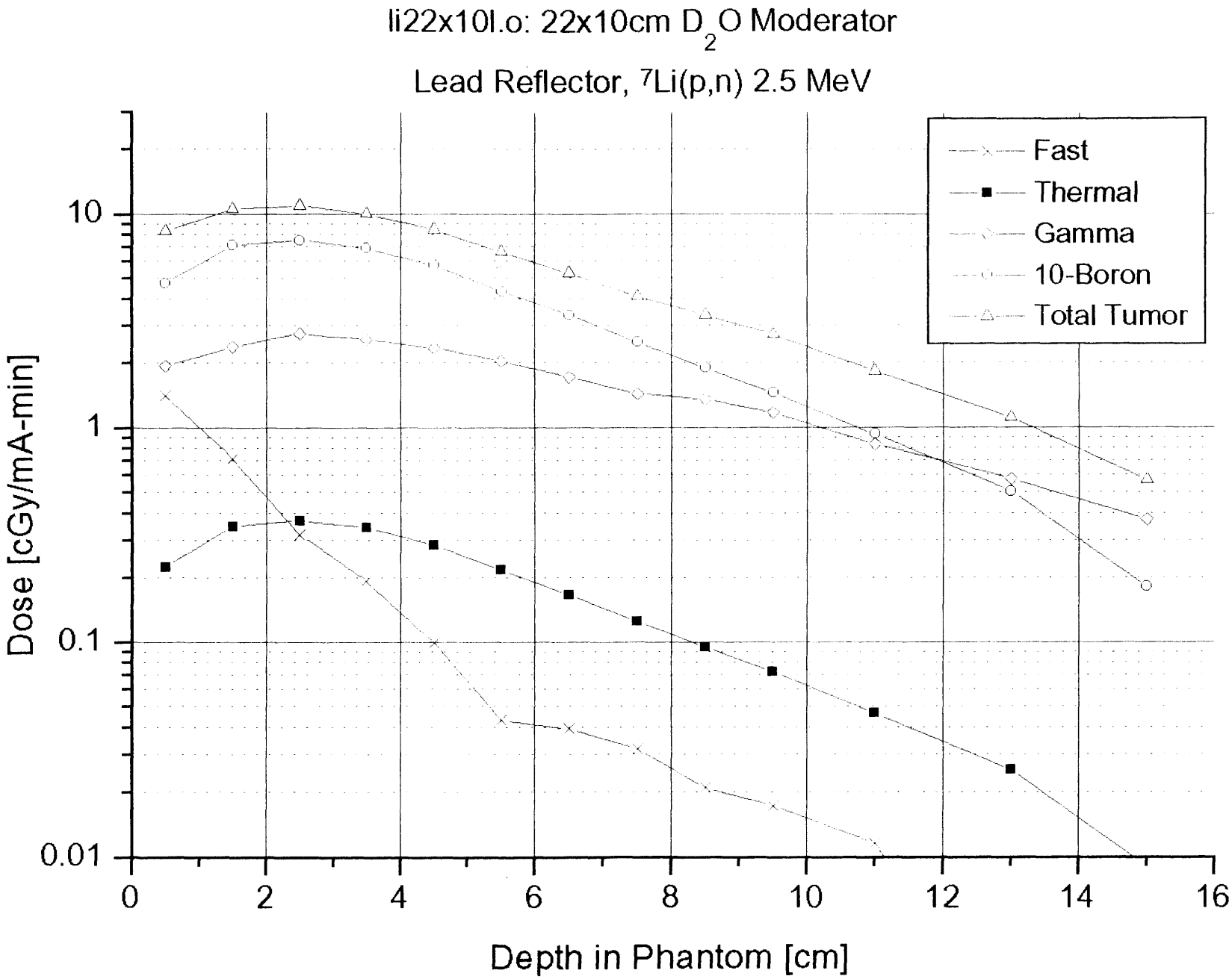
li22x10l.o: 22x10cm D2O Moderator
Lead Reflector, 7Li(p,n) 2.5 MeV
Fast
Thermal
Gamma
10-Boron
Total Tumor
Dose [cGy/mA-min]
10
1
0.1
0.01
0
2
4
6
8
10
12
14
16
Depth in Phantom [cm]

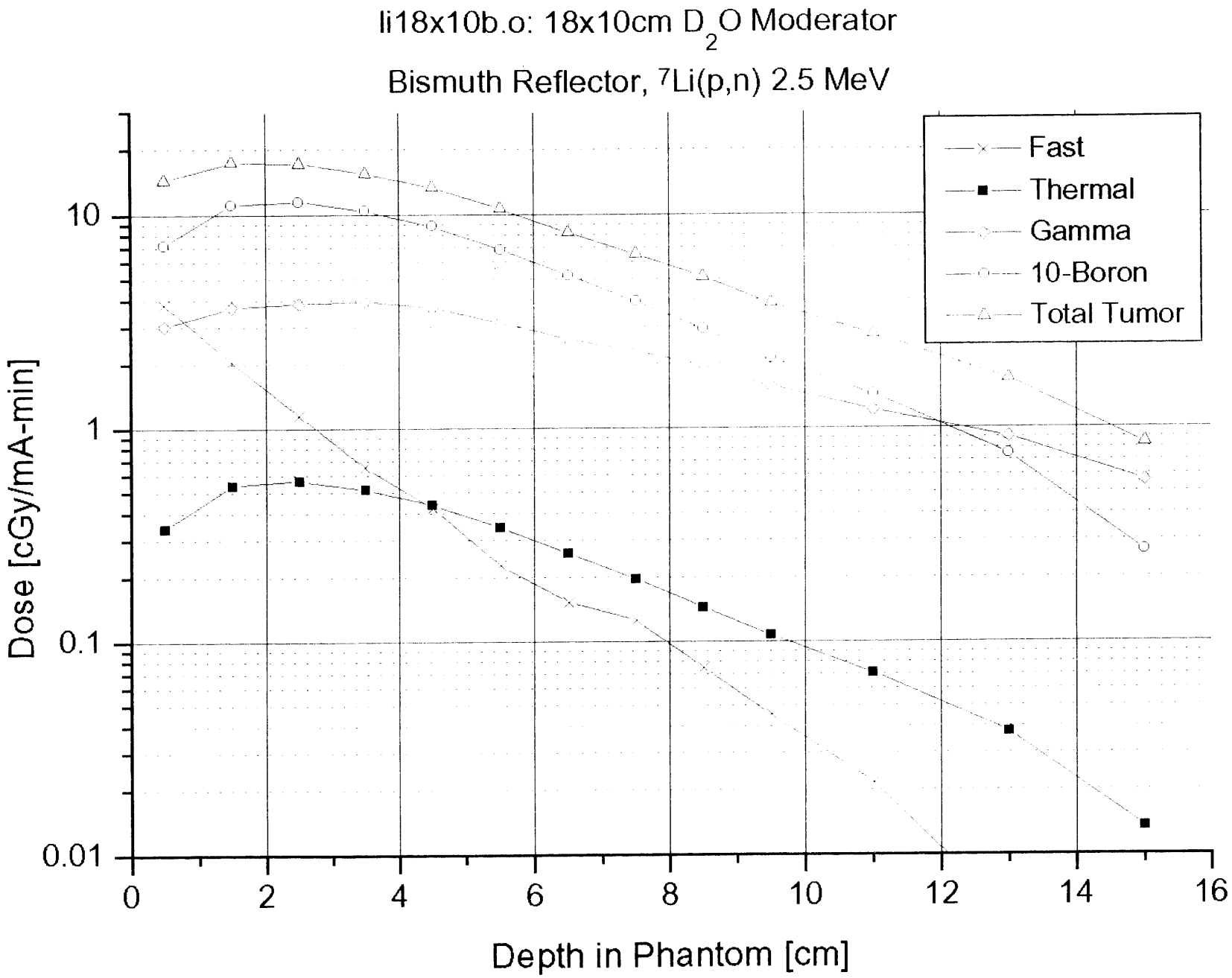
li18x10b.o: 18x10cm D2O Moderator
Bismuth Reflector, 7Li(p,n) 2.5 MeV
Fast
Thermal
Gamma
10-Boron
Total Tumor
Dose [cGy/mA-min]
10
1
0.1
0.01
0
2
4
6
8
10
12
14
16
Depth in Phantom [cm]

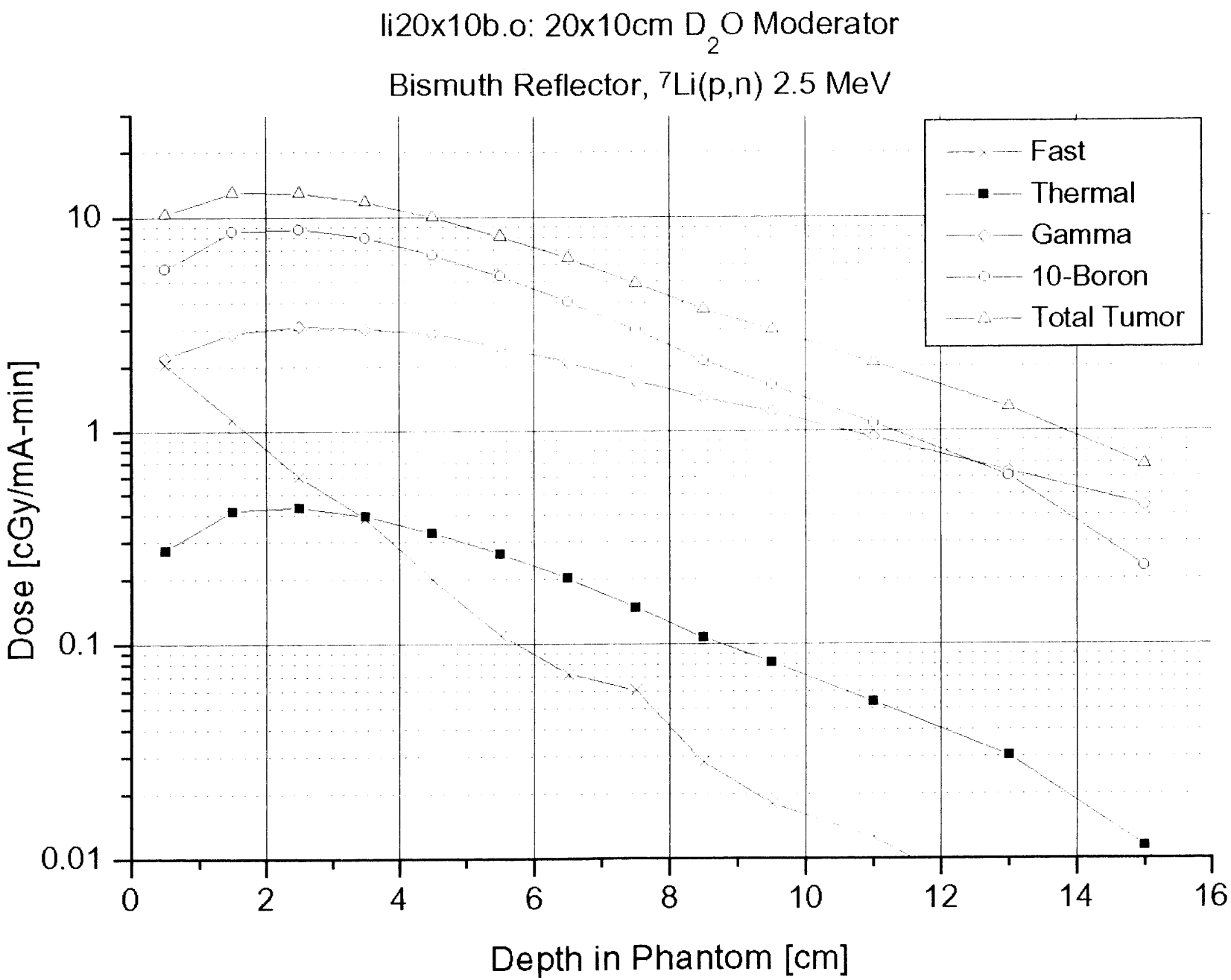
li20x10b.o: 20x10cm D2O Moderator
Bismuth Reflector, 7Li(p,n) 2.5 MeV
Fast
Thermal
Gamma
10-Boron
Total Tumor
Dose [cGy/mA-min]
10
1
0.1
0.01
0
2
4
6
8
10
12
14
16
Depth in Phantom [cm]

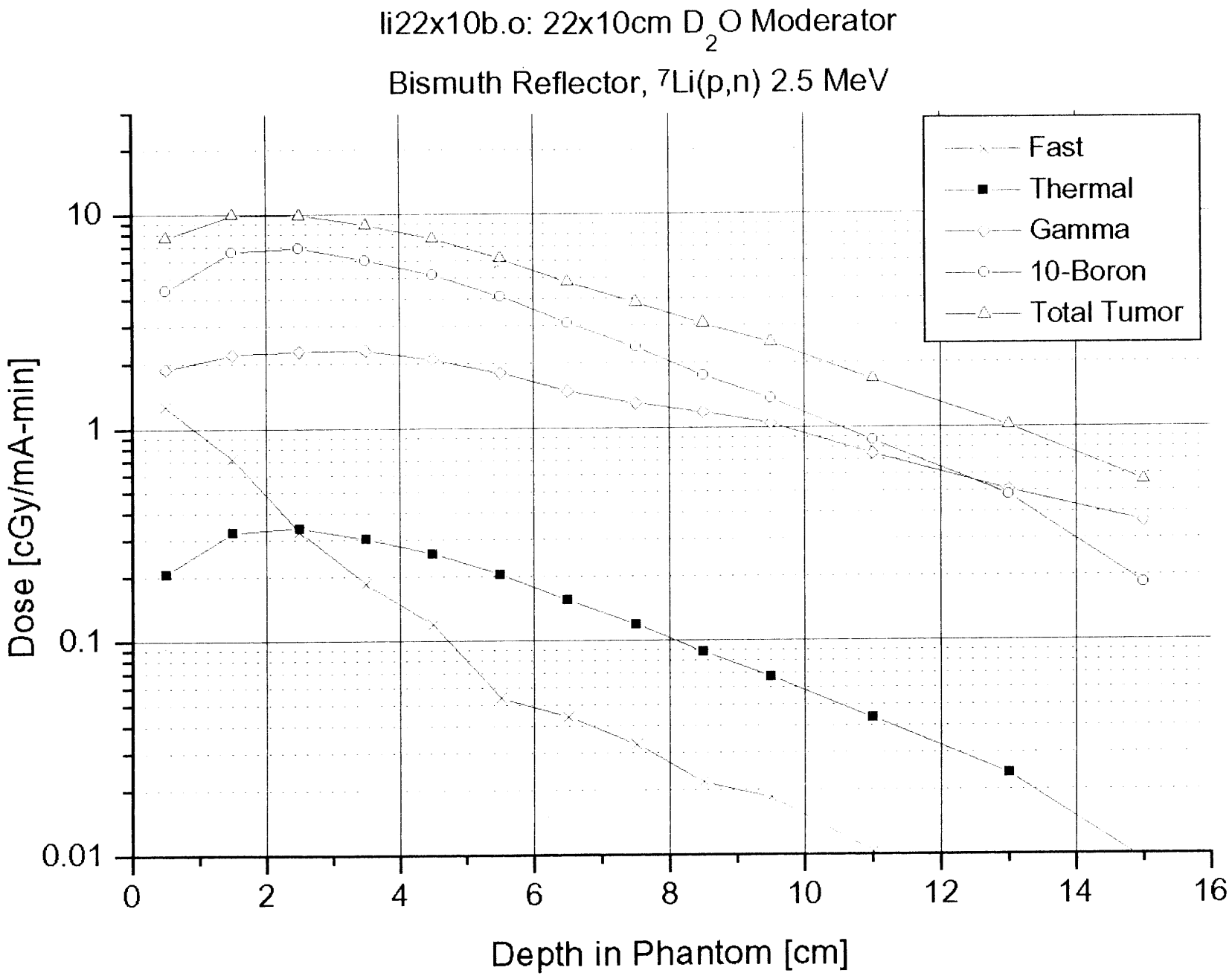
li22x10b.o: 22x10cm D2O Moderator
Bismuth Reflector, 7Li(p,n) 2.5 MeV
Fast
Thermal
Gamma
10-Boron
Total Tumor
Dose [cGy/mA-min]
10
1
0.1
0.01
0
2
4
6
8
10
12
14
16
Depth in Phantom [cm]

Table C-2: Therapy beam design configurations
for the reaction
9Be(p,n) E(p)=3.0 MeV

The following dimesions were not varied:
A=3 cm, C=10 cm, D=34 cm, E=34 cm, F=0.03 cm, H=0.03 cm, I=0.03 cm

Simulation Designation	Moderator material	Reflector material	Target Location [cm] (dimension A)	Moderator Length [cm] (dimension B)	Target to port Distance [cm] (dimension G)
30-gr-d2o-21x10	D2O	Graphite	3	21	18
30-gr-d2o-23x10	D2O	Graphite	3	23	20
30-gr-d2o-25x10	D2O	Graphite	3	25	22
30-pb-d2o-21x10	D2O	Lead	3	21	18
30-pb-d2o-23x10	D2O	Lead	3	23	20
30-pb-d2o-25x10	D2O	Lead	3	25	22
30-pb-d2o-27x10	D2O	Lead	3	27	24

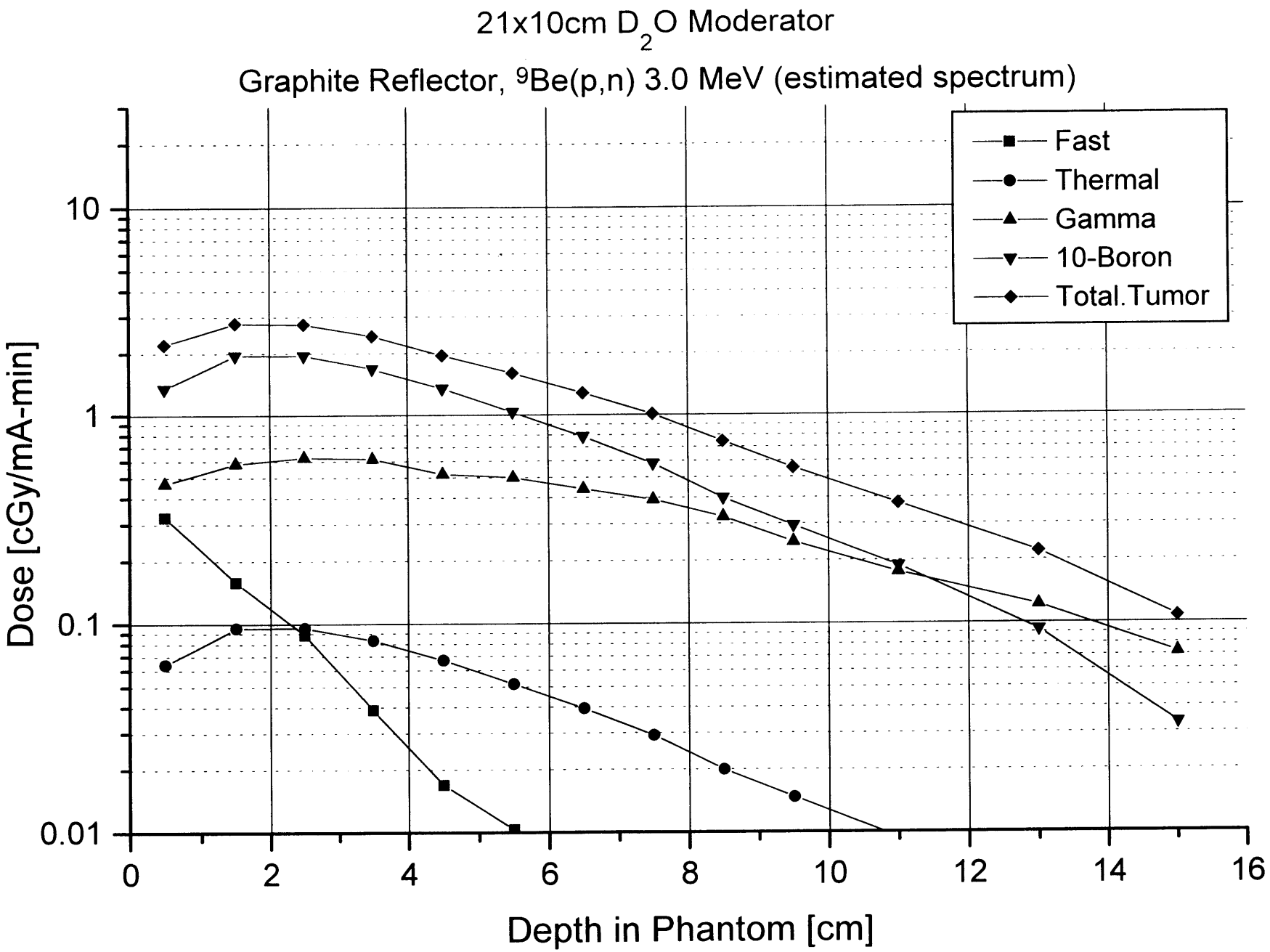
21x10cm D2O Moderator
Graphite Reflector, 9Be(p,n) 3.0 MeV (estimated spectrum)
Fast
Thermal
Gamma
10-Boron
Total.Tumor
Dose [cGy/mA-min]
10
1
0.1
0.01
0
2
4
6
8
10
12
14
16
Depth in Phantom [cm]

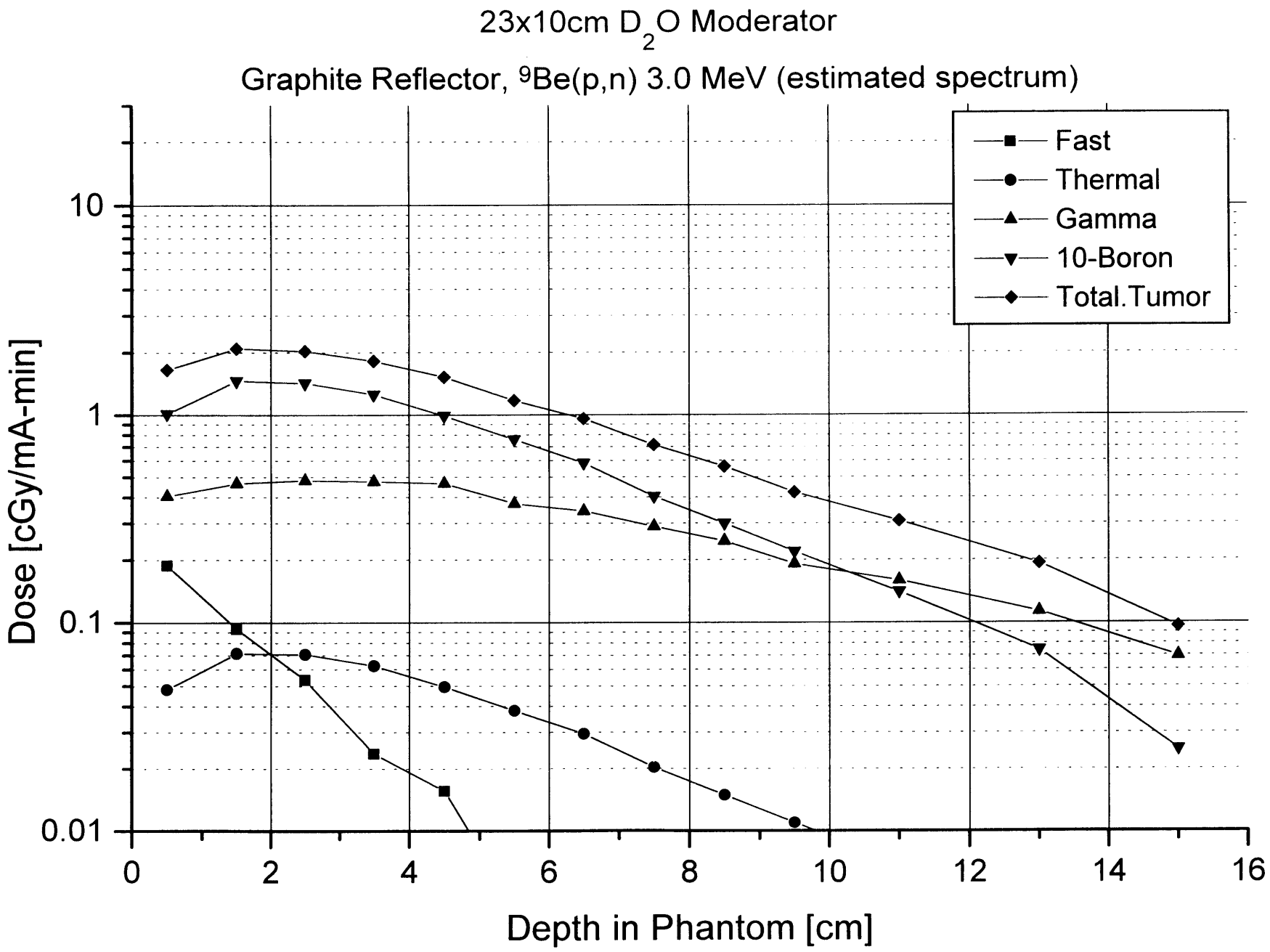
23x10cm D2O Moderator
Graphite Reflector, 9Be(p,n) 3.0 MeV (estimated spectrum)
Fast
Thermal
Gamma
10-Boron
Total.Tumor
Dose [cGy/mA-min]
10
1
0.1
0.01
0
2
4
6
8
10
12
14
16
Depth in Phantom [cm]

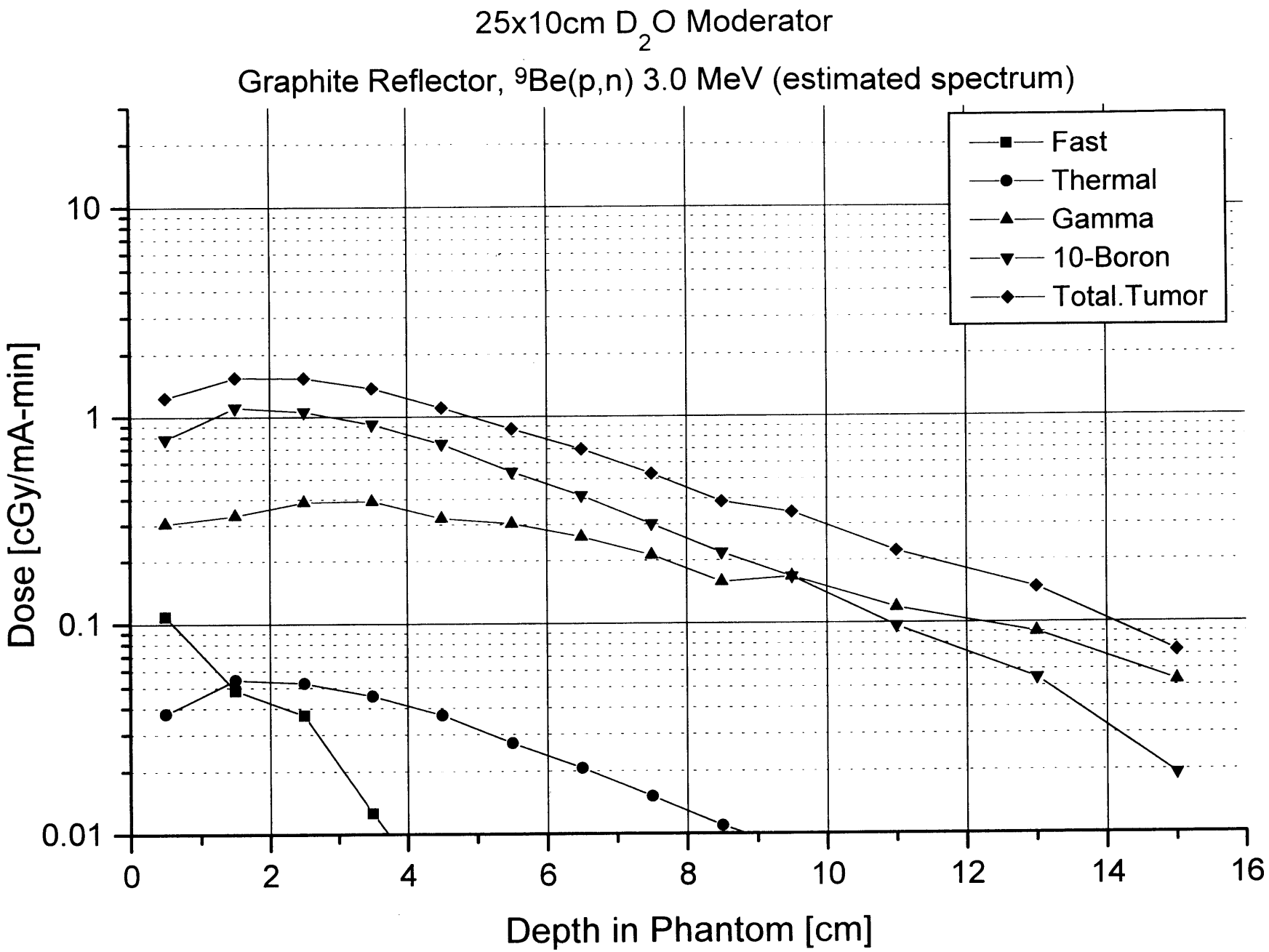
25x10cm D2O Moderator
Graphite Reflector, 9Be(p,n) 3.0 MeV (estimated spectrum)
Fast
Thermal
Gamma
10-Boron
Total.Tumor
Dose [cGy/mA-min]
10
1
0.1
0.01
0
2
4
6
8
10
12
14
16
Depth in Phantom [cm]

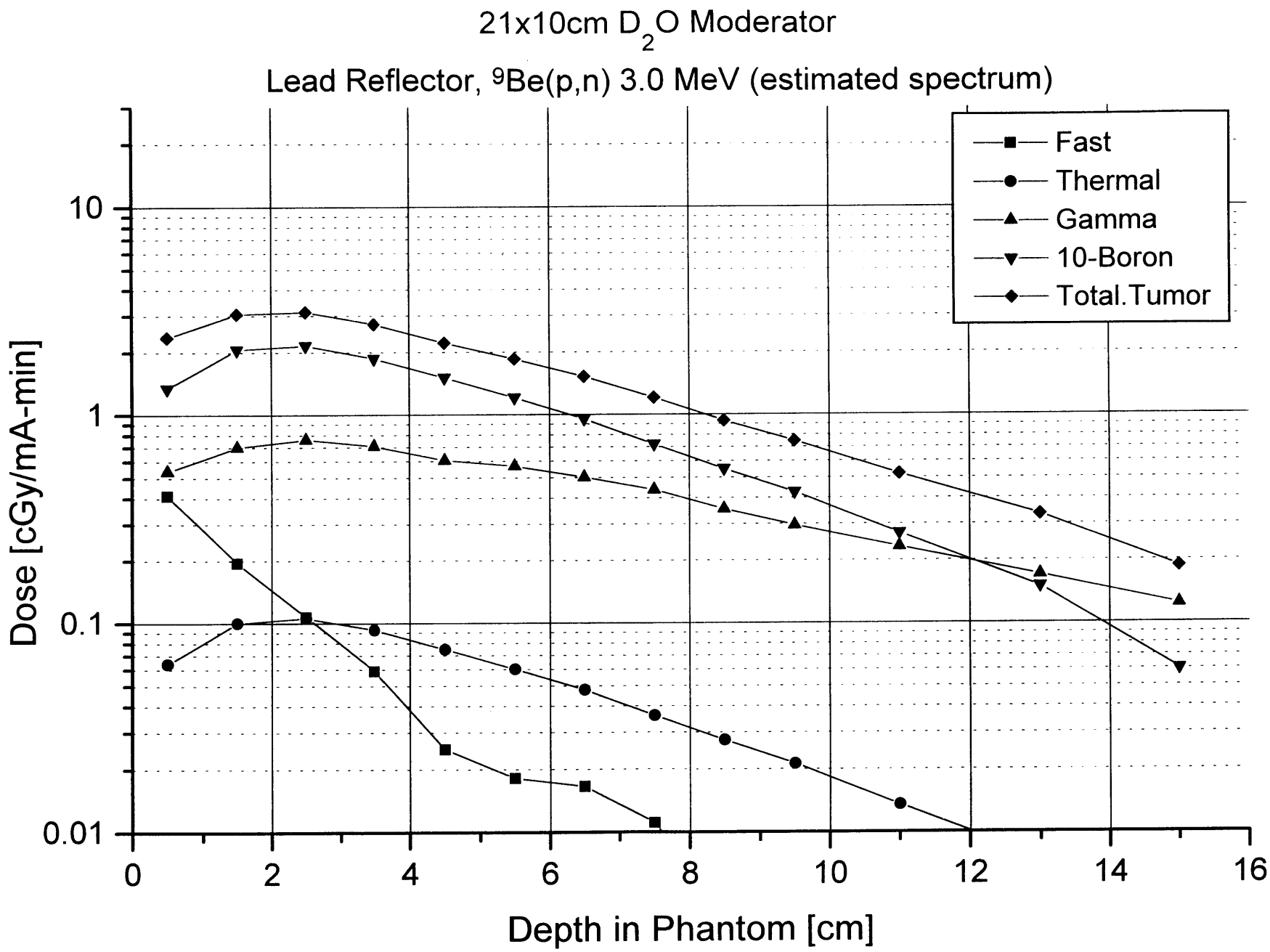
21x10cm D2O Moderator
Lead Reflector, 9Be(p,n) 3.0 MeV (estimated spectrum)
Fast
Thermal
Gamma
10-Boron
Total.Tumor
Dose [cGy/mA-min]
10
1
0.1
0.01
0
2
4
6
8
10
12
14
16
Depth in Phantom [cm]

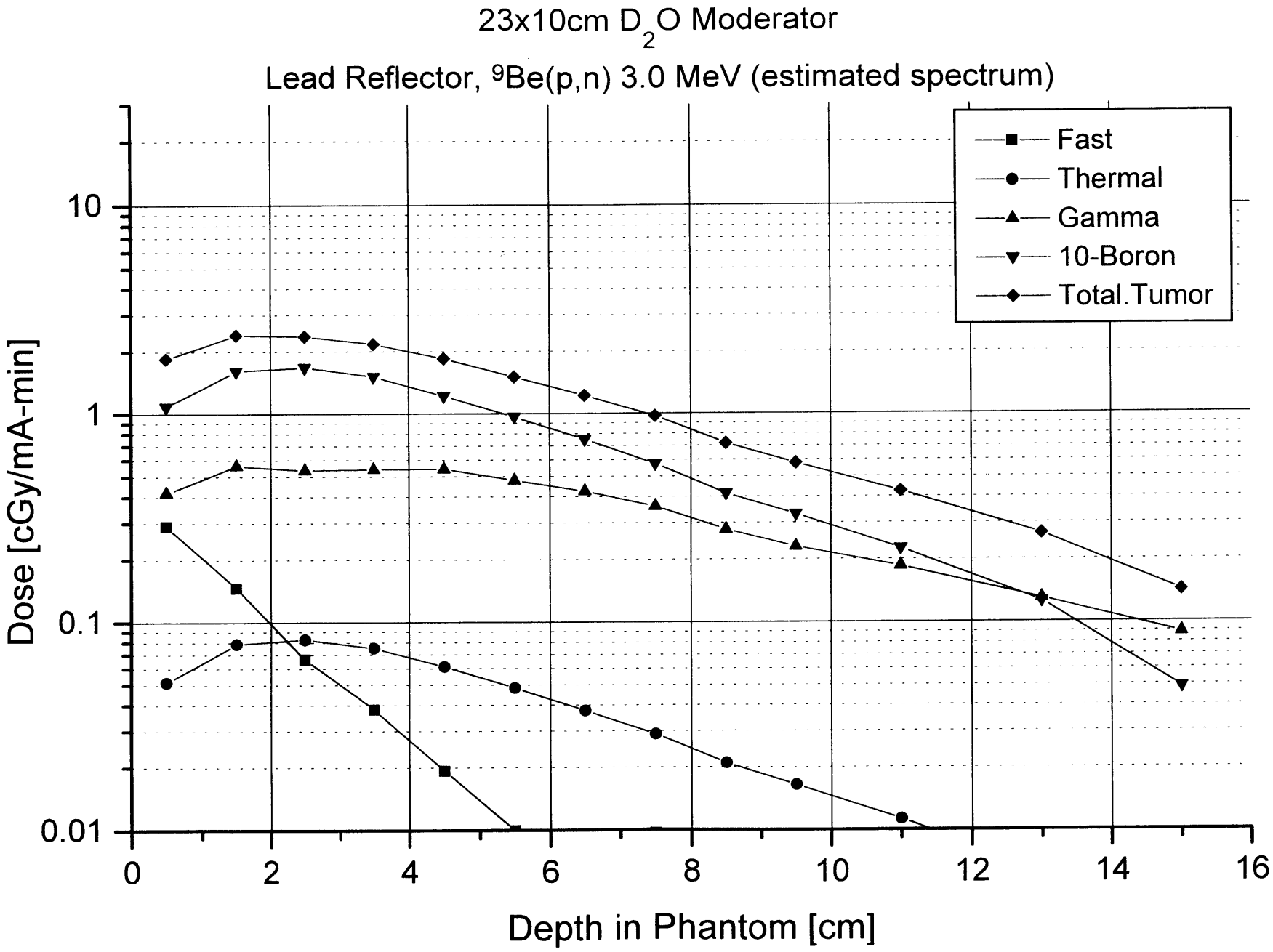
23x10cm D2O Moderator
Lead Reflector, 9Be(p,n) 3.0 MeV (estimated spectrum)
Fast
Thermal
Gamma
10-Boron
Total.Tumor
Dose [cGy/mA-min]
10
1
0.1
0.01
0
2
4
6
8
10
12
14
16
Depth in Phantom [cm]

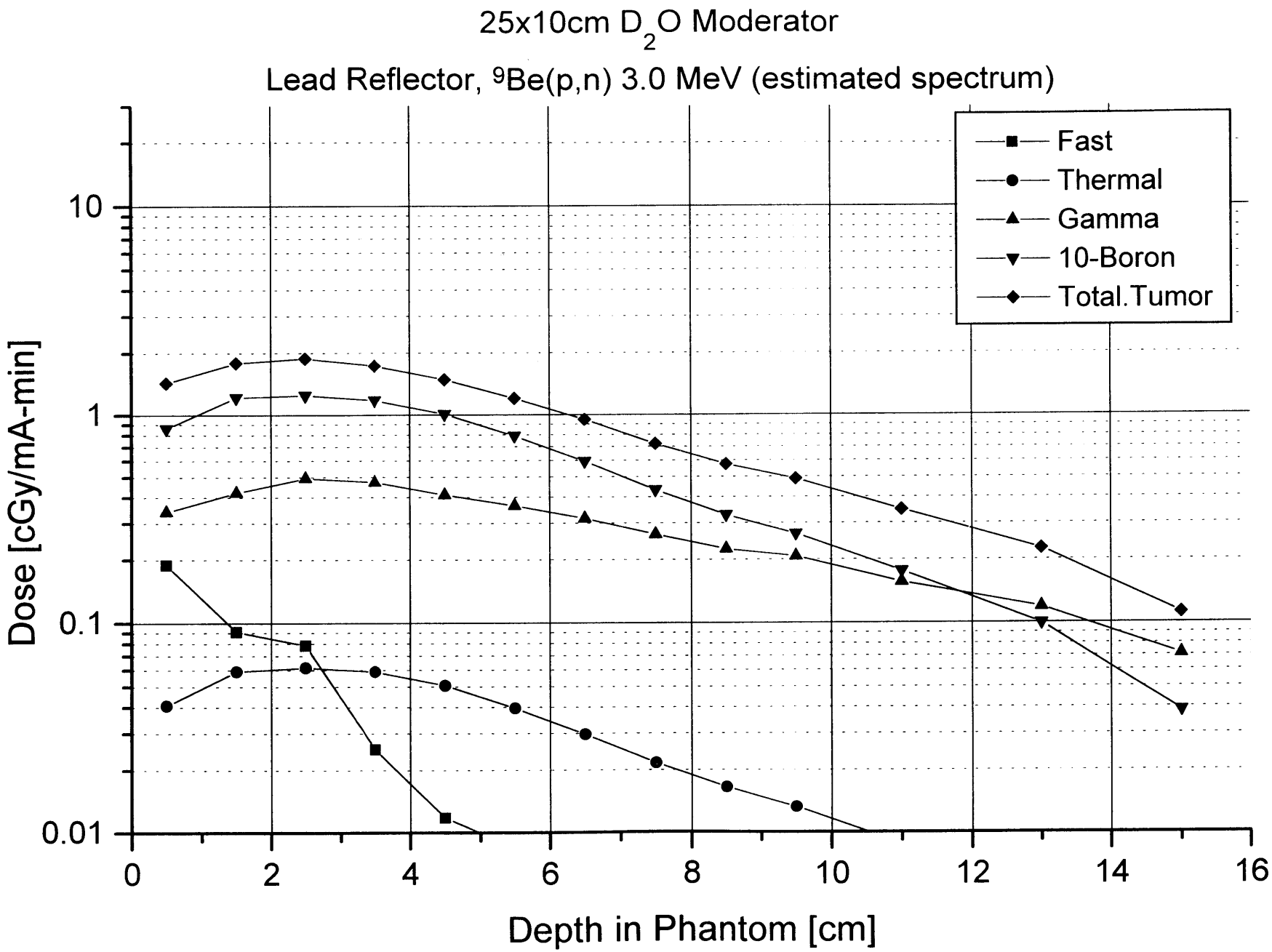
25x10cm D2O Moderator
Lead Reflector, 9Be(p,n) 3.0 MeV (estimated spectrum)
Fast
Thermal
Gamma
10-Boron
Total.Tumor
Dose [cGy/mA-min]
10
1
0.1
0.01
0
2
4
6
8
10
12
14
16
Depth in Phantom [cm]

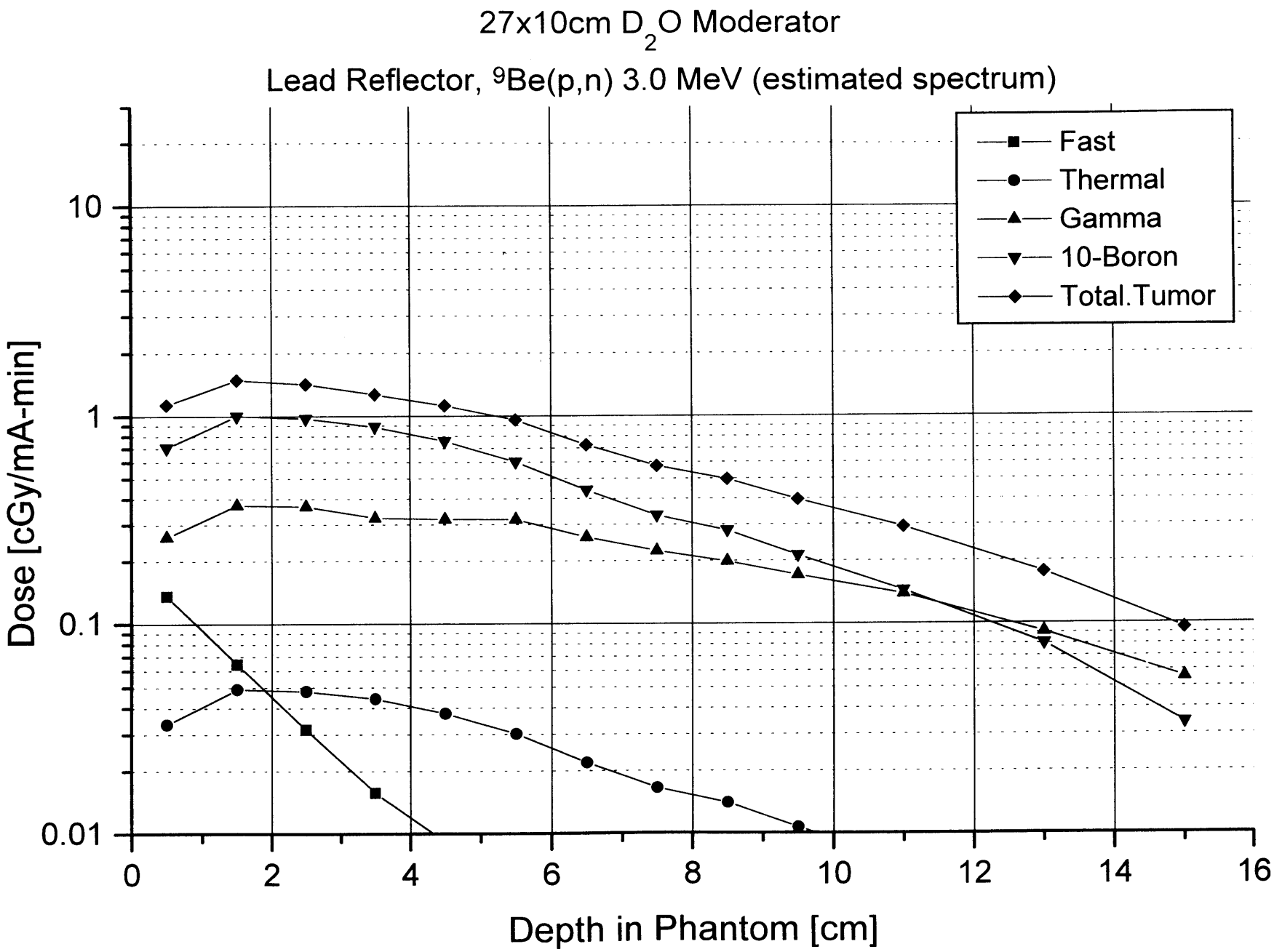
27x10cm D2O Moderator
Lead Reflector, 9Be(p,n) 3.0 MeV (estimated spectrum)
Fast
Thermal
Gamma
10-Boron
Total.Tumor
Dose [cGy/mA-min]
10
1
0.1
0.01
0
2
4
6
8
10
12
14
16
Depth in Phantom [cm]

Table C-3: Therapy beam design configurations
for the reaction
9Be(p,n) E(p)=3.4 MeV

The following dimesions were not varied:
A=3 cm, C=10 cm, D=34 cm, E=34 cm, F=0.03 cm, H=0.03 cm, I=0.03 cm

Simulation Designation	Moderator material	Reflector material	Target Location [cm] (dimension A)	Moderator Length [cm] (dimension B)	Target to port Distance [cm] (dimension G)
34-gr-d2o-21x10	D2O	Graphite	3	21	18
34-gr-d2o-23x10	D2O	Graphite	3	23	20
34-pb-d2o25x10	D2O	Lead	3	25	22
34-pb-d2o27x10	D2O	Lead	3	27	24

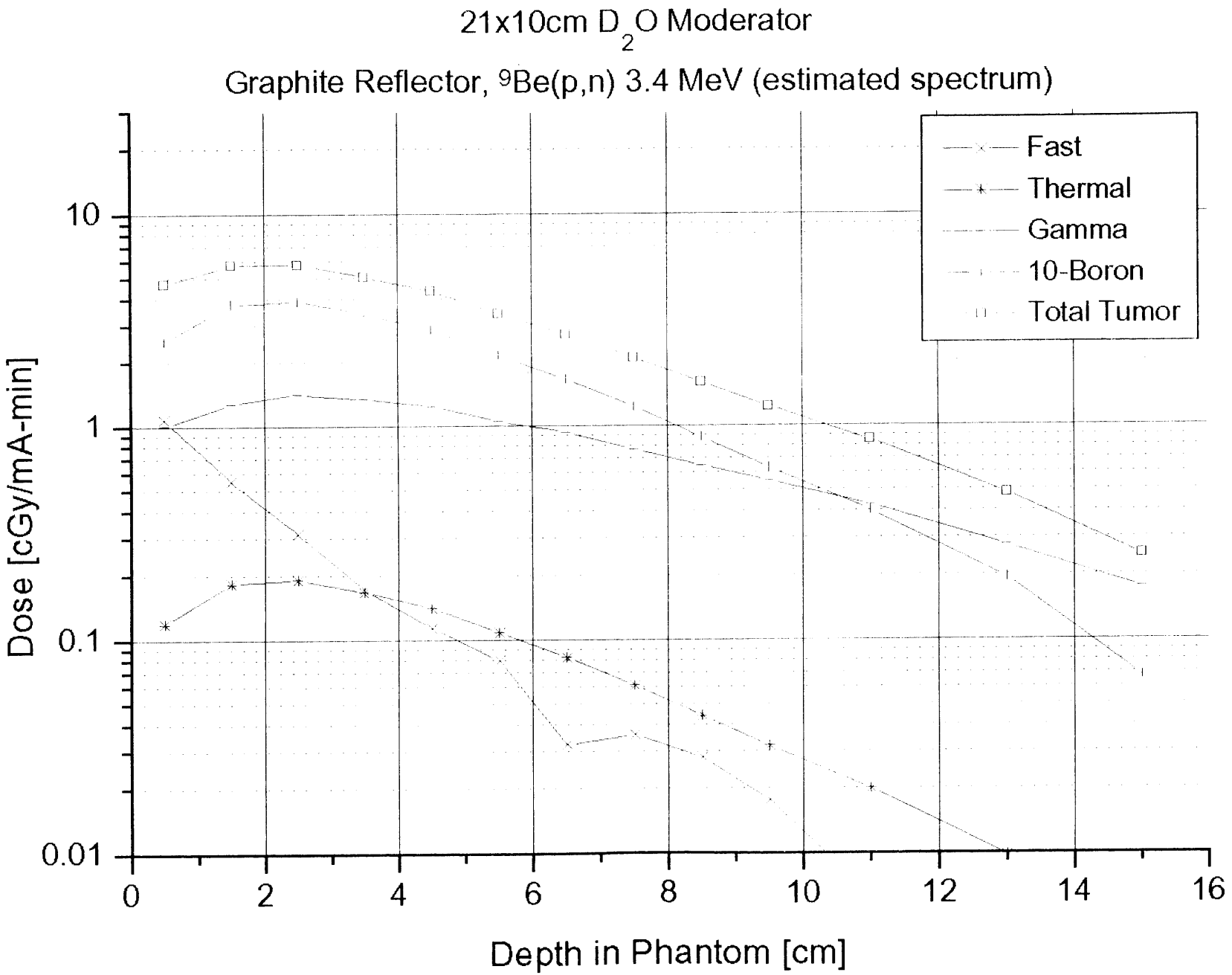
21x10cm D2O Moderator
Graphite Reflector, 9Be(p,n) 3.4 MeV (estimated spectrum)
Fast
Thermal
Gamma
10-Boron
Total Tumor
Dose [cGy/mA-min]
10
1
0.1
0.01
0
2
4
6
8
10
12
14
16
Depth in Phantom [cm]

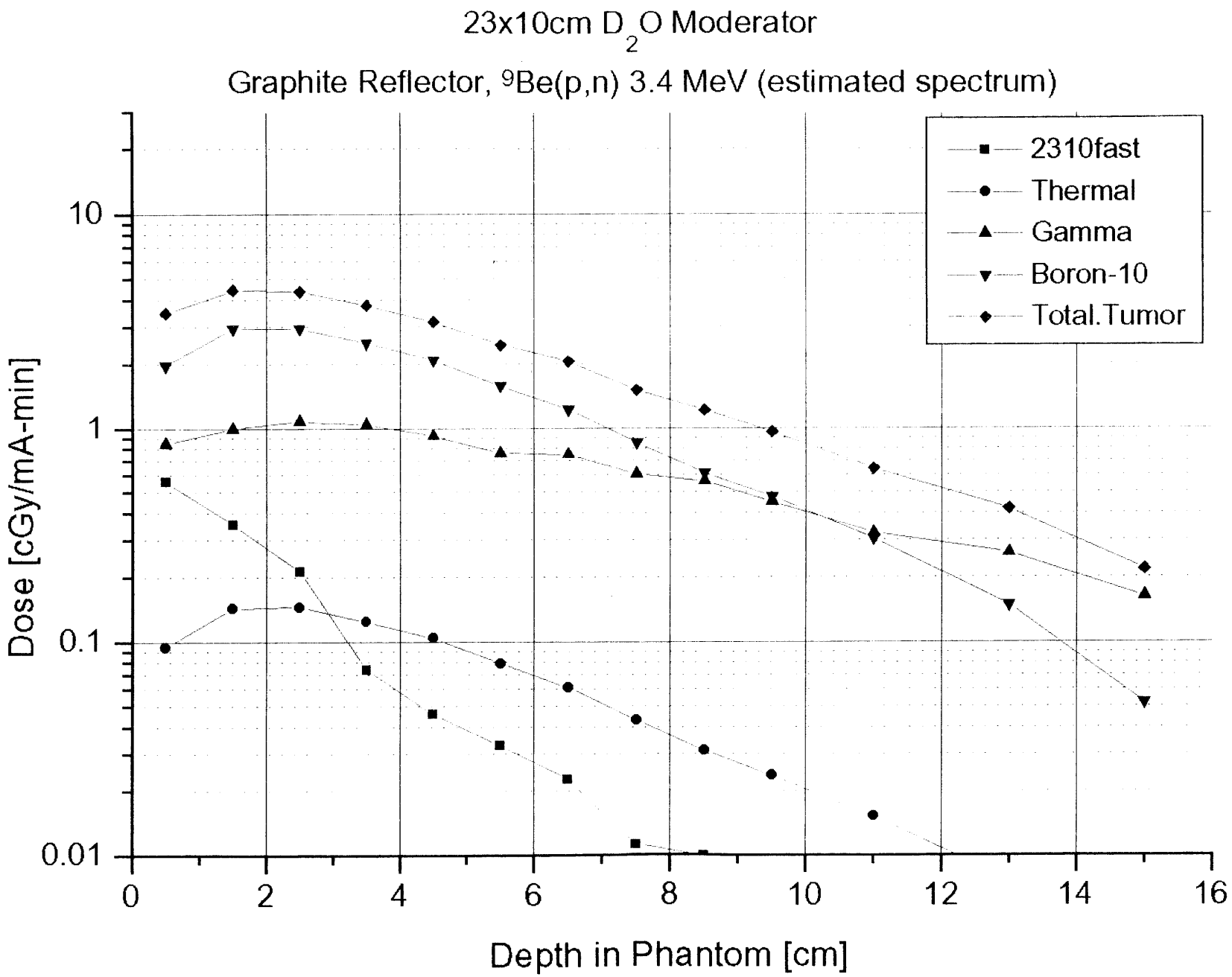
23x10cm D2O Moderator
Graphite Reflector, 9Be(p,n) 3.4 MeV (estimated spectrum)
2310fast
Thermal
Gamma
Boron-10
Total.Tumor
Dose [cGy/mA-min]
10
1
0.1
0.01
0
2
4
6
8
10
12
14
16
Depth in Phantom [cm]

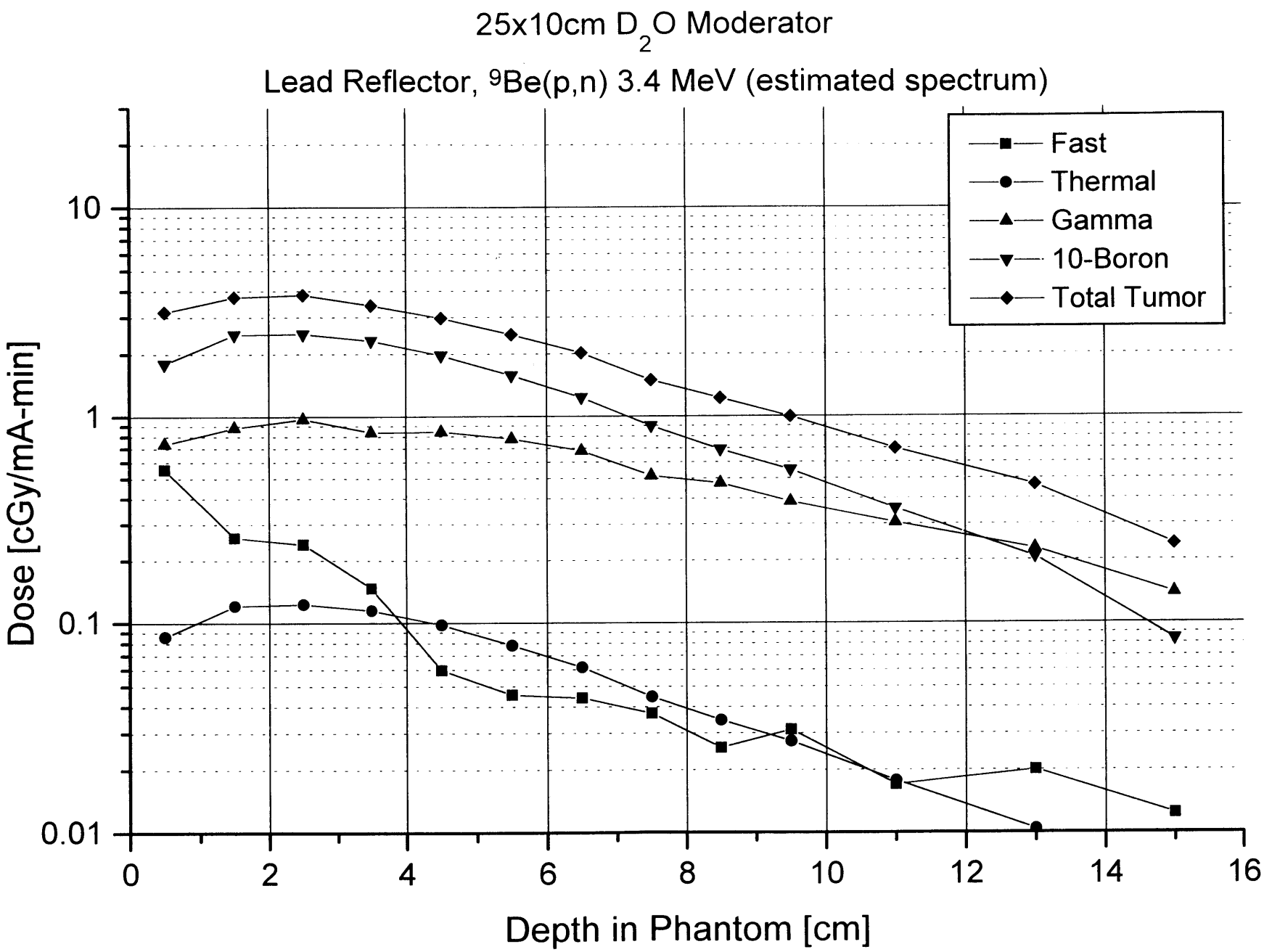
25x10cm D2O Moderator
Lead Reflector, 9Be(p,n) 3.4 MeV (estimated spectrum)
Fast
Thermal
Gamma
10-Boron
Total Tumor
Dose [cGy/mA-min]
10
1
0.1
0.01
0
2
4
6
8
10
12
14
16
Depth in Phantom [cm]

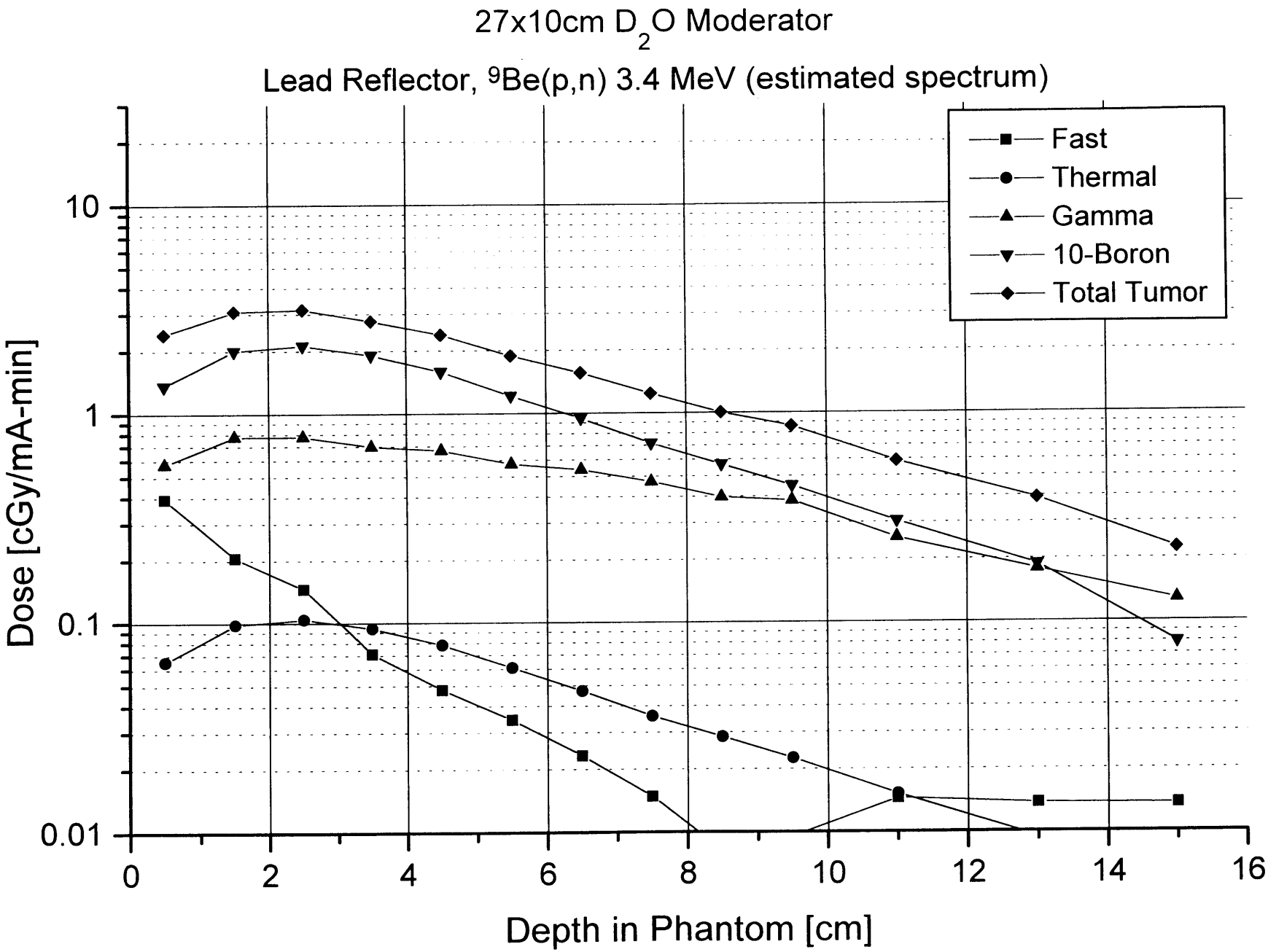
27x10cm D2O Moderator
Lead Reflector, 9Be(p,n) 3.4 MeV (estimated spectrum)
Fast
Thermal
Gamma
10-Boron
Total Tumor
Dose [cGy/mA-min]
10
1
0.1
0.01
0
2
4
6
8
10
12
14
16
Depth in Phantom [cm]

Table C-4: Therapy beam design configurations
for the reaction
9Be(p,n) E(p)=3.7 MeV

The following dimesions were not varied:
A=3 cm, C=10 cm, D=34 cm, E=34 cm, F=0.03 cm, H=0.03 cm, I=0.03 cm

Simulation Designation	Moderator material	Reflector material	Target Location [cm] (dimension A)	Moderator Length [cm] (dimension B)	Target to port Distance [cm] (dimension G)
37-gr-d2o-21x10	D2O	Graphite	3	21	18
37-gr-d2o-24x10	D2O	Graphite	3	24	21
37-gr-d2o-25x10	D2O	Graphite	3	25	22
37-gr-d2o-27x10	D2O	Graphite	3	27	24
37-pb-d2o-21x10	D2O	Lead	3	21	18
37-pb-d2o-24x10	D2O	Lead	3	24	21
37-pb-d2o-27x10	D2O	Lead	3	27	24
37-gr-alf-24x10	Al-AlF3	Graphite	3	24	21
37-gr-alf-27x10	Al-AlF4	Graphite	3	27	24

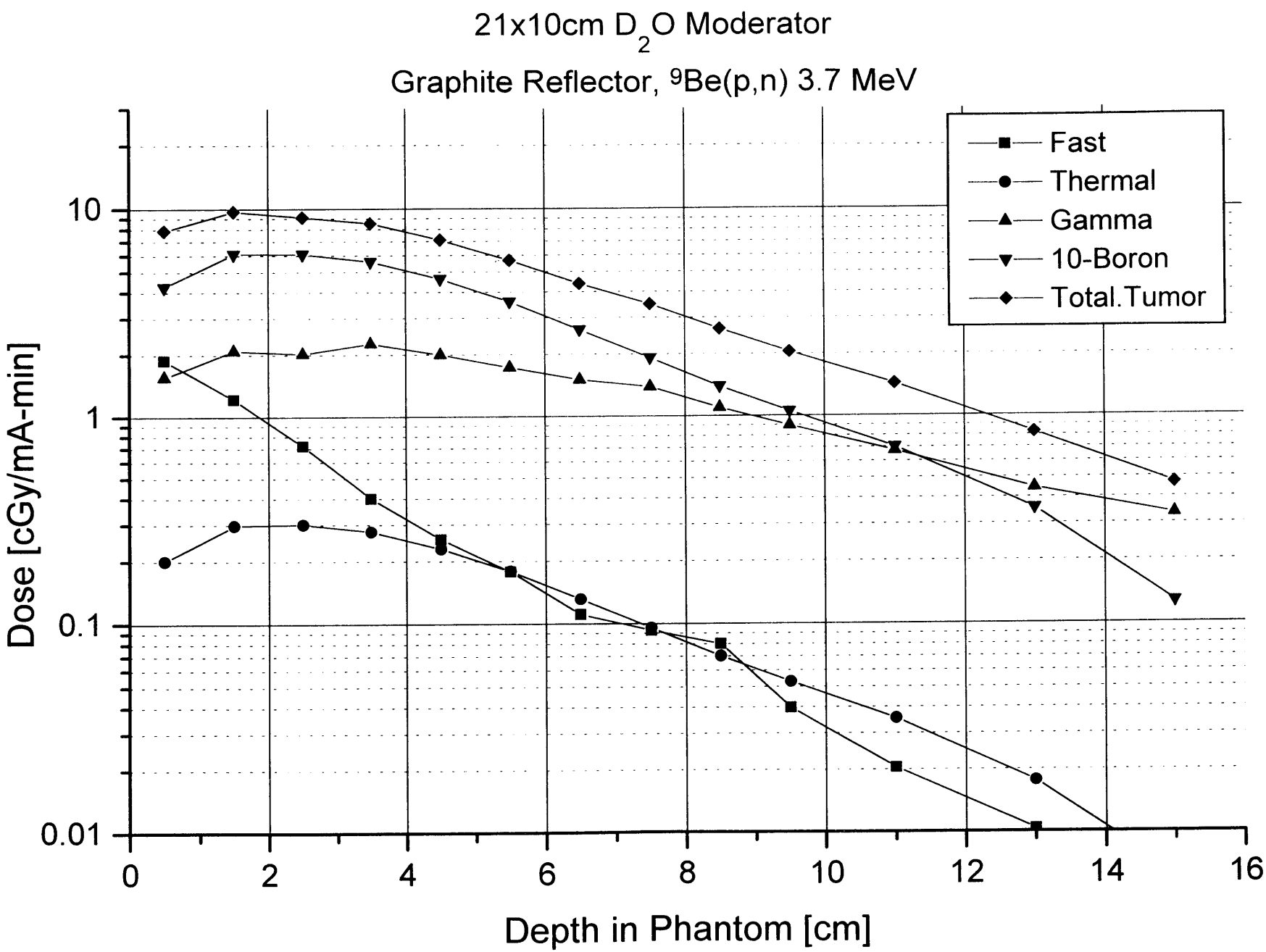
21x10cm D2O Moderator
Graphite Reflector, 9Be(p,n) 3.7 MeV
Fast
Thermal
Gamma
10-Boron
Total.Tumor
Dose [cGy/mA-min]
10
1
0.1
0.01
0
2
4
6
8
10
12
14
16
Depth in Phantom [cm]

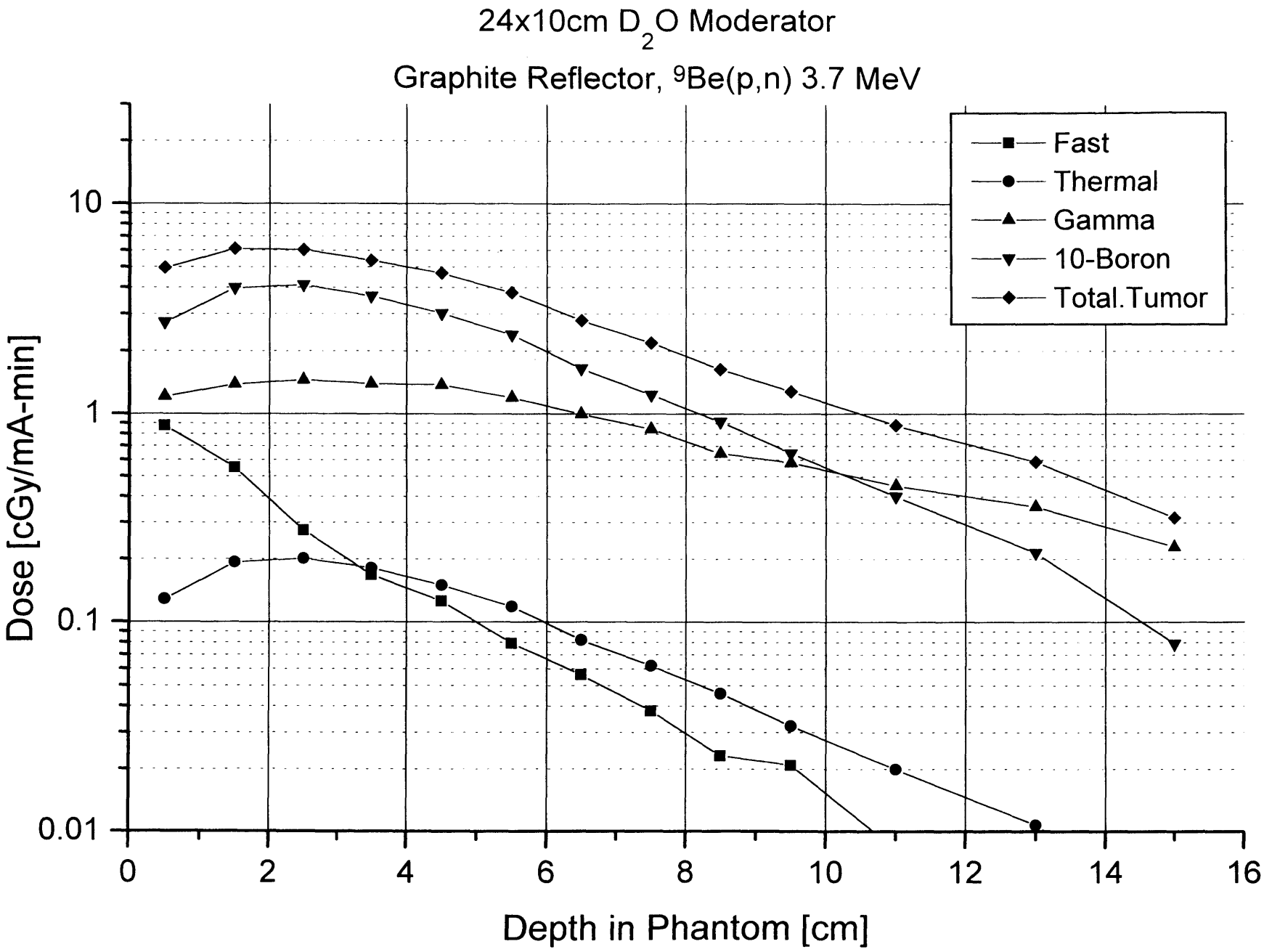
24x10cm D2O Moderator
Graphite Reflector, 9Be(p,n) 3.7 MeV
Fast
Thermal
Gamma
10-Boron
Total.Tumor
Dose [cGy/mA-min]
10
1
0.1
0.01
0
2
4
6
8
10
12
14
16
Depth in Phantom [cm]

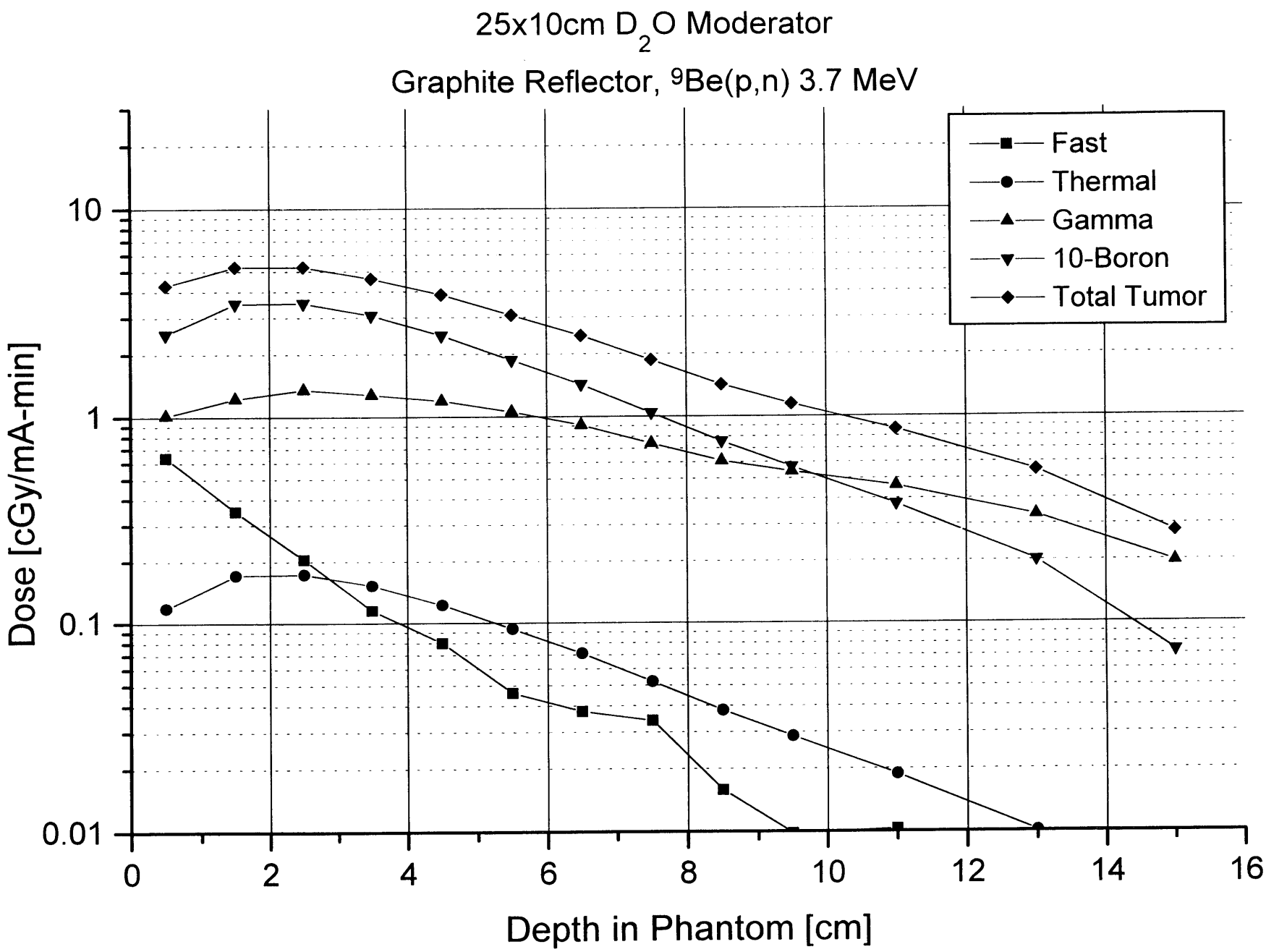
25x10cm D2O Moderator
Graphite Reflector, 9Be(p,n) 3.7 MeV
Fast
Thermal
Gamma
10-Boron
Total Tumor
Dose [cGy/mA-min]
10
1
0.1
0.01
0
2
4
6
8
10
12
14
16
Depth in Phantom [cm]

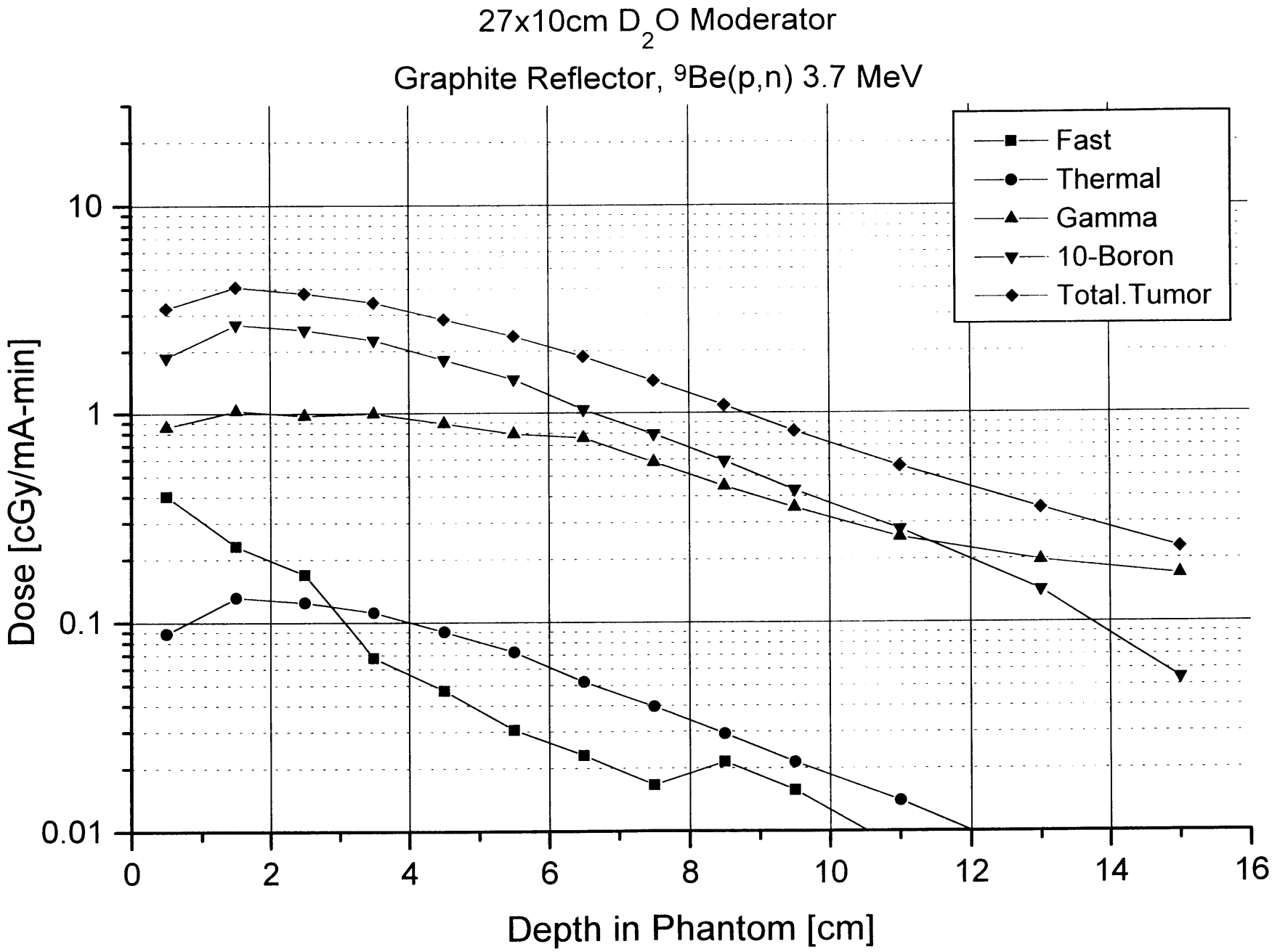
27x10cm D2O Moderator
Graphite Reflector, 9Be(p,n) 3.7 MeV
Fast
Thermal
Gamma
10-Boron
Total.Tumor
Dose [cGy/mA-min]
10
1
0.1
0.01
0
2
4
6
8
10
12
14
16
Depth in Phantom [cm]

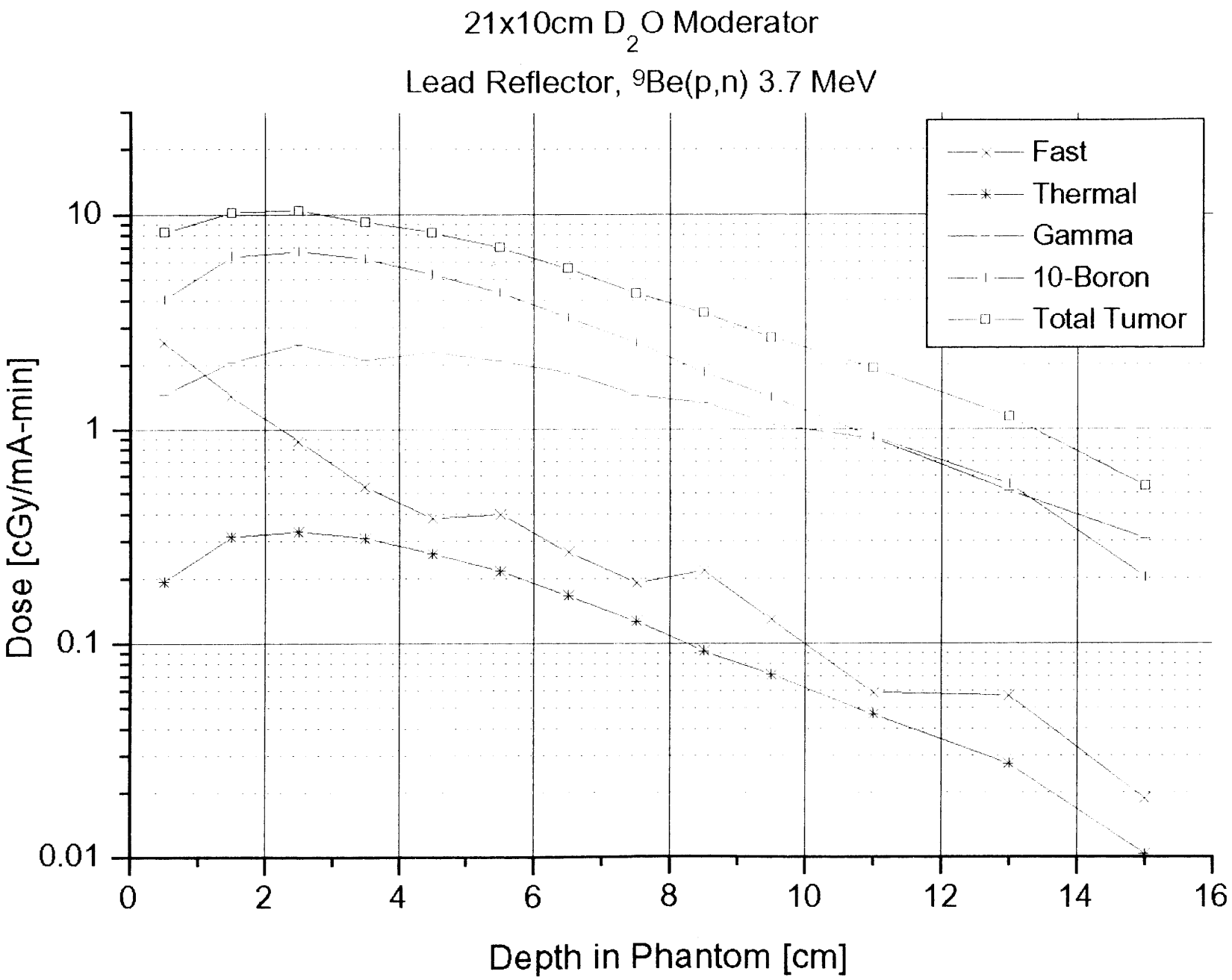
21x10cm D2O Moderator
Lead Reflector, 9Be(p,n) 3.7 MeV
Fast
Thermal
Gamma
10-Boron
Total Tumor
Dose [cGy/mA-min]
10
1
0.1
0.01
0
2
4
6
8
10
12
14
16
Depth in Phantom [cm]

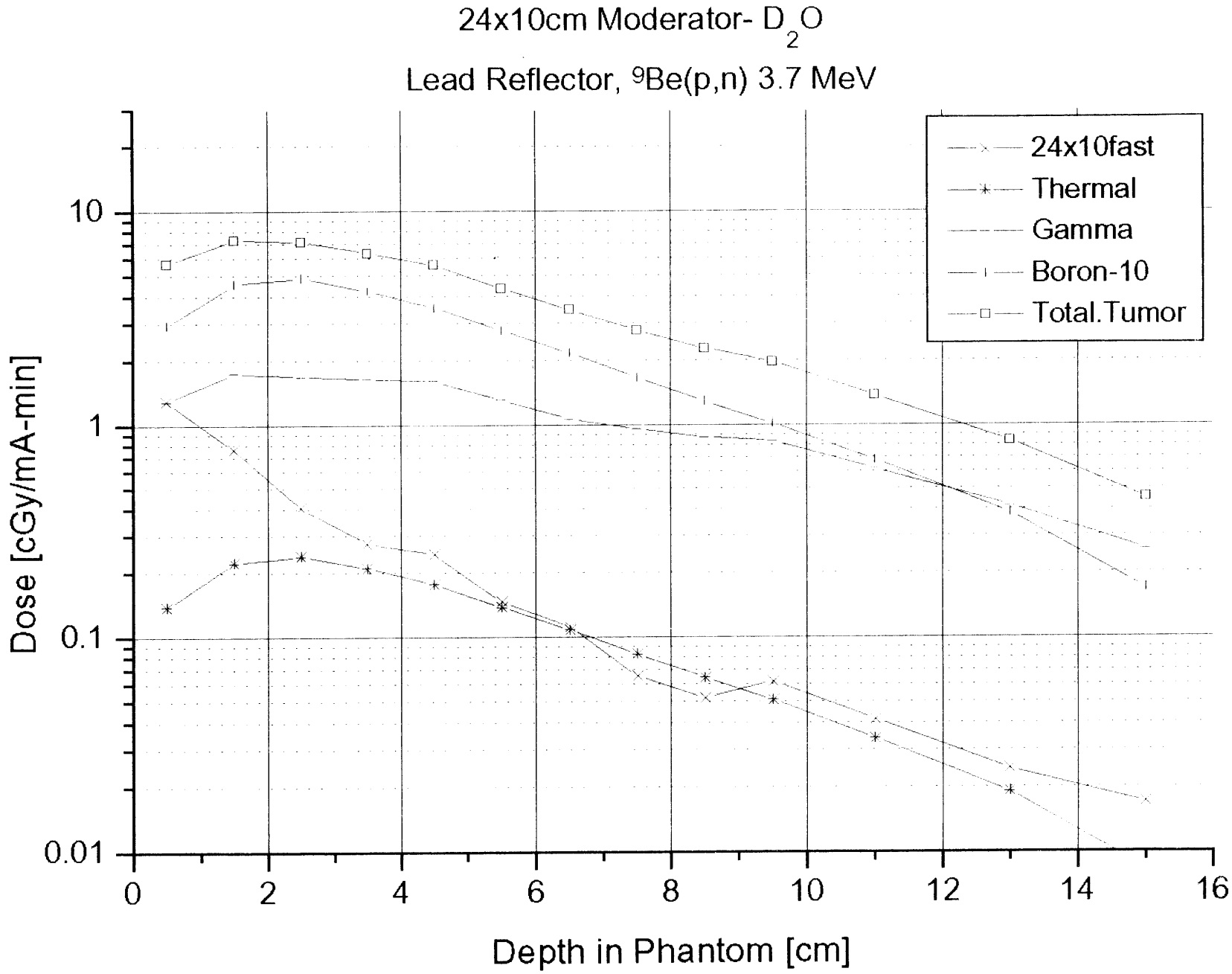
24x10cm Moderator- D_2O
Lead Reflector, $^9Be(p,n)$ 3.7 MeV
24x10fast
Thermal
Gamma
Boron-10
Total.Tumor
Dose [cGy/mA-min]
10
1
0.1
0.01
0
2
4
6
8
10
12
14
16
Depth in Phantom [cm]

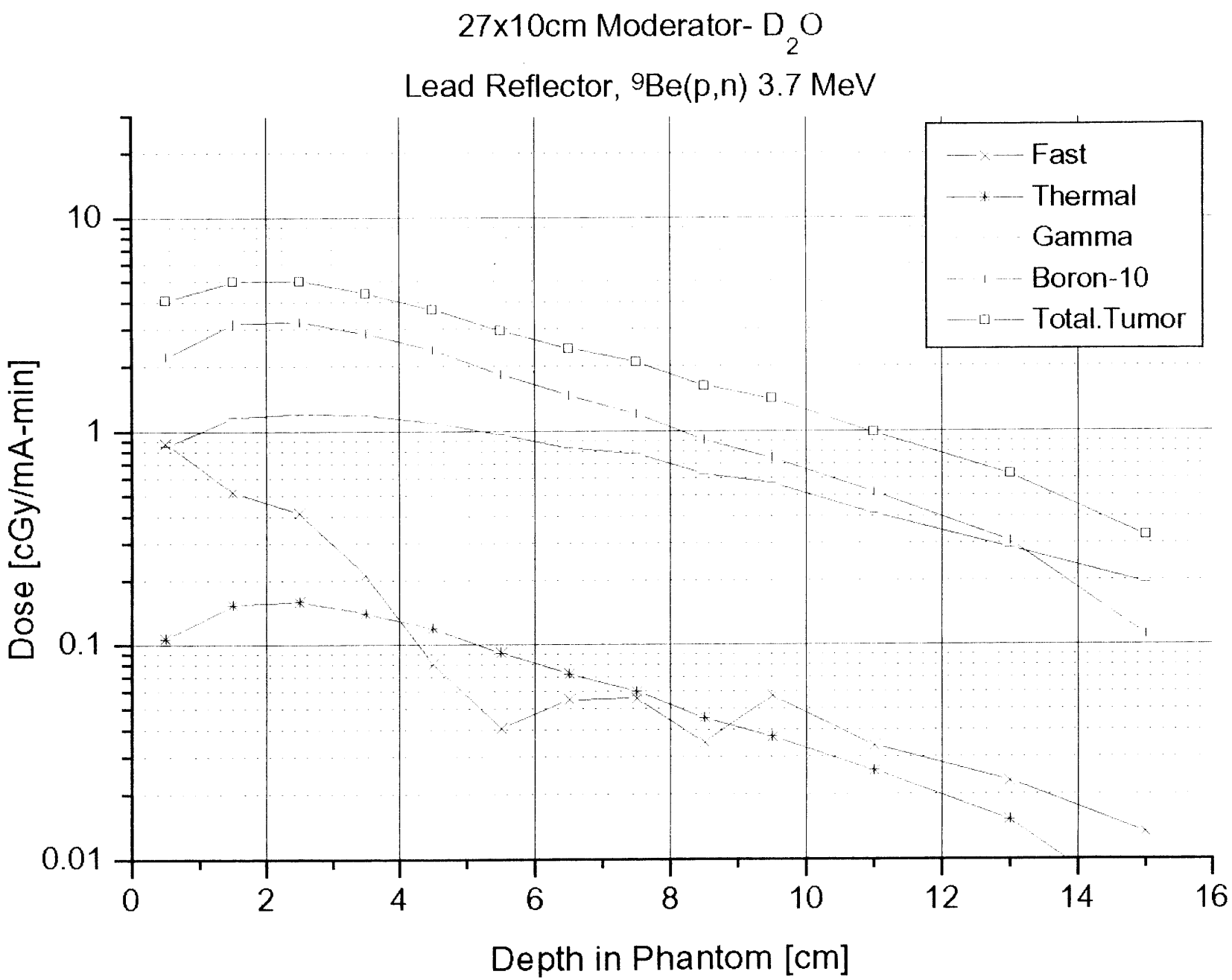
27x10cm Moderator- D_2O
Lead Reflector, $^9Be(p,n)$ 3.7 MeV
Fast
Thermal
Gamma
Boron-10
Total.Tumor
Dose [cGy/mA-min]
10
1
0.1
0.01
0
2
4
6
8
10
12
14
16
Depth in Phantom [cm]

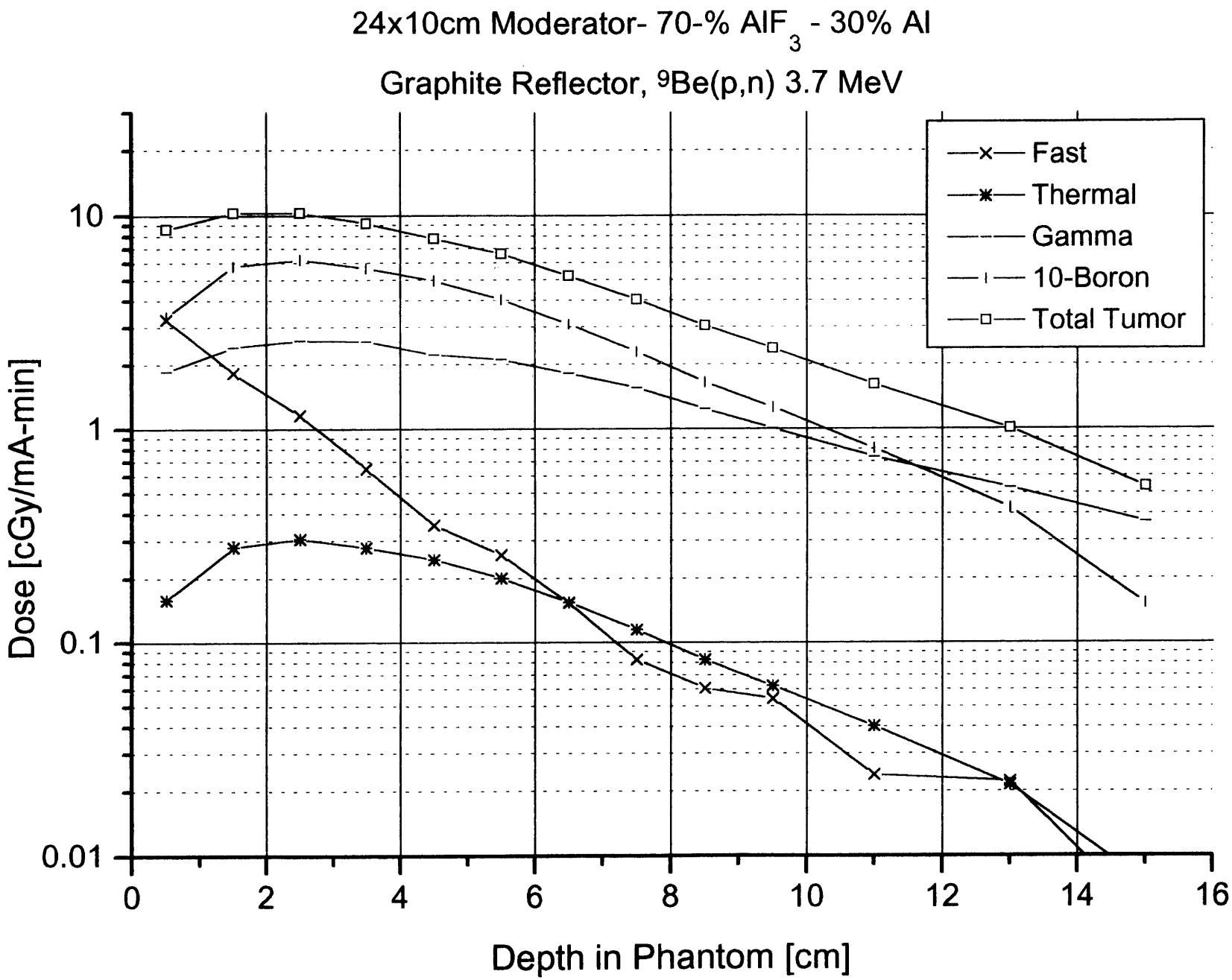
24x10cm Moderator- 70-% AlF3 - 30% Al
Graphite Reflector, 9Be(p,n) 3.7 MeV
Fast
Thermal
Gamma
10-Boron
Total Tumor
Dose [cGy/mA-min]
10
1
0.1
0.01
0
2
4
6
8
10
12
14
16
Depth in Phantom [cm]

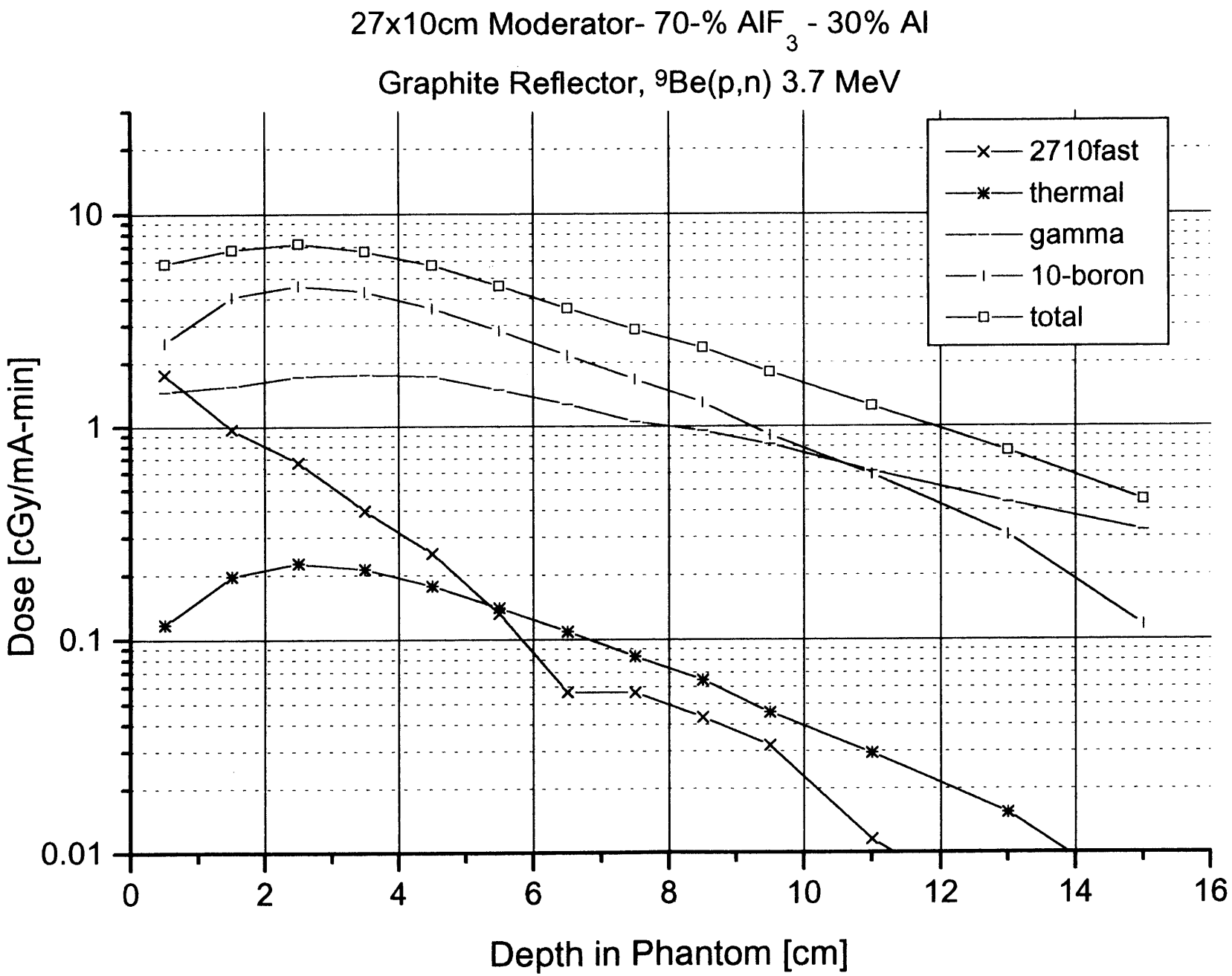
27x10cm Moderator- 70-% AlF3 - 30% Al
Graphite Reflector, 9Be(p,n) 3.7 MeV
2710fast
thermal
gamma
10-boron
total
Dose [cGy/mA-min]
10
1
0.1
0.01
0
2
4
6
8
10
12
14
16
Depth in Phantom [cm]

Table C-5: Therapy beam design configurations
for the reaction
9Be(p,n) E(p)=4.0 MeV

The following dimesions were not varied:
A=3 cm, D=34 cm, E=34 cm, F=0.03 cm, H=0.03 cm, I=0.03 cm

Simulation Designation	Moderator material	Reflector material	Target Location [cm] (dimension A)	Moderator Length [cm] (dimension B)	Moderator Radius [cm] (dimension C)	Target to port Distance [cm] (dimension G)
40-gr-d2o-24x10	D2O	Graphite	3	24	10	21
40-gr-d2o-27x8	D2O	Graphite	3	27	8	24
40-gr-d2o-27x10	D2O	Graphite	3	27	10	24
40-gr-d2o-27x12	D2O	Graphite	3	27	12	24
40-gr-d2o-30x10	D2O	Graphite	3	30	10	27
40-gr-d2o-26x10	D2O	Graphite	3	26	10	23
40-pb-d2o-24x10	D2O	Lead	3	24	10	21
40-pb-d2o-27x10	D2O	Lead	3	27	10	24
40-pb-d2o-30x10	D2O	Lead	3	30	10	27
40-bi-d2o-24x10	D2O	Bismuth	3	24	10	21
40-bi-d2o-27x10	D2O	Bismuth	3	27	10	24
40-bi-d2o-30x10	D2O	Bismuth	3	30	10	27
40-ni-d2O-24x10	D2O	Nickel	3	30	10	27
40-gr-alf-25x10	Al-AlF3	Graphite	3	25	10	22
40-gr-alf-30x10	Al-AlF4	Graphite	3	30	10	27
40-gr-alf-30x12	Al-AlF5	Graphite	3	30	12	27
40-gr-alf-34x10	Al-AlF6	Graphite	3	34	10	31
40-gr-alf-35x10	Al-AlF7	Graphite	3	35	10	32
40-gr-alf-40x10	Al-AlF8	Graphite	3	40	10	37
40-pb-alf-25x10	Al-AlF9	Lead	3	25	10	22
40-pb-alf-30x10	Al-AlF10	Lead	3	30	10	27
40-pb-alf-30x12	Al-AlF11	Lead	3	30	12	27
40-pb-alf-35x10	Al-AlF12	Lead	3	35	10	32
40-pb-alf-40x10	Al-AlF13	Lead	3	40	10	37

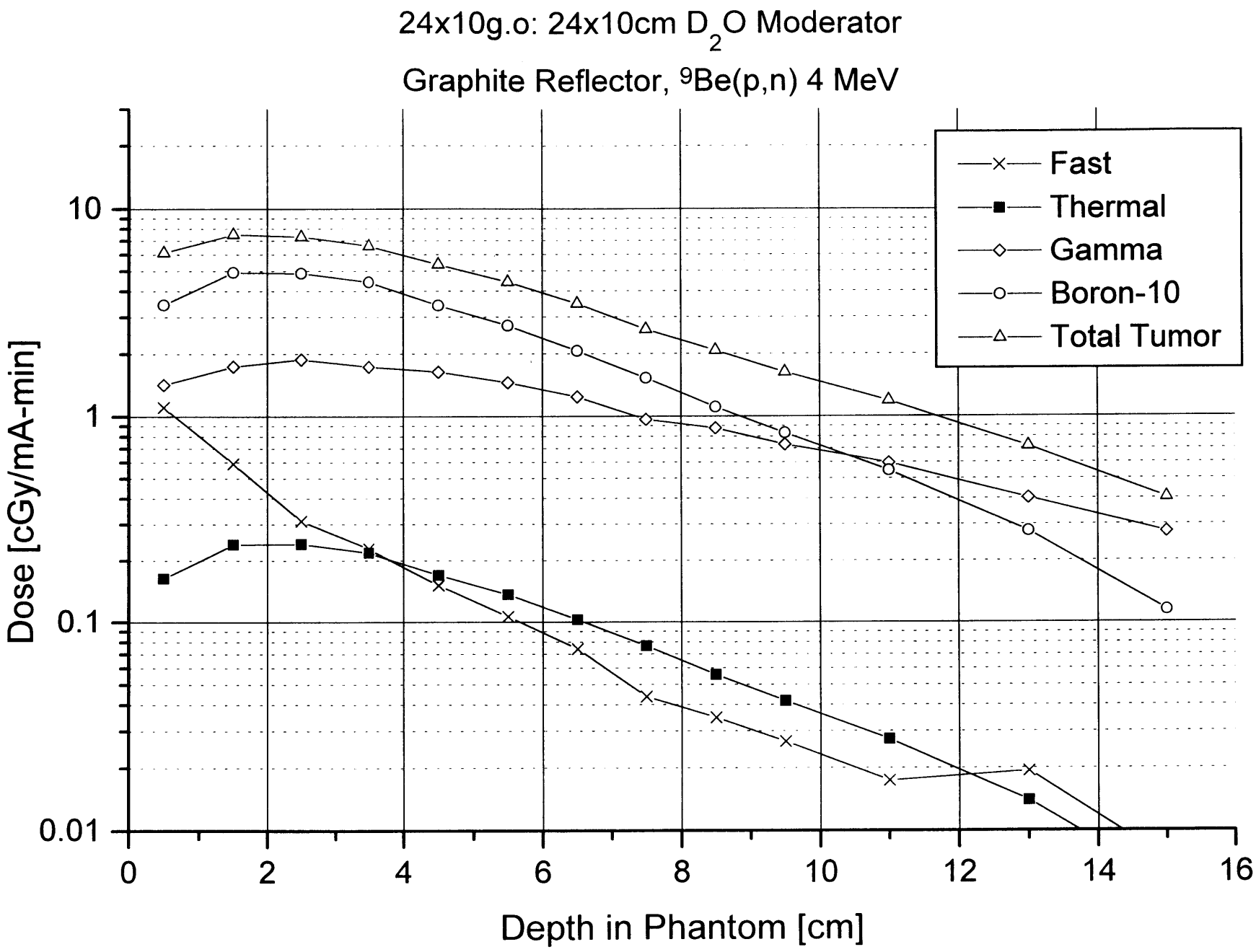
24x10g.o: 24x10cm D2O Moderator
Graphite Reflector, 9Be(p,n) 4 MeV
Fast
Thermal
Gamma
Boron-10
Total Tumor
Dose [cGy/mA-min]
10
1
0.1
0.01
0
2
4
6
8
10
12
14
16
Depth in Phantom [cm]

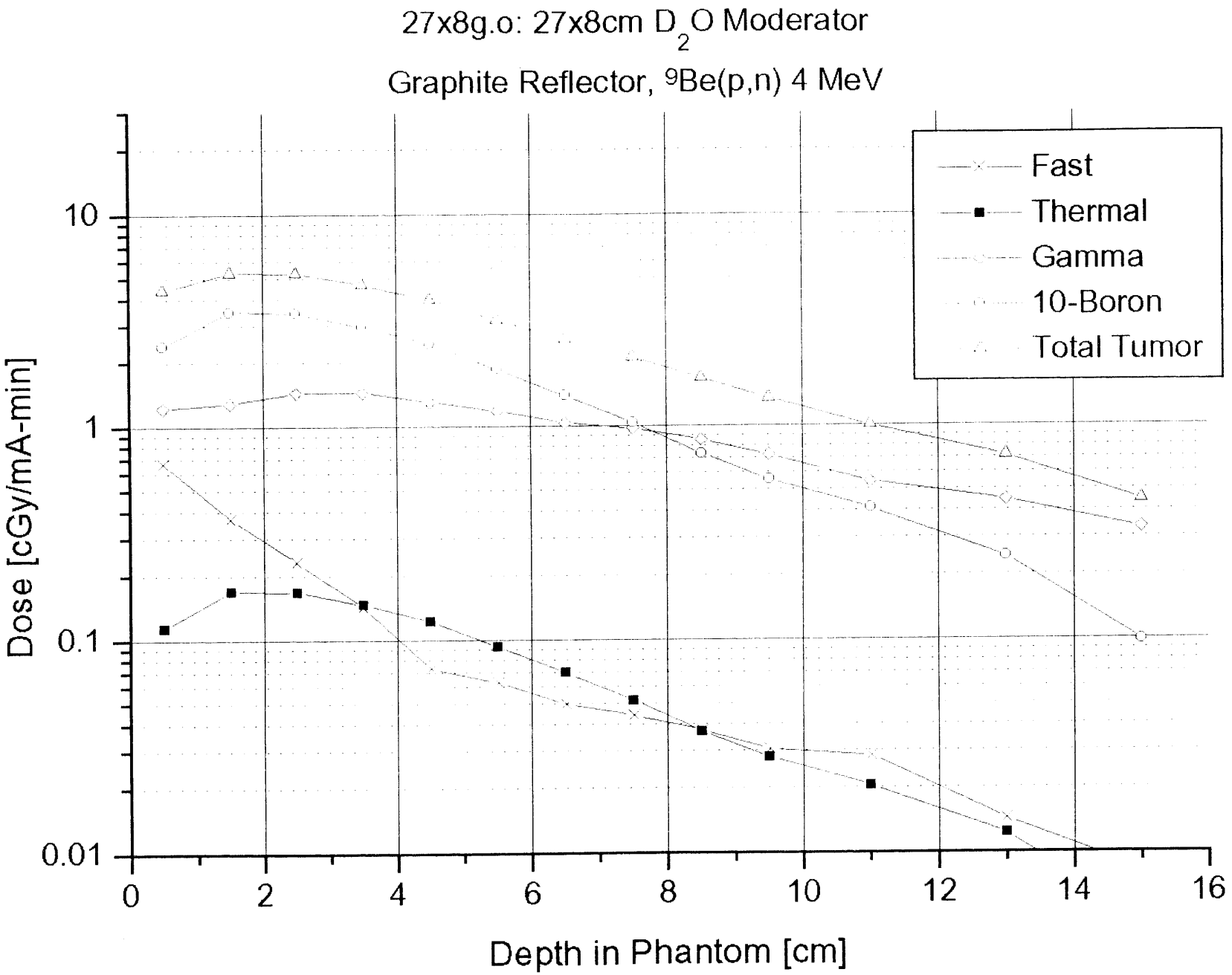
27x8g.o: 27x8cm D2O Moderator
Graphite Reflector, 9Be(p,n) 4 MeV
Fast
Thermal
Gamma
10-Boron
Total Tumor
Dose [cGy/mA-min]
10
1
0.1
0.01
0
2
4
6
8
10
12
14
16
Depth in Phantom [cm]

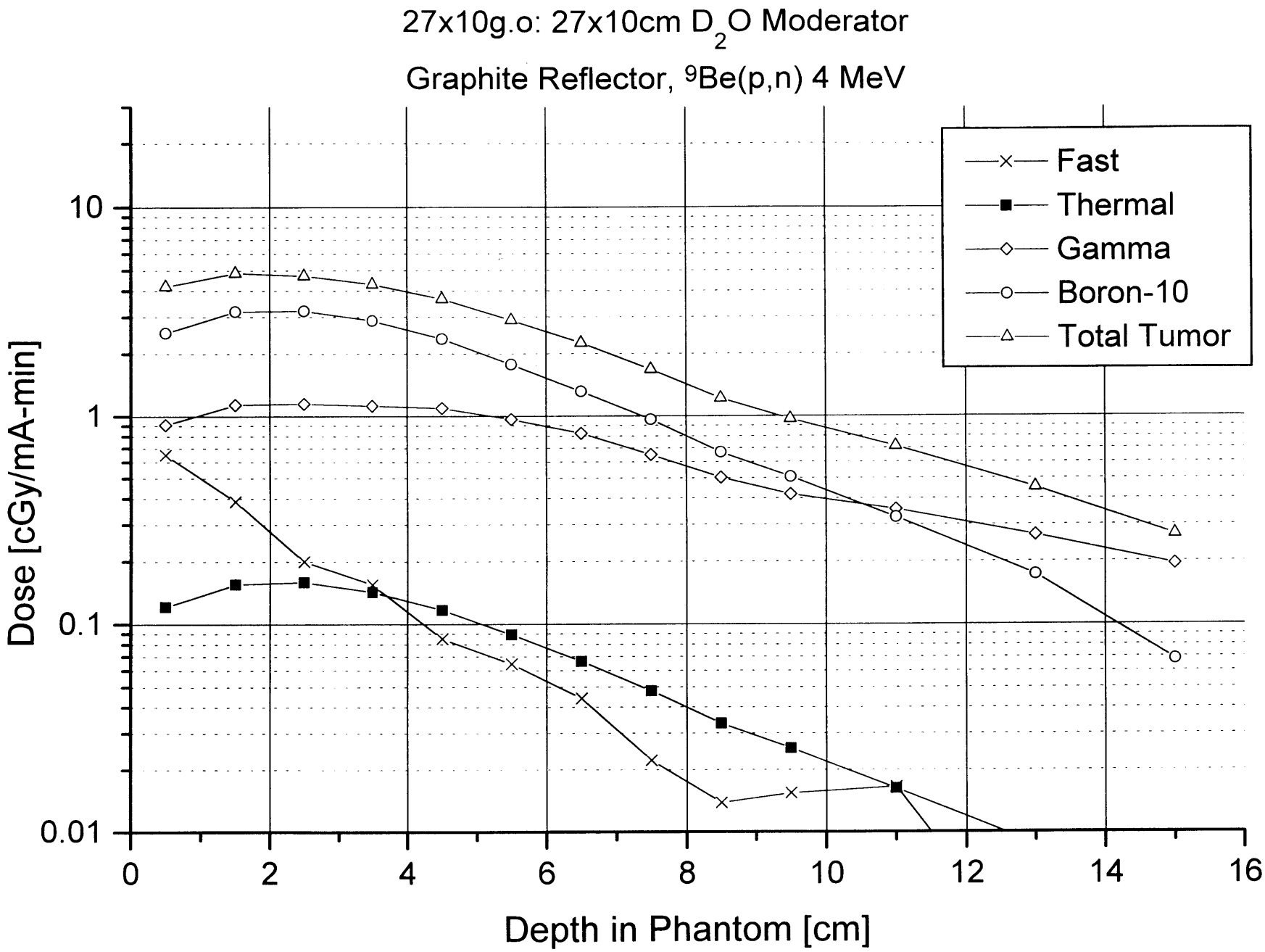
27x10g.o: 27x10cm D2O Moderator
Graphite Reflector, 9Be(p,n) 4 MeV
Fast
Thermal
Gamma
Boron-10
Total Tumor
Dose [cGy/mA-min]
10
1
0.1
0.01
0
2
4
6
8
10
12
14
16
Depth in Phantom [cm]

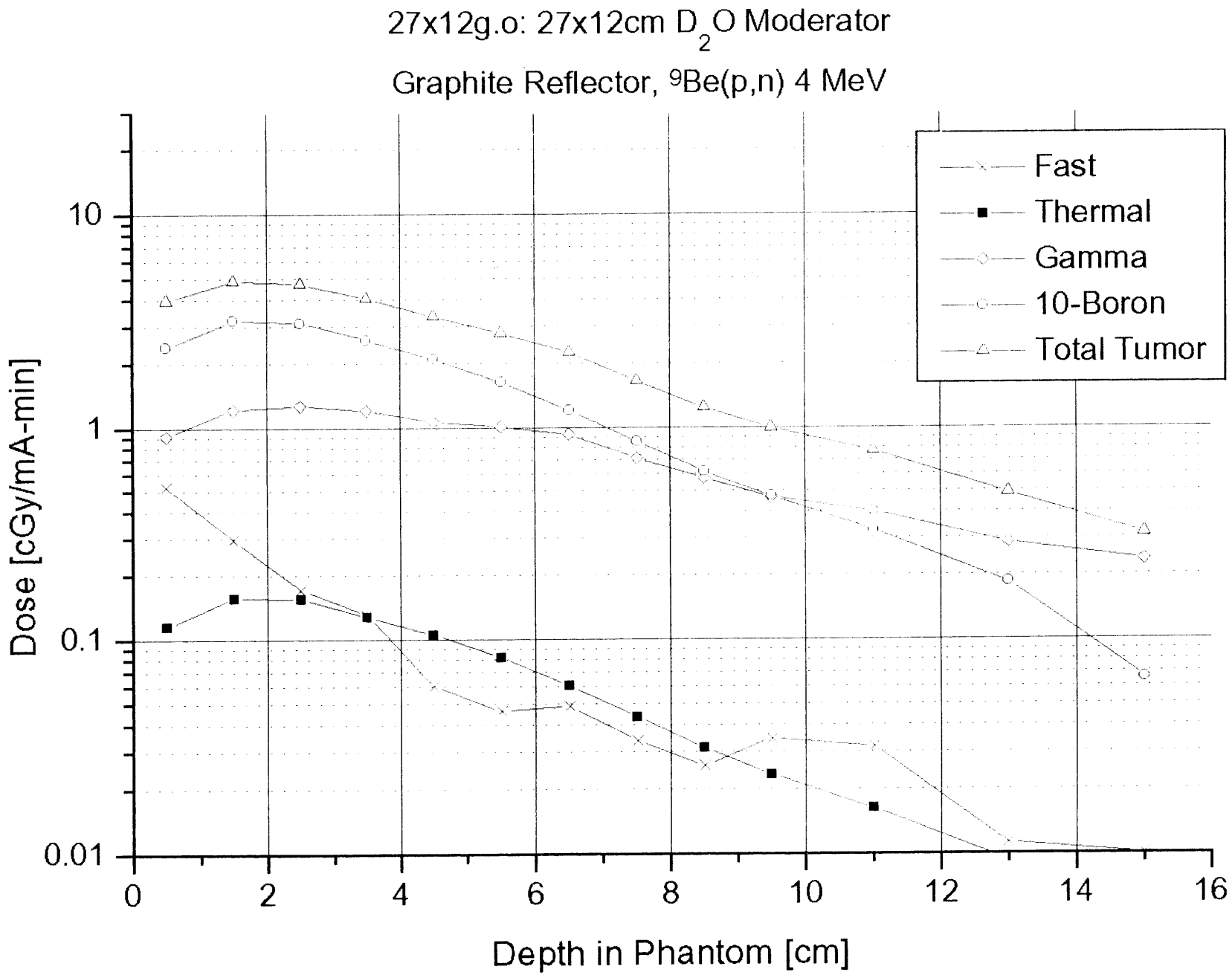
27x12g.o: 27x12cm D2O Moderator
Graphite Reflector, 9Be(p,n) 4 MeV
Fast
Thermal
Gamma
10-Boron
Total Tumor
Dose [cGy/mA-min]
10
1
0.1
0.01
0
2
4
6
8
10
12
14
16
Depth in Phantom [cm]

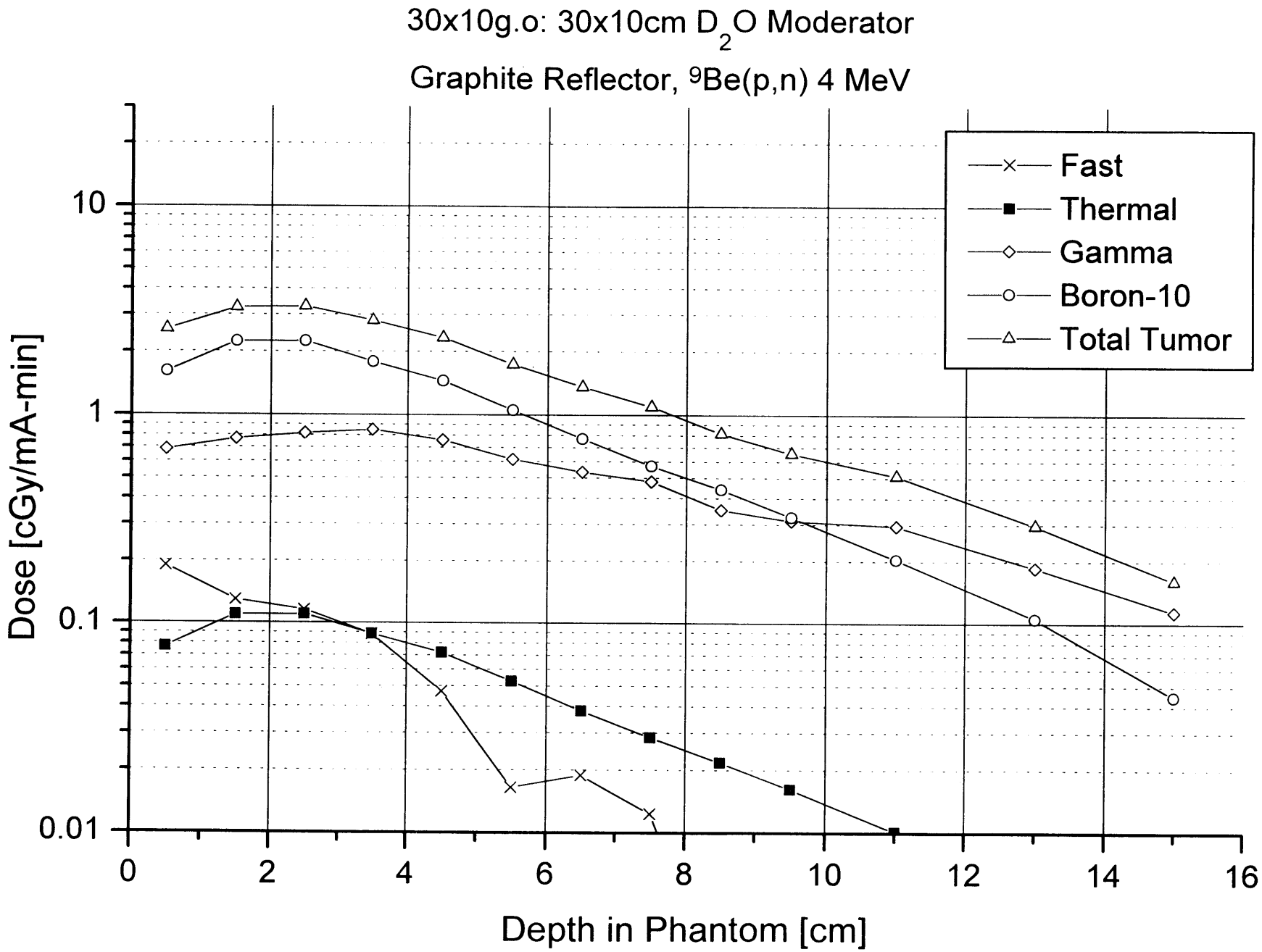
30x10g.o: 30x10cm D2O Moderator
Graphite Reflector, 9Be(p,n) 4 MeV
Fast
Thermal
Gamma
Boron-10
Total Tumor
Dose [cGy/mA-min]
10
1
0.1
0.01
0
2
4
6
8
10
12
14
16
Depth in Phantom [cm]

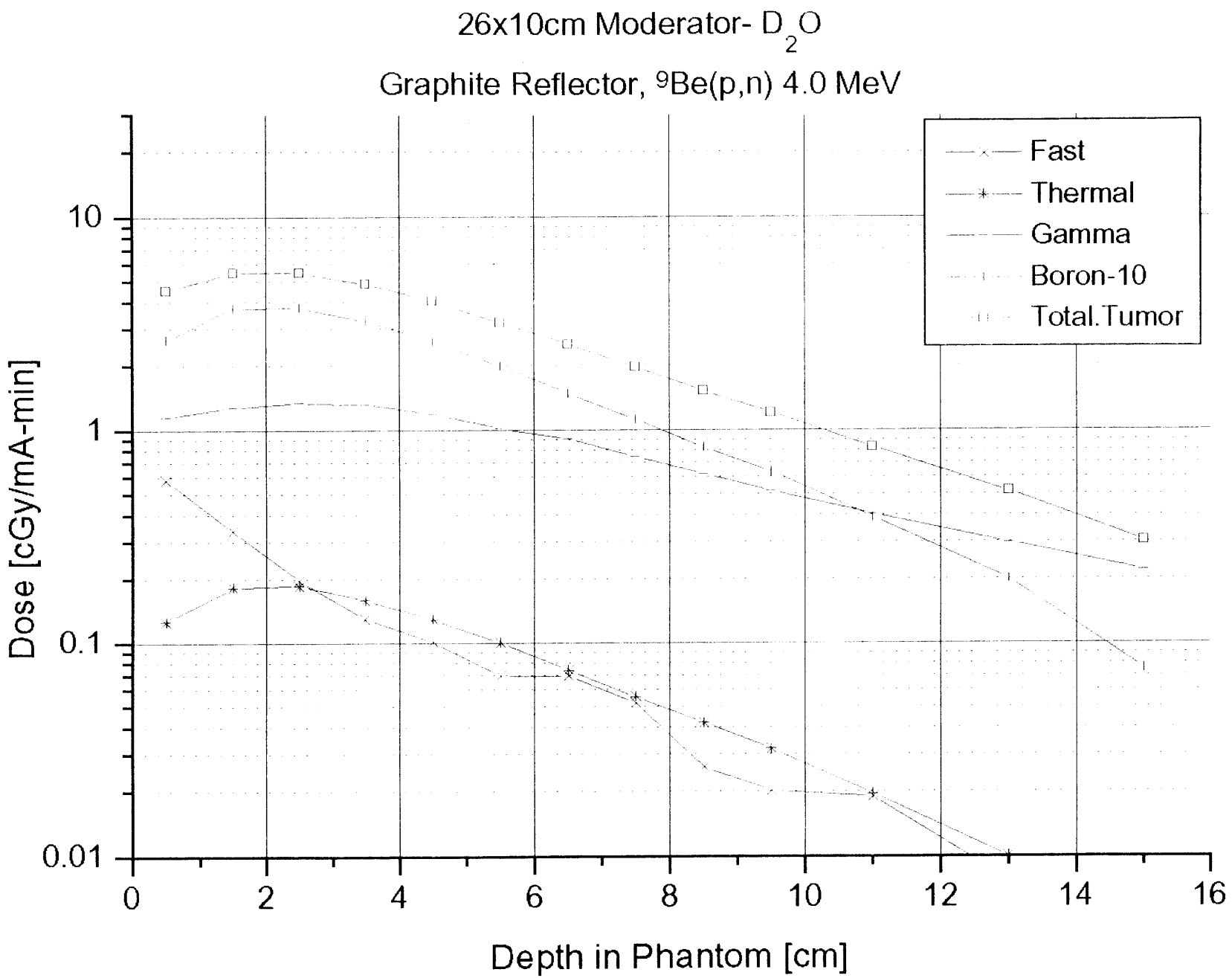
26x10cm Moderator- D_2O
Graphite Reflector, $^9Be(p,n)$ 4.0 MeV
Fast
Thermal
Gamma
Boron-10
Total.Tumor
Dose [cGy/mA-min]
10
1
0.1
0.01
0
2
4
6
8
10
12
14
16
Depth in Phantom [cm]

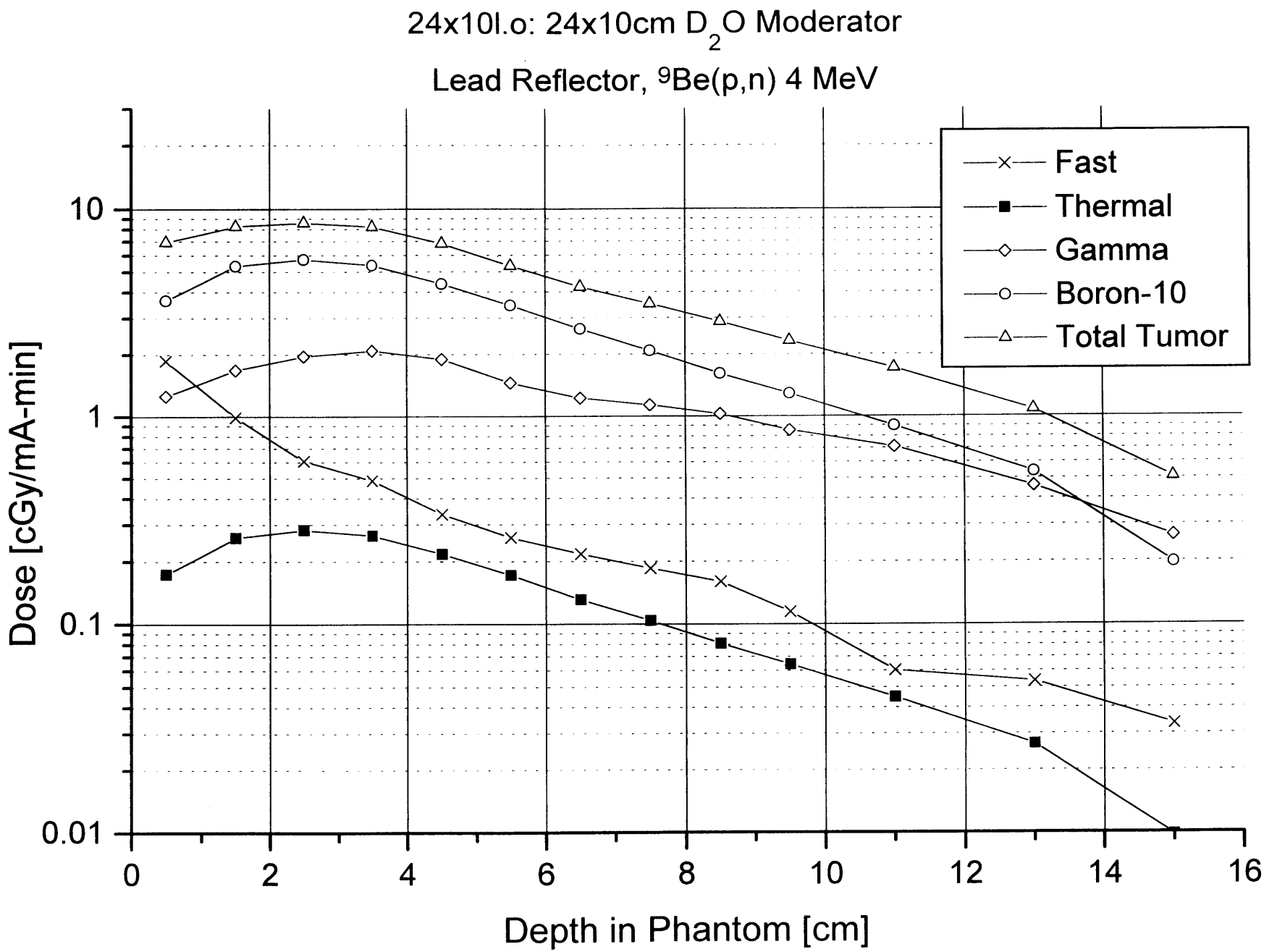
24x10l.o: 24x10cm D2O Moderator
Lead Reflector, 9Be(p,n) 4 MeV
Fast
Thermal
Gamma
Boron-10
Total Tumor
Dose [cGy/mA-min]
10
1
0.1
0.01
0
2
4
6
8
10
12
14
16
Depth in Phantom [cm]

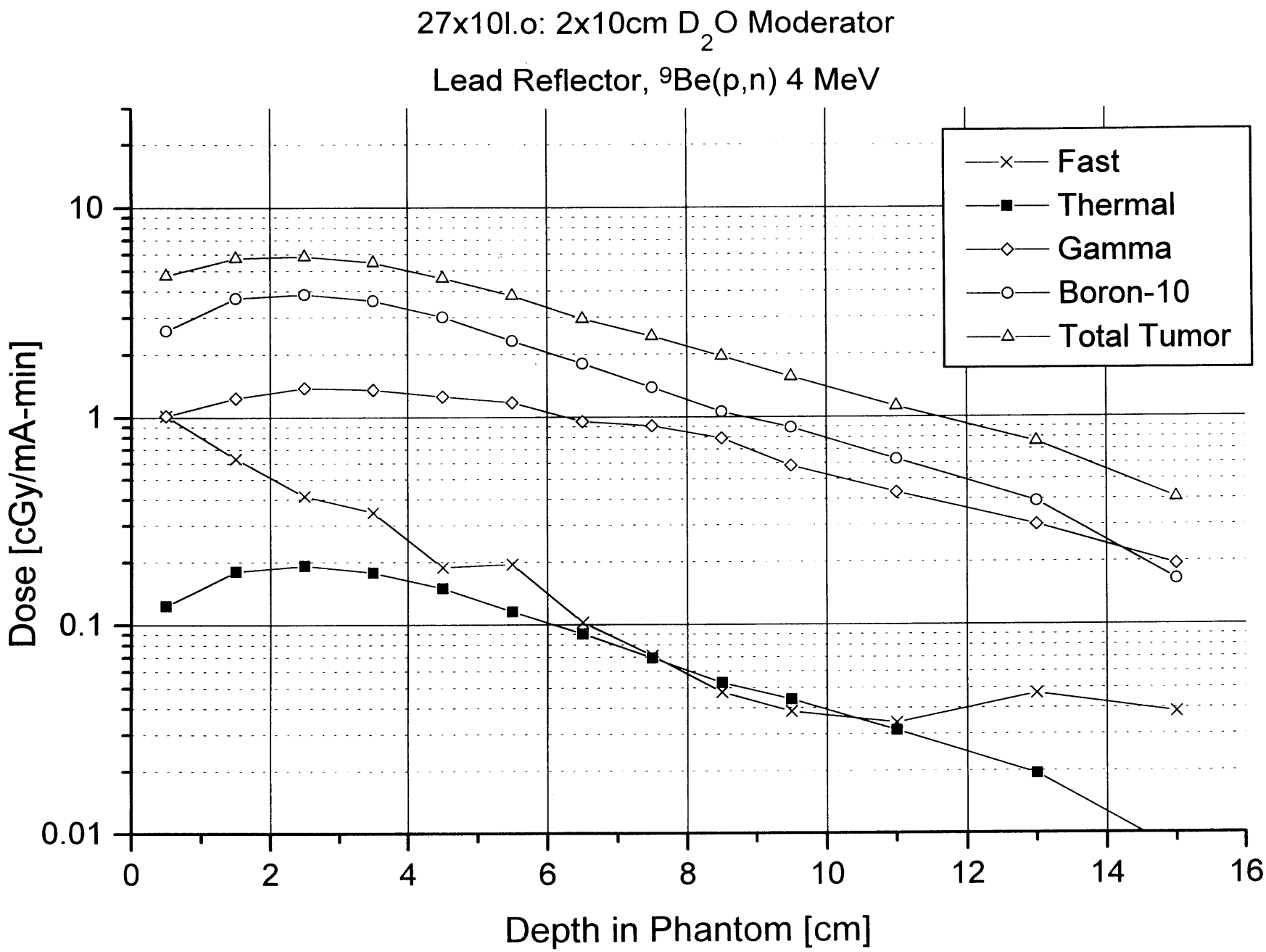
27x10l.o: 2x10cm D2O Moderator
Lead Reflector, 9Be(p,n) 4 MeV
Fast
Thermal
Gamma
Boron-10
Total Tumor
Dose [cGy/mA-min]
10
1
0.1
0.01
0
2
4
6
8
10
12
14
16
Depth in Phantom [cm]

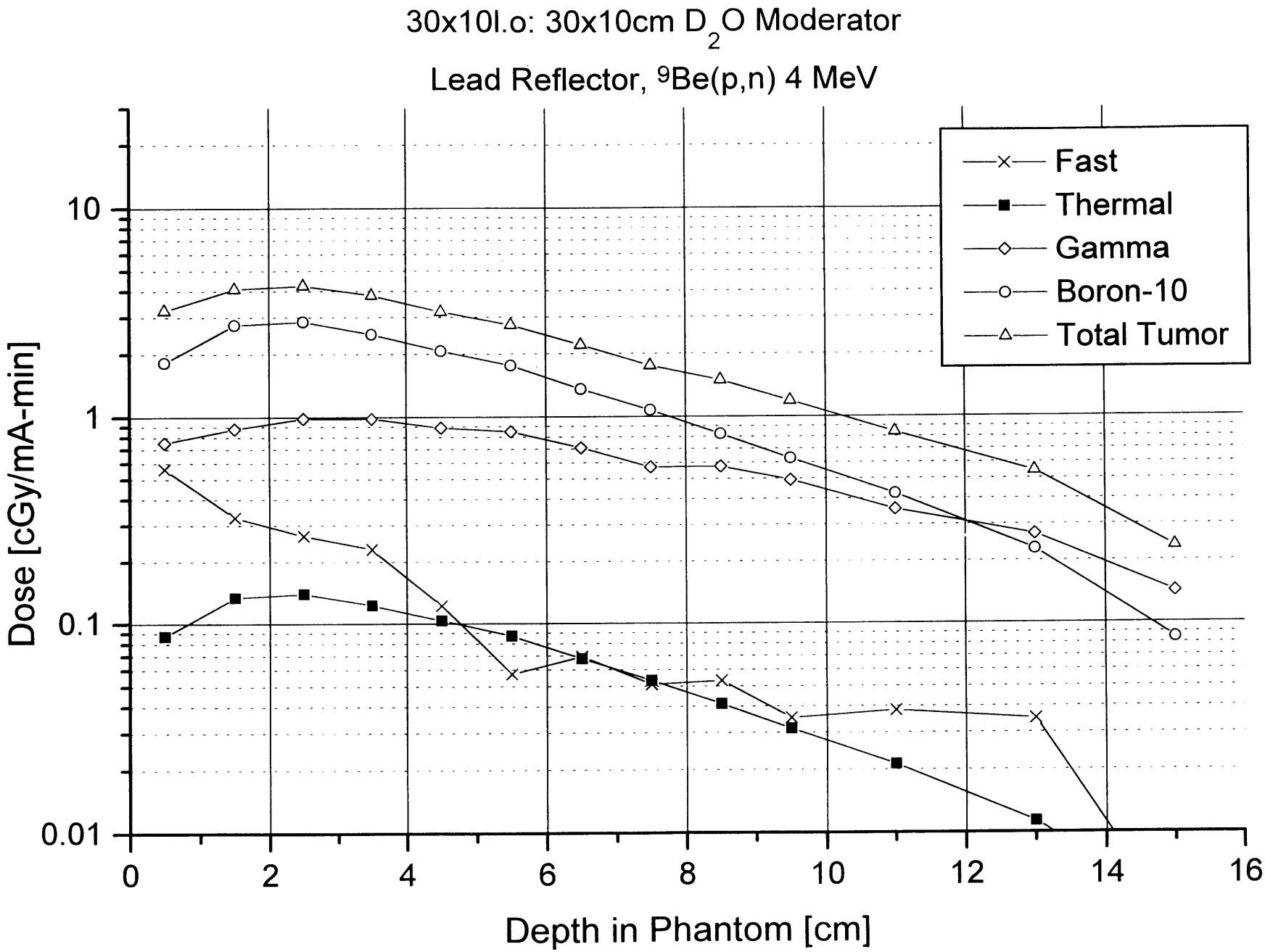
30x10l.o: 30x10cm D2O Moderator
Lead Reflector, 9Be(p,n) 4 MeV
Fast
Thermal
Gamma
Boron-10
Total Tumor
Dose [cGy/mA-min]
10
1
0.1
0.01
0
2
4
6
8
10
12
14
16
Depth in Phantom [cm]

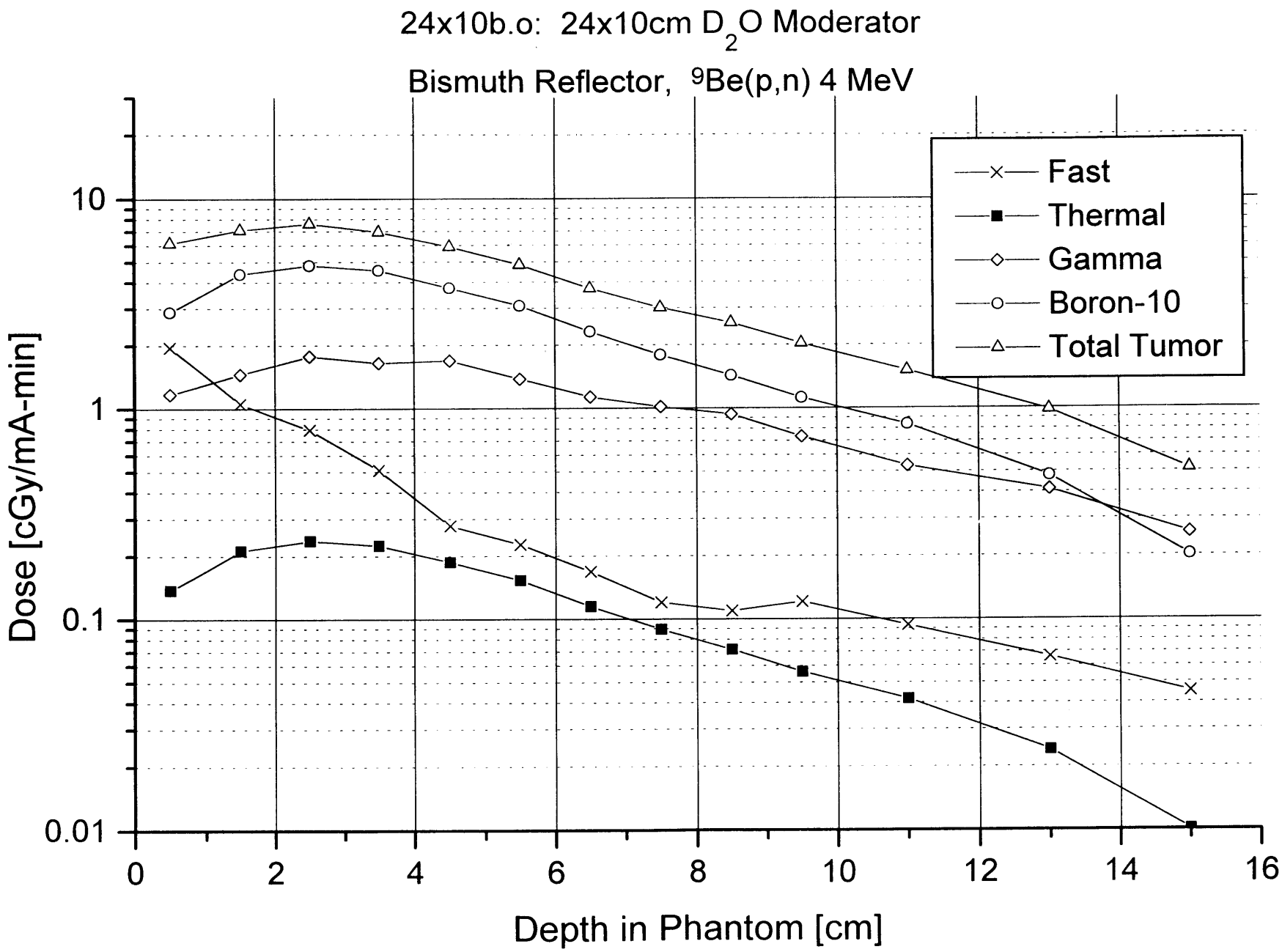
24x10b.o: 24x10cm D2O Moderator
Bismuth Reflector, 9Be(p,n) 4 MeV
Fast
Thermal
Gamma
Boron-10
Total Tumor
Dose [cGy/mA-min]
10
1
0.1
0.01
0
2
4
6
8
10
12
14
16
Depth in Phantom [cm]

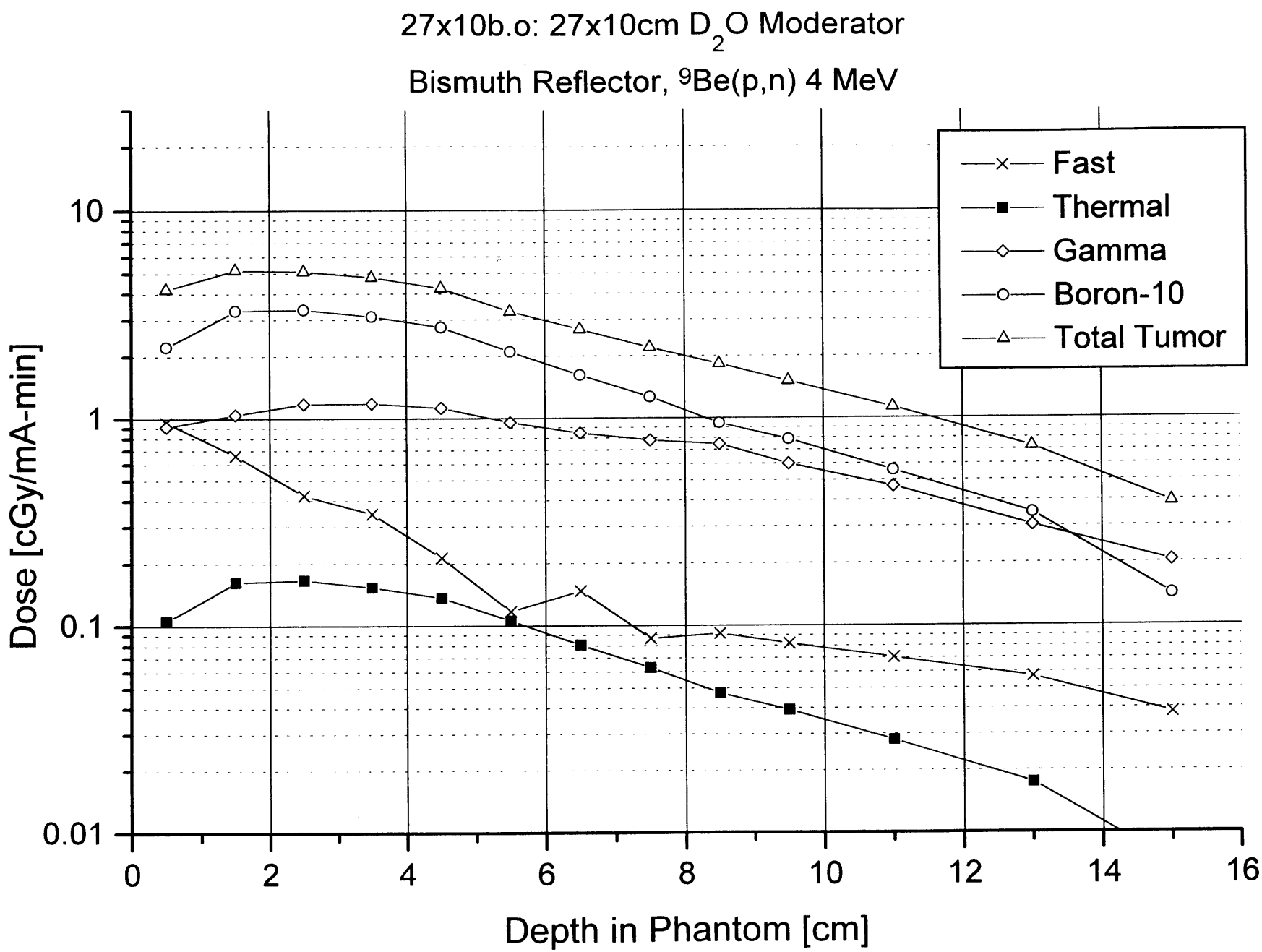
27x10b.o: 27x10cm D2O Moderator
Bismuth Reflector, 9Be(p,n) 4 MeV
Fast
Thermal
Gamma
Boron-10
Total Tumor
Dose [cGy/mA-min]
10
1
0.1
0.01
0
2
4
6
8
10
12
14
16
Depth in Phantom [cm]

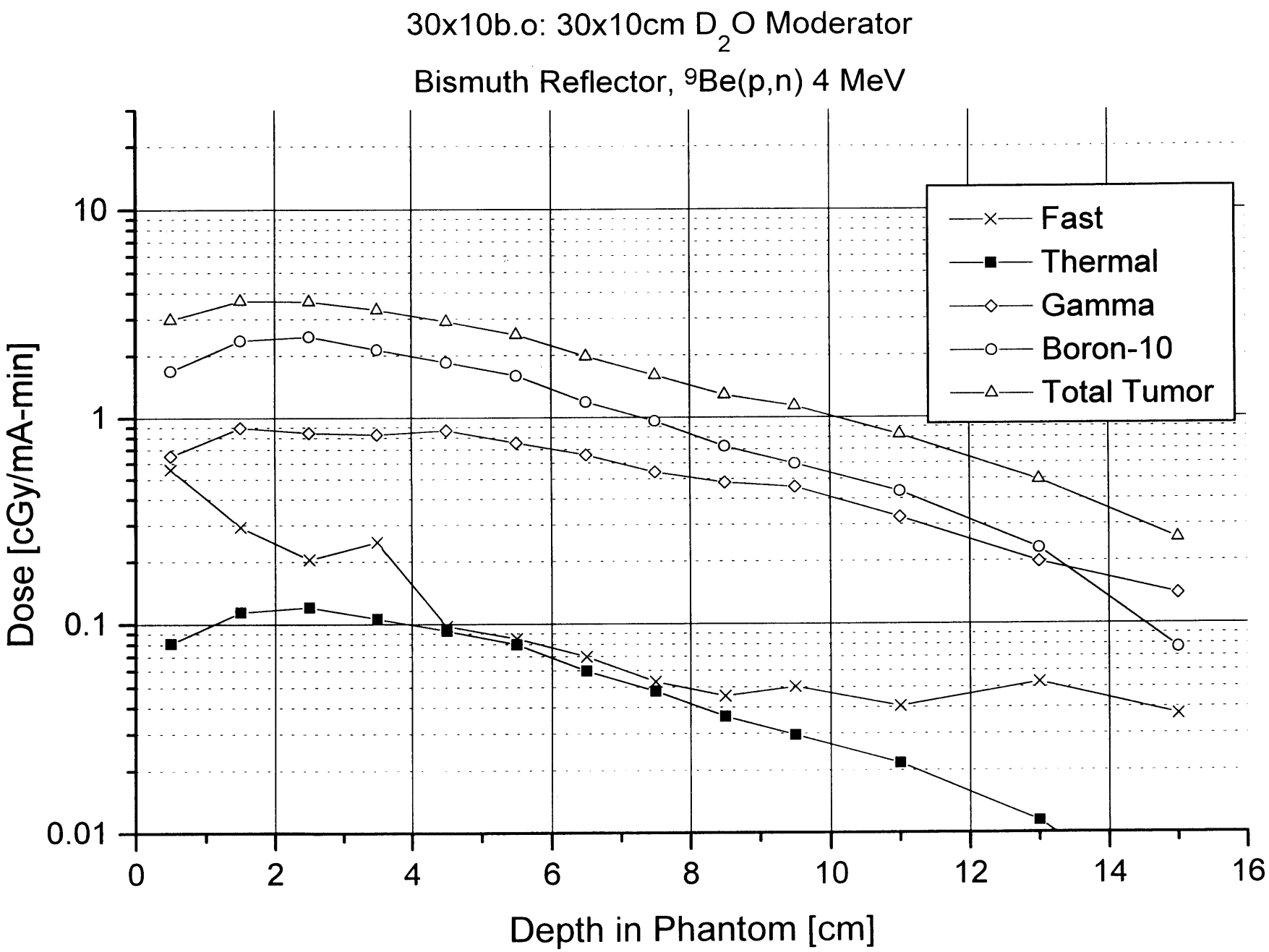
30x10b.o: 30x10cm D2O Moderator
Bismuth Reflector, 9Be(p,n) 4 MeV
Dose [cGy/mA-min]
Depth in Phantom [cm]
Fast
Thermal
Gamma
Boron-10
Total Tumor
10
1
0.1
0.01
0
2
4
6
8
10
12
14
16

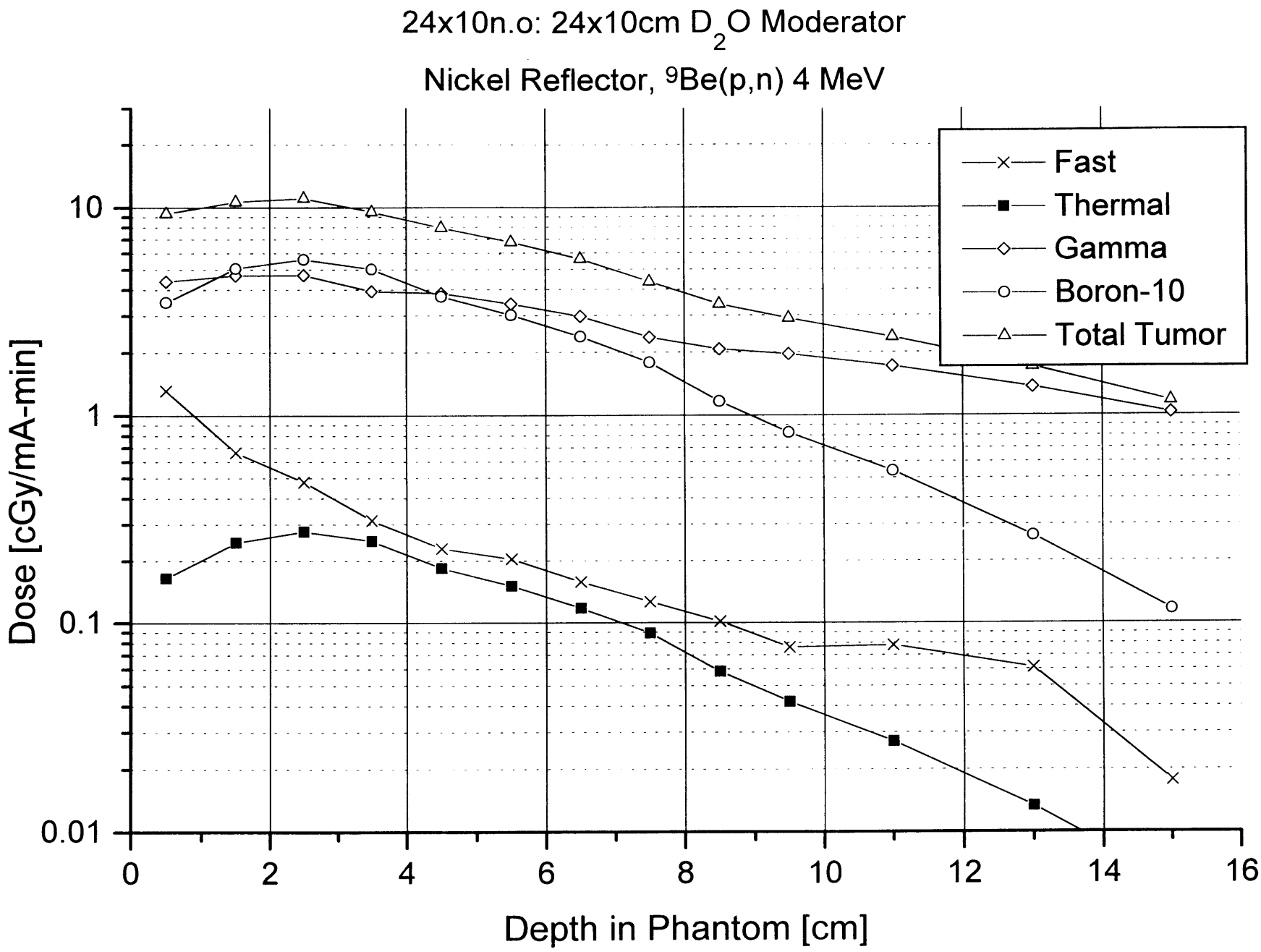
24x10n.o: 24x10cm D2O Moderator
Nickel Reflector, 9Be(p,n) 4 MeV
Fast
Thermal
Gamma
Boron-10
Total Tumor
Dose [cGy/mA-min]
10
1
0.1
0.01
0
2
4
6
8
10
12
14
16
Depth in Phantom [cm]

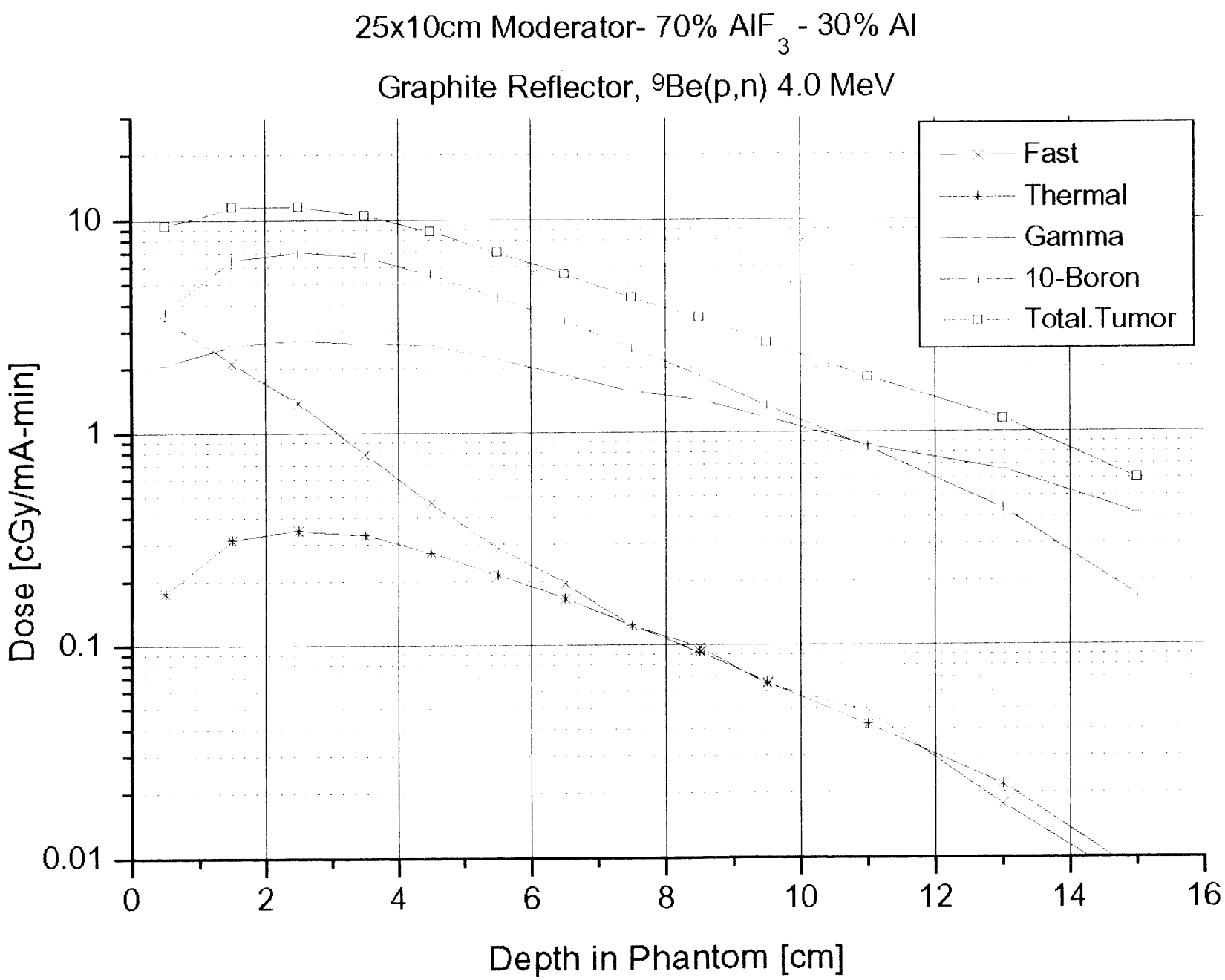
25x10cm Moderator- 70% AlF3 - 30% Al
Graphite Reflector, 9Be(p,n) 4.0 MeV
Fast
Thermal
Gamma
10-Boron
Total.Tumor
Dose [cGy/mA-min]
10
1
0.1
0.01
0
2
4
6
8
10
12
14
16
Depth in Phantom [cm]

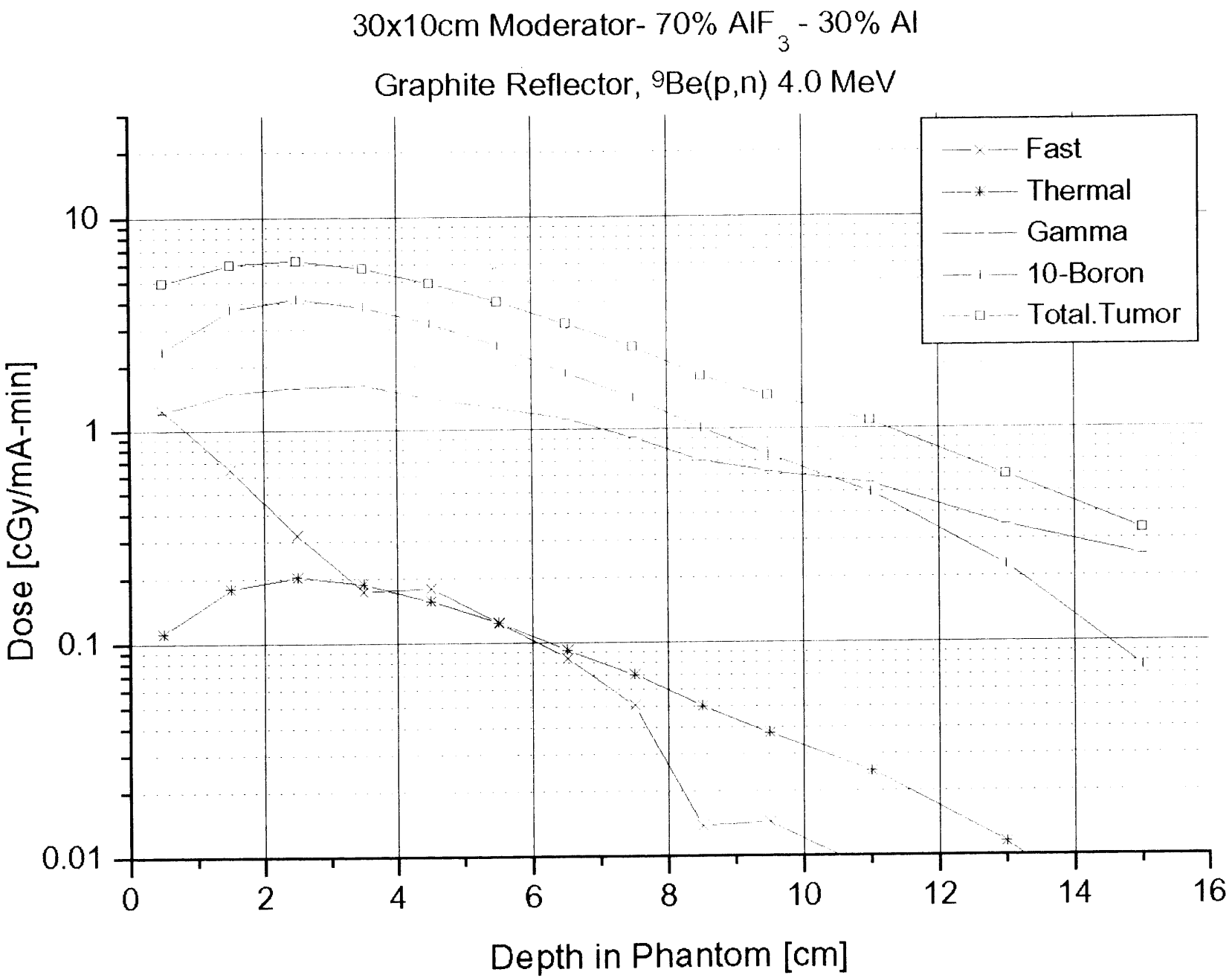
30x10cm Moderator- 70% AlF3 - 30% Al
Graphite Reflector, 9Be(p,n) 4.0 MeV
Fast
Thermal
Gamma
10-Boron
Total.Tumor
Dose [cGy/mA-min]
10
1
0.1
0.01
0
2
4
6
8
10
12
14
16
Depth in Phantom [cm]

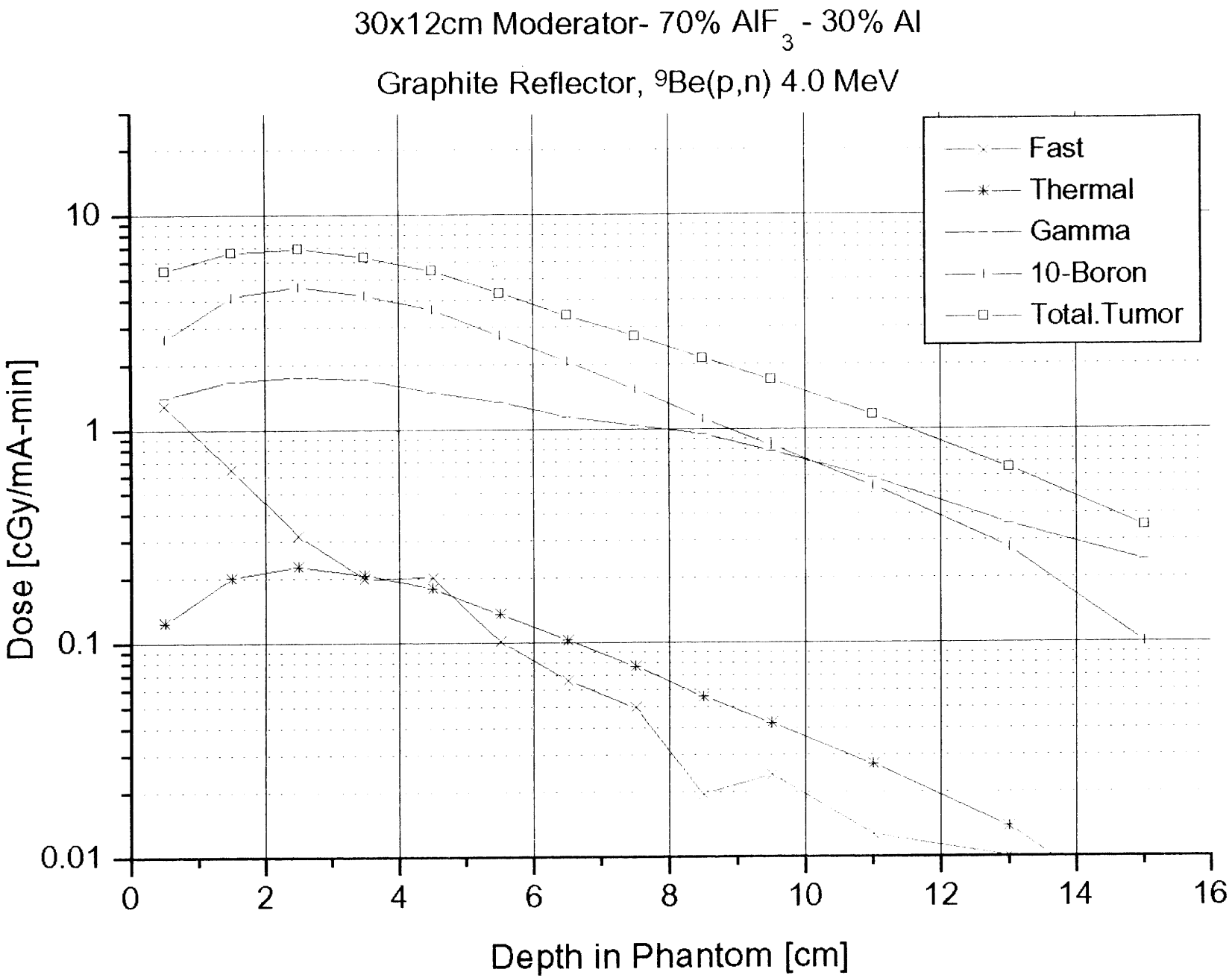
30x12cm Moderator- 70% AlF3 - 30% Al
Graphite Reflector, 9Be(p,n) 4.0 MeV
Fast
Thermal
Gamma
10-Boron
Total.Tumor
Dose [cGy/mA-min]
10
1
0.1
0.01
0
2
4
6
8
10
12
14
16
Depth in Phantom [cm]

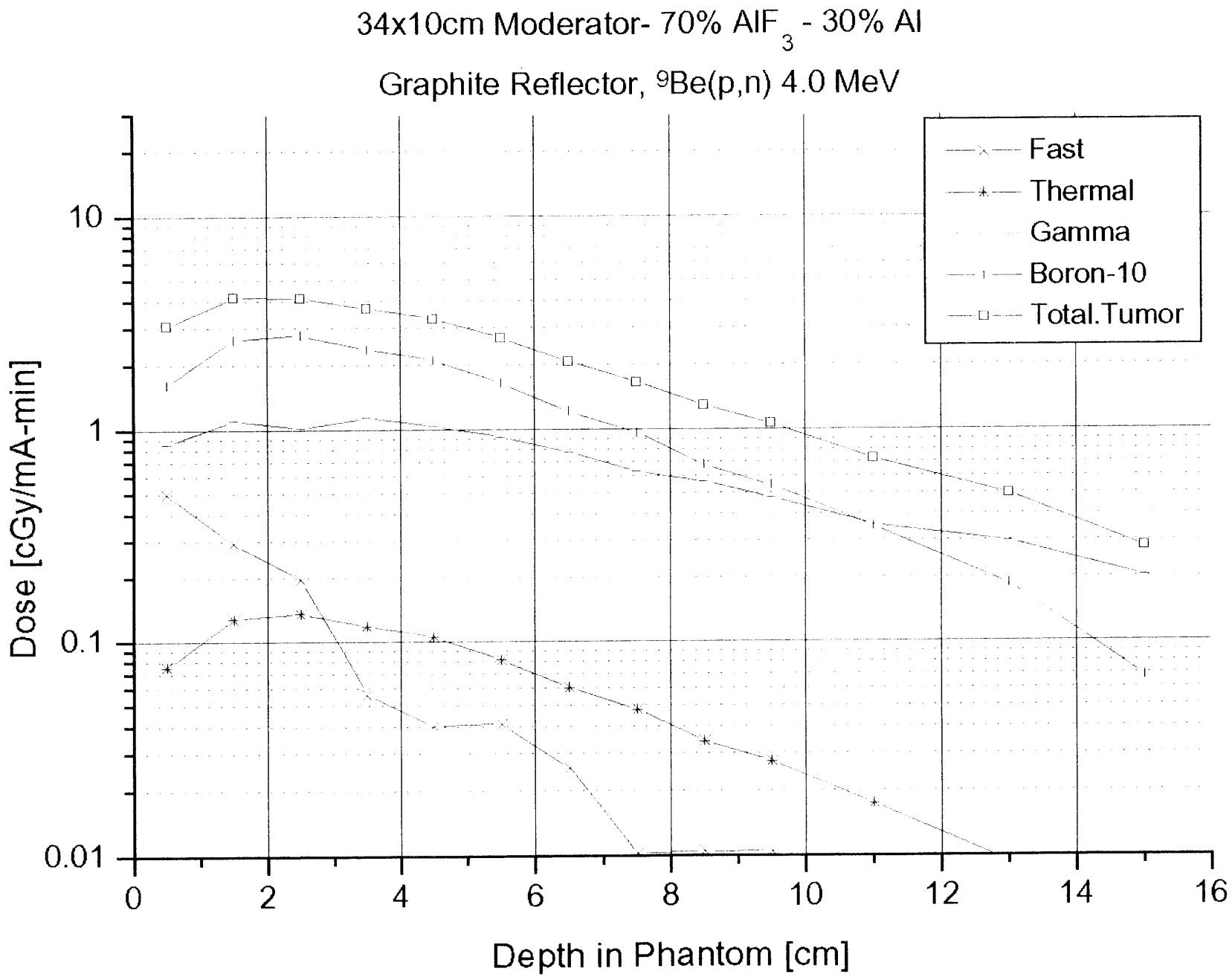
34x10cm Moderator- 70% AlF3 - 30% Al
Graphite Reflector, 9Be(p,n) 4.0 MeV
Fast
Thermal
Gamma
Boron-10
Total.Tumor
Dose [cGy/mA-min]
10
1
0.1
0.01
0
2
4
6
8
10
12
14
16
Depth in Phantom [cm]

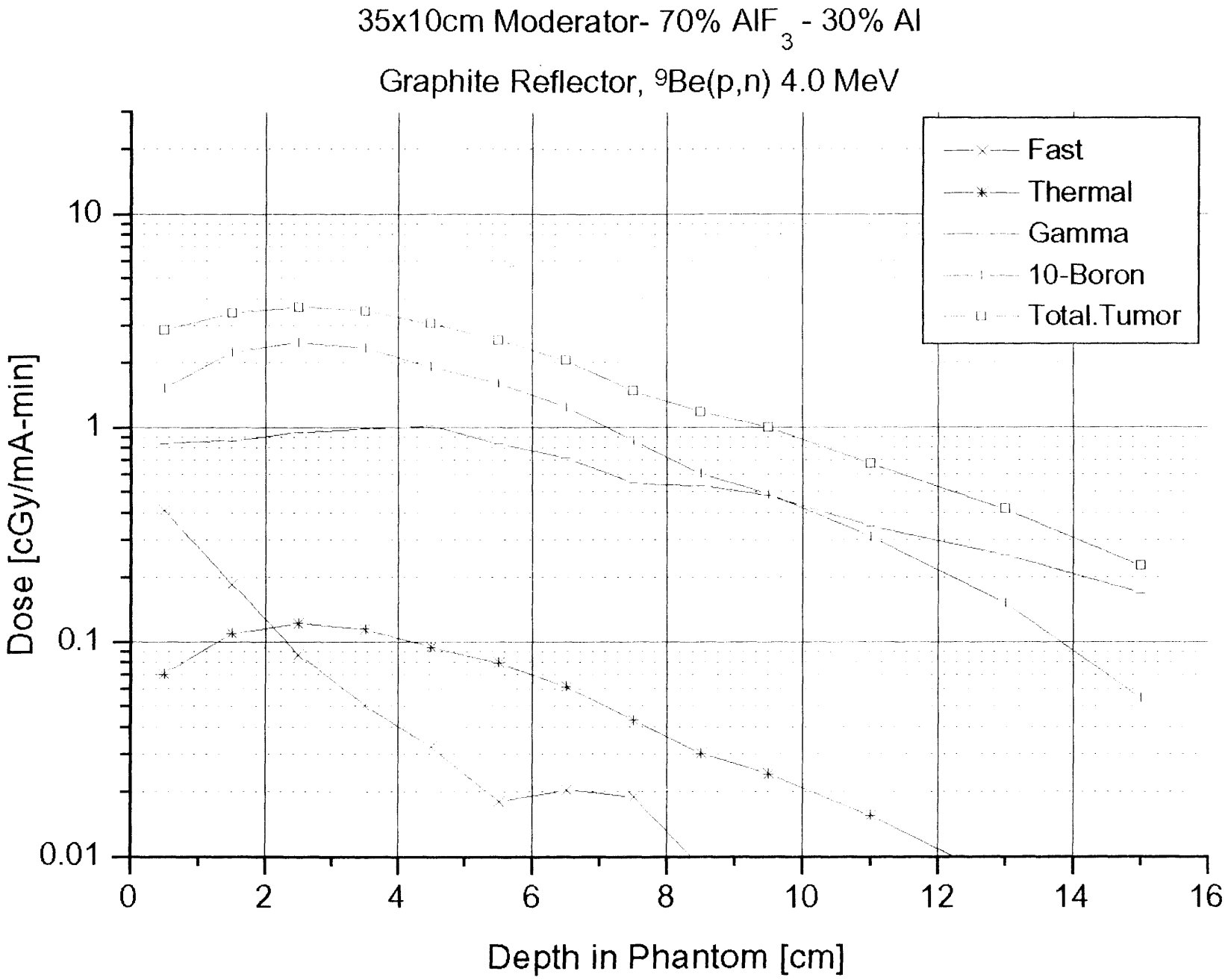
35x10cm Moderator- 70% AlF3 - 30% Al
Graphite Reflector, 9Be(p,n) 4.0 MeV
Fast
Thermal
Gamma
10-Boron
Total.Tumor
Dose [cGy/mA-min]
10
1
0.1
0.01
0
2
4
6
8
10
12
14
16
Depth in Phantom [cm]

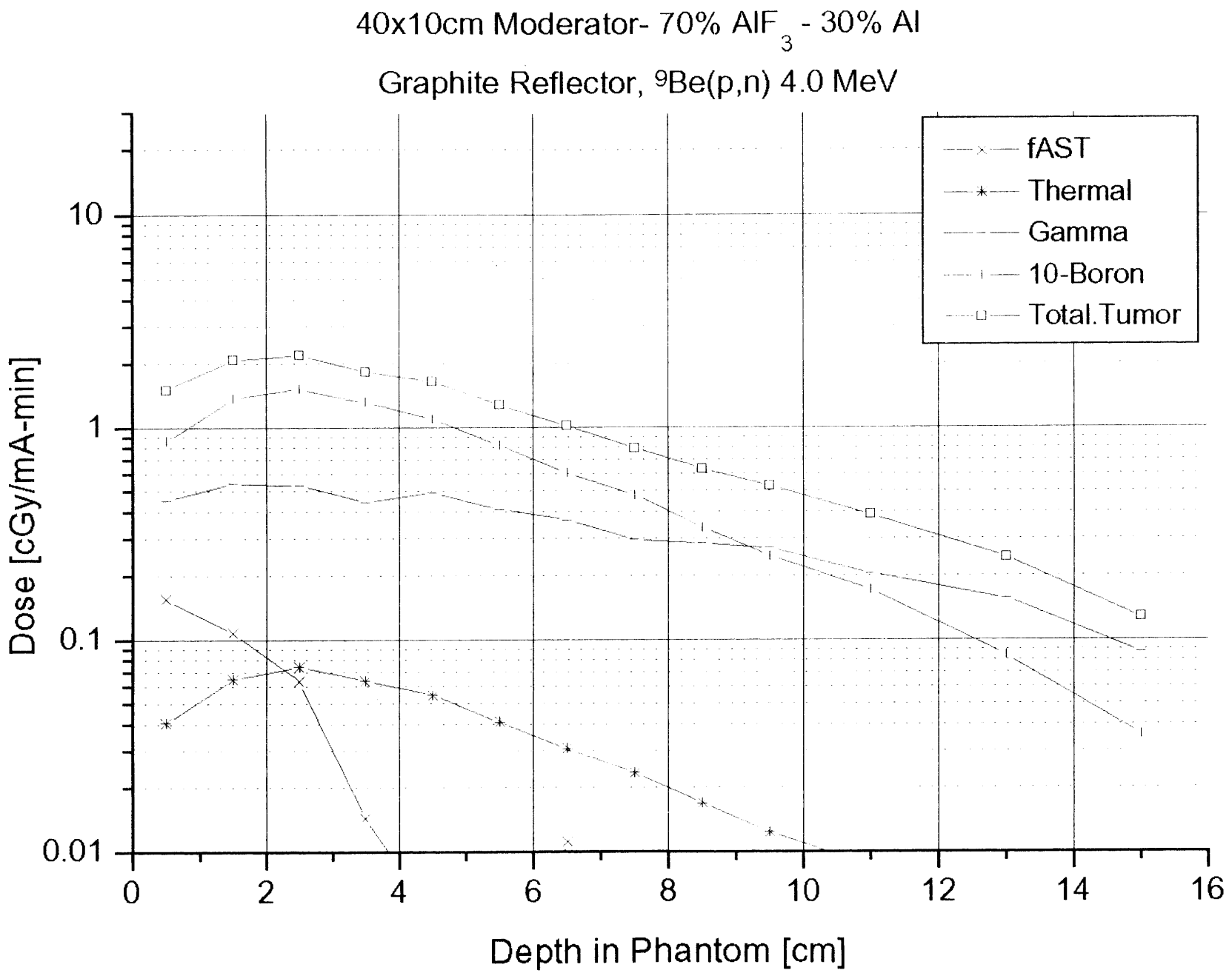
40x10cm Moderator- 70% AlF3 - 30% Al
Graphite Reflector, 9Be(p,n) 4.0 MeV
fAST
Thermal
Gamma
10-Boron
Total.Tumor
Dose [cGy/mA-min]
10
1
0.1
0.01
0
2
4
6
8
10
12
14
16
Depth in Phantom [cm]

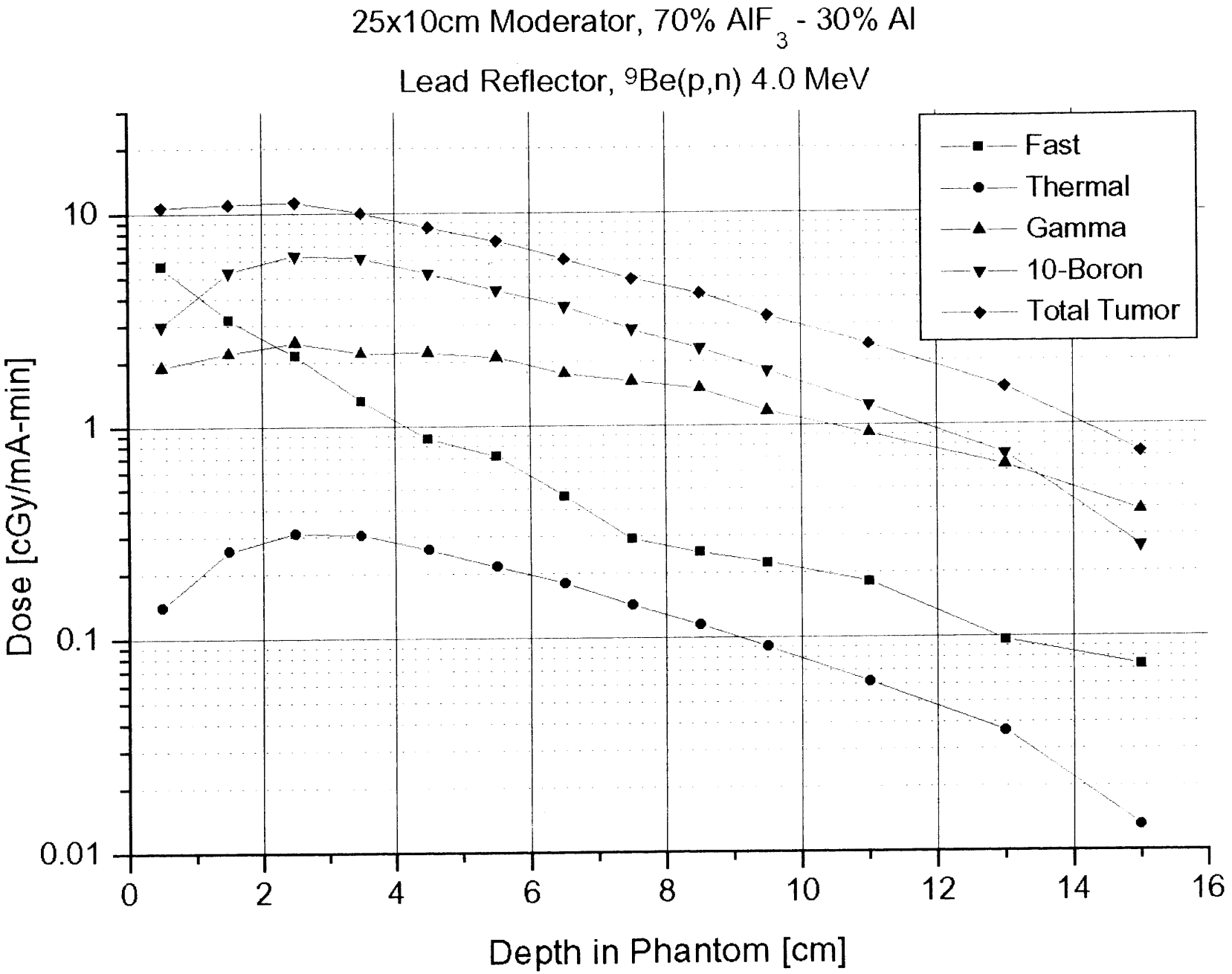
25x10cm Moderator, 70% AlF3 - 30% Al
Lead Reflector, 9Be(p,n) 4.0 MeV
Fast
Thermal
Gamma
10-Boron
Total Tumor
Dose [cGy/mA-min]
10
1
0.1
0.01
0
2
4
6
8
10
12
14
16
Depth in Phantom [cm]

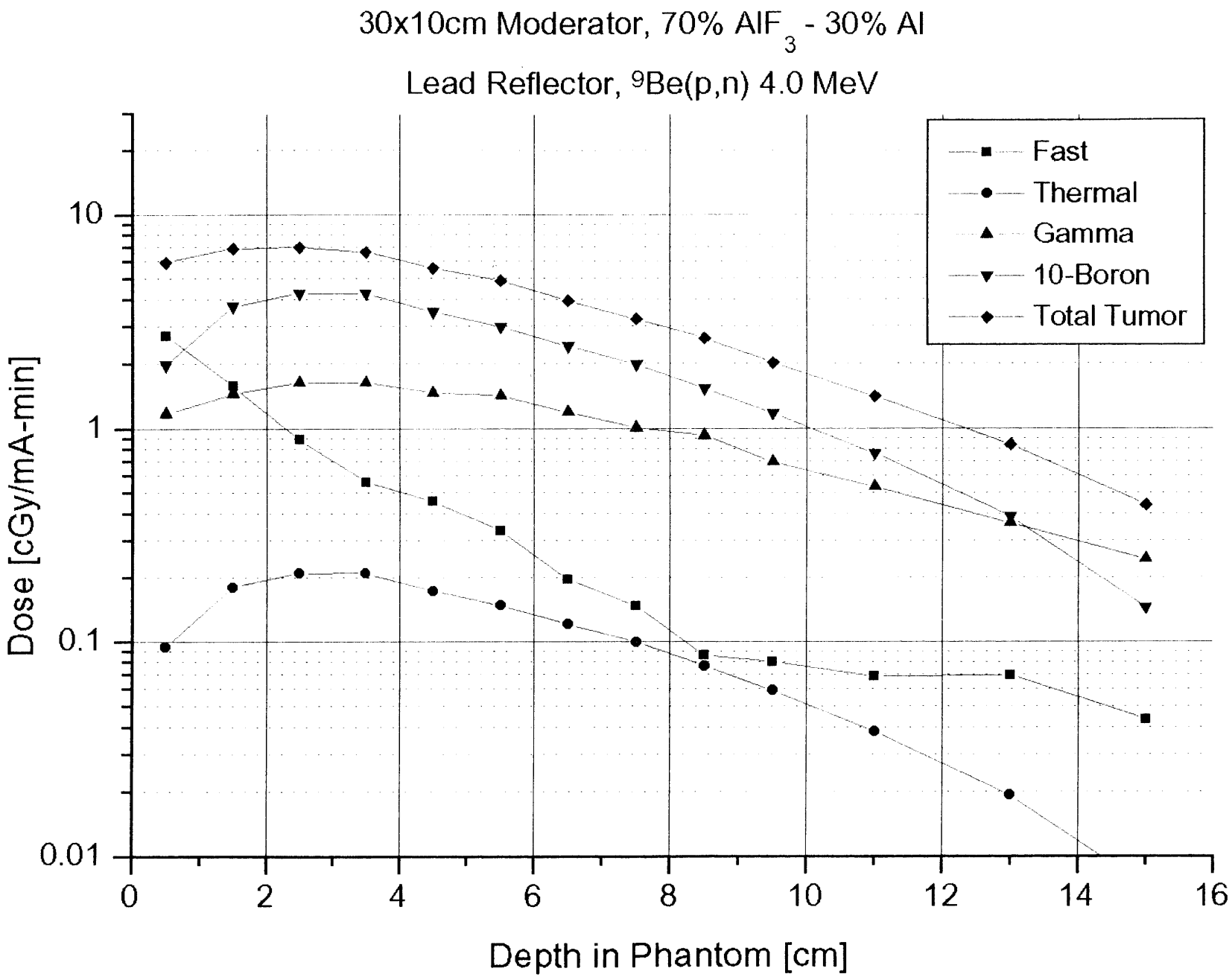
30x10cm Moderator, 70% AlF3 - 30% Al
Lead Reflector, 9Be(p,n) 4.0 MeV
Fast
Thermal
Gamma
10-Boron
Total Tumor
Dose [cGy/mA-min]
10
1
0.1
0.01
0
2
4
6
8
10
12
14
16
Depth in Phantom [cm]

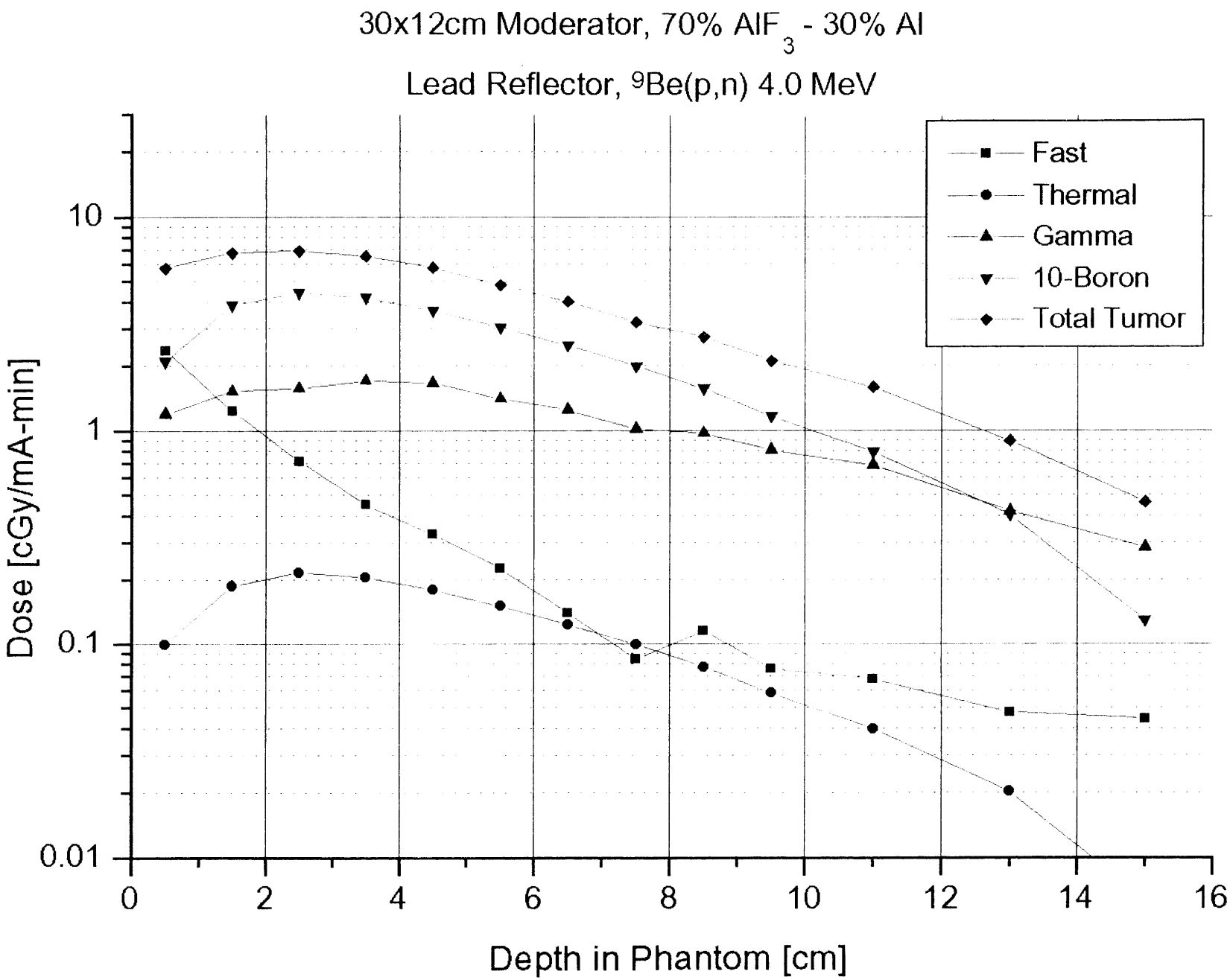
30x12cm Moderator, 70% AlF3 - 30% Al
Lead Reflector, 9Be(p,n) 4.0 MeV
Fast
Thermal
Gamma
10-Boron
Total Tumor
Dose [cGy/mA-min]
10
1
0.1
0.01
0
2
4
6
8
10
12
14
16
Depth in Phantom [cm]

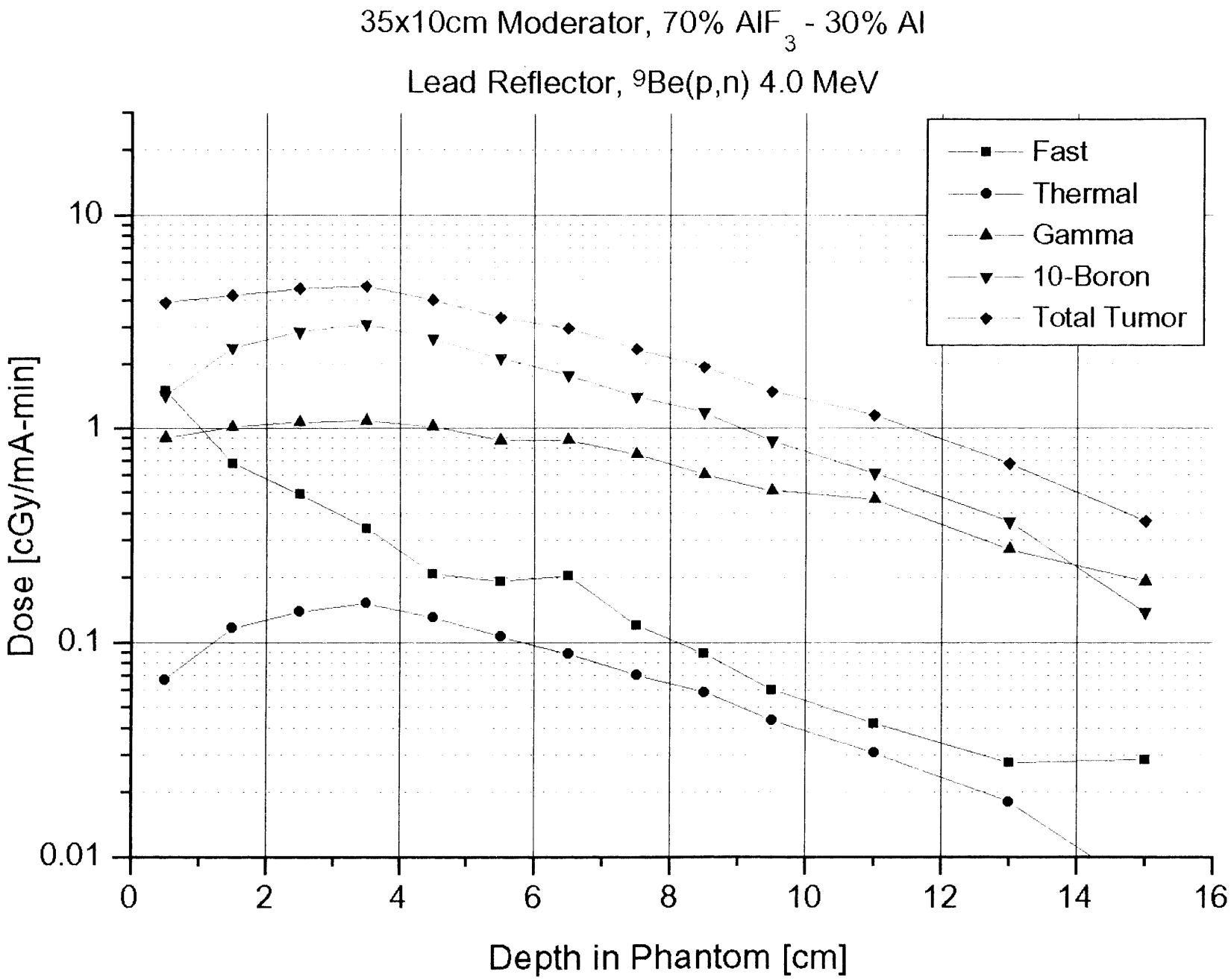
35x10cm Moderator, 70% AlF3 - 30% Al
Lead Reflector, 9Be(p,n) 4.0 MeV
Fast
Thermal
Gamma
10-Boron
Total Tumor
Dose [cGy/mA-min]
10
1
0.1
0.01
0
2
4
6
8
10
12
14
16
Depth in Phantom [cm]

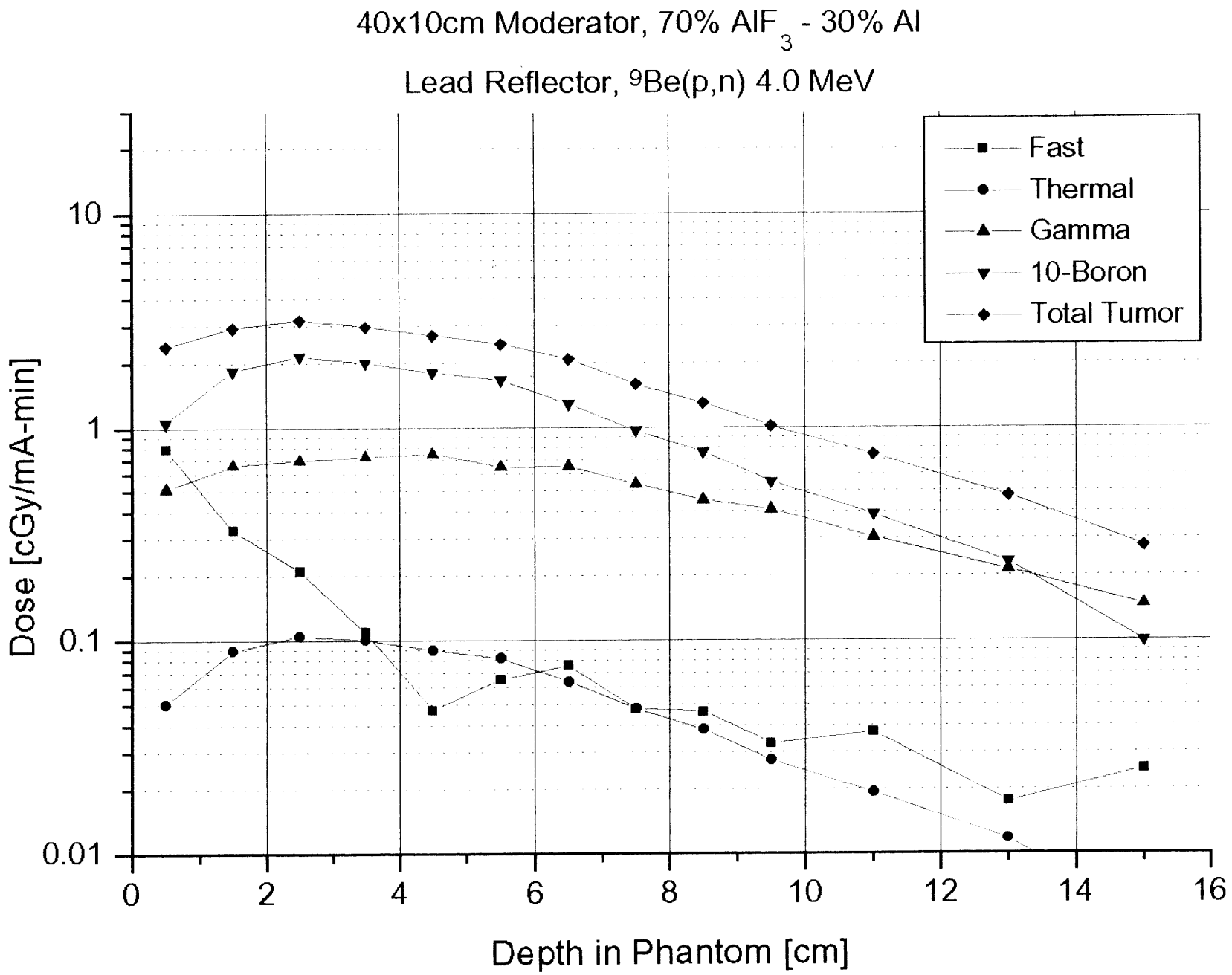
40x10cm Moderator, 70% AlF3 - 30% Al
Lead Reflector, 9Be(p,n) 4.0 MeV
Fast
Thermal
Gamma
10-Boron
Total Tumor
Dose [cGy/mA-min]
10
1
0.1
0.01
0
2
4
6
8
10
12
14
16
Depth in Phantom [cm]

Table C-6: Therapy beam design configurations
for the reaction
9Be(p,n) E(p)=4.0 MeV
These simulations examine
the effect of moving the target location

The following dimesions were not varied:
C=10 cm, D=34 cm, E=34 cm, F=0.03 cm, H=0.03 cm, I=0.03 cm

Simulation Designation	Moderator material	Reflector material	Target Location [cm] (dimension A)	Moderator Length [cm] (dimension B)	Moderator Radius [cm] (dimension C)	Target to port Distance [cm] (dimension G)
40-gr-d2o-27x10	D2O	Graphite	5	27	10	22
40-gr-d2o-27x10	D2O	Graphite	2	27	10	25
40-gr-d2o-27x10	D2O	Graphite	1	27	10	26
40-gr-d2o-27x10	D2O	Graphite	0	27	10	27
40-gr-d2o-27x10	D2O	Graphite	-1	27	10	28
40-gr-d2o-27x10	D2O	Graphite	-3	27	10	30
40-gr-d2o-27x10	D2O	Graphite	5	29	10	24
40-gr-d2o-27x10	D2O	Graphite	4	28	10	24
40-gr-d2o-27x10	D2O	Graphite	2	26	10	24
40-gr-d2o-27x10	D2O	Graphite	1	25	10	24
40-gr-d2o-27x10	D2O	Graphite	0	24	10	24
40-gr-d2o-27x10	D2O	Graphite	-1	23	10	24
40-gr-d2o-27x10	D2O	Graphite	-2	22	10	24
40-gr-d2o-27x10	D2O	Graphite	-3	21	10	24

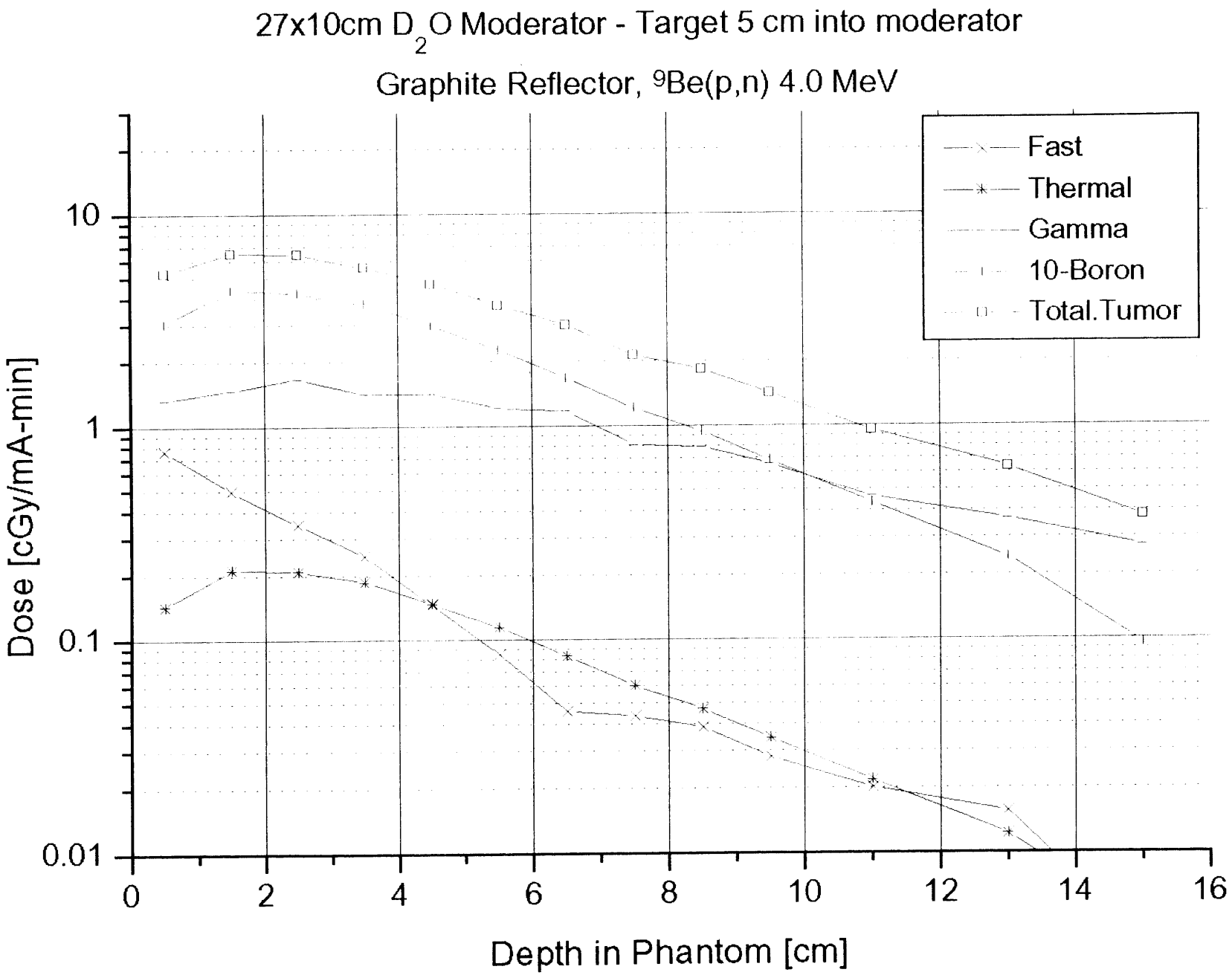
27x10cm D2O Moderator - Target 5 cm into moderator
Graphite Reflector, 9Be(p,n) 4.0 MeV
Fast
Thermal
Gamma
10-Boron
Total.Tumor
Dose [cGy/mA-min]
10
1
0.1
0.01
0
2
4
6
8
10
12
14
16
Depth in Phantom [cm]

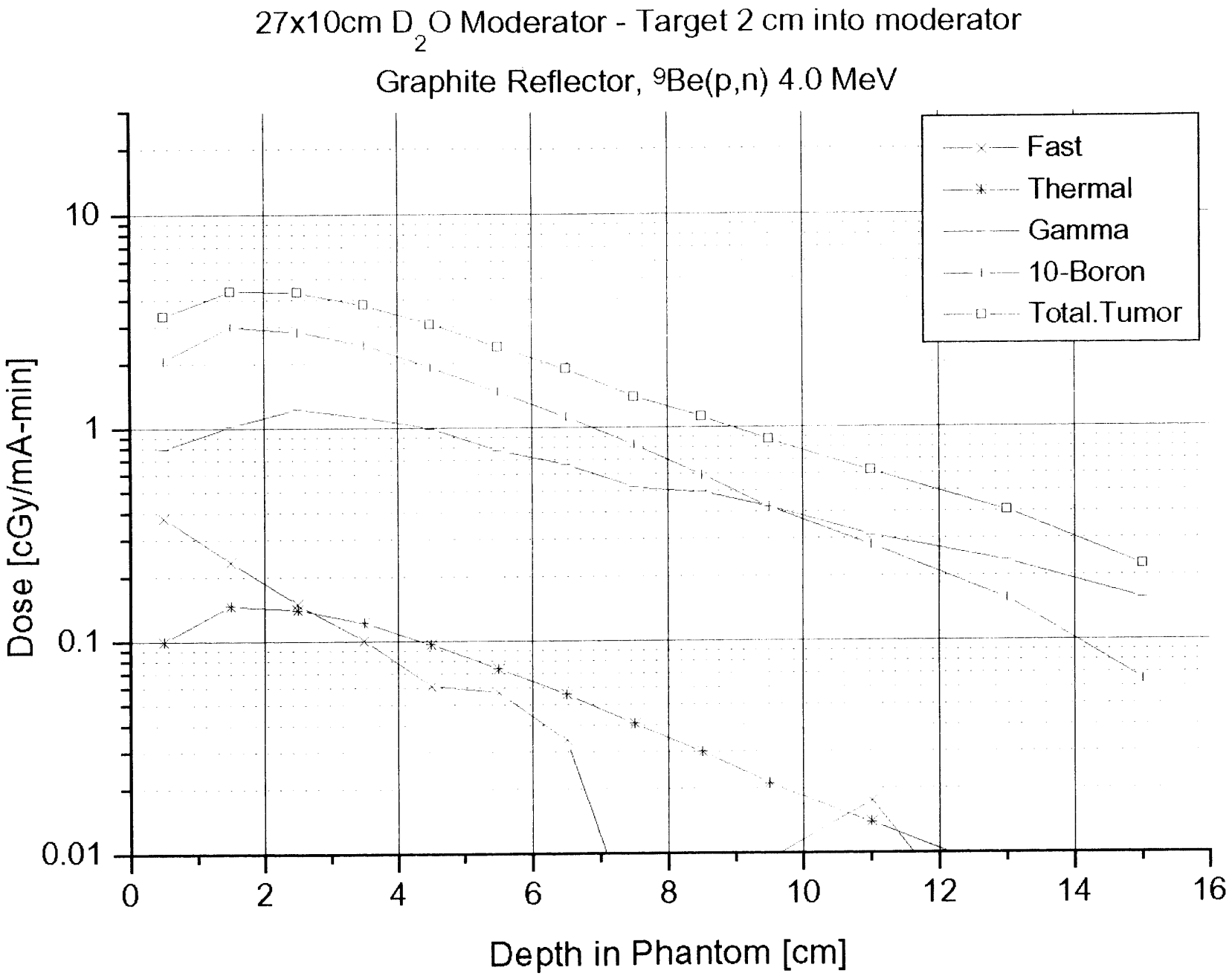
27x10cm D2O Moderator - Target 2 cm into moderator
Graphite Reflector, 9Be(p,n) 4.0 MeV
Fast
Thermal
Gamma
10-Boron
Total.Tumor
Dose [cGy/mA-min]
10
1
0.1
0.01
0
2
4
6
8
10
12
14
16
Depth in Phantom [cm]

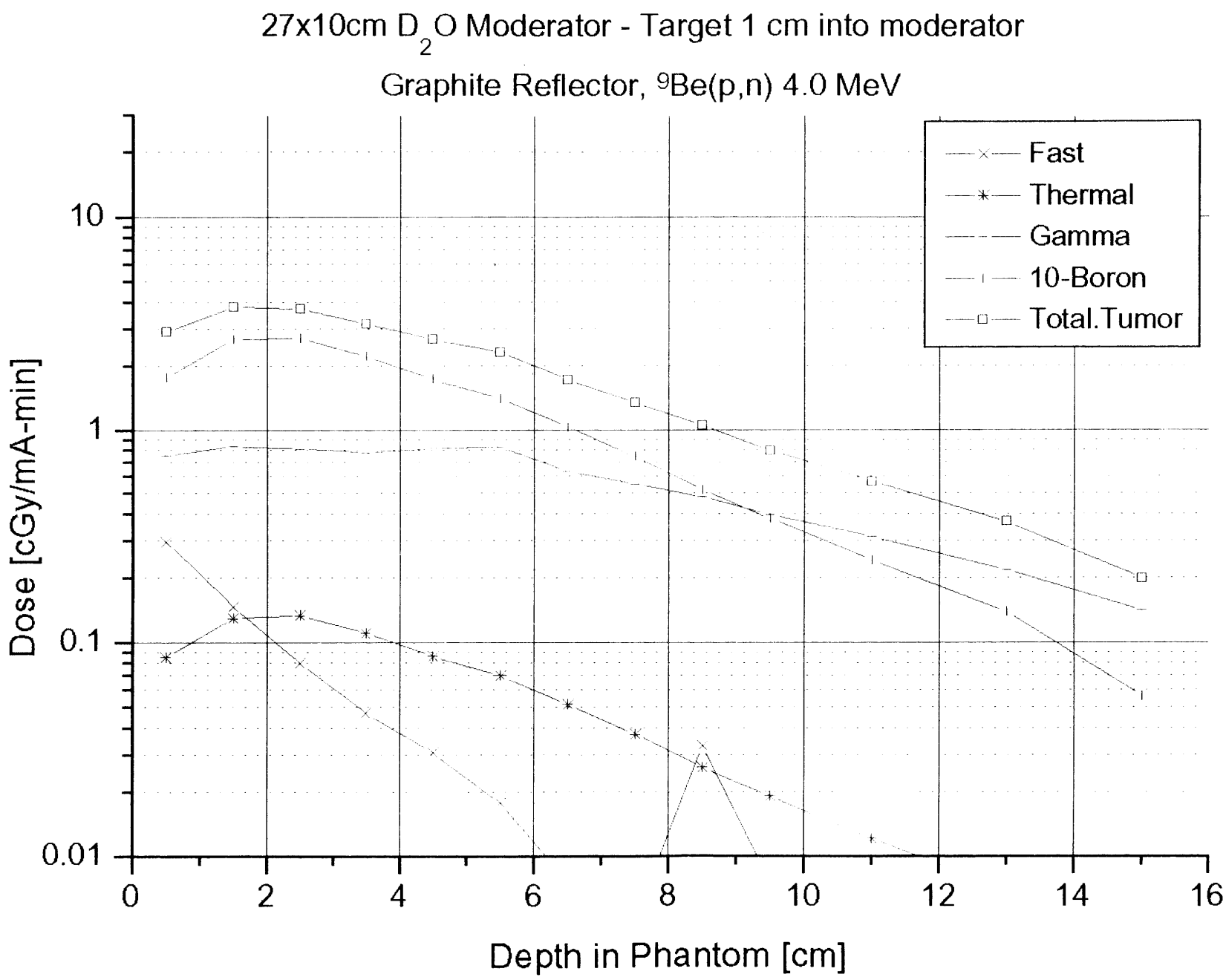
27x10cm D2O Moderator - Target 1 cm into moderator
Graphite Reflector, 9Be(p,n) 4.0 MeV
Fast
Thermal
Gamma
10-Boron
Total.Tumor
Dose [cGy/mA-min]
10
1
0.1
0.01
0
2
4
6
8
10
12
14
16
Depth in Phantom [cm]

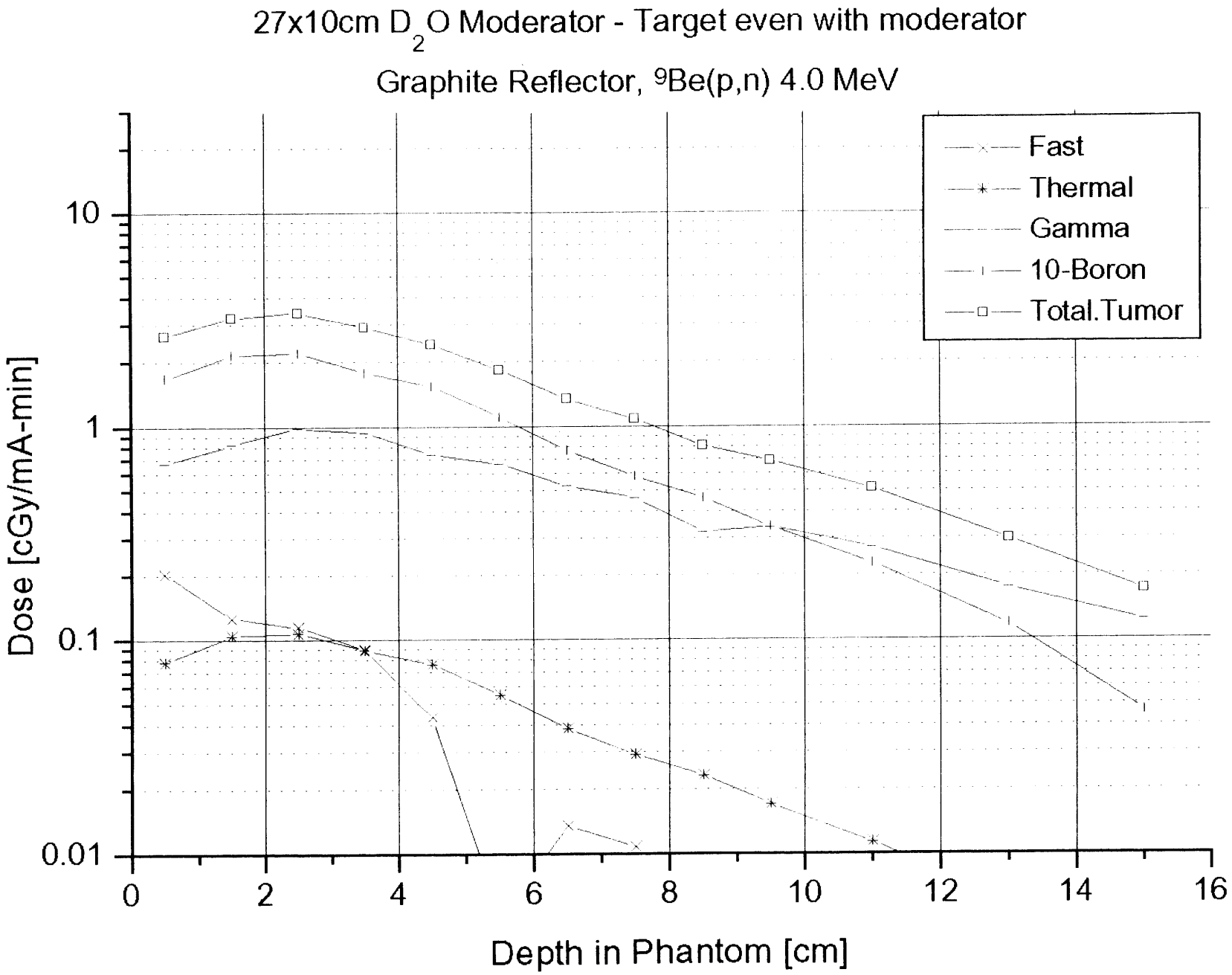
27x10cm D2O Moderator - Target even with moderator
Graphite Reflector, 9Be(p,n) 4.0 MeV
Fast
Thermal
Gamma
10-Boron
Total.Tumor
Dose [cGy/mA-min]
10
1
0.1
0.01
0
2
4
6
8
10
12
14
16
Depth in Phantom [cm]

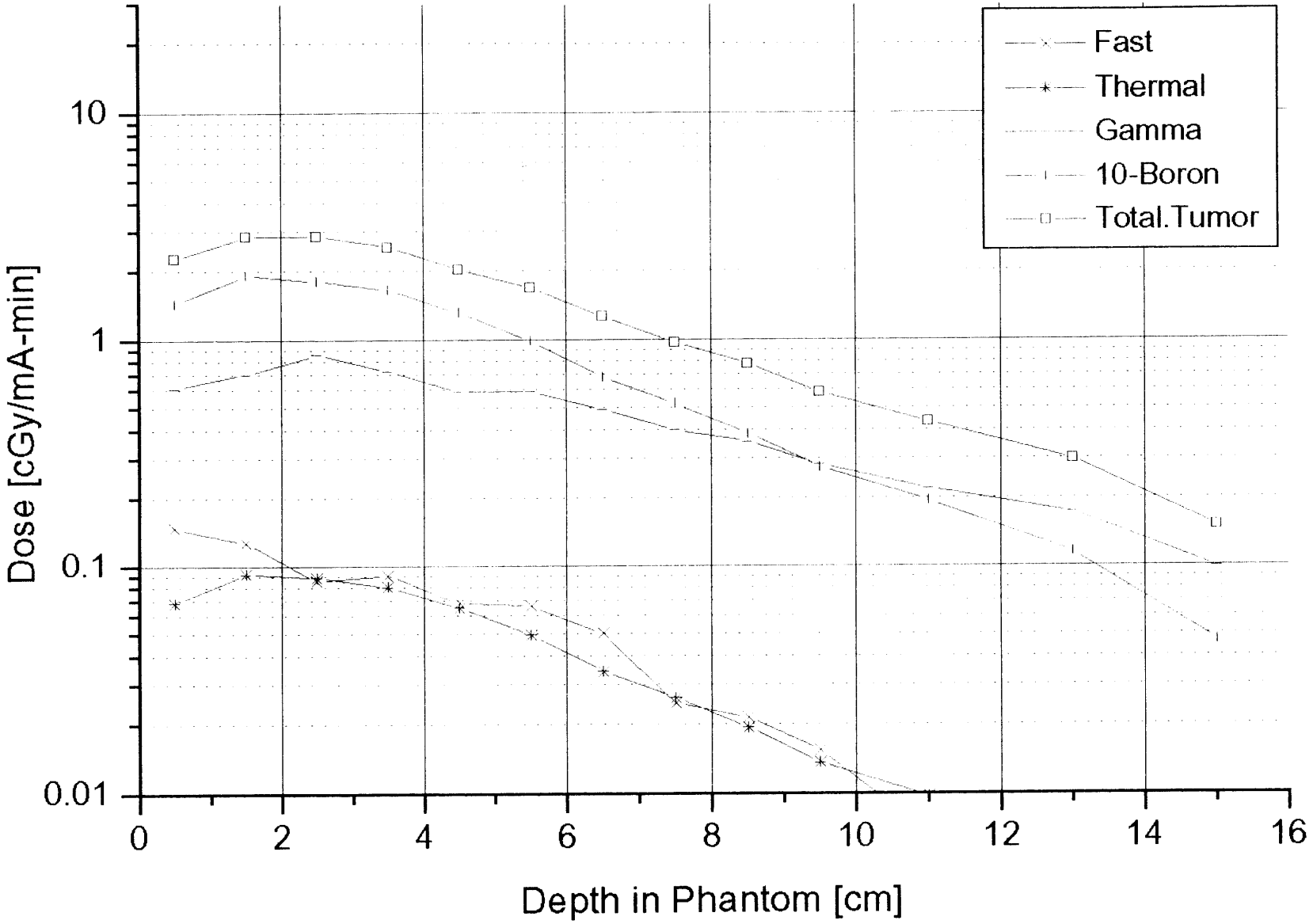
27x10cm D2O Moderator - Target 1 cm back from moderator
Graphite Reflector, 9Be(p,n) 4.0 MeV
Fast
Thermal
Gamma
10-Boron
Total.Tumor
Dose [cGy/mA-min]
10
1
0.1
0.01
0
2
4
6
8
10
12
14
16
Depth in Phantom [cm]

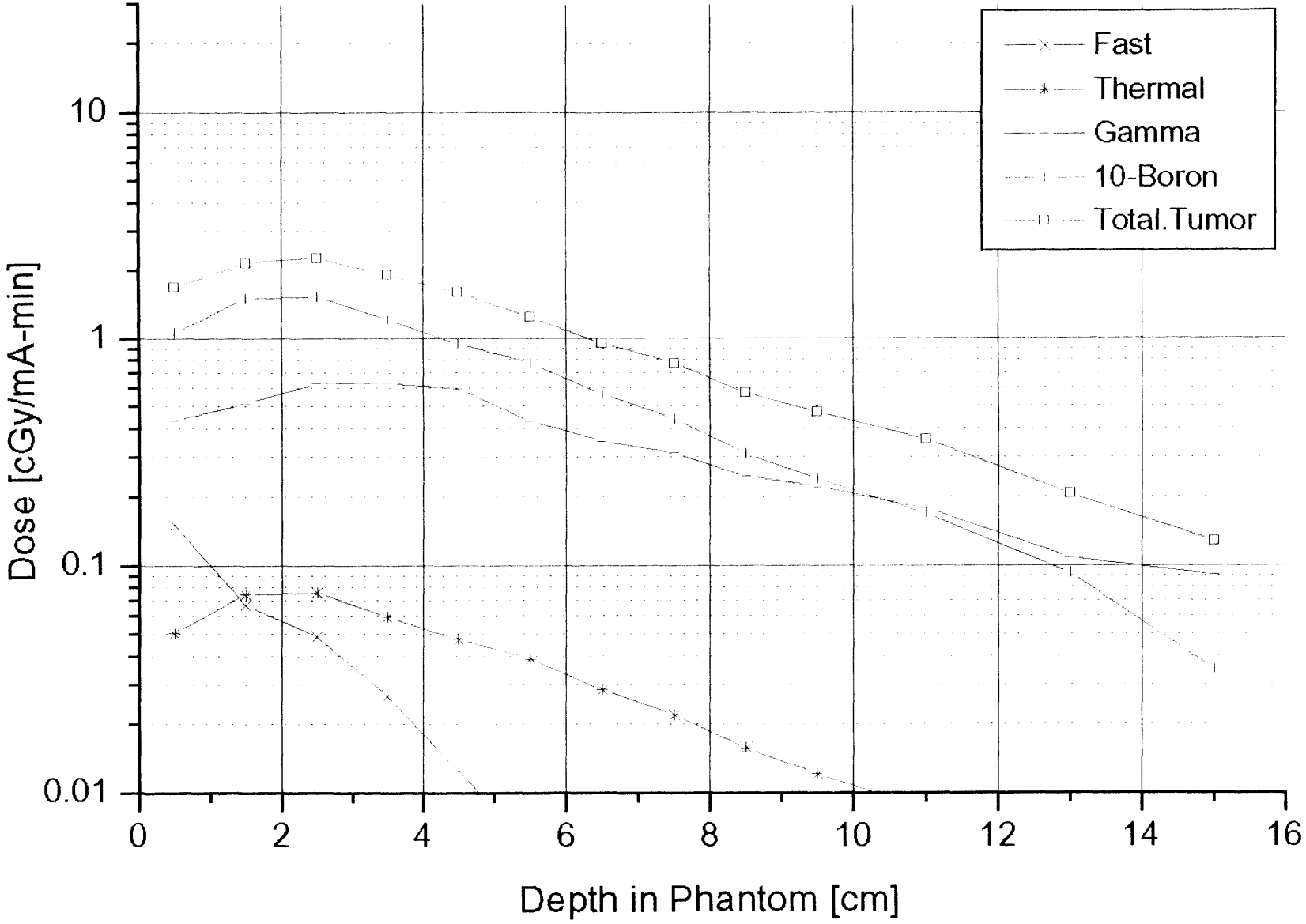
27x10cm D2O Moderator - Target 3 cm back from moderator
Graphite Reflector, 9Be(p,n) 4.0 MeV
Fast
Thermal
Gamma
10-Boron
Total.Tumor
Dose [cGy/mA-min]
10
1
0.1
0.01
0
2
4
6
8
10
12
14
16
Depth in Phantom [cm]

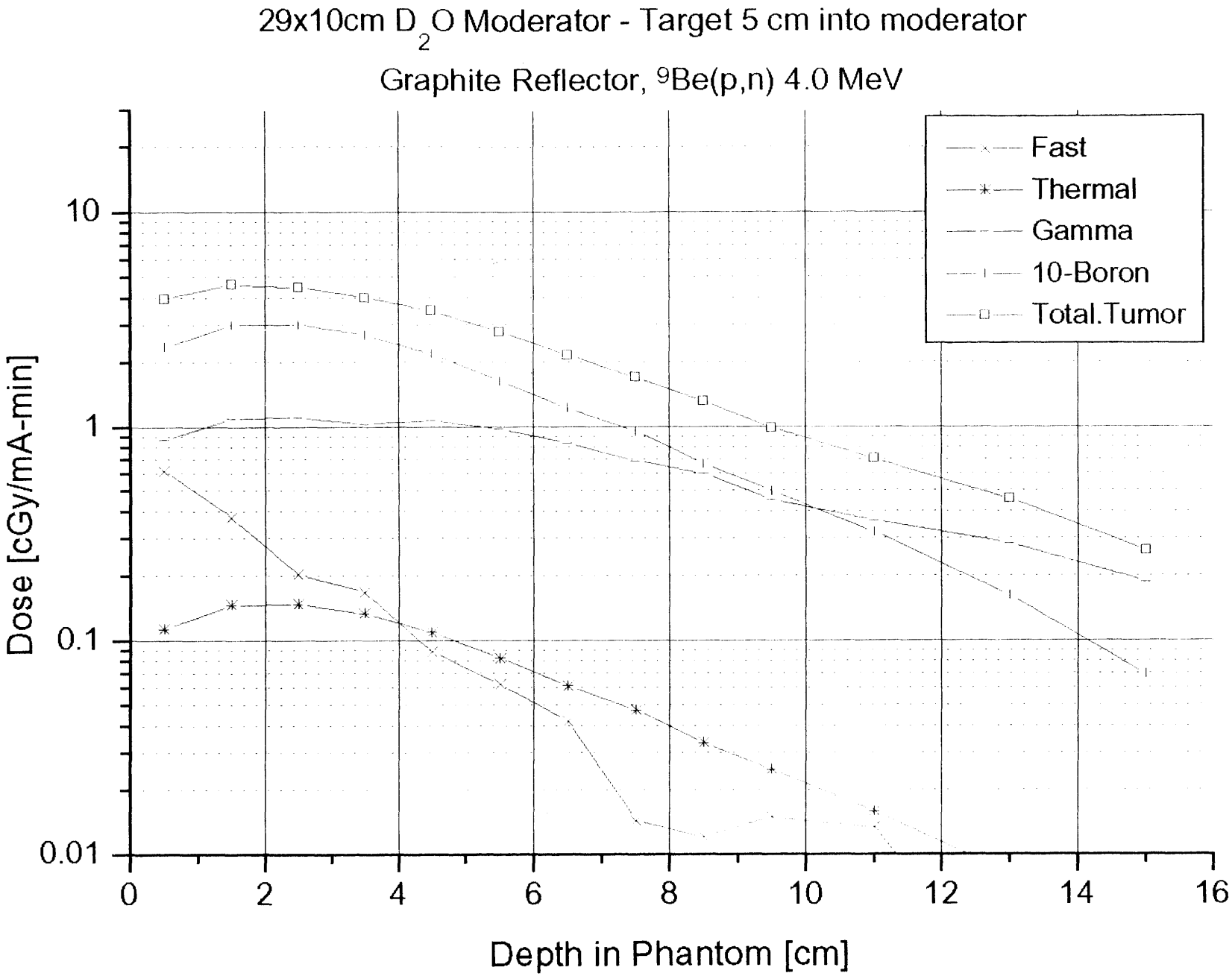
29x10cm D2O Moderator - Target 5 cm into moderator
Graphite Reflector, 9Be(p,n) 4.0 MeV
Fast
Thermal
Gamma
10-Boron
Total.Tumor
Dose [cGy/mA-min]
10
1
0.1
0.01
0
2
4
6
8
10
12
14
16
Depth in Phantom [cm]

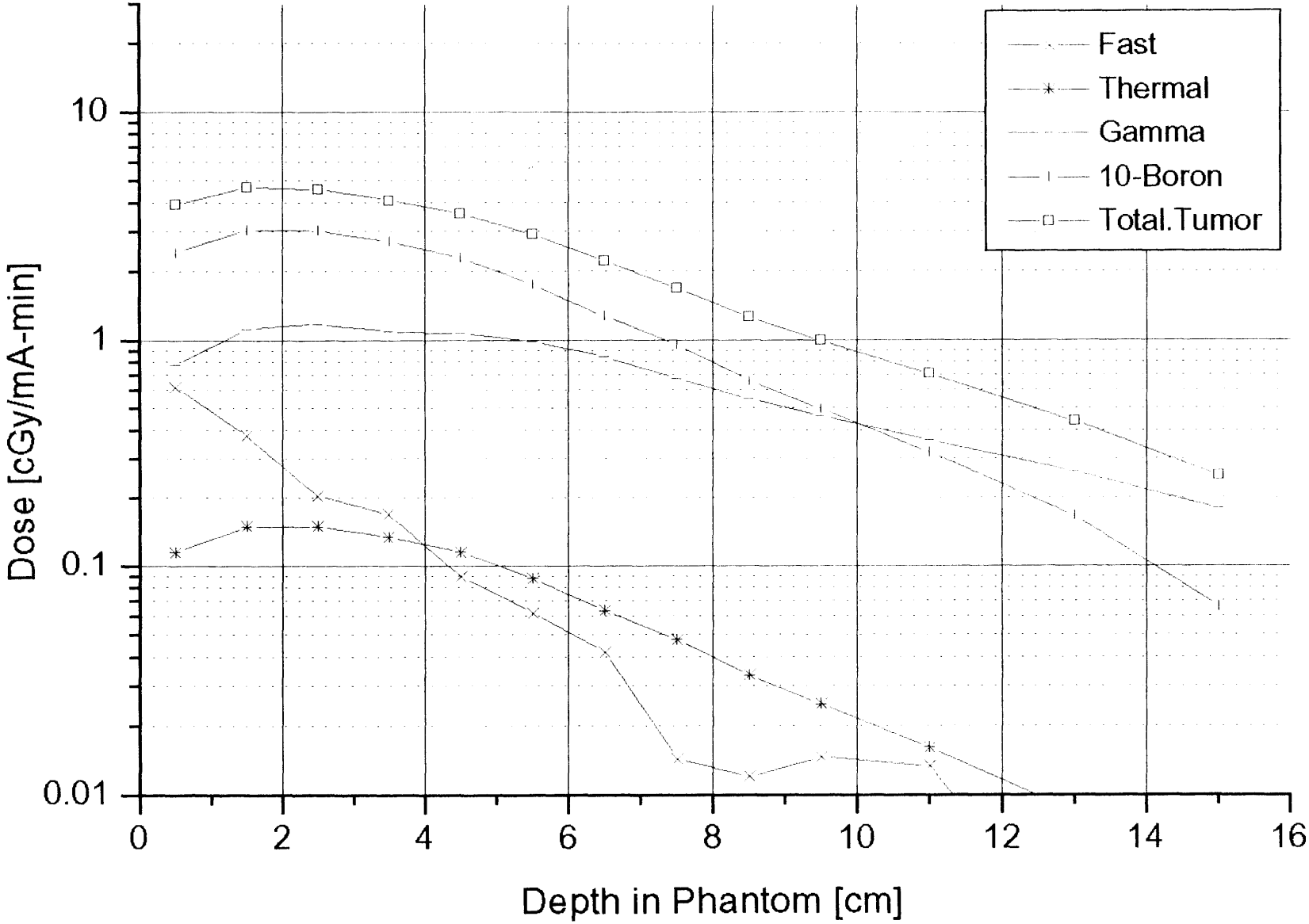
28x10cm D2O Moderator - Target 4 cm into moderator
Graphite Reflector, 9Be(p,n) 4.0 MeV
Fast
Thermal
Gamma
10-Boron
Total.Tumor
Dose [cGy/mA-min]
10
1
0.1
0.01
0
2
4
6
8
10
12
14
16
Depth in Phantom [cm]

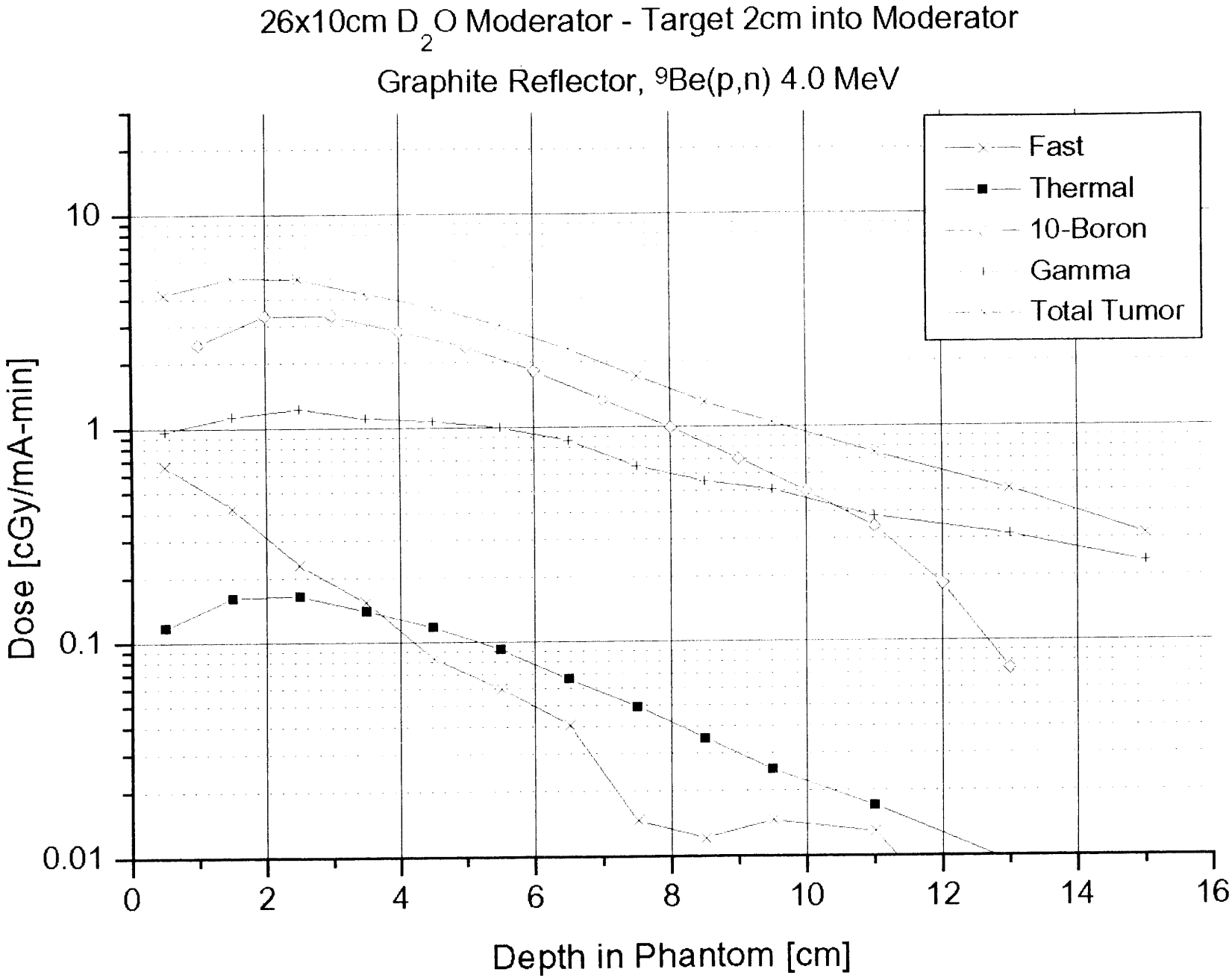
26x10cm D2O Moderator - Target 2cm into Moderator
Graphite Reflector, 9Be(p,n) 4.0 MeV
Fast
Thermal
10-Boron
Gamma
Total Tumor
Dose [cGy/mA-min]
10
1
0.1
0.01
0
2
4
6
8
10
12
14
16
Depth in Phantom [cm]

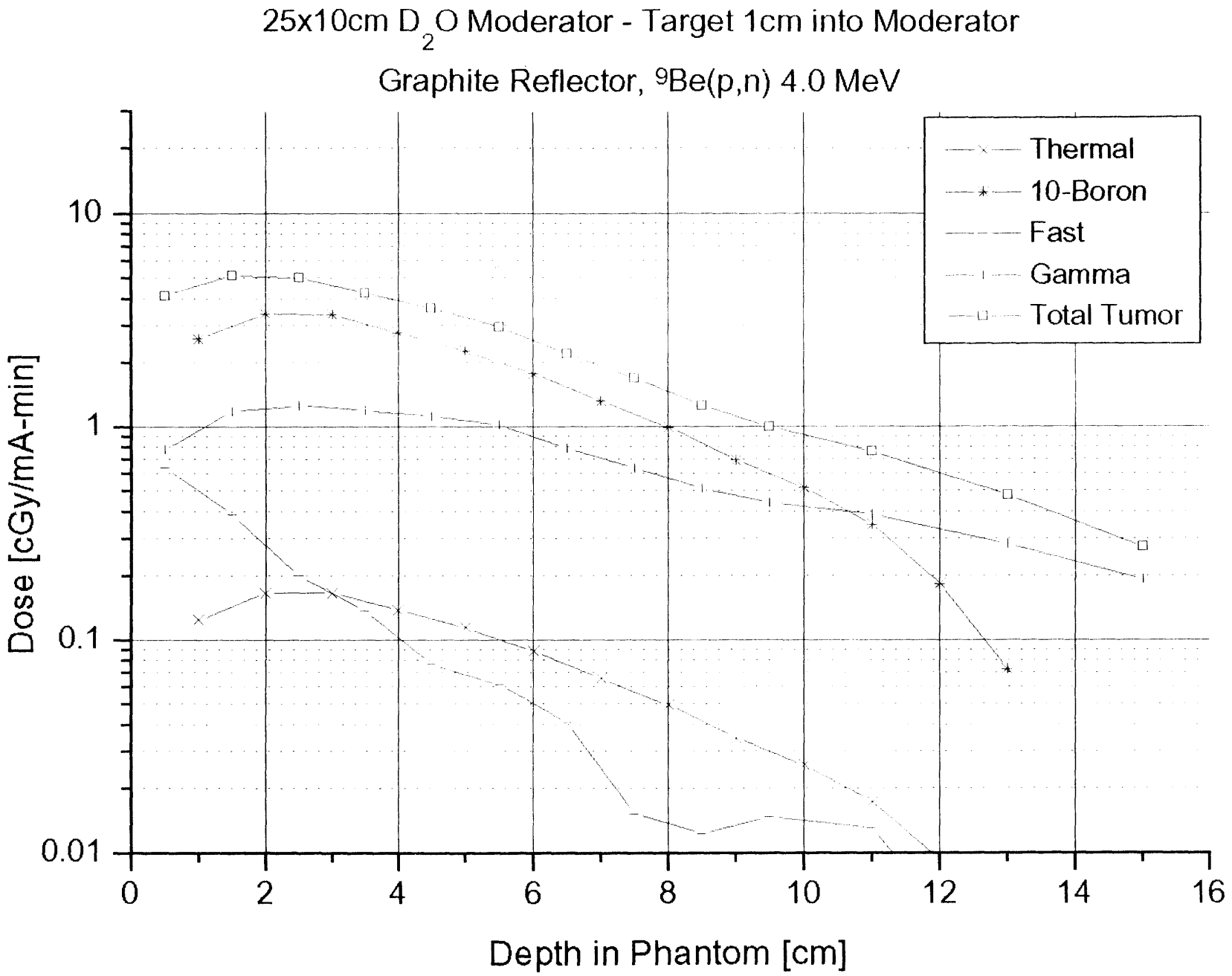
25x10cm D2O Moderator - Target 1cm into Moderator
Graphite Reflector, 9Be(p,n) 4.0 MeV
Thermal
10-Boron
Fast
Gamma
Total Tumor
Dose [cGy/mA-min]
10
1
0.1
0.01
0
2
4
6
8
10
12
14
16
Depth in Phantom [cm]

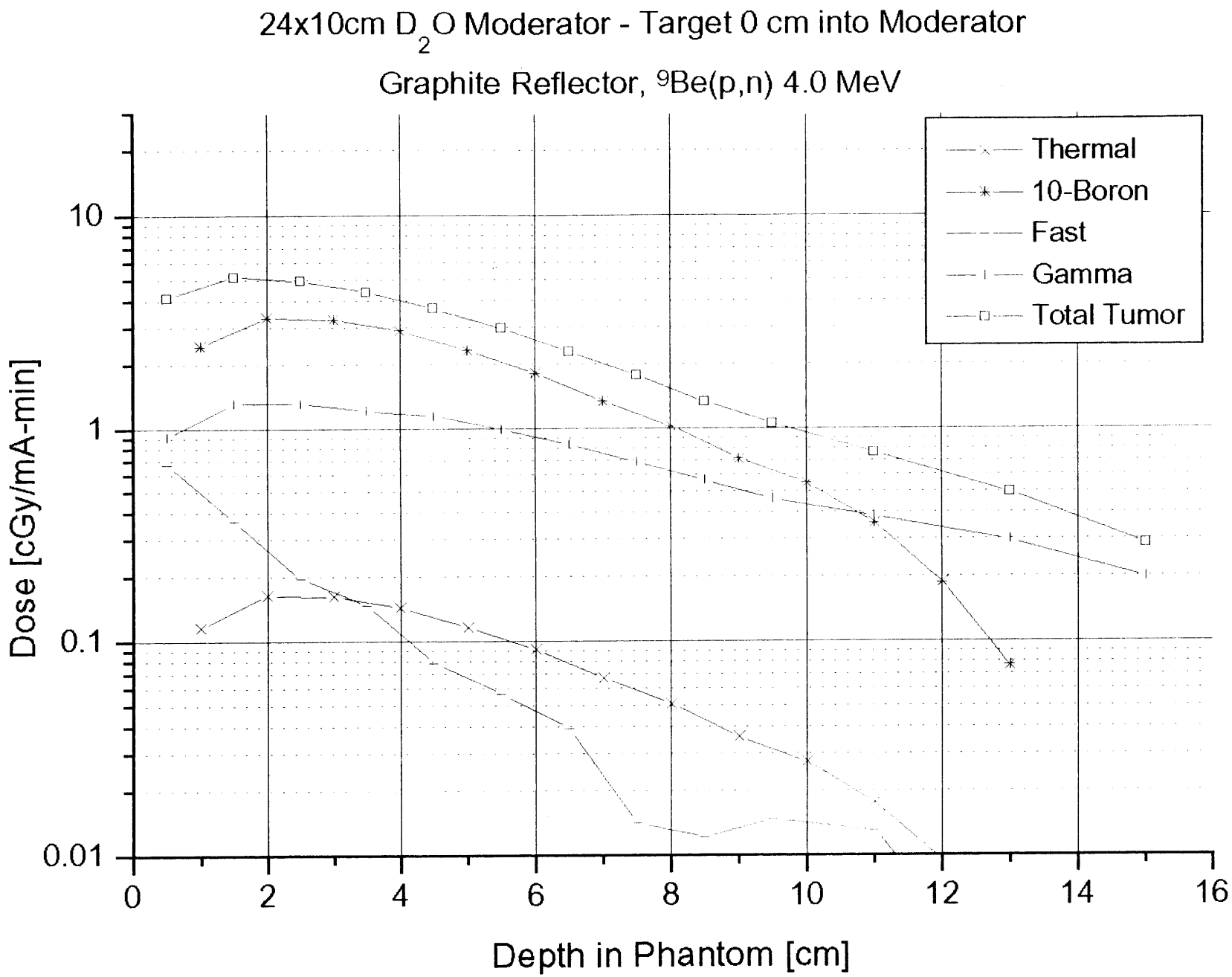
24x10cm D2O Moderator - Target 0 cm into Moderator
Graphite Reflector, 9Be(p,n) 4.0 MeV
Thermal
10-Boron
Fast
Gamma
Total Tumor
Dose [cGy/mA-min]
10
1
0.1
0.01
0
2
4
6
8
10
12
14
16
Depth in Phantom [cm]

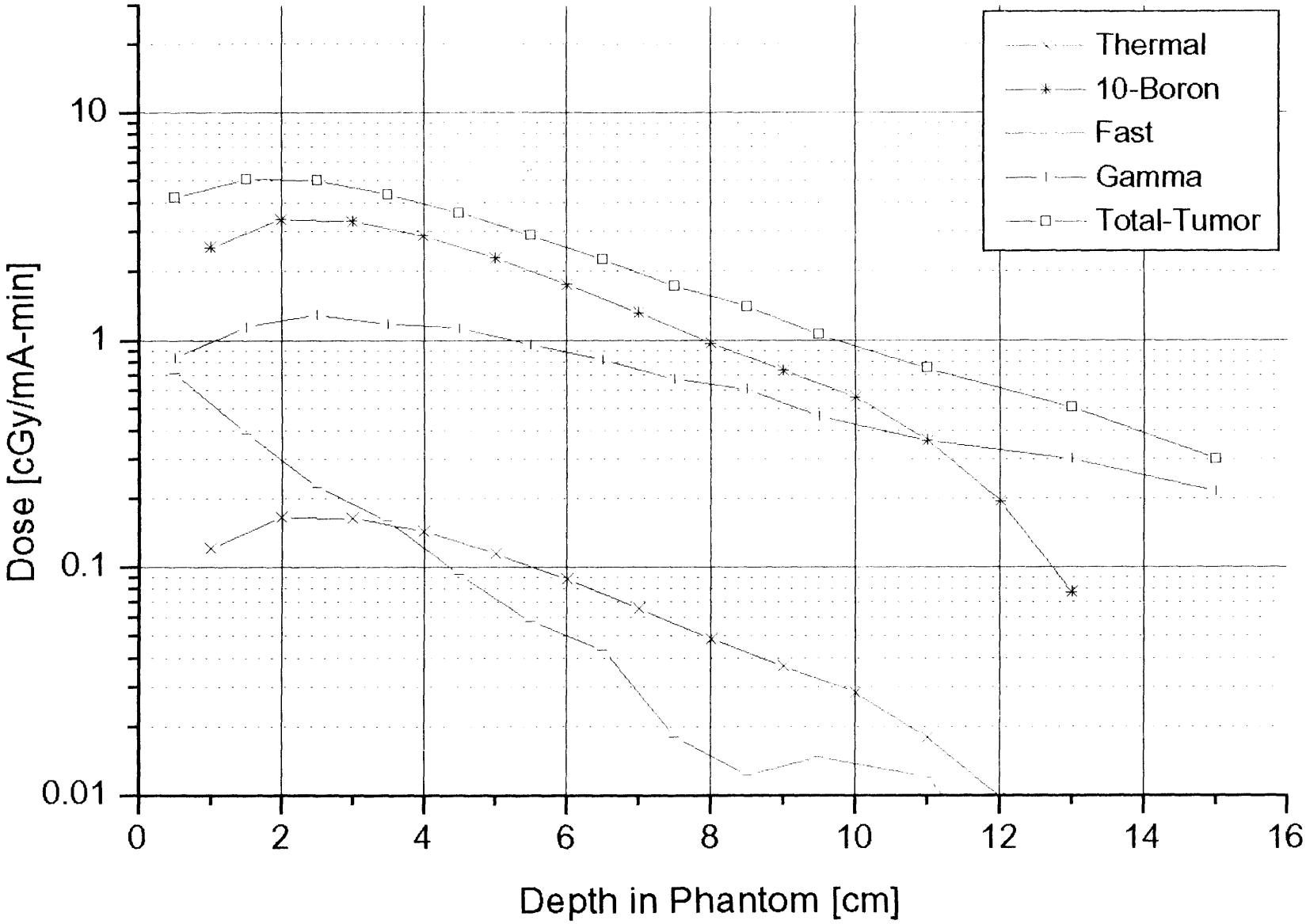
23x10cm D2O Moderator - Target 1 cm back from moderator
Graphite Reflector, 9Be(p,n) 4.0 MeV
Thermal
10-Boron
Fast
Gamma
Total-Tumor
Dose [cGy/mA-min]
10
1
0.1
0.01
0
2
4
6
8
10
12
14
16
Depth in Phantom [cm]

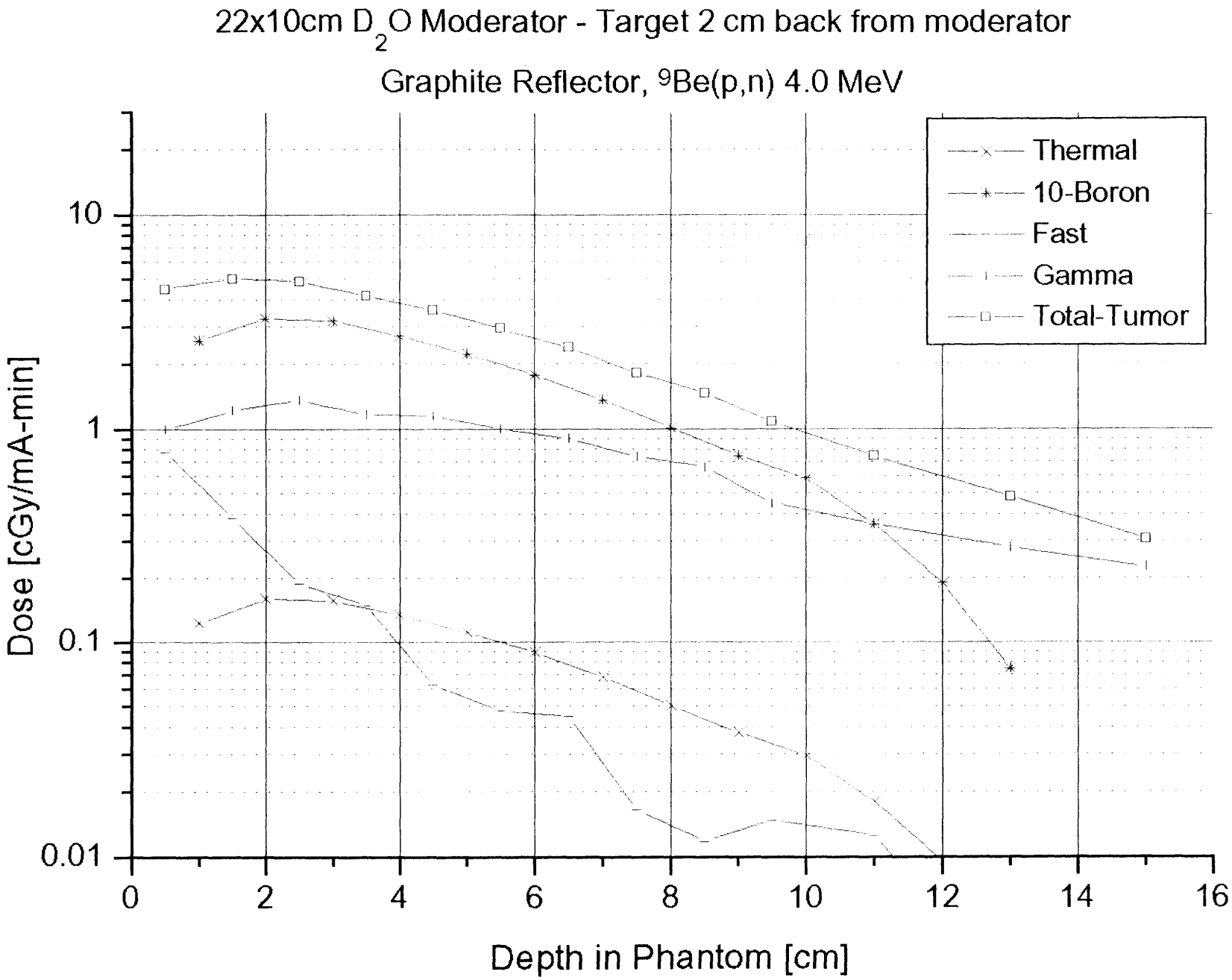
22x10cm D2O Moderator - Target 2 cm back from moderator
Graphite Reflector, 9Be(p,n) 4.0 MeV
Thermal
10-Boron
Fast
Gamma
Total-Tumor
Dose [cGy/mA-min]
10
1
0.1
0.01
0
2
4
6
8
10
12
14
16
Depth in Phantom [cm]

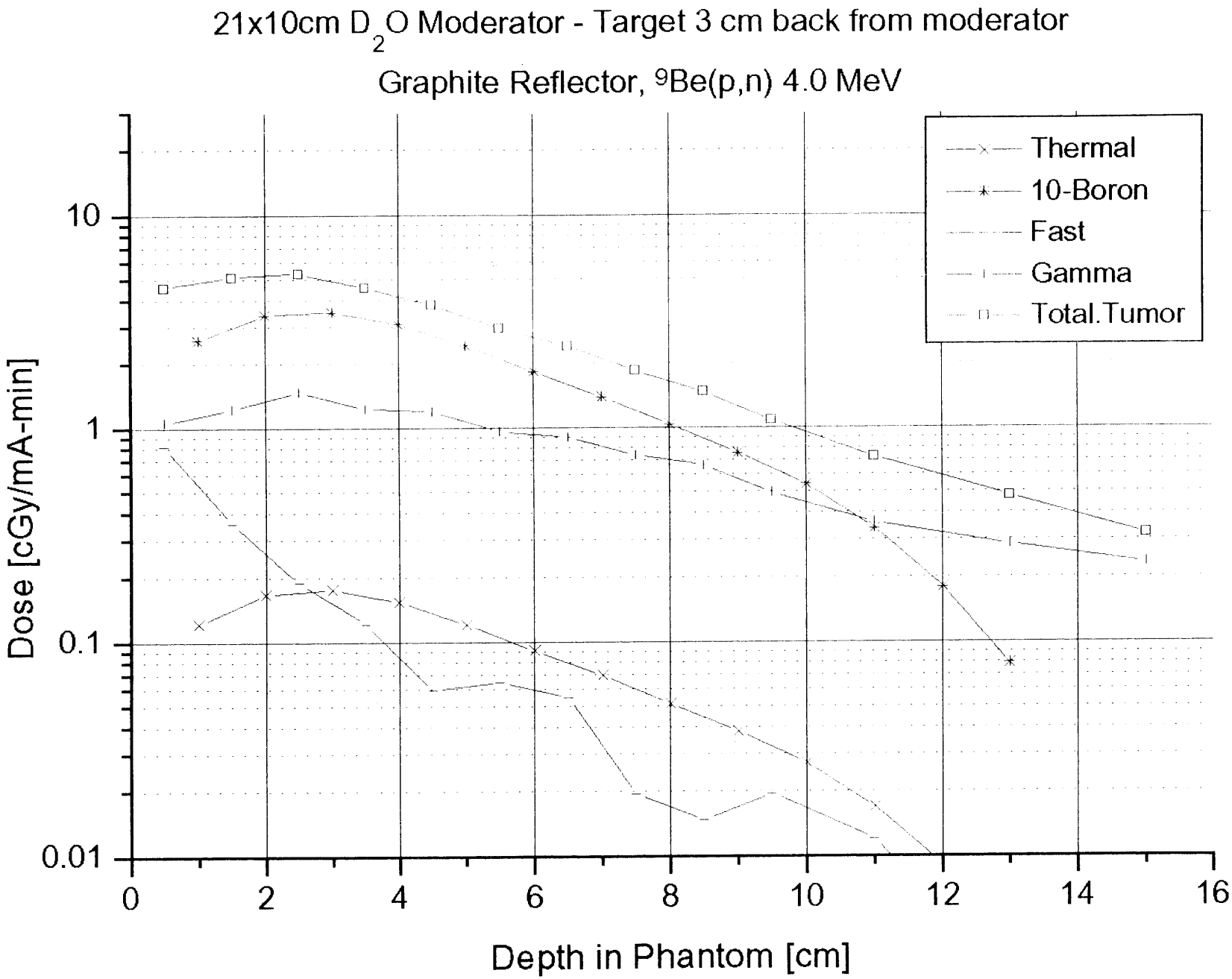
21x10cm D2O Moderator - Target 3 cm back from moderator
Graphite Reflector, 9Be(p,n) 4.0 MeV
Thermal
10-Boron
Fast
Gamma
Total.Tumor
Dose [cGy/mA-min]
10
1
0.1
0.01
0
2
4
6
8
10
12
14
16
Depth in Phantom [cm]

Table C-7: Therapy beam design configurations
for the reaction
9Be(p,n) E(p)=4.0 MeV
These simulations investigated
the effect of changing the reflector radius

The following dimesions were not varied:
A=3 cm, B=27 cm, C=10 cm, D=34 cm, F=0.03 cm, H=0.03 cm, I=0.03 cm

Simulation Designation	Moderator material	Reflector material	Reflector Radius [cm] (dimension E)
40-gr-d2o-27x10	D2O	Graphite	40
40-gr-d2o-27x10	D2O	Graphite	34
40-gr-d2o-27x10	D2O	Graphite	30
40-gr-d2o-27x10	D2O	Graphite	25
40-gr-d2o-27x10	D2O	Graphite	22
40-gr-d2o-27x10	D2O	Graphite	20
40-gr-d2o-27x10	D2O	Graphite	17
40-gr-d2o-27x10	D2O	Graphite	15

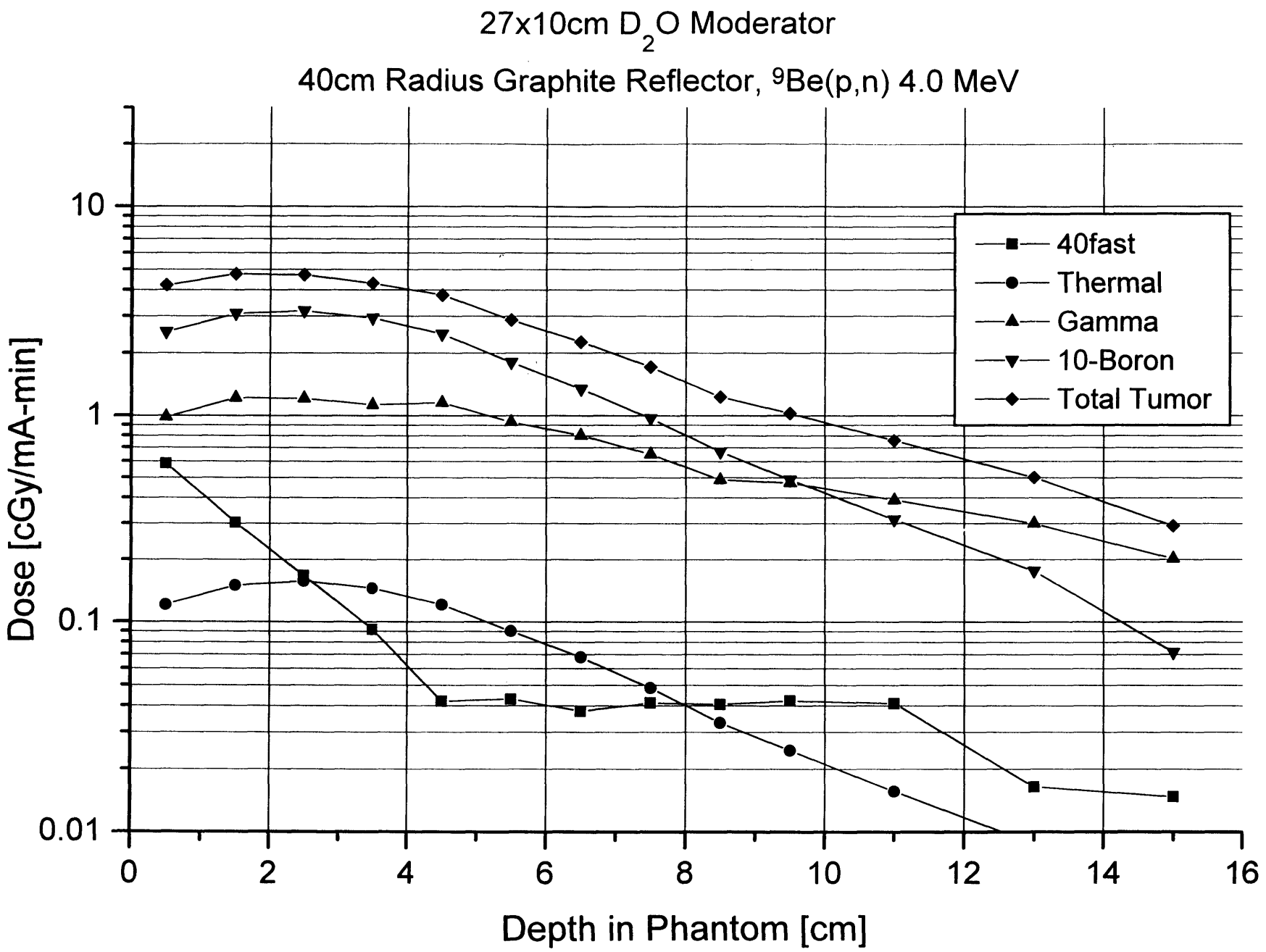
27x10cm D2O Moderator
40cm Radius Graphite Reflector, 9Be(p,n) 4.0 MeV
Dose [cGy/mA-min]
Depth in Phantom [cm]
10
1
0.1
0.01
0
2
4
6
8
10
12
14
16
40fast
Thermal
Gamma
10-Boron
Total Tumor

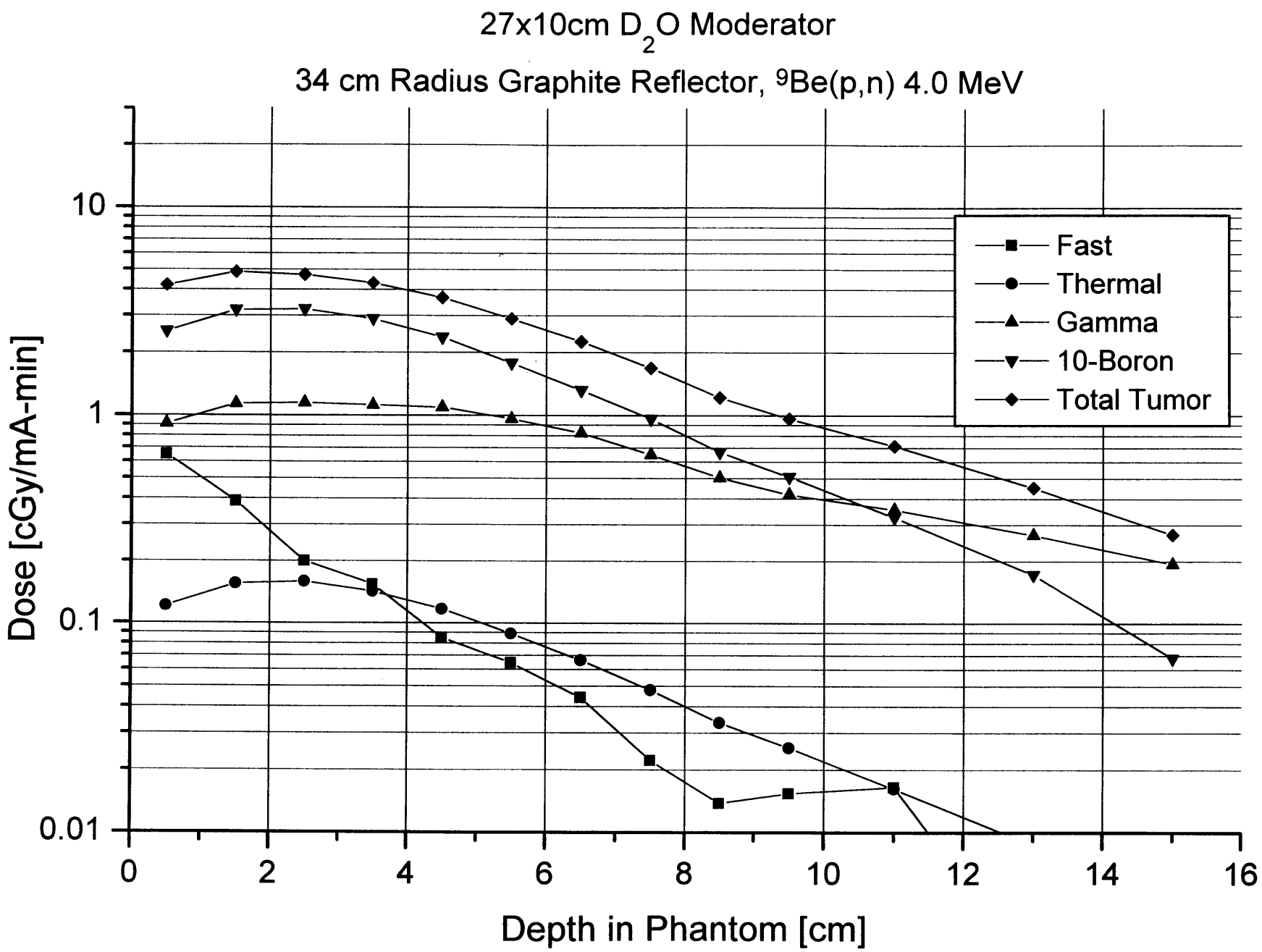
27x10cm D2O Moderator
34 cm Radius Graphite Reflector, 9Be(p,n) 4.0 MeV
Dose [cGy/mA-min]
10
1
0.1
0.01
0
2
4
6
8
10
12
14
16
Depth in Phantom [cm]
Fast
Thermal
Gamma
10-Boron
Total Tumor

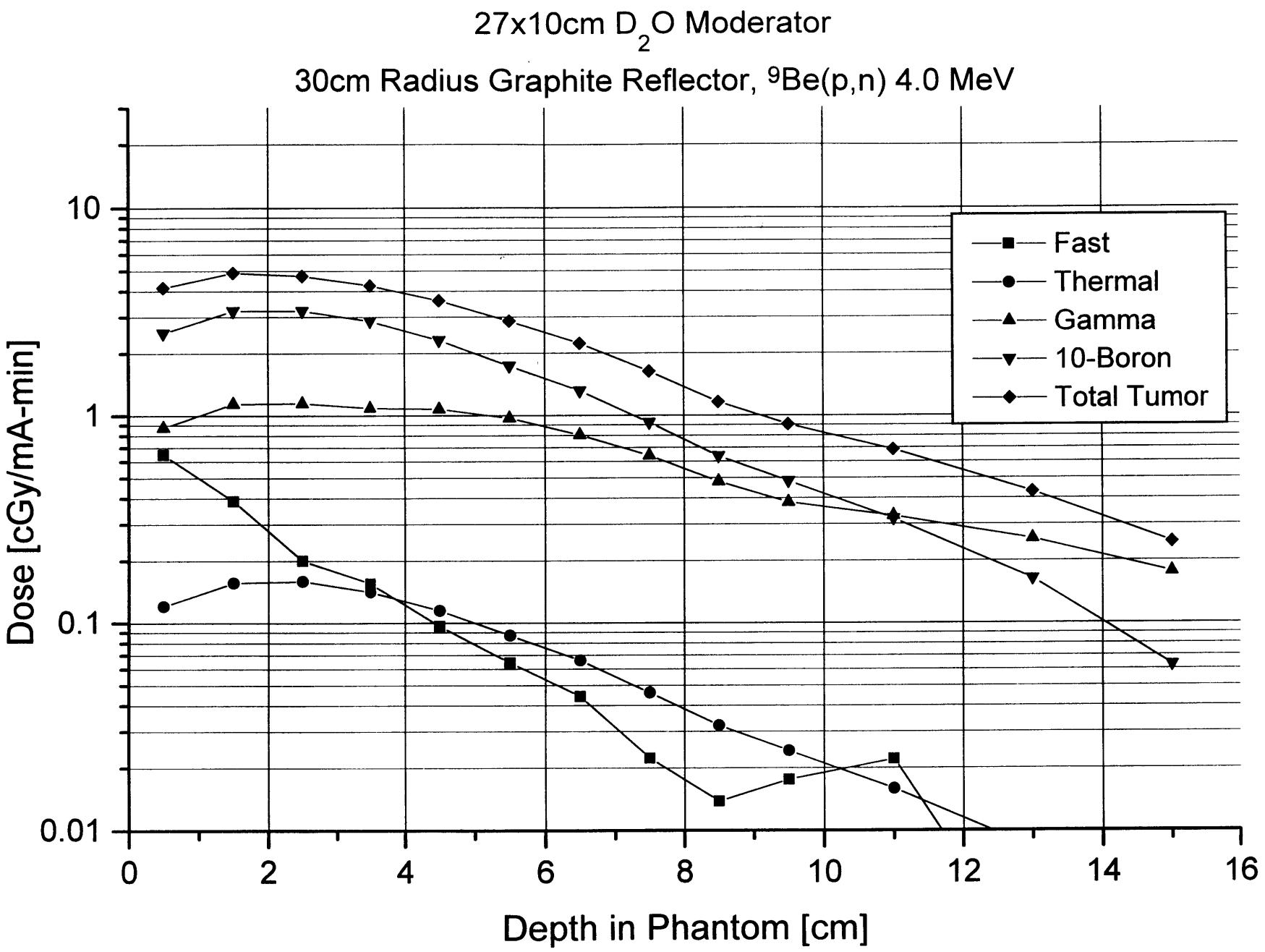
27x10cm D2O Moderator
30cm Radius Graphite Reflector, 9Be(p,n) 4.0 MeV
Dose [cGy/mA-min]
10
1
0.1
0.01
0
2
4
6
8
10
12
14
16
Depth in Phantom [cm]
Fast
Thermal
Gamma
10-Boron
Total Tumor

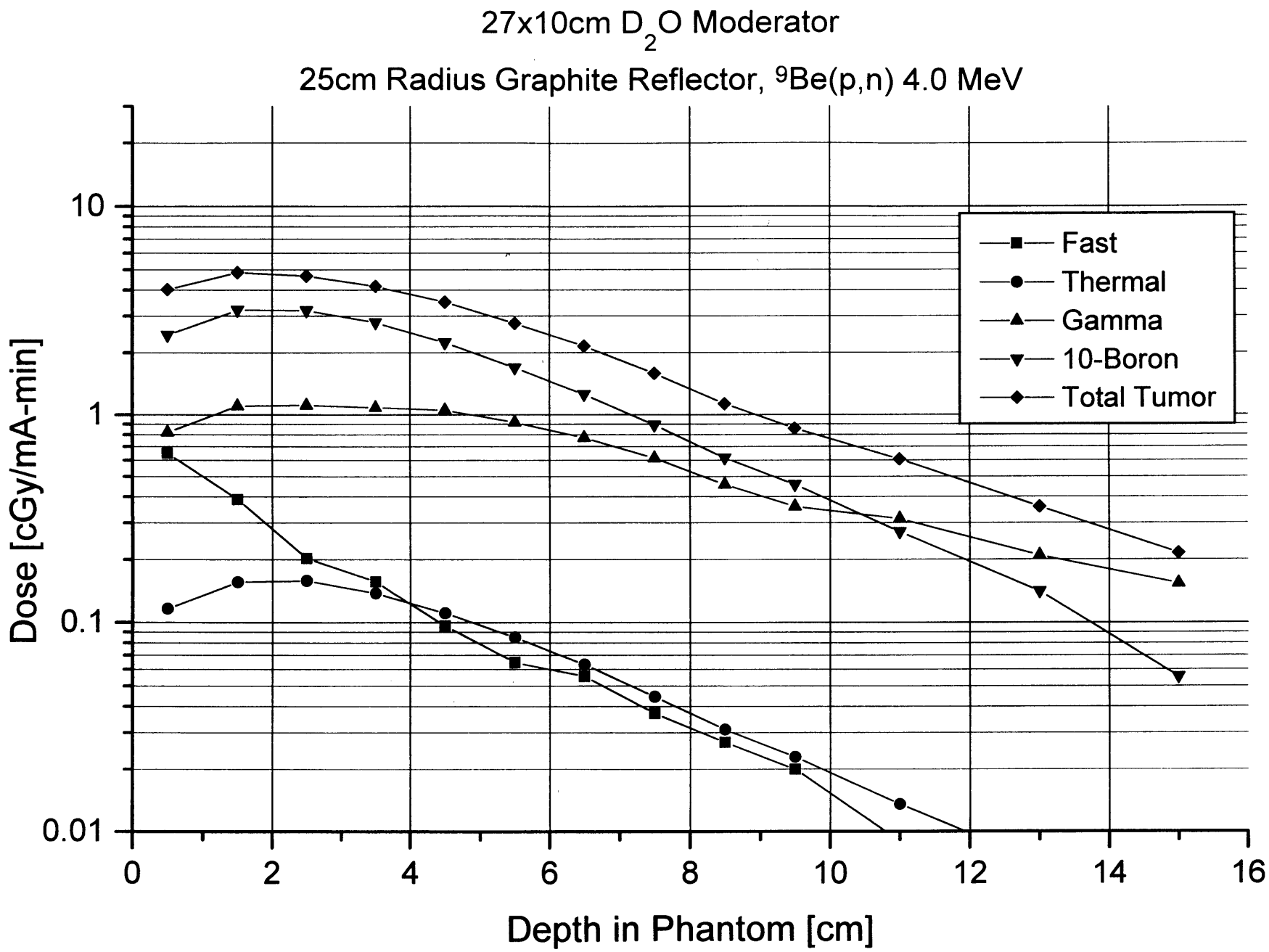
27x10cm D2O Moderator
25cm Radius Graphite Reflector, 9Be(p,n) 4.0 MeV
Dose [cGy/mA-min]
10
1
0.1
0.01
0
2
4
6
8
10
12
14
16
Depth in Phantom [cm]
Fast
Thermal
Gamma
10-Boron
Total Tumor

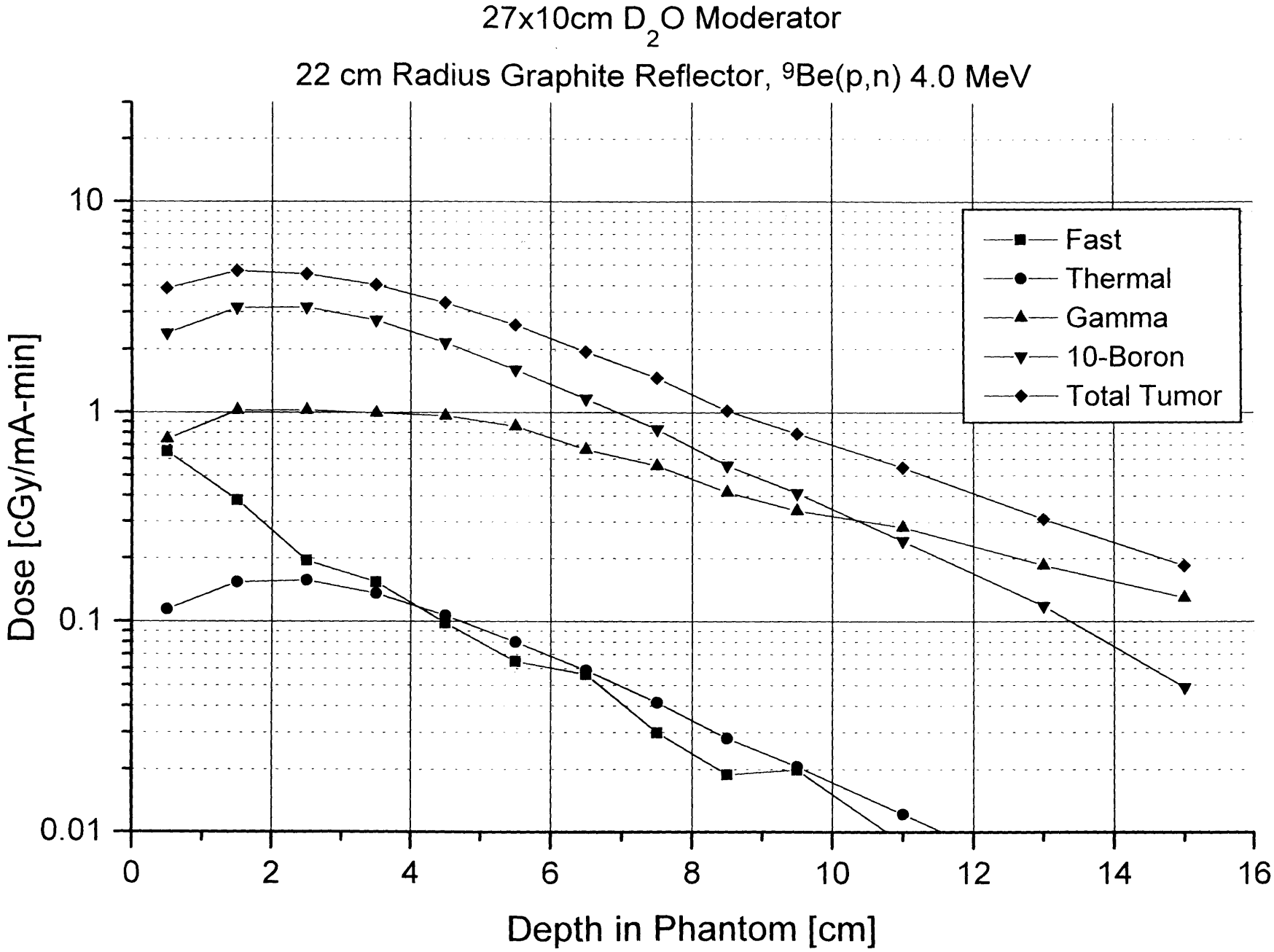
27x10cm D2O Moderator
22 cm Radius Graphite Reflector, 9Be(p,n) 4.0 MeV
Dose [cGy/mA-min]
Depth in Phantom [cm]
Fast
Thermal
Gamma
10-Boron
Total Tumor
10
1
0.1
0.01
0
2
4
6
8
10
12
14
16

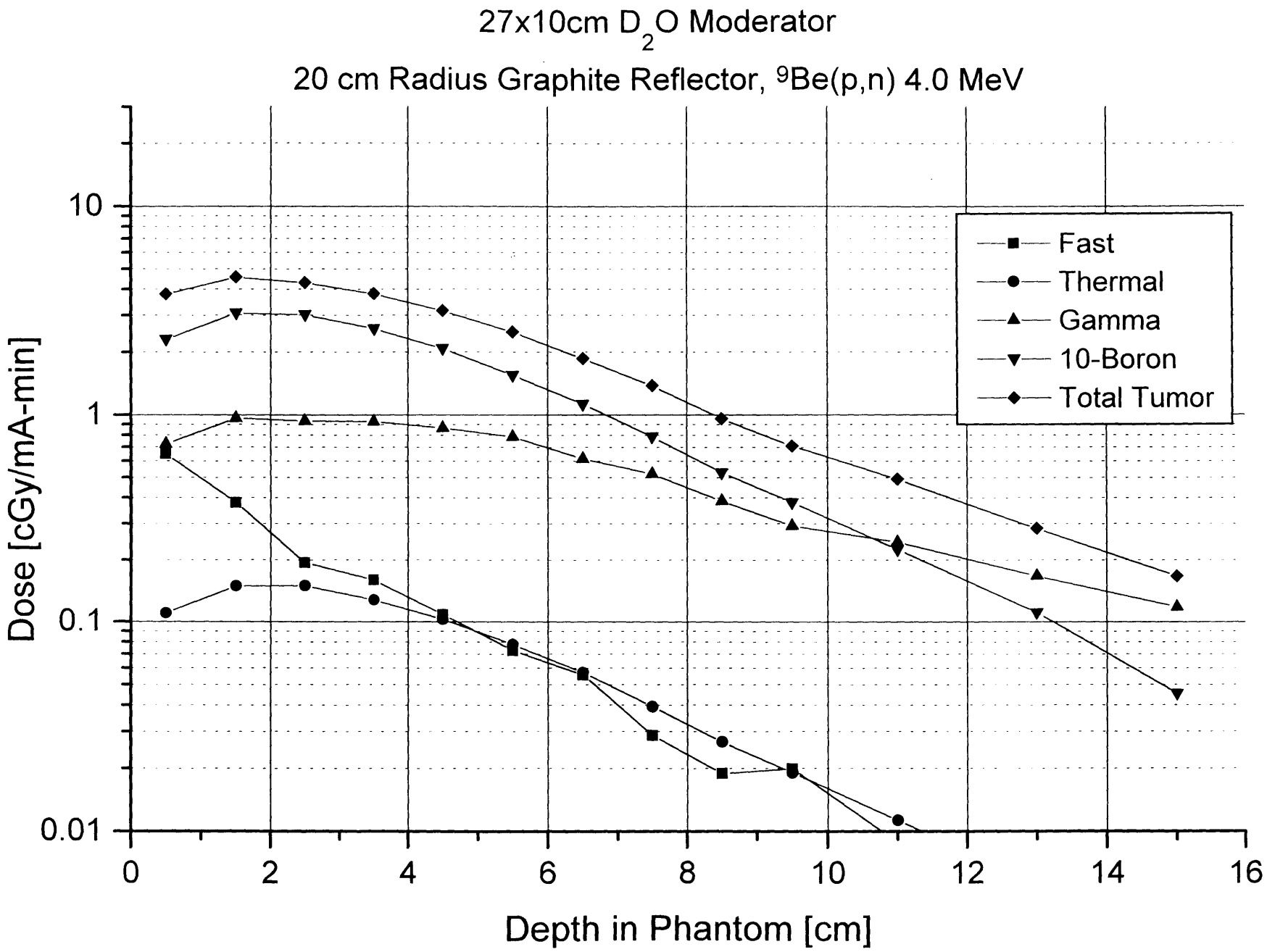
27x10cm D2O Moderator
20 cm Radius Graphite Reflector, 9Be(p,n) 4.0 MeV
Dose [cGy/mA-min]
Depth in Phantom [cm]
Fast
Thermal
Gamma
10-Boron
Total Tumor
10
1
0.1
0.01
0
2
4
6
8
10
12
14
16

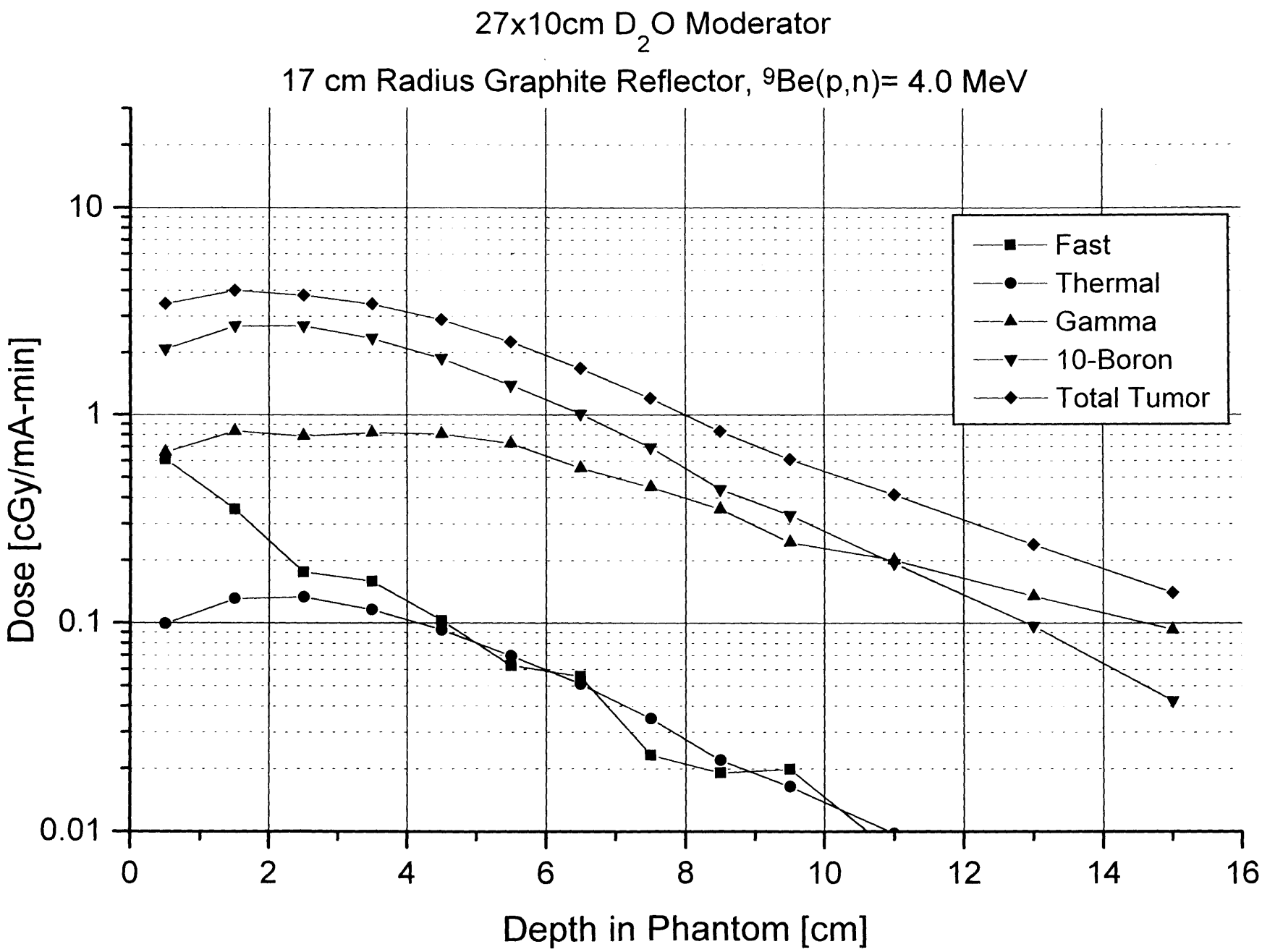
27x10cm D2O Moderator
17 cm Radius Graphite Reflector, 9Be(p,n)= 4.0 MeV
Dose [cGy/mA-min]
Depth in Phantom [cm]
Fast
Thermal
Gamma
10-Boron
Total Tumor
10
1
0.1
0.01
0
2
4
6
8
10
12
14
16

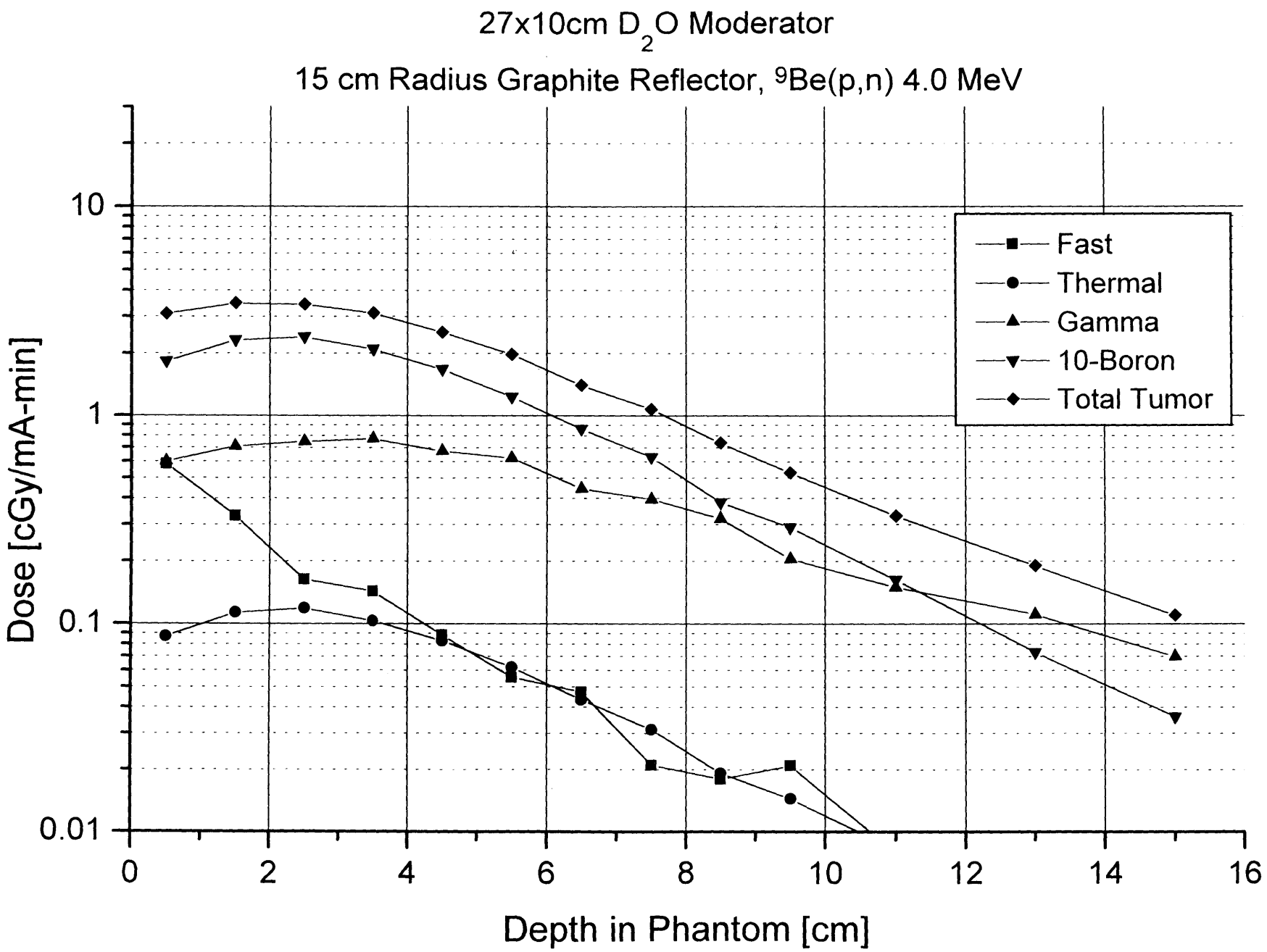
27x10cm D2O Moderator
15 cm Radius Graphite Reflector, 9Be(p,n) 4.0 MeV
Dose [cGy/mA-min]
Depth in Phantom [cm]
Fast
Thermal
Gamma
10-Boron
Total Tumor
10
1
0.1
0.01
0
2
4
6
8
10
12
14
16